Ultrafast Quadratic Nonlinear Dynamics and Soliton Formation in Parametric Amplifiers and Oscillators

Thesis by
Robert Matthew Gray

In Partial Fulfillment of the Requirements for the
Degree of
Doctor of Philosophy

Caltech

CALIFORNIA INSTITUTE OF TECHNOLOGY
Pasadena, California

2025
Defended May 28th, 2025

ACKNOWLEDGEMENTS

Completing my PhD has been a long journey filled with moments of joy, excitement, and discovery as well as moments of frustration, fatigue, and uncertainty. As with any such a journey, I would have been lost without direction and support from those around me who I have been blessed to call mentors, friends, and colleagues. I also appreciate that at times, their support has not been without incurring additional burden unto themselves, and I will be forever grateful for their willingness to extend their time, energy, and intellect to me.

To begin, I would like to thank my advisor, Professor Alireza Marandi. It was not until late in my undergraduate degree that I came to the realization that I was interested in pursuing a PhD (more on that below), so I think there were several ways in which I was admittedly not as well prepared as I could have been for the PhD experience. Beyond that, I came into the group with limited optics experience in a broad sense and little to no understanding of nonlinear optics. However, in my limited exposure, I had identified at least a few concepts of interest which happened to appear on the group website, such as "frequency combs" and "quantum," and I decided to apply. Lucky for me, Alireza saw something, whether in my application or in my nervous but enthusiastic responses in our interview, which persuaded him to take a chance on me.

I am so thankful he did. I remember leaving our first video interview feeling both excited and inspired, and I have continued to be regularly inspired by Alireza throughout my PhD. I think arguably that this ability to evoke such feelings of inspiration in a student is one of the most important qualities of any advisor, as it is this excitement which enables you to persist even in the face of great challenge (of which there are bound to be many in the course of a PhD), and it is something at which Alireza is extremely gifted. Beyond this, Alireza is thoughtful and has regularly demonstrated his care for me as an individual through being available for discussion in times of difficulty. He has furthermore made himself open to feedback on many an occasion regarding the group and his management style. He is a phenomenal scientist as well as a great speaker and presenter, and his ability to juggle many simultaneous duties and commitments while maintaining a level head has never ceased to amaze me. By his advice and example, he has helped me to grow in far more ways that just as an academic researcher, and I will be forever indebted to him for his investment in me.

I would also like to thank Professors Emami, Yang, and Vahala for serving on my thesis committee. I have additionally had the pleasure of engaging with them in different capacities through my time at Caltech. Professor Emami served as the Executive Officer of the Electrical Engineering (EE) department from 2018-2024, and in this capacity, she and I had several discussions during my time on the EE Local Student committee (LSC) regarding graduate student life in EE. I greatly appreciated her receptiveness to our feedback during those conversations, which was demonstrative of her continued commitment to the EE community and student experience. In my first year at Caltech, I took Professor Yang's Electromagnetic Engineering course, which helped to reinforce many important and relevant concepts in electromagnetism. Unfortunately, we were constrained to Zoom lectures at that time due to the COVID-19 pandemic, but Professor Yang's cheerful demeanor during lectures helped to brighten this otherwise dark period. Likewise, I had the opportunity to take Professor Vahala's Quantum Electronics course through my second year, also on Zoom. His careful presentation of many foundational concepts in laser physics, quantum optics, and nonlinear optics was extremely helpful in bridging the gaps in my understanding in these areas, many of which were of great relevance to my PhD work. Furthermore, I have enjoyed a burgeoning atmosphere of collaboration between Professor Vahala's group and our group, and I have appreciated the opportunity to exchange ideas and resources with his students in my time at Caltech, as well as his support in my postdoctoral search.

Next, I would like to thank all of the members of the Nonlinear Photonics Laboratory, led by Alireza. I have had innumerable great discussions and shared experiences with each and every member of the group throughout my PhD, for which I am extremely appreciative. I would like to begin by thanking the students in my year, starting with Ryoto Sekine. Ryoto and I first met when we shared a room at the Athenaeum during a visit in the year prior to joining, and it was not long after that we both had committed to joining the group. Deciding from that brief stint sharing a room that we would be compatible as flatmates, we chose to live together in our first year, and we have lived together for much of our time in Pasadena since. Ryoto is probably the most disciplined and hardworking person I know. Watching him consistently turn in to bed late at night and still beat me out the door in the morning has inspired and motivated me throughout the PhD. I am furthermore grateful to have collaborated with him on many of my projects in my time in the group, as I could always count on him to be meticulous and efficient, and I know that I (and the entire group) have benefited hugely from the tools that he developed through

his PhD work. Through our time together, Ryoto has become one of my closest friends, and I am appreciative of the meals, hikes, trips, soccer matches, and late night conversations we have shared. The other PhD student who joined in our year is Luis Ledezma. Luis embodies curiosity, and through his wealth of knowledge and willingness to help, he has been a consistent resource for me throughout my PhD. It always baffled me how he managed to juggle the workload of the PhD with his family responsibilities, and do so each day with a smile. I am so glad we had the opportunity to work together over these past years.

I would additionally like to extend my gratitude to the students in the year above me, Mingchen Liu, Arkadev Roy, and Christian Leefmans, who were the first cohort of students within the group. By the time that I joined, all three of them had already made tremendous progress in their respective projects and furthermore possessed a level of understanding which far exceeded what I think anyone could reasonably expect of a graduate student just beginning their second year, setting a very high standard for us newcomers to aspire to. I benefited tremendously from their mentorship and leadership. I would like to especially thank Mingchen and Arkadev, with whom I had more direct opportunities to collaborate. To say that Mingchen taught me everything I know about experimental optics would hardly be an overstatement. He dedicated countless hours to training me on all of the tools and procedures in the lab, from how to clean the optics to how to align an optical parametric oscillator. Many of those hours were over FaceTime as we navigated the challenges of research while adhering to the social distancing policies put forth in response to the COVID-19 pandemic. Mingchen is extremely thorough in his work, generous of his time, and kind-hearted; I am forever thankful to have had such a great first mentor, collaborator, and friend within the group. Likewise, Arkadev was instrumental in helping me to get acquainted with the theoretical side of the research. He very willingly shared his simulation code with me when I first joined, and he patiently assisted whenever I came to him with questions regarding numerical simulations or theoretical derivations. The simultaneous breadth and depth of scientific understanding that Arkadev has is admirable, and as such, he demonstrated within our group a knack for creatively tying together concepts from various sub-disciplines of optics and physics more broadly in his work, which always served to inspire me.

Many other graduate students have joined the group in the years since I joined, almost all of whom I have had the pleasure of working with. I feel lucky to have

been a part of such a thoughtful, intelligent, and curious team of researchers, and the support and insights I gained from my peers were instrumental to the work presented in this thesis. I would like to especially thank Thomas Zacharias, who joined the group at the start of my fourth year and very quickly became a close friend and collaborator on developing many of the ultrafast measurement capabilities in the group. Thomas's inquisitive and skeptical nature has forced me on several occasions to rethink my perspective and understanding of many core concepts related to the research, and I have both learned a lot and reinforced previous understanding through our discussions. He also is very goofy and cheerful, and has generally become an uplifting presence in the lab. I would additionally like to thank Selina Zhou, who first joined the group as an undergraduate during my second year and worked with me at that time on the optical parametric oscillator-based sensing projects. I was still learning a lot then, and Selina fearlessly joined me in venturing into the void, developing a small gas cell infrastructure for loading and measuring various gas samples in the cavity. Since then, Selina has continued grow tremendously in her knowledge and skill set as well as her confidence in working with the tools in the lab. We have had many insightful discussions on a variety of topics related to both research and life in our shared office space, and I am very grateful for Selina's collaboration and friendship.

Another graduate student who I had the opportunity to work with closely is Max Shen. He came to the group during my fifth year, and he has quickly developed many capabilities in chip design and fabrication, measurement, and simulation. He engages in research with a quiet determination and is fast to pick up on concepts and ideas. I am glad to have had the opportunity to work with Max through many late nights of pulse compression measurements. Furthermore, I owe a thank you to Justin Widjaja who, since joining the group at the start of my final year, has been a tremendous help in the numerical simulations related to the multi-octave supercontinuum generation project. He has come to the group with a lot of expertise in the world of Kerr solitons and is generally well-versed in optical physics. I have been very impressed with his thoughtfulness and appreciative of his contributions to this final project that I have worked on in my time in the group. Beyond these contributions, I am grateful to have had the opportunity to work with James Williams (my fellow Northwestern alumni) and Elina Sendonaris, with whom I shared many great discussions about quantum optics and enjoyed many shared lunches, Gordon Li, who could seemingly build a computer out of anything and who taught me a lot about computing in the process of working together, Ben Gutierrez and Rithvik

Ramesh, with whom I have enjoyed many conversations around laser physics and life more broadly, and Arda Deger, Yiting Wang, and Yingchu Xu, the newest members of the group, who have all demonstrated a great curiosity and additionally impressed me with their preparedness for tackling the challenges of the PhD.

My time in the group has also been enriched through the presence of wonderful postdoctoral scholars. Firstly, I must thank Nicolas Englebert, with whom I have shared a wonderful collaboration in my last few years in the group. He has taught me a lot, both in terms of technical knowledge around soliton theory and related numerical techniques as well as information for my life and career, particularly in regards to postdoctoral applications and funding opportunities. I also enjoyed many hours in the lab and office discussing with Raj Nehra, who enriched my understanding around quantum optics. Likewise, I learned a lot from both Midya Parto about computing and topological photonics, and I always appreciated his jovial demeanor. Luis Costa also taught me a lot about fiber optics, and has been a great gym buddy on many occasions. I additionally shared several meals and research discussions with Qiushi Guo, who was always up to date on the latest news in the photonics community. Each of them exhibited persistence and tenacity in their work, and together they set a wonderful example for me in terms of how to design and execute on a research project. Finally, I would like to thank Saman Jahani, Myoung-Gyun Suh, and Joong Hwan Bahng. Although I did not have the opportunity to work as much with them as the other postdoctoral researchers in the group, they made me feel extremely welcome in the group, and I have enjoyed their continued support and willingness to connect at conferences ever since.

Many outstanding undergraduates have also come through the group (in addition to Selina), including Rahul Chawlani, Shivam Mundhra, Jennifer Solgaard, Parthorn Ammawat, Adelynn Tang, and Louise Schul, among others. I have greatly appreciated their friendliness and curiousity. I would particularly like to thank Rahul, who worked closely with me on developing several tools related to ultrafast measurment in the group. I also enjoyed working with Shivam on numerical simulations. He asked great questions and was quick to pick things up. I know all of them will go on to achieve great things in their research.

Next, I would like to thank the group administrators, as well as the EE administrators, without whom we could not do our research. I am in particular thankful for Caroline Murphy and Liliana Chavarria, who have been incredibly wonderful administrators for the group. I am grateful for their support in purchasing, organizing group events

we have begun an exciting collaboration at the intersection of machine learning and nonlinear optical simulation and design, and I am excited to see what is achieved through the future of this project. Lastly, I have had the opportunity to work on two review papers during my last two years of my PhD. The first has been led by Prof. Dmitry Skryabin in collaboration with Prof. Hong Tang and Prof. Markku Vainio, and I have enjoyed learning from their perspectives regarding the history of quadratic soliton development as well as the future prospects for this line of research. The second has been in collaboration with Prof. Kartik Srinivasan and his group members, Jordan Stone and Xiyuan Lu. It has been wonderful sharing ideas back-and-forth with them regarding the similarities and differences of quadratic and cubic optical parametric oscillators.

I have also benefited through my PhD from many co-curricular activities and communities within Caltech. Firstly, I would like to thank Caltech Performing Arts, particularly Glenn Price and the members of the Caltech Orchestra as well as Hyesung Choe. I greatly enjoyed every performance I had in the orchestra with Glenn at the helm, and I similarly had fun in chamber music with Hyesung. I am also am grateful to everyone who I had the opportunity to play soccer with, particularly the members of RLC United, the Monrovia Bengals, and the Caltech Soccer Club. Furthermore, I fulfilled a longstanding dream of mine during the PhD by fronting a rock band, and I am thankful for Ryan Cosner, Berthy Feng, Piero Chiappina, Hirsh Kamakari, Mason McGill, and Nikhil Ranganathan, who all were members of our band, Measure Zero, during its chaotic existence through our time at Caltech. Beyond these outlets, I benefited greatly from my participation in the History, Ethics, and Identity Seminar Series, and I am especially appreciative of Jacque Tawney and Emily Palmer, who started this program, and Sean Mendoza and Federico Rios Tascon who I enjoyed working with in planning the series after inheriting it from Jacque and Emily. Likewise, it was a pleasure to serve on the EE LSC, and I want to express my gratitude to Pranav Kulkarni, Dominic Yurk, Richard Smith, Simon Mahler, James Williams, Thomas Zacharias, Rithvik Ramesh, Steven Bulfer, Volkan Gurses, Sergey Posnov, and all others who attended and helped with the organization of EE LSC events.

Beyond these endeavors, I have been lucky to have the support of many great friends at Caltech and beyond. They have celebrated with me in all my moments of success throughout the PhD and lifted me up during the most challenging times. I would like to extend a thank you in particular to Komron Shayegan, who has been a great friend

to me throughout my time at Caltech, for one year of which we were flatmates. We co-founded RLC United together and have enjoyed many moments together, both on and off the soccer pitch. He is a brilliant mind and a wonderful friend.

Next, I would like to thank my family. My parents, in particular, have supported me through my entire life. Without the values they instilled in me as well as their love and encouragement, I would be nowhere near the person I am today. Similarly, I would like to thank my brother, Chris, his wife, Jacey, and my nieces, who bring great joy into my life and always lend an interested ear when we have the opportunity to talk. I also adopted a cat, Appa, during my PhD, and I have appreciated many cuddles from her since she came into my life.

Lastly, but certainly not least, I owe a great thank you to my wonderful partner, Liz Frissell. Liz has been a constant source of love and support through many moments of confusion and frustration, late nights in the lab, and all of the other ups and downs of the PhD. We have also shared many moments of great joy together as we have adventured around Los Angeles and abroad. She constantly goes above and beyond as a partner, and I am incredibly grateful to her for all she does for me. I am also appreciative of the wonderful people she has brought into my life who have become an additional network of friendship and support.

To conclude, I would like to extend my thanks to everyone else who has been a part of my life and educational journey to this point. I have been blessed to have been touched by far more wonderful people than can possibly be listed in this acknowledgments section, and I am appreciative of all of the ways in which each of them has helped to shaped me in my life and work.

ABSTRACT

In the more than 60 years since the invention of the laser, complementary developments in nonlinear and ultrafast optics have revolutionized fundamental science and technology, enabling the measurement of atomic and electronic motion at their native timescales, optical timekeeping with unprecedented precision, information processing offering speeds beyond those attainable in electronics, and novel spectroscopy and sensing techniques capable of parallel detection of several analytes with fast acquisition times and high sensitivity. On the one hand, pulsed sources are particularly well-suited for driving nonlinear phenomena, as the strength of nonlinear interaction depends on the peak power of the optical input. Conversely, spectral broadening, pulse shaping, and temporal sampling mechanisms enabled by nonlinearity have been critical in developing ultrafast sources and systems.

In this thesis, we further explore this synergistic relationship between nonlinear and ultrafast optics. We specifically study nonlinear dynamical phenomena such as soliton formation and supercontinuum generation in parametric amplifiers and oscillators exhibiting a quadratic $\left(\chi^{(2)}\right)$ nonlinearity, and we show how these processes can be leveraged for the efficient generation of ultrashort pulses and coherent broadband spectra, with direct application in sensing and information processing. We begin by exploring the formation of mid-infrared temporal simultons in a free-space optical parametric oscillator, and we exploit their formation dynamics for enhanced molecular sensing. Next, we turn to the thin-film lithium niobate platform and demonstrate pJ pulse energy, two-color soliton pulse compression to the two-cycle regime in a dispersion-engineered waveguide. We additionally show that the strong nonlinearity in such waveguides enables the on-chip characterization of ultrashort, ultra-weak pulses. Next, we demonstrate a coherent, multi-octave frequency comb from a far-above-threshold nanophotonic parametric oscillator and investigate the dynamics underpinning its formation. Finally, we show simultaneous oscillation of 70 independent time-multiplexed parametric oscillators in a dispersion-engineered nanophotonic cavity. Our results pave the way to a new generation of scalable and efficient ultrafast sources, sensors, and information processing systems powered by quadratic nonlinearity.

PUBLISHED CONTENT AND CONTRIBUTIONS

First-author articles are listed first, in descending order by year, followed by other authorship contributions.

* indicates co-first authorship.

[1] **Robert M. Gray**, Ryoto Sekine, Maximilian Shen, Thomas Zacharias, James Williams, Selina Zhou, Rahul Chawlani, Luis Ledezma, Nicolas Englebert, and Alireza Marandi. "Two-optical-cycle pulses from nanophotonic two-color soliton compression." In: *arXiv preprint arXiv:2501.15381* (2025). DOI: 10.48550/arXiv.2501.15381.
R.M.G. participated in the conception and design of the project, performed the experiments, performed the data analysis, performed theoretical analysis and simulations, and participated in the writing of the manuscript.

[2] Thomas Zacharias*, **Robert Gray***, Ryoto Sekine, James Williams, Selina Zhou, and Alireza Marandi. "Energy-efficient ultrashort-pulse characterization using nanophotonic parametric amplification." In: *ACS Photonics* 12.3 (2025), pp. 1316–1320. DOI: 10.1021/acsphotonics.4c02620.
R.G. participated in the experiments and data analysis.

[3] **Robert M. Gray***, Ryoto Sekine*, Luis Ledezma, Gordon H. Y. Li, Selina Zhou, Arkadev Roy, Midya Parto, and Alireza Marandi. "Large-scale time-multiplexed nanophotonic parametric oscillators." In: *Newton* (2025). DOI: 10.1016/j.newton.2025.100108.
R.M.G. participated in the conception and design of the project, participated in the experiments, performed the data analysis, performed theoretical analysis, and participated in the writing of the manuscript.

[4] **Robert M. Gray**, Mingchen Liu, Selina Zhou, Arkadev Roy, Luis Ledezma, and Alireza Marandi. "Quadratic-soliton-enhanced mid-IR molecular sensing." In: *Nature Communications* 15.1 (2024), p. 9086. DOI: 10.1038/s41467-024-53447-3.
R.M.G. participated in the conception and design of the project, participated in the experiments, performed the data analysis, performed theoretical analysis, performed numerical simulations, and participated in the writing of the manuscript.

[5] Ryoto Sekine*, **Robert M. Gray***, Luis Ledezma, Selina Zhou, Qiushi Guo, and Alireza Marandi. "Multi-octave frequency comb from an ultra-low-threshold nanophotonic parametric oscillator." In: *arXiv preprint arXiv:2309.04545* (2023). DOI: 10.48550/arXiv.2309.04545.
R.M.G. participated in the experiments, performed numerical simulations, and participated in the writing of the manuscript.

[6] Mingchen Liu[*], **Robert M. Gray**[*], Arkadev Roy, Kirk A. Ingold, Evgeni Sorokin, Irina Sorokina, Peter G. Schunemann, and Alireza Marandi. "High-power mid-IR few-cycle frequency comb from quadratic solitons in an optical parametric oscillator." In: *Laser & Photonics Reviews* 16.11 (2022), p. 2200453. DOI: 10.1002/lpor.202200453.
R.M.G. participated in the experiments and data analysis and performed numerical simulations.

[7] Gordon H. Y. Li[*], Ryoto Sekine[*], Rajveer Nehra[*], **Robert M. Gray**[*], Luis Ledezma, Qiushi Guo, and Alireza Marandi. "All-optical ultrafast ReLU function for energy-efficient nanophotonic deep learning." In: *Nanophotonics* 12.5 (2023), pp. 847–855. DOI: 10.1515/nanoph-2022-0137.
R.M.G. participated in the experiments.

[8] Midya Parto[*], Christian Leefmans[*], James Williams, **Robert M. Gray**, and Alireza Marandi. "Enhanced sensitivity via non-Hermitian topology." In: *Light: Science & Applications* 14.1 (2025), p. 6. DOI: 10.1038/s41377-024-01667-z.
R.M.G. participated in the theoretical analysis.

[9] Midya Parto[*], Gordon H. Y. Li[*], Ryoto Sekine, **Robert M. Gray**, Luis L. Ledezma, James Williams, Arkadev Roy, and Alireza Marandi. "Ultrafast neuromorphic computing with nanophotonic optical parametric oscillators." In: *arXiv preprint arXiv:2501.16604* (2025). DOI: 10.48550/arXiv.2501.16604.
R.M.G. participated in the experiments.

[10] James Williams[*], Elina Sendonaris[*], Rajveer Nehra, **Robert M. Gray**, Ryoto Sekine, Luis Ledezma, and Alireza Marandi. "Ultrafast all-optical measurement of squeezed vacuum in a lithium niobate nanophotonic circuit." In: *arXiv preprint arXiv:2502.00518* (2025). DOI: 10.48550/arXiv.2502.00518.
R.M.G. participated in the experiments.

[11] Anni Li, Mehran Bahri, **Robert M. Gray**, Seowon Choi, Sajjad Hoseinkhani, Anchit Srivastava, Alireza Marandi, and Hanieh Fattahi. "0.7 MW Yb: YAG pumped degenerate optical parametric oscillator at 2.06 μm." In: *APL Photonics* 9.10 (2024). DOI: 10.1063/5.0230388.
R.M.G. assisted with the experiments.

[12] Mingchen Liu, **Robert M. Gray**, Arkadev Roy, Luis Ledezma, and Alireza Marandi. "Optical-parametric-amplification-enhanced background-free spectroscopy." In: *Optics Letters* 49.11 (2024), pp. 2914–2917. DOI: 10.1364/OL.520848.
R.M.G. assisted with numerical simulations.

[13] Elina Sendonaris[*], James Williams[*], Rajveer Nehra, **Robert Gray**, Ryoto Sekine, Luis Ledezma, and Alireza Marandi. "Ultrafast single-photon detection using nanophotonic parametric amplifiers." In: *arXiv preprint*

arXiv:2410.18397 (2024). DOI: `10.48550/arXiv.2410.18397`.
R.M.G. participated in the experiments.

[14] Shivam Mundhra, Elina Sendonaris, **Robert M. Gray**, James Williams, and Alireza Marandi. "Optimizing for a near single-mode type-0 optical parametric amplifier in nanophotonics." In: *arXiv preprint arXiv:2412.07004* (2024). DOI: `10.48550/arXiv.2412.07004`.
R.M.G. assisted with numerical simulations.

[15] James Williams, Rajveer Nehra, Elina Sendonaris, Luis Ledezma, **Robert M. Gray**, Ryoto Sekine, and Alireza Marandi. "Ultrashort pulse biphoton source in lithium niobate nanophotonics at 2 μm." In: *Nanophotonics* 13.18 (2024), pp. 3535–3544. DOI: `10.1515/nanoph-2024-0054`.
R.M.G. participated in the experiments.

[16] Qiushi Guo, Benjamin K. Gutierrez, Ryoto Sekine, **Robert M. Gray**, James A. Williams, Luis Ledezma, Luis Costa, Arkadev Roy, Selina Zhou, Mingchen Liu, et al. "Ultrafast mode-locked laser in nanophotonic lithium niobate." In: *Science* 382.6671 (2023), pp. 708–713. DOI: `10.1126/science.adj5438`.
R.M.G. participated in the experiments, performed theoretical analysis, and performed numerical simulations.

[17] Arkadev Roy[*], Luis Ledezma[*], Luis Costa, **Robert Gray**, Ryoto Sekine, Qiushi Guo, Mingchen Liu, Ryan M. Briggs, and Alireza Marandi. "Visible-to-mid-IR tunable frequency comb in nanophotonics." In: *Nature Communications* 14.1 (2023), p. 6549. DOI: `10.1038/s41467-023-42289-0`.
R.M.G. participated in the experiments and performed numerical simulations.

[18] Luis Ledezma, Arkadev Roy, Luis Costa, Ryoto Sekine, **Robert Gray**, Qiushi Guo, Rajveer Nehra, Ryan M. Briggs, and Alireza Marandi. "Octave-spanning tunable infrared parametric oscillators in nanophotonics." In: *Science Advances* 9.30 (2023), eadf9711. DOI: `10.1126/sciadv.adf9711`.
R.M.G. participated in the experiments.

[19] Mingchen Liu, **Robert M. Gray**, Luis Costa, Charles R. Markus, Arkadev Roy, and Alireza Marandi. "Mid-infrared cross-comb spectroscopy." In: *Nature Communications* 14.1 (2023), p. 1044. DOI: `10.1038/s41467-023-36811-7`.
R.M.G. participated in the experiments and data analysis and assisted with numerical simulations.

[20] Christian R. Leefmans[*], Nicolas Englebert[*], James Williams, **Robert M. Gray**, Nathan Goldman, Simon-Pierre Gorza, François Leo, and Alireza Marandi. "Cavity soliton-induced topological edge states." In: *arXiv preprint arXiv:2311.04873* (2023). DOI:

`10.48550/arXiv.2311.04873`.
R.M.G. participated in the experiments.

[21] Rajveer Nehra[*], Ryoto Sekine[*], Luis Ledezma, Qiushi Guo, **Robert M. Gray**, Arkadev Roy, and Alireza Marandi. "Few-cycle vacuum squeezing in nanophotonics." In: *Science* 377.6612 (2022), pp. 1333–1337. DOI: `10.1126/science.abo6213`.
R.M.G. participated in the experiments.

[22] Qiushi Guo[*], Ryoto Sekine[*], Luis Ledezma[*], Rajveer Nehra, Devin J. Dean, Arkadev Roy, **Robert M. Gray**, Saman Jahani, and Alireza Marandi. "Femtojoule femtosecond all-optical switching in lithium niobate nanophotonics." In: *Nature Photonics* 16.9 (2022), pp. 625–631. DOI: `10.1038/s41566-022-01071-2`.
R.M.G. participated in the experiments.

TABLE OF CONTENTS

LIST OF ILLUSTRATIONS

LIST OF TABLES

NOMENCLATURE

$f_{\mathbf{CEO}}$. Carrier-Envelope Offset Frequency.

f_{rep}. Repetition Rate.

$T_{\mathbf{rep}}$. Repetition Period.

ASE. Amplified Spontaneous Emission.

BBO. β-barium borate.

BOA. Booster Optical Amplifier.

CEO. Carrier-Envelope Offset.

CEP. Carrier-Envelope Phase.

CPA. Chirped Pulse Amplification.

CW. Continuous-Wave.

DFG. Difference-Frequency Generation.

DRO. Doubly Resonant Oscillator.

EO. Electro-Optic.

FPGA. Field-Programmable Gate Array.

FROG. Frequency-Resolved Optical Gating.

FWHM. Full-Width at Half-Maximum.

GaP. Gallium Phosphide.

GVD. Group Velocity Dispersion.

GVM. Group Velocity Mismatch.

HSQ. Hydrogen Silsesquioxane.

ICLAS. Intracavity Laser Absorption Sensing or Intracavity Laser Absorption Spectroscopy.

IM. Intensity Modulator.

IM. Phase Modulator.

IR. Infrared.

LAS. Linear Absorption Sensing.

LN. Lithium Niobate.

LO. Local Oscillator.

LPF. Long-Pass Filter or Low-Pass Filter.

MIR. Mid-Infrared.

MLL. Mode-Locked Laser.

MZI. Mach-Zehnder Interferometer.

NA. Numerical Aperture.

NEA. Noise-Equivalent Absorption.

NEP. Noise-Equivalent Power.

Nonlinear Optics. Field of study concerning phenomena in which the interaction of an intense optical field with a material modifies the optical response of that material.

OP. Orientation Patterning or Orientation-Patterned.

OPA. Optical Parametric Amplification.

OPG. Optical Parametric Generation.

OPO. Optical Parametric Oscillator or Optical Parametric Oscillation.

OSA. Optical Spectrum Analyzer.

PD. Photodetector.

PDF. Probability Density Function.

PMF. Probability Mass Function.

PP. Periodic Poling or Periodically Poled.

PZT. Lead Zirconate Titanate.

QCL. Quantum Cascade Laser.

QPM. Quasi-Phase Matching.

RF. Radio Frequency.

SCG. Supercontinuum Generation.

SFG. Sum-Frequency Generation.

SHG. Second-Harmonic Generation.

SM. Single-Mode.

SNR. Signal-to-Noise Ratio.

Soliton. Traveling wave which retains its shape during propagation, typically due to a balance of dispersion/diffraction and nonlinearity.

SPDC. Spontaneous Parametric Down-Conversion.

Supercontinuum. Extremely broad-bandwidth spectrum, typically spanning ~1 octave or greater.

TDM. Time-Domain Multiplexing or Time-Domain Multiplexed.

TE. Transverse Electric.

TFLN. Thin-Film Lithium Niobate.

TM. Transverse Magnetic.

YDFA. Ytterbium-Doped Fiber Amplifier.

Chapter 1

INTRODUCTION

1.1 The Need for Nonlinearity

Nonlinear optics concerns itself with a wide range of phenomena in which the interaction of an intense optical field with a material modifies the optical response of that material [1]. As will be discussed in more explicit mathematical detail in Chapter 2, the term "nonlinear" refers to the material's polarization density which is expanded in polynomial orders of the interacting electric field. The most studied nonlinear optical interactions are those involving the square or the cube of the electric field, which are referred to as quadratic and cubic nonlinear optics, respectively, as these are responsible for the strongest effects. In particular, quadratic nonlinear interactions are typically dominant in materials for which they occur, though they are limited to non-centrosymmetric materials, while cubic nonlinear effects may occur in any material for a sufficiently intense field.

One widely exploited consequence of nonlinear optics is that of frequency mixing, in which photons at one frequency may be converted via the nonlinear process to a different frequency. In the context considered here, these processes are parametric meaning that the quantum state of the material is left unaltered through the interaction. Thus, they are energy conserving in terms of the annihilated and created photons. Quadratic nonlinearity, which will be the focus of this thesis, governs three-wave mixing processes, in which photons may be exchanged between three disparate frequency bands. These include effects such as optical parametric generation (OPG), optical parametric amplification (OPA), difference-frequency generation (DFG), sum-frequency generation (SFG), and second-harmonic generation (SHG), to name a few. Meanwhile, cubic nonlinearity govern four-wave mixing processes.

As many of the most high-performing and inexpensive laser systems are in the visible and near-infrared spectral regions, this ability to convert input light between frequency bands has benefited many important applications. For example, down-conversion processes such as DFG [2–4] and optical parametric oscillation (OPO) [5–15], consisting of OPA in a resonator, may be used to efficiently generate mid- and far-infrared light. Such mid-infrared sources may be used for molecular

sensing and spectroscopy [16–22], with applications in areas such as greenhouse gas monitoring, industrial process control, and non-invasive medical diagnostics, as well as in free-space optical communications systems [23]. Meanwhile, up-conversion processes including SFG and SHG can be used for the generation of visible and ultraviolet light [24–26], benefiting applications such as atomic clocks [27, 28], astronomical spectrograph calibration [29], high-resolution imaging [30, 31], and biochemical sensing and spectroscopy [32, 33].

In addition to enabling frequency mixing, nonlinear interactions have several features of practical consequence. To begin, we note the important role that nonlinearity plays in computing and information processing systems. Modern electronic computing systems are enabled by the switching operation of the transistor, which relies on its having an extremely nonlinear response to input electronic signals [34]. Likewise, we may observe at a higher level that nonlinear activation functions represent a key building block in machine learning and artificial intelligence systems [35]. In a similar way, nonlinearity is an essential component in any optical information processing system [36–39]. Given the THz bandwidths of ultrafast optical systems, all-optical information processing promises opportunities to achieve high computation speeds which are beyond the reach of electronic systems [40–50].

Another important feature of parametric nonlinear processes is their phase-sensitive nature. This aspect allows for the direction of energy transfer between different frequency bands to be controlled by tuning the relative phase of the interacting waves. It is furthermore of great importance in the context of quantum optical systems [51, 52]. Here, the phase sensitivity of the nonlinear process can be used to generate squeezing or entanglement through spontaneous parametric down conversion (SPDC). As such, phase-sensitive nonlinear processes are foundational to many efforts in optical quantum sensing and information processing systems [53–64].

Finally, nonlinearity gives rise to rich physics and complex dynamics, for example soliton and pattern formation [65–68], supercontinuum generation [9, 69–71], and chaos [72]. On the one hand, these physics serve to engage the curious graduate student. On the other hand, when understood and properly harnessed, many of these dynamics can enable new applications. In particular, solitons, optical pulses which maintain their shape during propagation via a dynamical balance between linear dispersive or diffractive effects and nonlinearity, have long been of interest both from a fundamental perspective and due to their broad application in areas such as

communications [73], frequency synthesis [74, 75], sensing and spectroscopy [16, 18, 76–78], and ranging [79–81].

Combined, these properties motivate the need for nonlinearity. We hope that the claims of this section will be further supported by the results of this thesis, which have aimed to leverage the rich physics enabled by quadratic nonlinear interactions to enable new applications in areas such as ultrafast sensing, spectroscopy, and information processing.

1.2 Key Developments in Nonlinear and Ultrafast Optics

The history of nonlinear and ultrafast optics is long and storied. In this section, we briefly summarize a few key developments to give a flavor of the trajectory of the field and demonstrate the ways in which these two disciplines have remained fundamentally intertwined through the years.

Research into nonlinear optics has closely paralleled the development of laser technology, beginning with Theodore Maiman's invention of the laser in 1960 [82]. The interconnectedness of these two research areas is embodied through the proximity of its invention to the first observation of the nonlinear effect of SHG by Franken *et al.* in 1961, just one year later [83].

Both fields grew quickly in the years that followed. Within two years, Bloembergen, Armstrong, Pershan, and Ducuing had laid out the theoretical basis of the field [84, 85]. By 1965, the first demonstrations of OPO had been reported [86]. Parallel investigations into Q-switched and mode-locked lasers (MLLs) provided the groundwork for the areas of pulsed and ultrafast optics [87–91].

Following its invention in 1966 [92, 93] and subsequent mode-locking in 1968 [94], the dye laser provided the shortest pulse operation of available mode-locked laser technologies for several decades, including the first demonstration of sub-ps pulses in 1974 [95]. The additional development of colliding pulse mode-locking in 1981 enabled further reduction in the pulse widths by more than an order of magnitude [96].

Meanwhile, significant progress had been made into the study of optical solitons in Kerr nonlinear media, with seminal theoretical work by Hasegawa and Tappert in 1973 predicting that ps solitons could be realized and propagate undistorted in optical fibers [97, 98]. In the early 1980s, Mollenauer *et al.* verified these theoretical predictions through the experimental observation of ps pulse narrowing due to soliton pulse compression [99, 100]. Combining the soliton pulse compression

technique with then state-of-the art dye MLLs led to the first demonstrations of pulse durations on the order of single fs [101].

Mollenauer and Stolen went on to demonstrate a soliton fiber laser in 1984 [102]. The mechanism behind the mode-locking in this system was later understood as additive pulse mode-locking [103, 104]. Several mode-locking techniques, including nonlinear polarization rotation [105] and nonlinear amplifying loop mirrors [106, 107], were also developed around this time. Paired with the development of several rare-earth ion-doped fiber gain media, for example Erbium and Ytterbium, mode-locked fiber lasers continued to develop as low-noise, light weight, and compact generators of fs pulses [108]. Their commercial availability has made them ubiquitous in many ultrafast labs today.

The invention of the Ti:Sapphire laser in 1986 [109] and subsequent development of Kerr-lens mode-locking in 1991 [110, 111] marked another important turning point in the history of MLLs. The near-instantaneous action of the nonlinearity paired with the extremely large gain bandwidth and slow gain recovery time of the Ti:Sapphire provided nearly ideal conditions for achieving ultrashort pulse generation, and direct generation of sub-10 fs pulses from a dispersion-managed Ti:Sapphire MLL was achieved by the late 1990s [112, 113]. In 2001, the group of Ferenc Krausz reported the first observation of attosecond pulses in high-harmonic generation driven by high-energy, fs pulses from a Ti:Sapphire MLL [114]. In the years that have followed, availability of such extremely short pulses has seen the growth of the field of attosecond science [115, 116], which has provided many new insights into the underlying structures in atoms, molecules, and solids.

Another important development around this time, which enabled the generation of high-power laser pulses, was that of chirped pulse amplification (CPA) in 1985 by Strickland and Mourou [117]. They demonstrated that, through pre-chirping a pulse prior to amplification and subsequent re-compression, unwanted nonlinear effects and optical damage to the amplifier could be mitigated, leading to the generation of extremely high-energy laser pulses at the millijoule level. Dubietis *et al.* built upon this work to CPA in an OPA in 1992 [118], benefiting from the large bandwidths and wavelength tunability afforded through the nonlinear amplification process. Since its development, CPA has been widely used in high-energy laser physics experiments, include in the study of extreme nonlinear optical phenomena, and have benefited applications such as laser eye surgery [119, 120].

In parallel with the development of these various laser technologies, researchers sought to tackle another issue–that of absolute frequency measurement [121]. Early work in this area focused on laser referencing to molecular and atomic transitions [122, 123]. With the recognition that periodic signals in the time domain, from, for example, MLLs would correspond to frequency-periodic combs, it was soon demonstrated that by stabilizing both the optical frequency of one of the comb lines and the microwave frequency corresponding to the comb line spacing, one could translate coherence across broadband optical spectra, and focus shifted towards the generation of broadband frequency combs [124–128]. Perhaps the largest breakthrough came through the work of the groups of Theodore Hänsch and John Hall at the turn of the millennium, with the first demonstration of an octave-spanning frequency comb, benefiting from supercontinuum generation in the recently invented photonic crystal fiber [129, 130]. The generation of an octave-spanning comb enabled the direct measurement of the carrier-envelope-offset (CEO) frequency via f-2f interferometry through an SHG crystal [131, 132]. With the measurement, then, of just two microwave frequencies, the repetition rate and CEO frequency, one had complete knowledge and control over the entire comb spectrum. Since these developments, optical frequency comb technologies have served to bridge the radio-frequency and optical domains, and have revolutionized the area of optical metrology [133].

With the availability of femtosecond pulses came the first demonstration of a femtosecond OPO in 1989 [134], pumped by a mode-locked dye laser. Such femtosecond OPOs promised to extend the spectral coverage of MLLs into the important infrared spectral region. Since then, significant progress has been made in femtosecond OPO research [11]. OPOs have been demonstrated in many key wavelength bands of interest and been utilized for spectroscopy [18, 20, 135]. Below threshold, they have been leveraged as generators of squeezing for quantum information processing experiments [57, 58]. Moreover, the quantum randomness of the OPO output has been leveraged as a computational resource in the development of Ising solvers [45, 46]. More recently, improved theoretical understanding and experimental investigation into soliton formation in OPOs has revealed new operation regimes offering practical benefits such as improved efficiencies and pulse shortening [136, 137]. These works serve as a precursor to many of the results presented in this thesis.

Meanwhile, the last two decades have seen a boom in photonic integration of ultrafast optical sources [138]. Such sources critically promise reduced cost and improved

scalability over their bulk counterparts. One critical development in this direction has been that of high-Q microcavities [139–141]. Among other benefits, the energy storage capabilities of these cavities allows for substantial optical power to build up, requiring modest only pump levels. In 2007, it was demonstrated that this pump power could be enough to drive the formation of optical frequency combs via four-wave mixing processes in a high-Q microtoroid resonator [142]. The years that followed brought several additional demonstrations of Kerr combs in waveguide structures [143, 144]. Realization of driven cavity solitons [145] further enabled unprecedented comb stability, as well as the formation of localized pulses, in Kerr microcavities [146]. Since then, Kerr microcombs have become one of the dominant sources of integrated frequency combs, benefiting many application areas including laser ranging [79–81], astronomical calibration [147], spectroscopy [77, 78, 148], and microwave synthesis [75].

Among integrated photonic platforms, we single out the development of commercially available thin-film lithium niobate as a key precursor to the work presented in this thesis [149]. On the one hand, lithium niobate offers a large electro-optic coefficient, which has been leveraged for the integration of high-speed, low-energy modulators which can be used to generate broadband electro-optic frequency combs [150–152]. On the other hand, and key to the developments in this thesis, lithium niobate exhibits a strong quadratic nonlinearity. In this thesis, we build upon pioneering works leveraging quadratic nonlinearity in this platform, including demonstrations of pJ pulse energy supercontinuum generation[70, 153] and extremely broad bandwidth, high-gain parametric amplification [154, 155].

1.3 Dissertation Overview

In the preceding, we have attempted to motivate the far-reaching impacts of nonlinear and ultrafast optics in the development of optical technologies, with applications across a variety of academic fields and industries. Here, we comment more specifically on the work presented in this dissertation as well as its organization, in order to guide the reader.

Through the works of this thesis, we present several demonstrations of quadratic nonlinear phenomena which can benefit the development of scalable and efficient ultrafast sources, sensors, and information processing systems. A major focus of the thesis is on the formation of quadratic solitons and their application in spectroscopy and ultrashort pulse synthesis. However, other dynamical phenomena,

including supercontinuum generation, and properties, such as the phase-sensitive nature of parametric amplification, are explored. Many of the works harness the new opportunities provided by the development of thin-film lithium niobate as a nanophotonic platform capable of supporting quadratic nonlinear interactions.

The specific chapters are organized as follows. In Chapter 2, the pertinent theory of quadratic nonlinear optics is reviewed, and the main equations used for the modeling of the systems studied in this thesis are described. Following the derivation of the relevant equations, several additional concepts are discussed at the end of the chapter, including brief discussions on quasi-phase matching and resonant processes.

Chapters 3 and 4 present our work on extending the concept of temporal simultons in fs-pumped optical parametric oscillators to the mid-infrared (MIR) spectral region for sensing and spectroscopy. The studied OPO consists of a free-space cavity with a GaP crystal as the nonlinear medium. Chapter 3 focuses specifically on our characterization of the simulton OPO performance. Meanwhile, Chapter 4 presents our study of intracavity sensing in the simulton OPO, wherein we discover that the formation dynamics of the simulton can be exploited to obtain significant sensitivity enhancement.

In the remaining chapters, we turn to the nanophotonic platform of thin-film lithium niobate. Chapter 5 presents the generation of two-optical cycle pulses from two-color soliton pulse compression of pJ-energy pules in a dispersion-engineered nano-photonic waveguide. Through this work, we show that such dispersion engineering can benefit the design of systems supporting soliton formation compared what could be achieved in bulk systems.

Having demonstrated the formation of ultrashort pulses in a nanophotonic wave-guide, we show in Chapter 6 that nanophotonic OPAs may also be leveraged for on-chip pulse characterization. In particular, the high gain afforded by the tight mode confinement promises to enable measurement of ultra-weak pulses, beyond even our demonstrated measurement of a fJ-energy pulse. Likewise, the large gain bandwidths achievable through operation in the near-0 dispersion regime allow for measurement of ultrashort pulses.

Next, we turn to the study of nanophotonic parametric oscillators. In Chapter 7, we demonstrate multi-octave frequency comb formation requiring sub-pJ pump pulse energies from a high-gain, low-finesse nanophotonic OPO pumped far above thresh-old. Interestingly, the system exhibits decoherence and subsequent recoherence

as the pump power is increased, with the multi-octave comb formation occurring in this recoherent regime. We utilize an admixture of numerical simulation and experiments to study the dynamical features of this process in detail in Chapter 8.

Finally, in Chapter 9 we study the feasibility of supporting large-scale, time-multiplexed systems in nanophotonic OPOs through an experimental demonstration of simultaneous oscillation of 70 time-multiplexed OPOs in a single nanophotonic cavity at a 17.5-GHz repetition rate. Our results show that through dispersion engineering, independence of the pulses may be maintained, with application in quantum-random number generation and the development of scalable, time-multiplexed all-optical computers.

BIBLIOGRAPHY

[1]   Robert W. Boyd. *Nonlinear Optics.* 3rd ed. Cambridge, Massachusetts: Academic Press, 2008.

[2]   Ioachim Pupeza, Daniel Sánchez, Jinwei Zhang, Nicolai Lilienfein, Marcus Seidel, Nicholas Karpowicz, Tim Paasch-Colberg, Irina Znakovskaya, M. Pescher, Wolfgang Schweinberger, et al. "High-power sub-two-cycle mid-infrared pulses at 100 MHz repetition rate." In: *Nature Photonics* 9.11 (2015), pp. 721–724.

[3]   Grzegorz Soboń, Tadeusz Martynkien, Paweł Mergo, Lucile Rutkowski, and Aleksandra Foltynowicz. "High-power frequency comb source tunable from 2.7 to 4.2 μm based on difference frequency generation pumped by an Yb-doped fiber laser." In: *Optics Letters* 42.9 (2017), pp. 1748–1751.

[4]   Alexander J. Lind, Abijith Kowligy, Henry Timmers, Flavio C. Cruz, Nima Nader, Myles C. Silfies, Thomas K. Allison, and Scott A. Diddams. "Mid-infrared frequency comb generation and spectroscopy with few-cycle pulses and χ (2) nonlinear optics." In: *Physical Review Letters* 124.13 (2020), p. 133904.

[5]   Robert L. Byer. "Optical parametric oscillators." eng. In: *Quantum Electronics: A Treatise.* Vol. 1. New York: Academic Press, 1975, pp. 588–694. ISBN: 978-0-12-574041-8.

[6]   Mingchen Liu, Robert M. Gray, Arkadev Roy, Kirk A. Ingold, Evgeni Sorokin, Irina Sorokina, Peter G. Schunemann, and Alireza Marandi. "High-power mid-IR few-cycle frequency comb from quadratic solitons in an optical parametric oscillator." In: *Laser & Photonics Reviews* 16.11 (2022), p. 2200453. DOI: 10.1002/lpor.202200453.

[7]   Luis Ledezma, Arkadev Roy, Luis Costa, Ryoto Sekine, Robert Gray, Qiushi Guo, Rajveer Nehra, Ryan M. Briggs, and Alireza Marandi. "Octave-spanning tunable infrared parametric oscillators in nanophotonics." In: *Science Advances* 9.30 (2023), eadf9711. DOI: 10.1126/sciadv.adf9711.

[8]   Arkadev Roy, Luis Ledezma, Luis Costa, Robert Gray, Ryoto Sekine, Qiushi Guo, Mingchen Liu, Ryan M. Briggs, and Alireza Marandi. "Visible-to-mid-IR tunable frequency comb in nanophotonics." In: *Nature Communications* 14.1 (2023), p. 6549. DOI: 10.1038/s41467-023-42289-0.

[9]   Ryoto Sekine, Robert M. Gray, Luis Ledezma, Selina Zhou, Qiushi Guo, and Alireza Marandi. "Multi-octave frequency comb from an ultra-low-threshold nanophotonic parametric oscillator." In: *arXiv preprint arXiv:2309.04545* (2023). DOI: 10.48550/arXiv.2309.04545.

[10] Timothy P. McKenna, Hubert S. Stokowski, Vahid Ansari, Jatadhari Mishra, Marc Jankowski, Christopher J. Sarabalis, Jason F. Herrmann, Carsten Langrock, Martin M. Fejer, and Amir H. Safavi-Naeini. "Ultra-low-power second-order nonlinear optics on a chip." In: *Nature Communications* 13.1 (2022), p. 4532. DOI: 10.1038/s41467-022-31134-5.

[11] Yohei Kobayashi, Kenji Torizuka, Alireza Marandi, Robert L. Byer, Richard A. McCracken, Zhaowei Zhang, and Derryck T Reid. "Femtosecond optical parametric oscillator frequency combs." In: *Journal of Optics* 17.9 (2015), p. 094010.

[12] Luke Maidment, Peter G. Schunemann, and Derryck T. Reid. "Molecular fingerprint-region spectroscopy from 5 to 12 μm using an orientation-patterned gallium phosphide optical parametric oscillator." In: *Optics Letters* 41.18 (2016), pp. 4261–4264.

[13] Kana Iwakuni, Gil Porat, Thinh Q Bui, Bryce J. Bjork, Stephen B. Schoun, Oliver H. Heckl, Martin E. Fermann, and Jun Ye. "Phase-stabilized 100 mW frequency comb near 10 μm." In: *Applied Physics B* 124 (2018), pp. 1–7.

[14] Callum F. O'Donnell, Suddapalli Chaitanya Kumar, Peter G. Schunemann, and Majid Ebrahim-Zadeh. "Femtosecond optical parametric oscillator continuously tunable across 3.6–8 μm based on orientation-patterned gallium phosphide." In: *Optics Letters* 44.18 (2019), pp. 4570–4573.

[15] Chengxiao Ning, Pei Liu, Yingxiong Qin, and Zhaowei Zhang. "Continuous wavelength tuning of nondegenerate femtosecond doubly resonant optical parametric oscillators." In: *Optics Letters* 45.9 (2020), pp. 2551–2554.

[16] Nathalie Picqué and Theodor W. Hänsch. "Frequency comb spectroscopy." In: *Nature Photonics* 13.3 (2019), pp. 146–157.

[17] Jane Hodgkinson and Ralph P. Tatam. "Optical gas sensing: A review." In: *Measurement Science and Technology* 24.1 (2012), p. 012004.

[18] Mingchen Liu, Robert M. Gray, Luis Costa, Charles R. Markus, Arkadev Roy, and Alireza Marandi. "Mid-infrared cross-comb spectroscopy." In: *Nature Communications* 14.1 (2023), p. 1044. DOI: 10.1038/s41467-023-36811-7.

[19] Ioachim Pupeza, Marinus Huber, Michael Trubetskov, Wolfgang Schweinberger, Syed A. Hussain, Christina Hofer, Kilian Fritsch, Markus Poetzlberger, Lenard Vamos, Ernst Fill, Tatiana Amotchkina, Kosmas V. Kepesidis, Alexander Apolonski, Nicholas Karpowicz, Vladimir Pervak, Oleg Pronin, Frank Fleischmann, Abdallah Azzeer, Mihaela Žigman, and Ferenc Krausz. "Field-resolved infrared spectroscopy of biological systems." In: *Nature* 577.7788 (Jan. 2020), pp. 52–59. ISSN: 1476-4687. DOI: 10.1038/s41586-019-1850-7. URL: https://doi.org/10.1038/s41586-019-1850-7.

[20]   Andrey V. Muraviev, Viktor O. Smolski, Zachary E. Loparo, and Konstantin L. Vodopyanov. "Massively parallel sensing of trace molecules and their isotopologues with broadband subharmonic mid-infrared frequency combs." In: *Nature Photonics* 12.4 (2018), pp. 209–214. DOI: 10.1038/s41566-018-0135-2.

[21]   Ben Henderson, Amir Khodabakhsh, Markus Metsälä, Irène Ventrillard, Florian M Schmidt, Daniele Romanini, Grant A. D. Ritchie, Sacco te Lintel Hekkert, Raphaël Briot, Terence Risby, et al. "Laser spectroscopy for breath analysis: Towards clinical implementation." In: *Applied Physics B* 124 (2018), pp. 1–21.

[22]   Birgitta Bernhardt, Akira Ozawa, Patrick Jacquet, Marion Jacquey, Yohei Kobayashi, Thomas Udem, Ronald Holzwarth, Guy Guelachvili, Theodor W. Hänsch, and Nathalie Picqué. "Cavity-enhanced dual-comb spectroscopy." In: *Nature Photonics* 4.1 (2010), pp. 55–57.

[23]   Hemani Kaushal, Vijay K. Jain, and Subrat Kar. *Free space optical communication.* Vol. 60. Springer, 2017.

[24]   Tsung-Han Wu, Luis Ledezma, Connor Fredrick, Pooja Sekhar, Ryoto Sekine, Qiushi Guo, Ryan M. Briggs, Alireza Marandi, and Scott A. Diddams. "Visible-to-ultraviolet frequency comb generation in lithium niobate nanophotonic waveguides." In: *Nature Photonics* 18.3 (Mar. 2024), pp. 218–223. ISSN: 1749-4893. DOI: 10.1038/s41566-023-01364-0. URL: https://doi.org/10.1038/s41566-023-01364-0.

[25]   Emily Hwang, Nathan Harper, Ryoto Sekine, Luis Ledezma, Alireza Marandi, and Scott Cushing. "Tunable and efficient ultraviolet generation with periodically poled lithium niobate." In: *Optics Letters* 48.15 (2023), pp. 3917–3920.

[26]   Jan-Peter Meyn and Martin M. Fejer. "Tunable ultraviolet radiation by second-harmonic generation in periodically poled lithium tantalate." In: *Optics Letters* 22.16 (1997), pp. 1214–1216.

[27]   Andrew D. Ludlow, Martin M. Boyd, Jun Ye, Ekkehard Peik, and Piet O. Schmidt. "Optical atomic clocks." In: *Reviews of Modern Physics* 87.2 (2015), pp. 637–701.

[28]   Zachary L. Newman, Vincent Maurice, Tara Drake, Jordan R. Stone, Travis C Briles, Daryl T. Spencer, Connor Fredrick, Qing Li, Daron Westly, Bojan R. Ilic, et al. "Architecture for the photonic integration of an optical atomic clock." In: *Optica* 6.5 (2019), pp. 680–685.

[29]   Joss Bland-Hawthorn and Pierre Kern. "Astrophotonics: A new era for astronomical instruments." In: *Optics Express* 17.3 (2009), pp. 1880–1884.

[30]   Daniel Bratton, Da Yang, Junyan Dai, and Christopher K. Ober. "Recent progress in high resolution lithography." In: *Polymers for Advanced Technologies* 17.2 (2006), pp. 94–103.

[31] Jesper Østergaard. "UV imaging in pharmaceutical analysis." In: *Journal of Pharmaceutical and Biomedical Analysis* 147 (2018), pp. 140–148.

[32] Heinz-Helmut Perkampus. *UV-VIS spectroscopy and its applications.* Springer Science & Business Media, 2013.

[33] Kristina F. Chang, Daniel M. B. Lesko, Carter Mashburn, Peter Chang, Eugene Tsao, Alexander J Lind, and Scott A. Diddams. "Multi-harmonic near-infrared–ultraviolet dual-comb spectrometer." In: *Optics Letters* 49.7 (2024), pp. 1684–1687.

[34] Wei Cao, Huiming Bu, Maud Vinet, Min Cao, Shinichi Takagi, Sungwoo Hwang, Tahir Ghani, and Kaustav Banerjee. "The future transistors." In: *Nature* 620.7974 (2023), pp. 501–515.

[35] Munender Varshney and Pravendra Singh. "Optimizing nonlinear activation function for convolutional neural networks." In: *Signal, Image and Video Processing* 15.6 (2021), pp. 1323–1330.

[36] Gordon H. Y. Li, Ryoto Sekine, Rajveer Nehra, Robert M. Gray, Luis Ledezma, Qiushi Guo, and Alireza Marandi. "All-optical ultrafast ReLU function for energy-efficient nanophotonic deep learning." In: *Nanophotonics* 12.5 (2023), pp. 847–855. DOI: 10.1515/nanoph-2022-0137.

[37] Qiushi Guo, Ryoto Sekine, Luis Ledezma, Rajveer Nehra, Devin J. Dean, Arkadev Roy, Robert M. Gray, Saman Jahani, and Alireza Marandi. "Femtojoule femtosecond all-optical switching in lithium niobate nanophotonics." In: *Nature Photonics* 16.9 (2022), pp. 625–631. DOI: 10.1038/s41566-022-01071-2.

[38] Mario Miscuglio, Armin Mehrabian, Zibo Hu, Shaimaa I. Azzam, Jonathan George, Alexander V. Kildishev, Matthew Pelton, and Volker J. Sorger. "All-optical nonlinear activation function for photonic neural networks." In: *Optical Materials Express* 8.12 (2018), pp. 3851–3863.

[39] Peter L. McMahon. "The physics of optical computing." In: *Nature Reviews Physics* 5.12 (2023), pp. 717–734.

[40] Robert M. Gray, Ryoto Sekine, Luis Ledezma, Gordon H. Y. Li, Selina Zhou, Arkadev Roy, Midya Parto, and Alireza Marandi. "Large-scale time-multiplexed nanophotonic parametric oscillators." In: *Newton* (2025). DOI: 10.1016/j.newton.2025.100108.

[41] Gordon H. Y. Li, Midya Parto, Jinhao Ge, Qing-Xin Ji, Maodong Gao, Yan Yu, James Williams, Robert M. Gray, Christian R. Leefmans, Nicolas Englebert, et al. "All-optical computing with beyond 100-GHz clock rates." In: *arXiv preprint arXiv:2501.05756* (2025). DOI: 10.48550/arXiv.2501.05756.

[42] Gordon H. Y. Li, Christian R Leefmans, James Williams, Robert M. Gray, Midya Parto, and Alireza Marandi. "Deep learning with photonic neural cellular automata." In: *Light: Science & Applications* 13.1 (2024), p. 283. DOI: 10.1038/s41377-024-01651-7.

[43] Gordon H. Y. Li, Christian R. Leefmans, James Williams, and Alireza Marandi. "Photonic elementary cellular automata for simulation of complex phenomena." In: *Light: Science & Applications* 12.1 (2023), p. 132. DOI: 10.1038/s41377-023-01180-9.

[44] Midya Parto, Gordon H. Y. Li, Ryoto Sekine, Robert M. Gray, Luis L. Ledezma, James Williams, Arkadev Roy, and Alireza Marandi. "Ultrafast neuromorphic computing with nanophotonic optical parametric oscillators." In: *arXiv preprint arXiv:2501.16604* (2025). DOI: 10.48550/arXiv.2501.16604.

[45] Alireza Marandi, Zhe Wang, Kenta Takata, Robert L. Byer, and Yoshihisa Yamamoto. "Network of time-multiplexed optical parametric oscillators as a coherent Ising machine." In: *Nature Photonics* 8.12 (2014), pp. 937–942. DOI: 10.1038/nphoton.2014.249.

[46] Peter L. McMahon, Alireza Marandi, Yoshitaka Haribara, Ryan Hamerly, Carsten Langrock, Shuhei Tamate, Takahiro Inagaki, Hiroki Takesue, Shoko Utsunomiya, Kazuyuki Aihara, et al. "A fully programmable 100-spin coherent Ising machine with all-to-all connections." In: *Science* 354.6312 (2016), pp. 614–617. DOI: 10.1126/science.aah5178.

[47] Naeimeh Mohseni, Peter L. McMahon, and Tim Byrnes. "Ising machines as hardware solvers of combinatorial optimization problems." In: *Nature Reviews Physics* 4.6 (2022), pp. 363–379. DOI: 10.1038/s42254-022-00440-8.

[48] Toshimori Honjo, Tomohiro Sonobe, Kensuke Inaba, Takahiro Inagaki, Takuya Ikuta, Yasuhiro Yamada, Takushi Kazama, Koji Enbutsu, Takeshi Umeki, Ryoichi Kasahara, et al. "100,000-spin coherent Ising machine." In: *Science Advances* 7.40 (2021), eabh0952. DOI: 10.1126/sciadv.abh0952.

[49] Tingzhao Fu, Jianfa Zhang, Run Sun, Yuyao Huang, Wei Xu, Sigang Yang, Zhihong Zhu, and Hongwei Chen. "Optical neural networks: Progress and challenges." In: *Light: Science & Applications* 13.1 (2024), p. 263. DOI: 10.1038/s41377-024-01590-3.

[50] Yoshihisa Yamamoto, Kazuyuki Aihara, Timothee Leleu, Ken-ichi Kawarabayashi, Satoshi Kako, Martin Fejer, Kyo Inoue, and Hiroki Takesue. "Coherent Ising machines—optical neural networks operating at the quantum limit." In: *npj Quantum Information* 3.1 (2017), p. 49. DOI: 10.1038/s41534-017-0048-9.

[51] Christopher C. Gerry and Peter L. Knight. *Introductory quantum optics.* Cambridge University Press, 2023.

[52] Peter D. Drummond and Mark Hillery. *The quantum theory of nonlinear optics.* Cambridge University Press, 2014.

[53] Rajveer Nehra, Ryoto Sekine, Luis Ledezma, Qiushi Guo, Robert M. Gray, Arkadev Roy, and Alireza Marandi. "Few-cycle vacuum squeezing in nanophotonics." In: *Science* 377.6612 (2022), pp. 1333–1337. DOI: 10.1126/science.abo6213.

[54] James Williams, Rajveer Nehra, Elina Sendonaris, Luis Ledezma, Robert M. Gray, Ryoto Sekine, and Alireza Marandi. "Ultrashort pulse biphoton source in lithium niobate nanophotonics at 2 μm." In: *Nanophotonics* 13.18 (2024), pp. 3535–3544. DOI: 10.1515/nanoph-2024-0054.

[55] Elina Sendonaris, James Williams, Rajveer Nehra, Robert Gray, Ryoto Sekine, Luis Ledezma, and Alireza Marandi. "Ultrafast single-photon detection using nanophotonic parametric amplifiers." In: *arXiv preprint arXiv:2410.18397* (2024). DOI: 10.48550/arXiv.2410.18397.

[56] James Williams, Elina Sendonaris, Rajveer Nehra, Robert M. Gray, Ryoto Sekine, Luis Ledezma, and Alireza Marandi. "Ultrafast all-optical measurement of squeezed vacuum in a lithium niobate nanophotonic circuit." In: *arXiv preprint arXiv:2502.00518* (2025). DOI: 10.48550/arXiv.2502.00518.

[57] Mikkel V. Larsen, Xueshi Guo, Casper R. Breum, Jonas S. Neergaard-Nielsen, and Ulrik L. Andersen. "Deterministic generation of a two-dimensional cluster state." In: *Science* 366.6463 (2019), pp. 369–372. DOI: 10.1126/science.aay4354.

[58] Warit Asavanant, Yu Shiozawa, Shota Yokoyama, Baramee Charoensombutamon, Hiroki Emura, Rafael N. Alexander, Shuntaro Takeda, Jun-ichi Yoshikawa, Nicolas C. Menicucci, Hidehiro Yonezawa, et al. "Generation of time-domain-multiplexed two-dimensional cluster state." In: *Science* 366.6463 (2019), pp. 373–376. DOI: 10.1126/science.aay2645.

[59] Nicolas C. Menicucci, Peter Van Loock, Mile Gu, Christian Weedbrook, Timothy C. Ralph, and Michael A. Nielsen. "Universal quantum computation with continuous-variable cluster states." In: *Physical review letters* 97.11 (2006), p. 110501. DOI: 10.1103/PhysRevLett.97.110501.

[60] Seth Lloyd and Samuel L. Braunstein. "Quantum computation over continuous variables." In: *Physical Review Letters* 82.8 (1999), p. 1784. DOI: 10.1103/PhysRevLett.82.1784.

[61] Lars S. Madsen, Fabian Laudenbach, Mohsen Falamarzi Askarani, Fabien Rortais, Trevor Vincent, Jacob F. F. Bulmer, Filippo M. Miatto, Leonhard Neuhaus, Lukas G. Helt, Matthew J. Collins, et al. "Quantum computational

advantage with a programmable photonic processor." In: *Nature* 606.7912 (2022), pp. 75–81. DOI: `10.1038/s41586-022-04725-x`.

[62] Ryotatsu Yanagimoto, Edwin Ng, Marc Jankowski, Rajveer Nehra, Timothy P. McKenna, Tatsuhiro Onodera, Logan G. Wright, Ryan Hamerly, Alireza Marandi, Martin M. Fejer, et al. "Mesoscopic ultrafast nonlinear optics—the emergence of multimode quantum non-Gaussian physics." In: *Optica* 11.7 (2024), pp. 896–918. DOI: `10.1364/OPTICA.514075`.

[63] Manuel Erhard, Mario Krenn, and Anton Zeilinger. "Advances in high-dimensional quantum entanglement." In: *Nature Reviews Physics* 2.7 (2020), pp. 365–381. DOI: `10.1038/s42254-020-0193-5`.

[64] Juan M. Arrazola, Ville Bergholm, Kamil Brádler, Thomas R. Bromley, Matt J. Collins, Ish Dhand, Alberto Fumagalli, Thomas Gerrits, Andrey Goussev, Lukas G. Helt, et al. "Quantum circuits with many photons on a programmable nanophotonic chip." In: *Nature* 591.7848 (2021), pp. 54–60. DOI: `10.1038/s41586-021-03202-1`.

[65] Alexander V. Buryak, Paolo Di Trapani, Dmitry V. Skryabin, and Stefano Trillo. "Optical solitons due to quadratic nonlinearities: From basic physics to futuristic applications." In: *Physics Reports* 370.2 (2002), pp. 63–235.

[66] Govind P. Agrawal. "Chapter 5 - optical solitons". In: *Nonlinear Fiber Optics (Fifth Edition)*. Academic Press, 2013, pp. 129–191.

[67] Gian-Luca Oppo, Alison M. Yao, and Domenico Cuozzo. "Self-organization, pattern formation, cavity solitons, and rogue waves in singly resonant optical parametric oscillators." In: *Physical Review A* 88.4 (2013), p. 043813. DOI: `10.1103/PhysRevA.88.043813`.

[68] Robert M. Gray, Ryoto Sekine, Maximilian Shen, Thomas Zacharias, James Williams, Selina Zhou, Rahul Chawlani, Luis Ledezma, Nicolas Englebert, and Alireza Marandi. "Two-optical-cycle pulses from nanophotonic two-color soliton compression." In: *arXiv preprint arXiv:2501.15381* (2025). DOI: `10.48550/arXiv.2501.15381`.

[69] John M. Dudley, Goëry Genty, and Stéphane Coen. "Supercontinuum generation in photonic crystal fiber." In: *Reviews of Modern Physics* 78.4 (2006), pp. 1135–1184.

[70] Marc Jankowski, Carsten Langrock, Boris Desiatov, Marko Lončar, and Martin M. Fejer. "Supercontinuum generation by saturated second-order nonlinear interactions." In: *APL Photonics* 8.11 (2023).

[71] Christopher R. Phillips, Carsten Langrock, Jason S. Pelc, Martin M. Fejer, Ingmar Hartl, and Martin E. Fermann. "Supercontinuum generation in quasi-phasematched waveguides." In: *Optics Express* 19.20 (Sept. 2011), pp. 18754–18773. ISSN: 1094-4087. DOI: `10.1364/OE.19.018754`. (Visited on 02/18/2019).

[72] John M. Dudley, Frédéric Dias, Miro Erkintalo, and Goëry Genty. "Instabilities, breathers and rogue waves in optics." In: *Nature Photonics* 8.10 (2014), pp. 755–764. DOI: `10.1038/nphoton.2014.220`.

[73] Akira Hasegawa. "Soliton-based optical communications: An overview." In: *IEEE Journal of Selected Topics in Quantum Electronics* 6.6 (2002), pp. 1161–1172.

[74] Daryl T. Spencer, Tara Drake, Travis C. Briles, Jordan Stone, Laura C. Sinclair, Connor Fredrick, Qing Li, Daron Westly, B. Robert Ilic, Aaron Bluestone, et al. "An optical-frequency synthesizer using integrated photonics." In: *Nature* 557.7703 (2018), pp. 81–85. DOI: `10.1038/s41586-018-0065-7`.

[75] Erwan Lucas, Pierre Brochard, Romain Bouchand, Stéphane Schilt, Thomas Südmeyer, and Tobias J. Kippenberg. "Ultralow-noise photonic microwave synthesis using a soliton microcomb-based transfer oscillator." In: *Nature Communications* 11.1 (2020), p. 374.

[76] Robert M. Gray, Mingchen Liu, Selina Zhou, Arkadev Roy, Luis Ledezma, and Alireza Marandi. "Quadratic-soliton-enhanced mid-IR molecular sensing." In: *Nature Communications* 15.1 (2024), p. 9086. DOI: `10.1038/s41467-024-53447-3`.

[77] Liron Stern, Jordan R. Stone, Songbai Kang, Daniel C. Cole, Myoung-Gyun Suh, Connor Fredrick, Zachary Newman, Kerry Vahala, John Kitching, Scott A. Diddams, et al. "Direct Kerr frequency comb atomic spectroscopy and stabilization." In: *Science Advances* 6.9 (2020), eaax6230. DOI: `10.1126/sciadv.aax6230`.

[78] Myoung-Gyun Suh, Qi-Fan Yang, Kiyoul Yang, Xu Yi, and Kerry J. Vahala. "Microresonator soliton dual-comb spectroscopy." In: *Science* 354.6312 (2016), pp. 600–603.

[79] Myoung-Gyun Suh and Kerry J. Vahala. "Soliton microcomb range measurement." In: *Science* 359.6378 (2018), pp. 884–887.

[80] Philipp Trocha, Maxim Karpov, Denis Ganin, Martin H. P. Pfeiffer, Arne Kordts, Stefan Wolf, J. Krockenberger, Pablo Marin-Palomo, Claudius Weimann, Sebastian Randel, et al. "Ultrafast optical ranging using microresonator soliton frequency combs." In: *Science* 359.6378 (2018), pp. 887–891.

[81] Johann Riemensberger, Anton Lukashchuk, Maxim Karpov, Wenle Weng, Erwan Lucas, Junqiu Liu, and Tobias J. Kippenberg. "Massively parallel coherent laser ranging using a soliton microcomb." In: *Nature* 581.7807 (May 2020), pp. 164–170. ISSN: 1476-4687. DOI: `10.1038/s41586-020-2239-3`. URL: `https://doi.org/10.1038/s41586-020-2239-3`.

[82] Theodore H. Maiman. "Stimulated optical radiation in ruby." In: *Nature* 187.4736 (1960), pp. 493–494.

[83] Peter A. Franken, Alan E. Hill, C. W. Peters, and Gabriel Weinreich. "Generation of optical harmonics." In: *Physical Review Letters* 7.4 (1961), p. 118.

[84] John A. Armstrong, Nicolaas Bloembergen, Jacques Ducuing, and Peter S. Pershan. "Interactions between light waves in a nonlinear dielectric." In: *Physical Review* 127.6 (1962), p. 1918.

[85] Nicolaas Bloembergen and Peter S. Pershan. "Light waves at the boundary of nonlinear media." In: *Physical Review* 128.2 (1962), p. 606.

[86] Joseph Anthony Giordmaine and Robert C. Miller. "Tunable coherent parametric oscillation in $LiNbO_3$ at optical frequencies." In: *Physical Review Letters* 14.24 (1965), p. 973.

[87] Hermann Statz and Chung Liang Tang. "Multimode oscillations in solid-state masers." In: *Journal of Applied Physics* 35.5 (1964), pp. 1377–1383.

[88] Logan E. Hargrove, Richard L. Fork, and Martin A. Pollack. "Locking of He-Ne laser modes induced by synchronous intracavity modulation." In: *Applied Physics Letters* 5.1 (1964), pp. 4–5.

[89] Karl Gürs. "Beats and modulation in optical ruby-masers." In: *Quantum Electronics* (1964), p. 1113.

[90] Amnon Yariv. "Internal modulation in multimode laser oscillators." In: *Journal of Applied Physics* 36.2 (1965), pp. 388–391.

[91] Hans W. Mocker and Robert J. Collins. "Mode competition and self-locking effects in a Q-switched ruby laser." In: *Applied Physics Letters* 7.10 (1965), pp. 270–273.

[92] Peter P. Sorokin and John R. Lankard. "Stimulated emission observed from an organic dye, chloro-aluminum phthalocyanine." In: *IBM Journal of Research and Development* 10.2 (1966), pp. 162–163.

[93] Fritz P. Schäfer, Werner Schmidt, and Jürgen Volze. "Organic dye solution laser." In: *Applied Physics Letters* 9.8 (1966), pp. 306–309.

[94] William H. Glenn, Michael J. Brienza, and Anthony J. DeMaria. "Mode locking of an organic dye laser." In: *Applied Physics Letters* 12.2 (1968), pp. 54–56.

[95] Charles V. Shank and Erich P. Ippen. "Subpicosecond kilowatt pulses from a mode-locked cw dye laser." In: *Applied Physics Letters* 24.8 (1974), pp. 373–375.

[96] Richard L. Fork, Benjamin I. Greene, and Charles V. Shank. "Generation of optical pulses shorter than 0.1 psec by colliding pulse mode-locking." In: *Conference on Lasers and Electro-Optics*. Optica Publishing Group. 1981, WL1.

[97]   Akira Hasegawa and Frederick Tappert. "Transmission of stationary nonlinear optical pulses in dispersive dielectric fibers. I. Anomalous dispersion." In: *Applied Physics Letters* 23.3 (1973), pp. 142–144.

[98]   Akira Hasegawa and Frederick Tappert. "Transmission of stationary nonlinear optical pulses in dispersive dielectric fibers. II. Normal dispersion." In: *Applied Physics Letters* 23.4 (1973), pp. 171–172.

[99]   Linn F. Mollenauer, Roger H. Stolen, and James P. Gordon. "Experimental observation of picosecond pulse narrowing and solitons in optical fibers." In: *Physical Review Letters* 45.13 (1980), p. 1095.

[100] Linn F. Mollenauer, Roger H. Stolen, James P. Gordon, and W. Jack Tomlinson. "Extreme picosecond pulse narrowing by means of soliton effect in single-mode optical fibers." In: *Optics Letters* 8.5 (1983), pp. 289–291.

[101] Wayne H. Knox, Richard L. Fork, MC Downer, Roger H. Stolen, Charles V. Shank, and Janis A. Valdmanis. "Optical pulse compression to 8 fs at a 5-kHz repetition rate." In: *Applied Physics Letters* 46.12 (1985), pp. 1120–1121.

[102] Linn F. Mollenauer and Roger H. Stolen. "The soliton laser." In: *Optics Letters* 9.1 (1984), pp. 13–15.

[103] J. Mark, L. Y. Liu, Katherine L. Hall, Hermann A. Haus, and Erich P. Ippen. "Femtosecond pulse generation in a laser with a nonlinear external resonator." In: *Optics Letters* 14.1 (1989), pp. 48–50.

[104] Erich P. Ippen, Hermann A. Haus, and L. Y. Liu. "Additive pulse mode locking." In: *Journal of the Optical Society of America B* 6.9 (1989), pp. 1736–1745.

[105] V. J. Matsas, T. P. Newson, David J. Richardson, and David N. Payne. "Self-starting passively mode-locked fibre ring soliton laser exploiting nonlinear polarisation rotation." In: *Electronics Letters* 28.15 (1992), pp. 1391–1393.

[106] Irl N. Duling III. "All-fiber ring soliton laser mode locked with a nonlinear mirror." In: *Optics Letters* 16.8 (1991), pp. 539–541.

[107] Martin E. Fermann, F. Haberl, Martin Hofer, and H. Hochreiter. "Nonlinear amplifying loop mirror." In: *Optics Letters* 15.13 (1990), pp. 752–754.

[108] Jungwon Kim and Youjian Song. "Ultralow-noise mode-locked fiber lasers and frequency combs: Principles, status, and applications." In: *Advances in Optics and Photonics* 8.3 (2016), pp. 465–540.

[109] Peter F. Moulton. "Spectroscopic and laser characteristics of Ti: Al2O3." In: *Journal of the Optical Society of America B* 3.1 (1986), pp. 125–133.

[110] David E. Spence, P. N. Kean, and Wilson Sibbett. "60-fsec pulse generation from a self-mode-locked Ti: Sapphire laser." In: *Optics Letters* 16.1 (1991), pp. 42–44.

[111] David E. Spence, James M. Evans, W. E. Sleat, and Wilson Sibbett. "Regeneratively initiated self-mode-locked Ti: Sapphire laser." In: *Optics Letters* 16.22 (1991), pp. 1762–1764.

[112] Andreas Stingl, Matthias Lenzner, Christian Spielmann, Ferenc Krausz, and Róbert Szipöcs. "Sub-10-fs mirror-dispersion-controlled Ti: Sapphire laser." In: *Optics Letters* 20.6 (1995), pp. 602–604.

[113] S. Sartania, Zhao Cheng, Matthias Lenzner, Gabriel Tempea, Christian Spielmann, Ferenc Krausz, and Kárpát Ferencz. "Generation of 0.1-TW 5-fs optical pulses at a 1-kHz repetition rate." In: *Optics Letters* 22.20 (1997), pp. 1562–1564.

[114] Michael Hentschel, Reinhard Kienberger, Christian Spielmann, Georg A. Reider, Nenad Milosevic, Thomas Brabec, Paul Corkum, Ulrich Heinzmann, Markus Drescher, and Ferenc Krausz. "Attosecond metrology." In: *Nature* 414.6863 (2001), pp. 509–513.

[115] Paul B. Corkum and Ferenc Krausz. "Attosecond science." In: *Nature Physics* 3.6 (June 2007), pp. 381–387. ISSN: 1745-2481. DOI: `10.1038/nphys620`. URL: `https://doi.org/10.1038/nphys620`.

[116] Ferenc Krausz and Misha Ivanov. "Attosecond physics." In: *Reviews of modern physics* 81.1 (2009), pp. 163–234.

[117] Donna Strickland and Gerard Mourou. "Compression of amplified chirped optical pulses." In: *Optics Communications* 55.6 (1985), pp. 447–449.

[118] Audrius Dubietis, Gediminas Jonušauskas, and Algis Piskarskas. "Powerful femtosecond pulse generation by chirped and stretched pulse parametric amplification in BBO crystal." In: *Optics Communications* 88.4-6 (1992), pp. 437–440.

[119] Audrius Dubietis and Aidas Matijošius. "Table-top optical parametric chirped pulse amplifiers: Past and present." In: *Opto-Electronics Advances* 6.3 (2023), p. 220046.

[120] Franck Morin, Frédéric Druon, Marc Hanna, and Patrick Georges. "Microjoule femtosecond fiber laser at 1.6 μ m for corneal surgery applications." In: *Optics Letters* 34.13 (2009), pp. 1991–1993.

[121] John L. Hall. "Optical frequency measurement: 40 years of technology revolutions." In: *IEEE Journal of Selected Topics in Quantum Electronics* 6.6 (2002), pp. 1136–1144.

[122] R. L. Barger and John L. Hall. "Pressure shift and broadening of methane line at 3.39 μ studied by laser-saturated molecular absorption." In: *Physical Review Letters* 22.1 (1969), p. 4.

[123] Donald A. Jennings, Kenneth M. Evenson, and David J. E. Knight. "Optical frequency measurements." In: *Proceedings of the IEEE* 74.1 (1986), pp. 168–179.

[124] James N. Eckstein, Allister I. Ferguson, and Theodor W. Hänsch. "High-resolution two-photon spectroscopy with picosecond light pulses." In: *Physical Review Letters* 40.13 (1978), p. 847.

[125] Motonobu Kourogi, Ken'ichi Nakagawa, and Motoichi Ohtsu. "Wide-span optical frequency comb generator for accurate optical frequency difference measurement." In: *IEEE Journal of Quantum Electronics* 29.10 (1993), pp. 2693–2701.

[126] Scott A. Diddams, Long-Sheng Ma, Jun Ye, and John L. Hall. "Broadband optical frequency comb generation with a phase-modulated parametric oscillator." In: *Optics Letters* 24.23 (1999), pp. 1747–1749.

[127] Harald R. Telle, Dieter Meschede, and Theodor W. Hänsch. "Realization of a new concept for visible frequency division: Phase locking of harmonic and sum frequencies." In: *Optics Letters* 15.10 (1990), pp. 532–534.

[128] Joerg Reichert, Ronald Holzwarth, Thomas Udem, and Theodor W. Hänsch. "Measuring the frequency of light with mode-locked lasers." In: *Optics Communications* 172.1-6 (1999), pp. 59–68.

[129] Jonathan C. Knight, Tim A. Birks, Philip St. J. Russell, and Jean-Philippe De Sandro. "Properties of photonic crystal fiber and the effective index model." In: *Journal of the Optical Society of America A* 15.3 (1998), pp. 748–752.

[130] Jinendra K. Ranka, Robert S. Windeler, and Andrew J. Stentz. "Visible continuum generation in air–silica microstructure optical fibers with anomalous dispersion at 800 nm." In: *Optics Letters* 25.1 (2000), pp. 25–27.

[131] Scott A. Diddams, David J. Jones, Jun Ye, Steven T. Cundiff, John L. Hall, Jinendra K. Ranka, Robert S. Windeler, Ronald Holzwarth, Thomas Udem, and Theodor W Hänsch. "Direct link between microwave and optical frequencies with a 300 THz femtosecond laser comb." In: *Physical Review Letters* 84.22 (2000), p. 5102.

[132] David J. Jones, Scott A. Diddams, Jinendra K. Ranka, Andrew Stentz, Robert S. Windeler, John L. Hall, and Steven T. Cundiff. "Carrier-envelope phase control of femtosecond mode-locked lasers and direct optical frequency synthesis." In: *Science* 288.5466 (2000), pp. 635–639.

[133] Scott A. Diddams, Kerry Vahala, and Thomas Udem. "Optical frequency combs: Coherently uniting the electromagnetic spectrum." In: *Science* 369.6501 (2020), eaay3676.

[134] Daniel C. Edelstein, Elliot S. Wachman, and Chung-Liang Tang. "Broadly tunable high repetition rate femtosecond optical parametric oscillator." In: *Applied Physics Letters* 54.18 (1989), pp. 1728–1730.

[135] Alireza Marandi, Kirk A. Ingold, Marc Jankowski, and Robert L. Byer. "Cascaded half-harmonic generation of femtosecond frequency combs in the mid-infrared." In: *Optica* 3.3 (2016), pp. 324–327.

[136] Marc Jankowski, Alireza Marandi, Christopher R. Phillips, Ryan Hamerly, Kirk A. Ingold, Robert L. Byer, and Martin M. Fejer. "Temporal simultons in optical parametric oscillators." In: *Physical Review Letters* 120.5 (2018), p. 053904.

[137] Arkadev Roy, Rajveer Nehra, Saman Jahani, Luis Ledezma, Carsten Langrock, Martin Fejer, and Alireza Marandi. "Temporal walk-off induced dissipative quadratic solitons." In: *Nature Photonics* 16.2 (2022), pp. 162–168. DOI: 10.1038/s41566-021-00942-4.

[138] Lin Chang, Songtao Liu, and John E. Bowers. "Integrated optical frequency comb technologies." In: *Nature Photonics* 16.2 (2022), pp. 95–108.

[139] Kerry J. Vahala. "Optical microcavities." In: *Nature* 424.6950 (2003), pp. 839–846.

[140] Ming Cai, Oskar Painter, and Kerry J. Vahala. "Observation of critical coupling in a fiber taper to a silica-microsphere whispering-gallery mode system." In: *Physical Review Letters* 85.1 (2000), p. 74.

[141] Deniz K. Armani, Tobias J. Kippenberg, Sean M. Spillane, and Kerry J. Vahala. "Ultra-high-Q toroid microcavity on a chip." In: *Nature* 421.6926 (2003), pp. 925–928.

[142] Pascal Del'Haye, Albert Schliesser, Olivier Arcizet, Tom Wilken, Ronald Holzwarth, and Tobias J. Kippenberg. "Optical frequency comb generation from a monolithic microresonator." In: *Nature* 450.7173 (2007), pp. 1214–1217.

[143] Jacob S. Levy, Alexander Gondarenko, Mark A. Foster, Amy C. Turner-Foster, Alexander L. Gaeta, and Michal Lipson. "CMOS-compatible multiple-wavelength oscillator for on-chip optical interconnects." In: *Nature Photonics* 4.1 (2010), pp. 37–40.

[144] Luca Razzari, David Duchesne, Marcello Ferrera, Roberto Morandotti, Sai Chu, Brent E. Little, and David J. Moss. "CMOS-compatible integrated optical hyper-parametric oscillator." In: *Nature Photonics* 4.1 (2010), pp. 41–45.

[145] François Leo, Stéphane Coen, Pascal Kockaert, Simon-Pierre Gorza, Philippe Emplit, and Marc Haelterman. "Temporal cavity solitons in one-dimensional Kerr media as bits in an all-optical buffer." In: *Nature Photonics* 4.7 (2010), pp. 471–476.

[146] Tobias Herr, Victor Brasch, John D. Jost, Christine Y. Wang, Nikita M. Kondratiev, Michael L. Gorodetsky, and Tobias J. Kippenberg. "Temporal solitons in optical microresonators." In: *Nature Photonics* 8.2 (2014), pp. 145–152. DOI: 10.1038/nphoton.2013.343.

[147] Ewelina Obrzud, Monica Rainer, Avet Harutyunyan, Miles H. Anderson, Junqiu Liu, Michael Geiselmann, Bruno Chazelas, Stefan Kundermann, Steve Lecomte, Massimo Cecconi, et al. "A microphotonic astrocomb." In: *Nature Photonics* 13.1 (2019), pp. 31–35. DOI: `doi.org/10.1038/s41566-018-0309-y`.

[148] Mengjie Yu, Yoshitomo Okawachi, Austin G. Griffith, Nathalie Picqué, Michal Lipson, and Alexander L. Gaeta. "Silicon-chip-based mid-infrared dual-comb spectroscopy." In: *Nature Communications* 9.1 (2018), p. 1869.

[149] Mian Zhang, Cheng Wang, Rebecca Cheng, Amirhassan Shams-Ansari, and Marko Lončar. "Monolithic ultra-high-Q lithium niobate microring resonator." In: *Optica* 4.12 (2017), pp. 1536–1537.

[150] Mian Zhang, Cheng Wang, Prashanta Kharel, Di Zhu, and Marko Lončar. "Integrated lithium niobate electro-optic modulators: When performance meets scalability." In: *Optica* 8.5 (2021), pp. 652–667. DOI: `10.1038/s41586-018-0551-y`.

[151] Mian Zhang, Brandon Buscaino, Cheng Wang, Amirhassan Shams-Ansari, Christian Reimer, Rongrong Zhu, Joseph M. Kahn, and Marko Lončar. "Broadband electro-optic frequency comb generation in a lithium niobate microring resonator." In: *Nature* 568.7752 (2019), pp. 373–377.

[152] Yaowen Hu, Mengjie Yu, Brandon Buscaino, Neil Sinclair, Di Zhu, Rebecca Cheng, Amirhassan Shams-Ansari, Linbo Shao, Mian Zhang, Joseph M. Kahn, et al. "High-efficiency and broadband on-chip electro-optic frequency comb generators." In: *Nature Photonics* 16.10 (2022), pp. 679–685.

[153] Marc Jankowski, Carsten Langrock, Boris Desiatov, Alireza Marandi, Cheng Wang, Mian Zhang, Christopher R. Phillips, Marko Lončar, and Martin M. Fejer. "Ultrabroadband nonlinear optics in nanophotonic periodically poled lithium niobate waveguides." In: *Optica* 7.1 (2020), pp. 40–46.

[154] Luis Ledezma, Ryoto Sekine, Qiushi Guo, Rajveer Nehra, Saman Jahani, and Alireza Marandi. "Intense optical parametric amplification in dispersion-engineered nanophotonic lithium niobate waveguides." In: *Optica* 9.3 (2022), pp. 303–308. DOI: `10.1364/OPTICA.442332`.

[155] Marc Jankowski, Nayara Jornod, Carsten Langrock, Boris Desiatov, Alireza Marandi, Marko Lončar, and Martin M. Fejer. "Quasi-static optical parametric amplification." In: *Optica* 9.3 (2022), pp. 273–279.

Chapter 2

THEORETICAL BACKGROUND

2.1 Chapter Overview

In this chapter, we introduce the theoretical foundations required for the discussions found in later sections of this thesis. Our analysis is based on the presentations in [1–6]. We begin in 2.2 by introducing Maxwell's equations, which form the basis of the theoretical derivations in this section. We continue in 2.3 by introducing the idea of the nonlinear polarization. We next present in 2.4 the concept of spatial modes, which represent linear eigenmodes of Maxwell's equations. Using these ideas, we derive a propagation equation for multi-mode quadratic nonlinear interactions in a waveguide in 2.5. With appropriate simplifications, we reduce this model in 2.6 to the more commonly used multi-envelope equations. These propagation equations form the bedrock of the theoretical analyses presented in later sections of the thesis. The preceding derivations lead naturally into a discussion of quasi-phase matching in 2.7. Next, in 2.8, we present a basic theoretical analysis of OPOs. Finally, in 2.9, we introduce concepts related to pulse trains and optical frequency combs.

2.2 Maxwell's Equations

We begin our theoretical analysis by introducing Maxwell's equations. As we will show, nonlinear optical phenomena may be readily derived from Maxwell's equations with the inclusion of an appropriate nonlinear polarization term. Furthermore, we will see that in many physical systems of interest, appropriate spatial eigenmodes of Maxwell's equations may be found which can be used to greatly simplify the theoretical description of the system behaviors. We write Maxwell's equations in a medium as

$$\nabla \cdot \mathbf{D} = \rho, \tag{2.1a}$$

$$\nabla \cdot \mathbf{B} = 0, \tag{2.1b}$$

$$\nabla \times \mathbf{E} = -\frac{\partial \mathbf{B}}{\partial t}, \tag{2.1c}$$

$$\nabla \times \mathbf{H} = \mathbf{J} + \frac{\partial \mathbf{D}}{\partial t}. \tag{2.1d}$$

Here, $\mathbf{E}(\mathbf{r}, t)$ and $\mathbf{D}(\mathbf{r}, t)$ are the electric field and electric flux density, respectively, which are in general functions of space, $\mathbf{r}$ and time, t. Likewise, $\mathbf{H}(\mathbf{r}, t)$ and $\mathbf{B}(\mathbf{r}, t)$ represent the magnetic field and magnetic flux density, respectively. Finally, ρ represents the charge density and $\mathbf{J}$ the current density.

Before proceeding further, we briefly make a note about convention. In the following derivation, we consider the following Fourier transform relation. Quantities in the frequency domain, denoted with a tilde (i.e., $\tilde{f}(\omega)$) are related to their time-domain counterparts, $f(t)$, as

$$\tilde{f}(\omega) \equiv \mathcal{F}\{f(t)\} \equiv \int_{-\infty}^{\infty} f(t) e^{i\omega t} dt. \tag{2.2}$$

Tilde's will not be used, however, for certain quantities expressed only in the frequency domain, particularly the linear and nonlinear susceptibility tensors. With this definition of the Fourier transform, Maxwell's equations in the frequency domain become

$$\nabla \cdot \tilde{\mathbf{D}} = \tilde{\rho}, \tag{2.3a}$$

$$\nabla \cdot \tilde{\mathbf{B}} = 0, \tag{2.3b}$$

$$\nabla \times \tilde{\mathbf{E}} = i\omega \tilde{\mathbf{B}}, \tag{2.3c}$$

$$\nabla \times \tilde{\mathbf{H}} = \tilde{\mathbf{J}} - i\omega \tilde{\mathbf{D}}. \tag{2.3d}$$

In this thesis, we consider dielectric materials which are nonlinear, inhomogeneous, anisotropic, and non-magnetic. In this case, we have the following relations for the $\tilde{\mathbf{E}}$ and $\tilde{\mathbf{D}}$ fields as well as the $\tilde{\mathbf{B}}$ and $\tilde{\mathbf{H}}$ fields,

$$\tilde{\mathbf{D}} = \tilde{\epsilon}\tilde{\mathbf{E}} + \tilde{\mathbf{P}}_{\mathrm{NL}}, \tag{2.4a}$$

$$\tilde{\mathbf{B}} = \mu_0 \tilde{\mathbf{H}}, \tag{2.4b}$$

where $\tilde{\epsilon} = \epsilon_0(1 + \chi^{(1)}) = \epsilon_0 \tilde{\epsilon}_r$ is the linear permittivity which is in general a rank two tensor which may vary in both space and frequency, $\chi^{(1)}$ is the linear susceptibility, ϵ_0 is the permittivity of free space, ϵ_r is the relative permittivity, μ_0 is the permeability of free space, and $\tilde{\mathbf{P}}_{\mathrm{NL}}$ represents the nonlinear contributions to the polarization density. In the next section, we will discuss this nonlinear polarization in more detail.

2.3 Nonlinear Polarization

As discussed in section 1.1, nonlinear optics is called as such as it refers to processes for which the optical response of a material varies nonlinearly with respect to an incident electric field. This is typically expressed through the following Taylor expansion of the polarization density, $\tilde{\mathbf{P}}(\mathbf{r}, \omega)$, as

$$\tilde{\mathbf{P}} = \epsilon_0(\chi^{(1)}\tilde{\mathbf{E}} + \chi^{(2)} : \tilde{\mathbf{E}}\tilde{\mathbf{E}} + \chi^{(3)} : \tilde{\mathbf{E}}\tilde{\mathbf{E}}\tilde{\mathbf{E}} + ...) = \tilde{\mathbf{P}}_{\mathrm{L}} + \tilde{\mathbf{P}}_{\mathrm{NL}}. \qquad (2.5)$$

Here, $\chi^{(i)}$ is in general a tensor of rank $i + 1$ describing the nonlinear interaction of the ith order, the elements of which depend on the specific properties of the material under consideration. As was hinted at in the preceding section, we will commonly divide the polarization into a linear component, $\tilde{\mathbf{P}}_{\mathrm{L}} = \epsilon_0\chi^{(1)}\tilde{\mathbf{E}}$, and a nonlinear component, $\tilde{\mathbf{P}}_{\mathrm{NL}}$, which contains all remaining elements of the polarization.

In this thesis, we will focus on non-centrosymmetric materials exhibiting a quadratic ($\chi^{(2)}$) nonlinearity and further make the assumption that, in the systems considered, the quadratic response is a appreciably larger than the cubic and higher-order responses such that these higher order terms may be ignored. We may thus write the ith cartesian component of the nonlinear polarization in the frequency domain as

$$\tilde{P}_{\mathrm{NL},i}(\omega) = \epsilon_0 \sum_{j,k} \int \chi_{ijk}^{(2)}(\omega, \omega')\tilde{E}_j(\omega')\tilde{E}_k(\omega - \omega')d\omega'. \qquad (2.6)$$

We note here that throughout this thesis, we will sometimes interchange $\chi_{ijk}^{(2)}$ with $d_{ijk} = \frac{1}{2}\chi_{ijk}^{(2)}$. If we assume that the $\chi_{ijk}^{(2)}$ is non-dispersive and thus does not depend on frequency, we may remove it from the integral to obtain

$$\tilde{P}_{\mathrm{NL},i}(\omega) = \epsilon_0 \sum_{j,k} \chi_{ijk}^{(2)} \int \tilde{E}_j(\omega')\tilde{E}_k(\omega - \omega')d\omega' = \epsilon_0 \sum_{j,k} \chi_{ijk}^{(2)}\tilde{E}_j(\omega) * \tilde{E}_k(\omega). \qquad (2.7)$$

Finally, if we assume the light is linearly polarized along a single coordinate axis (as will typically be the case in the considered experiments using type 0 phase-matching), the sum reduces to a single term, which we write, dropping the coordinate labels, as

$$\tilde{P}_{\mathrm{NL}}(\omega) = \epsilon_0\chi^{(2)}\tilde{E}(\omega) * \tilde{E}(\omega), \qquad (2.8)$$

or, in the time domain,

$$P_{\text{NL}}(t) = \epsilon_0 \chi^{(2)} E(t) E(t). \tag{2.9}$$

2.4 Spatial Modes

In analyzing nonlinear optical systems, it is helpful to first decompose the electric (and magnetic) field into spatial modes, here defined as eigenmodes of Maxwell's equations in the system under consideration, ignoring nonlinear contributions. To start, let us look at equations 2.3c and 2.3d, ignoring the current source term. Taking the curl of both sides, we have

$$\nabla \times \nabla \times \tilde{\mathbf{E}} = i\omega\mu_0 \nabla \times \tilde{\mathbf{H}}, \tag{2.10a}$$

$$\nabla \times \nabla \times \tilde{\mathbf{H}} = -i\omega \nabla \times \tilde{\epsilon}\tilde{\mathbf{E}}, \tag{2.10b}$$

where we have made use of equations 2.4a and 2.4b, ignoring the nonlinear term. Using the vector curl identity along with equations 2.3a and 2.3b, this becomes

$$i\omega\mu_0 \nabla \times \tilde{\mathbf{H}} + \nabla^2 \tilde{\mathbf{E}} = 0, \tag{2.11a}$$

$$i\omega \nabla \times \tilde{\epsilon}\tilde{\mathbf{E}} - \nabla^2 \tilde{\mathbf{H}} = 0. \tag{2.11b}$$

Ignoring any spatial dependence of $\tilde{\epsilon}$, insertion of 2.3c and 2.3d yield the Helmholtz equation

$$\omega^2 \mu_0 \tilde{\epsilon}\tilde{\mathbf{E}} + \nabla^2 \tilde{\mathbf{E}} = 0, \tag{2.12a}$$

$$\omega^2 \mu_0 \tilde{\epsilon}\tilde{\mathbf{H}} + \nabla^2 \tilde{\mathbf{H}} = 0. \tag{2.12b}$$

We may readily find solutions to the system of the form

$$\tilde{\mathbf{E}}(\mathbf{r}, \omega) = \tilde{\mathbf{e}}(\omega) e^{\pm i\mathbf{k}\cdot\mathbf{r}}, \tag{2.13a}$$

$$\tilde{\mathbf{H}}(\mathbf{r}, \omega) = \tilde{\mathbf{h}}(\omega) e^{\pm i\mathbf{k}\cdot\mathbf{r}}. \tag{2.13b}$$

Here, $\tilde{\mathbf{e}}(\omega)$ and $\tilde{\mathbf{h}}(\omega)$ represent electric field and magnetic field mode functions at frequency ω and $\mathbf{k}$ is the wavenumber, which satisfies $|\mathbf{k}| = \sqrt{\omega^2 \mu_0 \tilde{\epsilon}} = \frac{n\omega}{c}$, $i \in \{x, y, z\}$. The $\pm$ solutions refer to forward and backwards-propagating waves,

respectively. We have here defined the refractive index, $n = \sqrt{\tilde{\epsilon}_r}$ (defined as such because the relative permeability was taken as 1 for the considered nonmagnetic medium), and speed of light in a vacuum, $c = \frac{1}{\sqrt{\mu_0 \epsilon_0}}$. Taking the inverse Fourier transform, we have

$$\mathbf{E}(\mathbf{r}, t) = \int_{-\infty}^{\infty} \tilde{\mathbf{e}}(\omega) e^{-i(\omega t \mp \mathbf{k} \cdot \mathbf{r})} d\omega, \tag{2.14a}$$

$$\mathbf{H}(\mathbf{r}, t) = \int_{-\infty}^{\infty} \tilde{\mathbf{h}}(\omega) e^{-i(\omega t \mp \mathbf{k} \cdot \mathbf{r})} d\omega. \tag{2.14b}$$

This shows that in this simplest case, where we have ignored any spatial dependence of $\tilde{\epsilon}$, the time-domain wave solutions may be represented as an infinite sum of monochromatic plane waves of the form $\tilde{\mathbf{e}}(\omega_n) e^{-i(\omega_n t \mp \mathbf{k_n} \cdot \mathbf{r})}$, and likewise for the magnetic field, where ω_n is the frequency of the wave and $\mathbf{k_n}$ is the corresponding wavenumber. Since the permittivity was taken to have no spatial dependence, we observe that the mode functions in this case also exhibit no spatial dependence.

In the context of the nonlinear systems we wish to study, typically driven by laser light, we desire to find the evolution of the wave as it propagates. To simplify our expressions without a loss of generality, we consider waves which propagate along z. We also wish to extend the spatially invariant plane wave modes we have derived in equations 2.13a and 2.13b to account for propagation in waveguides or other spatially varying systems (including capturing the finite beam width of a laser in a free-space system). As such, we consider a more general modal expansion of the following form

$$\tilde{\mathbf{E}}(\mathbf{r}, \omega) = \sum_n \tilde{C}_n(z, \omega) \tilde{\mathbf{e}}_n(\omega, x, y) e^{i\beta_n(\omega)z}, \tag{2.15a}$$

$$\tilde{\mathbf{H}}(\mathbf{r}, \omega) = \sum_n \tilde{C}_n(z, \omega) \tilde{\mathbf{h}}_n(\omega, x, y) e^{i\beta_n(\omega)z}. \tag{2.15b}$$

Here, as above, $\tilde{\mathbf{e}}_n(\omega, x, y) e^{i\beta_n(\omega)z}$ and $\tilde{\mathbf{h}}_n(\omega, x, y) e^{i\beta_n(\omega)z}$ represent eigenmodes of Maxwell's equation, ignoring any nonlinear contribution to the polarization, but we now allow for spatial dependence transverse to the direction of propagation. We additionally have replaced $k(\omega)$ with the closely related phase constants $\beta_n(\omega)$. Finally, we have introduced the quantity $\tilde{C}_n(z, \omega)$ which represents a unitless modal amplitude that describes the evolution of the fields as they propagate. The modes are orthogonal and are normalized to the following convention

$$\int_A (\text{Re}\{\tilde{\mathbf{e}}_n(\omega, x, y) \times \tilde{\mathbf{h}}_m^*(\omega, x, y) \cdot \hat{\mathbf{z}}\}) dx dy = 2\delta_{mn}\tilde{\Phi}(\omega), \qquad (2.16)$$

where δ_{mn} is a Kronecker delta function and Φ is a normalization constant with units of power, which we typically set as $\tilde{\Phi}(\omega) = 1$ W for convenience. The power in a single mode at a frequency ω and position z is given by

$$\begin{aligned}
\int_A \tilde{I}_n(\omega, x, y) dx dy &= \int_A \text{Re}\{\tilde{S}_{n,z}(\omega, x, y)\} dx dy \\
&= |\tilde{C}_n(z, \omega)|^2 \frac{1}{2} \int_A \text{Re}\{\tilde{\mathbf{e}}_n(\omega, x, y) \times \tilde{\mathbf{h}}_n(\omega, x, y) \cdot \hat{\mathbf{z}}\} dx dy \\
&= \tilde{\Phi}(\omega)|\tilde{C}_n(z, \omega)|^2. \quad (2.17)
\end{aligned}$$

In the first line, we have made reference to the intensity $\tilde{I}_n(\omega, x, y)$ and Poynting vector, $\tilde{\mathbf{S}}_n(\omega, x, y)$. This further shows why taking $\tilde{\Phi}(\omega) = 1$ W is a convenient normalization, as then the complex modal amplitude, $\tilde{C}_n(z, \omega)$, directly carries the information about the power in mode n at frequency ω. Another important quantity of interest is the mode area, $A_{\text{mode},n}(\omega)$, which can be calculated as

$$A_{\text{mode},n}(\omega) = \frac{(\int_A I_n(\omega, x, y) dx dy)^2}{\int_A I_n^2(\omega, x, y) dx dy}. \qquad (2.18)$$

It is then helpful in some situations to define normalized mode profiles, $\tilde{\mathbf{e}}_n'(\omega, x, y)$ and $\tilde{\mathbf{h}}_n'(\omega, x, y)$ as

$$\tilde{\mathbf{e}}_n(\omega, x, y) = \sqrt{\frac{2Z_0\tilde{\Phi}(\omega)}{n_{\text{eff},n}(\omega)A_{\text{mode},n}(\omega)}} \tilde{\mathbf{e}}_n'(\omega, x, y), \qquad (2.19a)$$

$$\tilde{\mathbf{h}}_n(\omega, x, y) = \sqrt{\frac{2n_{\text{eff},n}(\omega)\tilde{\Phi}(\omega)}{Z_0 A_{\text{mode},n}(\omega)}} \tilde{\mathbf{h}}_n'(\omega, x, y), \qquad (2.19b)$$

where Z_0 is the impedance of free space and $n_{\text{eff},n}$ is the effective index of mode n. In this normalization, $A_{\text{mode},n} = \int_A \text{Re}\{\tilde{\mathbf{e}}_n' \times \tilde{\mathbf{h}}_n'^* \cdot \hat{\mathbf{z}}\} dx dy$. This normalization helps to move seamlessly between integrated and bulk systems. Specifically, in bulk crystals, assuming the interaction occurs between focused fundamental Gaussian beams, one convenient choice is to approximate the beam as having a flat-top profile over a circle of radius $w_0(\omega)$, where $w_0(\omega)$ is the Gaussian beam waist. For example, assuming an x-polarized beam we may take

$$\tilde{\mathbf{e}}'(\omega, x, y) = \begin{cases} \hat{\mathbf{x}}, & x^2 + y^2 \le w_0(\omega)^2, \\ 0, & \text{otherwise}, \end{cases} \tag{2.20a}$$

$$\tilde{\mathbf{h}}'(\omega, x, y) = \begin{cases} \hat{\mathbf{y}}, & x^2 + y^2 \le w_0(\omega)^2, \\ 0, & \text{otherwise}. \end{cases} \tag{2.20b}$$

This allows for the finite width of the beam to be accounted for while maintaining the modes as solutions of the Helmholtz equation, apart from the discontinuity in the derivative at $x^2 + y^2 = w_0(\omega)^2$, being spatially truncated plane waves. The validity of this approximation generally demands that the waist of the Gaussian beam be significantly narrower than the smallest transverse dimension of the crystal and the length of the crystal be shorter than the confocal parameter (such that the phase front is flat and thus well-approximated by a plane wave over the course of the interaction). Another choice is

$$\tilde{\mathbf{e}}'(\omega, x, y) = e^{-\frac{x^2+y^2}{w_0(\omega)^2}} \hat{\mathbf{x}}, \tag{2.21a}$$

$$\tilde{\mathbf{h}}'(\omega, x, y) = e^{-\frac{x^2+y^2}{w_0(\omega)^2}} \hat{\mathbf{y}}. \tag{2.21b}$$

This choice better approximates the exact Gaussian beam profile but does not exactly solve the Helmholtz equation, as the Gaussian beam solution relies on making the paraxial approximation. For either choice, we find $A_{\text{mode}} = \pi w_0^2$, as expected. Mode profiles of waveguides and other more complex systems may be found using commercial solvers.

2.5 Nonlinear Propagation and the Single-Envelope Equation

Having introduced the nonlinear polarization and defined the waveguide modes, we may now derive the propagation equation for the electric field in a nonlinear medium. To start, we consider two distinct fields, which we refer to using superscripts, for example $\tilde{\mathbf{E}}^{(1)}$ and $\tilde{\mathbf{E}}^{(2)}$. We begin by taking the dot product of the complex conjugate of the electric and magnetic fields of the first wave, $\tilde{\mathbf{E}}^{(1)*}$ and $\tilde{\mathbf{H}}^{(1)*}$, with the appropriate Maxwell equations, respectively 2.3c and 2.3d, expressed in terms of the second wave, giving

$$\tilde{\mathbf{H}}^{(1)*} \cdot (\nabla \times \tilde{\mathbf{E}}^{(2)}) = i\omega\mu_0 \tilde{\mathbf{H}}^{(1)*} \cdot \tilde{\mathbf{H}}^{(2)}, \tag{2.22a}$$

$$\tilde{\mathbf{E}}^{(1)*} \cdot (\nabla \times \tilde{\mathbf{H}}^{(2)}) = -i\omega\tilde{\mathbf{E}}^{(1)*} \cdot \tilde{\epsilon}\tilde{\mathbf{E}}^{(2)} - i\omega\tilde{\mathbf{E}}^{(1)*} \cdot \tilde{\mathbf{P}}_{\text{NL}}^{(2)}, \qquad (2.22\text{b})$$

where we have again assumed the current density is 0 and made use of the relations 2.4a and 2.4b. Subtracting 2.22a from 2.22b gives

$$\tilde{\mathbf{E}}^{(1)*} \cdot (\nabla \times \tilde{\mathbf{H}}^{(2)}) - \tilde{\mathbf{H}}^{(1)*} \cdot (\nabla \times \tilde{\mathbf{E}}^{(2)}) =$$
$$- i\omega(\tilde{\mathbf{E}}^{(1)*} \cdot \tilde{\epsilon}\tilde{\mathbf{E}}^{(2)} + \tilde{\mathbf{E}}^{(1)*} \cdot \tilde{\mathbf{P}}_{\text{NL}}^{(2)} + \mu_0\tilde{\mathbf{H}}^{(1)*} \cdot \tilde{\mathbf{H}}^{(2)}). \quad (2.23)$$

Without repeating the above steps, we write the equivalent expression, interchanging the first and second fields, and take the complex conjugate to give

$$\tilde{\mathbf{E}}^{(2)} \cdot (\nabla \times \tilde{\mathbf{H}}^{(1)*}) - \tilde{\mathbf{H}}^{(2)} \cdot (\nabla \times \tilde{\mathbf{E}}^{(1)*}) =$$
$$i\omega(\tilde{\mathbf{E}}^{(2)} \cdot \tilde{\epsilon}\tilde{\mathbf{E}}^{(1)*} + \tilde{\mathbf{E}}^{(2)} \cdot \tilde{\mathbf{P}}_{\text{NL}}^{(1)*} + \mu_0\tilde{\mathbf{H}}^{(2)} \cdot \tilde{\mathbf{H}}^{(1)*}). \quad (2.24)$$

Here, we have assumed real $\tilde{\epsilon}$. Summing equations 2.23 and 2.24 and using the vector identity $\mathbf{A} \cdot (\nabla \times \mathbf{B}) = \mathbf{B} \cdot \nabla \times \mathbf{A} - \mathbf{A} \cdot \nabla \times \mathbf{B}$ gives

$$\nabla \cdot (\tilde{\mathbf{H}}^{(2)} \times \tilde{\mathbf{E}}^{(1)*} + \tilde{\mathbf{H}}^{(1)*} \times \tilde{\mathbf{E}}^{(2)}) = i\omega(\tilde{\mathbf{E}}^{(2)} \cdot \tilde{\mathbf{P}}_{\text{NL}}^{(1)*} - \tilde{\mathbf{E}}^{(1)*} \cdot \tilde{\mathbf{P}}_{\text{NL}}^{(2)}). \qquad (2.25)$$

We next integrate over the plane transverse to the direction of propagation. To do so, we use a corollary the divergence theorem which we will define below. The usual statement of the divergence theorem for a given function $\mathbf{F}$ is

$$\iiint_V (\nabla \cdot \mathbf{F})dV = \oiint_S (\mathbf{F} \cdot \hat{\mathbf{n}})dS, \qquad (2.26)$$

where $\hat{\mathbf{n}}$ is the surface normal. Next, we note that the desired area integral may be written in terms of a volume integral where the considered volume is infinite in x and y and infinitesimal in z. In particular, we have

$$\iint_A (\nabla \cdot \mathbf{F})dA = \lim_{\Delta z \to 0} \frac{1}{\Delta z} \iiint_V (\nabla \cdot \mathbf{F})dV. \qquad (2.27)$$

Through application of the divergence theorem, we arrive at the desired corollary which we write as

$$\iint_A (\nabla \cdot \mathbf{F}) dA = \oint_{l(A)} (\mathbf{F} \cdot \hat{\mathbf{r}}) dl + \frac{\partial}{\partial z} \iint_A (\mathbf{F} \cdot \hat{\mathbf{z}}) dA. \tag{2.28}$$

Here, $l(A)$ refers to the line integral around the area defined by A and $\hat{\mathbf{r}}$ represents the unit vector pointing radially outward in the xy-plane. By application of 2.28 to the area integral of 2.25, we find

$$\oint_{l(A)} ((\tilde{\mathbf{H}}^{(2)} \times \tilde{\mathbf{E}}^{(1)*} + \tilde{\mathbf{H}}^{(1)*} \times \tilde{\mathbf{E}}^{(2)}) \cdot \hat{\mathbf{r}}) dl$$
$$+ \frac{\partial}{\partial z} \iint_A ((\tilde{\mathbf{H}}^{(2)} \times \tilde{\mathbf{E}}^{(1)*} + \tilde{\mathbf{H}}^{(1)*} \times \tilde{\mathbf{E}}^{(2)}) \cdot \hat{\mathbf{z}}) dA$$
$$= i\omega \iint_A (\tilde{\mathbf{E}}^{(2)} \cdot \tilde{\mathbf{P}}_{\mathrm{NL}}^{(1)*} - \tilde{\mathbf{E}}^{(1)*} \cdot \tilde{\mathbf{P}}_{\mathrm{NL}}^{(2)}) dA. \tag{2.29}$$

To derive the desired dynamics, we take the second field, $\tilde{\mathbf{E}}^{(2)}$, to participate in the nonlinear interaction and consider the first field, $\tilde{\mathbf{E}}^{(1)}$, to be a linear mode of the system. As such, we expand $\tilde{\mathbf{E}}^{(2)}$ and $\tilde{\mathbf{H}}^{(2)}$ according to equations 2.15a and 2.15b and take $\tilde{\mathbf{P}}_{\mathrm{NL}}^{(2)} = \tilde{\mathbf{P}}_{\mathrm{NL}}$. Meanwhile, we set $\tilde{\mathbf{E}}^{(1)} = \tilde{\mathbf{e}}_m e^{i\beta_m z}$ and $\tilde{\mathbf{P}}_{\mathrm{NL}}^{(1)} = 0$. With these definitions, we find that equation 2.29 becomes

$$\frac{\partial}{\partial z} \sum_n e^{i(\beta_n - \beta_m)z} \tilde{C}_n \int_A ((\tilde{\mathbf{h}}_n \times \tilde{\mathbf{e}}_m^* + \tilde{\mathbf{h}}_n \times \tilde{\mathbf{e}}_m^*) \cdot \hat{\mathbf{z}}) dA$$
$$= -i\omega e^{-i\beta_m z} \int_A \tilde{\mathbf{e}}_m^* \cdot \tilde{\mathbf{P}}_{NL} dA. \tag{2.30}$$

Further simplification of the left-hand side using the mode orthogonality relation defined in equation 2.16 yields

$$\frac{\partial}{\partial z} \tilde{C}_m(z, \omega) = \frac{i\omega}{4\tilde{\Phi}(\omega)} e^{-i\beta_m(\omega)z} \int_A \tilde{\mathbf{e}}_m^*(x, y, \omega) \cdot \tilde{\mathbf{P}}_{\mathrm{NL}}(\mathbf{r}, \omega) dA. \tag{2.31}$$

To proceed, we introduce the fast-evolving envelope $\tilde{R}_m(z, \omega) = \tilde{C}_m(z, \omega) e^{i\beta_m z}$. Then, 2.31 becomes

$$\frac{\partial}{\partial z} \tilde{R}_m(z, \omega) = i\beta_m(\omega) \tilde{R}_m(z, \omega) + \frac{i\omega}{4\tilde{\Phi}(\omega)} \int_A \tilde{\mathbf{e}}_m^*(x, y, \omega) \cdot \tilde{\mathbf{P}}_{\mathrm{NL}}(\mathbf{r}, \omega) dA. \tag{2.32}$$

Next, we recall our previous definition of $\tilde{\mathbf{P}}_{\mathrm{NL}}$ from equation 2.6. Here, we expand this previous definition to further include interactions between different modes and then make some simplifying assumptions to reduce the complexity of the expression. The full expression may be written as

$$\tilde{P}_{\mathrm{NL},i}(\mathbf{r},\omega) = \epsilon_0 \sum_{n,l} \sum_{j,k} \int \chi_{ijk}^{(2)}(\mathbf{r},\omega,\omega') \tilde{E}_{n;j}(\mathbf{r},\omega') \tilde{E}_{l;k}(\mathbf{r},\omega-\omega') d\omega'$$

$$= \epsilon_0 \sum_{n,l} \sum_{j,k} \int \left(\chi_{ijk}^{(2)}(\mathbf{r},\omega,\omega') \tilde{e}_{n;j}(\mathbf{r},\omega') \tilde{e}_{l;k}(\mathbf{r},\omega-\omega') \right.$$

$$\left. \tilde{R}_n(\omega) \tilde{R}_l(\omega-\omega') \right) d\omega'. \quad (2.33)$$

In this expression, n and l refer to modes while i, j, and k are coordinate labels. The spatial dependence of both the modes and the nonlinearity have also been included. In this thesis, as previously mentioned, we will consider interactions between linearly polarized modes which act along the same tensor element of the nonlinearity, which we refer to as $\chi^{(2)}$, dropping any subscripts. With this approximation, the integral on the right-hand side of equation 2.32 becomes

$$\int_A \tilde{\mathbf{e}}_m^* \cdot \tilde{\mathbf{P}}_{NL} dA$$

$$= \epsilon_0 \sum_{n,l} \int_A \int \left(\chi^{(2)}(\mathbf{r},\omega,\omega') \tilde{e}_m^*(x,y,\omega) \tilde{e}_n(x,y,\omega') \tilde{e}_l(x,y,\omega-\omega') d\omega' \right.$$

$$\left. \tilde{R}_n(\omega) \tilde{R}_l(\omega-\omega') \right) d\omega' dA. \quad (2.34)$$

Exchanging the order of integration, we have

$$\epsilon_0 \sum_{n,l} \int \left(\tilde{R}_n(\omega) \tilde{R}_l(\omega-\omega') \right.$$

$$\left. \int_A \chi^{(2)}(\mathbf{r},\omega,\omega') \tilde{e}_m^*(x,y,\omega) \tilde{e}_n(x,y,\omega') \tilde{e}_l(x,y,\omega-\omega') d\omega' \right) dA$$

$$= \epsilon_0 \sum_{n,l} \int \tilde{R}_n(\omega) \tilde{R}_l(\omega-\omega') X_{mnl}^{(2)}(z,\omega,\omega') d\omega', \quad (2.35)$$

where in the final line, we have introduced $X_{mnl}(z, \omega, \omega')$, which represents the effective nonlinearity for the interaction between modes m, n, and l at frequencies ω, ω', and $\omega - \omega'$, and is a consequence of their mode overlap integral. Further simplification may be made through taking the nonlinearity to be non-dispersive, allowing us to further simplify $X_{mnl}(z, \omega, \omega') \approx X_{mnl}(z) = X_{mnl,0}\bar{d}(z)$. Here, $\bar{d}(z)$ contains the variation of the nonlinearity along z. This will allow us to model quasi-phase matching, a concept which we will discuss shortly. Through the ensuing discussion, we will allow $\bar{d}(z)$ to be complex and assume that $X_{mnl,0}$ is otherwise real.

With this simplification, we find

$$\int_A \tilde{\mathbf{e}}_m^* \cdot \tilde{\mathbf{P}}_{NL} dA = \epsilon_0 \sum_{n,l} X_{mnl,0}\bar{d}(z)\mathcal{F}\{R_n(z,t)R_l(z,t)\}. \tag{2.36}$$

Then, the propagation equation 2.31 may be rewritten as

$$\frac{\partial}{\partial z}\tilde{R}_m(z,\omega) = i\beta_m\tilde{R}_m(z,\omega) + \frac{i\omega}{4\tilde{\Phi}(\omega)}\epsilon_0 \sum_{n,l} X_{mnl,0}\bar{d}(z)\mathcal{F}\{R_n(z,t)R_l(z,t)\}. \tag{2.37}$$

Finally, if we assume that all interactions are between the same spatial mode, we may drop all subscripts m, l, n to arrive at

$$\frac{\partial}{\partial z}\tilde{R}(z,\omega) = i\beta(\omega)\tilde{R}(z,\omega) + \frac{i\omega}{4\tilde{\Phi}(\omega)}\epsilon_0 X_0\bar{d}(z)\mathcal{F}\{R(z,t)^2\}. \tag{2.38}$$

Until now, we have not made any constraints regarding the frequency extent of $\tilde{R}(z,\omega)$. However, we would like for our propagation equation to work for analytic signals containing only positive frequency components [7]. This requires a small modification of the equation as follows.

First, we establish the time-domain signal, $R(z,t)$ as real. We may then write it as a sum of complex envelope functions, $V(z,t)$. In particular, we have $R(z,t) = \frac{1}{2}[V(z,t)e^{-i(\omega_0 t - \beta_0 z - \frac{\omega_0}{v_0}z)} + V^*(z,t)e^{i(\omega_0 t - \beta_0 z - \frac{\omega_0}{v_0}z)}]$. Here, $\beta_0 = \beta(\omega_0)$, ω_0, and v_0 represent the reference phase constant, reference frequency, and reference velocity, respectively. We may then define the analytic signal, $U(z,t)$. $U(z,t)$ is related to $R(z,t)$ as

$$U(z,t) = R(z,t) + i\mathcal{H}[R](z,t), \tag{2.39}$$

where $\mathcal{H}[R](z,t) = \frac{1}{\pi}\text{p.v.}\int_{-\infty}^{\infty}\frac{R(z,t')}{t-t'}dt'$ represents the Hilbert transform and p.v. indicates the Cauchy principal value of the integral. In the frequency domain, we have that

$$
\tilde{U}(z,\omega) = \begin{cases} 2\tilde{R}(z,\omega), \ \omega > 0, \\ \tilde{R}(z,\omega), \ \omega = 0, \\ 0, \ \omega < 0. \end{cases} \tag{2.40}
$$

Since we have defined $R(z,t)$ to be real, we may reconstruct $\tilde{R}(z,\omega)$ from $\tilde{U}(z,\omega)$ as $\tilde{R}(z,\omega) = \frac{1}{2}[\tilde{U}(z,\omega) + \tilde{U}^*(z,-\omega)]$. Finally, we may relate $V(z,t)$ to $U(z,t)$ as $V(z,t) = U(z,t)e^{i(\omega_0 t - \beta_0 z - \frac{\omega_0}{v_0}z)}$. As $U(z,t)$ is an analytic signal, the demodulated signal $V(z,t)$ contains frequency content in $[-\omega_0, \infty)$. We had previously arrived at a frequency-domain propagation equation for $\tilde{R}(z,\omega)$ in equation 2.38. We may re-express it in the time domain as

$$
\frac{\partial}{\partial z}R(z,t) = i\mathcal{F}^{-1}\{\beta(\omega)\tilde{R}(z,\omega)\} - \mathcal{F}^{-1}\left\{\frac{1}{4\tilde{\Phi}(\omega)}\right\} * \frac{\partial}{\partial t}P_{\text{NL}}(z,t). \tag{2.41}
$$

Here, $P_{\text{NL}}(z,t)$ takes the simplistic form of equation 2.9, now expressed as $P_{\text{NL}}(z,t) = X_0 d(z)R(z,t)^2$. To find an evolution equation for the analytic signal $U(z,t)$, we have to find an analytic form for $P_{\text{NL}}(z,t)$, which we call $U_P(z,t)$. Here, we have

$$
U_P(z,t) = P_{\text{NL}}(z,t) + i\mathcal{H}[P_{\text{NL}}(z,t)]
$$
$$
\approx \epsilon_0 X_0 \frac{1}{2}[\bar{d}(z)U(z,t)^2 + \bar{d}^*(z)2|U(z,t)|^2], \tag{2.42}
$$

where we have made the approximation $|U(z,t)|^2 + i\mathcal{H}[|U(z,t)|^2] \approx 2|U(z,t)|^2$. This permits the generation of some small amount of negative frequency content, but it can be filtered out by other means in the propagation equation. We may now write the analytic propagation equation in the frequency domain as

$$
\frac{\partial}{\partial z}\tilde{U}(z,\omega) = i\beta(\omega)\tilde{U}(z,\omega) + \frac{i\omega}{8\tilde{\Phi}(\omega)}\epsilon_0 X_0 \mathcal{F}\{\bar{d}(z)U^2(z,t) + 2\bar{d}^*(z)|U(z,t)|^2\}. \tag{2.43}
$$

Finally, in terms of the complex envelope function, $\tilde{V}(z,\omega)$, we have

$$\frac{\partial}{\partial z}\tilde{V}(z,\Omega) = i\left(\beta(\omega) - \beta_0 - \frac{\Omega}{v_0} + i\frac{\alpha(\omega)}{2}\right)\tilde{V}(z,\Omega)$$

$$+ \frac{i\omega}{8\tilde{\Phi}(\omega)}\epsilon_0 X_0 H(\omega)\mathcal{F}_\Omega\left\{\bar{d}(z)V(z,\tau)^2 e^{-i\phi(z,\tau)} + 2\bar{d}^*(z)|V(z,\tau)|^2 e^{i\phi(z,\tau)}\right\}. \quad (2.44)$$

Here, we have introduced a new time coordinate, $\tau = t - \frac{1}{v_0}z$, which is shifted by the reference velocity as well as the envelope angular frequency, $\Omega = \omega - \omega_0$. The subscript Ω in the Fourier transform denotes that it is a transform with respect to this shifted frequency coordinate. We have furthermore defined the phase $\phi(z,\tau) = \omega_0\tau - \beta_0 z - \frac{\omega_0}{v_0}z$. In addition, we have multiplied the nonlinearity by $H(\omega)$, which here represents a Heaviside step function, to stifle interactions with negative frequencies. Lastly, we have added a frequency-dependent loss term in $\alpha(\omega)$.

Equation 2.44 represents the main result of this section. It allows us to model the evolution of broadband, complex envelopes while accounting for all involved quadratic nonlinear processes. As a final comment, we note that it may be readily extended to include, e.g., multiple spatial modes, multiple polarizations, or additional nonlinear processes by reverting some of the simplifications we have made along the way.

2.6 Multi-Envelope and Coupled Wave Equations

While equation 2.44 is extremely powerful, its implementation is often somewhat computationally cumbersome. Additionally, it is challenging to treat analytically. As such, we would like to find simplified models which still capture the dominant physics in a given quadratic nonlinear system of interest. Commonly, in the systems under study, the majority of the energy is localized to a few frequency harmonics, while the contributions of other frequency bands are negligible. In the extreme case where each harmonic is relatively narrow in bandwidth, the broadband complex envelope we have considered thus far is sparsely populated in frequency, making it not only a computationally cumbersome approach but also inefficient. This motivates the expansion of equation 2.44 into a set of multiple envelope equations describing the evolution of different harmonic orders N.

Let us begin by defining $\tilde{U}_N(z,\omega)$ which is an analytic function describing the evolution of the Nth harmonic. It is related to the previously defined $\tilde{U}(z,\omega)$ in that

$$\tilde{U}(z,\omega) = \sum_N \tilde{U}_N(z,\omega). \tag{2.45}$$

The 0th harmonic order corresponds to the DC component of the field, while the remaining harmonics are each localized around integer multiples the 1st harmonic, which may be selected arbitrarily. We write the propagation equation for the Nth harmonic, in analogy to 2.43, as

$$\frac{\partial}{\partial z}\tilde{U}_N(z,\omega) = i\beta(\omega)\tilde{U}_N(z,\omega) + \frac{i\omega}{4\tilde{\Phi}(\omega)}\tilde{P}_{\text{NL},N}(z,\omega). \tag{2.46}$$

Here, $\tilde{P}_{\text{NL},N}(z,\omega)$ describes all of the nonlinear interactions which can generate content at harmonic order N. In particular, it must include all DFG terms involving harmonic orders $N + P$ and P as well as all SFG terms involving orders $N - P$ and P.

Like before, we define complex harmonic envelopes, $V_N(z,t)$, which are related to $U_N(z,t)$ as $V_N(z,t) = U_N(z,t)e^{i(\omega_0 Nt - \beta_{0,N}z - \frac{N\omega_0}{v_0}z)}$. Here, ω_0 is the reference frequency of the first harmonic, $\beta_{0,N} = \beta(N\omega_0)$ is the reference phase constant of the Nth harmonic, and v_0 is the reference velocity. With these definitions, we may rewrite 2.46 in terms of $V_N(z,t)$ as

$$\frac{\partial}{\partial z}\tilde{V}_N(z,\omega) = i\left(\beta(\omega) - \beta_{0,N} - \frac{\Omega_N}{v_0} + i\frac{\alpha(\omega)}{2}\right)\tilde{V}_N(z,\omega) + \frac{i\omega}{4\tilde{\Phi}(\omega)}\tilde{P}_{\text{NL},N}(z,\omega), \tag{2.47}$$

where we now define $\tilde{P}_{\text{NL},N}(z,\omega)$ explicitly as

$$\tilde{P}_{\text{NL},N}(z,\omega)$$
$$= \epsilon_0 \frac{1}{2} \sum_P \left[X_0^{N,P,N-P} \bar{d}(z) \mathcal{F}_{\Omega_N}\{V_P(z,\tau)V_{N-P}(z,\tau)\}\right]e^{i(\beta_{0,P}+\beta_{0,N-P}-\beta_{0,N})z}$$
$$+ 2X_0^{N+P,N,P}\bar{d}^*(z)\mathcal{F}_{\Omega_N}\{V_P^*(z,\tau)V_{N+P}(z,\tau)\}]e^{-i(\beta_{0,P}+\beta_{0,N-P}-\beta_{0,N})z}\Bigg]. \tag{2.48}$$

Here, $\Omega_N = \omega - \omega_{0,N}$, and the $V_P V_{N-P}$ and $V_P^* V_{N+P}$ terms account for SFG and DFG interactions, respectively. We have also added the loss term, $\alpha(\omega)$. Finally, we have introduced the effective nonlinear coefficient, $X_0^{N,P,N-P}$, analogous to the previously defined X_0, which is defined through the mode overlap integral

$$X_0^{N,P,N-P} \bar{d}(z)$$
$$= \int_A \chi^{(2)}(\mathbf{r}, N\omega_0, P\omega_0) \tilde{e}^*(x, y, N\omega_0) \tilde{e}(x, y, P\omega_0) \tilde{e}(x, y, (N-P)\omega_0) dA. \quad (2.49)$$

We again evaluate the $\tilde{e}$'s and $\chi^{(2)}$ values at only a single frequency component to yield a constant $X_0^{N,P,N-P}$. However, we note that the harmonic envelope approach has one advantage over the single-envelope equation in this regard, as we may weakly account for the frequency dependence of both the nonlinearity and the mode shapes through calculation of the $X_0^{N,P,N-P}$'s involved in different harmonic interactions.

To conclude this section, we work through two examples of three-wave mixing which will be studied through the remainder of this thesis. The first is the interaction between harmonics 1, 2, and 3 which, in general, can be used to study SFG, OPA, and DFG. In the second, we consider the interaction between harmonics 1 and 2. The resulting equations can be used to model degenerate OPA and SHG.

For the case of SFG, considering harmonic orders 1, 2, and 3, we have

$$\frac{\partial}{\partial z}\tilde{V}_3 = i(\beta - \beta_{0,3} - \frac{\Omega_3}{v_0} + i\frac{\alpha}{2})\tilde{V}_3 + \frac{i\omega}{8\Phi}\epsilon_0\bar{d}(X_0^{3,2,1} + X_0^{3,1,2})\mathcal{F}_{\Omega_3}\{V_1 V_2\}e^{i\Delta\beta z}, \quad (2.50a)$$

$$\frac{\partial}{\partial z}\tilde{V}_2 = i(\beta - \beta_{0,2} - \frac{\Omega_2}{v_0} + \frac{\alpha}{2})\tilde{V}_2 + \frac{i\omega}{4\Phi}\epsilon_0\bar{d}^* X_0^{3,2,1}\mathcal{F}_{\Omega_2}\{V_1^* V_3\}e^{-i\Delta\beta z}, \quad (2.50b)$$

$$\frac{\partial}{\partial z}\tilde{V}_1 = i(\beta - \beta_{0,1} - \frac{\Omega_1}{v_0} + \frac{\alpha}{2})\tilde{V}_1 + \frac{i\omega}{4\Phi}\epsilon_0\bar{d}^* X_0^{3,1,2}\mathcal{F}_{\Omega_1}\{V_2^* V_3\}e^{-i\Delta\beta z}. \quad (2.50c)$$

In writing these equations, we have introduced the phase mismatch parameter, $\Delta\beta$ (also commonly referred to as Δk), which is defined as $\Delta\beta = \beta_{0,1} + \beta_{0,2} - \beta_{0,3}$. Achieving phase-matched interactions with $\Delta\beta = 0$, or intentionally phase-mismatched interactions, is a hugely important aspect of the design of nonlinear optical systems. One common method for achieving a desired phase matching condition, quasi-phase matching, will be discussed in the following section.

Turning back to equations 2.50c-2.50a, we note that they closely resemble the coupled-wave equations for SFG which are commonly used in nonlinear optical theory and simulation. Through minimal manipulation of the presented equations, we may show that they are equivalent. Let us first note that $X_0^{3,2,1} = X_0^{3,1,2}$, meaning the right-hand sides in each of the equations share the same prefactor, $\frac{i\omega}{4\Phi}\epsilon_0 X_0^{3,2,1}$.

Secondly, we make the substitution $\tilde{A}_N(z, \omega) = \sqrt{\tilde{\Phi}(\omega)}\tilde{V}_N(z, \omega)$ such that $\tilde{A}_N(z, \omega)$ represents a complex envelope function with units of $\sqrt{W}$. Finally, we wish to remove the frequency dependence of quantities such as $\alpha(\omega)$ as well as the prefactor term so that we may readily express the equations in the time domain. To do so, we evaluate the relevant terms in the Nth equation at $N\omega_0$. In the time domain, then, we have

$$\frac{\partial}{\partial z}A_3 = \hat{D}_3 A_3 - \Delta\beta'_{30}\frac{\partial}{\partial\tau}A_3 - \frac{\alpha_3}{2}A_3 + i\kappa_3\bar{d}A_1 A_2 e^{i\Delta\beta z}, \tag{2.51a}$$

$$\frac{\partial}{\partial z}A_2 = \hat{D}_2 A_2 - \Delta\beta'_{20}\frac{\partial}{\partial\tau}A_2 - \frac{\alpha_2}{2}A_2 + i\kappa_2\bar{d}^* A_1^* A_3 e^{-i\Delta\beta z}, \tag{2.51b}$$

$$\frac{\partial}{\partial z}A_1 = \hat{D}_1 A_1 - \Delta\beta'_{10}\frac{\partial}{\partial\tau}A_1 - \frac{\alpha_1}{2}A_1 + i\kappa_1\bar{d}^* A_2^* A_3 e^{-i\Delta\beta z}. \tag{2.51c}$$

Here, $\alpha_N = \alpha(N\omega_0)$, and we have defined the walk-off parameter, $\Delta\beta'_{N0} = \frac{1}{v_{g,N}} - \frac{1}{v_0}$, where $v_{g,N}$ represents the group velocity of the Nth wave, as well as the dispersion operator, $\hat{D}_N = \sum_{m=2}^{\infty}\left[\frac{(i)^{m+1}\beta_N^{(m)}}{m!}\right]\partial_t^m$, where $\beta_N^{(m)}$ represents the mth-order dispersion of the Nth harmonic. A common choice is to take the reference velocity, v_0, to be equal to the group velocity of one of the participating waves, such that one of the walk-off terms may be set to 0. In this case, the walk-off between the remaining waves and reference wave is referred to as the group velocity mismatch (GVM). Furthermore, the dispersion operator may be truncated at any order; often, the second-order dispersion, or group velocity dispersion (GVD), is sufficient to capture the majority of the dynamics unless the signal is extremely broadband or the GVD is small.

Finally, we have defined the nonlinear coupling coefficient of the Nth, $\kappa_N = \frac{N\omega_0}{4\tilde{\Phi}(N\omega_0)^{3/2}}\epsilon_0 X_0^{3,2,1}$. Recalling the definition of $X_0^{3,2,1}$ from equation 2.49, we see that

$$X_0^{3,2,1}\bar{d}(z) = \int_A \chi^{(2)}(3\omega_0, 2\omega_0)\tilde{e}^*(3\omega_0)\tilde{e}(2\omega_0)\tilde{e}(\omega_0)dA$$

$$\approx 2d(z)\sqrt{\frac{8Z_0^3\tilde{\Phi}(3\omega_0)\tilde{\Phi}(2\omega_0)\tilde{\Phi}(\omega_0)}{A_{\text{eff}}(3\omega_0, 2\omega_0, \omega_0)n_{\text{eff}}(3\omega_0)n_{\text{eff}}(2\omega_0)n_{\text{eff}}(\omega_0)}}, \tag{2.52}$$

where we have suppressed the spatial dimensions in the integral for compactness. We have additionally introduced the quantity, A_{eff}, which represents the effective

mode area of the nonlinear interaction. In its general form, it is defined in terms of the normalized modes introduced in equations 2.19a and 2.19b as

$$A_{\text{eff},mnl}(\omega, \omega', \omega - \omega') = \frac{A_{\text{mode},m}(\omega) A_{\text{mode},n}(\omega') A_{\text{mode},l}(\omega - \omega')}{|\int_A \sum_{ijk} \bar{\chi}_{ijk}^{(2)}(\omega, \omega') \tilde{e}_{m;i}'^{*}(\omega) \tilde{e}_{n;j}'(\omega') \tilde{e}_{l;k}'(\omega - \omega') dA|^2}.$$

$$(2.53)$$

Here, $A_{\text{eff},mnl}(\omega, \omega', \omega - \omega')$ is the effective mode area for the interaction between modes m, n, and l at frequencies ω, ω', and $\omega - \omega'$, respectively. Indices i, j, and k refer to spatial coordinates. $\bar{\chi}_{ijk}^{(2)}(\omega, \omega')$ represents a normalized nonlinear strength, which is normalized to the absolute value of the strongest tensor component. Since the relative strength of the participating tensor component is, therefore, already accounted form in A_{eff}, $d(z) = \frac{1}{2}\chi^{(2)}(z)$ in equation 2.52 is defined to be the strongest tensor component of $\chi^{(2)}$. We may furthermore separate the spatial dependence of $d(z)$ out to write $d(z) = \bar{d}(z)d$. Finally, taking $\tilde{\Phi}(3\omega_0) = \tilde{\Phi}(2\omega_0) = \tilde{\Phi}(\omega_0)$, we finally arrive at the usual expression for κ_N,

$$\kappa_N = \frac{\sqrt{2Z_0} N \omega_0 d}{c \sqrt{n_3 n_2 n_1 A_{\text{eff}}}}.$$

$$(2.54)$$

Here, we have made the notational simplification that $n_N = n_{\text{eff}}(N\omega_0)$.

Having found these coupled wave equations describing SFG, we next turn our attention to the equations for SHG. In this case, considering harmonic orders 1 and 2, we find

$$\frac{\partial}{\partial z}\tilde{V}_2 = i(\beta - \beta_{0,2} - \frac{\Omega_2}{v_0} + \frac{\alpha}{2})\tilde{V}_2 + \frac{i\omega}{8\Phi}\epsilon_0 \bar{d} X_0^{2,1,1} \mathcal{F}_{\Omega_2}\{V_1 V_1\} e^{i\Delta\beta z}, \qquad (2.55a)$$

$$\frac{\partial}{\partial z}\tilde{V}_1 = i(\beta - \beta_{0,1} - \frac{\Omega_1}{v_0} + \frac{\alpha}{2})\tilde{V}_1 + \frac{i\omega}{4\Phi}\epsilon_0 \bar{d}^* X_0^{2,1,1} \mathcal{F}_{\Omega_1}\{V_1^* V_2\} e^{-i\Delta\beta z}. \qquad (2.55b)$$

Making analogous simplifications to those made in the case of SFG, we have the following expression in the time domain

$$\frac{\partial}{\partial z}A_2 = \hat{D}_2 A_2 - \Delta\beta'_{20}\frac{\partial}{\partial \tau}A_2 - \frac{\alpha_2}{2}A_2 + i\kappa_2 \bar{d} A_1 A_1 e^{i\Delta\beta z}, \qquad (2.56a)$$

$$\frac{\partial}{\partial z}A_1 = \hat{D}_1 A_1 - \Delta\beta'_{10}\frac{\partial}{\partial \tau}A_1 - \frac{\alpha_1}{2}A_1 + i\kappa_1 \bar{d}^* A_1^* A_2 e^{-i\Delta\beta z}. \qquad (2.56b)$$

In this case, the nonlinear coupling coefficients are given by

$$\kappa_1 = \kappa_2 = \frac{\sqrt{2Z_0}\omega_0 d}{cn_1\sqrt{n_2 A_{\text{eff}}}}.\tag{2.57}$$

These two sets of coupled wave equations will form the basis of much of the theoretical analysis presented in this thesis. To conclude this section, we make a note about our usage of the time and frequency domain formalisms of the coupled wave equations equations. Typically, we utilize the time-domain formalisms to conduct analytic analysis, as analytic solutions are generally more tractable in the time domain, where the nonlinear term involves a product rather than a convolution.

In our simulations, however, we utilize the Fourier split-step technique, in which the evolution in z is calculated in small steps, with each step consisting of both a linear and a nonlinear operation. The nonlinear step is computed in the time domain using a numerical technique, typically fourth-order Runge Kutta, while the linear dispersive operations are performed in the frequency domain. As each step already demands fast Fourier transforms to move between the time and frequency domains between the linear and nonlinear steps, inclusion of the frequency dependence of, e.g., κ_N or α requires negligible additional computational overhead. As such, we typically include these frequency dependencies in our numerical models.

2.7 Quasi-Phase Matching

As was mentioned in the previous section, the phase mismatch parameter, $\Delta\beta = \beta_{0,1} + \beta_{0,2} - \beta_{0,3}$, is critical in shaping the behavior of nonlinear systems since it dictates the flow of energy between the participating harmonics. As such, being able to engineer a desired phase matching condition is a key component in the design of nonlinear systems. We will utilize a few techniques in this thesis, the most prevalent of which is the technique of quasi-phase matching (QPM). In this case, the sign of the nonlinearity is periodically inverted to induce what is referred to as a QPM grating, which compensates the phase mismatch due to the phase constants of the interacting waves. In particular, given a phase mismatch of $\Delta\beta = \beta_{0,1} + \beta_{0,2} - \beta_{0,3}$, the period, Λ, of the QPM grating required to achieve perfect phase matching may be calculated as

$$\Lambda = \frac{2\pi}{|\beta_{0,1} + \beta_{0,2} - \beta_{0,3}|}.\tag{2.58}$$

In our theoretical analysis above, the presence of such a QPM grating with a period of Λ would be expressed through the function $\bar{d}(z)$ as

$$\bar{d}(z) = \text{sgn}\left(\cos\left(\frac{2\pi z}{\Lambda}\right)\right). \tag{2.59}$$

Several approaches to QPM exist for different materials. The most widely discussed in this thesis is periodic poling (PP), which is a process compatible with ferroelectric materials, such as lithium niobate (LN). In this process, the directions of the ferroelectric domains of the material are periodically inverted to achieve the desired periodic inversion of the sign of the nonlinearity. Another QPM technique is orientation patterning, which is often used for semiconductor materials such as gallium phosphide (GaP). Here, the material growth direction is periodically inverted to induce the sign change in the nonlinear susceptibility. One may more generally allow the period of the QPM grating to also vary as a function of z, although no such structures are considered in this thesis.

A common approximation is to expand the poling function as a Fourier series. For the considered periodic poling function, we write

$$\bar{d}(z) = \sum_{m=-\infty}^{\infty} \bar{d}_m e^{im\frac{2\pi}{\Lambda}z}, \tag{2.60}$$

where the Fourier coefficients may be found as

$$\frac{2\sin\left(\frac{\pi m}{2}\right)}{m\pi} \tag{2.61}$$

for $m \neq 0$, and $\bar{d}_0 = 0$. Often, just the first Fourier component is sufficient to describe the interaction, in which case we approximate $\bar{d}(z)$ as $\frac{2}{\pi}e^{-i\frac{2\pi}{\Lambda}z}$. When such an approximation is made, it is typical to rewrite $d(z) = \bar{d}(z)d$, as defined previously, as $d(z) \approx d_{\text{eff}}e^{i\frac{2\pi}{\Lambda}z}$, where $d_{\text{eff}} = \frac{2}{\pi}d$ and we now redefine $\bar{d}(z)$ as $\bar{d}(z) = e^{i\frac{2\pi}{\Lambda}z}$. In equations 2.51c-2.51a, we see that $\bar{d}(z)$ defined this way may be combined with the phase mismatch term such that $\bar{d}(z)e^{i\Delta\beta z} = e^{i\Delta\beta_{\text{QPM}}z}$ with

$$\Delta\beta_{\text{QPM}} = \beta_{0,1} + \beta_{0,2} - \beta_{0,3} + \frac{2\pi}{\Lambda}. \tag{2.62}$$

2.8 Optical Parametric Oscillators

Having discussed the basics of optical resonators, we now introduce the basics of OPOs, consisting of an optical resonator with a quadratic nonlinear crystal inside.
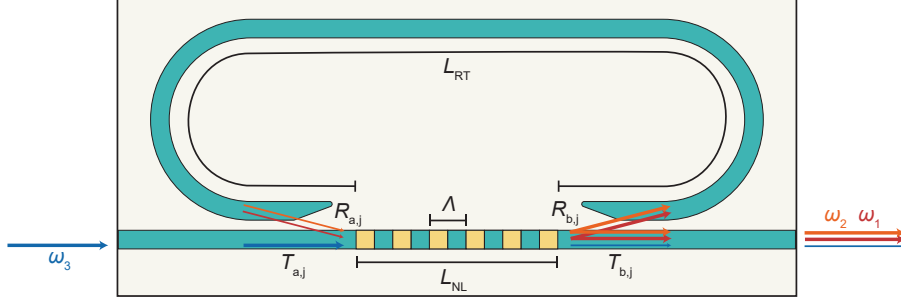
Figure 2.1: **Example OPO device.** A pump wave at frequency ω_3 generates signal and idler waves at frequencies ω_2 and ω_1, respectively. The input and output couplers are taken to have transmission (reflection) coefficients of $T_{a,j}$ ($R_{a,j}$) and $T_{b,j}$ ($R_{a,j}$), respectively, where $j \in \{1, 2, 3\}$. The nonlinear interaction takes place in a periodically poled region of length L_{NL} with poling period, Λ. The signal is coupled back through a resonator of length L_{RT}.

Many of the works presented in this thesis will involve the study of nonlinear phenomena occurring in OPOs.

In quadratic OPOs, a pump wave at frequency ω_3 generates signal and idler waves at frequencies ω_2 and ω_1, respectively. Here, $\omega_3 > \omega_2 \geq \omega_1$ and conservation of energy requires $\omega_3 = \omega_2 + \omega_1$. For the analysis that follows, we consider a racetrack resonator (Fig. 2.1), as is commonly used in nanophotonics, as well as a continuous-wave (CW) pump. The input coupler is taken to have transmission and reflection coefficients in power of $T_{a,j}$ and $R_{a,j}$, respectively, for the jth wave, $j \in \{1, 2, 3\}$. Likewise, the output coupler has transmission and reflection coefficients of $T_{b,j}$ and $R_{b,j}$. For our analysis, we further consider first propagation through a lossless nonlinear medium of length L_{NL} followed by propagation through a lossy waveguide of roundtrip length L_{RT} with an absorption coefficient of α_j for the jth wave. With this in mind, we may rewrite the reflection coefficients as $R_{a,j} = e^{-\alpha_{R_a,j} L_{\mathrm{RT}}}$ and $R_{b,j} = e^{-\alpha_{R_b,j} L_{\mathrm{RT}}}$ such that the total loss for wave j may be characterized by the absorption coefficient $\alpha_j' = \alpha_j + \alpha_{R_a,j} + \alpha_{R_b,j}$. As derived in Section 2.6 the nonlinear interaction along the propagation direction, z, is modeled using the coupled wave equations

$$\frac{d}{dz} A_1 = i\kappa_1 A_2 A_3^* e^{-i\Delta k z}, \tag{2.63a}$$

$$\frac{d}{dz} A_2 = i\kappa_2 A_1 A_3^* e^{-i\Delta k z}, \tag{2.63b}$$

$$\frac{d}{dz} A_3 = i\kappa_3 A_1 A_2 e^{i\Delta k z}. \tag{2.63c}$$

Here, as defined before, $A_j(z)$ represents the complex electric field amplitude for wave $j \in \{1, 2, 3\}$, normalized such that $|A_j|^2$ is the power. The nonlinear coupling coefficients are given by $\kappa_j = \frac{\sqrt{2Z_0}\omega_j d_{\text{eff}}}{c\sqrt{n_1 n_2 n_3 A_{\text{eff}}}}$, where Z_0 is the impedance of free space, d_{eff} is the effective nonlinearity, c is the speed of light, n_j is the refractive index of the jth wave, and A_{eff} is the effective mode area. Finally, $\Delta k = k_2 + k_1 - k_3 + \frac{2\pi}{\Lambda}$ is the phase mismatch parameter, where Λ is the poling period, when applicable.

In this thesis, we will primarily consider doubly resonant oscillators (DROs), for which the pump is non-resonant but the signal and idler waves are both made to resonate. Our analysis closely follows that of [2, 8]. To start, we wish to find the threshold condition. For this, we make the undepleted pump approximation by assuming that the pump amplitude remains constant, $A_3 = A_3(0)$, through the nonlinear section. With this approximation, we may directly integrate equations 2.63a and 2.63b to find the following relationships for the signal and idler waves at the input and output of the nonlinear section

$$\begin{bmatrix} A_1(L_{\text{NL}}) \\ A_2^*(L_{\text{NL}}) \end{bmatrix} = \begin{bmatrix} g_{11} & g_{12} \\ g_{21}^* & g_{22}^* \end{bmatrix} \begin{bmatrix} A_1(0) \\ A_2^*(0) \end{bmatrix}, \tag{2.64}$$

where

$$g_{11} = g_{22} = e^{-i\frac{1}{2}\Delta k L_{\text{NL}}} \left(\cosh\left(\Gamma L_{\text{NL}}\right) + i\frac{\Delta k}{2\Gamma} \sinh\left(\Gamma L_{\text{NL}}\right) \right), \tag{2.65a}$$

$$g_{12} = i\frac{\kappa_1 E_3(0)}{\Gamma} \sinh\left(\Gamma L_{\text{NL}}\right) e^{-i\frac{1}{2}\Delta k L_{\text{NL}}}, \tag{2.65b}$$

$$g_{21} = i\frac{\kappa_2 E_3(0)}{\Gamma} \sinh\left(\Gamma L_{\text{NL}}\right) e^{-i\frac{1}{2}\Delta k L_{\text{NL}}}, \tag{2.65c}$$

and we have defined $\Gamma = \sqrt{\kappa_1 \kappa_2 |E_3(0)|^2 - (\frac{\Delta k}{2})^2}$. To reach threshold, the nonlinear gain accumulated by the signal and idler waves must balance the roundtrip loss, leading to the following roundtrip equation

$$\begin{bmatrix} A_1(0) \\ A_2^*(0) \end{bmatrix} = \begin{bmatrix} e^{-\frac{\alpha_1'}{2} L_{\text{RT}}} & 0 \\ 0 & e^{-\frac{\alpha_2'}{2} L_{\text{RT}}} \end{bmatrix} \begin{bmatrix} g_{11} & g_{12} \\ g_{21}^* & g_{22}^* \end{bmatrix} \begin{bmatrix} A_1(0) \\ A_2^*(0) \end{bmatrix}. \tag{2.66}$$

Solving this system leads to the characteristic equation $(g_{11}e^{-\frac{\alpha_1'}{2}L_{\mathrm{RT}}}-1)(g_{22}^*e^{-\frac{\alpha_2'}{2}L_{\mathrm{RT}}}-1) - g_{12}g_{21}^*e^{\frac{(\alpha_1'+\alpha_2')}{2}L_{\mathrm{RT}}}$, which may be solved to find the threshold condition. Here, we write the solution for perfect phase matching with $\Delta k = 0$. Defining $\Gamma_{\mathrm{PM}} = \sqrt{\kappa_1\kappa_2|A_3(0)|^2}$, we have the threshold condition

$$\cosh\left(\Gamma_{\mathrm{PM}}L_{\mathrm{NL}}\right) = \frac{\cosh\left(\frac{1}{4}(\alpha_1' + \alpha_2')L_{\mathrm{RT}}\right)}{\cosh\left(\frac{1}{4}(\alpha_1' - \alpha_2')L_{\mathrm{RT}}\right)}. \tag{2.67}$$

By expanding the left-hand and right-hand sides to first order, assuming the roundtrip loss is small, we find an approximate expression for the threshold power

$$P_{\mathrm{th}} \approx \frac{1}{4}\frac{a_1 a_2}{\kappa_1\kappa_2 L_{\mathrm{NL}}^2}, \tag{2.68}$$

where $a_i = \alpha_i' L_{\mathrm{RT}}$.

Having found the threshold condition, we next wish to analyze the steady-state dynamics of the above-threshold OPO. In particular, we would like to find the conversion efficiency of the OPO, given as $\eta = \frac{P_{1+2}^{\mathrm{out}}}{P_3(0)}$, where P_{1+2}^{out} is the combined output power of the signal and idler waves. To do so, we first seek the internal efficiency, $\eta_{\mathrm{int}} = \frac{\Delta P_3}{P_3(0)}$, as well as the escape efficiency, $\eta_{\mathrm{escape}} = \frac{P_{1+2}^{\mathrm{out}}}{\Delta P_3}$, where $\Delta P_3 = P_3(0) - P_3(L_{\mathrm{NL}})$. The conversion efficiency may then be found as $\eta = \eta_{\mathrm{int}}\eta_{\mathrm{escape}}$. To find the internal efficiency, we first turn to equation 2.63c. Here, we make the approximation that $A_1(0)$ and $A_2(0)$ remain approximately constant in a single-pass through the nonlinear section. This is a reasonable approximation when the roundtrip loss is small such that $\Delta P_3 =<< P_2(0) + P_3(0)$. We additionally re-write the fields as $A_j = |A_j|e^{i\phi_j}$ where ϕ_j is the phase of the jth wave. This yields the following equation

$$|A_3(L_{\mathrm{NL}})| = |A_3(0)| + \kappa_3|A_1(0)||A_2(0)|L_{\mathrm{NL}}\mathrm{sinc}(\frac{\Delta k L_{\mathrm{NL}}}{2})e^{i(\Delta\phi+\pi/2+\frac{1}{2}\Delta k L_{\mathrm{NL}})}. \tag{2.69}$$

Here, we have defined $\Delta\phi = \phi_1 + \phi_2 - \phi_3$. We note also that, as expected, maximum transfer of energy from the pump to the signal and idler occurs when $\Delta\phi + \frac{1}{2}\Delta k L_{\mathrm{NL}} = -\pi/2$. This phase-sensitive nature of the amplification process is responsible for several interesting properties of OPOs. At degeneracy, $\phi_2 = \phi_1$, leading to a

constrained phase relationship for the signal, $\Delta\phi = 2\phi_2 - \phi_3$. Thus, the amplified signal may take on only one of two relative phases in reference to the pump, a property which has been exploited for binary random number generation and creation of coherent Ising solvers [9–11], which will be discussed in more detail in Chapter 9. It furthermore results in a phase-locking between the signal and pump, which can enable a transfer of coherence between the pump and signal [12]. Meanwhile, for non-degenerate operation, the relative phases of the signal and idler are constrained through the pump.

In what follows, we will assume that the cavity feedback is well-optimized to ensure the phase relationship for signal amplification, and we furthermore consider the phase-matched case in which $\Delta k = 0$. We will additionally make use of the conservation of energy condition that $\Delta P_3 = \Delta P_1 + \Delta P_2$ and the Manley-Rowe relations which require $\frac{\Delta P_3}{\omega_3} = \frac{\Delta P_2}{\omega_2} = \frac{\Delta P_1}{\omega_1}$. Finally, we will make use of the feedback condition that $\Delta P_j \approx |E_j^2(0)|a_j$ where $j \in \{1, 2\}$. Using these relationships, we may write equation 2.69 in terms of only the pump and idler waves to find

$$\frac{\Delta P_1}{P_3(0)} = 4\frac{\omega_1}{\omega_3}\frac{1}{N}(\sqrt{N} - 1), \tag{2.70}$$

where $N = \frac{P_3(0)}{P_{\text{th}}}$ is the number of times above threshold, and P_{th} is given by equation 2.68. An equivalent expression may be found for the signal. Combining the two expressions yields the internal efficiency:

$$\eta_{\text{int}} = \frac{4}{N}(\sqrt{N} - 1). \tag{2.71}$$

Meanwhile, the output idler power may be related to the power in the resonator as

$$P_1^{\text{out}} = P_1(L_{\text{NL}})T_{b,1} = \Delta P_1 \frac{e^{\alpha_1' L_{\text{RT}}}}{e^{\alpha_1' L_{\text{RT}}} - 1}T_{b,1}, \tag{2.72}$$

and a similar expression may be derived for the signal. This leads to the following expression for the escape efficiency

$$\eta_{\text{escape}} = \frac{\omega_1}{\omega_3}T_{b,1}\frac{e^{\alpha_1' L_{\text{RT}}}}{e^{\alpha_1' L_{\text{RT}}} - 1} + \frac{\omega_2}{\omega_3}T_{b,2}\frac{e^{\alpha_2' L_{\text{RT}}}}{e^{\alpha_2' L_{\text{RT}}} - 1}. \tag{2.73}$$

Finally, we may write the total efficiency as

$$\eta = \frac{4}{N}(\sqrt{N} - 1)\left(\frac{\omega_1}{\omega_3}T_{b,1}\frac{e^{\alpha_1' L_{\text{RT}}}}{e^{\alpha_1' L_{\text{RT}}} - 1} + \frac{\omega_2}{\omega_3}T_{b,2}\frac{e^{\alpha_2' L_{\text{RT}}}}{e^{\alpha_2' L_{\text{RT}}} - 1}\right). \tag{2.74}$$

While many of the results in this thesis pertain to physical regimes where the assumptions made in deriving these CW solutions are violated, they can provide guidance for the design and interpretation of results from the studied OPOs. Firstly, equations 2.67 or 2.68 may be utilized to ensure that a DRO system can go above threshold. Even in the pulsed pumping regime, the CW threshold can generally be used as a first-order estimate the required peak power of the pump pulse. Additionally, from equation 2.74, we see that the optimum operating point for maximizing the conversion efficiency is typically four times above the DRO threshold in conventional OPOs. Furthermore, we see the importance of the coupler design for the OPO system in dictating both the threshold and the efficiency. In particular, a significantly improved escape efficiency may be achieved when the majority of the roundtrip loss is a consequence of the output coupler.

The formalism developed here also provides basic intuition into how our numerical simulations are conducted. We typically follow the Ikeda map approach [13], in which the propagation through the nonlinear equation is performed using a Fourier split-step method, as described in Section 2.6, and the roundtrip propagation is simulated using a linear transfer function which captures the dispersion and loss of the roundtrip. Further descriptions on the particular models used will be provided in each individual chapter.

2.9 Pulse Trains and Frequency Combs

To conclude this theoretical introduction, we briefly introduce the key relations between a train of pulses in the time domain and a frequency comb in the frequency domain. As mentioned in Chapter 1, this Fourier transform relationship is at the heart of many of the key developments and applications in ultrafast optics. The figure and discussion in this section closely follow those presented in [14, 15].
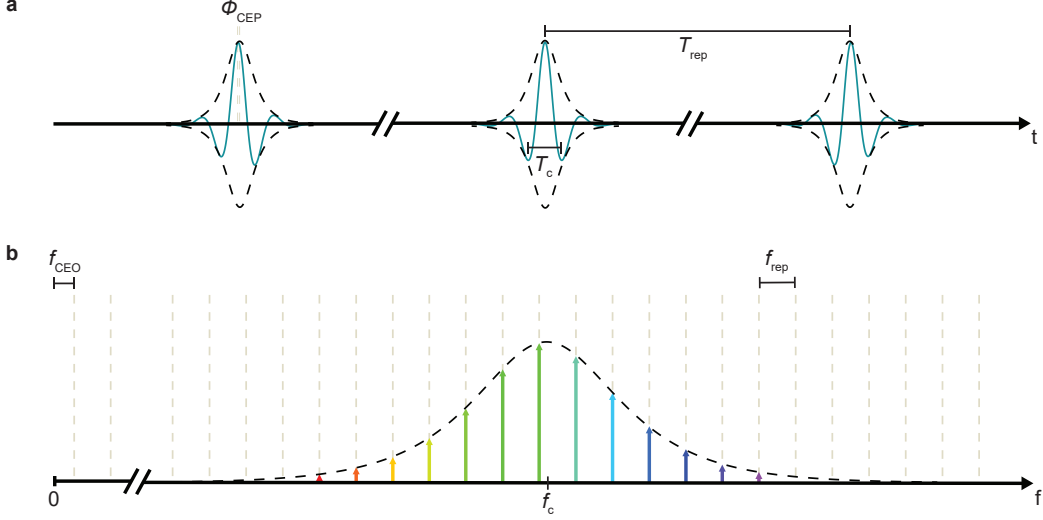
Figure 2.2: **Pulse trains and frequency combs. a,** A train of pulses in the time domain corresponds to **b,** a comb of equidistant lines in the frequency domain. T_{rep}, repetition period; ϕ_{CEP}, carrier-envelope offset phase; T_{c}, carrier period, f_{CEO}, carrier-envelope offset frequency, f_{c}, carrier frequency, f_{rep}, repetition rate.

As depicted in Fig. 2.2a, we consider a train of ultrashort pulses in the time domain. Ignoring any spatial dependence, we may describe the complex electric field, $E(t)$ associated with this pulse train in the time domain as

$$E(t) = e^{-i(\omega_{\text{c}}t+\phi_{\text{c}})} \sum_{n=-\infty}^{\infty} A(t - nT_{\text{rep}})e^{-in\Delta\phi_{\text{CEP}}}$$

$$= e^{-i(\omega_{\text{c}}t+\phi_{\text{c}})} \left(A(t) * \sum_{n=-\infty}^{\infty} \delta(t - nT_{\text{rep}})e^{-i\omega_{\text{CEO}}t} \right). \quad (2.75)$$

Here, $A(t)$ represents a complex field envelope function, $\omega_{\text{c}} = 2\pi f_{\text{c}}$ is the carrier frequency, ϕ_{c} is the carrier phase, T_{rep} is the pulse repetition period, ϕ_{CEP} is the carrier-envelope offset phase, and $\Delta\phi_{\text{CEP}}$ is the pulse-to-pulse variation in the carrier-envelope phase. We have also defined $\omega_{\text{CEO}}/2\pi = f_{\text{CEO}} = \frac{\text{mod}\{\phi_{\text{CEP}},2\pi\}}{2\pi} f_{\text{rep}}$, where f_{CEO} is the carrier-envelope-offset frequency. In the frequency domain, this corresponds to

$$\tilde{E}(\omega) = e^{-i\phi_{\text{c}}}\tilde{A}(\omega) \sum_{n=-\infty}^{\infty} \delta\left(\Omega - (\omega_{\text{CEO}} + n\omega_{\text{rep}}) \right). \quad (2.76)$$

There are several important relations between the quantities of 2.76 and those of equation 2.75. Firstly, $\tilde{A}(\Omega) = \mathcal{F}\{A(t)\}$, where $\Omega = \omega - \omega_{\text{c}}$. Next, $\omega_{\text{rep}}/2\pi =$

$f_{rep} = 1/T_{rep}$, where f_{rep} is the repetition rate. Together, the f_{CEO} and f_{rep} (typically radio frequencies) precisely define the exact position of all of the optical comb lines which constitute the frequency comb.

BIBLIOGRAPHY

[1]   Christopher R. Phillips, Marc Jankowski, Noah Flemens, and Martin M. Fejer. "General framework for ultrafast nonlinear photonics: Unifying single and multi-envelope treatments". In: *Optics Express* 32.5 (2024), pp. 8284–8307.

[2]   Luis M. Ledezma. "Towards universal integrated laser sources with non-linear photonics." en. PhD thesis. California Institute of Technology, 2023. URL: https://www.proquest.com/dissertations-theses/towards-universal-integrated-laser-sources-with/docview/3132880104/se-2.

[3]   Christopher Richard Phillips. *Broadband optical sources based on highly nonlinear quasi-phasematched interactions.* Stanford University, 2012.

[4]   Marc Jankowski, Jatadhari Mishra, and Martin M. Fejer. "Dispersion-engineered nanophotonics: A flexible tool for nonclassical light." In: *Journal of Physics: Photonics* 3.4 (2021), p. 042005.

[5]   Frank P. Payne and Allan W. Snyder. "The slowly varying envelope approximation in non-linear optics". In: *IEE Colloquium on Non-Linear Optical Waveguides.* IET. 1988, pp. 9–1.

[6]   Martin Michael Fejer. *Single crystal fibers: Growth dynamics and nonlinear optical interactions.* Stanford University, 1986.

[7]   Matteo Conforti, Fabio Baronio, and Costantino De Angelis. "Nonlinear envelope equation for broadband optical pulses in quadratic media." In: *Phys. Rev. A* 81 (5 May 2010), p. 053841. DOI: 10.1103/PhysRevA.81.053841. URL: https://link.aps.org/doi/10.1103/PhysRevA.81.053841.

[8]   Robert L. Byer. "Optical parametric oscillators." eng. In: *Quantum Electronics: A Treatise.* Vol. 1. New York: Academic Press, 1975, pp. 588–694. ISBN: 978-0-12-574041-8.

[9]   Alireza Marandi, Nick C. Leindecker, Konstantin L. Vodopyanov, and Robert L. Byer. "All-optical quantum random bit generation from intrinsically binary phase of parametric oscillators." In: *Optics Express* 20.17 (2012), pp. 19322–19330. DOI: 10.1364/OE.20.019322.

[10] Peter L. McMahon, Alireza Marandi, Yoshitaka Haribara, Ryan Hamerly, Carsten Langrock, Shuhei Tamate, Takahiro Inagaki, Hiroki Takesue, Shoko Utsunomiya, Kazuyuki Aihara, et al. "A fully programmable 100-spin coherent Ising machine with all-to-all connections." In: *Science* 354.6312 (2016), pp. 614–617. DOI: 10.1126/science.aah5178.

[11] Robert M. Gray, Ryoto Sekine, Luis Ledezma, Gordon H. Y. Li, Selina Zhou, Arkadev Roy, Midya Parto, and Alireza Marandi. "Large-scale time-multiplexed nanophotonic parametric oscillators." In: *Newton* (2025). DOI: 10.1016/j.newton.2025.100108.

[12] Alireza Marandi, Nick C. Leindecker, Vladimir Pervak, Robert L. Byer, and Konstantin L. Vodopyanov. "Coherence properties of a broadband femtosecond mid-IR optical parametric oscillator operating at degeneracy." en. In: *Optics Express* 20.7 (Mar. 2012), p. 7255. ISSN: 1094-4087. DOI: 10.1364/OE.20.007255. URL: https://opg.optica.org/oe/abstract.cfm?uri=oe-20-7-7255 (visited on 03/17/2025).

[13] Kensuke Ikeda. "Multiple-valued stationary state and its instability of the transmitted light by a ring cavity system." In: *Optics Communications* 30.2 (Aug. 1979), pp. 257–261. ISSN: 0030-4018. DOI: 10.1016/0030-4018(79)90090-7. URL: https://www.sciencedirect.com/science/article/pii/0030401879900907 (visited on 03/16/2025).

[14] Scott A. Diddams, Kerry Vahala, and Thomas Udem. "Optical frequency combs: Coherently uniting the electromagnetic spectrum." In: *Science* 369.6501 (2020), eaay3676.

[15] Nathalie Picqué and Theodor W. Hänsch. "Frequency comb spectroscopy." In: *Nature Photonics* 13.3 (2019), pp. 146–157.

Chapter 3

HIGH-POWER MID-IR FEW-CYCLE FREQUENCY COMB FROM QUADRATIC SOLITONS IN AN OPTICAL PARAMETRIC OSCILLATOR

Mingchen Liu[*], **Robert M. Gray**[*], Arkadev Roy, Kirk A. Ingold, Evgeni Sorokin, Irina Sorokina, Peter G. Schunemann, and Alireza Marandi. "High-power mid-IR few-cycle frequency comb from quadratic solitons in an optical parametric oscillator." In: *Laser & Photonics Reviews* 16.11 (2022), p. 2200453. DOI: 10.1002/lpor.202200453.

3.1   Introduction

Optical frequency comb generation in the MIR spectral region (3–25 µm) has been a subject of intensive research over the past decades, driven by its numerous applications ranging from precise sensing to fundamental science [1], of which notable examples are molecular spectroscopy [2, 3], astronomical spectrograph calibration [4, 5], and high-harmonic generation [6, 7]. Referred to as the "molecular fingerprint region," the MIR portion of the electromagnetic spectrum contains strong rovibrational absorption features of many molecules, the detection of which is useful for a plethora of applications such as medicine, environmental science, agriculture, energy, and defense. In particular, the 3–5 µm band is of high interest as it contains strong absorptions of many important molecules, including greenhouse gases (e.g., carbon dioxide at ~4.2 µm, nitrous oxide at ~4.5 µm, and methane at ~3.3 µm), species used in breath analysis (e.g., ethane at ~3.3 µm and carbon monoxide at ~4.7 µm), and major air pollutants (e.g., nitrogen dioxide at ~3.5 µm and sulfur dioxide at ~4 µm) [8, 9]. Given its significance, it is highly desirable to produce frequency combs in this band with great power, efficiency, bandwidth, and stability.

The most widely used techniques to produce MIR frequency combs include DFG, OPOs, quantum cascade lasers (QCLs), microresonators, supercontinuum generation (SCG), and direct MIR lasing. DFG-based sources feature single-pass configuration and passive cancellation of the carrier-envelope offset frequency (f_{CEO}) [10–12] but are limited by their relatively low powers and efficiencies. QCLs have been demonstrated to be a promising alternative to optical nonlinear methods for frequency comb generation [13–15] but currently exhibit narrow instantaneous band-

width and limited spectral coverage. Other MIR frequency comb sources, including microresonators [16], SCG [17, 18], and direct MIR lasing [19] are still facing challenges to reach beyond 3.5 µm.

Compared to other techniques, OPOs have high powers and efficiencies with broad spectral coverages and wide tuning ranges [20–25]. Among the various OPO configurations, synchronously pumped degenerate OPOs have been demonstrated to be particularly promising, featuring high conversion efficiencies [26, 27], two-octave-wide spectra [28], few-cycle pulses [29], scalability to a multi-GHZ repetition rate [30], and more importantly, intrinsic phase and frequency locking of the output to the pump [31]. However, the demonstrated OPOs with a wavelength coverage beyond 3 µm have either an MIR conversion efficiency smaller than 20% [20, 22–24, 26] or a limited MIR output power under 250 mW [27, 28].

Recently, there has been increasing interest in realization of purely dissipative cavity solitons [32, 33] with the promise of frequency comb sources outside the well-developed near-IR region. The temporal simulton, a special form of quadratic solitons characterized by the generation of simultaneous bright-dark solitons of the signal at ω and the pump at 2ω [34, 35], has emerged as a novel state of operation in OPOs [36, 37]. The simulton-based OPO can be considered as a combination of a degenerate OPA and a positively detuned cavity, in which a double balance of energy and timing is achieved [37], as illustrated in Figure 3.1a–d. While the energy balance results from the interplay of dissipation and amplification, the timing balance is rooted in the compensation of cavity detuning by the nonlinear acceleration. Running in an uncommon high-gain low-finesse regime, simulton-based OPOs feature even higher power and efficiency as well as favorable power-dependent bandwidth scaling without losing any advantages of conventional OPOs. Although operation in the simulton regime has offered a promising new avenue for frequency comb generation in the MIR spectral region, it has remained challenging to extend it to longer wavelengths due to an incomplete understanding of its formation requirements and challenges in experiment.

In this chapter, we demonstrate an OPO working in the simulton regime which generates a frequency comb centered at 4.18 µm with a high average power of 565 mW, a record conversion efficiency of 44%, an instantaneous full-width at half-maximum (FWHM) bandwidth from 3.6 to 4.5 µm, and pulses of 45 fs duration, making it an outstanding mid-IR frequency comb source. A direct experimental comparison between the simulton and conventional regimes under the exact same
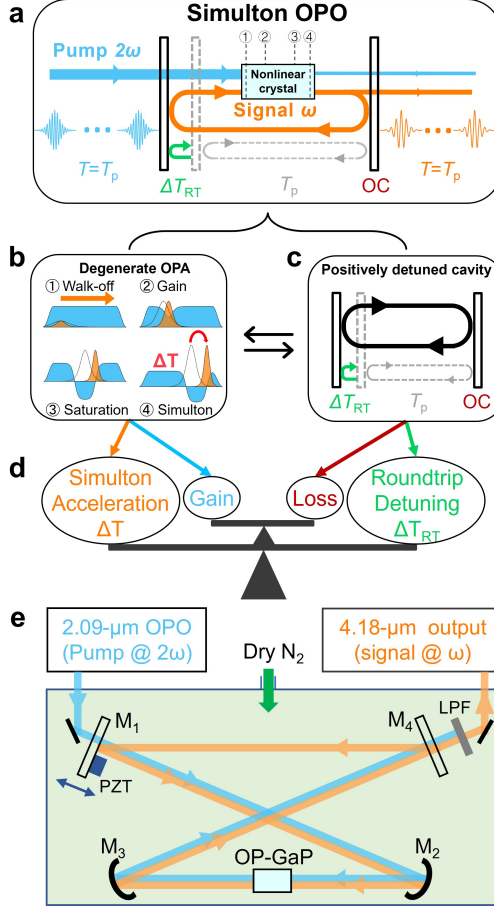
Figure 3.1: **The simulton-based OPO. a**, Simplified diagram of the oscillator. T_p, pump and signal repetition period; ΔT_{RT}, roundtrip group delay; OC, output coupler. The oscillator can be considered a combination of, **b**, a degenerate OPA and, **c**, a positively detuned cavity, striking, **d**, a double balance of timing and energy. **b**, Illustration of simulton formation: signal (orange) at ω and pump (blue) at 2ω. For comparison, uncolored solid lines denote a perfectly synchronous ($\Delta T_{RT} = 0$) half-harmonic pulse undergoing linear propagation. ①: on each roundtrip, a small group delay, ΔT_{RT}, is acquired by the resonating signal pulse with respect to the newly in-coupled pump pulse due to the detuning of the cavity roundtrip time. ②,③: Passing through the crystal, the signal is amplied by extracting gain from the pump until the pump is depleted, meanwhile accumulating a simulton group advance. ④: Once depleted, the pump forms a dark soliton and co-propagates with the signal at the simulton velocity. **e**, Schematic of the 4.18 µm OPO cavity. The cavity length is controlled by mounting M_1 on a piezo stage (PZT). The whole cavity resides in a box purged with dry nitrogen to reduce the effects of atmospheric absorption on the OPO operation. LPF, long-pass filter.

pump condition attributes many of these outstanding characteristics to the simulton formation. Moreover, we perform numerical simulations to capture the behavior

exhibited by different regimes of the OPO, which agree well with our experimental results. The simulation also indicates a pathway to further improve the performance of the simulton-based OPO. Lastly, we highlight key features of the simulton build-up dynamics and offer a discussion on the impact of the pump carrier-envelope offset frequency on simulton formation, with many practical implications. This work presents a powerful scheme for MIR frequency comb generation and demonstrates its potential to be extended to longer wavelengths and integrated platforms [38].

3.2 Theory of Temporal Simultons

Before presenting our experimental results, we briefly review the theory of temporal simulton formation in optical parametric oscillators. The simulton solution can be readily found for a traveling wave optical parametric amplifier (OPA) operating at degeneracy by considering the coupled wave equations, keeping only the walk-off and nonlinear coupling terms [34, 35, 37]. In this section, we derive the simulton solution following the notation of ref. [39] and utilize the analytic expressions for its dynamical evolution to provide intuition for the presented sensing mechanism. We begin with the coupled wave equations for the fields at degeneracy:

$$\frac{\partial}{\partial z} A_\omega(z,t) = \kappa A_{2\omega} A_\omega^*, \tag{3.1a}$$

$$\frac{\partial}{\partial z} A_{2\omega}(z,t) = -\Delta\beta' \frac{\partial}{\partial t} A_{2\omega} - \kappa A_\omega^2. \tag{3.1b}$$

Here, κ is the nonlinear coupling coefficient, $\Delta\beta'$ is the group velocity mismatch, and A_ω and $A_{2\omega}$ refer to the signal and pump fields, respectively, normalized so that $|A_i|^2$ gives the power in wave $i \in \{\omega, 2\omega\}$. The nonlinear coupling coefficient is κ. The time coordinate is defined to be co-moving with the group velocity of the signal wave. Assuming wave solutions of the form $A_\omega(z,t) = A_\omega(t + \nu z)$ and $A_{2\omega} = A_{2\omega}(t + \nu z)$ with inverse group velocity ν gives:

$$\nu \frac{\partial}{\partial t} A_\omega(z,t) = \kappa A_{2\omega} A_\omega^*, \tag{3.2a}$$

$$(\nu + \Delta\beta') \frac{\partial}{\partial z} A_{2\omega}(z,t) = -\kappa A_\omega^2. \tag{3.2b}$$

This system of equations can be solved analytically to yield the simulton solution:

$$A_\omega(z,t) = \frac{a}{\sqrt{2\tau}} \operatorname{sech}\left(\frac{t-T}{\tau}\right), \tag{3.3a}$$

$$A_{2\omega}(z,t) = -A_{2\omega,0} \tanh\left(\frac{t-T}{\tau}\right). \tag{3.3b}$$

In these equations, we have re-parameterized the system in terms of τ, the signal pulse duration, T, the simulton centroid position, $A_{2\omega,0}$, the pump amplitude, and a, the simulton signal amplitude. Defining the small-signal gain coefficient, $\gamma_0 = \kappa A_{2\omega,0}$, we find that $a^2 = \frac{2\gamma_0}{\kappa^2}(\Delta\beta' + \gamma_0\tau)$ and $T = -\gamma_0\tau z$.

Thus, we see that the simulton consists of a tanh-shaped dark soliton in the pump and sech-shaped bright soliton in the signal which are co-moving with a group velocity greater than the signal group velocity by a factor $v = \gamma_0\tau$. Now, we wish to extend this solution to the dynamical regime where we can understand the impact of gain and loss on the system, following the manifold projection method presented in ref. [36]. We begin again with the coupled wave equations and use the method of characteristics to derive a solution for the pump field. We have:

$$\frac{\partial A_{2\omega}(z,t)}{\partial z} + \Delta\beta'\frac{\partial A_{2\omega}(z,t)}{\partial t} = -\kappa A_\omega^2(z,t). \tag{3.4}$$

Solving for $A_{2\omega}$ gives:

$$A_{2\omega}(z,t) = A_{2\omega}(0, t - \Delta\beta'z) - \kappa \int_0^z A_\omega^2(z', t + \Delta\beta'(z'-z))dz'. \tag{3.5}$$

To simplify the integral, we make the change of variables $t' = t + \Delta\beta'(z'-z)$, giving:

$$A_{2\omega}(z,t) = A_{2\omega}(0, t - \Delta\beta'z) - \frac{\kappa}{\Delta\beta'} \int_{t-\Delta\beta'z}^t A_\omega^2(z, t')dt'. \tag{3.6}$$

Now, we invoke the gain without distortion assumption, which says generally that $A_\omega(z,t) \approx e^{\gamma_{av}z}\bar{A}_\omega(z,t)$ such that $\bar{A}_\omega(z,t)$ is slowly varying in z and γ_{av} satisfies $re^{\gamma_{av}l} = 1$ for an OPO cavity with mirror reflectivity r and crystal length l. Under the present change of variables, this gives $A_\omega(z,t') \approx e^{\frac{\gamma_{av}}{\Delta\beta'}(t'-t)}\bar{A}_\omega(z,t')$. Noticing that the primary variation in the signal comes from this exponential term and thus vanishes exceedingly fast for increasingly negative t', we can assume the lower limit of the integral extends to $-\infty$ to good approximation:

$$A_{2\omega}(z,t) = A_{2\omega}(0, t - \Delta\beta'z) - \frac{\kappa}{\Delta\beta'} \int_{-\infty}^t A_\omega^2(z, t')dt'. \tag{3.7}$$

Next, we can plug this expression for the pump into equation 3.1a, the differential equation describing the evolution of the signal. This yields:

$$\frac{\partial A_\omega(z,t)}{\partial z} = \kappa A_\omega(z,t) A_{2\omega}(0, t - \Delta\beta' z) - \frac{\kappa^2}{\Delta\beta'} A_\omega(z,t) \int_{-\infty}^{t} A_\omega^2(z,t') dt'. \quad (3.8)$$

From here, we assume the field envelope takes on the sech-like form given above for the simulton, but we allow the parameters T, τ, and a to vary in z:

$$A_{\text{sim}}(z,t) = \frac{a(z)}{\sqrt{2\tau(z)}} \operatorname{sech}\left(\frac{t - T(z)}{\tau(z)}\right). \quad (3.9)$$

Plugging this into equation 3.8 for $A_\omega(z,t)$ and assuming a constant pump, $A_{2\omega,0}$, gives:

$$\frac{\partial A_\omega(z,t)}{\partial z} = \kappa A_{2\omega,0} \frac{a(z)}{\sqrt{2\tau(z)}} \operatorname{sech}\left(\frac{t - T(z)}{\tau(z)}\right) -$$
$$\frac{\kappa^2 a^2(z)}{2\Delta\beta' \sqrt{2\tau(z)}} \operatorname{sech}\left(\frac{t - T(z)}{\tau(z)}\right) \left[\tanh\left(\frac{t - T(z)}{\tau(z)}\right) + 1\right]. \quad (3.10)$$

Defining the right-hand side of equation 3.10 as $g(z,t)$, we now perform the manifold projection to obtain equations for the evolution of the signal pulse parameters. To perform the projection, we must first define an inner product, which we take to be $\langle f | g \rangle = \int f(t) g(t) dt$. The full derivative of A_{sim} with respect to z is given by:

$$\frac{dA_{\text{sim}}}{dz} = \frac{\partial A_{\text{sim}}}{\partial T} \frac{dT}{dz} + \frac{\partial A_{\text{sim}}}{\partial \tau} \frac{d\tau}{dz} + \frac{\partial A_{\text{sim}}}{\partial a} \frac{da}{dz}. \quad (3.11)$$

Letting $\frac{dA_{\text{sim}}}{dz} = g(z,t)$, and using the orthogonality of the partial derivatives under the defined inner product, e.g., $\left\langle \frac{\partial A_{\text{sim}}}{\partial \xi} \middle| \frac{\partial A_{\text{sim}}}{\partial \eta} \right\rangle = 0$ where $\xi, \eta \in \{T, \tau, a\}$ and $\xi \neq \eta$, we find the following expression for the evolution of parameter ξ:

$$\frac{\partial \xi}{\partial z} = \frac{\int g(z,t) \frac{\partial A_{\text{sim}}}{\partial \xi} dt}{\int \frac{\partial A_{\text{sim}}}{\partial \xi}^2 dt}. \quad (3.12)$$

Applying this to our three parameters of interest gives the following system of equations for their evolution:

$$\frac{\partial T}{\partial z} = -\gamma_0 \tau \frac{a^2}{a_{\text{sim}}^2}, \tag{3.13a}$$

$$\frac{\partial \tau}{\partial z} = 0, \tag{3.13b}$$

$$\frac{\partial a}{\partial z} = \gamma_0 a \left(1 - \frac{a^2}{a_{\text{sim}}^2}\right). \tag{3.13c}$$

Here, a_{sim} is the steady-state simulton amplitude, given by $a_{\text{sim}}^2 = \frac{2\gamma_0 \Delta \beta'}{\kappa^2}$. In the limit of the approximations made here, the simulton is a stable attractor of the OPA system, such that a sech-shaped pulse which is injected into an OPA will experience either gain or back conversion until its amplitude reaches a_{sim} [37]. This system of equations can be solved analytically to find $T(z)$, $\tau(z)$, and $a(z)$, giving:

$$T(z) = \tau_0 \ln\left(\frac{a(z)}{a(0)e^{\gamma_0 z}}\right) + T(0), \tag{3.14a}$$

$$\tau(z) = \tau_0, \tag{3.14b}$$

$$a(z) = \frac{a(0)e^{\gamma_0 z}}{\sqrt{1 + \frac{a(0)^2}{a_{\text{sim}}^2}(e^{2\gamma_0 z} - 1)}}. \tag{3.14c}$$

We may now extend this solution to the case of the simulton OPO by considering the effects of the roundtrip feedback, including loss and detuning, on the system. In particular, we assume a roundtrip group delay of ΔT_{RT} and a roundtrip loss of $e^{-\alpha_\omega \frac{L_{\text{RT}}}{2}}$, where α_ω, represents the loss per unit length in power over the resonator of total length L_{RT}. Assuming the nonlinear crystal is length L_{NL}, we get for the roundtrip evolution that:

$$T(n+1) = -\frac{\tau_0}{2} \ln\left(1 + \frac{a(n)^2}{a_{\text{sim}}^2}(e^{2\gamma_0 L_{\text{NL}}} - 1)\right) + T(n) + \Delta T_{\text{RT}}, \tag{3.15a}$$

$$\tau(n+1) = \tau_0, \tag{3.15b}$$

$$a(n+1) = \frac{a(n)e^{\gamma_0 L_{\text{NL}} - \alpha_\omega \frac{L_{\text{RT}}}{2}}}{\sqrt{1 + \frac{a(n)^2}{a_{\text{sim}}^2}(e^{2\gamma_0 L_{\text{NL}}} - 1)}}. \tag{3.15c}$$

Steady-state is reached when $a(n+1) = a(n)$ and $T(n+1) = T(n)$. From this first relation, an expression for the steady-state signal amplitude, $\tilde{a}$, may be derived:

$$\tilde{a}^2 = a_{\text{sim}}^2 \frac{e^{2\gamma_0 L_{\text{NL}} - \alpha_\omega L_{\text{RT}}} - 1}{e^{2\gamma_0 L_{\text{NL}}} - 1}. \tag{3.16}$$

This gives the first requirement for simulton threshold, which is that the gain must compensate the roundtrip loss, meaning that $e^{2\gamma_0 l - \alpha_\omega L} \geq 1$. The second steady-state condition, that $T(n+1) = T(n)$, gives the timing requirement for stable simulton formation, which is that $\Delta T = -\frac{\tau_0}{2} \ln\left(1 + \frac{a(n)^2}{a_{\text{sim}}^2}(e^{2\gamma_0 l} - 1)\right) = -\Delta T_{\text{RT}}$. by plugging in the steady-state signal amplitude, $\tilde{a}$, for $a(n)$, we find the following expression for the signal pulse width:

$$\tau_0 = \frac{2\Delta T_{\text{RT}}}{2\kappa E_{2\omega,0} L_{\text{NL}} - \alpha_\omega L_{\text{RT}}}. \tag{3.17}$$

Equation 3.17 describes the characteristic narrowing of the pulse width with increasing pump powers in the simulton regime.

In addition to these steady-state solutions, we can also see the interdependence of the energy and timing conditions, as the steady-state centroid position T depends on how quickly the simulton amplitude a saturates to its steady-state value. Since the growth of the amplitude depends on the interplay of gain and loss, the steady-state centroid position is therefore ultimately dictated by the gain and loss of the system. While here we have approximated the pump as continuous, this interplay becomes very important for a pulsed pump, as used in our experiments, where the pump defines a temporal gain window for the signal. Then, a more thorough description must also account for the effects of dispersion and gain clipping [36], though the inclusion of these additional terms does not always permit exact steady-state analytic solutions. In this case, the bright soliton in the signal cannot go above threshold if its amplitude does not grow quickly enough to satisfy the timing condition before the detuning pulls it out of the gain window, leading to an increased threshold for further-detuned simultons. We explore these concepts in more detail through the numerical simulations presented in Section 3.4.

3.3 Results

Having reviewed the simulton theory, we now present our experimental results. Because the parametric gain is phase sensitive, the signal of the OPO only oscillates around the cavity lengths where it acquires a 0 or π phase shift relative to the pump on each roundtrip. This results in signal resonances at a discrete set of cavity lengths, which are separated by about half the signal center wavelength. In the

context of this paper, the cavity length is denoted by the deviation of the cold-cavity roundtrip time from the repetition period of the pump pulses, i.e., ΔT_{RT}. Depending on the ΔT_{RT}, the different resonances can be classified into three regimes of operation: simulton ($\Delta T_{RT} > 0$), conventional ($\Delta T_{RT} = 0$), also referred to as "synchronous"), and nondegenerate ($\Delta T_{RT} < 0$) [36, 37]. Note that the positive ΔT_{RT} corresponds to a longer cavity length. Observation of the simulton in this regime follows naturally from the analysis in Section 3.2, where we found that synchrony of the simulton requires the simulton group advance, ΔT, to be compensated by the roundtrip detuning. Figure 3.2a shows the measured output spectrum as a function of relative cavity timing detuning (ΔT_{RT}) at the highest pump power of 1290 mW. When the cold cavity is most nearly synchronized to the pump repetition period (ΔT_{RT}), the OPO is identified to run in the conventional (synchronous) regime (labeled "0"), which has a degenerate spectrum and the lowest threshold. One additional degenerate resonance, the simulton regime (labeled "+1"), is found when the cavity is positively detuned. Conversely, when the cavity is negatively detuned, the OPO operates in the nondegenerate regime, with the output spectra split into distinguishable signal and idler bands (labeled "-1, -2, -3, and -4"). With parameters comparable to the experiment, a simulation of the output spectrum as a function of ΔT_{RT} is conducted (see Section 3.6 for additional details), which is depicted in Figure 3.2b. The simulation exhibits a good agreement with the experimental result for all three regimes.

Figure 3.2c presents output-input power dependencies for each resonance measured with locked cavity lengths. With the lowest threshold, the conventional regime has a slope efficiency of 45% and a conversion efficiency of 42%. For the nondegenerate resonances, as ΔT_{RT} becomes increasingly negative, the thresholds increase uniformly, with conversion efficiencies decreasing and limited to less than 35%. In contrast, the simulton resonance has an irregularly located high threshold and the highest conversion efficiency of 44%. Furthermore, it measures a 350% slope efficiency near the threshold and a 70% slope efficiency well above the threshold, much higher than those of the conventional and nondegenerate regimes.

To demonstrate the difference between the power-dependent bandwidth scaling of the conventional and simulton regimes, we measure spectra of the signal at each output power corresponding to the experimental points in Figure 3.2c, the results of which are shown in Figure 3.3a–c. In the simulton regime, as the power increases, the bandwidth of the signal spectrum increases if the pump power is not too high
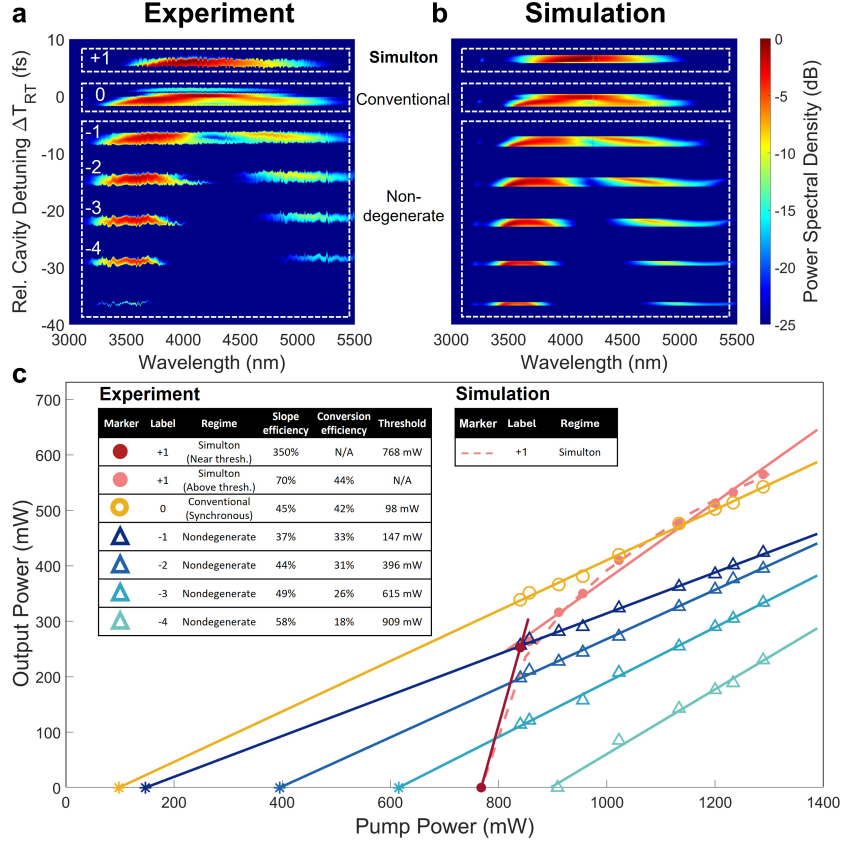
Figure 3.2: **Simulton OPO characterization.** **a**, Measured signal spectrum as a function of cavity detuning at the highest pump power of 1290 mW, labeled with resonance numbers. The y-axis denotes the relative cavity detuning, the zero of which is set at the center of the conventional resonance. **b**, Simulated signal spectrum as a function of cavity detuning corresponding to **a**, with the three identified regimes indicated on the left. **c**, Output–input power dependencies for each resonance measured with locked cavity lengths. Filled circle, unfilled circles, and triangles denote experimental measured points of simulton (+1), conventional (0), and nondegenerate (-1 to -4) resonances, respectively. Solid lines represent their linear fitting for estimation of their slope efficiencies. Note that the thresholds of resonance 0, -1, -2, and -3 cannot be directly measured since the pump is not stable at such low powers; therefore, they are instead estimated by extrapolations of their linearly fitted lines, denoted by asterisks. Two slope efficiencies, one just above the threshold (dark red solid line) and the other well above the threshold (pink solid line), are estimated for the simulton resonance, given its distinct behavior from other resonances. Conversion efficiencies for all resonances are calculated at the highest pump power of 1290 mW. The simulation corresponding to resonance +1 is denoted by the pink dashed curve.

(Figure 3.3a), while in the conventional regime, it monotonically decreases (Figure 3.3b). These tendencies are in accordance with the simulton theory (Section 3.2) [37]

and conventional box-pulse scaling [36]. It should be noted that at the three highest pump powers, the signal bandwidth of the simulton regime stops broadening further, which also agrees with our theoretical prediction that the simulton theory would fail if the signal is too far above threshold [36]. This transition from simulton scaling to box-pulse scaling far above threshold also accounts for the observed nonlinear reduction in the simulton slope efficiency in Figure 3.2c. Nonetheless, at high pump power around 1200 mW, the simulton regime wins about 40% in bandwidth. This power-dependent signal spectral characterization shows that the simulton regime outperforms the conventional regime not only in power and efficiency but also in spectral bandwidth. At the highest available pump power of 1290 mW, the FWHM bandwidth of the signal spectra for simulton and conventional regimes are 14 and 10 THz, which can support pulses as short as 22 and 32 fs, respectively. Figure 3.3d depicts the interferometric autocorrelation of the simulton pulse measured by a two-photon extended-InGaAs detector, together with its fitted pulse intensity. This measurement corresponds to an FWHM pulse width of about 45 fs, assuming no chirp. However, chirp exists due to the dispersion from the substrates of the output coupler (1 mm ZnSe) and two long pass filters (1 mm Ge and 1 mm Si) in the path to the autocorrelator.

In this experiment, the efficiency advantage of the simulton regime is limited by the available pump power. To further demonstrate the efficiency potential of the simulton regime, we use numerical simulations with higher pump power under different output coupling ratios, and the results are shown in Figure 3.4a. As suggested by the simulation, higher output coupling should be employed with higher pump power to realize higher conversion efficiency, and the conversion efficiency can be improved to as high as 63% if 4.2-W pump power and 0.65 (65%) output coupling ratio are used. This simulation result can also be used as a design rule for choosing the output coupling of the simulton OPO under different available pump powers. Figure 3.4b presents the highest possible conversion efficiency that the simulton regime can reach under different pump powers (red circles), with the labels of the corresponding output coupling (red decimals). As a comparison, under each pump power, the highest conversion efficiencies that the conventional regime can achieve are also plotted in Figure 3.4b (blue circles), labeled with the corresponding output coupling ratios (blue decimals). The comparison shows that the return of the simulton regime can increase sharply with increasing pump power. It is worth noting that the pump intensity used in the simulation is similar to those of the previously demonstrated experiments [28, 40], which is expected to be below the
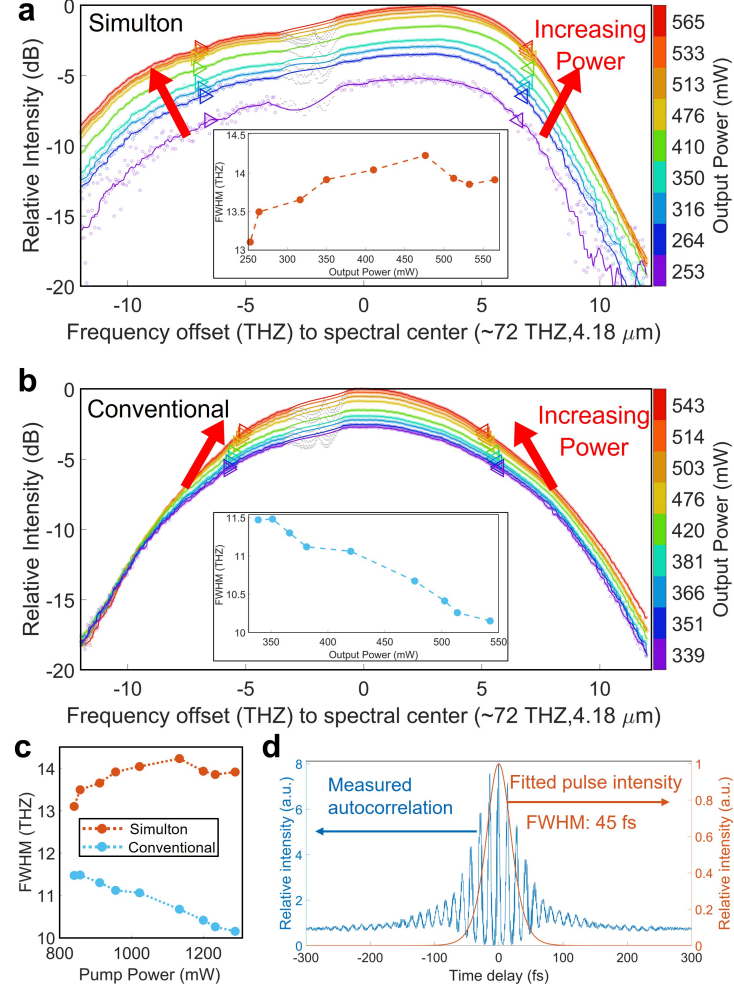
Figure 3.3: **Temporal and spectral power scaling.** Spectra recorded as a function of output power for the OPO working in the **a**, simulton regime and **b**, conventional (synchronous) regime. The signal power and corresponding FWHM bandwidth for each curve are presented in the insets. The FWHM bandwidths are also denoted by the triangular arrows on the curves. The unfilled circles denote the raw data points obtained by the Fourier-transform infrared spectroscopy (FTIR), and curves present the interpolation of them for a better visualization of results and estimation of FWHM bandwidths. Note that a portion of the raw data near the strong atmospheric absorption around 4.2 μm is discarded during the interpolation, which is denoted by smaller filled gray circles. **c**, FWHM bandwidths of the signal spectra as a function of pump power for both regimes, corresponding to **a** and **b**. Solid circles denote experimentally measured points, and dotted curves are to guide the eye. **d**, Two-photon interferometric autocorrelation (blue) and fitted intensity (red) of the signal pulse at the highest pump power of 1290 mW, for the OPO working in the simulton regime.

damage threshold of OP-GaP.
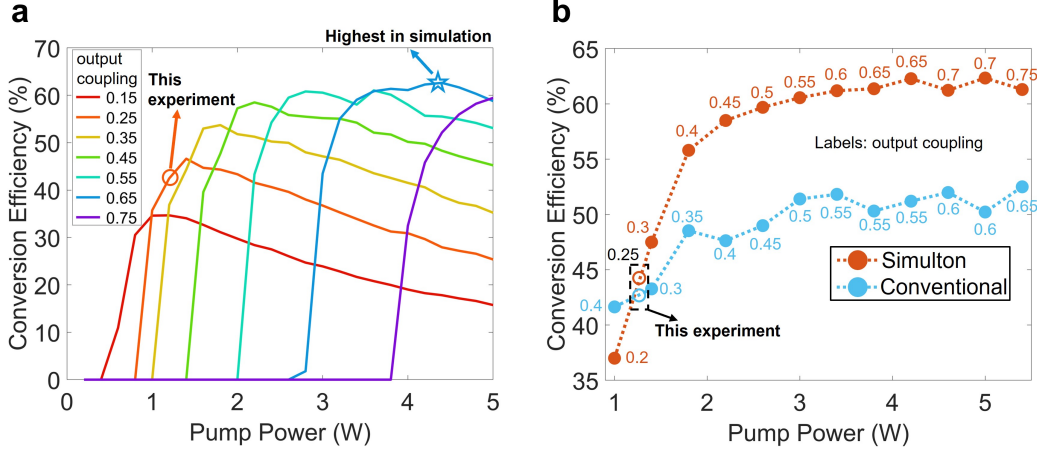
Figure 3.4: **Numerical simulation of the simulton OPO with different output coupling ratios.** **a**, Conversion efficiency (in percentage) as a function of pump power. Curves in different colors denote different output coupling ratio (in decimal), as indicated in the legend box. The orange circle denotes the result that is realized in our experiment and the blue pentagram denotes the suggested highest conversion efficiency that can be achieved by this simulton OPO. **b**, Highest conversion efficiency (in percentage) that the OPO can achieve under different pump power. The red circles denote the results (in percentage) in the simulton regime, labeled with the output coupling ratio (red decimal) that should be used. The blue circles, as a comparison to the red ones, denote the results in the conventional regime, also labeled with the corresponding output coupling ratio (blue decimal). The unfilled red and blue circles denote our experimental results of simulton and conventional regime, respectively.

3.4 Discussion

As is evident from our experimental and theoretical results, developing a better understanding of simulton formation is crucial for further improvement of the OPO performance. Here, we use our simulation results to build upon the understanding of simulton formation dynamics presented in ref. [37] and offer practical tools for optimizing simulton performance. We begin with a discussion of the relationship between the simulton formation dynamics and the high slope efficiencies and conversion efficiencies offered by this regime. Figure 3.5a shows schematically the interaction between pump (blue) and signal (orange) in the single-pass OPA process which occurs each roundtrip in the OPO. From the crystal input (left) to its output (right), the signal walks through the pump, depleting it and extracting gain in the process. Two terms contribute to the walk-off, the product of the group velocity

mismatch (GVM), $\Delta\beta'$, with the crystal length, $L_{\text{NL}} = L$, and the nonlinear timing advance due to simulton acceleration, ΔT, leading to a combined walk-off of $\Delta\beta' L + \Delta T$ relative to the signal starting position. This walk-off along the fast time axis and simultaneous depletion of the pump by the signal determines the available gain for the signal. For the signal to resonate above threshold, the gain extracted in consecutive roundtrips must consistently overcome the loss.

Figure 3.5b–e shows the signal centroid position at the input facet of the crystal as a function of roundtrip, with the color indicating the normalized logarithm of the pulse energy, to illustrate the signal build up dynamics in the conventional and simulton regimes. In the conventional case (Figure 3.5b,c), there is no timing condition, so the signal goes above threshold as soon as the gain experienced through the linear walk-off, $\Delta\beta' L$, equals the loss. This results in there being no clear trends in the dynamics of the signal below threshold, as shown in Figure 3.5b, with amplified noise being unable to build up. Above threshold, the noise quickly grows into a strong signal pulse, located near the center of the gain window set by the pump (Figure 3.5c). In the simulton case (Figure 3.5d,e), however, the cavity detuning, ΔT_{RT}, creates a linear delay which causes the amplified signal noise to move away from the gain window set by the pump. Since the simulton acceleration relies on pump depletion by the leading edge of the signal and subsequent back-conversion of the trailing edge, going above threshold requires that the simulton build up enough to accelerate and satisfy the timing condition before falling out of the gain window due to the linear delay. This intertwines the simulton energy and timing conditions, as large simulton acceleration requires the presence of high enough signal gain. Figure 3.5d shows the case of the below threshold simulton, in which the delayed and amplified noise attempts to build up but ultimately does not experience enough gain to sufficiently accelerate and falls off. By contrast, Figure 3.5e shows the simulton build-up above threshold, in which the simulton acceleration leads to a timing advance, ΔT, which compensates the delay, ΔT_{RT}. Unlike the conventional case, the simulton just above threshold builds up near the edge of the gain window. These observations correspond to important features of the simulton. First, the high threshold for the simulton is a consequence of the requirement for there to be high gain for the timing condition to be satisfied. The burst slope efficiency of the simulton near threshold then results as the acceleration pulls the simulton to the center of the gain window. Once well-confined to the gain window, the longer walk-off for the simulton due to the additional nonlinear acceleration term, ΔT, suggests that simulton operation can often enable more efficient extraction of the pump gain. This
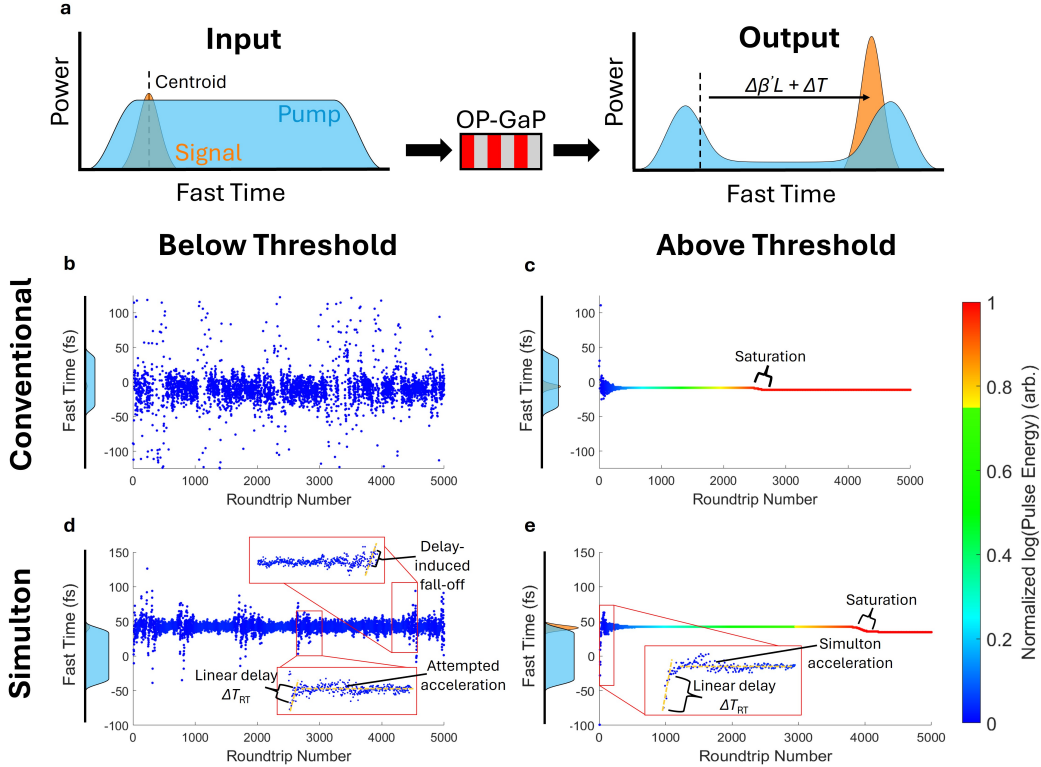
Figure 3.5: **Depiction of simulton formation dynamics as compared to the conventional regime. a**, Schematic illustration of the pump-signal interaction in the crystal. Between the input (left) and output (right) facets of the crystal, the signal (orange) walks through the pump (blue) from its starting point according to product of the GVM, $\Delta\beta'$, with the crystal length, L, plus any timing advance, ΔT, due to simulton acceleration. This walk-off and concurrent pump depletion define a gain window for the signal along the fast time axis. **b–e**, Simulated comparison of simulton (**b**,**c**) and conventional (**d**,**e**) signal centroid positions along the fast time axis as a function of roundtrip number in the below (**b**,**d**) and above (**c**,**e**) threshold cases. The normalized logarithm of the pulse energy is indicated by the color of each point. **b**, The conventional case below threshold has few discernible features as noise and loss dominate; noise amplified by the pump is unable to build up. **c**, Above threshold, the noise quickly builds into a strong signal pulse. A small timing shift is observed when the gain saturates. **d**, For the simulton, noise amplified by the pump experiences a linear delay due to the cavity detuning, ΔT_{RT}. Below threshold, since the gain cannot enable sufficient acceleration for the timing condition to be satisfied, the delay results in the signal falling out of the gain window before signal build up can be achieved. **e**, The simulton goes above threshold when the gain is sufficient for the simulton acceleration to compensate the linear delay and enable signal build up. As in the conventional case, a small timing shift is observed when the gain saturates.

gives rise to observed trends of slope efficiencies and overall conversion efficiencies for simulton operation that exceed what is observed for conventional OPO operation. Practically, one should match $\Delta\beta' L + \Delta T$ to the length of the gain window defined by the pump for optimum signal generation.

An additional parameter which is critical to simulton formation is the carrier-envelope offset (CEO) frequency (f_{CEO}) of the pump, the impact of which is illustrated in Figure 3.6. The pump f_{CEO} imposes a phase $\Delta\phi_{CEO}$ between consecutive pump pulses. Due to the aforementioned phase-sensitive gain which demands a relative phase of 0 or π between pump and signal for signal build-up, this pulse-to-pulse phase shift in the pump must be mirrored in the signal, as shown in Figure 3.6a. For signal resonance to occur, the phase accumulated in the roundtrip must be $\Delta\phi_{CEO}/2 + n\pi$, where n is an integer, with π signal phase corresponding to a detuning of 7 fs between resonances for the 4.18 µm OPO. The case for n even is shown by the upper signal branch while the case where n is odd, in which the signal accumulates an additional phase shift of π between pulses, is depicted in the lower signal branch. The signal roundtrip phase accumulation, $\phi(\Omega)$, relative to a perfectly synchronous signal pulse is given by $\phi(\Omega) = \Delta T_{RT}(\frac{\omega c}{\lambda_{2\omega}} + \Omega)$, where Ω is the normalized frequency, ΔT_{RT} is the detuning as defined previously, c is the speed of light, $\lambda_{2\omega}$ is the pump wavelength, and $\phi(\Omega)$ represents the higher-order effects of dispersion from mirrors and additional cavity elements [37]. From this equation, we see the required pulse-to-pulse phase shift for the signal can be achieved through varying ΔT_{RT} such that the constant phase term $\Delta\phi_{RT} = \Delta T_{RT}\frac{\pi c}{\lambda_{2\omega}} = \Delta\phi_{CEO} + \pi n$, the desired phase shift. In other words, $\Delta\phi_{CEO}$ determines the detuning values where the OPO can resonate. However, varying ΔT_{RT} also causes a change in the signal timing, modeled through the linear phase term $\Delta T_{RT}\Omega$, and consequently the simulton threshold and slope efficiency. This implies that, through tuning of the pump f_{CEO}, one can adjust the timing of the signal resonances to optimize simulton performance.

Figure 3.6b–e shows the simulated signal resonances for a few values of $\Delta\phi_{CEO}$. As the focus of this study is on simulton behavior, only the first few resonances are shown. Resonance labels denote the roundtrip phase, $\Delta\phi_{RT}$, acquired by the signal, and an additional label denotes the timing shift from 0 fs of the most positively detuned resonance with $\Delta\phi_{RT} = \Delta\phi_{CEO}/2$. As seen in Figure 3.6b, when $\Delta\phi_{CEO} = 0$, the signal at $\Delta\phi_{RT} = \Delta\phi_{CEO}/2$ is a typical conventional resonance with $\Delta T_{RT} = 0$. Note that no simulton exists at the expected location, $\Delta\phi_{RT} = \Delta\phi_{CEO}/2 + \pi$ (shown
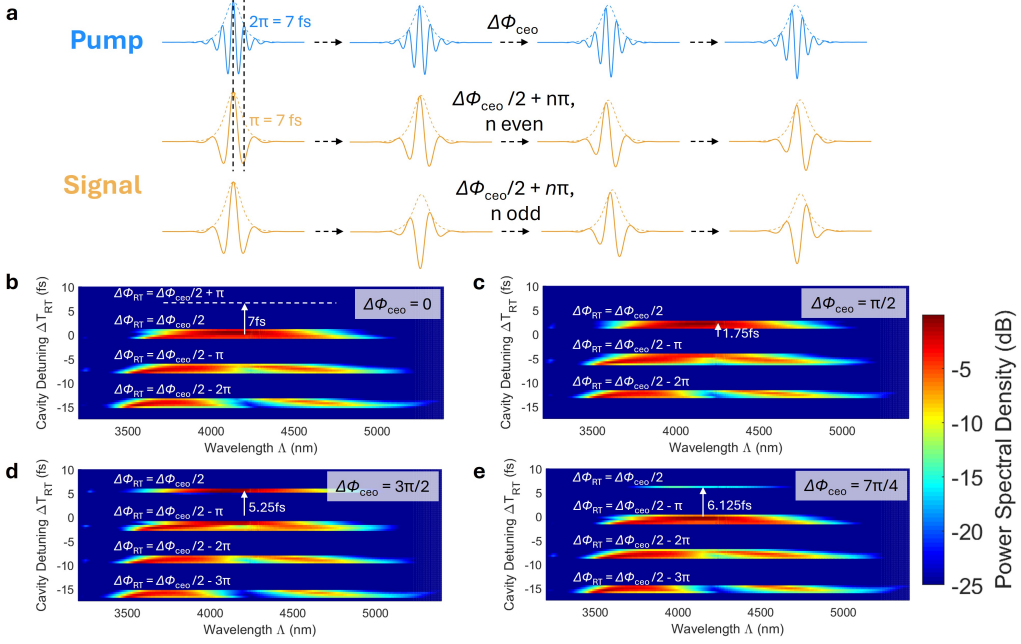
Figure 3.6: **Simulated impact of the pump carrier-envelope offset frequency, f_{CEO}, on simulton performance.** **a**, Illustration of the pump-signal phase relationships for the OPO resonances. For a pulse-to-pulse phase slip of $\Delta\phi_{CEO}$ in the pump, the OPO can resonate when the roundtrip phase accumulation, $\Delta\phi_{RT}$, is $\Delta\phi_{CEO}/2 + n\pi$, where n is an integer, with π signal phase corresponding to a detuning of 7 fs between resonances. The upper signal branch depicts the case of n even, where a pulse-to-pulse phase of $\Delta\phi_{CEO}/2$ is accrued, while the lower shows n odd, which adds an additional π phase shift between consecutive pulses. **b**, First three cavity resonances for $\Delta\phi_{CEO} = 0$, showing that no simulton behavior is observed, with the topmost resonance occurring at $\Delta T_{RT} = 0$ and exhibiting both strongly degenerate and nondegenerate features. **c**, As $\Delta\phi_{CEO}$ is increased to $\pi/2$, simulton-like behavior is observed as the topmost resonance becomes more positively detuned. **d**, Example of a strongly degenerate simulton at $\Delta\phi_{CEO} = 3\pi/2$, showing that tuning of $\Delta\phi_{CEO}$ to this region can enable optimum simulton performance for the given gain. **e**, As $\Delta\phi_{CEO}$ is further increased beyond $7\pi/2$, the simulton disappears as the timing condition can no longer be satisfied by the gain, which is why no simulton resonance is observed in panel **b** at the $\Delta\phi_{CEO}/2 + \pi$ resonance, indicated by the white, dashed line.

by the white, dashed line), due to a lack of gain. For values between 0 and π, the $\Delta\phi_{RT} = \Delta\phi_{CEO}/2$ resonance becomes simulton-like but still behaves more like a conventional OPO, with both nondegenerate and degenerate regions as shown in Figure 3.6c. Beyond $\Delta\phi_{CEO} = \pi$, a strong simulton is observed, like that shown in Figure 3.6d for $\Delta\phi_{CEO} = 3\pi/2$. In tandem with the $\Delta\phi_{RT} = \Delta\phi_{CEO}/2$ resonance transitioning from more conventional behavior to the simulton regime, we also

observe strengthening of the degenerate side of the $\Delta\phi_{RT} = \Delta\phi_{CEO}/2 - \pi$ resonance such that it behaves more like a conventional OPO as it approaches $\Delta T_{RT} = 0$. Finally, as exemplified by Figure 3.6e, when $\Delta\phi_{CEO}$ is greater than 1.5π, the power in the resonance quickly drops off as the gain struggles to satisfy the timing condition, with the OPO repeating the resonance structure shown in Figure 3.6b as $\Delta\phi_{CEO}$ approaches 2π. Our experiment corroborates these findings, as we observe such a shift in simulton behavior as the $\Delta\phi_{CEO}$ is varied, with presented data representing the strongest observed simulton. This suggests that, for given experimental values of gain and loss, $\Delta\phi_{CEO}$ can be a crucial experimental parameter for optimizing simulton performance.

3.5   Conclusion

In summary, we present the generation of a high-power and efficient MIR frequency comb centered at 4.18 µm based on an OPO operating in the simulton regime, achieving 565 mW average power together with a 14 THz instantaneous FWHM bandwidth, sub-three-cycle pulses, a 350% slope efficiency near the threshold, a 70% slope efficiency above the threshold, and a record high 44% conversion efficiency. By a direct comparison with the conventional regime in terms of cavity detuning, output power, threshold, slope and conversion efficiency, instantaneous bandwidth, and bandwidth scaling, we are able to ascribe the favorable performances of this novel regime to the simulton formation, based on the agreement between the experiment, simulation, and theory. The performance of this simulton OPO is expected to be further improved by tuning the pump and optimizing dispersion and loss within the cavity. Especially, the numerical simulation suggests that a conversion efficiency >60% can be achieved if 4 W pump power and 65% output coupling are employed. Finally, we further explore simulton build-up dynamics and analyze the impact of the pump f_{CEO} on simulton formation, and we tie these results to practical design considerations for a simulton OPO. In addition, we want to emphasize that the half-harmonic signal of femtosecond degenerate OPOs are frequency combs that are intrinsically phase- and frequency-locked to their pump combs, which is well-established in previous works [26, 31, 41]. Very recently, we have used the OPO presented in this work as the comb source for a dual-comb-based spectroscopy experiment in the mid-IR [42], enabled by its comb character and intrinsic locking. Moreover, it is experimentally shown that the CEO frequency noise can be reduced by 6 dB through the half-harmonic generation [43].

In short, this work paves the way to realization of a compelling new source of ultrashort-pulse frequency combs in the mid-infrared region which can benefit numerous applications, for example, spectroscopy methods that require high-power, broadband, and short-pulse MIR frequency combs [41, 42]. This work sheds new lights on soliton generation based on the quadratic nonlinearity and its potential in the MIR region. Recent advances in integrated quadratic platforms [33, 38, 44] promise on-chip realization of such sources in the future.

3.6 Supporting Information

Experimental Details

The experimental setup of the MIR OPO is illustrated in Figure 3.1e. For the pump, another OPO based on periodically poled lithium niobate with a 250 MHz repetition rate generating pulses centered at 2.09 µm was used. Its average power reached up to 1290 mW with an FWHM bandwidth around 155 nm. The MIR OPO cavity consisted of a bow-tie resonator with a tunable cold-cavity time of 4 ns that could be scanned or locked around the pump repetition period using a piezoelectric actuator. The input coupler (M1) was a flat dielectric-coated mirror that was highly transmissive for the pump range (around 2.09 µm) and highly reflective for the signal range (around 4.18 µm). The focusing and collimating of the beams were provided by two concave gold mirrors (M2 and M3) with a 24-mm radius of curvature, which had a high reflection for both signal and pump. The nonlinear gain was provided by a plane-parallel orientation-patterned gallium phosphide (OP-GaP) crystal with a length of 0.5 mm and a poling period of 92.7 µm for type-0 phase matching at room temperature. The crystal had a broadband antireflection coating for both the signal and pump range. The output coupler (M4) was a dielectric mirror coated for broadband transmission (T = 25%) from 3.5 to 5.5 µm, the value of which was chosen based on a rough experimental optimization of the output coupling using a coated pellicle beamsplitter [27]. The length of the OPO was locked using the "dither-and-lock" procedure described in ref. [31].

As mentioned in the figure caption, the OPO is placed in a box purged with dry nitrogen to reduce the impact of atmospheric absorption. Although the OPO can still run without purging, degenerate operation is not possible due to the strong absorption of carbon dioxide centered at 4.2 µm, prohibiting the OPO from operating in the simulton regime. We also contain the measurement instruments for characterization of the OPO output in the purging box to limit the artifacts caused by the atmospheric absorption.

Numerical Simulation

Here, we describe the methodology behind the simulations used for numerical modeling of our experiment. Using the notation of [37], the coupled wave equations describing the phase-matched nonlinear interaction of pump and signal in the crystal are given by

$$\frac{\partial}{\partial z} A_\omega(z,t) = \kappa A_{2\omega} A_\omega^* - \frac{\alpha_\omega}{2} + \hat{D}_\omega A_\omega, \tag{3.18a}$$

$$\frac{\partial}{\partial z} A_{2\omega}(z,t) = -\Delta\beta' \frac{\partial}{\partial t} A_{2\omega} - \kappa A_\omega^2 - \frac{\alpha_{2\omega}}{2} + \hat{D}_{2\omega} A_{2\omega}, \tag{3.18b}$$

where compared to equations 3.1a and 3.1b, we have included explicitly the loss in the crystal for the jth wave, α_j, as well as the dispersion operator, $\hat{D}_j = \sum_{m=2}^{\infty} \left[\frac{(i)^{m+1} \beta_j^{(m)}}{m!} \right] \partial_t^m$.

Simulations of the field envelope evolutions in the crystal are performed using the split-step Fourier method, in which the OPA process in the crystal is divided into fifty segments. In each segment, we solve the linear and nonlinear portions of the coupled wave equations as lumped elements. The nonlinear step is computed by solving the nonlinear terms in the coupled wave equations using the fourth-order Runge-Kutta method. This is followed by a linear filter containing the dispersion and loss for the crystal, which is applied in the frequency domain to the pump and signal. We calculate four orders of dispersion for both pump and signal from the Sellmeier equation given in [45].

The roundtrip propagation is modeled by a linear feedback loop which contains the frequency-dependent losses as well as the dispersion for all cavity elements. Specifically, for the nth roundtrip, the signal at the input of the crystal, $A_\omega^{n+1}(0,t)$ is related to the output of the OPA process, $A_\omega^n(L,t)$ by the equation

$$A_\omega^{n+1}(0,t) = \mathcal{F}^{-\infty} \{ e^{-\frac{\alpha_{\text{RT}}(\omega)}{2}} e^{-i\phi_\Omega} \mathcal{F} \{ A_\omega^n(L,t) \} \}. \tag{3.19}$$

Here, Ω is the normalized Fourier frequency and $\mathcal{F}$ and $\mathcal{F}^{-1}$ are the Fourier transform and inverse Fourier transform, respectively. $\alpha_{\text{RT}}(\Omega)$ gives the roundtrip loss of the signal, including the frequency-dependent losses from the output coupling, the AR coatings on the crystal interfaces, the cavity mirrors, and the residual atmospheric gases in the cavity after purging, modeled using data provided by the HITRAN database [46]. Similarly, $\phi(\Omega) = \Delta T_{\text{RT}}(\frac{\pi c}{\lambda_{2\omega}} + \Omega) + \Delta\phi(\Omega)$ gives the

roundtrip phase accumulated by the signal, measured relative to a perfectly synchronous signal pulse, as mentioned in Section 3.4. ΔT_{RT} is the detuning and contributes to both a constant phase term, $\frac{\Delta T_{\mathrm{RT}} \pi c}{\lambda_{2\omega}}$, and a linear phase term, $\Delta T_{\mathrm{RT}} \Omega$, which accounts for the timing delay. Here, c is the speed of light and $\lambda_{2\omega}$ is the wavelength of the pump. $\Delta \phi(\Omega)$ accounts for higher-order contributions to the phase due to the dispersion of the cavity mirrors, the AR coatings on the crystal, and the residual gas in the cavity.

BIBLIOGRAPHY

[1] Albert Schliesser, Nathalie Picqué, and Theodor W. Hänsch. "Mid-infrared frequency combs." In: *Nature Photonics* 6.7 (2012), pp. 440–449.

[2] Nathalie Picqué and Theodor W. Hänsch. "Frequency comb spectroscopy." In: *Nature Photonics* 13.3 (2019), pp. 146–157.

[3] Fritz Keilmann, Christoph Gohle, and Ronald Holzwarth. "Time-domain mid-infrared frequency-comb spectrometer." In: *Optics Letters* 29.13 (2004), pp. 1542–1544.

[4] Tilo Steinmetz, Tobias Wilken, Constanza Araujo-Hauck, Ronald Holzwarth, Theodor W. Hänsch, Luca Pasquini, Antonio Manescau, Sandro D'Odorico, Michael T. Murphy, Thomas Kentischer, et al. "Laser frequency combs for astronomical observations." In: *Science* 321.5894 (2008), pp. 1335–1337.

[5] Joss Bland-Hawthorn and Pierre Kern. "Astrophotonics: A new era for astronomical instruments." In: *Optics Express* 17.3 (2009), pp. 1880–1884.

[6] Tenio Popmintchev, Ming-Chang Chen, Dimitar Popmintchev, Paul Arpin, Susannah Brown, Skirmantas Ališauskas, Giedrius Andriukaitis, Tadas Balčiunas, Oliver D. Mücke, Audrius Pugzlys, et al. "Bright coherent ultrahigh harmonics in the keV x-ray regime from mid-infrared femtosecond lasers." In: *Science* 336.6086 (2012), pp. 1287–1291.

[7] Shambhu Ghimire and David A. Reis. "High-harmonic generation from solids." In: *Nature Physics* 15.1 (Jan. 2019), pp. 10–16. ISSN: 1745-2481. DOI: 10.1038/s41567-018-0315-5. URL: https://doi.org/10.1038/s41567-018-0315-5.

[8] Markku Vainio and Lauri Halonen. "Mid-infrared optical parametric oscillators and frequency combs for molecular spectroscopy." In: *Physical Chemistry Chemical Physics* 18.6 (2016), pp. 4266–4294.

[9] Ben Henderson, Amir Khodabakhsh, Markus Metsälä, Irène Ventrillard, Florian M Schmidt, Daniele Romanini, Grant A. D. Ritchie, Sacco te Lintel Hekkert, Raphaël Briot, Terence Risby, et al. "Laser spectroscopy for breath analysis: Towards clinical implementation." In: *Applied Physics B* 124 (2018), pp. 1–21.

[10] Ioachim Pupeza, Daniel Sánchez, Jinwei Zhang, Nicolai Lilienfein, Marcus Seidel, Nicholas Karpowicz, Tim Paasch-Colberg, Irina Znakovskaya, M. Pescher, Wolfgang Schweinberger, et al. "High-power sub-two-cycle mid-infrared pulses at 100 MHz repetition rate." In: *Nature Photonics* 9.11 (2015), pp. 721–724.

[11] Grzegorz Soboń, Tadeusz Martynkien, Paweł Mergo, Lucile Rutkowski, and Aleksandra Foltynowicz. "High-power frequency comb source tunable from 2.7 to 4.2 μm based on difference frequency generation pumped by an Yb-doped fiber laser." In: *Optics Letters* 42.9 (2017), pp. 1748–1751.

[12] Alexander J. Lind, Abijith Kowligy, Henry Timmers, Flavio C. Cruz, Nima Nader, Myles C. Silfies, Thomas K. Allison, and Scott A. Diddams. "Mid-infrared frequency comb generation and spectroscopy with few-cycle pulses and χ (2) nonlinear optics." In: *Physical Review Letters* 124.13 (2020), p. 133904.

[13] Andreas Hugi, Gustavo Villares, Stéphane Blaser, Hui Chun Liu, and Jérôme Faist. "Mid-infrared frequency comb based on a quantum cascade laser." In: *Nature* 492.7428 (2012), pp. 229–233.

[14] Jérôme Faist, Gustavo Villares, Giacomo Scalari, Markus Rösch, Christopher Bonzon, Andreas Hugi, and Mattias Beck. "Quantum cascade laser frequency combs." In: *Nanophotonics* 5.2 (2016), pp. 272–291.

[15] Manijeh Razeghi and Alexei N. Baranov. "Terahertz emitters, receivers, and applications IX." In: *Proc. of SPIE Vol*. Vol. 10756. 2018, pp. 1075601–1.

[16] Mengjie Yu, Yoshitomo Okawachi, Austin G. Griffith, Nathalie Picqué, Michal Lipson, and Alexander L. Gaeta. "Silicon-chip-based mid-infrared dual-comb spectroscopy." In: *Nature Communications* 9.1 (2018), p. 1869.

[17] Davide Grassani, Eirini Tagkoudi, Hairun Guo, Clemens Herkommer, Fan Yang, Tobias J. Kippenberg, and Camille-Sophie Brès. "Mid infrared gas spectroscopy using efficient fiber laser driven photonic chip-based supercontinuum." In: *Nature Communications* 10.1 (2019), p. 1553.

[18] Hairun Guo, Wenle Weng, Junqiu Liu, Fan Yang, Wolfgang Hänsel, Camille-Sophie Brès, Luc Thévenaz, Ronald Holzwarth, and Tobias J. Kippenberg. "Nanophotonic supercontinuum-based mid-infrared dual-comb spectroscopy." In: *Optica* 7.9 (2020), pp. 1181–1188.

[19] Sergey Vasilyev, Viktor Smolski, Jeremy Peppers, Igor Moskalev, Mike Mirov, Yury Barnakov, Sergey Mirov, and Valentin Gapontsev. "Middle-IR frequency comb based on Cr: ZnS laser." In: *Optics Express* 27.24 (2019), pp. 35079–35087.

[20] Florian Adler, Kevin C. Cossel, Michael J. Thorpe, Ingmar Hartl, Martin E. Fermann, and Jun Ye. "Phase-stabilized, 1.5 W frequency comb at 2.8–4.8 μ m." In: *Optics letters* 34.9 (2009), pp. 1330–1332.

[21] Yohei Kobayashi, Kenji Torizuka, Alireza Marandi, Robert L. Byer, Richard A. McCracken, Zhaowei Zhang, and Derryck T Reid. "Femtosecond optical parametric oscillator frequency combs." In: *Journal of Optics* 17.9 (2015), p. 094010.

[22] Luke Maidment, Peter G. Schunemann, and Derryck T. Reid. "Molecular fingerprint-region spectroscopy from 5 to 12 μm using an orientation-patterned gallium phosphide optical parametric oscillator." In: *Optics Letters* 41.18 (2016), pp. 4261–4264.

[23] Kana Iwakuni, Gil Porat, Thinh Q Bui, Bryce J. Bjork, Stephen B. Schoun, Oliver H. Heckl, Martin E. Fermann, and Jun Ye. "Phase-stabilized 100 mW frequency comb near 10 μm." In: *Applied Physics B* 124 (2018), pp. 1–7.

[24] Callum F. O'Donnell, Suddapalli Chaitanya Kumar, Peter G. Schunemann, and Majid Ebrahim-Zadeh. "Femtosecond optical parametric oscillator continuously tunable across 3.6–8 μm based on orientation-patterned gallium phosphide." In: *Optics Letters* 44.18 (2019), pp. 4570–4573.

[25] Chengxiao Ning, Pei Liu, Yingxiong Qin, and Zhaowei Zhang. "Continuous wavelength tuning of nondegenerate femtosecond doubly resonant optical parametric oscillators." In: *Optics Letters* 45.9 (2020), pp. 2551–2554.

[26] Alireza Marandi, Kirk A. Ingold, Marc Jankowski, and Robert L. Byer. "Cascaded half-harmonic generation of femtosecond frequency combs in the mid-infrared." In: *Optica* 3.3 (2016), pp. 324–327.

[27] Evgeni Sorokin, Alireza Marandi, Peter G. Schunemann, Martin M. Fejer, Robert L. Byer, and Irina T. Sorokina. "Efficient half-harmonic generation of three-optical-cycle mid-IR frequency comb around 4 μm using OP-GaP." In: *Optics Express* 26.8 (2018), pp. 9963–9971.

[28] Qitian Ru, Taiki Kawamori, Peter G. Schunemann, Sergey Vasilyev, Sergey B. Mirov, and Konstantin L. Vodopyanov. "Two-octave-wide (3–12 μm) sub-harmonic produced in a minimally dispersive optical parametric oscillator cavity." In: *Optics Letters* 46.4 (2021), pp. 709–712.

[29] Richard A. McCracken and Derryck T. Reid. "Few-cycle near-infrared pulses from a degenerate 1 GHz optical parametric oscillator." In: *Optics Letters* 40.17 (2015), pp. 4102–4105.

[30] Richard A. McCracken, Yuk Shan Cheng, and Derryck T. Reid. "10-GHz femtosecond degenerate optical parametric oscillator." In: *CLEO: QELS_Fundamental Science*. Optica Publishing Group. 2018, FTh1M–1.

[31] Alireza Marandi, Nick C. Leindecker, Vladimir Pervak, Robert L. Byer, and Konstantin L. Vodopyanov. "Coherence properties of a broadband femtosecond mid-IR optical parametric oscillator operating at degeneracy." en. In: *Optics Express* 20.7 (Mar. 2012), p. 7255. ISSN: 1094-4087. DOI: 10.1364/OE.20.007255. URL: https://opg.optica.org/oe/abstract.cfm?uri=oe-20-7-7255 (visited on 03/17/2025).

[32] Arkadev Roy, Rajveer Nehra, Saman Jahani, Luis Ledezma, Carsten Langrock, Martin Fejer, and Alireza Marandi. "Temporal walk-off induced dissipative quadratic solitons." In: *Nature Photonics* 16.2 (2022), pp. 162–168. DOI: 10.1038/s41566-021-00942-4.

[33] Alexander W. Bruch, Xianwen Liu, Zheng Gong, Joshua B. Surya, Ming Li, Chang-Ling Zou, and Hong X. Tang. "Pockels soliton microcomb." In: *Nature Photonics* 15.1 (2021), pp. 21–27.

[34] Sergei Akhmanov, Anatolii Chirkin, Konstantin Drabovich, Al Kovrigin, Rem Khokhlov, and Anatoly Sukhorukov. "Nonstationary nonlinear optical effects and ultrashort light pulse formation." In: *IEEE Journal of Quantum Electronics* 4.10 (1968), pp. 598–605.

[35] Stefano Trillo. "Bright and dark simultons in second-harmonic generation." In: *Optics Letters* 21.15 (1996), pp. 1111–1113.

[36] Ryan Hamerly, Alireza Marandi, Marc Jankowski, Martin M. Fejer, Yoshihisa Yamamoto, and Hideo Mabuchi. "Reduced models and design principles for half-harmonic generation in synchronously pumped optical parametric oscillators." In: *Physical Review A* 94.6 (2016), p. 063809.

[37] Marc Jankowski, Alireza Marandi, Christopher R. Phillips, Ryan Hamerly, Kirk A. Ingold, Robert L. Byer, and Martin M. Fejer. "Temporal simultons in optical parametric oscillators." In: *Physical Review Letters* 120.5 (2018), p. 053904.

[38] Luis Ledezma, Ryoto Sekine, Qiushi Guo, Rajveer Nehra, Saman Jahani, and Alireza Marandi. "Intense optical parametric amplification in dispersion-engineered nanophotonic lithium niobate waveguides." In: *Optica* 9.3 (2022), pp. 303–308. DOI: 10.1364/OPTICA.442332.

[39] Marc Jankowski. *Pulse formation and frequency conversion in dispersion-engineered nonlinear waveguides and resonators*. Stanford University, 2020.

[40] Luke Maidment, Oguzhan Kara, Peter G. Schunemann, Jonathon Piper, Kenneth McEwan, and Derryck T. Reid. "Long-wave infrared generation from femtosecond and picosecond optical parametric oscillators based on orientation-patterned gallium phosphide." In: *Applied Physics B* 124 (2018), pp. 1–8.

[41] Andrey V. Muraviev, Viktor O. Smolski, Zachary E. Loparo, and Konstantin L. Vodopyanov. "Massively parallel sensing of trace molecules and their isotopologues with broadband subharmonic mid-infrared frequency combs." In: *Nature Photonics* 12.4 (2018), pp. 209–214. DOI: 10.1038/s41566-018-0135-2.

[42] Mingchen Liu, Robert M. Gray, Luis Costa, Charles R. Markus, Arkadev Roy, and Alireza Marandi. "Mid-infrared cross-comb spectroscopy." In: *Nature Communications* 14.1 (2023), p. 1044. DOI: 10.1038/s41467-023-36811-7.

[43] Chenchen Wan, Peng Li, Axel Ruehl, and Ingmar Hartl. "Coherent frequency division with a degenerate synchronously pumped optical parametric oscillator." In: *Optics Letters* 43.5 (2018), pp. 1059–1062.

[44] Marc Jankowski, Nayara Jornod, Carsten Langrock, Boris Desiatov, Alireza Marandi, Marko Lončar, and Martin M. Fejer. "Quasi-static optical parametric amplification." In: *Optica* 9.3 (2022), pp. 273–279.

[45] Jean Wei, Joel M. Murray, Jacob O. Barnes, Douglas M. Krein, Peter G. Schunemann, and Shekhar Guha. "Temperature dependent Sellmeier equation for the refractive index of GaP." In: *Optical Materials Express* 8.2 (2018), pp. 485–490.

[46] Iouli E. Gordon, Laurence S. Rothman, Robert J. Hargreaves, R. Hashemi, Ekaterina V. Karlovets, Frances M. Skinner, Eamon K. Conway, Christian Hill, Roman V. Kochanov, Yan Tan, et al. "The HITRAN2020 molecular spectroscopic database." In: *Journal of Quantitative Spectroscopy and Radiative Transfer* 277 (2022), p. 107949.

Chapter 4

QUADRATIC-SOLITON-ENHANCED MID-IR MOLECULAR SENSING

Robert M. Gray, Mingchen Liu, Selina Zhou, Arkadev Roy, Luis Ledezma, and Alireza Marandi. "Quadratic-soliton-enhanced mid-IR molecular sensing." In: *Nature Communications* 15.1 (2024), p. 9086. DOI: 10.1038/s41467-024-53447-3.

4.1 Introduction

Since their discovery, optical solitons [1, 2] have been the subject of intense study due to the rich physics underlying their dynamics [3–6], relying on a delicate interplay of linear and nonlinear effects, as well as their broad application in areas including low-noise frequency synthesis [7], astronomy [8], and spectroscopy [9, 10], among others. Quadratic solitons [11–14] can benefit from the inherent strength of the quadratic nonlinearity, which relaxes the requirement on resonator finesse or pump power for achieving soliton formation, as well as the ability to achieve efficient conversion between disparate spectral bands.

Temporal simultons are one such quadratic soliton, which consist of a co-propagating bright-dark soliton pair at the fundamental and second harmonic frequencies, respectively [15, 16]. More recently, cavity simultons have been demonstrated in synchronously-pumped degenerate OPOs operating in the high-gain, low-finesse regime [17]. Such temporal cavity simultons are shown to have several favorable properties including broader bandwidths, which increase with increasing pump power, and higher efficiencies. When extended to the MIR regime [18], where many important molecules have their strongest absorption features [19], these properties make the simulton OPO a powerful frequency comb source for molecular sensing and spectroscopy.

In this work, we utilize the formation dynamics of quadratic cavity simultons for molecular sensing, in particular, the uniquely high sensitivity of simulton formation to the intracavity loss (Figs. 4.1a-b). In a proof-of-principle experiment sensing CO_2 in a 1.2-m-long OPO operating in the simulton regime at around 4.18 µm [18], we measure an equivalent path length enhancement of up to 6000 and additionally
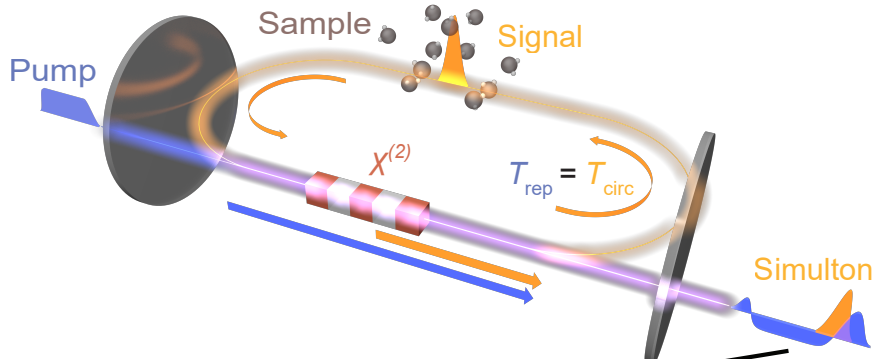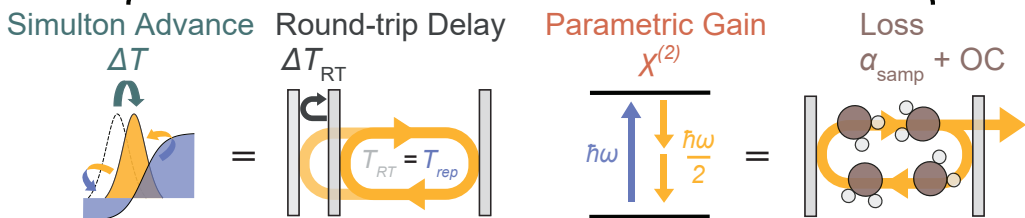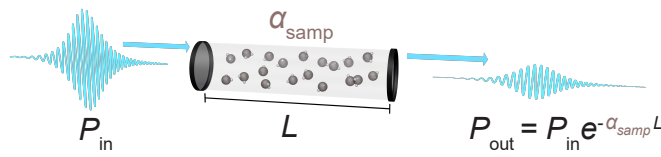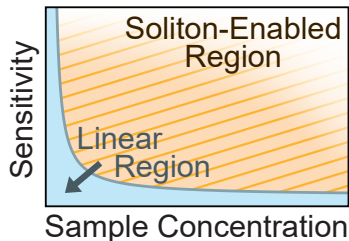
Figure 4.1: **Enhanced sensing using quadratic cavity simultons**. **a**, Schematic depiction of sensing in the simulton regime of a synchronously-pumped optical parametric oscillator at degeneracy. The bright soliton in the signal interacts with the sample every round trip, and the resulting competing nonlinear dynamics generate the measured signal response. **b**, Specifically, stable simulton operation requires the simulton group advance, ΔT, to balance the round-trip group delay, ΔT_{RT}, and the parametric gain to balance the sample loss, α_{samp}, and output coupling. **c**, Schematic representation of linear absorption sensing governed by the Beer-Lambert Law for light interacting with a sample over a path length L. **d**, Linear methods (light blue region) face limitations in the achievable sensitivity at high sample concentrations. In contrast, active cavity sensing with quadratic cavity (orange) can achieve high sensitivities at high sample concentrations. T_{rep}, pump repetition period; T_{circ}, pulse circulation time in the cavity; ΔT, simulton group advance; T_{RT}, cold cavity round-trip time ΔT_{RT}, round-trip group delay; $\chi^{(2)}$, second-order susceptibility; ω, angular frequency; α_{samp}, sample absorption coefficient; OC, output coupling; P_{in}, input power; P_{out}, output power; L, path length; $\hbar$, reduced Planck's constant.

show a maximum sensitivity at concentrations of CO_2 as high as atmospheric levels that is orders of magnitude larger than what can theoretically be achieved through linear methods using a source of equivalent power and bandwidth to the output of our broadband OPO. We additionally extend our experimental results to estimate a detector-limited normalized noise equivalent absorption (NEA) of $1.05*10^{-10}$ $cm^{-1}/\sqrt{Hz}$ for realistic system parameters. Finally, we use numerical simulation to investigate the unique dynamics responsible for this sensing behavior and show the potential of the method to achieve high linearity across a dynamic range of 10^7.

Sensing based on simulton formation dynamics enables a fundamentally different scaling behavior compared to typical linear absorption sensing (LAS) following the Beer-Lambert Law [20], as illustrated in Figs. 4.1c-d. In particular, although passive cavity enhancement [21–23] can offer extremely high sensitivities at low analyte concentrations, the dynamic range is limited. For example, recent works [24] have demonstrated normalized noise-equivalent absorption (NEA) values on the order of 10^{-13} $cm^{-1}/\sqrt{Hz}$, while their dynamic range is constrained to about 4 orders of magnitude [25] if not extended through a frequency [26, 27] or path-length multiplexed [28] approach. By contrast, cavity soliton dynamics can achieve high sensitivity and significant signal enhancement even at large sample concentrations, thereby promising precision and extended dynamic range for mid-infrared gas sensing while avoiding the typical requirements of high-finesse and high-power operation. Furthermore, in contrast to intracavity laser absorption sensing (ICLAS) techniques [29–34], cavity-simulton enhancement mitigates the limitations in sensitivity imposed by spontaneous emission and difficulty in measuring the low signal powers required for near-threshold operation [29]. Moreover, simultons can be achieved at arbitrary wavelengths, paving the way towards a universal molecular sensing scheme, especially in wavelength ranges where lasers are not readily available.

4.2 Results

Theory of Cavity Simulton Formation

Since we previously derived the simulton solutions and discussed their formation in OPOs, we only briefly recount here the details necessary for understanding the sensing mechanism. As discussed in Section 3.2, the simulton consists of a co-propagating bright-dark soliton pair of the pump at frequency 2ω and signal at ω, given by

$$A_\omega(z, t) = \frac{a}{\sqrt{2\tau}} \operatorname{sech}\left(\frac{t - T}{\tau}\right), \tag{4.1a}$$

$$A_{2\omega}(z, t) = -A_{2\omega,0} \tanh\left(\frac{t - T}{\tau}\right). \tag{4.1b}$$

Here, A_j, $j\epsilon\{\omega, 2\omega\}$, is the field amplitude of the jth wave, $A_{2\omega,0}$ is the pump amplitude, a is the simulton signal amplitude, T is the simulton centroid position, and τ is the simulton pulse width. As before, we may use the nonlinear manifold projection method to find the evolution of T, τ, and a [35]. In this case, we assume in particular an OPO with a nonlinear crystal of length l, a total cavity length of L, a roundtrip group delay of ΔT_{RT}, and a roundtrip loss of coefficient of $\alpha_\omega = \alpha_R + \alpha_{\text{samp}} + \alpha_{\text{oth}}$, where α_R is the loss due to the output coupler reflectivity $R = e^{-\alpha_R L}$, α_{samp} is loss due to the sample, and α_{oth} encapsulates all other roundtrip losses. Then, the evolution of the system from the nth roundtrip to the $n + 1^{\text{th}}$ roundtrip is given by

$$T(n + 1) = \Delta T(n) + T(n) + \Delta T_{\text{RT}}, \tag{4.2a}$$

$$\tau(n + 1) = \tau_0, \tag{4.2b}$$

$$a(n + 1) = \frac{a(n)e^{\kappa E_{2\omega,0}l - \alpha_\omega \frac{L}{2}}}{\sqrt{1 + \frac{a(n)^2}{a_{\text{sim}}^2}\left(e^{2\kappa E_{2\omega,0}l} - 1\right)}}, \tag{4.2c}$$

where a_{sim} is the steady-state simulton amplitude, τ_0 is the simulton pulse width, κ is the nonlinear coupling coefficient, and $\Delta T(n) = -\frac{\tau_0}{2} \ln\left(1 + \frac{a(n)^2}{a_{\text{sim}}^2}\left(e^{2\kappa E_{2\omega,0}l} - 1\right)\right)$ is the simulton centroid shift due to nonlinear acceleration caused by pump depletion and subsequent back conversion.

From these equations, we see the requirements for stable cavity simulton formation, as depicted in Fig. 4.1b. Firstly, we see that achieving a non-zero steady-state amplitude requires that the gain balance the loss; here, this demands $e^{\kappa E_{2\omega,0}l - \alpha_\omega \frac{L}{2}} \geq 1$. Secondarily, the simulton centroid shift, ΔT, must balance the roundtrip group delay due to the cavity length detuning, ΔT_{RT}. This allows the simulton to re-synchronize with the pump, such that signal pulse circulation time $T_{\text{circ}} = T_{\text{RT}} + \Delta T_{\text{RT}} + \Delta T$ equals the pump repetition period, T_{rep}. Further, we see the interdependence of these two conditions, as achieving a sufficient timing advance to compensate the roundtrip delay requires a sufficient amount of gain and pump depletion, which results in the dynamics responsible for the simulton sensing mechanism.

Principle of Simulton Enhancement
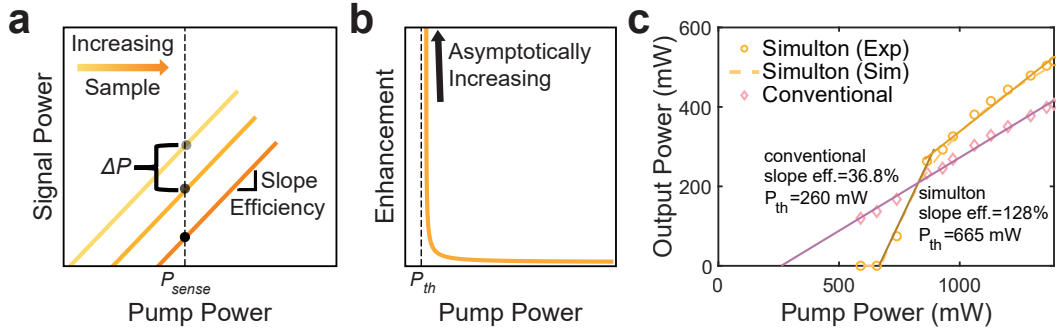
Figure 4.2: **Quadratic cavity simulton enhancement mechanism. a,** Theoretical behavior of near-threshold sensing, wherein the addition of sample causes an increase in threshold, resulting in a decrease in signal power at the sensing point. **b,** The corresponding signal enhancement grows asymptotically as threshold is approached. **c,** Experimentally measured input-output power relationships for the simulton (orange) and conventional (pink) regimes show the extremely high slope efficiency and high threshold of the simulton, suggesting its potential for near-threshold sensing with high SNR. Solid lines capture the trends through linear fits of the experimental data while the orange, dashed line shows the corresponding simulton simulation.

The simulton-based sensing mechanism exploits the interplay between energy and timing in the simulton regime to attain high sensitivity to the sample of interest. The theoretical principle of threshold sensing as leveraged by the simulton sensing mechanism is depicted in Fig. 4.2a. For a given pump power, the addition of a small amount of loss due to the sample causes a threshold increase, resulting in a corresponding decrease in the output power, ΔP. The absolute change in power is proportional to the local slope efficiency at the sensing point, meaning a higher slope efficiency results in a higher sensitivity.

In such a scenario, the corresponding equivalent path length enhancement is given by:

$$\frac{L_{\text{eff}}}{L} = \frac{-1}{L\Delta\alpha_{\text{samp}}} \ln\left(\frac{P_{\text{signal}}(\alpha_{\text{samp}} + \Delta\alpha_{\text{samp}})}{P_{\text{signal}}(\alpha_{\text{samp}})}\right) \approx \frac{\Delta P_{\text{signal}}}{L\Delta\alpha_{\text{samp}}P_{\text{signal}}}, \qquad (4.3)$$

where L_{eff} is the effective path length, L is the cavity roundtrip length and, equivalently, the sample interaction length, P_{signal} is the signal power, α_{samp} is the sample absorption coefficient, and $\Delta\alpha_{\text{samp}}$ represents a small change in the absorption due to the addition of sample. Simplified models using single-mode laser theory [29] or OPO theory [35, 36] show the enhancement to asymptotically approach infinity as

the number of times above threshold, $N = P_{\text{pump}}/P_{\text{th}}$, approaches unity, as shown schematically in Fig. 4.2b. Specifically, using degenerate OPO theory and assuming a roundtrip loss in power for the signal of α_ω, we compute the equivalent path-length enhancement as:

$$\frac{\Delta P_{\text{signal}}}{L\Delta\alpha_{\text{samp}}P_{\text{signal}}} = \frac{1}{L\alpha_\omega}\frac{1}{\sqrt{N}-1}. \tag{4.4}$$

In typical intracavity laser systems, such threshold enhancement has been achieved through operation of the system close to the lasing threshold and subsequent addition of sample. In our degenerate OPO system, we show that such asymptotic enhancement may also be attained by pumping above the sample-free oscillation threshold, at a point P_{sense} (Fig. 4.2a), and adding sufficient sample to raise the threshold to the level of the pump power. We benefit here from a feature of degenerate OPO systems that the addition of roundtrip loss does not change the theoretical sensitivity, which contrasts single-mode laser theory (see Section 4.4). This enables tuning of the enhancement region through variation of the pump rate, thereby extending the dynamic range. In describing our results, therefore, we use N to describe specifically the number of times above the sample-free simulton threshold.

This large enhancement near threshold is theoretically followed by a decrease in the signal-to-noise ratio (SNR). However, the combination of the low spontaneous emission rate of the OPO[37] as well as the large slope efficiency and high threshold in the simulton regime makes this SNR reduction extremely slow in comparison to other intracavity laser sensors. As an example, in our experiments (see Section 4.4), the measured simulton threshold is approximately a factor of 2.5 larger than that of the conventional regime, and the slope efficiency is a factor of 3.5 larger, as illustrated in Fig. 4.2c. The net result is an ability to operate nearly 9 times closer to threshold in the simulton regime at the same output power for detector-limited measurements. This ability to achieve measurable signals very near to the simulton threshold can lead to an extremely large enhancement, making the simulton an ideal candidate for intracavity sensing.

From the fundamental perspective, such cavity-simulton-enhanced sensing cannot be achieved in a general multi-mode laser or conventional OPO as other modes which do not experience the absorption can compensate for the loss in the absorbing modes, leading to a limited change in the laser threshold or output power with the addition of the sample [29]. This is observed in the far above threshold conventional regime
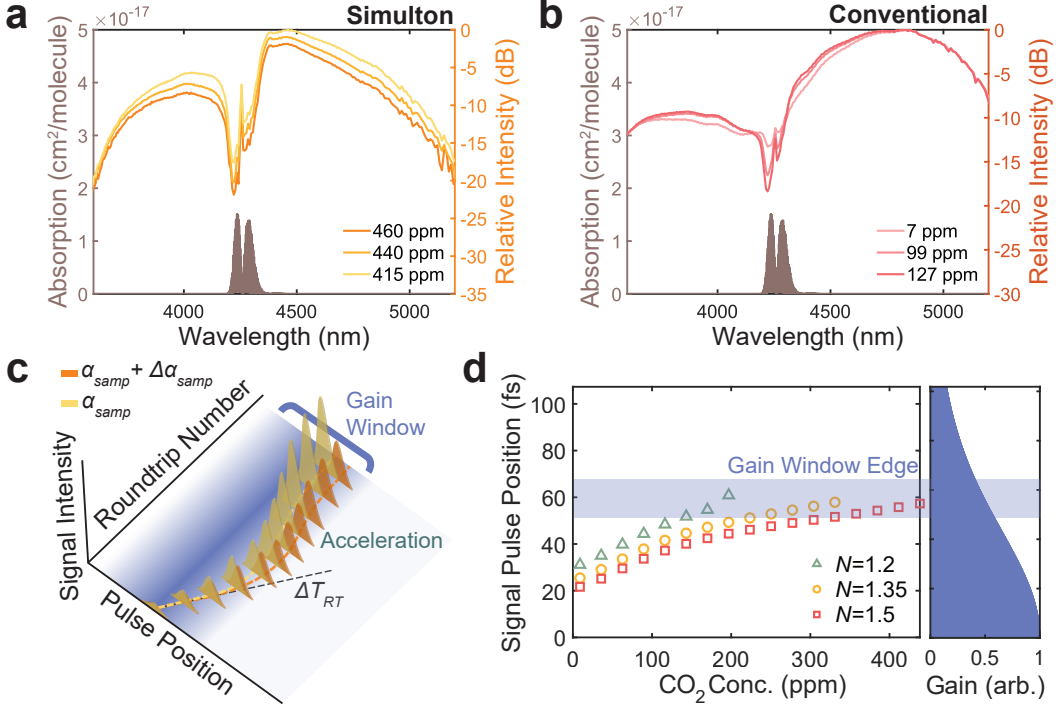
Figure 4.3: **Simulton dynamics responsible for sensing. a**, Experimental power spectral densities demonstrate reduced power across the entire simulton spectrum with the addition of sample despite the relatively narrow CO_2 absorption feature. **b**, In the far above threshold conventional regime, like other general multi-mode lasers, power in non-absorbing modes increases with the addition of sample, largely compensating the loss in the absorbing modes. **c**, Schematic depiction of the temporal dynamics of cavity simulton formation which enable the sensing enhancement mechanism. Additional loss in the round trip limits the ability of the simulton to deplete the pump and accelerate, leading to a reduced gain for all modes at steadystate. **d** Simulated steady-state pulse position as a function of gas concentration (left). Comparison with the theoretical gain window (right) shows the simulton moving further towards the gain window edge as the sample concentration is increased, in accordance with **c**.

of our synchronously-pumped OPO but not for the simulton regime, as shown in Figs. 4.3a-b. Here, the experimental spectrum data in both the simulton (Fig. 4.3a) and conventional regimes (Fig. 4.3b) is given for three different intracavity CO_2 concentrations. In the conventional regime, spectral modes which do not experience the absorption are observed to increase in power, largely compensating the loss due to the sample. In sharp contrast, the power in all the spectral modes of the simulton regime decreases nearly uniformly with the addition of even a narrow-band sample, mimicking that of a single-mode sensor for which threshold sensing is possible. In contrast to single-mode lasers, however, the simulton enhancement provides SNR

advantages, can be achieved in wavelength ranges that are typically not easy to reach with lasers, particularly in the infrared, and provides broadband operation, which relaxes the requirement for fine tuning of the laser line to a single absorption line, though at the cost of selectivity without increasing system complexity.

This collective response of the spectral modes of the simulton to the addition of sample results from the interplay between the energy and timing requirements of simulton formation. This interplay is shown in Fig. 4.3c, where the formation of the simulton pulses over multiple roundtrips in the resonator is schematically depicted for two different values of the absorption. Due to the roundtrip delay, ΔT_{RT}, required for stable simulton formation, the newly formed pulse slowly falls out of the gain window, determined by the pump pulse and walk-off length, until it has grown enough to experience a sufficiently strong nonlinear acceleration to compensate the delay. The addition of a small amount of loss in the roundtrip to the signal will reduce the amount of acceleration and, correspondingly, the amount of gain experienced by all spectral modes of the simulton at steady-state as it interacts with the pump in the nonlinear crystal, leading to a spectrally uniform reduction of power despite the relatively narrow absorption spectrum, as shown in the measured spectrum of Fig. 4.3a.

This dynamical behavior is confirmed through our simulation. Figure 4.3d depicts the steady-state signal pulse position as a function of CO_2 concentration (left) in comparison to the available gain (right) for three different number of times above threshold, $N = 1.2$ (green triangles), $N = 1.35$ (orange circles), and $N = 1.5$ (red squares). The gain here is calculated as the convolution between the pump pulse shape and the walk-off, with the center of the gain window positioned at 0 fs. The approximate gain window edge can be calculated by halving the sum of the pump pulse length and the walk-off length. Further details can be found in Section 4.4. As sample is added to the cavity, the steady-state position of the signal pulse moves towards the gain window edge due to the reduced acceleration of the simulton until it no longer experiences sufficient gain to resonate. This sharp reduction in gain as sample is added to the cavity enables a high sensitivity for the simulton near threshold. Additional theoretical analysis and comparisons regarding the sensitivity, sensitivity enhancement, and SNR of single-mode intracavity lasers, single-mode degenerate OPOs, and simulton OPOs may be found in Section 4.4.
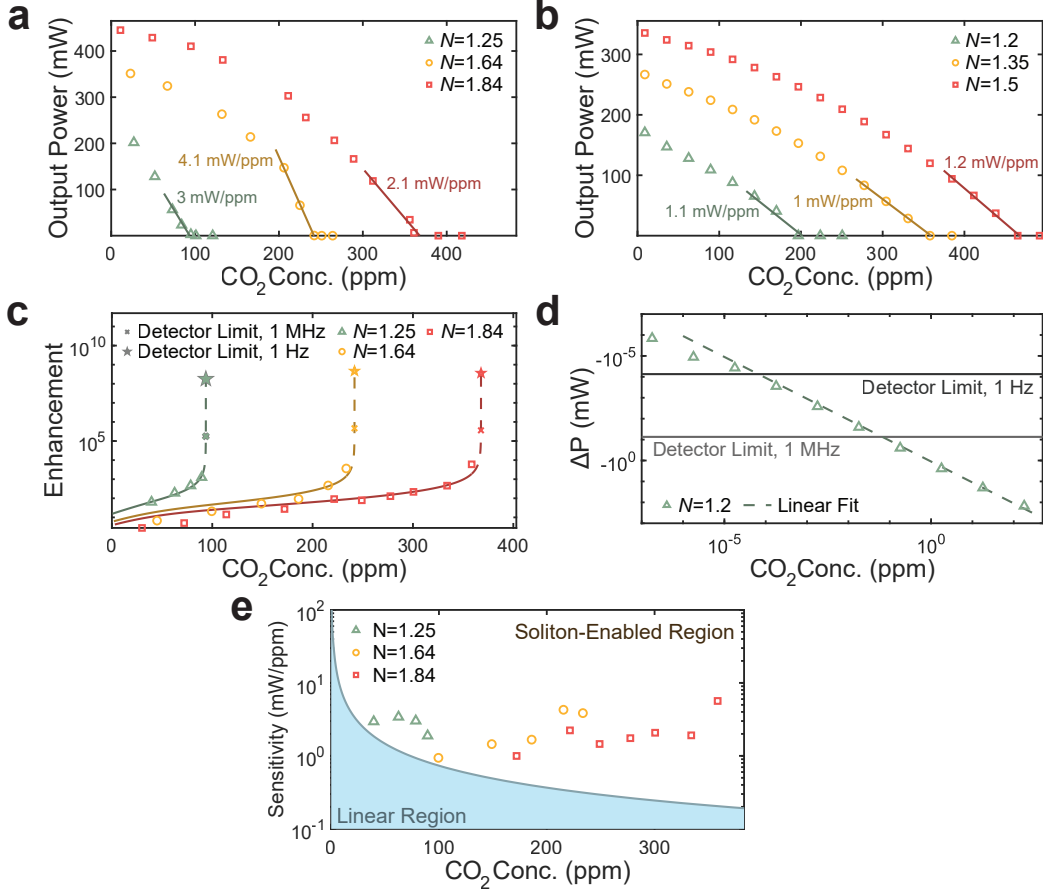
Figure 4.4: **Sensing behaviors of quadratic cavity solitons. a**, Measured output power as a function of CO_2 concentration for different number of times above threshold, N. A high sensitivity of 4.1 mW/ppm is measured near threshold, emphasized using the solid trend lines. **b**, Simulations of the simulton response to the addition of CO_2 at various number of times above threshold exhibit good qualitative agreement with the experimental data. **c**, Equivalent path-length enhancement calculated for neighboring points in the experiment, showing a measured enhancement as large as 6000. Solid lines show the expected asymptotic enhancement corresponding to the linear fits in **b**, with dashed lines extending these fits to enable extrapolation of detector-limited enhancements for detection bandwidths of 1 MHz (x's) and 1 Hz (stars). **d** Simulated change in output power as a function of CO_2 concentration with a linear fit (dashed line) showing good linearity over a dynamic range of 10^7. **e**, Measured sensitivity as a function of CO_2 concentration in direct comparison with linear sensing (light blue), demonstrating orders of magnitude sensitivity improvement over linear methods at high sample concentrations.

Sensing Behavior

Figure 4.4a depicts the measured simulton output power as the CO_2 concentration in the cavity is varied. Green triangles, orange circles, and red squares correspond to

pumping at different number of times above threshold (here, $N = 1.25$, 1.64, and 1.84, respectively). Similar to the input-output power dependence shown previously, the output power dependence on CO_2 changes most sharply close to threshold. Solid lines show linear fits of the near-threshold data. Their slope is used to find the sensitivity, with the highest fitted sensitivity calculated to be 4.1 mW/ppm. This unit of sensitivity is convenient as it both represents the slope of our calibration curve, defined at any concentration, and carries physical meaning as a detector-independent metric for characterizing the strength of the system response to the addition of sample. Additionally, it allows for easy analytical comparison with linear absorption spectroscopy through the Beer-Lambert Law. Finally, we observe that by tuning the pump power, one can change the region of high sensitivity, thereby extending the dynamic range of the system.

These observations are consistent with our simulated sensing results, shown in Fig. 4.4b. Here, we again see the large sensitivity near threshold and tuning of the sensitive region through variation in the number of times above threshold. The calculated sensitivity is also shown to be consistent across the different pump conditions. Our simulated sensitivity is slightly lower than what is observed experimentally, which we attribute primarily to imperfections in our modeling of the gas response.

We also find the equivalent path length enhancement for the experimental data, as shown in Fig. 4.4c. To do so, we define $\Delta\alpha_{\text{eff}}$ as the effective absorption coefficient experienced by a pump of the same bandwidth as the simulton which has experienced 1.2 m of CO_2 absorption at the reference concentration. Using this, we calculate $\frac{-1}{L\Delta\alpha_{\text{eff}}} \ln\left(\frac{P_{\text{signal}}(\alpha_{\text{eff}}+\Delta\alpha_{\text{eff}})}{P_{\text{signal}}(\alpha_{\text{eff}})}\right)$ for neighboring points in our experimental measurement. Further details on this calculation may be found in Section 4.4. The largest enhancement of 6000 is observed near threshold for the case where $N = 1.84$, though similar enhancements are observed near threshold for the other cases. Solid lines show the enhancement corresponding to the linear fits from Fig. 4.4a in accordance with theory. The close fits near threshold illustrate the nearly asymptotic trend for the enhancement, with deviations at lower sample concentrations coming from the observed saturation of the simulton response far above threshold.

To additionally demonstrate the potential of this asymptotic enhancement, we extend the theoretical fits (dashed lines) and plot the detector-limited enhancement for two different measurement bandwidths, 1 MHz (x's) and 1 Hz (stars). We select these bandwidth values as the current measurement is performed at a 1 MHz bandwidth, while 1 Hz is the standard for normalized comparison with other reported results.

The detector-limited value is found by dividing our noise-equivalent power (NEP), given by the 1σ variance of our detector noise, by our measured sensitivity (see Section 4.4 for more information). For output powers of 74 µW and 74 nW, the calculated NEPs at a 1 MHz and 1 Hz bandwidth, respectively, we see enhancements on the order of 100s of thousands and 10s of millions.

In addition to the estimated enhancement, we compute the detector-limited normalized NEA, which we find to be $1.05*10^{-10}$ cm$^{-1}/\sqrt{\text{Hz}}$, corresponding to a concentration of 18 ppt. Taken in tandem with our experimentally measured concentrations of up to nearly 400 ppm, this is suggestive of a dynamic range on the order of 10^7 for the method, which can be further extended through use of a higher-power pump laser. To further validate this estimated dynamic range, we use our simulation to characterize the linearity of the sensor response across many orders of magnitude of CO_2 concentrations. The results are plotted in Fig. 4.4d, where the y-axis, ΔP, indicates the difference between the output power at a given concentration and the power at 0 ppm. A dashed line indicates a linear fit of the data, with solid lines showing the detector limits for measurement bandwidths of 1 Hz and 1 MHz. Here, we again see that sample concentrations can be measured down to the level of 10s of ppt, and good linearity is observed over nearly 7 orders of magnitude of dynamic range. While such detector-limited measurements would require careful stabilization of the measurement system and finer control over the measured gas concentration than was achieved in the present experiment, which is currently limited by the precision of our reference sensor (see Section 4.4), these theoretical values show high potential for the simulton sensing mechanism.

Finally, we can make direct comparisons with the sensitivity achievable using linear methods for varying concentrations. Figure 4.4e shows the sensitivity in mW/ppm, calculated for neighboring points in our experimental measurement. Note that through variation of the number of times above threshold, a sensitivity near the measured value of 4.1 mW/ppm may be achieved across all concentrations.

By comparison, we have plotted the theoretically achievable sensitivities using linear methods (light blue region). Here, we model a linear cavity pumped by a pulsed source with the same bandwidth as our measured simulton and an average power of 500 mW, equivalent to the sample-free output power of the simulton OPO for the highest pump power. We have additionally assumed a path-length-multiplexed approach in which the path length enhancement is varied to achieve the maximum sensitivity at each point, up to a length corresponding to an enhancement of 10^6 and

corresponding finesse of over 1.5 million for a cavity length of 1.2 m, equivalent to the length of our OPO, compared to our sample-free cavity finesse of ~20. We believe this to be a large enough enhancement limit for linear methods to represent practically achievable values of the finesse. Further discussion and additional points of comparison, including with single-mode systems, may be found in Section 4.4. Though high sensitivities can be maintained at low concentrations for this path-length-multiplexed approach, an inverse scaling is observed in accordance with theory, emphasizing the limitations of linear techniques for achieving high sensitivities at high sample concentrations. In contrast, the nearly constant and orders of magnitude higher sensitivity demonstrated by the simulton sensing mechanism at high sample concentrations illustrates the potential for this method to achieve precision at large concentrations, which can benefit many applications while avoiding the typical requirements of high-finesse cavities.

4.3 Discussion

It is worth noting that other methods exist which address some of the aforementioned limitations of LAS, including dispersion sensing as well as photoacoustic and photothermal sensing. Dispersion spectroscopy techniques achieve high linearity and consequently large dynamic range through direct measurement of the refractive index rather than the absorption of the sample of interest [38]. A recent demonstration of cavity-mode dispersion spectroscopy [39], which marries the benefits of dispersion spectroscopy with cavity-enhanced techniques, has achieved a dynamic range of $2*10^5$ and a NEA of $5*10^{-11}$ cm^{-1}. Photothermal and photoacoustic methods work by measuring the heat-induced refractive index change and pressure change due to the absorption of light by the sample, respectively. A recent demonstration of mode-phase-difference photothermal spectroscopy [40] has shown a dynamic range of $2*10^7$ and a NEA of $1.6*10^{-11}$ cm^{-1}. Meanwhile, measurements using intracavity quartz-enhanced photoacoustic spectroscopy [41] have exhibited a dynamic range of $>10^5$ and a normalized NEA of $1.5*10^{-8}$ cm$^{-1}/\sqrt{Hz}$. As these results show, these methods demonstrate effective ways of overcoming limitations of absorption-based sensing but at the cost of introducing additional system complexity and potential susceptibility to environmental noise.

The sensing performance of the simulton could be further improved in several ways. Here, we have only explored the first simulton due to limitations in our pump power, but OPOs will often exhibit multiple simulton peaks as the cavity length is further increased. These further-detuned simultons can exhibit even higher slope efficien-

cies, leading to potentially larger sensitivities and sensitivity enhancements [17]. Additionally, simultons benefit from operation in the high-gain, low-finesse regime. Recent advances in thin-film lithium niobate nanophotonics, where gains as large as 100 dB/cm have been demonstrated [42, 43], could push OPOs even further into this regime, adding to a growing push for the creation of high-sensitivity, highly scalable molecular sensors [44–46]. Low-finesse operation also makes simulton-based sensing compatible with waveguide structures such as slot [47] and suspended rib waveguides [48] aimed at improving evanescent wave interaction with the molecular sample of interest but generally at the cost of additional propagation loss. Finally, other nonlinear behaviors in OPOs such as spectral phase transitions offer additional means to achieve high sensitivity for intracavity sensing in OPOs [49]. Exploration of different operation regimes of OPOs for molecular sensing will be the subject of future work.

There are a few additional considerations for use of the simulton enhancement mechanism for practical sensing applications. The first is with regards to selectivity, as previously noted. Since the simulton response is broadband, the ability to distinguish between molecules using the simulton response alone can be limited, so care must be taken in the system design to ensure that only the molecule of interest is captured in the simulton bandwidth. With that said, one may also perform a spectrally-resolved measurement of the output signal to gain information about the molecules present. Additionally, since other regimes of OPO operation contain different frequency content, exploration of other OPO regimes could enable multi-species sensing using only a detector for signal read-out (see Section 4.4) [50]. Secondly, to achieve the theoretically suggested detector-limited performance, one must ensure that other noise contributions are minimized; in particular, the relative intensity noise (RIN) is of concern. Here, we consider the signal RIN as being dominated by the RIN of the pump, coupled into the signal through the slope efficiency. To remain detector-noise limited, we require that the signal RIN in a 1 Hz bandwidth is less than the NEP of 74 nW. Considering our measured slope efficiency of 128% and 665-mW threshold, this would necessitate a pump RIN of less than -70.5 dBc/Hz. Such a value is practically achievable in many mode-locked fiber laser systems [51], among other pulsed sources.

In summary, we have proposed and demonstrated a mid-infrared molecular sensing mechanism which benefits from the formation dynamics of quadratic cavity simultons in optical parametric oscillators to achieve strong performance. Our

proof-of-principle experimental demonstration measuring CO_2 in an OPO at 4.18 µm and complementary simulations show an equivalent path length enhancement of 6000 and orders of magnitudes sensitivity enhancement at large gas concentrations when compared to linear cavity-enhanced methods. This distinct scaling behavior of the simulton suggests the potential for achieving high sensitivity, large dynamic range, and good precision using this method, in accordance with our theoretical estimates of the detector-limited performance in the current experimental configuration, and illustrates how nonlinear dynamics in low-finesse resonators may be exploited for enhanced sensing.

4.4   Supporting Information

Experimental Details

In this section, we explain in detail our experimental setup, which is similar to ref. [18], as described in Chapter 3, as well as our experimental procedure. Our system consists of a synchronously-pumped free-space optical parametric oscillator (OPO) at 4.18 µm, shown in Fig. 4.5a. The OPO is pumped by another PPLN-based OPO which provides pulses at 2.09 µm with a full-width, half-maximum bandwidth of 155 nm and a 250-MHz repetition rate. The pump can provide up to 1400 mW of average power, though the full power is not necessary for the performed sensing experiment. Dielectric-coated mirror M1 is highly reflective for the signal at 4.18 µm and highly transmissive for the pump at 2.09 µm, enabling coupling of the pump into the resonator. An anti-reflection coated, plane-parallel orientation-patterned gallium phosphide (OP-GaP) crystal of length 0.5 mm with a poling period of 92.7 µm for type-0 phase matching of the pump and signal at room temperature enables the nonlinear interaction. Concave gold mirrors M3 and M4 with a radius of curvature of 24 mm on either side of the OP-GaP crystal provide focusing and collimating of the beam on the input and output sides of the crystal, respectively. Mirror M2 is a dielectric mirror designed for 25% transmission of the signal around 4.18 µm, enabling outcoupling and measurement of the generated signal. A piezoelectric actuator (PZT) on cavity mirror M1 allows for tuning of the cavity length for entry into the simulton regime. The cavity can be locked using the dither-and-lock protocol.

Measurement of the signal can be performed using either a photodetector (PD) or a commercial Fourier-transform infrared spectrometer (FTIR) placed after the cavity. Mirror MM, a magnetic-mounted gold mirror, allows for easy transition between the two. For performing sensing measurements, only the photodetector
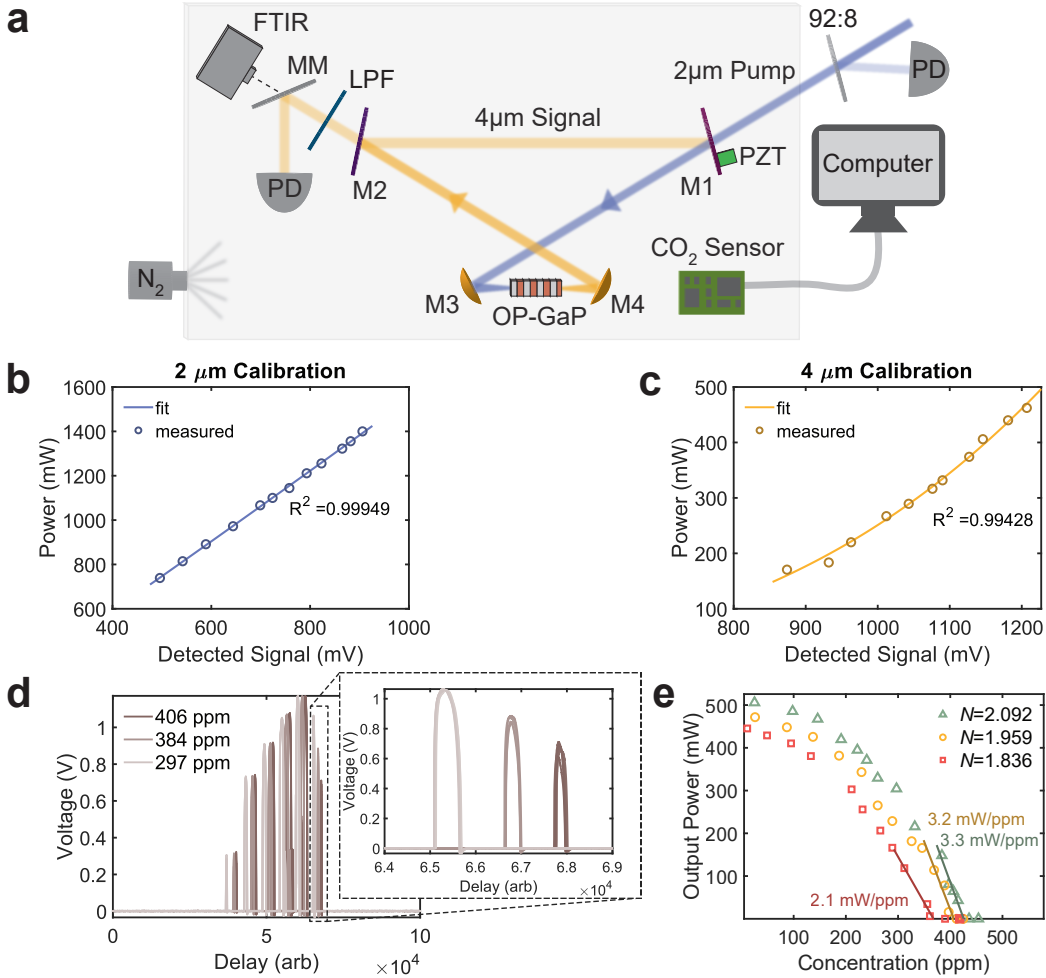
Figure 4.5: **Experimental details**. **a**, The experimental setup consists of the 4 µm OPO cavity placed inside a purging box alongside all necessary measurement equipment. **b**, Calibration curve for mapping the voltage on the pump photodetector to optical power. **c**, Corresponding calibration curve for the signal. **d**, Example of the raw trace measured by the 4 µm photodetector as the round trip delay in the cavity is scanned at 406 ppm, 384 ppm, and 297 ppm. Overlaid traces with different shading correspond to the five traces that are averaged to generate the final value. The inset shows a zoom-in of the simulton peak. **f**, Experimental data showing how fine tuning of N can allow for high sensitivity at desired values of the concentration. The example traces in **d** were taken from the data set corresponding to $N = 2.092$. M1, input coupler; M2, output coupler; M3 and M4, concave gold mirrors; OP-GaP, orientation-patterned gallium phosphide crystal; PZT, piezoelectric actuator; MM, magnetic mirror; FTIR, Fourier-transform infrared spectrometer; 92:8, pellicle beamsplitter with 92:8 splitting ratio; PD, photodetector.

(or, equivalently, a power meter) must be used, but the FTIR allows for studying of the spectral behavior of the OPO in the presence of the sample. The entire

cavity and all measurement tools are placed inside a purging box. Purging of the cavity is achieved with nitrogen (N_2) supplied to the cavity. Through adjusting the flow of nitrogen to the cavity, the amount of atmospheric gas, and thereby the concentration of CO_2, inside the cavity is varied. The potential contribution of other atmospheric gases to the observed sensing behavior is discussed below. Due to the large size of the purging box and numerous gas outlets, we expect the internal pressure to remain approximately constant. The CO_2 concentration is monitored using a commercial CO_2 sensor (CO2meter.com K-30) which records real-time measurements on a computer, enabling calibration of the sensing measurements. Currently, our measurement is limited by the specifications of the reference sensor and measurement setup; in particular, the reference sensor has a 20 s response time diffusion and +/-30 ppm accuracy, limiting our ability to reliably fine-tune the concentration.

Our experimental procedure is as follows. First, a small fraction of the 2 µm power is siphoned off to a detector using a pellicle beamsplitter with a 92:8 splitting ratio, placed at the input side of the cavity (Fig. 4.5a). We then create a calibration curve (Fig. 4.5b) mapping the 2 µm power to the detector value using an optical power meter. A similar procedure is used to create a calibration curve for the 4 µm signal in both the conventional and simulton regimes mapping the measured voltage on the photodetector to optical power with the 4 µm OPO cavity locked and purged. An example calibration curve for the simulton can be seen in Fig. 4.5c. The R^2 values for the calibration curves are shown in each plot and indicate the goodness of the fits.

After finishing the detector calibration, we perform the sensing measurement. For this, the PZT is continuously scanned with a ramp function supplied by a function generator. This enables near-simultaneous monitoring of all OPO peaks and also allows measurement of the output nearer to threshold, where the locking is generally less stable. The output is measured on the 4 µm photodetector and then mapped to optical power using the calibration curve. Five measurements are taken at each CO_2 concentration using a data acquisition unit, triggered on the ramp function used to scan the cavity length. An example of the raw data that is measured from the system can be seen in Fig. 4.5d. Here, we show examples from 3 different CO_2 concentrations, 406 ppm, 384 ppm, and 297 ppm. The five different traces are overlaid in different shades; they are for the most part almost identical, but there is some fluctuation due to instability in the locking of our pump OPO and the

dynamic nature of our measurement. The inset shows a zoomed-in picture of the simulton peak. Through visual comparison with other peaks, it is clear to see that the simulton exhibits a significantly more dramatic response to the addition of gas. However, as discussed later in detail, we believe that the behaviors of the other peaks contain additionally useful information about the gas being monitored, and a sensor designed to utilize data from all of the OPO peaks will be the subject of future works. The final presented value for the output power at any single concentration value, as in Fig. 4.4a as well as Fig. 4.5e, is the result of averaging the five measured simulton peaks and finding the maximum voltage of this averaged measurement which is then mapped back to optical power through the calibration curve. In Fig. 4.5e, we show this output power as a function of concentration for three different number of times above threshold, $N = 2.092$ (green triangles), $N = 1.959$ (orange circles), and $N = 1.837$ (red squares). These three values are significantly closer together than the values shown in Section 4.2, highlighting the ability to do fine tuning of the pump power to achieve high sensitivity at any concentration of interest.

Numerical Methods

In this section, we describe the methods used for computing the numerical results presented in this work. We also show some additional results which help to both substantiate claims made in the paper and illuminate areas where further theoretical and numerical work could help to improve our understanding. Our simulations are primarily based on the methodology presented in ref. [17], so our notation will largely follow that of the analysis in that work. The key parameters of our simulation may be found in Table 4.4.

The roundtrip propagation of the signal in the cavity is modeled in two parts: the nonlinear interaction of the pump, taken to be a 35-fs sech-shaped pulse, and signal in the crystal and the free space propagation of the light around the cavity, described by a linear transfer function. The nonlinear interaction is essentially a single-pass OPA, governed by the coupled wave equations,

$$\partial_z A_\omega(z,t) = \kappa A_{2\omega} A_\omega^* - \frac{\alpha_\omega}{2} + \hat{D}_\omega A_\omega, \tag{4.5a}$$

$$\partial_z A_{2\omega}(z,t) = -\kappa A_\omega^2 - \frac{\alpha_{2\omega}}{2} - \Delta\beta' \partial_t A_{2\omega} + \hat{D}_{2\omega} A_{2\omega}, \tag{4.5b}$$

where t, the time coordinate, is set to be co-moving with the group velocity of the signal wave, and the pump envelope phase is shifted by $\pi/2$ to ensure real solutions if

higher order dispersion is not considered. The subscripts ω and 2ω refer to the signal and pump, respectively. The field envelopes are given by A_j, where $j \in \{\omega, 2\omega\}$, and are normalized such that the instantaneous power is given by $|A_j|^2$. The strength of the nonlinear interaction is governed by the nonlinear coupling coefficient, $\kappa = \sqrt{2\eta_0}\omega d_{\text{eff}}/(w_0 n_\omega \sqrt{\pi n_{2\omega}}c)$, where η_0 is the impedance of free space, d_{eff} is the effective nonlinearity, w_0 is the Gaussian beam waist inside the crystal (assuming the crystal length is small compared to the confocal parameter), n_j is the refractive index, and c is the speed of light. The absorption coefficients, α_j, account for the material loss in the crystal. $\Delta\beta'$ gives the group velocity mismatch between pump and signal. Finally, the dispersion operator $\hat{D}_j = \sum_{m=2}^{\infty} \left[\frac{(i)^{m+1}\beta_j^{(m)}}{m!} \right] \partial_t^m$ describes the material dispersion experienced by the pump and signal in the crystal, with $\beta_j^{(m)}$ describing the mth-order dispersion of wave j.

Simulation of the nonlinear step in each roundtrip is done using the split-step Fourier method. For this, the spatial coordinate z, corresponding to propagation distance into the 0.5 mm crystal, is divided into 50 discrete steps. In a given step, the output of the nonlinear interaction is solved numerically using a fourth-order Runge-Kutta method. Then, a linear filter accounting for the dispersion and loss in the step is applied in the frequency domain. Dispersion is computed to fourth order using the Sellmeier equation for GaP found in ref. [52].

After the nonlinear step is completed, we apply an additional linear filter in the frequency domain to account for the roundtrip propagation of the beam. Specifically, the input to the coupled wave equations for roundtrip n+1, $A_\omega^{n+1}(0, t)$, is related to the output from the previous OPA, $A_\omega^n(L, t)$, where L is the length of the crystal, by the equation

$$A_\omega^{n+1}(0, t) = \mathcal{F}^{-1}\{e^{-\frac{\alpha(\Omega)}{2}} e^{-i\Phi(\Omega)} \mathcal{F}\{A_\omega^n(L, t)\}\}. \tag{4.6}$$

Here, $\mathcal{F}$ and $\mathcal{F}^{-1}$ represent the Fourier and inverse Fourier transforms, respectively, and Ω is the normalized Fourier frequency coordinate. The absorption coefficient $\alpha(\Omega)$ accounts for the frequency-dependent losses in the cavity coming from the mirrors, the output coupling, AR coatings on the crystal surface, and the gas in the cavity. Similarly, the accumulated roundtrip phase, measured relative to a perfectly synchronous signal pulse, is considered in $\Phi(\Omega) = \Delta T_{\text{RT}}(\pi c/\lambda_{2\omega} + \Omega) + \Delta\Phi(\Omega)$, where ΔT_{RT} is the cavity detuning, c is the speed of light, and $\lambda_{2\omega}$ is the

Parameter	Description	Value	Units
τ_P	pump pulse width	35	fs
T	outcoupler transmission	0.25	
w_0	beam waist, signal	25	µm
$n_{2\omega}$	refractive index, pump	3.0348	
n_ω	refractive index, signal	3.0123	
d_{eff}	effective nonlinearity	32.3	pm/V
α_ω	crystal loss, signal	0.01	1/mm
$\alpha_{2\omega}$	crystal loss, pump	0.01	1/mm
$\Delta\beta'$	crystal GVM	143.6	fs/mm
$\beta_\omega^{(2)}$	crystal GVD, signal	103.4	fs^2/mm
$\beta_\omega^{(3)}$	crystal TOD, signal	1580	fs^3/mm
$\beta_\omega^{(4)}$	crystal 4OD, signal	-10235	fs^4/mm
$\beta_{2\omega}^{(2)}$	crystal GVD, pump	489.2	fs^2/mm
$\beta_{2\omega}^{(3)}$	crystal TOD, pump	681.0	fs^3/mm
$\beta_{2\omega}^{(4)}$	crystal 4OD, pump	-24.31	fs^4/mm
$\phi_\omega^{(2)}$	roundtrip GDD, signal	70	fs^2
$\phi_\omega^{(3)}$	roundtrip TOD, pump	1300	fs^3
$\phi_\omega^{(4)}$	roundtrip 4OD, pump	0	fs^4
$\phi_\omega^{(5)}$	roundtrip 5OD, pump	15e6	fs^5

Table 4.1: Simulation parameters for the simulton OPO.

pump wavelength. $\Delta\Phi(\Omega)$ contains the dispersion terms from the various cavity components as well as from the gas.

Critical to accurate simulation of the sensing behavior is our model for the gas. In our simulation, we use the Lorentz oscillator model to compute the complex refractive index experienced by the signal in the roundtrip [53]. Specifically, the index, $n(\omega)$, is given as

$$n^2(\omega) = 1 + \sum_{ij} \frac{f_{ij}N_j q^2}{2\varepsilon_0 m_e(\omega_{ij}^2 - \omega^2 + i\gamma_{ij}\omega)}, \tag{4.7}$$

where the indices i,j refer, respectively, to the upper and lower state of the transition of interest, f_{ij} is the oscillator strength, N_j is the density of molecules in state j, q is the electron charge, ε_0 is the vacuum permittivity, m_e is the mass of an electron, ω_{ij} is the center frequency of the transition, and γ_{ij} is the linewidth of the transition. Modeling of the CO_2 response is done using parameters taken from the HITRAN database [54]. All simulations assume room temperature and atmospheric pressure. While the dominant contribution in our experiment is from CO_2, this model allows for easy inclusion of additional atmospheric gases, as discussed further in below.

After computing the complex refractive index using Equation 4.7, the absorption and dispersion can be separately considered from the relationship

$$n(\omega) = n^{'}(\omega) - i\kappa(\omega), \tag{4.8}$$

where the real part of the refractive index, $n^{'}(\omega)$, contains the dispersion information and the imaginary part $\kappa(\omega)$ defines the contribution to the loss. Examples of the imaginary and real parts of the complex refractive index for the CO_2 bands of interest at atmospheric concentrations can be found in Fig. 4.6a and Fig. 4.6b, respectively. Interestingly, while much of our theoretical analysis centers around the impact of loss, we have found that accurate simulation of the sensing behavior additionally requires a correct model for the dispersion, likely due to the effective loss imposed by dispersion resulting from the phase-sensitive nature of the gain. This suggests that a complete theoretical description of the sensing behavior should also include dispersion; such a model will be the subject of future works.

Besides helping to confirm the behaviors observed in experiment, our numerical analysis can extend those results to different regimes where the sensing performance
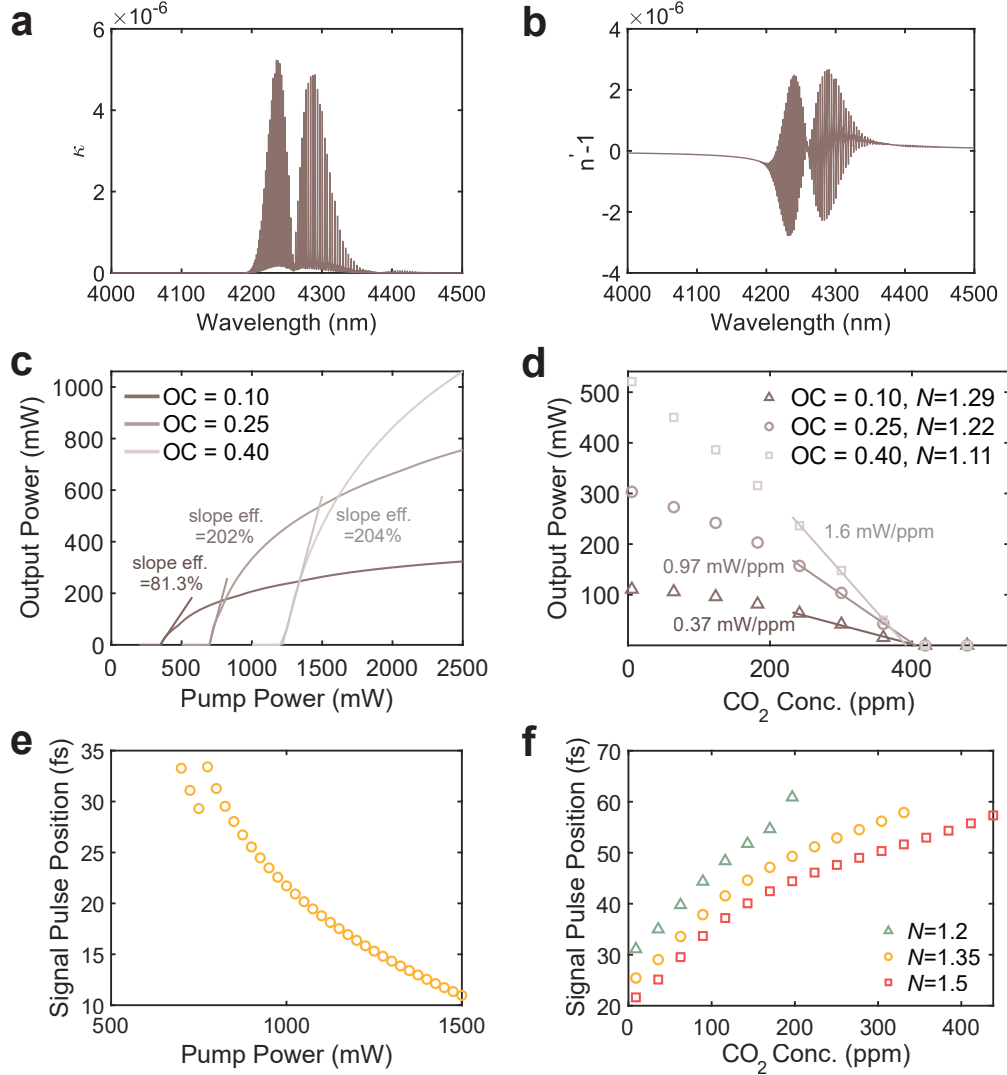
Figure 4.6: **Numerical methods and results.** **a**, Calculated κ, the imaginary part of the complex refractive index, for the CO_2 bands of interest at atmospheric levels of CO_2. **b**, Corresponding result for $n' - 1$, the real part of the complex refractive index. **c**, Simulated simulton slope efficiency for various values of the output coupling; the experiment most closely corresponds to 0.25 (orange). **d**, Simulated sensing behaviors for the three different values of the output coupling shown in **c**, demonstrating higher sensitivities as the slope efficiency and threshold are increased. **e**, Steady-state signal pulse position as a function of pump power, shown to trend towards the center of the gain window as the pump power is increased. **f**, Relative steady-state signal pulse position along the fast time axis with increasing CO_2 concentration for three different number of times above threshold. Note that the observed trend is opposite that of **e**, illustrating the way in which the gain and loss work as counteracting forces for near-threshold simulton operation.

may be further improved. In Figs. 4.6c and 4.6d, we highlight the importance of low-finesse operation for the observed sensing behavior. As mentioned in Section 4.2, the sensitivity benefits from a higher slope efficiency and a higher threshold. In the simulton regime, both the slope efficiency and threshold can be increased through use of a low finesse cavity. Fig. 4.6c shows the output power as a function of input power for output coupling values of 0.1, 0.25, and 0.4, with an output coupling value of 0.25 being approximately correspondent to our experiment. Here, we observe a threshold increase from around 350 mW for an output coupling of 0.1 to around 1200 mW for an output coupling of 0.4. Additionally, we see that the slope efficiency more than doubles, from an efficiency of 81.3% to 204%. Correspondingly, we note a more than 4-fold increase in the sensitivity, as illustrated in Fig. 4.6d. This ability to achieve both a higher slope efficiency and threshold in the simulton regime through low-finesse operation is critical to the uniquely large sensitivity enhancement provided by the simulton.

Additionally, our numerical results can help us to better understand the nonlinear dynamics involved in simulton formation which contribute to the sensing. As shown in Figs. 4.3c and 4.3d, it is the interplay of the energy and timing conditions which result in the enhanced sensing behavior for the simulton. Specifically, in Fig. 4.3d, which has been repeated in Fig. 4.6f, we illustrate that the dynamical feature responsible for the high sensitivity is the movement of the steady-state signal pulse position away from the center of the gain window as loss is added to the cavity. The gain window is determined by the pump pulse and walk-off length and can be approximately found by convolving the pump pulse (here, a sech-shaped pulse with duration of 35 fs) with a square pulse of duration equivalent to the walk-off length, $\Delta\beta'L$ (here, 72 fs). The steady-state signal pulse position is computed by finding the "center of mass" of the signal, $\frac{\sum_i P_i t_i}{\sum_i P_i}$, where P_i and t_i represent the pulse power and time in the ith Fourier bin. The "center of mass" metric is useful in providing consistency across measurements, since the addition of sample tends to distort the temporal features of the pulse.

To further emphasize the opposing roles of the gain and loss, we contrast the steady-state pulse position as a function of pump power (Fig. 4.6e) with the pulse position as a function of concentration (Fig. 4.6f). In both cases, 0 fs along the y-axis represents the center of the gain window. Here, we see that the addition of gain through increasing the pump power pushes the steady-state pulse position towards the center of the gain window while the addition of loss pulls it away. Thus, we see

how the same interplay of energy and timing which result in a high slope efficiency for the simulton regime can also enable high sensitivity. The observed jump in Fig. 4.6e near 775 mW is an artifact resulting from the discrete nature of the simulation. To mimic the experiment, in which we generally lock to the detuning value ΔT_{RT} which gives the maximum power, we simulate multiple detuning values and record the one which results in the highest output power. As the pump power is increased, this optimum detuning can change, resulting in a discrete jump such as the one observed; however, we believe the behavior should be smooth for the experiment for which the detuning can be continuously varied.

Comparison with Linear Absorption Sensing

In analyzing the performance of our method, it is helpful to perform a direct comparison with LAS. The analysis here is informed by the presentation in ref. [55]. Note that, although we perform most of the analysis here in terms of the absorption coefficient, α, it may be easily applied to the parts-per notation, as the two are generally linearly related. We begin with the Beer-Lambert Law for light of intensity I_{in} passing through a sample of length L with absorption coefficient α which says that the output intensity, I_{out}, is given by

$$I_{\text{out}} = I_{\text{in}}e^{-\alpha L}. \tag{4.9}$$

The most common way of quantifying sensitivity enhancement is to consider the path length enhancement. This metric is particularly appropriate for cavity-enhanced sensing, where the physical mechanism at play can be directly understood as an increase of the interaction length between the light and the sample. In a symmetric Fabry-Pèrot cavity of length L with mirror transmission T and reflection R (in intensity) filled with the absorbing sample, the input-output power relationship is given as

$$I_{\text{out}}/I_{\text{in}} = \frac{T^2 e^{-\alpha L}}{(1 - Re^{-\alpha L})^2} \approx \frac{T^2}{(1 - R)^2}\left(1 - \frac{\alpha L(1 + R)}{1 - R}\right). \tag{4.10}$$

The approximation made here is to expand the entire expression to first order in α. By noting that $\frac{\alpha L(1+R)}{1-R} \approx \frac{2\sqrt{R}L\alpha}{1-R} = \frac{2FL\alpha}{\pi}$, where F is the cavity finesse, and making use of the fact that $T \approx 1 - R$, we find that

$$I_{\text{out}}/I_{\text{in}} \approx 1 - \alpha\frac{2FL}{\pi} \approx e^{-\alpha L_{\text{eff}}}, \tag{4.11}$$

where we have defined $L_{\text{eff}} = \frac{2FL}{\pi}$, the effective path length. This is just the typical Beer-Lambert Law but with the path length L replaced by L_{eff}. Thus, we see that the linear cavity enhances the path length by a factor of $\xi = \frac{L_{\text{eff}}}{L} = \frac{2F}{\pi}$ whenever this linearization of the exponential is valid. Comparing 4.11 with equation 4.9, we can then find a direct expression for the path length enhancement, ξ,

$$\xi = \frac{L_{\text{eff}}}{L} = -\frac{1}{\alpha L} \ln \frac{I_{\text{out}}}{I_{\text{in}}}. \tag{4.12}$$

This expression is very practically useful as it enables the computation of ξ or, equivalently, L_{eff} from measured values of the intensity. It can also be generalized to include measurements where some baseline concentration of the sample exists already in the system. In particular, if the output intensity is measured before and after the addition of some small amount of sample, $\Delta\alpha$, the expression becomes

$$\xi = -\frac{1}{\Delta\alpha L} \ln \frac{I_{\text{out}}(\alpha + \Delta\alpha)}{I_{\text{out}}(\alpha)}. \tag{4.13}$$

This is equivalent to equation 4.3, though we have, in equation 4.3, replaced intensities with powers under the assumption that the spatial profile of the beam remains constant between measurements such that the mode area can be taken out of both the numerator and denominator. It is clear then that with knowledge of $\Delta\alpha$, the path length L, and a measurement of the change in power as sample is added, one can easily calculate the path length enhancement. With that said, computation of this quantity using solely the measured change in intensity for a broadband signal requires slightly more care since $\alpha = \alpha(\omega)$ is a function of frequency. To address this, we consider the case of performing LAS with a multimode source containing several frequency modes i such that $I_{\text{in}} = \sum_i I_{\text{in,i}}$. Then, the Beer-Lambert Law would suggest the following expression for the output intensity given that each frequency mode experiences an absorption coefficient α_i

$$I_{\text{out}} = \sum_i I_{\text{out,i}} = \sum_i I_{\text{in,i}} e^{-\alpha_i L} = I_{\text{in}} e^{-\alpha_{\text{eff}} L}. \tag{4.14}$$

Assuming $\alpha_i L$ small, we find

$$I_{\text{out}} \approx \sum_i I_{\text{in,i}} - \sum_i I_{\text{in,i}} \alpha_i L \approx I_{\text{in}} - I_{\text{in}} \alpha_{\text{eff}} L. \tag{4.15}$$

Dividing by $I_{in}L$ and rearranging terms, we arrive at the following expression for α_{eff}

$$\alpha_{eff} = \frac{\sum_i I_{in,i}\alpha_i}{I_{in}}. \tag{4.16}$$

This expression is what one might expect; α_{eff} is given by a weighted sum of the $\alpha_i's$ with the various mode intensities, normalized to the total intensity, as weights. Using this expression, one can extend equation 4.13 to the case of a broadband source as long as the spectral shape of the source is known.

These results allow us to make a comparison between the experimentally measured simulton behavior and linear methods. To do so, we calculate the equivalent path length enhancement, which is the enhancement that would be necessary for a source with the same spectrum as the simulton at the reference absorption, α, to experience the same change in intensity with the further addition of sample, $\Delta\alpha$, in a linear cavity. For this computation, we first take our experimental simulton spectrum for the purged cavity with a measured CO_2 concentration of 11 ppm (Fig. 4.7a, orange line) and use interpolation to reconstruct the CO_2-free spectrum (blue, dashed line). We then use the CO_2 absorption spectrum provided by HITRAN to estimate $P_i(\alpha_i)$, the mode strengths of a source with a spectrum equivalent to the simulton, after propagation through 1.2 m (the length of our OPO cavity) of a sample with modal absorption coefficients α_i assuming no enhancement [54]. Figure 4.7b shows the resulting spectra for three different example concentrations. Using the mode strengths from these calculated spectra as weights along with the provided absorption coefficients, we find $\Delta\alpha_{eff}$ according to equation 4.16 and plug the resulting value along with the measured values of the intensities $I(\alpha)$ and $I(\alpha + \Delta\alpha)$ into equation 4.13 to compute the equivalent path length enhancement.

As shown in Fig. 4.4c, the calculated enhancement is significant, reaching a value as large as 6000. Using the L_{eff} defined for equation 4.11, we see that this is equivalent to the enhancement provided by a cavity with a finesse of 9400. This is important as it demonstrates the ability of quadratic cavity solitons in a low-finesse cavity near threshold to achieve similar sensitivity enhancements to those achieved through linear methods in high-finesse cavities.

With that said, the measurement of path length enhancement, as defined in 4.13, serves primarily to quantify relative power rather than sensitivity. Additionally, it is difficult to make fair comparisons since the enhancement in the simulton case is
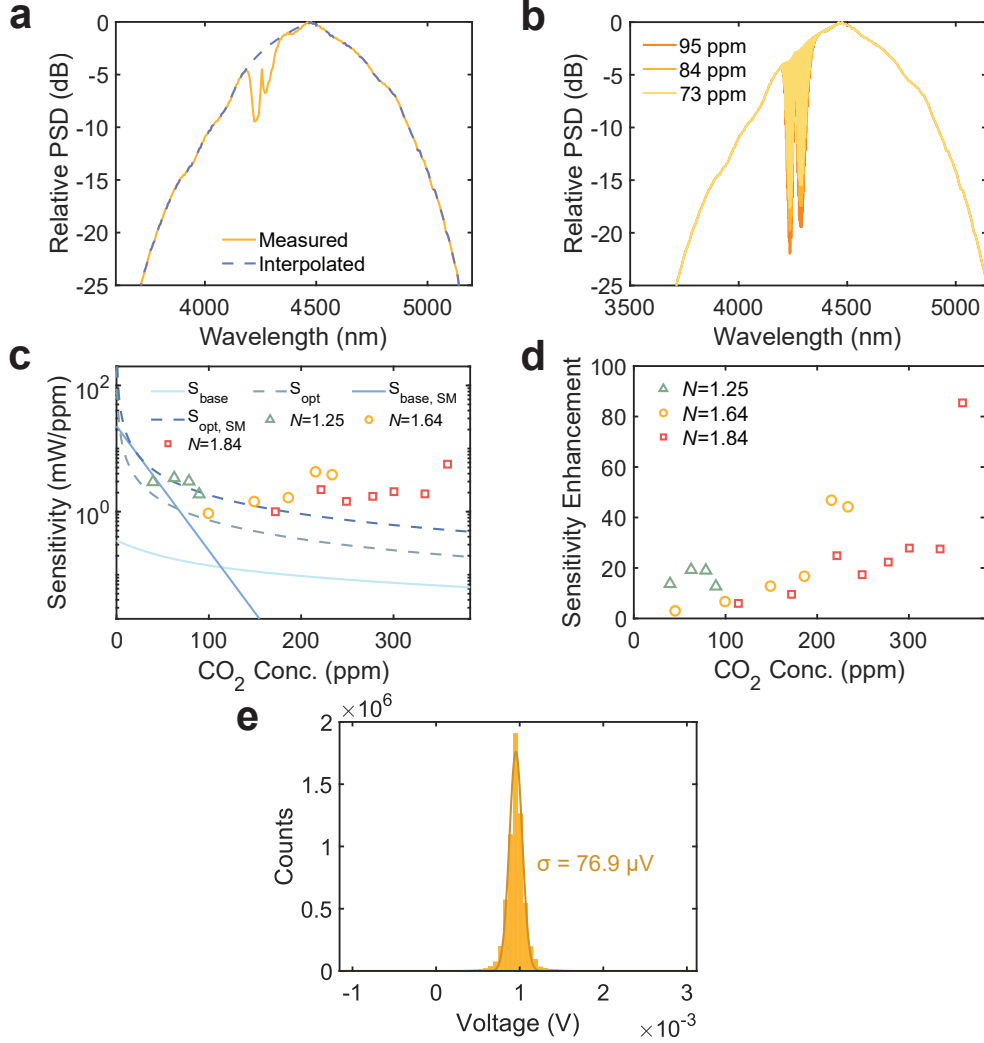
Figure 4.7: **Enhancement calculations for direct comparison with linear absorption sensing. a**, Interpolated simulton PSD (blue, dashed line) plotted on top of measured PSD (orange). **b**, PSD of calculated spectrum corresponding to passage of a signal with the interpolated spectrum from **a** through 1.2 m of CO_2, for 3 different concentrations. The resulting mode strengths are used as weights for calculating α_{eff}. **c**, Measured experimental sensitivities for 3 different numbers of times above threshold, compared to the baseline linear sensitivity, S_{base}, and optimum linear sensitivity achieved through path-length multiplexing, S_{opt}. **d**, Sensitivity enhancement computed through direct comparison of measured sensitivity and S_{base}, as plotted in **c**. **e**, Histogram of the experimentally measured detector noise with a Gaussian fit.

not coming from an extension of the path length but from the nonlinear dynamics which result in a broadband loss. This difficulty is especially pronounced in the case where there is already some significant baseline level of sample in the cavity, where linear methods will generally have already experienced significant depletion

in the absorbing modes that would not be seen in the simulton spectrum used for calculation of α_{eff}. In the extreme case of very large absorption, the notion of L_{eff} as defined in equation 4.11 even breaks down, since its derivation was reliant on being able to approximate αL as small. Thus, it is also worthwhile to make a direct sensitivity comparison with LAS for a pump with the same optical properties as the output of our simulton OPO. Let us begin by analytically calculating the sensitivity of LAS. The sensitivity is the rate of change of the signal, I_{out}, with respect to the absorption coefficient, given as the derivative of 4.9,

$$S = \left| \frac{dI_{\text{out}}}{d\alpha} \right| = I_{\text{in}} L e^{-\alpha L}. \tag{4.17}$$

From this, we see that the maximum sensitivity occurs when $\alpha = 0$ and is given by $I_{\text{in}} L$. This sensitivity can be quite large, given the large effective path lengths that can be achieved in high-finesse cavities. Comparison of the enhanced sensitivity, S_{enh}, of a system with effective path length L_{eff} and the sensitivity, S_{base}, of a baseline LAS system with path length L gives the following expression for sensitivity enhancement, ζ,

$$\zeta = \frac{S_{\text{enh}}}{S_{\text{base}}} = \frac{L_{\text{eff}}}{L} e^{-\alpha(L_{\text{eff}} - L)}. \tag{4.18}$$

Here, we have assumed both systems are pumped with the same power. At $\alpha = 0$, we see that the sensitivity enhancement does correspond exactly to the above computed path length enhancement, ξ. However, it is clear that this sensitivity enhancement quickly decays with increasing α for $L_{\text{eff}} > L$. This gives rise to an inherent trade-off between sensitivity at low concentrations and sensitivity at high concentrations in the linear case, as illustrated in Fig. 4.1, since achieving a higher sensitivity near $\alpha = 0$ through increasing of L (or, equivalently, L_{eff}) results in significantly lower sensitivities at larger values of α. This can limit dynamic range and/or precision in practical implementations, further highlighting the importance of direct consideration of the sensitivity for analyzing sensor performance. To perform this comparison, we seek the maximum attainable sensitivity using linear methods for arbitrary α. By optimizing equation 4.17 with respect to L, we find the sensitivity is maximized when $L = \frac{1}{\alpha}$, giving the optimized sensitivity

$$S_{\text{opt}} = \frac{I_{\text{in}}}{e\alpha}. \tag{4.19}$$

This optimized sensitivity, which is inversely related to α, defines the sensitivity limit for LAS shown in Fig. 4.1b and Fig. 4.4d. For the comparison plot in Fig. 4.4d, we assume a source with the same bandwidth as the simulton and an average power of 500 mW, which is approximately the maximum output power of our system when fully purged. In practice, the asymptotic behavior near $\alpha = 0$ for LAS is limited by spatial constraints and the finesses achievable with available cavity mirrors. For our comparison, we assume a cavity length of 1.2 m, the same as the length of our OPO cavity, and a maximum path length enhancement of 10^6, corresponding to a finesse of over 1.5 million. We believe this to be a fair choice as such a high finesse is extremely difficult to achieve in practice, particularly over such a large bandwidth.

The sensitivity given by equation 4.17 and sensitivity enhancement of equation 4.18 are plotted for our measured data in Figs. 4.7c and 4.7d. Figure 4.7c is very similar to Fig. 4.4d, but here we have distilled the linear region into four lines. The first two lines include the sensitivity limit, S_{opt}, and the baseline sensitivity, S_{base}, computed for a source of the same bandwidth and power as the simulton, as discussed in the preceding. While these multimode trendlines provide the most direct comparison with our experiment (hence our use of S_{opt} as the linear reference in Fig. 4.4d), we also show the sensitivity limit, $S_{\text{opt, SM}}$, and baseline sensitivity, $S_{\text{base, SM}}$ for a single-mode source of the same power as our OPO. The best linear performance is observed for the path-length-multiplexed single-mode source ($S_{\text{opt, SM}}$), since non-absorbing modes in the multimode case limit the achievable sensitivity. However, better linearity is observed for the baseline sensitivity in the multimode case due to the intrinsic multiplexing that comes with having multiple frequency modes. In all cases, the sensitivity is seen to decrease with increasing concentration, in contrast to the simulton sensing behavior. Figure 4.7d shows the corresponding sensitivity enhancement for the simulton measurement, found by taking the ratio of our measured sensitivity and S_{base}, with the maximum sensitivity enhancement reaching a value of 90. This large sensitivity enhancement can greatly improve the achievable sensor precision when compared to the linear baseline.

In addition to calculating the sensitivity and sensitivity enhancement for our measured data, we further extend the plot of Fig. 4.4c to include the detector-limited measurements for a bandwidth of 1 MHz, the bandwidth of our presented experimental data, and a bandwidth of 1 Hz. Here, we make the assumption that the cavity is locked to the simulton resonance such that continuous measurement of the

simulton output is taken over the full measurement time. To find the detector-limited output, we must consider the noise-equivalent power (NEP) of our detection system. We do so by first making a histogram of the measured voltage at times when no signal was incident on the detector; the resulting histogram is shown in Fig. 4.7e. We then fit it with a Gaussian distribution and find the standard deviation, $\sigma = 76.9$ µV, which is valid if we assume the detector noise distribution to be close to white noise. Next, we use the 4 µm calibration curve, shown previously in Fig. 4.5c, to estimate the equivalent optical power. As the curve is not perfectly linear, we use the average slope across the measured data.

The resulting NEP is 74.2 µW. Since our measurement was taken in a 1 MHz bandwidth, given by the bandwidth of our detector (Thorlabs PDAVJ5), we can divide by the square root of our bandwidth to find the normalized NEP of our measurement of 74.2 nW/$\sqrt{\text{Hz}}$. One might note that this is far from Thorlabs' reported value for the detector of 14 pW/$\sqrt{\text{Hz}}$. The discrepancy, however, comes primarily from our calibration curve which has a slope close to 1 V/W compared to the specified conversion gain of 1500 V/W on the Thorlabs website. This difference is due to our focusing only a fraction of our output power onto the detector area to limit detector saturation at high powers as well as the broadband nature of our signal, since the specified NEP is at the wavelength with the peak responsivity. Accounting for this difference in conversion from optical power to voltage, our measured value is in pretty good agreement with the specified value. Using our measured value for the NEP, we find that the detector-limited enhancement can be extremely large, benefiting from the asymptotic behavior close to threshold. In particular, around an output power of 74.2 µW (the NEP for a 1 MHz bandwidth), we find enhancements on the order of 100s of thousands while, around a measured power of 74.2 nW (the NEP for a 1 Hz bandwidth), enhancement on the order of 10s of millions could be possible.

Finally, we may find the detector-limited NEA. Here, we divide the normalized NEP of 74.2 nW/$\sqrt{\text{Hz}}$ by our maximum measured sensitivity of 4.1 mW/ppm to find a minimum detectable concentration of 18 ppt in a 1 Hz measurement time. We may find the effective absorption coefficient for a concentration of 18 ppt, calculated as specified above in equation 4.16 to be 5.84 cm^{-1}, to give a NEA of 1.05*10^{-10} cm^{-1}/$\sqrt{\text{Hz}}$. While there are limitations in practice to achieving a detector-limited measurement for the simulton sensing mechanism, including the need for a well-stabilized cavity, careful control over the sample concentration, and suppression of

the relative intensity noise (RIN) of the pump laser, we believe that these theoretical estimates showcase the potential for achieving high sensitivity and precision as well as a large dynamic range using this mechanism.

Selectivity and Impact of Other Atmospheric Molecules

Another important consideration of our experiment is that, while the dominant response of the simulton is attributable to CO_2, our experiment is performed using atmosphere which contains an abundance of other molecular species in addition to CO_2. Thus, while the simulations in Section 4.2 are done using only CO_2, as described above, it is worth characterizing the impact of other molecules on the sensing behavior. The second notable molecule in the spectral region of our OPO output is H_2O, but we additionally consider contributions from CH_4, N_2O, and O_3 which also exist in small concentrations in the atmosphere and have strong absorption features near our degenerate signal at 4180 nm. In our model, we assume molecular fractions of 78.084% for N_2, 20.946% for O_2, 0.0415% for CO_2, 0.000179% for CH_4, 0.00005% for N_2O, and 0.000001% for O_3 in dry atmosphere [56, 57]. These molecular fractions are scaled proportionally with the addition of H_2O, which is assumed to have a molecular fraction of 1.25%, typical of the temperature and humidity of our lab.

Figures 4.8a and 4.8b show the imaginary and real parts of the complex refractive index, $\kappa(\omega)$ and $n'(\omega)$, for the full atmospheric model. As expected, the strongest contributions by far are from atmospheric CO_2 and H_2O. Figure 4.8c shows the simulated simulton response using the full atmospheric model. Here, we mimic our experimental procedure by varying the modeled concentration of N_2 and changing the concentrations of all other gases proportionally. Compared to the simulation using only CO_2 shown in Fig. 4.4b, the observed change in output power with CO_2 concentration is slightly larger, indicating a small contribution from other atmospheric gases. Figure 4.8d depicts the simulated simulton response to H_2O alone for reasonable atmospheric concentrations. While the effect is less pronounced than in the case of CO_2, validating our experimental assumption that the dominant response is coming from CO_2, this also highlights the sensitivity of the simulton to any molecule within the simulton bandwidth. This can be advantageous for certain applications as it enables the same sensor to be used for sensing of multiple molecules, as long as one has a priori knowledge of the molecular species being varied. However, it poses an additional challenge with respect to selectivity, since one cannot distinguish the separate contributions from different species in a mixture.
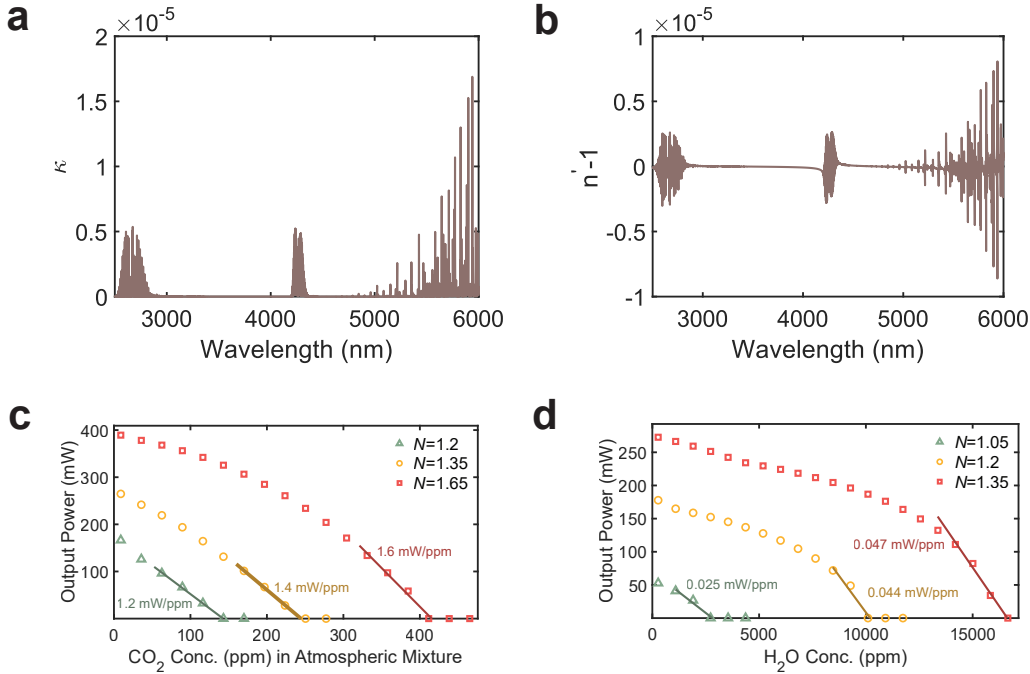
Figure 4.8: **Modeling of full atmospheric absorption. a**, Calculated κ, the imaginary part of the complex refractive index, for full atmospheric model. **b**, Corresponding result for $n' - 1$, the real part of the complex refractive index. **c**, Output power as a function of CO_2 concentration in the atmospheric mixture, where all atmospheric gases are changed proportionally to the N_2 concentration, consistent with the experimental purging setup. **d**, Output power as a function of H_2O concentration, the second strongest atmospheric absorber in the vicinity of the broadband simulton resonance.

One solution to this challenge which we elucidate here is to consider the response of multiple OPO peaks rather than just the simulton regime [50]. These multiple OPO peaks may be addressed through varying the detuning, T_{RT}, corresponding to a roundtrip delay in the cavity. As each peak contains different spectral content, their collective response to the addition of gas can contain information regarding the molecular makeup of a given gas mixture of interest. Figure 4.9a shows the simulated power spectrum for a pump power of 1.2 W as the detuning is swept, highlighting the different OPO regimes. A more positive detuning, T_{RT}, indicates a longer cavity, with the most postively detuned peak (T_{RT} = 3.5 fs) corresponding to operation in the simulton regime, the second most positively detuned peak (T_{RT} = -3.5 fs) indicating the conventional regime, and the rest corresponding to non-degenerate operation.

Figure 4.9b shows the collective response of all OPO peaks as the atmospheric mixture is varied in proportion to the addition of N_2, replicating our experimental setup.
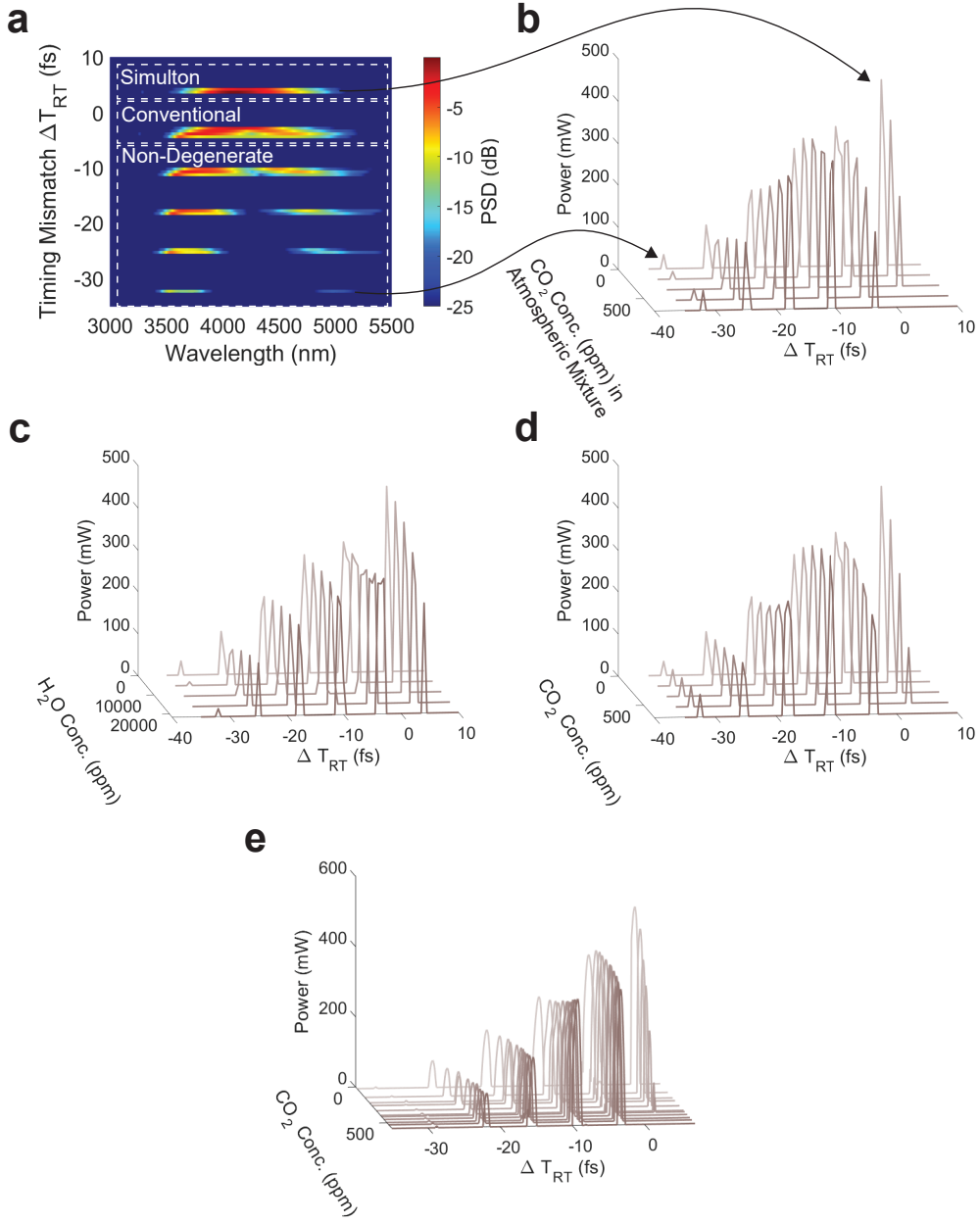
Figure 4.9: **Selectivity in multi-species sensing using OPOs. a**, Simulated power spectrum of OPO output as the detuning, ΔT_{RT}, is swept, with labels indicating different OPO regimes. **b**, Simulated response of all OPO peaks for the addition of CO_2 in an atmospheric mixture to the cavity. **c**, Simulated response of OPO peaks with changing H_2O concentration. **d**, Simulated response of OPO peaks with addition of CO_2. **e**, Experimental response of all OPO peaks as the cavity is purged with N_2.

Here, the peak structure corresponds to a detected power or voltage, equivalent to taking the integral over wavelength for the data of Fig. 4.9a. The pump power is

held constant at 1.2 W. As the CO_2 concentration in the atmospheric mixture is increased, we observe a strong decrease in power for the simulton (T_{RT} = 3.5 fs), as expected. By contrast, the conventional (T_{RT} = -3.5 fs) and first non-degenerate (T_{RT} = -10.5 fs) peaks are seen to increase slightly at low concentrations and then decrease at higher concentrations. Furthermore, the most non-degenerate peak (T_{RT} = -31.5 fs) exhibits the opposite behavior, decreasing at low concentrations and then increase at higher concentrations.

This response can be broken down into the contributions from CO_2 and H_2O by analyzing the behaviors of the peaks while varying only one gas at a time. Figure 4.9c shows the simulated OPO behavior as the concentration of H_2O is varied, while the CO_2 response is shown in Fig. 4.9d. In the case of CO_2, the simulton (T_{RT} = 3.5 fs) is seen to sharply decrease, while more non-degenerate peaks, such as the peak at T_{RT} = -17.5 fs, are seen to monotonically increase. The most non-degenerate peak exhibits very little change, except for a small increase in power. In contrast, besides also causing a decrease in power for the simulton, the addition of H_2O is seen to produce additional features on the conventional peak (T_{RT} = -3.5 fs) and cause the most non-degenerate peak (T_{RT} = -31.5 fs) to decrease for low concentrations and increase again at high concentrations. Taken together, one can see that the response of the non-degenerate peaks for the case where the full atmospheric mixture is considered is dominated by the addition of H_2O, whereas the more degenerate peaks largely follow the CO_2 behavior. This unique response to the different gases indicates that, by considering all the OPO peaks together, information about multiple species may be gleaned from the OPO output.

An equivalent plot for our experimental system is shown in Fig. 4.9d. Qualitatively, we see good agreement with Fig. 4.9b as the CO_2 concentration is increased. The simulton (T_{RT} = 3.5 fs) is observed to rapidly decrease while the conventional peak (T_{RT} = -3.5 fs) grows at low concentrations and then begins to decrease. More non-degenerate resonances are seen to increase in power. With that said, the farthest non-degenerate peaks (T_{RT} = -31.5 fs and T_{RT} = -24.5 fs) neither increase as much as those for the simulation of CO_2 alone nor exhibit the decrease and subsequent increase expected for the full atmospheric case which includes H_2O. This suggests that there is some small impact from atmospheric water in our experiment but that we have likely overestimated its contribution in the parameters considered for the presented simulation.

Single-Mode Intracavity Absorption Sensing

In this section, we briefly review the theory of single-mode intracavity absorption sensing (SM ICAS), following the formalism presented in ref. [29]. We begin with the rate equations for a laser system. Defining the mean photon number M, the mean population inversion ρ, the broadband cavity loss γ, the pump rate R, the rate of spontaneous decay of the upper laser level A, and the rate of induced emission per photon per excited atom or molecule B, we have

$$\frac{dM}{dt} = -\gamma M + B\rho(M + 1), \tag{4.20a}$$

$$\frac{d\rho}{dt} = R - A\rho - \rho BM. \tag{4.20b}$$

The last term in equation 4.20a, $B\rho$, is the mean spontaneous emission rate. This term is often omitted in analysis of single-cavity intracavity absorption sensing. Here, we will give the solutions both with and without this term which will enable discussion of its practical importance. Setting both equations to 0 and solving for the steady-state mean photon number gives

$$M = \frac{1}{2}\left(\frac{R}{\gamma} - \frac{A}{B}\right) + \sqrt{\frac{1}{4}\left(\frac{R}{\gamma} - \frac{A}{B}\right)^2 + \frac{R}{\gamma}}. \tag{4.21}$$

In the case where spontaneous emission is not considered, or when $(\frac{R}{\gamma} - \frac{A}{B})^2 >> \frac{R}{\gamma}$, the last term under the root may be neglected, giving

$$M = \frac{R}{\gamma} - \frac{A}{B}. \tag{4.22}$$

The intracavity power, P_{int} may be found from the mean photon number, M, as $P_{int} = \hbar\omega\frac{c}{L}M$, where $\hbar$ is the reduced Planck's constant, c is the speed of light, ω is the laser frequency, and we have assumed a free-space cavity of roundtrip length L. Taking the transmission of the output coupler as T, the output power, P_{out} can be found by computing $P_{out} = TP_{int}$. In terms of equation 4.22, then, we have

$$P_{out} = TP_{int} = T\hbar\omega\frac{c}{L}M = T\hbar\omega\frac{c}{L}\left(\frac{R}{\gamma} - \frac{A}{B}\right) = \hbar\omega\frac{T}{\mathcal{L}}(R - R_{th}), \tag{4.23}$$

where $\mathcal{L}$ is the total loss, and the relations $R_{th} = \frac{A\gamma}{B}$ and $\gamma = \frac{c\mathcal{L}}{L}$ have been used. As a final manipulation before proceeding, we may also rewrite $T = 1 - R = 1 - e^{-\alpha_R L} \approx$

$\alpha_R L$, where R is the reflection of the output coupler. The total loss, similarly, can be defined as $\mathcal{L} = 1 - e^{-\alpha_{\text{tot}} L} \approx \alpha_{\text{tot}} L$ where $\alpha_{\text{tot}} = \alpha_R + \alpha_{\text{samp}} + \alpha_{oth}$ is a lumped absorption coefficient which includes the output coupling loss, α_R, the loss due to the sample, α_{samp}, and the loss due to other intracavity elements, α_{oth}. Rewriting equation 4.23 in terms of these absorption coefficients gives

$$P_{\text{out}} = \hbar\omega\alpha_R\left(\frac{R}{\alpha_{\text{tot}}} - \frac{cA}{B}\right) = \hbar\omega\frac{\alpha_R}{\alpha_{\text{tot}}}(R - R_{\text{th}}). \tag{4.24}$$

To find the enhancement factor according to equation 4.13, we seek the quantity $\ln\left(\frac{P_{\text{out}}(\alpha_{\text{samp}})}{P_{\text{out}}(\alpha_{\text{samp}}+\Delta\alpha_{\text{samp}})}\right)$, where $\Delta\alpha_{\text{samp}}$ is some small change in the loss due to the presence of an intracavity absorber. Defining $\Delta P_{\text{out}} = P_{\text{out}}(\alpha_{\text{samp}}) - P_{\text{out}}(\alpha_{\text{samp}}+\Delta\alpha_{\text{samp}})$ and assuming $\frac{\Delta P_{\text{out}}}{P_{\text{out}}} \ll 1$, then $\ln\left(\frac{P_{\text{out}}(\alpha_{\text{samp}})}{P_{\text{out}}(\alpha_{\text{samp}}+\Delta\alpha_{\text{samp}})}\right) \approx \frac{P_{\text{out}}(\alpha_{\text{samp}})-P_{\text{out}}(\alpha_{\text{samp}}+\Delta\alpha_{\text{samp}})}{P_{\text{out}}(\alpha_{\text{samp}})} = \frac{\Delta P_{\text{out}}}{P_{\text{out}}}$. Using 4.24, we can find this quantity as

$$\frac{\Delta P_{\text{out}}}{P_{\text{out}}} = \frac{\Delta\alpha_{\text{samp}}R}{\alpha_{\text{tot}}(\alpha_{\text{tot}} + \Delta\alpha_{\text{samp}})\left(\frac{R}{\alpha_{\text{tot}}} - \frac{cA}{B}\right)} = \frac{\Delta\alpha_{\text{samp}}N}{(\alpha_{\text{tot}} + \Delta\alpha_{\text{samp}})(N - 1)}, \tag{4.25}$$

where we have re-parameterized the system in terms of the number of times above threshold, $N = \frac{R}{R_{\text{th}}}$. Finally, we compute the enhancement $\xi = \frac{L_{eff}}{L}$, making the approximation that $\Delta\alpha_{\text{samp}} \ll \alpha_{\text{samp}}$

$$\xi \approx \frac{1}{\alpha_{\text{tot}}L}\frac{N}{N - 1}. \tag{4.26}$$

Thus, we see that if spontaneous emission can be neglected, an enhancement asymptotically approaching infinity can be expected as threshold is approached. Figure4.10a shows the enhancement calculated using the full model from equation 4.21 in comparison with the analytic solution ignoring spontaneous emission given by equation 4.26 for the realistic laser parameters given in ref. [29], namely $A = 1.7 * 10^8$ s^{-1}, $B = 10^{-2}$ s^{-1}, $L = 1$ m, and $\alpha_R = 0.01$ m^{-1}. We take the frequency to be $\omega = 4.5 * 10^{14}$ rad/s, equivalent to the center frequency of our OPO output. For these parameters, the agreement is excellent, with the primary variation occurring extremely near to $N = 1$, where the simplified model asymptotes to infinity while the full model approaches a peak. Generally, agreement is better the lower the spontaneous emission rate.

To maximize the enhancement, then, we would like our system to operate as close to $N = 1$ as possible. However, we face a signal-to-noise ratio (SNR) trade-off in
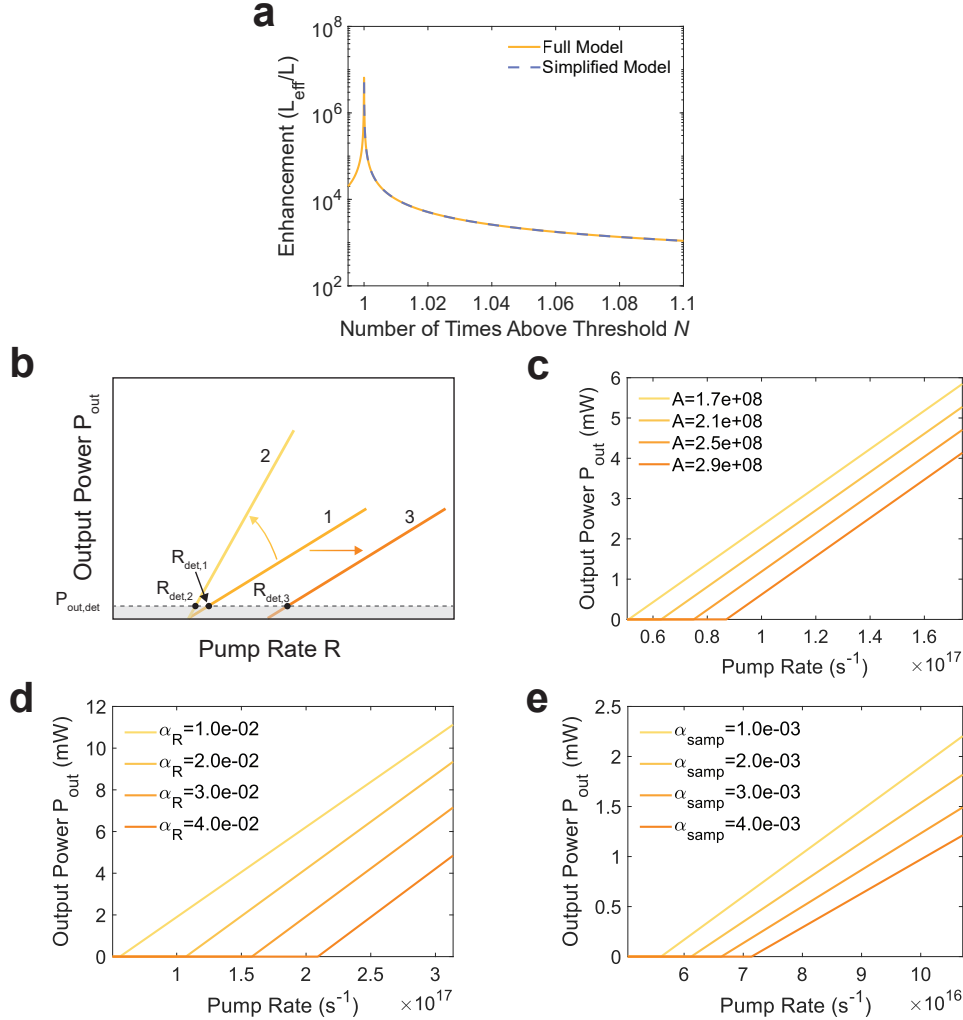
Figure 4.10: **Enhanced sensing in a single-mode laser. a**, Comparison between the enhancement calculated for the full model including spontaneous emission (orange) and simplified model ignoring spontaneous emission (blue), showing the extreme benefit of near-threshold operation. The y-axis is on a logarithmic scale. **b**, For a given minimum detectable output power, $P_{\text{out,det}}$, there are two ways to achieve sensing closer to threshold compared to some reference (line 1). The first is increase the slope efficiency (line 2), and the second is to increase the threshold (line 3). **c**, Increasing the spontaneous decay rate A (or, equivalently, decreasing B, the rate of stimulated emission) can increase the threshold of the laser system without changing the slope efficiency. **d**, Increasing the output coupling loss, $alpha_{\text{R}}$, increases the threshold and can also benefit the slope efficiency. **e**, Increasing other losses increases the threshold but decreases the slope in the same proportion and thus does not enable detector-limited sensing closer to threshold.

doing so because the signal goes to zero as N approaches 1. Intuitively, there are two ways to improve the situation, depicted in Fig. 4.10b. Here, the output power,

P_{out}, as a function of the pump rate, R, is shown for a reference line (line 1, medium orange) and compared to two modified lines, line 2 in light orange and line 3 in dark orange. The minimum detectable power, $P_{\text{out,det}}$, is shown with the dashed gray line; the shaded gray region below represents photon numbers which cannot be detected. $R_{\text{det,i}}$ where $i \in \{1, 2, 3\}$ represents the minimum pump rate for which the number of signal photons exceeds $P_{\text{out,det}}$. The first path towards improvement would be to alter the slope efficiency, or the rate of the change of the output power with a changing pump rate above threshold. As shown by line 2, a higher slope efficiency enables operation closer to threshold while maintaining a large enough output power to have a sufficiently large SNR. Alternatively, one can increase the threshold, as exemplified by line 3. For the same slope efficiency and output power, a larger threshold will mean a smaller N; in other words, $R_{\text{det,3}}/R_{\text{th,3}} < R_{\text{det,1}}/R_{\text{th,1}}$. With this intuition, we can then look at the equation 4.24 and see how each parameter can help to tune the enhancement. First, we rewrite equation 4.24 in terms of $P_{\text{out,det}}$

$$P_{\text{out,det}} = \alpha_R \hbar \omega \left(\frac{R}{\alpha_{\text{tot}}} - \frac{cA}{B} \right). \tag{4.27}$$

We may then rearrange to solve for R_{det}

$$R_{\text{det}} = \alpha_{\text{tot}} \left(\frac{cA}{B} + \frac{P_{\text{out,det}}}{\alpha_R \hbar \omega} \right). \tag{4.28}$$

Knowing that $R_{\text{th}} = \frac{\alpha_{\text{tot}} cA}{B}$, we find that the detector-limited number of times above threshold, N_{det} is given by

$$N_{\text{det}} = \frac{R_{\text{det}}}{R_{\text{th}}} = 1 + \frac{B P_{\text{out,det}}}{\alpha_R \hbar \omega cA}. \tag{4.29}$$

This expression tells us which parameters can be tuned to operate closer to threshold while keeping the signal level the same, thus improving the SNR for a detector-limited measurement. Here, we see clearly that increasing increasing the ratio $\frac{A}{B}$ can help to bring N_{det} closer to 1 while holding the signal constant. This is consistent with Fig. 4.10c, which shows the output power as a function of the pump rate for varying A. As A is increased, the threshold increases, which should enable operation closer to threshold. With that said, the rates A and B come from fundamental properties of the lasing system and may be difficult to tune in practice. More notable is that the only loss present in equation 4.29 is the loss due to the

output coupling, α_R. As may be expected, a larger output coupling results in a larger extraction efficiency, which increases the threshold and may also benefit the slope efficiency. This is illustrated in Fig. 4.10d. By contrast, other intracavity loss mechanisms result simultaneously in an increase in the threshold and a decrease in the slope efficiency, as shown in Fig. 4.10e. The net result is that the two effects cancel one another out, leading to no net gain in terms of operation closer to threshold.

As a final point of comparison, we can find an expression for the sensitivity

$$S = |\frac{\partial P_{\text{out}}}{\partial \alpha_{\text{samp}}}| = \alpha_R \hbar \omega \frac{R}{\alpha_{\text{tot}}^2}. \tag{4.30}$$

Assuming we are operating at the pump rate given by R_{det}, we find

$$S_{\text{det}} = \alpha_R \hbar \omega \frac{R_{\text{det}}}{\alpha_{\text{tot}}^2} = \frac{\alpha_R \hbar \omega}{\alpha_{\text{tot}}} \left(\frac{cA}{B} + \frac{P_{\text{out,det}}}{\alpha_R \hbar \omega} \right), \tag{4.31}$$

where S_{det} is the sensitivity at the point dictated by $P_{\text{out,det}}$. As with the SNR for near-threshold operation, we see that the ratio $\frac{A}{B}$ can benefit the absolute sensitivity, further highlighting the benefit of using a laser with a low spontaneous emission rate. Furthermore, we see that the sensitivity is related to α_{tot}^{-1}. This suggests the same limitation in dynamic range for ICAS with traditional lasers as we observed for linear methods; for given system parameters, the maximum achievable sensitivity scales with an inverse relationship to the sample loss. Between this relationship and our finding in equation 4.26 that the enhancement factor is also inversely related to the loss, it is clear that traditional intracavity absorption sensing with a single-mode laser benefits from a high-finesse cavity and is best suited towards trace gas detection. These conclusions will be critically important as we analyze the contrasting case of intracavity absorption sensing in a CW OPO in the next section.

ICAS in a Continuous-Wave OPO

While the focus of this work is on the simulton regime, which is a pulsed mode of operation, it is desirable also to have a basic analytical framework for understanding ICAS in an OPO. The CW theory can give us such a framework, allowing for direct comparison with the general laser case presented above and for the simulton theory presented in the following subsection. Specifically, here, we seek to derive the enhancement factor for ICAS in a CW OPO. We additionally derive an expression

for the sensitivity, and we see how these quantities scale with critical parameters of the OPO.

To begin, we directly quote equation 2.74 derived in Section 2.8 for the OPO efficiency, η, as

$$\eta = \frac{4}{N}(\sqrt{N} - 1)\left(\frac{\omega_1}{\omega_3}T_1\frac{e^{\alpha_1 L_{RT}}}{e^{\alpha_1 L_{RT}} - 1} + \frac{\omega_2}{\omega_3}T_2\frac{e^{\alpha_2 L_{RT}}}{e^{\alpha_2 L_{RT}} - 1}\right), \qquad (4.32)$$

where we have considered the interaction between a pump, signal, and idler at ω_3, ω_2, and ω_1, respectively. Additionally, $N = P_{30}/P_{th}$ is the number of times above threshold, T_j is the outcoupling in power of wave j, and we have defined α_j is the total loss for wave j. Assuming the loss is small and considering operation at degeneracy with $\omega_1 = \omega_2$, we find

$$P_\omega^{out} = \frac{T}{\alpha_\omega L_{RT}}\frac{4P_{2\omega}(0)}{N}(\sqrt{N} - 1) = \frac{4TP_{th}}{\alpha_\omega L_{RT}}\left(\sqrt{\frac{P_{2\omega}(0)}{P_{th}}} - 1\right)$$

$$= \frac{2T}{\kappa L_{NL}}(\sqrt{P_{2\omega}(0)} - \frac{\alpha_\omega L_{RT}}{2\kappa L_{NL}}). \quad (4.33)$$

This equation allows us to characterize the OPO behavior in the case of single-mode ICAS. First, we look at the enhancement factor. For a small change in the loss, $\Delta\omega$, we have the following change in signal

$$\Delta P_\omega^{out} = \frac{T\Delta\alpha_\omega L_{RT}}{\kappa^2 L_{NL}^2}. \qquad (4.34)$$

Then, the enhancement $\xi = \frac{\Delta P_\omega^{out}}{L_{RT}\Delta\alpha_\omega P_\omega^{out}}$ is given by

$$\xi = \frac{1}{L_{RT}\alpha_\omega}\frac{1}{\sqrt{N} - 1}. \qquad (4.35)$$

This is a very similar behavior as the one predicted by the SM laser theory. However, one advantage of the OPO according to this result is the $\sqrt{N} - 1$ behavior in the denominator which grows to large values further away from threshold than the $N - 1$ behavior exhibited in the SM laser case, as illustrated in Fig. 4.11a. Here, we see that the CW OPO (orange) grows more quickly as $N = 1$ is approached when compared to SM ICAS (pink).

In addition to the enhancement, we may also look at the other scaling behaviors of the CW OPO system, as we did in the case of SM ICAS. Firstly, let us make some simplifications. To begin, we return to our earlier observation that the output coupling has been included implicitly in the loss; in fact, the loss α_ω consists of three components such that $\alpha_\omega = \alpha_{\mathrm{samp}} + \alpha_R + \alpha_{\mathrm{oth}}$. Here, α_{samp} is the loss from the sample of interest, α_R is the loss from the output coupling such that the reflection $R = e^{-\alpha_R L_{\mathrm{RT}}}$, and α_{oth} accounts for all other roundtrip losses in the OPO cavity. Then, $T = 1 - R = 1 - e^{-\alpha_R L_{\mathrm{RT}}} \approx \alpha_R L_{\mathrm{RT}}$. Furthermore, we define the parameter $\gamma = \frac{1}{\kappa}$, giving

$$P_\omega^{\mathrm{out}} = \alpha_R \gamma \frac{2 L_{\mathrm{RT}}}{L_{\mathrm{NL}}} \left(\sqrt{P_{2\omega}(0)} - \alpha_\omega \gamma \frac{L_{\mathrm{RT}}}{2 L_{\mathrm{NL}}} \right). \tag{4.36}$$

Let us now define the detector-limited ouptut power, P_ω^{det}. The corresponding input intensity, $P_{2\omega}^{\mathrm{det}}$ is

$$P_{2\omega}^{\mathrm{det}} = \left(\frac{P_\omega^{\mathrm{out}}}{\alpha_R \gamma} \frac{L_{\mathrm{NL}}}{2 L_{\mathrm{RT}}} + \alpha_\omega \gamma \frac{L_{\mathrm{RT}}}{2 L_{\mathrm{NL}}} \right)^2 = \left(\frac{P_\omega^{\mathrm{out}}}{\alpha_R \gamma} \frac{L_{\mathrm{NL}}}{2 L_{\mathrm{RT}}} \right)^2 + \frac{P_\omega^{\mathrm{out}} \alpha_\omega}{4 \alpha_R} + \alpha_\omega^2 \gamma^2 \left(\frac{L_{\mathrm{RT}}}{2 L_{\mathrm{NL}}} \right)^2. \tag{4.37}$$

Using this, we find that the number of times above threshold needed to achieve an output intensity of P_ω^{det}, N^{det}, is

$$N^{\mathrm{det}} = 1 + \frac{P_\omega^{\mathrm{out}}}{\alpha_R \alpha_\omega} \left(\frac{L_{\mathrm{NL}}}{L_{\mathrm{RT}} \gamma} \right)^2 + \left(\frac{P_\omega^{\mathrm{out}}}{\alpha_R \alpha_\omega} \right)^2 \left(\frac{L_{\mathrm{NL}}}{\gamma L_{\mathrm{RT}}} \right)^4. \tag{4.38}$$

Here we see that, unlike the SM laser case, the number of times above threshold for the OPO can be brought closer to 1 through tuning of the loss. This is a result of the loss contributing to the threshold directly through the offset term in the OPO case rather than through the slope, as it did in the case of the SM laser. Additionally, we see that tuning of the output coupling can provide the largest benefit, since it serves to simultaneously increase the slope efficiency and threshold. Finally, increasing γ can also be used to improve the detector-limited sensitivity enhancement, with a benefit similar to that of the output coupling. These observations are consistent with the scaling behaviors of equation 4.36, plotted in Figs. 4.11b, 4.11c, and 4.11d for variation in the output coupling, loss, and γ parameter, respectively. The output coupling and γ parameter can both be tuned to simultaneously increase the threshold and slope efficiency, while increasing the roundtrip loss can increase the threshold without impacting the slope efficiency.
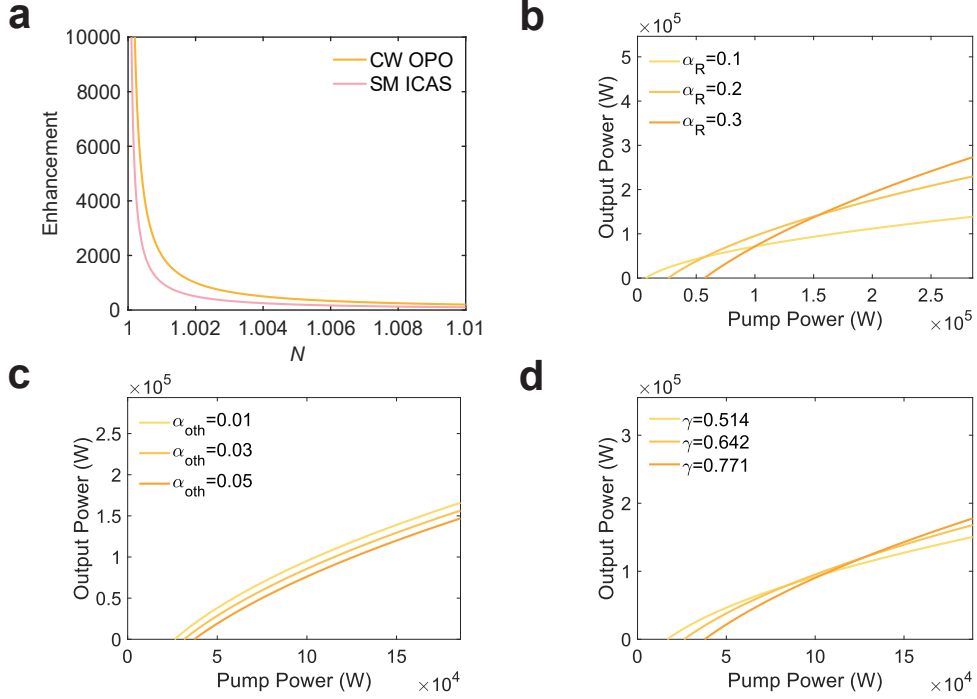
Figure 4.11: **Enhanced sensing in a continuous-wave OPO. a**, Comparison between the theoretical enhancement from a CW OPO and that of SM ICAS in a laser system, showing the faster growth of the CW OPO as $N = 1$ is approached. **b**, Output intensity versus input intensity for different values of the output coupling, showing how the output coupling can be increased to simultaneously increase both the threshold and slope efficiency, enabling a better SNR for detector-limited near-threshold sensing in the low-finesse regime. **c**, Varying the round-trip loss coming from components other than the output coupling can increase the threshold without degrading the slope efficiency. **d**, Changing the γ parameter can benefit the system in a similar way to the output coupling by simultaneously increasing the threshold and slope efficiency.

In addition to looking at the detector-limited enhancement, we can compute the sensitivity, which is given here as:

$$S = \left| \frac{\partial P_\omega^{\text{out}}}{\partial \alpha_{\text{samp}}} \right| = \alpha_R \gamma^2 \Big(\frac{L_{\text{RT}}}{L_{\text{NL}}} \Big)^2. \tag{4.39}$$

Again, there is a notable difference as compared to the SM laser case. Specifically, the loss term due to the sample does not appear anywhere in the equation. However, both the output coupling and γ parameter can be increased to improve the sensitivity, consistent with what we saw in equation 4.38 for the detector-limited enhancement. These results suggest that, unlike the SM laser case, the CW OPO can benefit from

operation in the low-finesse regime, provided there is sufficient gain to go above threshold. Additionally, this lack of dependence on the sample loss allows for a high dynamic range to be achieved for sensing measurements performed in the OPO system. These differences arise due to the different gain mechanisms of the two systems as represented in their respective rate equations, where the laser gain arises from an energy exchange in which an atomic transition results in emission of a photon while the parametric gain comes from an interaction between the pump and signal electric fields through the quadratic nonlinearity.

ICAS in a Simulton OPO

Having studied ICAS in a CW OPO, we finish our discussion by turning to the case of the simulton OPO. Here, we begin by directly quoting the result from equation 3.16 in section 3.2, where the steady-state simulton amplitude, $\tilde{a}$, was given as

$$\tilde{a}^2 = a_{\text{sim}}^2 \frac{e^{2\gamma_0 l - \alpha_\omega L} - 1}{e^{2\gamma_0 l} - 1}. \tag{4.40}$$

As mentioned previously, this gives the first requirement for simulton threshold, which is that the gain must compensate the round-trip loss, meaning that $e^{2\gamma_0 L_{\text{NL}} - \alpha_\omega L_{\text{RT}}} \geq 1$. Using the definition of $\gamma_0 = \kappa A_{2\omega,0}$ to re-express things in terms of the pump power, we see that the threshold pump power, P_{th}, is given by $P_{\text{th}} = A_{2\omega,\text{th}}^2 = \frac{(\alpha_\omega L_{\text{RT}})^2}{(2\kappa L_{\text{NL}})^2}$. We see also that for sufficiently large gains, the steady-state signal amplitude saturates to the simulton amplitude, a_{sim}. From equation 4.40, assuming an output coupling, $T = 1 - R \approx \alpha_R L_{\text{RT}}$, and by expanding the exponential terms to first order, we arrive at the following expression for the steady-state output power, $\tilde{P}_{\text{out}}$:

$$\tilde{P}_{\text{out}} = \frac{\alpha_R L_{\text{RT}}}{\kappa L_{\text{NL}}} \frac{\Delta\beta' L_{\text{NL}}}{\tau_0} \left(A_{2\omega,0} - \frac{\alpha_\omega L_{\text{RT}}}{2\kappa L_{\text{NL}}}\right) = \frac{\alpha_R L_{\text{RT}}}{\kappa L_{\text{NL}}} \frac{\Delta\beta' L_{\text{NL}}}{\tau_0} A_{2\omega,\text{th}}(\sqrt{N} - 1). \tag{4.41}$$

This is, perhaps unsurprisingly, a similar expression to what was observed in the CW OPO case. In particular, the equivalent path-length enhancement $\xi = \frac{\Delta\tilde{P}_{\text{out}}}{L_{\text{RT}}\Delta\alpha_\omega \tilde{P}_{\text{out}}}$ follows the same asymptotic scaling:

$$\xi = \frac{1}{\alpha_\omega L_{\text{RT}}} \frac{1}{\sqrt{N} - 1}. \tag{4.42}$$

The sensitivity $S = \left|\frac{\partial \tilde{P}_{\text{out}}}{\partial \alpha_\omega}\right|$ also has a similar expression, given as:

$$S = \left| \frac{\Delta\beta' L_{\mathrm{NL}}}{\tau_0} \frac{\alpha_R L_{\mathrm{RT}}^2}{\kappa^2 L_{\mathrm{NL}}^2} \right|. \tag{4.43}$$

One key difference, however, is the factor $\frac{\Delta\beta' L_{\mathrm{NL}}}{\tau_0}$, which is given by the ratio between the walk-off length and the pulse width. This additional factor accounts for the extra gain that the simulton may extract from the pump due to the relative motion of the pump and signal which is not accounted for in the static dynamics of the CW regime. In our experimental system, $\Delta\beta' = 144$ fs/mm, $l = 0.5$ mm, and $\tau_0 = 22$ fs in the simulton regime assuming a transform-limited sech-shaped pulse [18], so this factor gives a sensitivity enhancement of approximately 3.27. If we assume the conventional regime can be approximately described by the CW theory, which would be largely consistent with the box-pulse scaling behavior described in ref. [35], we may observe that this factor of 3.27 is strikingly close to the measured difference in slope efficiency between the simulton and conventional regimes, as shown in Fig. 4.2c and repeated here in Fig. 4.12a, as well as the difference in sensitivity, as in Fig. 4.12b. This also suggests that further increasing this ratio may enable even larger sensitivity enhancement. Paired with the discussion regarding the gain clipping in the case of pulsed pumping in section 4.2, the studied dynamics suggest a complex toolbox which one may use to optimize the performance of a simulton-based sensor through modification of the walk-off parameter, cavity length detuning, pump pulse shape, and output coupling.
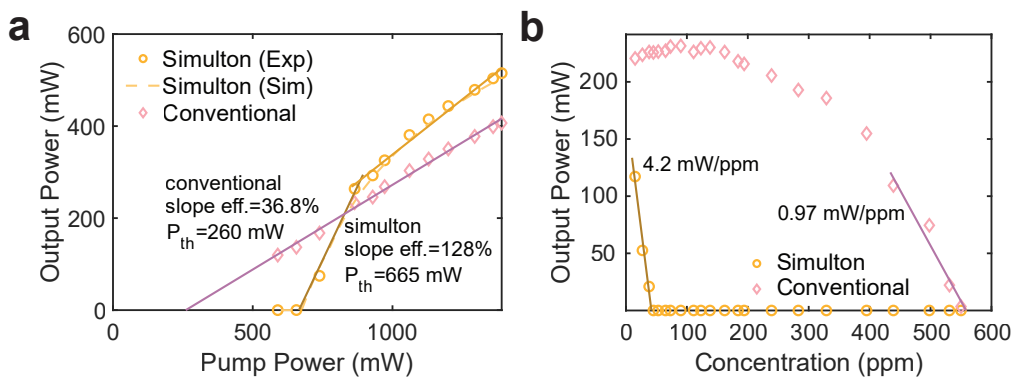
Figure 4.12: **Sensitivity comparison between the simulton and conventional regimes. a**, Output power as a function of input power in the simulton (orange) and conventional (pink) regimes. Solid lines show the linear fits, while the orange, dashed line shows the simulton simulation. **b**, Output power as a function of CO_2 concentration in both the simulton and conventional regimes at a factor of $N = 1.25$ times above threshold, which is sufficiently low for the conventional regime to also be depleted.

BIBLIOGRAPHY

[1]   Akira Hasegawa and Frederick Tappert. "Transmission of stationary nonlinear optical pulses in dispersive dielectric fibers. I. Anomalous dispersion." In: *Applied Physics Letters* 23.3 (1973), pp. 142–144.

[2]   Govind P. Agrawal. "Chapter 5 - optical solitons". In: *Nonlinear Fiber Optics (Fifth Edition)*. Academic Press, 2013, pp. 129–191.

[3]   Daniel C. Cole, Erin S. Lamb, Pascal Del'Haye, Scott A. Diddams, and Scott B. Papp. "Soliton crystals in Kerr resonators." In: *Nature Photonics* 11.10 (2017), pp. 671–676. DOI: `10.1038/s41566-017-0009-z`.

[4]   Maxim Karpov, Martin H. P. Pfeiffer, Hairun Guo, Wenle Weng, Junqiu Liu, and Tobias J. Kippenberg. "Dynamics of soliton crystals in optical microresonators." In: *Nature Physics* 15.10 (2019), pp. 1071–1077.

[5]   Xu Yi, Qi-Fan Yang, Kiyoul Yang, and Kerry Vahala. "Imaging soliton dynamics in optical microcavities." In: *Nature Communications* 9.1 (2018), p. 3565.

[6]   Mengjie Yu, Jae K. Jang, Yoshitomo Okawachi, Austin G. Griffith, Kevin Luke, Steven A. Miller, Xingchen Ji, Michal Lipson, and Alexander L. Gaeta. "Breather soliton dynamics in microresonators." In: *Nature Communications* 8.1 (2017), p. 14569.

[7]   Daryl T. Spencer, Tara Drake, Travis C. Briles, Jordan Stone, Laura C. Sinclair, Connor Fredrick, Qing Li, Daron Westly, B. Robert Ilic, Aaron Bluestone, et al. "An optical-frequency synthesizer using integrated photonics." In: *Nature* 557.7703 (2018), pp. 81–85. DOI: `10.1038/s41586-018-0065-7`.

[8]   Ewelina Obrzud, Monica Rainer, Avet Harutyunyan, Miles H. Anderson, Junqiu Liu, Michael Geiselmann, Bruno Chazelas, Stefan Kundermann, Steve Lecomte, Massimo Cecconi, et al. "A microphotonic astrocomb." In: *Nature Photonics* 13.1 (2019), pp. 31–35. DOI: `doi.org/10.1038/s41566-018-0309-y`.

[9]   Vladimir L. Kalashnikov and Evgeni Sorokin. "Soliton absorption spectroscopy." In: *Physical Review A* 81.3 (2010), p. 033840.

[10] Myoung-Gyun Suh, Qi-Fan Yang, Kiyoul Yang, Xu Yi, and Kerry J. Vahala. "Microresonator soliton dual-comb spectroscopy." In: *Science* 354.6312 (2016), pp. 600–603.

[11] Alexander V. Buryak, Paolo Di Trapani, Dmitry V. Skryabin, and Stefano Trillo. "Optical solitons due to quadratic nonlinearities: From basic physics to futuristic applications." In: *Physics Reports* 370.2 (2002), pp. 63–235.

[12] Arkadev Roy, Rajveer Nehra, Saman Jahani, Luis Ledezma, Carsten Langrock, Martin Fejer, and Alireza Marandi. "Temporal walk-off induced dissipative quadratic solitons." In: *Nature Photonics* 16.2 (2022), pp. 162–168. DOI: 10.1038/s41566-021-00942-4.

[13] Mingming Nie and Shu-Wei Huang. "Quadratic solitons in singly resonant degenerate optical parametric oscillators." In: *Physical Review Applied* 13.4 (2020), p. 044046.

[14] Alexander W. Bruch, Xianwen Liu, Zheng Gong, Joshua B. Surya, Ming Li, Chang-Ling Zou, and Hong X. Tang. "Pockels soliton microcomb." In: *Nature Photonics* 15.1 (2021), pp. 21–27.

[15] Sergei Akhmanov, Anatolii Chirkin, Konstantin Drabovich, Al Kovrigin, Rem Khokhlov, and Anatoly Sukhorukov. "Nonstationary nonlinear optical effects and ultrashort light pulse formation." In: *IEEE Journal of Quantum Electronics* 4.10 (1968), pp. 598–605.

[16] Stefano Trillo. "Bright and dark simultons in second-harmonic generation." In: *Optics Letters* 21.15 (1996), pp. 1111–1113.

[17] Marc Jankowski, Alireza Marandi, Christopher R. Phillips, Ryan Hamerly, Kirk A. Ingold, Robert L. Byer, and Martin M. Fejer. "Temporal simultons in optical parametric oscillators." In: *Physical Review Letters* 120.5 (2018), p. 053904.

[18] Mingchen Liu, Robert M. Gray, Arkadev Roy, Kirk A. Ingold, Evgeni Sorokin, Irina Sorokina, Peter G. Schunemann, and Alireza Marandi. "High-power mid-IR few-cycle frequency comb from quadratic solitons in an optical parametric oscillator." In: *Laser & Photonics Reviews* 16.11 (2022), p. 2200453. DOI: 10.1002/lpor.202200453.

[19] Andrey V. Muraviev, Viktor O. Smolski, Zachary E. Loparo, and Konstantin L. Vodopyanov. "Massively parallel sensing of trace molecules and their isotopologues with broadband subharmonic mid-infrared frequency combs." In: *Nature Photonics* 12.4 (2018), pp. 209–214. DOI: 10.1038/s41566-018-0135-2.

[20] Jane Hodgkinson and Ralph P. Tatam. "Optical gas sensing: A review." In: *Measurement Science and Technology* 24.1 (2012), p. 012004.

[21] Anthony O'Keefe and David A. G. Deacon. "Cavity ring-down optical spectrometer for absorption measurements using pulsed laser sources." In: *Review of Scientific Instruments* 59.12 (1988), pp. 2544–2551.

[22] Michael J. Thorpe, Kevin D. Moll, R. Jason Jones, Benjamin Safdi, and Jun Ye. "Broadband cavity ringdown spectroscopy for sensitive and rapid molecular detection." In: *Science* 311.5767 (2006), pp. 1595–1599.

[23] Birgitta Bernhardt, Akira Ozawa, Patrick Jacquet, Marion Jacquey, Yohei Kobayashi, Thomas Udem, Ronald Holzwarth, Guy Guelachvili, Theodor W. Hänsch, and Nathalie Picqué. "Cavity-enhanced dual-comb spectroscopy." In: *Nature Photonics* 4.1 (2010), pp. 55–57.

[24] Gang Zhao, Thomas Hausmaninger, Weiguang Ma, and Ove Axner. "Shot-noise-limited Doppler-broadened noise-immune cavity-enhanced optical heterodyne molecular spectrometry." In: *Optics Letters* 43.4 (2018), pp. 715–718.

[25] Aleksandra Foltynowicz, Florian M. Schmidt, Weiguang Ma, and Ove Axner. "Noise-immune cavity-enhanced optical heterodyne molecular spectroscopy: Current status and future potential." In: *Applied Physics B* 92 (2008), pp. 313–326.

[26] Ming Dong, Chuantao Zheng, Dan Yao, Guoqiang Zhong, Shuzhuo Miao, Weilin Ye, Yiding Wang, and Frank K. Tittel. "Double-range near-infrared acetylene detection using a dual spot-ring Herriott cell (DSR-HC)." In: *Optics Express* 26.9 (2018), pp. 12081–12091.

[27] Béla Tuzson, Markus Mangold, Herbert Looser, Albert Manninen, and Lukas Emmenegger. "Compact multipass optical cell for laser spectroscopy." In: *Optics Letters* 38.3 (2013), pp. 257–259.

[28] Xiutao Lou, Yabo Feng, Shunhu Yang, and Yongkang Dong. "Ultra-wide-dynamic-range gas sensing by optical pathlength multiplexed absorption spectroscopy." In: *Photonics Research* 9.2 (2021), pp. 193–201.

[29] Valery M. Baev, Torsten Latz, and Peter E. Toschek. "Laser intracavity absorption spectroscopy." In: *Applied Physics B* 69.3 (1999), pp. 171–202.

[30] Evgeny N. Antonov, Vsevolod G. Koloshnikov, and Vladimir R. Mironenko. "Quantitative measurement of small absorption coefficients in intracavity absorption spectroscopy using a cw dye laser." In: *Optics Communications* 15.1 (1975), pp. 99–103.

[31] Daniel A. Gilmore, Pajo V. Cvijin, and George H. Atkinson. "Intracavity absorption spectroscopy with a Titanium: Sapphire laser." In: *Optics Communications* 77.5-6 (1990), pp. 385–389.

[32] Mikhail A. Belkin, Marko Lončar, Benjamin G. Lee, Christian Pflügl, Ross Audet, Laurent Diehl, Federico Capasso, David Bour, Scott Corzine, and Gloria Höfler. "Intra-cavity absorption spectroscopy with narrow-ridge microfluidic quantum cascade lasers." In: *Optics Express* 15.18 (2007), pp. 11262–11271.

[33] Benjamin Löhden, Svetlana Kuznetsova, Klaus Sengstock, Valery M. Baev, Anatoly Goldman, Sergey Cheskis, and Bera Pálsdóttir. "Fiber laser intracavity absorption spectroscopy for in situ multicomponent gas analysis in the atmosphere and combustion environments." In: *Applied Physics B* 102.2 (2011), pp. 331–344.

[34] Pavel Melentiev, Aleksei Kalmykov, Anton Gritchenko, Anton Afanasiev, Victor Balykin, Aleksandr S. Baburin, E. Ryzhova, Ivan Filippov, Ilya A. Rodionov, Igor A. Nechepurenko, et al. "Plasmonic nanolaser for intracavity spectroscopy and sensorics." In: *Applied Physics Letters* 111.21 (2017), p. 213104.

[35] Ryan Hamerly, Alireza Marandi, Marc Jankowski, Martin M. Fejer, Yoshihisa Yamamoto, and Hideo Mabuchi. "Reduced models and design principles for half-harmonic generation in synchronously pumped optical parametric oscillators." In: *Physical Review A* 94.6 (2016), p. 063809.

[36] Robert L. Byer. "Optical parametric oscillators." eng. In: *Quantum Electronics: A Treatise*. Vol. 1. New York: Academic Press, 1975, pp. 588–694. ISBN: 978-0-12-574041-8.

[37] Witlof Brunner and Harry Paul. "The optical parametric oscillator as a means for intracavity absorption spectroscopy." In: *Optics Communications* 19.2 (1976), pp. 253–256.

[38] Michal Nikodem and Gerard Wysocki. "Molecular dispersion spectroscopy–new capabilities in laser chemical sensing." In: *Annals of the New York Academy of Sciences* 1260.1 (2012), pp. 101–111.

[39] Agata Cygan, Piotr Wcisło, Szymon Wójtewicz, Grzegorz Kowzan, Mikołaj Zaborowski, Dominik Charczun, Katarzyna Bielska, Ryszard S. Trawiński, Roman Ciuryło, Piotr Masłowski, et al. "High-accuracy and wide dynamic range frequency-based dispersion spectroscopy in an optical cavity." In: *Optics Express* 27.15 (2019), pp. 21810–21821.

[40] Pengcheng Zhao, Yan Zhao, Haihong Bao, Hoi Lut Ho, Wei Jin, Shangchun Fan, Shoufei Gao, Yingying Wang, and Pu Wang. "Mode-phase-difference photothermal spectroscopy for gas detection with an anti-resonant hollow-core optical fiber." In: *Nature communications* 11.1 (2020), p. 847.

[41] Qiang Wang, Zhen Wang, Wei Ren, Pietro Patimisco, Angelo Sampaolo, and Vincenzo Spagnolo. "Fiber-ring laser intracavity QEPAS gas sensor using a 7.2 kHz quartz tuning fork." In: *Sensors and Actuators B: Chemical* 268 (2018), pp. 512–518.

[42] Luis Ledezma, Ryoto Sekine, Qiushi Guo, Rajveer Nehra, Saman Jahani, and Alireza Marandi. "Intense optical parametric amplification in dispersion-engineered nanophotonic lithium niobate waveguides." In: *Optica* 9.3 (2022), pp. 303–308. DOI: 10.1364/OPTICA.442332.

[43] Luis Ledezma, Arkadev Roy, Luis Costa, Ryoto Sekine, Robert Gray, Qiushi Guo, Rajveer Nehra, Ryan M. Briggs, and Alireza Marandi. "Octave-spanning tunable infrared parametric oscillators in nanophotonics." In: *Science Advances* 9.30 (2023), eadf9711. DOI: 10.1126/sciadv.adf9711.

[44] Zongyin Yang, Tom Albrow-Owen, Weiwei Cai, and Tawfique Hasan. "Miniaturization of optical spectrometers." In: *Science* 371.6528 (2021), eabe0722.

[45] Hong Zhou, Zhihao Ren, Cheng Xu, Liangge Xu, and Chengkuo Lee. "MOF/polymer-integrated multi-hotspot mid-infrared nanoantennas for sensitive detection of CO2 gas." In: *Nano-Micro Letters* 14.1 (2022), p. 207.

[46] Cheng Li, Trevor Lohrey, Phuong-Diem Nguyen, Zhouyang Min, Yisha Tang, Chang Ge, Zachary P. Sercel, Euan McLeod, Brian M. Stoltz, and Judith Su. "Part-per-trillion trace selective gas detection using frequency locked whispering-gallery mode microtoroids." In: *ACS Applied Materials & Interfaces* 14.37 (2022), pp. 42430–42440.

[47] Veer Chandra and Rakesh Ranjan. "Performance analysis of different slot waveguide structures for evanescent field based gas sensor applications." In: *Optical and Quantum Electronics* 53 (2021), pp. 1–15.

[48] Marek Vlk, Anurup Datta, Sebastián Alberti, Henock Demessie Yallew, Vinita Mittal, Ganapathy Senthil Murugan, and Jana Jágerská. "Extraordinary evanescent field confinement waveguide sensor for mid-infrared trace gas spectroscopy." In: *Light: Science & Applications* 10.1 (2021), p. 26.

[49] Arkadev Roy, Saman Jahani, Carsten Langrock, Martin Fejer, and Alireza Marandi. "Spectral phase transitions in optical parametric oscillators." In: *Nature Communications* 12.1 (2021), p. 835. DOI: 10.1038/s41467-021-21048-z.

[50] Selina Zhou, Robert Gray, Mingchen Liu, Arkadev Roy, and Alireza Marandi. "Towards gas sensing without spectroscopy using mid-infrared optical parametric oscillators." In: *Optical Sensors*. Optica Publishing Group. 2022, SM1E–1.

[51] Jungwon Kim and Youjian Song. "Ultralow-noise mode-locked fiber lasers and frequency combs: Principles, status, and applications." In: *Advances in Optics and Photonics* 8.3 (2016), pp. 465–540.

[52] Jean Wei, Joel M. Murray, Jacob O. Barnes, Douglas M. Krein, Peter G. Schunemann, and Shekhar Guha. "Temperature dependent Sellmeier equation for the refractive index of GaP." In: *Optical Materials Express* 8.2 (2018), pp. 485–490.

[53] Wolfgang Demtröder. *Laser spectroscopy 1: Basic principles.* Springer, 2014.

[54] Iouli E. Gordon, Laurence S. Rothman, Robert J. Hargreaves, R. Hashemi, Ekaterina V. Karlovets, Frances M. Skinner, Eamon K. Conway, Christian Hill, Roman V. Kochanov, Yan Tan, et al. "The HITRAN2020 molecular spectroscopic database." In: *Journal of Quantitative Spectroscopy and Radiative Transfer* 277 (2022), p. 107949.

[55] Daniele Romanini, Irène Ventrillard, Guillaume Méjean, Jérôme Morville, and Erik Kerstel. "Introduction to cavity enhanced absorption spectroscopy." In: *Cavity-Enhanced Spectroscopy and Sensing*. Springer, 2014, pp. 1–60.

[56] Arthur N. Cox. *Allen's astrophysical quantities.* Springer, 2015.

[57] Earth System Research Laboratory. *Trends in atmospheric carbon dioxide.* 2019.

Chapter 5

TWO-OPTICAL-CYCLE PULSES FROM NANOPHOTONIC TWO-COLOR SOLITON COMPRESSION

Robert M. Gray, Ryoto Sekine, Maximilian Shen, Thomas Zacharias, James Williams, Selina Zhou, Rahul Chawlani, Luis Ledezma, Nicolas Englebert, and Alireza Marandi. "Two-optical-cycle pulses from nanophotonic two-color soliton compression." In: *arXiv preprint arXiv:2501.15381* (2025). DOI: 10.48550/arXiv.2501.15381.

5.1 Introduction

Ultrashort pulses with temporal widths on the order of a few or even a single cycle [1–3] of their carrier frequency have enabled many key breakthroughs in recent decades. Pulses with timescales on the order of femtoseconds and, more recently, attoseconds allow the direct measurement and control of molecular, atomic, and electronic motion [4–8] as well as field-resolved measurements of ultrafast phenomena [9, 10]. Additionally, the large peak powers associated with ultrashort pulses can enable extreme nonlinear optical phenomena [11, 12] such as high-harmonic generation [13, 14], where specifically two-color, few-cycle pulses have been demonstrated to offer numerous benefits in shaping the generated high-harmonic spectrum and probing the underlying dynamics [15–18]. Furthermore, ultrashort pulses serve as ultrafast carriers of information in time-multiplexed optical systems [19], benefiting a variety of applications in communications [20] and information processing [21, 22].

The generation and control of ultrashort pulses typically consists of two stages. The first stage is used to generate an ultra-broadband coherent spectrum or supercontinuum, after which the second stage is used to manipulate the phase of different spectral components in order to produce the desired pulse [23]. The systems required for achieving this spectral broadening and subsequent phase compensation are typically bulky and complex, limiting their scalability.

One way to reduce the system complexity has been to leverage soliton pulse compression, where the nonlinear phase accumulated through the spectral broadening process is compensated by linear dispersive effects [24, 25]. This allows for direct generation of clean short pulses, with limited need for additional spectral phase

compensation following the soliton compressor. Typically, soliton pulse compression has been achieved using cubic (Kerr) nonlinearity, including several integrated demonstrations in the many 10s of fs to ps regime [26–29], requiring a suitable nonlinear medium with anomalous dispersion at the wavelength of interest.

Soliton pulse compression has also been investigated leveraging phase-mismatched second-harmonic generation in quadratic nonlinear optical systems, including experimental demonstrations to the few-cycle regime [30–32]. Such systems have typically operated in the cascading limit, with a large phase mismatch, where the dynamics at the fundamental frequency are similar to those of cubic soliton compression [33, 34]. However, they have the additional advantages of utilizing the inherently stronger quadratic nonlinearity and operating in either dispersion regime (normal or anomalous) through correct selection of the sign of the phase mismatch. Furthermore, the quadratic compression mechanism lends itself naturally to the generation of two-color ultrashort waveforms [35] through the accompanying generated second harmonic. That said, the presence of walk-off due to the GVM between the fundamental and second-harmonic waves in typical bulk media has limited the performance and broad application of quadratic soliton compression [36].

Here, we show that these challenges may be overcome through dispersion engineering in nanophotonic quadratic nonlinear optical systems [37, 38]. By designing for a low walk-off, we illustrate that compression may be achieved beyond the cascading limit, allowing the realization of a host of two-color pulses through suitable adjustment of the dispersion of the fundamental and second-harmonic waves. We perform experiments in nanophotonic lithium niobate in which we demonstrate compression to the two-cycle regime. We experimentally measure a pulse FWHM of 13 fs at the fundamental frequency and 16 fs at the second harmonic, respectively 143.5 THz (2090 nm) and 287 THz (1045 nm). Our results show good agreement with theoretical predictions, validating the use of our theoretical framework as a holistic toolbox for the design of such soliton compression systems. Finally, we illustrate how the two-color compressed pulses can be directly leveraged for the synthesis of single-cycle waveforms. These results pave the way towards scalable next-generation ultrashort pulse synthesizers.

5.2 Theory of Quadratic Two-Color Soliton Compression

The concept of two-color soliton pulse compression is illustrated in Fig. 5.1a. A pulse at the fundamental frequency is coupled into the nanophotonic waveguide
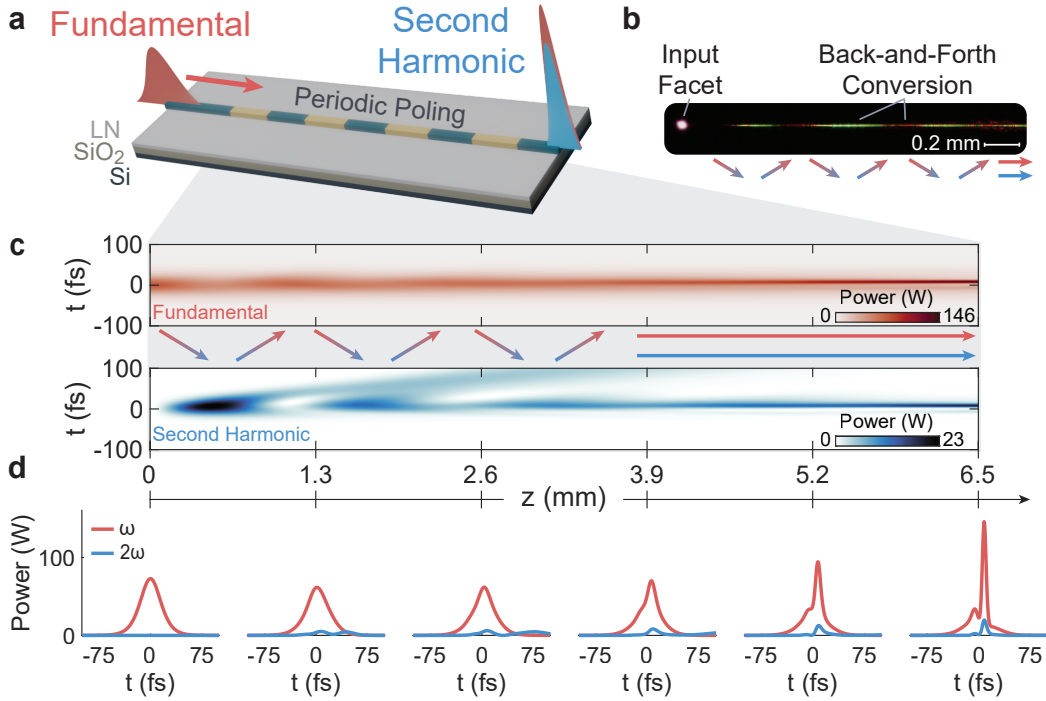
Figure 5.1: **Two-color soliton pulse compression in nanophotonics. a**, A pulse at the fundamental frequency (ω) is used to pump the dispersion-engineered nanophotonic waveguide designed for phase-mismatched second-harmonic (2ω) generation. Co-propagating compressed pulses at the fundamental and second harmonic are achieved through the two-color soliton compression. **b**, Microscope image of the measured waveguide, showing back-and-forth conversion between harmonics. **c**, Simulated evolution of the fundamental (top) and second harmonic (bottom) as a function of normalized propagation distance, z, in the waveguide. **d**, Temporal profiles of the fundamental and second harmonic at labeled locations in the waveguide.

designed for slightly phase-mismatched second-harmonic generation. By precisely engineering the dispersion and nonlinearity, pulse shortening at both the fundamental frequency and generated second harmonic is achieved over the course of propagation in the waveguide. This stands in contrast to other quadratic spectral broadening mechanisms [39–41], for which broad supercontinuum may be observed but without the formation of a clean short pulse.

The dynamics of this regime of operation are illuminated through the microscope image of the experimentally measured device shown in Fig. 5.1b and simulations of Figs. 5.1c and 5.1d. The soliton pulse compression relies on the linear dispersion in the waveguide balancing the nonlinear phase accumulated through the back-and-forth energy transfer between the fundamental (ω) and second-harmonic (2ω) waves due to the slightly phase-mismatched interaction. Figure 5.1b shows this back-and-

forth conversion during the first few millimeters of propagation in our waveguide device. The microscope camera is not receptive to the fundamental light at 2090 nm, so periodic bright and dark spots correspond to the generation and back-conversion of second-harmonic light at 1045 nm. In areas where the generated second harmonic is strongest, we also observe third and fourth harmonic generation to 700 nm (red) and 512 nm (green), respectively.

This behavior is consistent with our simulations based on the coupled wave equations in Fig. 5.1c, which show the temporal evolution of both the fundamental (top) and second-harmonic (bottom) pulses as a function of propagation distance z in the waveguide. Figure 5.1d presents snapshots of the temporal profile of both harmonics at labeled locations along the waveguide. Compression over a few cycles of back-and-forth conversion ultimately results in their forming a co-propagating two-color bright-bright pulse pair in the waveguide, characteristic of the two-color soliton compression. In addition to pulse shortening, we also observe significant peak power enhancement.

To confirm the solitonic nature of the compression mechanism, we first turn to the soliton solutions of the coupled wave equations describing phase-mismatched second-harmonic generation (see Section 5.7). When the GVD sign is the same for both the fundamental and second harmonic waves, there exists a well-known family of bright-bright soliton solutions [42]. Assuming 0 GVM, the shapes of the normalized fundamental and second-harmonic soliton envelopes, $a_\omega(\xi)$ and $a_{2\omega}(\xi)$, respectively, as a function of the dimensionless time coordinate ξ are approximately given by [43]:

$$a_\omega(\xi) = a_{\omega,0} \operatorname{sech}^p(\frac{\xi}{p}), \tag{5.1a}$$

$$a_{2\omega}(\xi) = a_{2\omega,0} \operatorname{sech}^2(\frac{\xi}{p}), \tag{5.1b}$$

where the parameters p, $a_{\omega,0}$, and $a_{2\omega,0}$ may be found using the equations:

$$p = \frac{1}{a_{2\omega,0} - 1}, \tag{5.2a}$$

$$a_{\omega,0}^2 = \frac{\alpha a_{2\omega,0}^2}{a_{2\omega,0} - 1}, \tag{5.2b}$$

$$\alpha = \frac{4(a_{2\omega,0} - 1)^3}{2 - a_{2\omega,0}}. \tag{5.2c}$$

Here, $a_{\omega,0}$ and $a_{2\omega,0}$ represent the normalized amplitudes of the fundamental and second-harmonic solitons. From this, we see that the soliton shape is completely determined by $\alpha = \left|\frac{\beta_\omega^{(2)}}{\beta_{2\omega}^{(2)}}\right|(2 + \frac{\Delta k}{\beta})$, where $\beta_\omega^{(2)}$ and $\beta_{2\omega}^{(2)}$ are respectively the GVD of the fundamental and second harmonic, Δk is the phase mismatch, and β represents shifts in the phase velocity due to the nonlinear interaction. This solution exhibits good agreement with the exact soliton solution, capturing both the behavior of the soliton amplitudes and tails. Furthermore, the solution shape asymptotes to that of the soliton in the cascading limit [44] where $\alpha \gg 1$ and precisely captures the known exact soliton solution [45] with $\alpha = 1$.
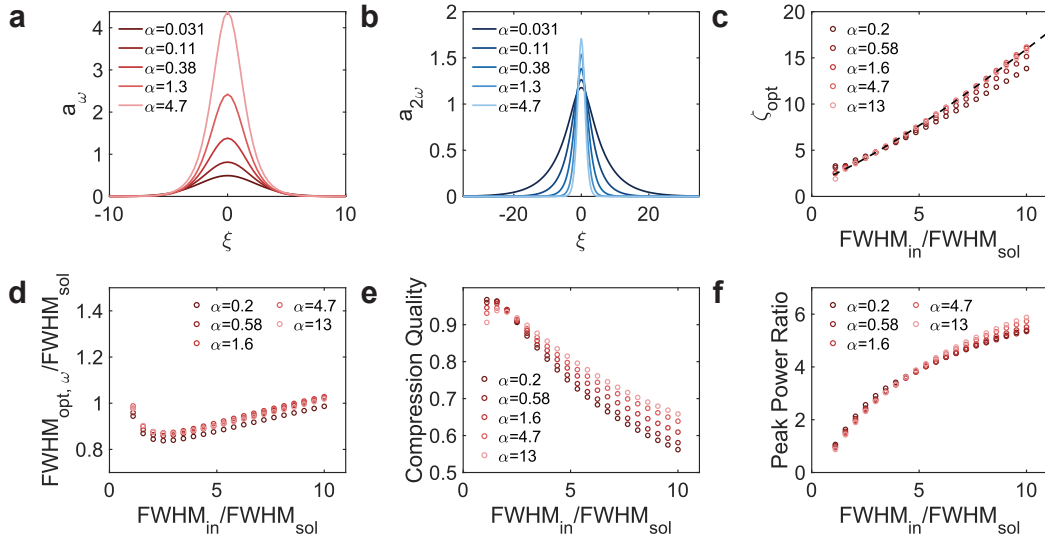
Figure 5.2: **Scaling behaviors of two-color soliton pulse compression. a**, Soliton solutions of the fundamental wave for varying α. **b**, Corresponding soliton solutions for the second harmonic. **c**, Optimum ζ for achieving compression. A fit is given by the dashed black line. **d-f**, Scaling behaviors for varying α of the **d**, fundamental FWHM, **e**, compression quality, and **f**, fundamental peak power ratio at ζ_{opt}. FWHM, full-width at half-maximum.

In addition to this approximate analytic solution, we compute the soliton solution branch using numerical continuation (see Section 5.7). Several examples of bright solitons for various α values are shown in Figs. 5.2a-b. As expected from equation 5.2b, the amplitude of the normalized fundamental wave (Fig. 5.2a) is significantly larger than that of the second harmonic (Fig. 5.2b) for large α and vice versa for small α.

Having to this point neglected walk-off, we next consider the effects of GVM, $\Delta\beta'$, on the soliton solution. Here, we find that a soliton solution exists only in the stationary regime [32] with $\left|\beta_{2\omega}^{(2)}\beta\right|(2 + \frac{\Delta k}{\beta}) \geq \frac{(\Delta\beta')^2}{2}$. This has presented a large challenge for achieving two-color soliton compression bulk systems with limited control over the dispersion, as overcoming the intrinsic GVM in the material has required operation in the cascading limit with large phase mismatch, limiting the power in the generated second-harmonic wave.

With the soliton solution in hand, we next use it to better understand the compression behavior. By investigating its stability, we find that the soliton is a saddle point with respect to the pulse amplitude, phase, and pulse width (see Section 5.7). Thus, during the compression process, the fundamental and second-harmonic pulses approach the soliton solution, near which the evolution of the two waves is slow, and then are observed to again broaden. One must therefore optimize the length of the waveguide to achieve an optimally compressed pulse.

To determine this optimum length, we simulate the pulse evolution as a function of the normalized propagation coordinate, $\zeta = |\beta|z$ for a variety of input parameters. We then define the optimum distance, ζ_{opt}, at which point the minimum pulse width is achieved for the fundamental wave. Figure 5.2c shows ζ_{opt} as a function of the ratio of the input pulse FWHM to that of the fundamental soliton, $\text{FWHM}_{\text{in}}/\text{FWHM}_{\text{sol}}$. As can be seen, the scaling behavior is similar for all values of α and nearly identical for $\alpha \geq 1$. By fitting the $\alpha \geq 1$ data (dashed, black line), we arrive at the following design heuristic:

$$\zeta_{\text{opt}} = 1.49 + 0.86\left(\frac{\text{FWHM}_{\text{in}}}{\text{FWHM}_{\text{sol}}}\right)^{1.23}. \tag{5.3}$$

From these simulations, we may also study several key properties of the compressed pulse at the point ζ_{opt}. To begin, we analyze the FWHM of the fundamental wave, $\text{FWHM}_{\text{opt},\omega}$, and we compare it to FWHM_{sol}. The results are shown in Fig. 5.2d. For all simulated input pulse widths, the width of the compressed pulse is within 20% of the soliton width, with the pulses under-shooting the soliton pulse width for smaller values of $\text{FWHM}_{\text{in}}/\text{FWHM}_{\text{sol}}$.

A second parameter of interest is the compression quality [32], which is a measure of how well the energy remains localized in the pulse following compression. Here, it is defined as the ratio between the combined energy of the output fundamental and second-harmonic pulses and the input pulse energy. For the output, the energy

is calculated from the pulse FWHM and amplitudes, assuming a sech-shaped pulse profile. As expected, the compression quality, shown in Fig. 5.2e, is higher for inputs with a FWHM closer to the soliton FWHM. However, a compression quality greater than 0.5 is observed even for the highest simulated ratio of $FWHM_{in}/FWHM_{sol} = 10$.

Finally, we are interested in the peak power enhancement provided by the compression mechanism, as an important benefit of the compressed pulses is their ability to drive nonlinear optical phenomena requiring large peak powers. The ratio between the peak power in the fundamental output and the input is plotted in Fig. 5.2f. Again, the trend is similar for all values of α, with significant peak power enhancement observed for all simulated values of the input pulse FWHM.
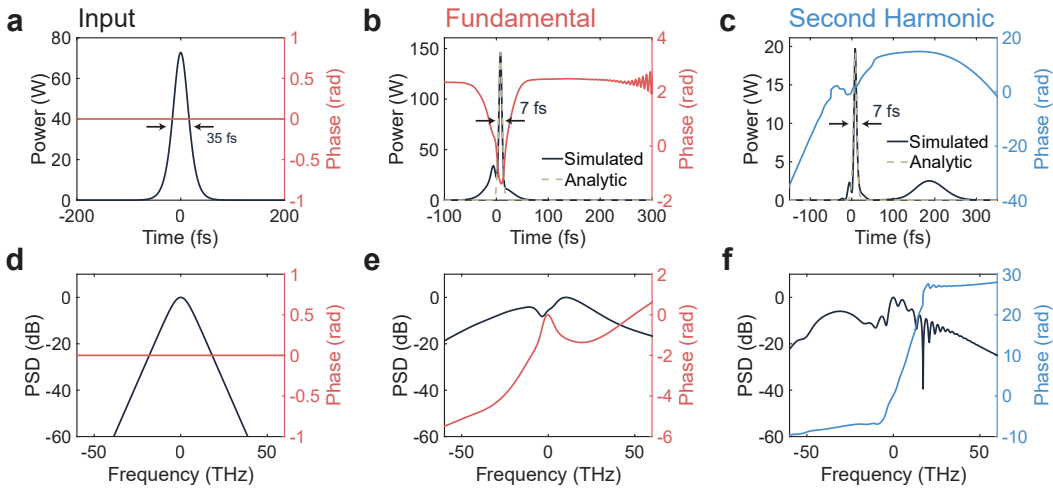
Figure 5.3: **Simulation of designed single-cycle pulse compressor.** **a**, Input, **b**, output fundamental, and **c**, output second-harmonic pulses. **d**, Corresponding input, **e**, output fundamental, and **f**, output second-harmonic spectra. Dashed, tan lines show the pulse profiles predicted from soliton theory.

These observations have several important consequences for the design of two-color soliton pulse compression systems. Firstly, since the compressed pulse exhibits a pulse width similar to that of the soliton solution and furthermore retains most of the input energy, the soliton solution given by equations 5.1 and 5.2 can be used to estimate the compressed pulse profile. Secondly, control over the dispersion parameters offers new opportunities for two-color pulse compression compared to previous demonstrations in the cascading limit with large Δk, including operation in the small α regime and compression with small Δk. This can allow two-color compression with a variety of resultant pulse shapes and peak power ratios between

the fundamental and second harmonics. Further discussion around the design of two-color soliton compression systems based on the presented theoretical framework may be found in Section 5.7.

5.3 Device Design

Based on these principles, we design a device for experimentally demonstrating two-color pulse compression to the near-single cycle regime. In our design, we aim to operate away from the cascading limit, in the small α regime. Furthermore, we seek to operate with low pump pulse energies on the order of a few pJ, as may be achieved by integrated ultrafast sources [46, 47]. The designed waveguide (see Section 5.7) has a fundamental and second-harmonic GVD of $\beta_\omega^{(2)}$ = 9.2 fs^2/mm and $\beta_{2\omega}^{(2)}$ = 141 fs^2/mm, respectively, as well as a GVM of $\Delta\beta' = 27$ fs/mm between the two waves.

With these parameters, and considering our transform-limited input pulse width of 35 fs as well as a phase mismatch of Δk = -4 rad/mm, we find that the soliton solution has a FWHM of 8 fs for an input energy of 3 pJ. This is nearly single-cycle for the fundamental wave at 143.5 THz. The corresponding normalized parameters in our system are $\beta = -1.02$ rad/mm and $\alpha = 0.39$. The optimum waveguide length, L, is then found using equation 5.3 to be 6.5 mm, the designed length for our nanophotonic device.

Simulation results for our designed device parameters are plotted in Fig. 5.3. The input is taken to be a 2.9-pJ, 35-fs sech-shaped pulse at 2090 nm, with temporal and spectral profiles shown in Figs. 5.3a and 5.3d. The fundamental output in time domain is shown in Fig 5.3b. The pulse profile is shown in dark gray, with the corresponding phase shown in red. Overlaid is the soliton solution given by equations 5.1 and 5.2 (tan, dashed line), exhibiting very good agreement. We normalize the peak power of the analytic solution to the peak power of the simulation, but we emphasize here that the soliton shape is otherwise unaltered. The pulse FWHM is 7 fs, close to the theoretical value (8 fs). This also equates exactly to a single cycle at the carrier frequency. Despite the inclusion of loss in the simulated waveguide, we additionally observe an approximately two-fold peak power enhancement at the fundamental. The corresponding carrier-free spectrum is shown in Fig. 5.3e and is characterized by a relatively flat phase across the entirety of the broadband spectrum.

The second-harmonic output is shown in Figs. 5.3c and 5.3f. As with the funda-

mental, the soliton solution is overlaid in the time domain plot (Fig. 5.3c). In this case, we perform no additional normalization, preserving the predicted peak power ratio of about 7.6:1 from the analytic solution. Yet, the agreement is again excellent. As with the fundamental, the FWHM is 7 fs. Although we operate in the soliton regime, the presence of some walk-off leads to the small secondary lobe at around 175 fs = $\Delta\beta' L$. Correspondingly, we see that the carrier-free spectrum has more structure than for the fundamental wave, though the low-frequency side is observed to be smooth and to exhibit a fairly flat phase.

5.4 Results
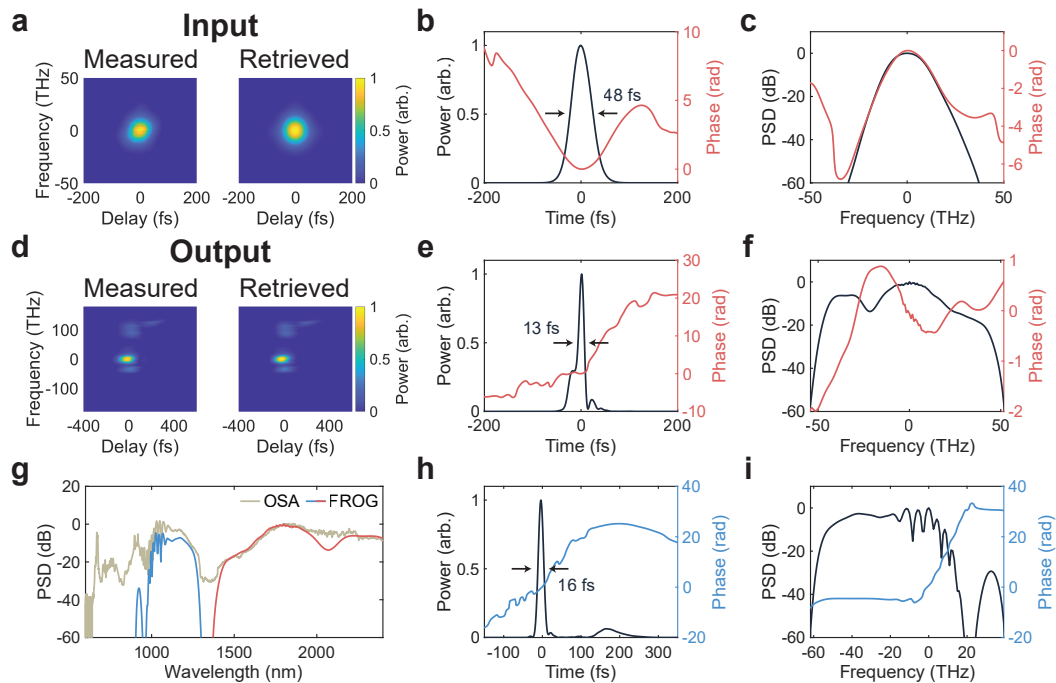
Figure 5.4: **Experimental quadratic soliton compression. a**, Measured and retrieved SHG FROG traces of fundamental input pulse. **b**, Input pulse temporal profile and **c**, spectrum. **d**, Measured and retrieved X-FROG traces of compressor output. **e**, Output temporal profile and **f**, spectrum for the fundamental. **g**, Reconstructed FROG spectrum overlaid with measured OSA spectrum. **h**, Output temporal profile and **i**, spectrum for the second harmonic. FROG, frequency-resolved optical gating; OSA, optical spectrum analyzer. FROG errors of 0.0032 and 0.0046 were measured for the SHG FROG and X-FROG, respectively.

To experimentally demonstrate the pulse compression, we fabricate the designed device and then temporally characterize the input and output pulses with a frequency-resolved optical gating (FROG) system (see Section 5.7). Figure 5.4a shows the measured and retrieved SHG FROG spectrograms for the input pulse. Qualitatively,

we see good agreement, corresponding to a reasonable FROG error of 0.0032. The reconstructed pulse and spectrum are shown in Figs. 5.4b-c. We observe a small amount of anomalous chirp due to propagation through various optical elements on the way to the chip setup, with the dominant contribution coming from a variable ND filter used for adjusting the input power.

The measured and retrieved cross-FROG (X-FROG) traces for the device output at a pump power of 3 pJ are shown in Fig. 5.4d. Again, good qualitative agreement is observed along with a reasonable FROG error of 0.0046. As further confirmation of the FROG performance, we compare the retrieved FROG spectrum with a secondary measurement on an optical spectrum analyzer (OSA). The result is shown in Fig. 5.4g, exhibiting good agreement across the entire spectrum. The largest discrepancy around 2090 nm is due to the presence of higher-order spatial modes, which are captured by the OSA but temporally gated by the X-FROG measurement due to their propagating at a different group velocity compared to the fundamental mode (see Section 5.7). The slight under-estimation of power on the short-wavelength side of the spectrum and cut-off around 950 nm is predominantly due to a combination of the phase-matching bandwidth of the nonlinear crystal used in the FROG and the frequency response of a short-pass filter used at the FROG output to block residual light from the strong gate beam which can otherwise saturate the spectrum (see Section 5.7). Finally, the discontinuity in the center of the FROG spectrum is due to the limited SNR of the FROG measurement.

The recovered fundamental pulse and spectrum are plotted in Figs. 5.4e and 5.4f, respectively. The pulse and spectrum exhibit qualitatively very similar behavior to the simulation, verifying the two-color soliton compression mechanism. The spectrum is broad and largely unstructured, besides a central dip, and the spectral phase exhibits only slow variation. The FWHM of the pulse is measured to be 13 fs, corresponding to less than two optical cycles for the fundamental carrier. Likewise, the recovered second-harmonic pulse and spectrum are plotted in Figs. 5.4h and 5.4i, respectively. Again, there is good agreement with the simulation. The pulse FWHM is also measured to be 16 fs. Furthermore, a small bump is observed in the vicinity of 175 fs as expected. Like the simulation, the spectrum is more structured than the fundamental but exhibits a flat phase and amplitude on the low-frequency side. While the measured pulses agree qualitatively well with the simulations, we finally note that discrepancies in the experimentally measured FWHM and simulation arise due to the impact of the chirp on the input pulse, higher

order dispersion in the waveguide, and limitations in our current measurement setup (see Section 5.7).

5.5 Towards Single-Cycle Synthesis

One unique feature of the two-color soliton compression is the opportunity it presents for facilitating on-chip single-cycle pulse synthesis. By manipulating the relative phase $\phi_\omega - \phi_{2\omega}$ of the two distinct harmonics, their combination can provide a variety of ultrashort waveforms. Interestingly, as the soliton solution occurs for a fixed phase relationship, $2\phi_\omega - \phi_{2\omega} = 0$ (see Section 5.7), the relative phase between the two co-propagating harmonics may be manipulated through control of the envelope phase of the input. Thus, with a carrier-envelope phase (CEP)-stabilized input and relatively few additional components on-chip, an integrated single-cycle synthesizer may be envisaged (Fig. 5.5a). In our proposal, a voltage supplied to an integrated electro-optic modulator is used to directly tune the CEP of the input pulse [48].
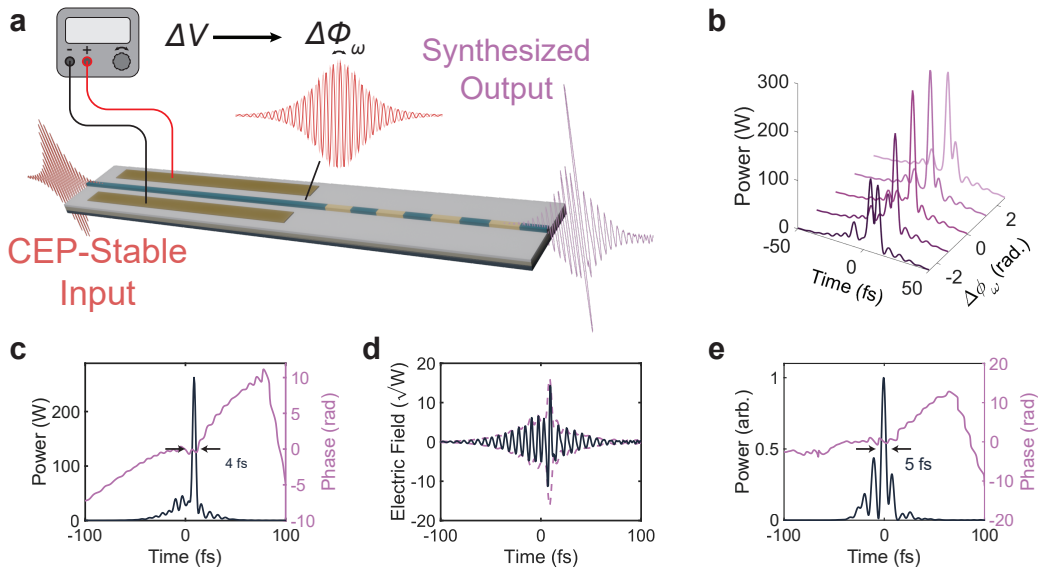
Figure 5.5: **Towards integrated single-cycle pulse synthesizers.** **a**, Proposed nanophotonic circuit architecture for single-cycle pulse synthesis. **b**, Simulated waveforms that may be achieved through manipulation of the input envelope phase, $\Delta\phi_\omega$. **c**, Simulated synthesized single-cycle waveform and **d**, corresponding electric field. **e**, Expected waveform from synthesis of experimentally measured pulses.

Figure 5.5b shows several examples of simulated synthesized pulse profiles as a function of the input pulse phase shift, $\Delta\phi_\omega$, for the parameters of Fig. 5.3. Figure 5.5c shows an example of a single-cycle pulse which may be realized through such a scheme, with a pulse FWHM of 4 fs and a combined carrier of 159 THz. The

single-cycle nature of the pulse is highlighted through the plot of the corresponding electric field (solid line) and electric field envelope (purple, dashed line) shown in Fig. 5.5d. Additionally, we consider the synthesized pulse that may be realized using the experimentally measured 13 fs and 16 fs pulses, as plotted in Fig. 5.5e. Through overlapping and manipulating the relative phases of the measured traces, we observe that an ultrashort pulse with a FWHM of 5 fs may already be realized.

Finally, we note that typical intensities required for entering the regime of extreme nonlinear optics [12] are on the order of 10^{12} W/cm^2. With mode areas of ~ 2 μm^2 in the waveguide for the synthesized pulse, this requires peak powers on the order of 10 kW, whereas our current proposal using pJ pump pulses exhibits peak powers on the order of 100 W. However, with the continued development of nanophotonic sources, achieving the required 100-pJ pulse energies on chip may soon be feasible.

5.6 Discussion

To summarize, we have demonstrated two-color soliton pulse compression in lithium niobate nanophotonics requiring only a few pJ of pump pulse energy. The experimentally measured fundamental pulse duration of 13 fs corresponds to less than two optical cycles of the carrier. Our results exhibit good agreement with theoretical models based on the analytic soliton solutions of the waveguide and numerical simulations of the coupled wave equations. We have further shown how the intrinsic phase relationship between the co-propagating fundamental and second-harmonic waves may be directly leveraged for single-cycle pulse synthesis. The compression mechanism may also be extended to longer pump pulses, making it compatible with integrated sources (see Section 5.7). Taken together, our results offer a holistic design framework for achieving two-color soliton compression in quadratic media and illuminate the great potentials of this technique for realizing a new generation of scalable single-cycle pulse generators, enabling many applications in ultrafast integrated photonics. For example, the resultant ultrashort pulses can be leveraged to realize extremely high bandwidth information processing systems [22]. Furthermore, as higher-energy integrated pulsed sources become available, the compressed pulses may be used to drive high-harmonic generation as a compact source for high-resolution imaging and lithography [14].

5.7 Supporting Information

Experimental Details

Experimental Setup

The experimental setup is shown in Fig. 5.6a. The input pulses at 2090 nm (red lines) which drive the compression are taken from the output of a free-space degenerate optical parametric oscillator based on periodically poled lithium niobate. It is pumped by a commercial mode-locked laser at 1045 nm (Menlo Orange, blue lines) which delivers 103-fs pulses at a repetition rate of 250 MHz. The OPO output consists of nearly transform-limited 35-fs, sech-shaped pulses centered at 2090 nm. It is then passed through a long-pass filter, beam expander, and variable ND wheel before being sent to the chip. This results in a small amount of anomalous pre-chirp on the pulses. To avoid additionally dispersing the pulses, they are coupled in and out of the thin-film lithium niobate (TFLN) chip using reflective objectives. A pair of magnetic mirrors placed before the chip may also be used to re-direct the 2 µm beam to our home-built frequency-resolved optical gating (FROG) system, described in the following.

The output of the TFLN device (purple lines) may be directed along one of two measurement paths. Along one path (dashed line), the output is coupled to a multimode fiber using a reflective collimator for direct spectrum measurements using an OSA. Along the second path, the output is guided using plano-metallic mirrors to our FROG. A magnetic mounted beamsplitter at the FROG input can be used to switch between SHG auto-FROG and SFG X-FROG geometries. The solid lines in the figure illustrate the X-FROG geometry. An off-axis parabolic mirror is used for collimation into the nonlinear crystal, which is a 50-µm-long β-barium borate (BBO) crystal cut for type I non-collinear phase matching of SFG between 1045 nm and 1300 nm. The crystal is mounted with rotational and translational degrees of freedom to optimize the SHG or SFG signal at the FROG output.

The FROG output is sent through a pinhole to filter the residual input beams and then passed through a collimating lens. Finally, a reflective collimator is used to couple the beam to a multi-mode fiber before detection on a spectrometer. The 1045-nm mode-locked laser and 2090-nm OPO output are measured using the auto-FROG geometry. The low-power chip output, however, is measured using an X-FROG, gated by a portion the 1045-nm MLL output. In this X-FROG configuration, we additionally use a short-pass filter (Thorlabs FESH0800), which has a pass band of 500-789 nm, to filter any scattered light at 1045 nm from the high-power gate beam.
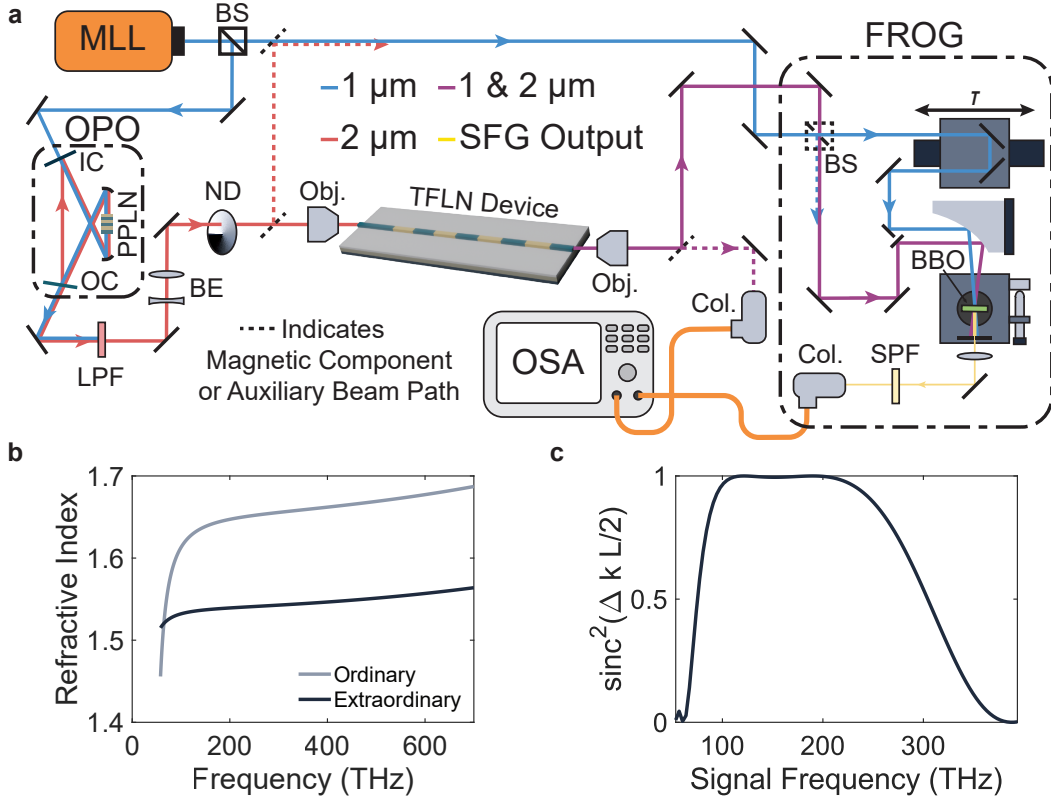
Figure 5.6: **Experimental setup for measuring two-color soliton pulse compression.** **a**, Setup for generation and measurement of compressed pulses. **b**, Refractive index of BBO crystal used in FROG setup. **c**, Phase-matching curve for sum-frequency generation between the 1045-nm gate pulse and the compressed signal pulse. MLL, mode-locked laser; BS, beam-splitter; OPO, optical parametric oscillator; IC, input coupler; OC, output coupler; PPLN, periodically poled lithium niobate; Obj., reflective objective; TFLN, thin-film lithium niobate; Col., reflective collimator; FROG, frequency-resolved optical gating; BBO, β-barium borate; LPF, long-pass filter; SPF, short-pass filter

This limits the bandwidth of our X-FROG measurement to wavelengths between 950 nm and 3220 nm coming from the chip, although this well-captures the most crucial spectral window for the two-color soliton pulse compression.

To verify the feasibility of using our FROG to measure the broadband pulses coming out of the chip, we simulate the phase-matching bandwidth of the BBO crystal. The refractive index of BBO, shown in Fig. 5.6a for both the ordinary and extraordinary rays, is found using the Sellmeier equation of ref. [49]. We then compute the phase-matching curve, assuming a fixed gate pulse at 1045 nm and a variable signal frequency. We consider a crystal angle of 23.74 degrees, optimized for phase-
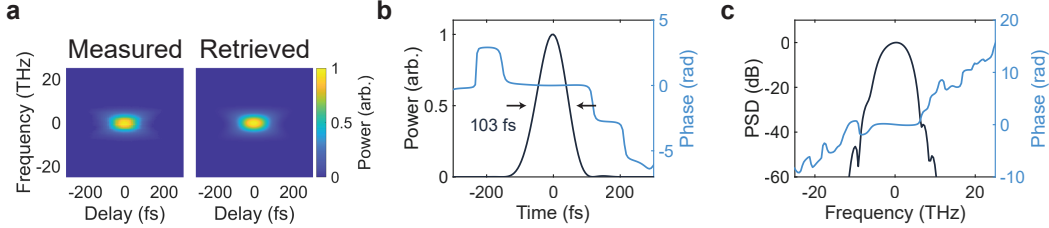
Figure 5.7: **Gate pulse characterization. a**, Measured (left) and retrieved (right) SHG FROG spectrograms for the gate pulse used in the measurement. **b**, Corresponding retrieved temporal profile and **c**, spectrum. FROG error = 0.0018.

matched SFG of 1045 nm and 1550 nm. In practice, this requires rotation of the crystal by -1.26 degrees with respect to normal based on the calculated cut angle of the crystal of 25 degrees. We further consider an input beam angle of 8.5 degrees for both beams, based on a 1.2" separation between the beams prior to the parabolic mirror and the 4" focal length of the mirror.

The resulting plot of $\mathrm{sinc}(\Delta k L/2)$, where $L = 50$ µm is the length of the crystal and Δk is the calculated phase mismatch, is shown in Fig. 5.6c. Here, we observe that the 3-dB bandwidth extends from about 75 THz to 305 THz, well-capturing both the fundamental and second harmonic frequencies at 143.5 THz and 287 THz, respectively. However, in combination with the short-pass filter response, we believe the observed decrease in phase matching at high frequencies to be responsible for the slight under-estimation of the second-harmonic power in our FROG reconstruction as compared to the measured spectrum on the OSA.

An SHG FROG characterization of 1045-nm gate pulses may be seen in Figure 5.7. Figure 5.7a shows the measured and retrieved FROG spectrograms. Good qualitative agreement is observed as well as a reasonable FROG error of 0.0018. The retrieved temporal profile and spectrum are shown in Figs. 5.7b and 5.7c, respectively.

FROG Processing

The output of an SFG X-FROG is an intensity spectrogram [50], which approximately takes the form:

$$I_{\mathrm{FROG}}(\omega, \tau) = \left| \int_{-\infty}^{\infty} E_S(t) E_G(t - \tau) e^{-i\omega t} dt \right|^2. \tag{5.4}$$

Here, $E_S(t)$ and $E_G(t)$ are the electric field amplitudes of the signal and gate pulses, respectively. In our FROG system (Fig. 5.6a), τ is imposed through a mechanical delay stage on the gate arm. Moving from an SFG X-FROG to an SHG auto-FROG merely requires setting $E_G(t)$ equal to $E_S(t)$.

For accurate measurement of broadband few- or single-cycle pulses, several additional considerations come into play. These can include the phase-matching bandwidth, the frequency response of the spectrometer, the frequency dependence of the nonlinear susceptibility, and the frequency dependence of the nonlinear coupling coefficient [50]. As discussed above, the phase-matching bandwidth is sufficiently broad to include the dominant fundamental and second harmonic components well within the 3 dB bandwidth, so we do not factor it into our post processing. We additionally do not consider the effects of the frequency dependence of the nonlinear susceptibility nor the spectrometer response, beyond the built-in amplitude correction of the Thorlabs CCS200 instrument used in the X-FROG measurement.

With these considerations in mind, our post-processing consists of the following. We first perform background subtraction by measuring an empty trace (where no signal is present on the spectrometer) and subtracting it from all other measured traces. After subtraction, we set all values less than 0 to be 0, as a measured value of less than 0 in the spectrogram would be unphysical. Next, we perform thresholding of any content that is more than 20 dB below the maximum measured intensity. After thresholding, we correct for the frequency dependence of the nonlinear coupling coefficient by rescaling the spectrogram by a factor of ω^2. Lastly, we normalize the spectrogram to contain only values between 0 and 1 and perform interpolation using the MATLAB interp1 function onto a Fourier grid for processing. For the X-FROG traces, a Fourier grid size of 1024 is used with a total time window length of 2500 fs. For the 2 µm input measurement, a grid size of 1024 is also used, while a grid size of 512 is used for reconstructing the 1 µm gate pulses.

Our FROG algorithm uses a slightly modified version of the open-source code provided by Wyatt and Byrnes [51, 52]. It employs the principal component generalized projections algorithm developed by Kane [53, 54]. The definition of the Fourier grid and overall performance of the algorithm has been tested against the suggestions made by DeLong, et al [55]. We run the algorithm for 1000 iterations, although convergence is typically observed within the first 100 iterations. Typical errors for our FROG retrievals are on the order of 10^{-3}, consistent with reported guidelines.

FROG Measurement Limitations

Our current experimental apparatus has several limitations which prohibit our successfully measuring shorter pulses than what is shown in Fig. 5.4, although current measurements and simulations suggest that shorter pulse widths should be observed at slightly higher pulse energies. The current limitations are experimentally demonstrated through the measurements presented in Fig. 5.8.
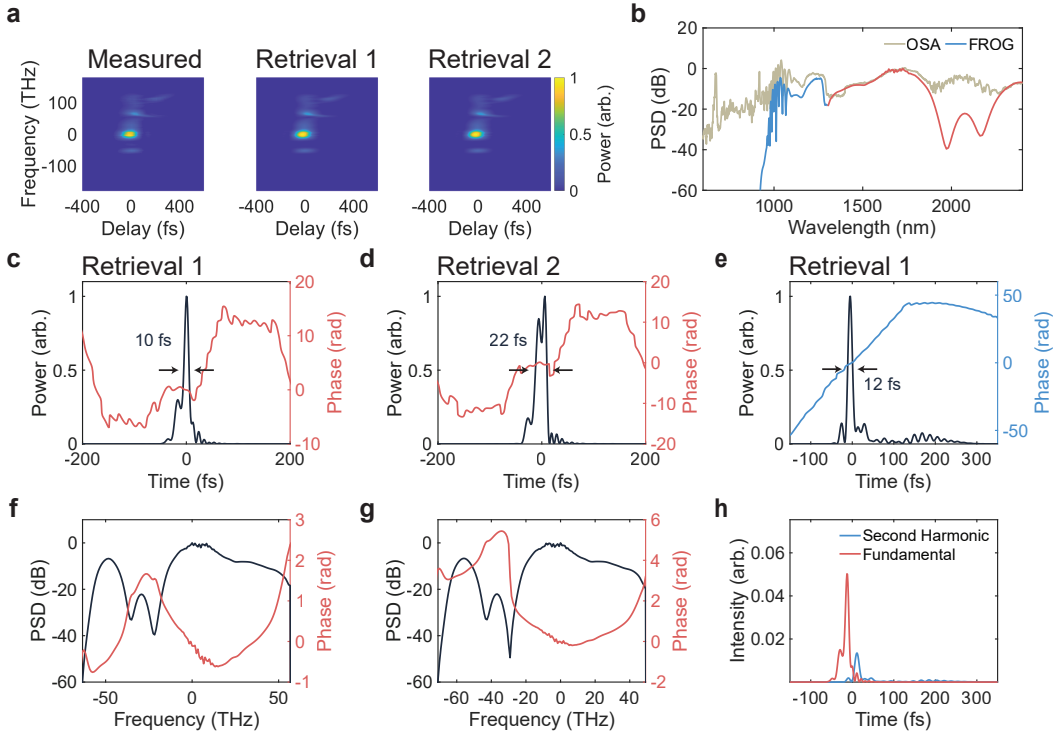
Figure 5.8: **Experimental FROG ambiguities. a**, Measured (left) SFG FROG spectrogram for an input energy of 5 pJ along with two example retrievals (right). **b**, Overlaid OSA and FROG spectra, showing good agreement. **c**, Fundamental pulse corresponding to retrieval 1. **d**, Fundamental pulse corresponding to retrieval 2. **e**, Second harmonic pulse corresponding to retrieval 1. **f**, Fundamental spectrum corresponding to retrieval 1 and **g**, retrieval 2. **h**, Overlay of directly retrieved fundamental and second harmonic temporal profiles. Both FROG retrievals show an error of 0.0045.

The measured and retrieved spectrograms for an input pulse energy of 5 pJ are shown in Fig. 5.8a. Both retrievals show good agreement with the measured spectrogram as well as a low error of 0.0045. Furthermore, good agreement is seen between the retrieved spectrum and measured spectrum on the OSA (Fig. 5.8b), besides the expected discrepancies due to the FROG bandwidth and presence of higher-order spatial modes. For retrieval 1, ultrashort pulses of duration 10 fs and 12 fs are

observed at both the fundamental and second harmonic, respectively, as shown in Figs. 5.8c and 5.8e. The spectral shape and short durations are both consistent with expectations based on simulation. However, despite exhibiting similar error, retrieval 2 recovers a different profile for the fundamental wave, depicted in Fig. 5.8d. Instead of a single, 10-fs pulse, we observe a double-humped pulse of total duration 22-fs. The second harmonic for retrieval 2 is not shown, as it is nearly identical to that of retrieval 1. As can be seen through the corresponding spectra in Figs. 5.8f and 5.8g, the predominant discrepancy between the two retrievals is attributable to the relative phase between the high-frequency and low-frequency components of the fundamental wave. When in phase, a single sharp feature is observed, whereas the double-humped pulse of retrieval 2 is a consequence of the two spectral bands being out of phase. A secondary issue is depicted in Fig. 5.8h. Although the fundamental and second harmonic waves are expected to co-propagate, retrievals consistently indicate an approximately 20-fs separation between the two harmonics. We believe this to be a consequence of dispersion in the measurement path, which can be resolved by limiting the number of mirror bounces and propagation distance between the chip output and FROG.

We believe the observed phase ambiguity in the fundamental traces at high powers to be predominantly a consequence of the f_{CEO} of the driving laser being unlocked and non-zero. Because of this, the relative phase of the fundamental and and second harmonic waveforms drifts from pulse to pulse, resulting in a non-repeating pulse train at the FROG. Such non-repeating pulse trains are known to cause ambiguities in FROG and have been the subject many experimental and numerical investigations [56, 57]. To illustrate the consequence of the unlocked f_{CEO} on our FROG retrieval, we numerically construct a spectrogram which approximates the simulated spectrogram. This is by averaging the spectrograms generated from five distinct simulated waveforms made by summing the simulated fundamental and second harmonic components with different relative phases. In our simulation, we assume an input energy of 3.7 pJ. As in the synthesis proposal of Fig. 5.5, the relative phase is varied by changing the input envelope phase, ϕ_ω. The simulated fundamental and second harmonic pulses are shown in Figs. 5.9a and 5.9b, respectively.

The combined spectral amplitudes and phases for the five simulated values of the input phase are shown in Figs. 5.9c and 5.9d. As may be expected, the spectral amplitudes and phases are similar everywhere except for in the overlap region around
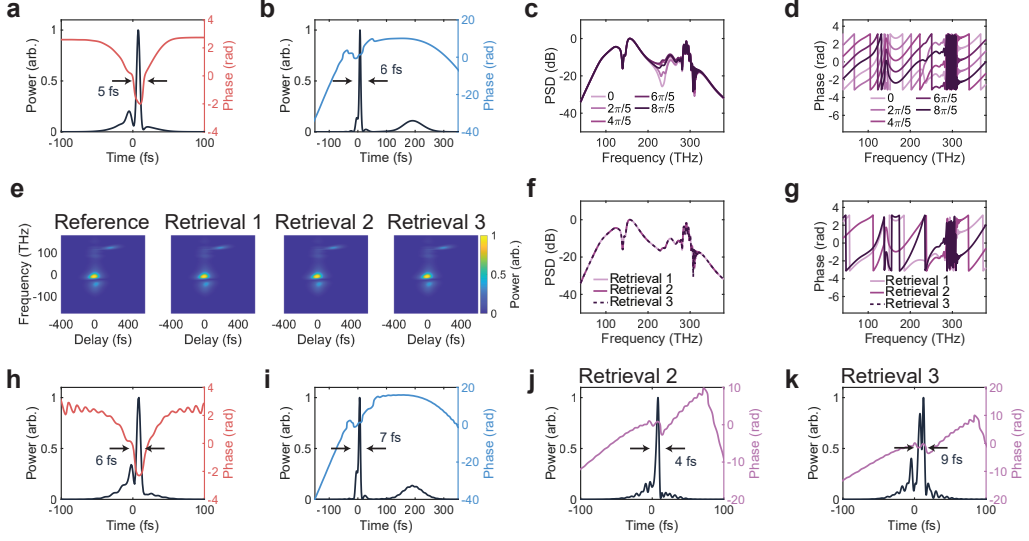
Figure 5.9: **Simulation of FROG ambiguity.** **a**, Simulated fundamental and **b**, second harmonic waveforms for 3.7 pJ of pump pulse energy. **c**, Combined spectral amplitudes for different fundamental envelope phases. **d**, Corresponding spectral phases. **e**, Numerically constructed ambiguous FROG trace along with three example retrievals. **f**, Retrieved spectral amplitudes and **g**, phases. **h**, Retrieved fundamental and **i**, second harmonic pulses. **j**, Combined pulses for retrieval 2 and **k**, retrieval 3. FROG retrievals 1, 2, and 3 show errors of 0.00037, 0.00046, and 0.00067, respectively.

230 THz. Here, interference results in significant spectral amplitude variation, and the spectral phases are observed to change at different rates. The average spectrogram constructed from these different waveforms is shown in Fig. 5.9e along with three different example retrieved spectrograms. The retrieval algorithm is run for 1000 iterations, resulting in similar errors for the retrieved spectrograms of 0.00037, 0.00046, and 0.00067 for retrievals 1, 2, and 3, respectively. As shown in Figs. 5.9f and 5.9g, all three retrievals result in similar spectral amplitudes; however, significant spectral phase variation in the vicinity of 230 THz is observed across retrievals.

The consequences of this are illustrated in Figs. 5.9h-k. In all cases, the fundamental and second harmonic temporal profiles are pretty faithfully reconstructed; examples corresponding to retrieval 1 are shown in Figs. 5.9h and 5.9i. However, vastly different combined temporal profiles may be observed, corresponding to the different relative phases between the fundamental and second harmonic components, as demonstrated by the examples of Figs. 5.9j and 5.9k. This ambiguity mirrors that of the experimentally measured fundamental pulses; however, it is not entirely clear

why the ambiguity occurs experimentally in the middle of the fundamental pulse rather than between the two harmonics. We believe, however, that it is due to there being low SNR in this region due to the significant dip in spectral amplitude. This results in the optimal retrieval misattributing the phase ambiguity to this spectral region, as such a phase ambiguity typically exists between spectrally separated components in a FROG measurement [58].

Device Design and Characterization

We design our device according to the design principles laid in the theory section of the manuscript and also in the theoretical analysis to follow, and we refer the reader to those sections for definitions of the parameters. We wish to operate in the $\alpha \approx 1$ regime with small Δk, such that similar soliton pulse widths and amplitudes may be observed at both the fundamental and second harmonics. This requires a low group velocity mismatch between the two harmonics to ensure small δ. In addition, we wish for the GVD at 2 µm to be sufficiently small so that the characteristic timescale of the system is on the order femtoseconds at moderate input pulse energies in the pJ range. This demonstrates the feasibility of performing soliton compression towards the single-cycle regime using available integrated pulsed laser sources [46].

The key parameters contributing to the dispersion of our device are shown in Fig. 5.10a. They include the thin-film thickness, h, etch depth, d, and waveguide top width, w. Our fabrication process additionally results in a sidewall angle, θ, of 60°, which must also be accounted for. Using Lumerical, we may sweep these three main parameters to find a geometry that satisfies our design requirements. The fabricated device geometry has $h = 709$ nm, $d = 330$ nm, and $w = 2938$ nm. With these parameters, the waveguide supports 3 transverse electric (TE) modes at the fundamental wavelength of 2090 nm, the electric field intensities of which are shown in Figs. 5.10a, 5.10b, and 5.10c. The fundamental mode at the second-harmonic wavelength of 1045 nm is shown in Fig. 5.10d.

We also use Lumerical to calculate the effective index, n_{eff}, group index, n_g, and GVD, β_2, of the fundamental mode as a function of wavelength. The results are shown in Fig. 5.10e. From this, we find the GVD at 2090 nm to be 9 fs^2/mm, and at 1045 nm to be 141 fs^2/mm. The GVM between the two is calculated to be 27 fs/mm. Spikes in the dispersion around 1350 nm, 930 nm, and 690 nm are the result of mode crossings near these wavelengths. However, all occur sufficiently far away from the fundamental and second harmonic carriers as to not significantly impede
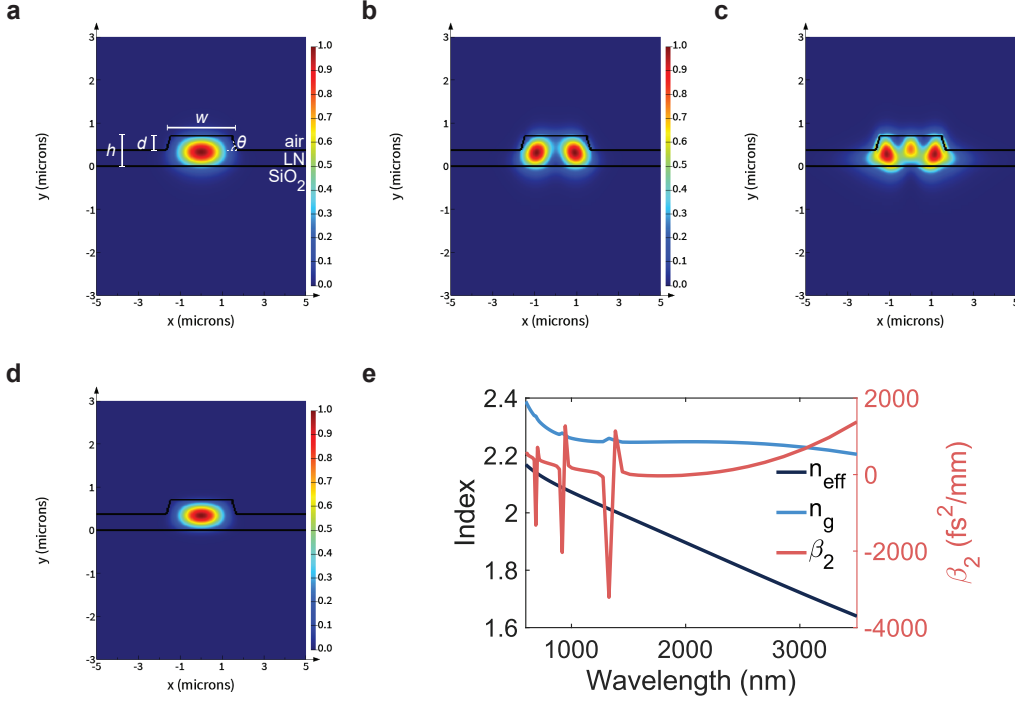
Figure 5.10: **Waveguide design. a**, TE0 mode at 2090 nm, with key design parameters indicated. **b**, TE1 mode at 2090 nm. **c**, TE2 mode at 2090 nm. **d**, TE0 mode at 1045 nm **e**, Dispersion parameters for TE0 mode.

the broadening. Additionally, the poling period required for phase-matched SHG is calculated to be 5.69 µm from the effective indices of the fundamental and second harmonic, 1.88034 and 2.06409, respectively. The measured phase-mismatched device is designed to have a poling length of 6.5 mm with a period of 5.73 µm.

As mentioned in the 5.4, some of our input power is coupled into the higher order modes at 2090 nm, resulting in there being content at 2090 nm in the OSA measurement that is not observed in the FROG retrieval. This is because the higher-order modes are temporally gated out in the X-FROG geometry. To illustrate this, we calculate the expected temporal separation between the TE0 and TE1 modes at the chip output. From the group indices of the two modes, we calculate a group velocity mismatch of 258 fs/mm. This results in there being a temporal separation of about 2 ps over the 8-mm-long device. This is well-separated from the X-FROG trace, which spans about 1 ps of time delay, centered about the TE0 mode. As the higher-order modes are not phase-matched for efficient nonlinear conversion, their spectra do not change significantly from that of the input, accounting for the additional spectral content around 2090 nm in the OSA trace.

We fabricate the device following the procedure described in ref. [38]. It is fabricated on X-cut MgO-doped thin-film lithium niobate on a SiO$_2$/Si substrate (NANOLN). To achieve the periodic poling, we pattern Cr poling electrodes using lift-off. By applying a voltage across the electrodes, we periodically flip the ferro-electric domains. Following poling, we etch the waveguides using Ar-milling with hydrogen silsesquioxane (HSQ) as the etch mask. Finally, we mechanically polish the waveguide facets to enable end-fire coupling into the devices.

After fabrication, we characterize the throughput of our device and from them estimate the coupling losses. From free-space to free-space, we observe a 22 dB loss at 2090 nm through the chip. Based on the index contrast at the output, we expect a 10% reflection at the output facet of the chip. Furthermore, based on the numerical aperture (NA) of our output objective (Thorlabs LMM40X-P01), which is 0.5, we use Lumerical to estimate the power coupling between the fundamental TE mode and a Gaussian beam which fills the objective and is focused to the waveguide output facet. A more accurate calculation may be achieved by using a slightly elliptical free-space mode, but we believe the symmetric Gaussian mode to be a fair choice given that the $1/e^2$ width of the fundamental TE mode is close to the diffraction-limited beam waist, which we calculate as 1.33 µm. With these assumptions, the power coupling is 0.43. Finally, we must include the obscuration factor, which is reported to be 24% for the objective. Approximating the chip output as an ideal spherical wavefront, this obscuration factor can be directly taken as the loss. Based on these values, our output coupling is calculated to be 5.3 dB, which is similar to the output coupling that has previously been measured from our devices using other techniques. In our analysis, we round this value up to 6 dB, accounting for other non-idealities in our system such as scattering loss due to imperfect polishing, and use 16 dB as the input coupling calibration factor between off-chip and on-chip powers.

Theoretical Analysis

Soliton Solutions to Coupled Wave Equations

We begin our analysis with the coupled wave equations [37, 59], written as:

$$\frac{\partial A_\omega}{\partial z} = i\kappa A_{2\omega} A_\omega^* e^{-i\Delta k z} - \frac{i\beta_\omega^{(2)}}{2}\frac{\partial^2 A_\omega}{\partial t^2}, \tag{5.5a}$$

$$\frac{\partial A_{2\omega}}{\partial z} = i\kappa A_\omega^2 e^{i\Delta k z} - \Delta\beta'\frac{\partial A_{2\omega}}{\partial t} - \frac{i\beta_{2\omega}^{(2)}}{2}\frac{\partial^2 A_{2\omega}}{\partial t^2}, \tag{5.5b}$$

where $A_\omega(z, t)$ and $A_{2\omega}(z, t)$ represent the amplitudes of the fundamental and second harmonic waves at frequencies ω and 2ω, respectively, normalized such that the instantaneous power in each wave is given by $|A_j|^2$, $j\epsilon\{\omega, 2\omega\}$. The time coordinate is defined such that the reference frame is co-moving at the group velocity of the fundamental wave. The phase mismatch parameter is $\Delta k = \frac{2\pi}{\Lambda} + 2k_\omega - k_{2\omega}$, where Λ is the poling period. $\kappa = \frac{\sqrt{2\eta_0}\omega d_{\text{eff}}}{n_\omega \sqrt{A_{\text{eff}} n_{2\omega}} c}$ is the nonlinear coupling coefficient, where d_{eff} is the effective nonlinearity, n_j is the refractive index of wave j, A_{eff} is the effective mode area, c is the speed of light, and η_0 is the impedance of free space. The group velocity mismatch is given by $\Delta\beta' = \frac{1}{v_{g,2\omega}} - \frac{1}{v_{g,\omega}}$, where $v_{g,j}$ is the group velocity of wave j. Finally, $\beta_j^{(2)}$ is the group velocity dispersion of the jth wave. For the purposes of this analysis, we neglect higher dispersion orders.

We next introduce the normalized waves $a_\omega = -\frac{\sqrt{2}\kappa}{\beta}\sqrt{\left|\frac{\beta_\omega^{(2)}}{\beta_{2\omega}^{(2)}}\right|}A_\omega e^{-i\beta z}$ and $a_{2\omega} = \frac{\kappa}{\beta}A_{2\omega}e^{-i(2\beta+\Delta k)z}$, where β accounts for shifts in the phase velocity induced by the nonlinear interaction [60]. Additionally, we define a new spatial coordinate $\zeta = |\beta|z$ and a new temporal coordinate $\xi = \sqrt{\left|\frac{2\beta}{\beta_\omega^{(2)}}\right|}t$. Note that we have implicitly required that β be real. Although our analysis focuses on these bright soliton solutions, we note that a wide variety soliton solutions exists in other parameter regimes, so compression in those regimes may be also possible. Making these substitutions yields the following system of equations:

$$-is_1\frac{\partial a_\omega}{\partial \zeta} = s_2\frac{\partial^2 a_\omega}{\partial \xi^2} - a_\omega + a_{2\omega}a_\omega^*, \tag{5.6a}$$

$$-is_1\frac{\partial a_{2\omega}}{\partial \zeta} = s_3\left|\frac{\beta_{2\omega}^{(2)}}{\beta_\omega^{(2)}}\right|\frac{\partial^2 a_{2\omega}}{\partial \xi^2} + is_3\Delta\beta'\sqrt{-\frac{2}{\beta_\omega^{(2)}\beta}}\frac{\partial a_{2\omega}}{\partial \xi} - (2 + \frac{\Delta k}{\beta})a_{2\omega} + \left|\frac{\beta_{2\omega}^{(2)}}{\beta_\omega^{(2)}}\right|\frac{a_\omega^2}{2}. \tag{5.6b}$$

Here, $s_1 = \text{sgn}(\beta)$, $s_2 = -\text{sgn}(\frac{\beta_\omega^{(2)}}{\beta})$, and $s_3 = -\text{sgn}(\frac{\beta_{2\omega}^{(2)}}{\beta})$. In what follows, we take $s_2 = s_3 = 1$, requiring that $\beta_\omega^{(2)}$ and $\beta_{2\omega}^{(2)}$ share the same sign, opposite that of β, as this is known to yield bright soliton solutions [61]. Finally, defining $\sigma = \left|\frac{\beta_\omega^{(2)}}{\beta_{2\omega}^{(2)}}\right|$, $\delta = s_1\Delta\beta'\sqrt{\left|\frac{2\beta_\omega^{(2)}}{\beta_{2\omega}^{(2)}\beta}\right|}$, and $\alpha = \sigma(2 + \frac{\Delta k}{\beta})$, we arrive at the normalized coupled wave equations:

$$-is_1\frac{\partial a_\omega}{\partial \zeta} = \frac{\partial^2 a_\omega}{\partial \xi^2} - a_\omega + a_{2\omega}a_\omega^*, \tag{5.7a}$$

$$-is_1\sigma\frac{\partial a_{2\omega}}{\partial\zeta} = \frac{\partial^2 a_{2\omega}}{\partial\xi^2} + i\delta\frac{\partial a_{2\omega}}{\partial\xi} - \alpha a_{2\omega} + \frac{a_\omega^2}{2}. \tag{5.7b}$$

Let us first study the soliton solutions with $\delta = 0$, assuming no walk-off between the fundamental and second-harmonic waves. Setting the spatial derivatives on the left-hand side of equations 5.7a and 5.7b to 0, we have:

$$0 = \frac{\partial^2 a_\omega}{\partial\xi^2} - a_\omega + a_{2\omega}a_\omega^*, \tag{5.8a}$$

$$0 = \frac{\partial^2 a_{2\omega}}{\partial\xi^2} - \alpha a_{2\omega} + \frac{a_\omega^2}{2}. \tag{5.8b}$$

To begin, we find the continuous-wave solutions, $a_{j,CW}$, $j\epsilon\{\omega, 2\omega\}$, by setting the time derivatives to 0. Assuming real solutions, which requires $\alpha > 0$, we find the following non-zero solutions:

$$a_{2\omega,CW} = 1, \tag{5.9a}$$

$$a_{\omega,CW} = \pm\sqrt{2\alpha}. \tag{5.9b}$$

The existence of two CW solutions with opposite phases at the fundamental wave is a well-known feature of degenerate quadratic nonlinear systems. For the analysis that follows, we will take the positive solution; however, the analysis would follow equivalently from the negative solution. Secondarily, we see that the two waves have an amplitude ratio which is given by $\sqrt{2\alpha}$, the normalized phase mismatch parameter. Next, we seek particular solutions of the form:

$$a_\omega(\xi) = a_{\omega,CW}\tilde{a}_\omega(\xi) = \sqrt{2\alpha}\tilde{a}_\omega(\xi), \tag{5.10a}$$

$$a_{2\omega}(\xi) = a_{2\omega,CW}\tilde{a}_{2\omega}(\xi) = \tilde{a}_{2\omega}(\xi). \tag{5.10b}$$

To proceed, we assume a large phase mismatch, $\alpha \gg 1$, and perform an asymptotic expansion of $\tilde{a}_{2\omega}(\xi)$ and $\tilde{a}_\omega(\xi)$ in orders of the small parameter $\frac{1}{\alpha}$:

$$\tilde{a}_j(\xi) = \tilde{a}_{j,0}(\xi) + \frac{1}{\alpha}\tilde{a}_{j,2}(\xi) + \frac{1}{\alpha^2}\tilde{a}_{j,3}(\xi) + \dots \tag{5.11}$$

Using this expansion in conjunction with equations 5.10a and 5.10b and plugging into equations 5.8a and 5.8b gives the following system of equations for terms of order $(\frac{1}{\alpha})^0$:

$$0 = \frac{\partial^2 \tilde{a}_{\omega,0}}{\partial \xi^2} - \tilde{a}_{\omega,0} + \tilde{a}_{2\omega,0}\tilde{a}_{\omega,0}^*, \tag{5.12a}$$

$$0 = -\tilde{a}_{2\omega,0} + \tilde{a}_{\omega,0}^2. \tag{5.12b}$$

Plugging equation 5.12b into 5.12a gives a second-order differential equation for $\tilde{a}_{\omega,0}$:

$$0 = \frac{\partial^2 \tilde{a}_{\omega,0}}{\partial \xi^2} - \tilde{a}_{\omega,0} + \tilde{a}_{\omega,0}\left|\tilde{a}_{\omega,0}\right|^2, \tag{5.13}$$

which closely resembles the nonlinear Schrödinger equation governing cubic non-linear optical systems [44]. Solving for $\tilde{a}_{\omega,0}$ assuming $\tilde{a}_{\omega,0}$ real gives the bright soliton solution:

$$\tilde{a}_{\omega,0}(\xi) = \sqrt{2}\,\text{sech}(\xi), \tag{5.14a}$$

$$\tilde{a}_{2\omega,0}(\xi) = 2\,\text{sech}^2(\xi). \tag{5.14b}$$

From this, we see that the temporal duration of the soliton solution is given by the characteristic timescale of the system, $\left|\frac{2\beta}{\beta_\omega^{(2)}}\right|$. This first-order solution of the asymptotic expansion is what has been predominantly studied in works on quadratic soliton pulse compression, due to its similarity to the fundamental Kerr soliton. Next, we may repeat the procedure to find solutions for higher orders of $\frac{1}{\alpha}$. For brevity, we directly write here the solutions for $(\frac{1}{\alpha})^1$ and $(\frac{1}{\alpha})^2$. For $(\frac{1}{\alpha})^1$, we have:

$$\tilde{a}_{\omega,1}(\xi) = 2\sqrt{2}\,\text{sech}(\xi)\,\text{tanh}^2(\xi), \tag{5.15a}$$

$$\tilde{a}_{2\omega,1}(\xi) = 4\,\text{sech}^2(\xi)[4 - 5\,\text{sech}^2(\xi)], \tag{5.15b}$$

while for $(\frac{1}{\alpha})^2$, we see:

$$\tilde{a}_{\omega,2}(\xi) = \frac{2\sqrt{2}}{3}\,\text{sech}(\xi)[28\,\text{sech}^4(\xi) + 32\,\text{sech}^2(\xi) - 97], \tag{5.16a}$$

$$\tilde{a}_{2\omega,2}(\xi) = \frac{8\sqrt{2}}{3}\,\text{sech}^2(\xi)[181\,\text{sech}^4(\xi) - 106\,\text{sech}^2(\xi) - 76]. \tag{5.16b}$$

Together, then, the asymptotic expansion in $\frac{1}{\alpha}$ for the soliton solutions of the coupled wave equations is given by:

$$a_\omega(\xi) = 2\sqrt{\alpha}\,\text{sech}(\xi)\Bigg(1 + \frac{2}{\alpha}\tanh^2(\xi)$$

$$+ \frac{2}{3\alpha^2}[28\,\text{sech}^4(\xi) + 32\,\text{sech}^2(\xi) - 97] + O(\frac{1}{\alpha^3})\Bigg), \quad (5.17a)$$

$$a_{2\omega}(\xi) = 2\,\text{sech}^2(\xi)\Bigg(1 + \frac{2}{\alpha}[4 - 5\,\text{sech}^2(\xi)]$$

$$+ \frac{4\sqrt{2}}{3\alpha^2}[181\,\text{sech}^4(\xi) - 106\,\text{sech}^2(\xi) - 76] + O(\frac{1}{\alpha^3})\Bigg). \quad (5.17b)$$

While this asymptotic solution works well to first order for cases when $\alpha \gg 1$ and can be made more exact for cases with $\alpha \approx 1$ by including higher-order terms, it would be preferable to have a more succinct expression for the soliton solution for arbitrary α. Such a solution may be obtained by making the observation that the soliton solutions in both the pump and signal take the form of powers of sech functions, and that they share the same approximate pulse width. Thus, we make make the following ansatz [43]:

$$a_\omega(\xi) = a_{\omega,0}\,\text{sech}^p(\frac{\xi}{\tau}), \quad (5.18a)$$

$$a_{2\omega}(\xi) = a_{2\omega,0}\,\text{sech}^q(\frac{\xi}{\tau}), \quad (5.18b)$$

where $a_{\omega,0}$ and $a_{2\omega,0}$ are the pulse amplitudes, assumed to be real, and τ will define the pulse width scaling. Plugging into the system of equations 5.8a and 5.8b gives:

$$\frac{a_{\omega,0}}{\tau^2}[p^2\,\text{sech}^p(\frac{\xi}{\tau}) - (p^2 + p)\,\text{sech}^{(p+2)}(\frac{\xi}{\tau})]$$

$$- a_{\omega,0}\,\text{sech}^p(\frac{\xi}{\tau}) + a_{\omega,0}a_{2\omega,0}\,\text{sech}^{p+q}(\frac{\xi}{\tau}) = 0 \quad (5.19a)$$

$$\frac{a_{2\omega,0}}{\tau^2}[q^2\,\text{sech}^q(\frac{\xi}{\tau}) - (q^2 + q)\,\text{sech}^{(q+2)}(\frac{\xi}{\tau})]$$

$$- \alpha a_{2\omega,0}\,\text{sech}^q(\frac{\xi}{\tau}) + \frac{a_{\omega,0}^2}{2}\,\text{sech}^{2p}(\frac{\xi}{\tau}) = 0. \quad (5.19b)$$

From here, we may note that the first equation can be solved exactly when q = 2, requiring that $\tau = p$ and the second-harmonic pulse amplitude be given by:

$$a_{2\omega,0} = 1 + \frac{1}{p}.$$ (5.20)

With these constraints, one may find an exact solution [45] using equation 5.19b when p = 2, corresponding to $\alpha = 1$. In this case, the solution is given by:

$$a_\omega(\xi) = \frac{3}{\sqrt{2}} \operatorname{sech}^2(\frac{\xi}{2}),$$ (5.21a)

$$a_{2\omega}(\xi) = \frac{3}{2} \operatorname{sech}^2(\frac{\xi}{2}).$$ (5.21b)

However, an approximate analytical solution which gives exactly the behavior around the pulse peak and tails may be derived by making a few observations. The first is that, at the pulse peak ($\xi = 0$), all of the sech terms go to 1. Thus, satisfaction of equation 5.19b at $\xi = 0$ requires that:

$$a_{\omega,0}^2 = 2a_{2\omega,0}(\frac{2}{p^2} + \alpha).$$ (5.22)

Here, we note also that equation 5.19b is already satisfied at the tails of the pulses, as all of the sech terms approach 0 as $\xi \to \pm\infty$. The second observation that can be made is that the normalized equations 5.8a and 5.8b exactly describe a particle in a potential U, where U is given by:

$$U = \frac{a_\omega^2 a_{2\omega}}{2} - \frac{1}{2}a_\omega^2 - \frac{1}{2}\alpha a_{2\omega}^2.$$ (5.23)

The Hamiltonian for the system is:

$$H = \frac{1}{2}\left(\frac{\partial a_\omega}{\partial \xi}\right)^2 + \frac{1}{2}\left(\frac{\partial a_{2\omega}}{\partial \xi}\right)^2 + U.$$ (5.24)

For such a conservative system, we expect the Hamiltonian to remain constant for all values of ξ. By noting that at the wings, where $\xi \to \pm\infty$, $H \to 0$, we see that this requires $H = 0$ for all values of ξ. As such, correct behavior at the pulse peak, where $\frac{\partial a_\omega}{\partial \xi} = \frac{\partial a_{2\omega}}{\partial \xi} = 0$, requires $H|_{\xi=0} = U|_{\xi=0} = 0$. This leads to a second equation:

$$a_{\omega,0}^2 a_{2\omega,0} - a_{\omega,0}^2 - \alpha a_{2\omega,0}^2 = 0. \tag{5.25}$$

We may combine the above arguments along with equations 5.20, 5.22, and 5.25 to arrive at the following set of soliton solutions, originally proposed by Sukhorukov [43]:

$$a_\omega(\xi) = a_{\omega,0} \operatorname{sech}^p\left(\frac{\xi}{p}\right), \tag{5.26a}$$

$$a_{2\omega}(\xi) = a_{2\omega,0} \operatorname{sech}^2\left(\frac{\xi}{p}\right), \tag{5.26b}$$

where the scaling behaviors for the parameters $a_{2\omega,0}$, $a_{\omega,0}$, and p are given as:

$$p = \frac{1}{a_{2\omega,0} - 1}, \tag{5.27a}$$

$$a_{\omega,0}^2 = \frac{\alpha a_{2\omega,0}^2}{a_{2\omega,0} - 1}, \tag{5.27b}$$

$$\alpha = \frac{4(a_{2\omega,0} - 1)^3}{2 - a_{2\omega,0}}. \tag{5.27c}$$

Numerical Soliton Solutions

We may numerically find the soliton solutions using Newton's Method with the solutions given by equations 5.26 and 5.27 as a seed. To do so, we encode the two equations for which we wish to find the zeros, 5.8a and 5.8b, where we numerically compute derivatives in ξ in the Fourier domain using the Fast Fourier Transform. For a Fourier grid of size N, the state vector a_{curr} is size 2N, consisting of the value of a_ω at each of the N points in ξ along with the value of $a_{2\omega}$ at all N points. Newton's Method requires iteratively computing the 2N-by-2N Jacobian J, composed by taking partial derivatives of the equations 5.8a and 5.8b with respect to the 2N points in the current state vector, and inverting it to compute $a_{\text{next}} = a_{\text{curr}} - J^{-1} f(a_{\text{curr}})$. Here, $f(a_{\text{curr}})$ is a vector of size 2N consisting of the solutions of equations 5.8a and 5.8b for the 2N values of the state vector a_{curr}.

The numerically computed soliton solutions for different values of α along with scaling behaviors of the soliton pulse amplitude and full width at half maximum
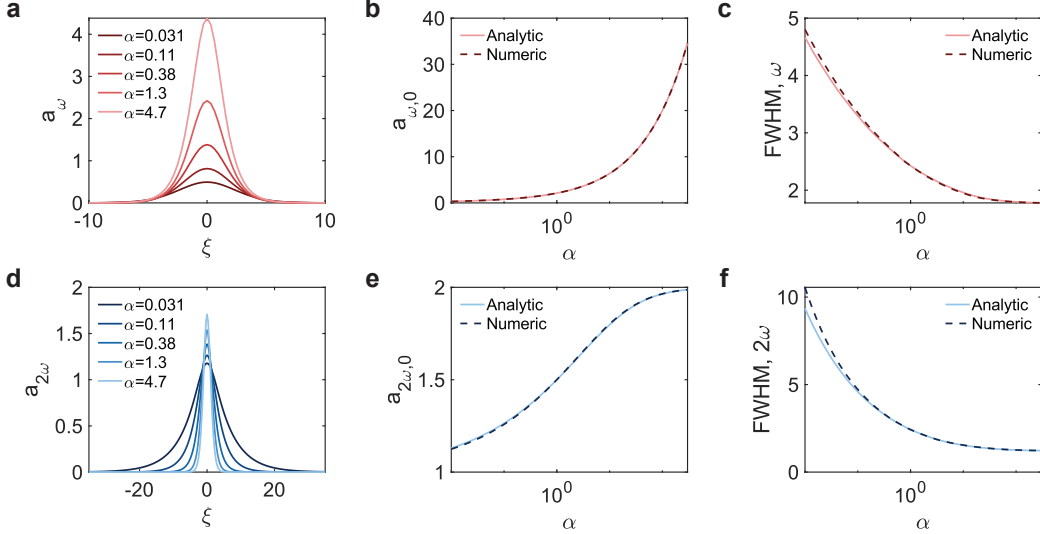
Figure 5.11: **Soliton solutions with $\delta = 0$. a**, Fundamental soliton solutions. **b**, Amplitude of fundamental soliton. **c**, FWHM of fundamental soliton. **d-f**, Corresponding plots for second harmonic soliton. FWHM, full width at half maximum.

(FWHM) are shown in Figure 5.11. The pulse profiles are shown in Figs. 5.11a and 5.11d for the fundamental and second harmonic, respectively. As noted in Section 5.2, we see that at large values of α, the fundamental amplitude greatly exceeds that of the second harmonic and vice versa for small values of α. This behavior is shown more clearly in Figs. 5.11b and 5.11e, where the pulse amplitudes are plotted as a function of α. The numerically computed solutions are shown by dark dashed lines, and exhibit near-perfect agreement with the light, solid lines showing the analytic solutions of 5.26 and 5.27. Similarly, we plot the analytic and numerically computed soliton FWHM for both waves in Figs. 5.11c and 5.11f. Again, good agreement between the numeric and analytic solutions is observed, particularly for large α. Here, we see that the FWHM is relatively stable for $\alpha > 1$ as the asymptotic solution of equations 5.17a and 5.17b is approached but quickly grows for $\alpha < 1$.

After solving for the system of equations 5.8a and 5.8b, we may additionally use numerical continuation to find solutions to the modified system where $\delta \neq 0$, given by setting the right-hand side of equations 5.7a and 5.7b equal to 0:

$$0 = \frac{\partial^2 a_\omega}{\partial \xi^2} - a_\omega + a_{2\omega} a_\omega^*, \tag{5.28a}$$

$$0 = \frac{\partial^2 a_{2\omega}}{\partial \xi^2} + i\delta \frac{\partial a_{2\omega}}{\partial \xi} - \alpha a_{2\omega} + \frac{a_\omega^2}{2}. \tag{5.28b}$$

Here, we begin with the solutions found using Newton's Method at $\delta = 0$ and find the solution for increasing values of δ, using the solution for the previous value of δ as a seed. An example of how the soliton solution changes for varying δ with fixed $\alpha = 1.64$ is given in Fig. 5.12. The real parts of the soliton solutions at the fundamental and second harmonic are shown in Figs. 5.12a and 5.12c, with corresponding imaginary parts shown in Figs. 5.12b and 5.12d. As may be observed, increasing δ results in a growing imaginary component of the soliton. In addition, the real component is observed to skew; here, we've shown positive values of δ for which the skew shifts the center of mass in the direction of the positive time coordinate. However, we observe also that for sufficiently small values of δ, the soliton is still extremely well-approximated by the $\delta = 0$ solution.
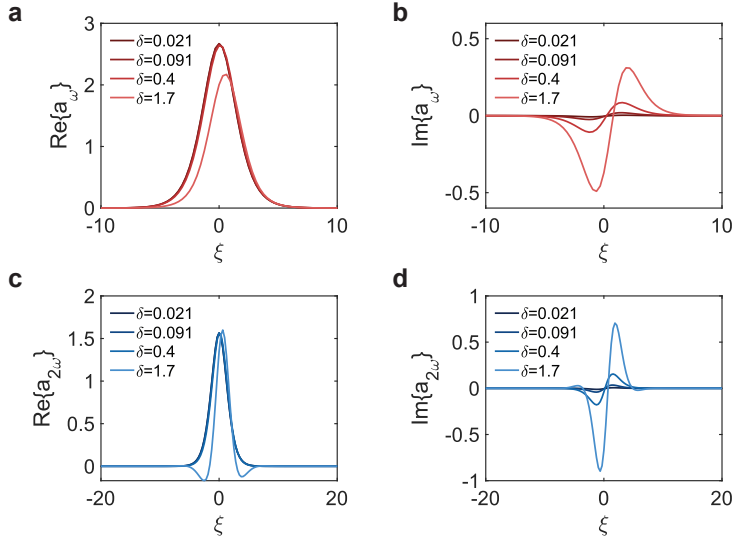
Figure 5.12: **Soliton solutions with $\delta \neq 0$. a**, Real and **b**, imaginary parts of fundamental soliton solutions. **c**, Corresponding real and **d**, imaginary parts of second harmonic solitons.

At large values of δ, we note that our continuation algorithm no longer converges to a soliton solution but either blows up to infinity or converges to the trivial solution, $a_\omega = a_{2\omega} = 0$. To better understand where this transition occurs between the existence and non-existence of a stable soliton solution, we again consider the equations 5.28a and 5.28b. A solution for $a_{2\omega}$ in terms of a_ω may be found through direct integration of equation 5.28b. Doing so yields the solution:

$$a_{2\omega}(\xi) = \int_{-\infty}^{\infty} \frac{a_\omega^2(\xi - \xi')}{4\sqrt{\alpha - \delta^2/4}} e^{-i\frac{\delta}{2}} R_\pm(\xi')d\xi', \tag{5.29}$$

where $R_+(\xi') = e^{-\sqrt{\alpha-\delta^2/4}|\xi'|}$ is used if $\alpha-\delta^2/4 \geq 0$ and $R_-(\xi') = \sin\left(\sqrt{\alpha-\delta^2/4}|\xi'|\right)$ is used if $\alpha - \delta^2/4 < 0$. Thus, we see that a non-oscillatory soliton solution is expected only if $\alpha \geq \delta^2/4$, which has previously been referred to as the stationary regime of pulse compression [34]. To confirm that this analysis is consistent with what we observe numerically, we plot (Fig. 5.13a) the soliton existence (dark blue) and non-existence regimes (light blue), as determined by the convergence of our Newton's Method to a non-zero stationary solution, as a function of α and δ. The analytically computed boundary, $\alpha = \delta^2/4$ is shown by the solid, black line, in good agreement with our numerical solver.
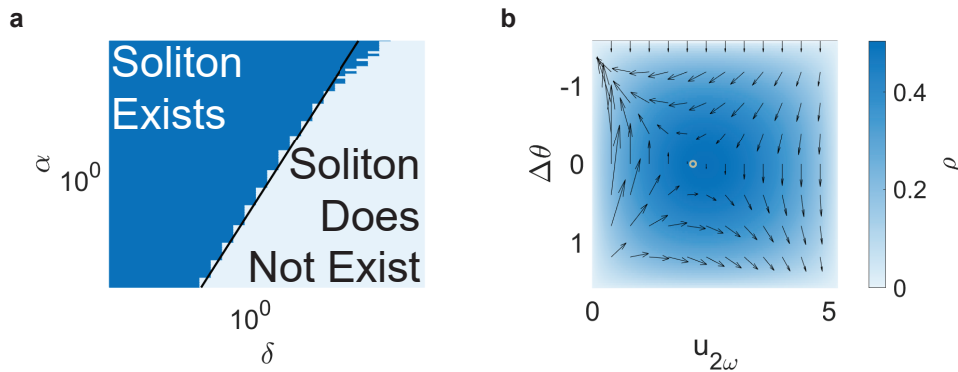
Figure 5.13: **Soliton existence and stability. a**, Soliton existence and non-existence regimes determined by convergence of Newton's method to a non-zero solution. The expected boundary $\alpha = \delta^2/4$ is given by the solid, black line. **b**, Phase space diagram with $\alpha = 1$ of the second harmonic soliton amplitude, $u_{2\omega}$, relative phase, $\Delta\theta$ found using the Lagrangian analysis. The color map shows the value of the pulse width parameter, ρ, corresponding to the given values of $u_{2\omega}$ and $\Delta\theta$. The soliton solution is indicated by the open tan circle.

Lagrangian Analysis

To better understand the stability of the soliton solution and the compression dynamics near the soliton solution, we may perform a Lagrangian analysis [62] on the system 5.7a and 5.7b, setting $\delta = 0$. In this case, the Lagrangian density may be written as:

$$L = \sigma \operatorname{Im}\left\{a_{2\omega}^* \frac{\partial a_{2\omega}}{\partial \zeta}\right\} + \operatorname{Im}\left\{a_\omega^* \frac{\partial a_\omega}{\partial \zeta}\right\} + \left|\frac{\partial a_\omega}{\partial \zeta}\right|^2 + \left|\frac{\partial a_{2\omega}}{\partial \zeta}\right|^2$$
$$+ |a_\omega|^2 + \alpha|a_{2\omega}|^2 - \operatorname{Re}\{a_\omega^2 a_{2\omega}^*\}. \quad (5.30)$$

To proceed, we assume the following simplified forms for the fundamental and second harmonic waves based on the known exact soliton solution for $\alpha = 1$:

$$a_\omega(\zeta, \xi) = u_\omega(\zeta)\sqrt{\rho(\zeta)} \operatorname{sech}^2\left(\rho(\zeta)\xi\right)e^{i\frac{\theta_\omega(\zeta)}{2}}, \tag{5.31a}$$

$$a_{2\omega}(\zeta, \xi) = u_{2\omega}(\zeta)\sqrt{\rho(\zeta)} \operatorname{sech}^2\left(\rho(\zeta)\xi\right)e^{i\theta_{2\omega}(\zeta)}, \tag{5.31b}$$

where u_ω, $u_{2\omega}$, θ_ω, and $\theta_{2\omega}$ are the fundamental and second harmonic pulse amplitudes and phases, respectively, and ρ is the pulse width parameter, assumed to be the same for both the fundamental and second harmonic. The time-averaged Lagrangian density, $\mathcal{L}$, is then obtained inserting this ansatz into equation 5.30 and integrating over ξ:

$$\mathcal{L} = \int_{-\infty}^{\infty} L(\xi, \zeta)d\xi. \tag{5.32}$$

Finally, the equations of motion for the system parameters can be found using the Euler-Lagrange equation, $\frac{\partial}{\partial\zeta}\left(\frac{\partial\mathcal{L}}{\left(\frac{\partial f}{\partial\zeta}\right)}\right) = \frac{\partial\mathcal{L}}{\partial f}$, where $f \in \{\rho, \theta_\omega, \theta_{2\omega}, u_\omega, u_{2\omega}\}$. Steady-state solutions may be found by setting the resulting ζ derivatives to 0, yielding the following set of algebraic equations:

$$4\rho^{3/2}(u_{2\omega}^2 + u_\omega^2) = u_\omega^2 u_{2\omega}, \tag{5.33a}$$

$$2 + \frac{8}{5}\rho^2 = \frac{8}{5}\sqrt{\rho}u_{2\omega}, \tag{5.33b}$$

$$2\alpha + \frac{8}{5}\rho^2 = \frac{4}{5}\sqrt{\rho}\frac{u_\omega^2}{u_{2\omega}}. \tag{5.33c}$$

In the case of $\alpha = 1$, the known soliton solution given by equations 5.21a and 5.21 is recovered exactly, as expected. Away from $\alpha = 1$, the system approximates the soliton solution but deviates slightly due to the assumption that the fundamental and second harmonic share the same pulse profile and width. The dynamics of the system can be reduced to two algebraic equations and two differential equations as follows:

$$\rho^{3/2} = \frac{1}{4}\frac{u_{2\omega}u_\omega^2}{u_{2\omega}^2 + u_\omega^2}\cos(\Delta\theta), \tag{5.34a}$$

$$\frac{u_\omega^2}{2} + \sigma u_{2\omega}^2 = \eta_{\text{tot}}, \tag{5.34b}$$

$$\frac{du_{2\omega}}{d\zeta} = -\frac{2}{5\sigma}\sqrt{\rho}u_\omega^2 \sin(\Delta\theta), \tag{5.34c}$$

$$\frac{d\Delta\theta}{d\zeta} = -\frac{2}{5}\left(\frac{u_\omega^2}{\sigma u_\omega} - 4u_{2\omega}\right)\sqrt{\rho}\cos(\Delta\theta) + \frac{4}{5}\left(\frac{1}{\sigma} - 2\right)\rho^2 + \left(\frac{\alpha}{\sigma} - 2\right), \tag{5.34d}$$

where we have re-parameterized the phase in terms of $\Delta\theta = \theta_\omega - \theta_{2\omega}$. Equation 5.34b is an energy conservation relation for the normalized system, with η_{tot} being a constant representing the total energy of the system.

The phase space diagram corresponding to equations 5.34c and 5.34d for $\alpha = 1$ can be found in Fig. 5.13b. The color gradient in the background further shows the value of ρ, computed using the algebraic equations 5.34a and 5.34b, where η_{tot} is computed from the soliton solution given by the system of equations 5.33. We observe that, in the space of the considered parameters, the soliton solution (open, tan circle) is a saddle point. We note also that the soliton solution corresponds very nearly to the largest value of ρ (corresponding to the minimum value of the pulse width). Although this simplified model does not capture the full compression behavior (for example, the observed back-and-forth conversion), the behavior is consistent with the overall compression dynamics of Fig. 5.1b. Specifically, we observe that the pulse nearly compresses to the soliton solution, around which pulse evolution is observed to be slow, but eventually begins to broaden again. This slow evolution, but ultimate instability, of the pulse near the soliton solution is consistent with the finding from the Lagrangian analysis that the soliton is a saddle point.

This analysis additionally highlights another important property of the soliton solution of the system, which is that $\Delta\theta = 0$ for the soliton state. We note here that in terms of the fundamental second harmonic envelope phases, respectively $\phi_\omega = \frac{\theta_\omega}{2}$ and $\phi_{2\omega} = \theta_{2\omega}$, this result implies that $2\phi_\omega = \phi_{2\omega}$ in the soliton state. Therefore, a change $\Delta\phi_\omega$ in the fundamental phase results in a change $\Delta\phi_{2\omega}$ that is twice as large. This is the basis of the synthesis method proposed in Section 5.5, as a simple modulation of the envelope phase of the fundamental input to the two-color compression can be used to directly shape the relative phase of the two output harmonics for the realization of a variety of waveforms.

Pulse Compression Simulations

To further explore the compression dynamics and provide finally some basic design guidelines, we perform Fourier split-step simulations of the coupled wave equations,

5.7a and 5.7b. To seed the simulations, we first take the numerically computed soliton solutions, as described above, and find the pulse width of the fundamental soliton as well as the total normalized energy in the combined fundamental and second harmonic soliton solutions. We then input a sech-shaped pulse at the fundamental with a pulse energy equal to the total soliton energy. To study the compression dynamics, we vary the ratio of the FWHM of the input, FWHM_{in}, to that of the soliton, FWHM_{sol} for different values of α, δ, and σ. For simplicity, we have assumed $\text{sgn}(\beta) = 1$ in our simulations, but identical scaling behaviors would be observed for $\text{sgn}(\beta) = -1$, with the primary difference being in the accumulated propagation phase.
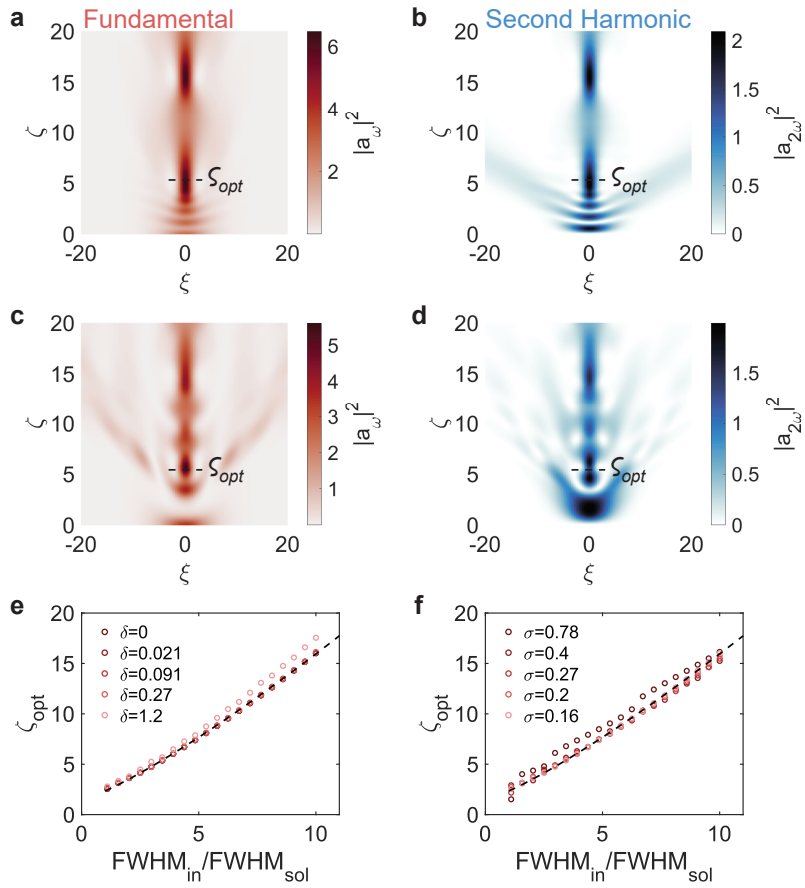
Figure 5.14: **Normalized compression results with constant $\alpha = 1.64$. a,** Phase-mismatched compression with $\sigma = \alpha/5$ for the fundamental and **b,** second harmonic. **c,** Nearly phase-matched compression with $\sigma = \alpha/2.1$ for the fundamental and **d,** second harmonic. The optimum compression length, ζ_{opt} is indicated in all four cases. **e,** ζ_{opt} as a function of $\text{FWHM}_{\text{in}}/\text{FWHM}_{\text{sol}}$ for various values of σ, showing similar scaling behavior. **f,** Likewise, ζ_{opt} exhibits similar scaling behaviors for different values of δ.

The results of this analysis are used to generate the scaling behavior plots of Figs. 5.2c-f. Several supporting results are shown in Fig. 5.14. Figures 5.14a and 5.14b show the evolution of the fundamental and second harmonic as a function of the normalized propagation distance with $\alpha = 1.64$, $\sigma = \alpha/5$, and $\delta = 0$. This case represents compression in the phase-mismatched regime, where several back-and-forth conversions are observed before the waves approaches the soliton solution near the optimum compression point, ζ_{opt}, indicated by the dashed, white line. As mentioned in Section 5.2, we define ζ_{opt} as the point at which the minimum pulse width is observed at the fundamental. Another interesting feature of note, as predicted by the Lagrangian analysis, is that the waves do not remain in the compressed soliton state but are then observed to broaden. A second regime of compression is observed near $\zeta = 3\zeta_{\text{opt}}$, indicative of breathing dynamics for the compression system. By contrast, we show compression in the near phase-matched regime with $\sigma = \alpha/2.1$ in Figs. 5.14c and 5.14d. Here, only about two cycles of back-and-forth conversion are observed before ζ_{opt} is reached. However, the shape of the compressed pulse and optimum distance, ζ_{opt}, are observed to be similar in both the phase-mismatched and near phase-matched cases.

Having shown a few examples of the compression dynamics, we turn now to the claim that α is the dominant parameter in determining the compression behavior. In Fig. 5.14e, we show ζ_{opt} for many values of σ with constant $\alpha = 1.64$ and $\delta = 0$. Besides some small deviation for the largest value of σ, where the system is very nearly phase-matched, we observe extremely similar scaling behavior, all of which follows well the fit of equation 5.3. Likewise, we show the scaling behavior for different values of δ in Fig. 5.14f. Again, we see nearly identical scaling behavior besides the extreme case of large δ, where we are near the edge of the soliton existence regime.

Theoretically-Informed Design Rules

Having now studied the soliton solutions of the normalized coupled wave equations 5.7a and 5.7b and characterized the corresponding pulse compression behaviors, we may offer several design guidelines for achieving two-color soliton compression. There are several considerations for the design of the soliton compression system. The first is the desired pulse shape, which is fully determined by α, as discussed above. Secondly, one must consider the ratio of fundamental to second harmonic peak power, which we recall is given in physical units by $\dfrac{|A_{\omega,0}|^2}{|A_{2\omega,0}|^2} = \left|\dfrac{\beta_{2\omega}^{(2)}}{2\beta_{\omega}^{(2)}}\right|\dfrac{|a_{\omega,0}|^2}{|a_{2\omega,0}|^2}$.

Here, $A_{j,0}$ refers to the soliton amplitude in the jth wave, in direct analogy to the normalized soliton amplitudes, $a_{j,0}$. The third is the resultant pulse FWHM, which we have observed is on the order of the characteristic time of the system, $\sqrt{\left|\frac{\beta_\omega^{(2)}}{2\beta}\right|}$, for most reasonable values of α. Finally, we must satisfy the constraint $\alpha \geq \delta^2/4$, which translates in physical parameters to $\frac{2\left|\beta_{2\omega}^{(2)}\beta\right|}{(\Delta\beta')^2}(2 + \frac{\Delta k}{\beta}) \geq 1$.

Before continuing, we must also find an expression for β. One approach is to use conservation of energy. Specifically, we have that:

$$E_{\text{tot}} = \left|\frac{\beta}{\kappa}\right|^2 \left(\left|\frac{1}{2\sigma}\right| \int_{-\infty}^{\infty} a_\omega^2\left(\sqrt{\left|\frac{2\beta}{\beta_\omega^{(2)}}\right|}t\right)dt + \int_{-\infty}^{\infty} a_{2\omega}^2\left(\sqrt{\left|\frac{2\beta}{\beta_\omega^{(2)}}\right|}t\right)dt\right), \qquad (5.35)$$

where $a_\omega(\xi)$ and $a_{2\omega}(\xi)$, $\xi = \sqrt{\left|\frac{2\beta}{\beta_\omega^{(2)}}\right|}t$, may be taken as the soliton solutions of equation 5.26, and E_{tot} is, therefore, the total energy in the soliton solution. As we have observed, the majority of the pulse energy is retained in the soliton solution for moderate compression factors (less than a factor of ≈ 10). Thus, we may consider E_{tot} also to be the required input energy. This allows us therefore to relate β precisely to 5.35 for a given soliton solution.

With these key parameters in mind and a solution for β, we offer a suggested work flow for designing a compression system. The most stringent requirement is that the signs of $\beta_\omega^{(2)}$ and $\beta_{2\omega}^{(2)}$ must be the same to satisfy our initial assumptions for $s2$ and $s3$. After meeting this requirement, one should then try to minimize $\left|\Delta\beta'\right|$, as a smaller walk-off will give more flexibility on the other parameters of the system.

Once such a regime has been found, one may optimize for the desired soliton shape, FWHM, and peak power ratio. As discussed above, the shape of the soliton solutions is determined by α. In the cascading limit of large α, we observe a sech-shaped field envelope for the fundamental and a sech^2-shaped field envelope for the second harmonic. This results in narrower pulses for the second harmonic than the fundamental. Conversely, shorter pulses are observed at the fundamental in the case of small α. Both envelopes take the same sech^2 shape at $\alpha = 1$. In our experiment, we aim to operate near $\alpha = 1$ to achieve similar pulse widths at both harmonics.

After determining the desired value of α, one may consider the peak power ratio. By definition, we require $\sigma \leq \alpha/2$. If one selects $\beta_\omega^{(2)}$ and $\beta_{2\omega}^{(2)}$ such that $\sigma \approx \alpha/2$, very little phase-mismatch is required for achieving the desired compression, resulting

in nearly equal distributions of power between the two pulses. This may be readily observed in the cascading limit, where $\frac{|a_{\omega,0}|^2}{|a_{2\omega,0}|^2} = |\alpha| \approx |2\sigma| = \left|\frac{2\beta_\omega^{(2)}}{\beta_{2\omega}^{(2)}}\right|$. Then, in terms of physical parameters, we have that $\frac{|A_{\omega,0}|^2}{|A_{2\omega,0}|^2} = \left|\frac{\beta_{2\omega}^{(2)}}{2\beta_\omega^{(2)}}\right|\frac{|a_{\omega,0}|^2}{|a_{2\omega,0}|^2} = 1$. If one wishes, however, to compress the fundamental only with limited conversion to the second harmonic, then one should design for $\sigma \ll \alpha$, and a large Δk should be used. In our system, we have $\sigma = 0.065$, so we require a moderate Δk to operate near $\alpha = 1$.

While the desired peak power ratio informs the ratio of $\beta_\omega^{(2)}$ to $\beta_{2\omega}^{(2)}$, design of their absolute values is determined by the soliton existence condition, desired FWHM, and available pulse energy. Specifically, we see that a larger magnitude of $\beta_{2\omega}^{(2)}$ can compensate the walk-off $\Delta\beta'$ in satisfying the existence condition, $\frac{2|\beta_{2\omega}^{(2)}\beta|}{(\Delta\beta')^2}(2 + \frac{\Delta k}{\beta}) \geq 1$. However, with a fixed ratio of $\left|\frac{\beta_\omega^{(2)}}{\beta_{2\omega}^{(2)}}\right|$, this means also increasing $\left|\beta_\omega^{(2)}\right|$, which will result in a longer soliton pulse width for the same $|\beta|$. Offsetting this through increasing $|\beta|$ requires a larger input pulse energy. A well-optimized system will therefore maximize the magnitude of $\beta_{2\omega}^{(2)}$, while still maintaining that the desired pulse width is achievable in the range of available pump energies. This may be done iteratively through the use of equation 5.35. In our system, we have prioritized operation with a small $\left|\beta_\omega^{(2)}\right|$ to show that few-cycle pulse compression is attainable with pJ pump pulse energies, as may be achieved with available integrated pulsed sources.
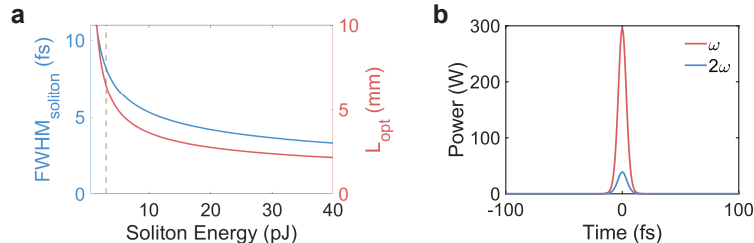
Figure 5.15: **Device design and soliton solution**. **a**, Predicted soliton FWHM and optimum device length as a function of input energy. The tan, dashed line shows the experimentally desired operation point. **b**, Predicted soliton solution corresponding to the experimental parameters.

Finally, having determined the other system parameters, one may calculate the required waveguide length. To do so, should take desired compression factor as the ratio of the input pulse FWHM to that of the desired soliton solution and use equation 5.3 to calculate the corresponding ζ_{opt}. The device length may then be

Parameter	Description	Value	Units
A_{eff}	effective mode area	2.18	µm^2
n_ω	refractive index, fundamental	1.88034	
$n_{2\omega}$	refractive index, second harmonic	2.06409	
Δk	phase mismatch	-4	rad/mm
d_{eff}	effective nonlinearity	11	pm/V
α_ω	loss, fundamental	0.023	1/mm
$\alpha_{2\omega}$	loss, second harmonic	0.023	1/mm
$\Delta\beta'$	GVM	27	fs/mm
$\beta_\omega^{(2)}$	GVD, fundamental	9.22	fs^2/mm
$\beta_{2\omega}^{(2)}$	GVD, second harmonic	141	fs^2/mm

Table 5.1: **Simulation parameters for the soliton compression.**

directly calculated as $L_{\text{opt}} = \frac{\zeta_{\text{opt}}}{|\beta|}$. To illustrate this process for our own device parameters, we plot FWHM$_{\text{soliton}}$ and L_{opt} as a function of the input energy in Fig. 5.15a. Our desired operation point is shown by the tan, dashed line, corresponding to a FWHM$_{\text{soliton}}$ of 8 fs and L_{opt} of 6.5 mm. The resulting soliton solution is shown in Fig. 5.15b.

Full Simulation and Mapping to Experiment

For comparison with experiment, we directly simulate equations 5.5a and 5.5b but with the additional inclusion of loss terms for the fundamental and second harmonic, α_ω and $\alpha_{2\omega}$. As in the normalized simulations described previously, we employ a Fourier split-step simulation using a fourth-order Runge-Kutta method for the nonlinear step. A full list of simulation parameters may be found in Table 5.7. We note here that the simulated magnitude of Δk is slightly lower than what may be expected based on the poling period and geometry of the device. Similarly, the d_{eff} used is slightly smaller than what has been previously reported for PPLN. Both numbers were adjusted to optimize the match between simulation and experiment as non-idealities such as thin-film thickness variation, fabrication error, and imperfect poling can create uncertainty in these quantities.

The results of these numerical simulations are used to generate the results of Figs.

5.1b and 5.1c as well as the entirety of Figure 5.2. Although very good agreement is observed between these simulations and our experiments, some discrepancies may be observed which we investigate here. The first is that our theory and simulation have assumed a transform-limited 35-fs pulse as our input to the compression device. In reality, as mentioned previously, some pre-chirp is accumulated on the pulse due to propagation through several optical elements, with the main contribution being anomalous chirp from the ND wheel used to tune the input pulse energy to the compression system. We estimate the total accumulated group delay dispersion, accounting for chirp from the ND wheel, beam expander, and waveguide section prior to compression to be -260 fs^2.
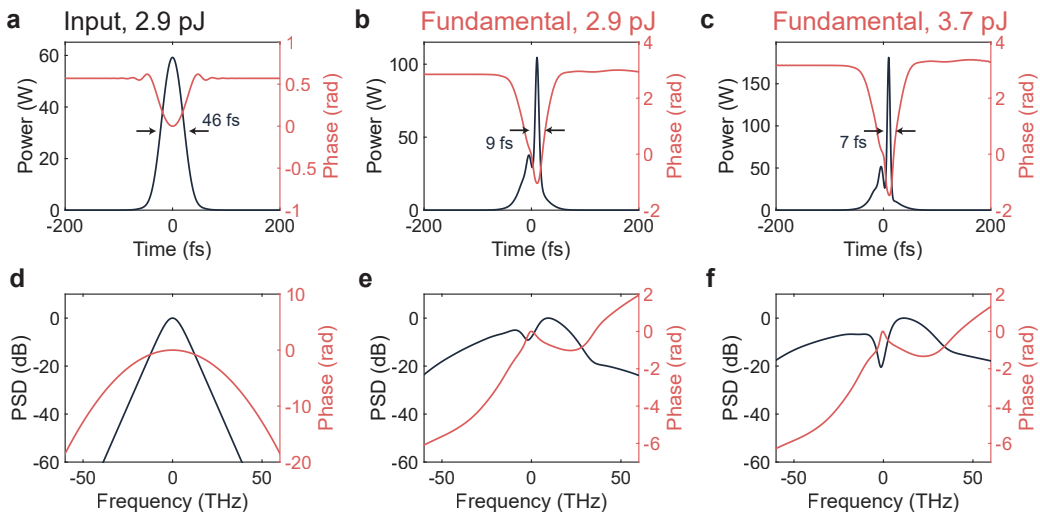
Figure 5.16: **Simulation results with pre-chirped input pulse**. **a**, Chirped input pulse used in simulation. **b**, Output at the fundamental for a 2.9-pJ input pulse. **c**, Output at the fundamental for a 3.7-pJ input pulse. **d**, Input spectrum. **e**, Output fundamental spectrum for a 2.9-pJ and **f**, 3.7-pJ input

Simulation results including this pre-chirp are shown in Fig. 5.16. The chirped input pulse is given in Fig. 5.16a and is shown to be 46 fs, similar to the measured 48-fs input pulses. The primary consequence of this pre-chirp is to slow the rate of compression down compared to the transform-limited case of Fig. 5.2. In particular, we see that the pulse is compressed to 9 fs at 2.9 pJ, compared to 7 fs in the unchirped case (Fig. 5.16b). Instead, compression to 7 fs is observed at 3.7 pJ of input energy (Fig. 5.16c). A small secondary consequence of the pre-chirp is that more energy flows into the small secondary lobe on the leading edge of the pulse. Corresponding spectra for the input and two output pulses are shown in Figs. 5.16d-f.

That said, this result does not fully explain why the compressed pulses have a slightly longer duration than predicted, as it suggests that we should achieve the ideal 7-fs pulses by merely increasing the input pulse energy. To investigate this further, we turn to a more full model which includes the effects of higher-order dispersion. Modeling the higher-order dispersion requires the following modification of equations 5.5a and 5.5b:

$$\frac{\partial A_\omega}{\partial z} = i\kappa A_{2\omega} A_\omega^* e^{-i\Delta k z} + \hat{D}_\omega A_\omega - \frac{\alpha_\omega}{2}, \tag{5.36a}$$

$$\frac{\partial A_{2\omega}}{\partial z} = i\kappa A_\omega^2 e^{i\Delta k z} - \Delta\beta' \frac{\partial A_{2\omega}}{\partial t} + \hat{D}_{2\omega} A_{2\omega} - \frac{\alpha_{2\omega}}{2}, \tag{5.36b}$$

where we have considered the dispersion operator $\hat{D}_j = \sum_{m=2}^{\infty} \left[\frac{(i)^{m+1} \beta_j^{(m)}}{m!} \right] \partial_t^m$. Here, $\beta_j^{(m)}$ refers to the mth dispersion order in the jth wave. In our simulations, we include all orders of higher-order dispersion by calculating the propagation constant from the frequency-dependent index of Fig. 5.7e and subtracting the first two terms of the Taylor expansions about the fundamental and second harmonic frequencies for the respective equations.

The results of this full simulation are shown in Fig. 5.17 for an input pulse energy of 2.9 pJ, mirroring the on-chip input energy used in the experiment. As in Fig. 5.16, we use a chirped input pulse to better capture the behaviors of the experiment. The output pulse profiles at the fundamental and second harmonic are shown in Figs. 5.17a and 5.17c, respectively. The fundamental pulse measures 16 fs, and the second harmonic measures 14 fs, in better agreement with the experimentally measured pulse durations compared to the simulations including only quadratic dispersion. Corresponding spectra in Figs. 5.17e and 5.17g also exhibit very similar behavior to the experimentally reconstructed spectra.

The shortest pulses observed in simulation occur for energies closer to 5 pJ. Here, we show a simulated example at 4.6 pJ of pump pulse energy. In this case, pulse widths of 11 fs (Fig. 5.17b) and 10 fs (Fig. 5.17d) at the fundamental and second harmonic are observed. Corresponding spectra are shown in Figs. 5.17f and 5.17h. Most interestingly, a more prominent dip with two features is observed in the fundamental spectrum. The pulse widths and spectral shape agree well with experimental traces taken at 5 pJ of pump pulse energy; however, as discussed previously, a phase ambiguity in the FROG measurement at these power levels prohibit a deterministic retrieval.
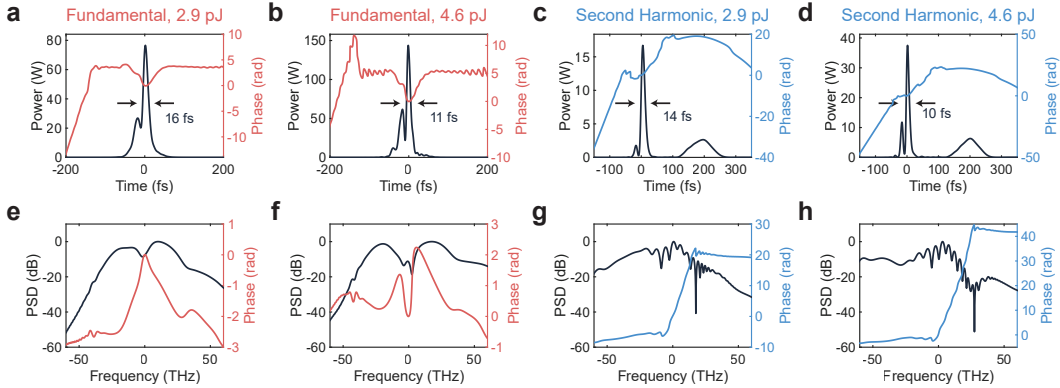
Figure 5.17: **Simulated output including higher-order dispersion**. **a**, Output fundamental pulse at 2.9 pJ and **b**, 4.6 pJ of pump pulse energy. **c**, Output second harmonic pulse at 2.9 pJ and **d** 4.6 pJ of pump pulse energy. The corresponding spectra are also plotted for the **e**, output fundamental at 2.9 pJ, **f**, output fundamental 4.6 pJ, **g**, output second harmonic at 2.9 pJ, and **h**, output second harmonic at 4.6 pJ.

To further study the agreement between our model and experiment, we examine the spectrum and output pulse profile as a function of the input energy. The results are shown in Fig. 5.18. Figure 5.18a shows the spectrum evolution as the pump energy is increased for our simplified model which includes only quadratic dispersion. We note that the pump energy (y-axis) is plotted on a logarithmic scale. By comparison, the spectrum for the full simulation is shown in Fig. 5.18d. Finally, the experimental spectrum evolution as measured by the OSA is shown in Fig. 5.18g. Extremely good agreement with experiment is observed with both of the simulations, but especially for the full model. In particular, the fundamental and second harmonic spectral components begin to strongly overlap at a similar point, near 4 pJ. Additionally, significant spectral splitting is observed near the center of the fundamental wavelength at 2090 nm for powers greater than 5 pJ in all cases.
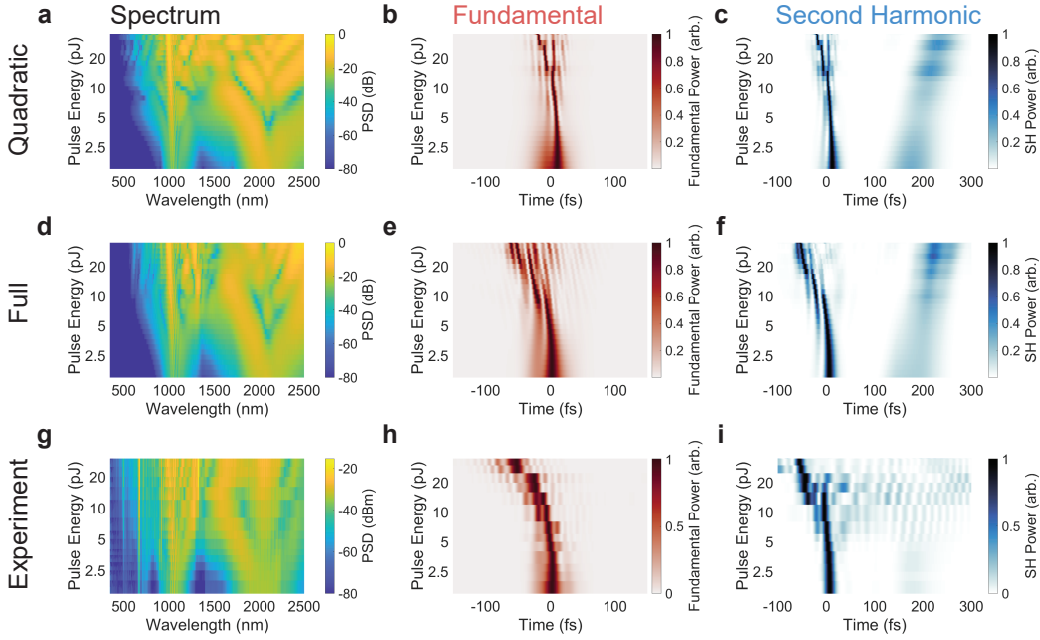
Figure 5.18: **Simulated vs. experimental energy-dependent outputs**. **a**, Simulated spectrum, **b**, fundamental pulse profile, and **c**, second harmonic profile for various input energies, including only quadratic dispersion. For comparison, we show the **d**, spectrum, **e**, fundamental pulse, and **f**, second harmonic pulse for the full simulation including higher-order dispersion. Finally, we show the experimentally-measured **g**, spectrum, **h**, fundamental pulse, and **i**, second harmonic pulse for various input energies. The experimental pulse measurements are shifted according to the maximum of the cross-correlation with the full simulation at the same pump pulse energy.

We additionally compare the temporal profiles between the simulations and measurement. The fundamental pulse as a function of input energy for the three cases is shown in Figs. 5.18b, 5.18e, and 5.18h, while the second harmonic is shown in Figs. 5.18c, 5.18f, and 5.18i. As our FROG retrieval does not provide absolute temporal positioning for the measured pulses, we instead use the simulation including the full dispersion as a reference and position the measured pulses according to the maximum of their cross-correlation with the simulation for the same input energy. Each row, corresponding to different input energies, has been independently normalized to the pulse maximum. The measured pulses have further been interpolated onto the same time grid as the simulation to improve clarity.

For lower input energies, we see improved compression as the energy is increased, as expected. After the input energy exceeds about 5 pJ, however, the length of the device begins to exceed the optimum device length for compression, and the

compression quality begins to degrade. In the case where only quadratic dispersion is included, the degradation is slower, with a single central feature being maintained until an input energy of around 12 pJ is reached. At this point, the device length is nearly double the calculated optimum for compression, and the pulse is seen to split into two distinct lobes. With the inclusion of higher-order dispersion, splitting is observed much sooner. This agrees well with our experiment, where the optimum compression is observed to occur with 3-5 pJ of pump pulse energy, and the quality quickly degrades for higher powers. In the experiment, however, the separate lobes predicted by the simulation are not well resolved at high powers. We attribute this primarily to the limitations of our measurement setup.
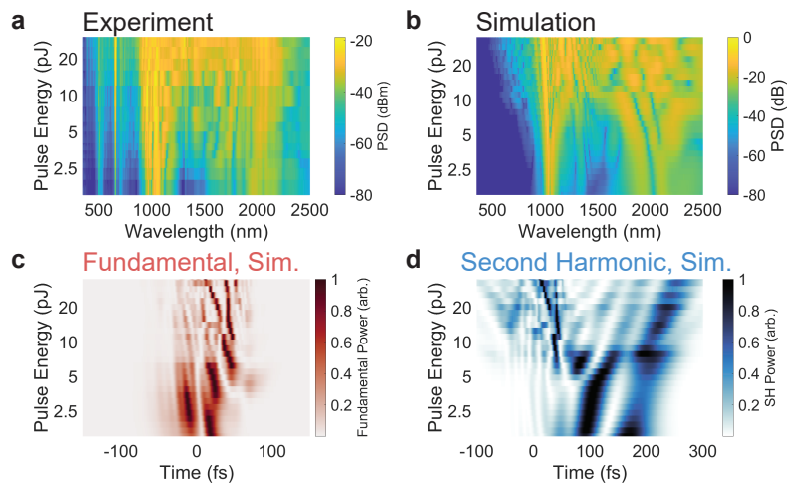
Figure 5.19: **Phase-matched supercontinuum generation**. **a**, Experimentally measured spectral broadening in the phase-matched regime. **b**, Simulation of phase-matched broadening using the full dispersion. **c**, Corresponding simulations of fundamental and **d**, second harmonic output pulses, demonstrating that temporal shortening is not observed in this regime.

As a final point of comparison between experiment and simulation, and to illustrate the importance of operation in the soliton regime for such compression to occur, we characterize the behavior of a neighboring device which is nearly phase matched. The results are shown in Fig. 5.19. The measured spectrum as a function of input energy is shown in Fig. 5.19a, and the corresponding simulation including the full dispersion profile is shown in Fig. 5.19b. Although significant spectral broadening is seen to occur, we see many additional spectral features when compared to the soliton regime of Fig. 5.18. The simulated pulse profiles at the fundamental and second harmonic are shown in Figs. 5.19c and 5.19d, respectively. Here, significant pulse shortening is not observed, and the pulses are seen to split into many

distinct lobes. This highlights the power of soliton pulse compression for achieving both broadband spectra and ultrashort pulses compared to other supercontinuum generation processes in quadratic media.

Extension to Longer Pump Pulses

While in our work we have begun with 35-fs input pulses, which are already quite short, the presented compression scheme may be readily extended to longer pump pulses. Here, we simulate the compression of an 80-fs pulse using the realistic parameters of our fabricated waveguide. Based on equation 5.3, we calculate that for such a longer pulse, a 15.4-mm waveguide is required. Otherwise, the simulation parameters remain unchanged from those in 5.7. We additionally consider an unchirped pump pulse.
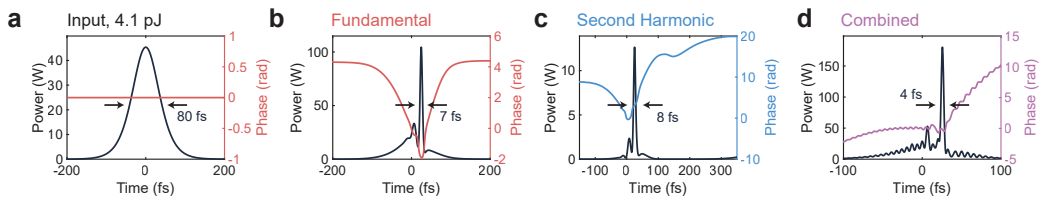
Figure 5.20: **Compression of 80-fs pulses**. **a**, Input 4.1-pJ, 80-fs pulse. **b**, Simulated temporal at the fundamental and **c**, corresponding second harmonic. **d**, Combined fundamental and second harmonic pulses.

Our simulation results are shown in Fig. 5.20. Due to the additional 9 mm of length in the waveguide, the pulse incurs an additional 1.8 dB of loss which must be compensated by pumping at a slightly higher power than the previously simulated 2.9-pJ inputs. The input 80-fs, 4.1-pJ pulse is shown in Fig. 5.20a. At the output of the waveguide, compressed 7-fs (5.20b) and 8-fs (5.20c) pulses are observed at the fundamental and second harmonic, similar to the outputs observed for the case of 35-fs pump pulses. The primary difference is the presence of a larger pedestal in the case of the longer pump pulse. Likewise, Fig. 5.20d shows the combined 4-fs pulse, indicating the possibility of using the compressed outputs for single-cycle pulse synthesis.

These results further demonstrate how the presented design framework may be flexibly used for the compression of a wide variety of input pulses. This flexibility ensures compatibility with emerging nanophotonic sources towards the development of integrated ultrafast systems.

BIBLIOGRAPHY

[1] Shu-Wei Huang, Giovanni Cirmi, Jeffrey Moses, Kyung-Han Hong, Siddharth Bhardwaj, Jonathan R. Birge, Li-Jin Chen, Enbang Li, Benjamin J. Eggleton, Giulio Cerullo, et al. "High-energy pulse synthesis with sub-cycle waveform control for strong-field physics." In: *Nature Photonics* 5.8 (2011), pp. 475–479.

[2] Adrian Wirth, Mohammed Th. Hassan, Ivanka Grguraš, Justin Gagnon, Antoine Moulet, Tran Trung Luu, Stefan Pabst, Robin Santra, Zeyad A. Alahmed, Abdallah M. Azzeer, et al. "Synthesized light transients." In: *Science* 334.6053 (2011), pp. 195–200.

[3] Peter Krogen, Haim Suchowski, Houkun Liang, Noah Flemens, Kyung-Han Hong, Franz X. Kärtner, and Jeffrey Moses. "Generation and multi-octave shaping of mid-infrared intense single-cycle pulses." In: *Nature Photonics* 11.4 (Apr. 2017), pp. 222–226. ISSN: 1749-4893. DOI: `10 . 1038/nphoton.2017.34`. URL: `https://doi.org/10.1038/nphoton.2017.34`.

[4] Ahmed H. Zewail. "Laser femtochemistry." In: *Science* 242.4886 (1988), pp. 1645–1653. DOI: `10 . 1126 / science . 242 . 4886 . 1645`. URL: `https://www.science.org/doi/abs/10.1126/science.242.4886.1645`.

[5] Ferenc Krausz and Misha Ivanov. "Attosecond physics." In: *Reviews of modern physics* 81.1 (2009), pp. 163–234.

[6] Francesca Calegari, Giuseppe Sansone, Salvatore Stagira, Caterina Vozzi, and Mauro Nisoli. "Advances in attosecond science." In: *Journal of Physics B: Atomic, Molecular and Optical Physics* 49.6 (2016), p. 062001.

[7] Adrian L. Cavalieri, Norbert Müller, Thorsten Uphues, Vladislav S. Yakovlev, Andrius Baltuška, Balint Horvath, Bruno Schmidt, Ludwig Blümel, Ronald Holzwarth, Stefan Hendel, Markus Drescher, Ulf Kleineberg, Pedro M. Echenique, Reinhard Kienberger, Ferenc Krausz, and Ulrich Heinzmann. "Attosecond spectroscopy in condensed matter." In: *Nature* 449.7165 (Oct. 2007), pp. 1029–1032. ISSN: 1476-4687. DOI: `10 . 1038 / nature06229`. URL: `https://doi.org/10.1038/nature06229`.

[8] Dandan Hui, Husain Alqattan, Shunsuke Yamada, Vladimir Pervak, Kazuhiro Yabana, and Mohammed Th. Hassan. "Attosecond electron motion control in dielectric." In: *Nature Photonics* 16.1 (Jan. 2022), pp. 33–37. ISSN: 1749-4893. DOI: `10.1038/s41566-021-00918-4`. URL: `https://doi.org/10.1038/s41566-021-00918-4`.

[9] Ioachim Pupeza, Marinus Huber, Michael Trubetskov, Wolfgang Schweinberger, Syed A. Hussain, Christina Hofer, Kilian Fritsch, Markus Poetzlberger, Lenard Vamos, Ernst Fill, Tatiana Amotchkina, Kosmas V. Kepesidis, Alexander Apolonski, Nicholas Karpowicz, Vladimir Pervak, Oleg Pronin, Frank Fleischmann, Abdallah Azzeer, Mihaela Žigman, and Ferenc Krausz. "Field-resolved infrared spectroscopy of biological systems." In: *Nature* 577.7788 (Jan. 2020), pp. 52–59. ISSN: 1476-4687. DOI: 10.1038/s41586-019-1850-7. URL: https://doi.org/10.1038/s41586-019-1850-7.

[10] Claudius Riek, Philipp Sulzer, Maximilian Seeger, Andrey S. Moskalenko, Guido Burkard, Denis V. Seletskiy, and Alfred Leitenstorfer. "Subcycle quantum electrodynamics." In: *Nature* 541.7637 (2017), pp. 376–379.

[11] Eleftherios Goulielmakis, Martin Schultze, Michael Hofstetter, Vladislav S. Yakovlev, Juestin Gagnon, Matthias Uiberacker, Andrew L. Aquila, Eric M. Gullikson, David T. Attwood, Reinhard Kienberger, Ferenc Krausz, and Ulf Kleineberg. "Single-cycle nonlinear optics." In: *Science* 320.5883 (June 2008), pp. 1614–1617. DOI: 10.1126/science.1157846. URL: https://doi.org/10.1126/science.1157846.

[12] Martin Wegener. *Extreme nonlinear optics: An introduction.* Advanced Texts in Physics. Springer Berlin Heidelberg, 2006. ISBN: 9783540266884. URL: https://books.google.com/books?id=pZI0erZXgdcC.

[13] Shambhu Ghimire and David A. Reis. "High-harmonic generation from solids." In: *Nature Physics* 15.1 (Jan. 2019), pp. 10–16. ISSN: 1745-2481. DOI: 10.1038/s41567-018-0315-5. URL: https://doi.org/10.1038/s41567-018-0315-5.

[14] Eleftherios Goulielmakis and Thomas Brabec. "High harmonic generation in condensed matter." In: *Nature Photonics* 16.6 (2022), pp. 411–421.

[15] Sylvianne D. C. Roscam Abbing, Filippo Campi, Alexandra Zeltsi, Peter Smorenburg, and Peter M. Kraus. "Divergence and efficiency optimization in polarization-controlled two-color high-harmonic generation." In: *Scientific Reports* 11.1 (2021), p. 24253.

[16] Giulio Vampa, TJ Hammond, Nicolas Thiré, Bruno E. Schmidt, Francois Légaré, Chris R. McDonald, Thomas Brabec, and Paul B. Corkum. "Linking high harmonics from gases and solids." In: *Nature* 522.7557 (2015), pp. 462–464.

[17] Cheng Jin and Chii D. Lin. "Control of soft X-ray high harmonic spectrum by using two-color laser pulses." In: *Photonics Research* 6.5 (2018), pp. 434–442.

[18] Mikhail V. Frolov, Nikolai L. Manakov, Alexander A. Silaev, and Nikolay V. Vvedenskii. "Analytic description of high-order harmonic generation by

atoms in a two-color laser field." In: *Physical Review A—Atomic, Molecular, and Optical Physics* 81.6 (2010), p. 063407.

[19]   Christian Leefmans, Avik Dutt, James Williams, Luqi Yuan, Midya Parto, Franco Nori, Shanhui Fan, and Alireza Marandi. "Topological dissipation in a time-multiplexed photonic resonator network." In: *Nature Physics* 18.4 (2022), pp. 442–449. DOI: `10.1038/s41567-021-01492-w`.

[20]   Toshihiko Hirooka, Ryoya Hirata, Jianping Wang, Masato Yoshida, and Masataka Nakazawa. "Single-channel 10.2 Tbit/s (2.56 Tbaud) optical Nyquist pulse transmission over 300 km." In: *Optics Express* 26.21 (2018), pp. 27221–27236.

[21]   Robert M. Gray, Ryoto Sekine, Luis Ledezma, Gordon H. Y. Li, Selina Zhou, Arkadev Roy, Midya Parto, and Alireza Marandi. "Large-scale time-multiplexed nanophotonic parametric oscillators." In: *Newton* (2025). DOI: `10.1016/j.newton.2025.100108`.

[22]   Gordon H. Y. Li, Midya Parto, Jinhao Ge, Qing-Xin Ji, Maodong Gao, Yan Yu, James Williams, Robert M. Gray, Christian R. Leefmans, Nicolas Englebert, et al. "All-optical computing with beyond 100-GHz clock rates." In: *arXiv preprint arXiv:2501.05756* (2025). DOI: `10.48550/arXiv.2501.05756`.

[23]   Cristian Manzoni, Oliver D. Mücke, Giovanni Cirmi, Shaobo Fang, Jeffrey Moses, Shu-Wei Huang, Kyung-Han Hong, Giulio Cerullo, and Franz X. Kärtner. "Coherent pulse synthesis: Towards sub-cycle optical waveforms." In: *Laser & Photonics Reviews* 9.2 (2015), pp. 129–171. DOI: `https://doi.org/10.1002/lpor.201400181`. eprint: `https://onlinelibrary.wiley.com/doi/pdf/10.1002/lpor.201400181`. URL: `https://onlinelibrary.wiley.com/doi/abs/10.1002/lpor.201400181`.

[24]   Linn F. Mollenauer, Roger H. Stolen, and James P. Gordon. "Experimental observation of picosecond pulse narrowing and solitons in optical fibers." In: *Physical Review Letters* 45.13 (1980), p. 1095.

[25]   John M. Dudley, Goëry Genty, and Stéphane Coen. "Supercontinuum generation in photonic crystal fiber." In: *Reviews of Modern Physics* 78.4 (2006), pp. 1135–1184.

[26]   Pierre Colman, Chad Husko, Sylvain Combrié, Isabelle Sagnes, Chee Wei Wong, and Alfredo De Rossi. "Temporal solitons and pulse compression in photonic crystal waveguides." In: *Nature Photonics* 4.12 (2010), pp. 862–868.

[27]   Andrea Blanco-Redondo, Chad Husko, Daniel Eades, Yanbing Zhang, Juntao Li, Thomas F. Krauss, and Benjamin J. Eggleton. "Observation of soliton compression in silicon photonic crystals." In: *Nature Communications* 5.1 (2014), p. 3160.

[28] Ju Won Choi, Byoung-Uk Sohn, George F. R. Chen, Doris K. T. Ng, and Dawn T. H. Tan. "Soliton-effect optical pulse compression in CMOS-compatible ultra-silicon-rich nitride waveguides." In: *APL Photonics* 4.11 (2019).

[29] Richard Oliver, Yoshitomo Okawachi, Xingchen Ji, Adrea R. Johnson, Alexander Klenner, Michal Lipson, and Alexander L. Gaeta. "Soliton-effect compression of picosecond pulses on a photonic chip." In: *Optics Letters* 46.18 (2021), pp. 4706–4709.

[30] Binbin Zhou, Andy Chong, Frank W. Wise, and Morten Bache. "Ultrafast and octave-spanning optical nonlinearities from strongly phase-mismatched quadratic interactions." In: *Physical Review Letters* 109.4 (2012), p. 043902.

[31] Hairun Guo, Xianglong Zeng, Binbin Zhou, and Morten Bache. "Few-cycle solitons and supercontinuum generation with cascaded quadratic nonlinearities in unpoled lithium niobate ridge waveguides." In: *Optics Letters* 39.5 (2014), pp. 1105–1108.

[32] Morten Bache, Jeffrey Moses, and Frank W. Wise. "Scaling laws for soliton pulse compression by cascaded quadratic nonlinearities." In: *Journal of the Optical Society of America B* 24.10 (2007), pp. 2752–2762.

[33] Curtis R. Menyuk, Roland Schiek, and Lluis Torner. "Solitary waves due to χ (2): χ (2) cascading." In: *Journal of the Optical Society of America B* 11.12 (1994), pp. 2434–2443.

[34] Morten Bache, Ole Bang, Jeffrey Moses, and Frank W. Wise. "Nonlocal explanation of stationary and nonstationary regimes in cascaded soliton pulse compression." In: *Optics Letters* 32.17 (2007), pp. 2490–2492.

[35] Xianglong Zeng, Satoshi Ashihara, Xianfeng Chen, Tsutomu Shimura, and Kazuo Kuroda. "Two-color pulse compression in aperiodically-poled lithium niobate." In: *Optics Communications* 281.17 (2008), pp. 4499–4503.

[36] Morten Bache, Ole Bang, Wieslaw Krolikowski, Jeffrey Moses, and Frank W. Wise. "Limits to compression with cascaded quadratic soliton compressors." In: *Optics Express* 16.5 (2008), pp. 3273–3287.

[37] Marc Jankowski, Jatadhari Mishra, and Martin M. Fejer. "Dispersion-engineered nanophotonics: A flexible tool for nonclassical light." In: *Journal of Physics: Photonics* 3.4 (2021), p. 042005.

[38] Luis Ledezma, Ryoto Sekine, Qiushi Guo, Rajveer Nehra, Saman Jahani, and Alireza Marandi. "Intense optical parametric amplification in dispersion-engineered nanophotonic lithium niobate waveguides." In: *Optica* 9.3 (2022), pp. 303–308. DOI: 10.1364/OPTICA.442332.

[39] Christopher R. Phillips, Carsten Langrock, Jason S. Pelc, Martin M. Fejer, Ingmar Hartl, and Martin E. Fermann. "Supercontinuum generation in quasi-phasematched waveguides." In: *Optics Express* 19.20 (Sept. 2011), pp. 18754–18773. ISSN: 1094-4087. DOI: `10.1364/OE.19.018754`. (Visited on 02/18/2019).

[40] Marc Jankowski, Carsten Langrock, Boris Desiatov, Marko Lončar, and Martin M. Fejer. "Supercontinuum generation by saturated second-order nonlinear interactions." In: *APL Photonics* 8.11 (2023).

[41] Yang Yue, Yuxi Fang, Wenpu Geng, and Changjing Bao. "SCG involving second-order nonlinearity." In: *Integrated Optical Supercontinuum Generation: Physics, Advances, and Applications*. Springer, 2024, pp. 141–160.

[42] Hao He, Michael J. Werner, and Peter D. Drummond. "Simultaneous solitary-wave solutions in a nonlinear parametric waveguide." In: *Physical Review E* 54.1 (1996), p. 896.

[43] Andrey A. Sukhorukov. "Approximate solutions and scaling transformations for quadratic solitons." In: *Physical Review E* 61.4 (2000), p. 4530.

[44] Alexander V. Buryak and Yuri S. Kivshar. "Spatial optical solitons governed by quadratic nonlinearity." In: *Optics Letters* 19.20 (1994), pp. 1612–1614.

[45] Yu N. Karamzin and Anatoly P. Sukhorukov. "Nonlinear interaction of diffracted light beams in a medium with quadratic nonlinearity: Mutual focusing of beams and limitation on the efficiency of optical frequency converters." In: *Journal of Experimental and Theoretical Physics Letters* 20.11 (1974), pp. 339–343.

[46] Qiushi Guo, Benjamin K. Gutierrez, Ryoto Sekine, Robert M. Gray, James A. Williams, Luis Ledezma, Luis Costa, Arkadev Roy, Selina Zhou, Mingchen Liu, et al. "Ultrafast mode-locked laser in nanophotonic lithium niobate." In: *Science* 382.6671 (2023), pp. 708–713. DOI: `10.1126/science.adj5438`.

[47] Mengjie Yu, David Barton III, Rebecca Cheng, Christian Reimer, Prashanta Kharel, Lingyan He, Linbo Shao, Di Zhu, Yaowen Hu, Hannah R Grant, et al. "Integrated femtosecond pulse generator on thin-film lithium niobate." In: *Nature* 612.7939 (2022), pp. 252–258.

[48] Olivier Gobert, Pierre-Mary Paul, Jean-François Hergott, Olivier Tcherbakoff, Fabien Lepetit, Pascal D'Oliveira, François Viala, and Michel Comte. "Carrier-envelope phase control using linear electro-optic effect." In: *Optics Express* 19.6 (2011), pp. 5410–5418.

[49] Gintaras Tamošauskas, Gvidas Beresnevičius, Darius Gadonas, and Audrius Dubietis. "Transmittance and phase matching of BBO crystal in the 3- 5 μm range and its application for the characterization of mid-infrared laser pulses." In: *Optical Materials Express* 8.6 (2018), pp. 1410–1418.

[50] Rick Trebino. *Frequency-resolved optical gating: The measurement of ultrashort laser pulses.* Springer Science & Business Media, 2012.

[51] Adam Wyatt. *Frequency-resolved optical gating (FROG).* June 6, 2023. URL: `https : / / www . mathworks . com / matlabcentral / fileexchange / 16235 - frequency - resolved - optical - gating-frog`.

[52] Steven Byrnes. *Frequency-resolved optical gating (FROG).* June 6, 2023. URL: `https : / / www . mathworks . com / matlabcentral / fileexchange / 34986 - frequency - resolved - optical - gating-frog`.

[53] Daniel J. Kane. "Real-time measurement of ultrashort laser pulses using principal component generalized projections." In: *IEEE Journal of Selected Topics in Quantum Electronics* 4.2 (1998), pp. 278–284.

[54] Daniel J. Kane. "Recent progress toward real-time measurement of ultrashort laser pulses." In: *IEEE Journal of Quantum Electronics* 35.4 (1999), pp. 421–431.

[55] Kenneth W. Delong, David N. Fittinghoff, and Rick Trebino. "Practical issues in ultrashort-laser-pulse measurement using frequency-resolved optical gating." In: *IEEE Journal of Quantum Electronics* 32.7 (1996), pp. 1253–1264.

[56] Justin Ratner, Günter Steinmeyer, Tsz Chun Wong, Randy Bartels, and Rick Trebino. "Coherent artifact in modern pulse measurements." In: *Optics Letters* 37.14 (2012), pp. 2874–2876.

[57] Charles Bourassin-Bouchet and Marie-Emmanuelle Couprie. "Partially coherent ultrafast spectrography." In: *Nature Communications* 6.1 (2015), p. 6465.

[58] Dorine Keusters, Howe-Siang Tan, Patrick O'Shea, Erik Zeek, Rick Trebino, and Warren S. Warren. "Relative-phase ambiguities in measurements of ultrashort pulses with well-separated multiple frequency components." In: *Journal of the Optical Society of America B* 20.10 (2003), pp. 2226–2237.

[59] Robert W. Boyd. *Nonlinear Optics.* 3rd ed. Cambridge, Massachusetts: Academic Press, 2008.

[60] Yuri S. Kivshar and Govind P. Agrawal. *Optical solitons: From fibers to photonic crystals.* Academic Press, 2003.

[61] Alexander V. Buryak, Paolo Di Trapani, Dmitry V. Skryabin, and Stefano Trillo. "Optical solitons due to quadratic nonlinearities: From basic physics to futuristic applications." In: *Physics Reports* 370.2 (2002), pp. 63–235.

[62] Allan D. Boardman, Kang Xie, and Anil Sangarpaul. "Stability of scalar spatial solitons in cascadable nonlinear media." In: *Physical Review A* 52.5 (1995), p. 4099.

Chapter 6

ENERGY-EFFICIENT ULTRASHORT-PULSE CHARACTERIZATION USING NANOPHOTONIC PARAMETRIC AMPLIFICATION

Thomas Zacharias[*], **Robert Gray**[*], Ryoto Sekine, James Williams, Selina Zhou, and Alireza Marandi. "Energy-efficient ultrashort-pulse characterization using nanophotonic parametric amplification." In: *ACS Photonics* 12.3 (2025), pp. 1316–1320. DOI: `10.1021/acsphotonics.4c02620`.

6.1 Introduction

Ultrafast integrated photonics aims to bring the advantages of ultrashort pulses largely limited to expensive, bulky optical systems to scalable, compact nanophotonic platforms [1]. Developments in this field have so far been focused on either generating ultrafast pulses on-chip [2–5] or on leveraging ultrashort pulses for applications in time-keeping [6], quantum information processing [7], and computing [8]. Demonstrations of ultrashort pulse characterization techniques on nanophotonic platforms [9, 10] have been limited due to the requirements of strong optical nonlinearity and the non-collinear nature of many typical pulse characterization techniques. Ultrashort pulse characterization is a critical tool for leveraging the unique properties of ultrashort pulses - short pulse width, high peak power, and high repetition rate - for probing ultrafast phenomena [11], enhancing nonlinear interactions [12], and increasing information density for ultrafast information processing [13]. Developing ultrashort pulse characterization techniques in nanophotonics is an important step toward developing integrated ultrafast photonic systems. Additionally, the challenges associated with off-chip temporal characterization, weak pulse energies, and temporal distortions resulting from pulse extraction necessitate the need for energy-efficient ultrashort on-chip pulse characterization techniques.

Here, we experimentally demonstrate a novel pulse characterization technique compatible with integrated photonics for energy-efficient on-chip pulse characterization. Our technique uses dispersion-engineered OPAs in lithium niobate nanophotonic waveguides combined with a FROG-based retrieval algorithm [14] for on-chip pulse characterization. XFROG based on non-collinear OPAs has been previously demon-

strated in bulk optics as one of the most sensitive ultrashort pulse characterization techniques [15]. However, its non-collinear nature makes it incompatible with nanophotonics motivating the need for a modified measurement technique [16–19]. Additionally, fJ pulse characterization using the bulk OPA-XFROG has required tens of μJ of gate pulse energies [15, 20]. Here, we overcome these limitations by operating in the degenerate and collinear regime, making our technique compatible with nanophotonic realization. Moreover, on-chip degenerate OPAs provide unparalleled gain, especially in nanophotonic lithium niobate with low-energy pump pulses [21]. A combination of the spatial mode confinement due to the waveguides and temporal mode confinement due to dispersion engineering enables gain-bandwidth levels unavailable to bulk crystals. This results in operating the degenerate OPA (DOPA)-XFROG using a fraction of the pump energy compared to the bulk counterpart. Our scheme paves the way toward the measurement of ultrashort-ultraweak optical pulses that were not possible with bulk crystals.

6.2 Methods

Principle of Operation for DOPA-XFROG

The FROG [14] uses an iterative 2D phase-retrieval algorithm to recover the intensity and phase of an unknown optical field from an intensity spectrogram. The phase retrieval uses a generalized projections optimization algorithm that iteratively searches for the electric field that can create the intensity spectrogram while satisfying an optical nonlinearity constraint. In our DOPA-XFROG, the optical nonlinearity is defined by the degenerate optical parametric amplification process which can be mathematically modeled as

$$E^{DOPA}(t,\tau) = E(t)\cosh(\kappa|G(t-\tau)|) + iE^*(t)\sinh(\kappa|G(t-\tau)|)\exp(i\angle G(t-\tau)),$$

$$(6.1)$$

where $E^{DOPA}(t,\tau)$ is the pulse field resulting from the nonlinear process, $E(t)$ is the unknown signal pulse field to be measured, $G(t)$ is the known gate pulse field that pumps the OPA, and τ is the time delay between the signal and the pump. $\kappa^2 = \frac{2\omega_s^2 d_{eff}^2 z^2}{n_s^2 n_p \epsilon_0 c^3 A_{eff}}$ is the gain parameter for the OPA where $d_{eff} = \frac{2}{\pi}d_{33}$ is the effective nonlinear coefficient [21], z is the length of the nonlinear interaction process, and n_s, n_p are the effective indices of the signal and pump, respectively. The carrier frequency of the gate pulse is twice that of the unknown pulse. The degenerate OPA process is sensitive to the relative phase of the signal and gate pulses which

determines whether the signal to be measured is amplified through parametric gain or deamplified through second harmonic generation. The dependence of the OPA process on the relative signal and gate phases within the order of an optical cycle makes the output field sensitive to experimental fluctuations. These include non-idealities such as stage nonrepeatability and nonlinearity, timing jitter, temperature fluctuations, alignment fluctuations, etc. These fluctuations are calibrated using a modified spectrogram measurement technique that allows for the simultaneous collection of a calibration signal. The spectrogram is created by continuously scanning the stage while detecting the output signal one frequency component at a time on an optical spectrum analyzer. The output signal is simultaneously collected in a slow detector that acts as the calibration signal. The slow detector is expected to see the same signal for each consecutive scan of the delay stage and can therefore be used for calibration. The calibrated spectrogram can then be passed through the custom DOPA-XFROG algorithm for pulse retrieval.

The custom recovery algorithm uses generalized projections algorithm [14] to enforce the mathematical constraint defined in Eq. 6.1 through iterative gradient descent. The corresponding gradients were analytically derived from Eq. 6.1 and can be found in Section 6.5. Equation 6.1 accurately models the amplification process when operating in the quasistatic regime - where dispersion and walk-off are negligible. Dispersion-engineering, unavailable in bulk crystals, achieved through precise control over waveguide geometry enables operating nanophotonic OPAs in the quasistatic regime [21, 22] thus ensuring the validity of Eq. 6.1.

Device Design and Fabrication

The design and fabrication of the dispersion-engineered nanophotonic OPA used here follow the techniques described in [21]. The waveguides were designed to have minimal dispersion and walk-off between the signal at 2090 nm and the pump at 1045 nm. The waveguides were fabricated on a 704-nm thin film of lithium niobate on a silica substrate and were measured using atomic force microscopy to have a top width of 1790 nm and an etch depth of 330 nm.

The etched waveguide geometry was simulated using Lumerical to estimate a group velocity mismatch between 1045 nm and 2090 nm of 1.7 fs/mm, group velocity dispersion around 2090 nm of -3 fs^2/mm, group velocity dispersion around 1045 nm of 54 fs^2 /mm (see Fig. 6.1). The total length of the waveguide was 10 mm with a 4-mm-long periodically poled region and a 5.2 µm poling period. The OPA
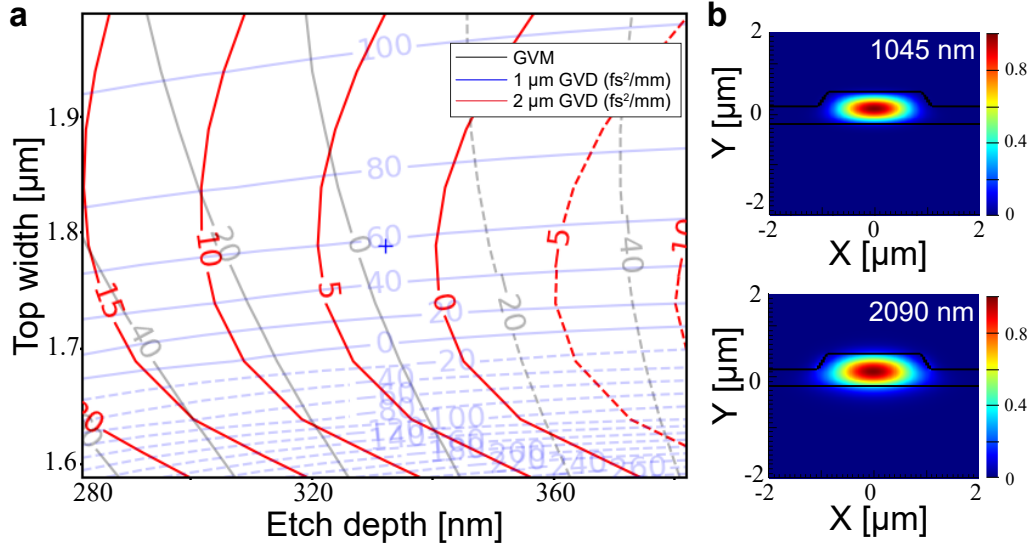
Figure 6.1: **Device design. a**, Simulated GVM between 1045 nm and 2090 nm, GVD at 1045 nm, and GVD at 2090 nm while scanning for different top widths and etch depths. The blue cross corresponds to the dimensions of the etched waveguide. **b**, Electric field profiles of the fundamental TE modes at pump and signal wavelengths.

was measured to have a gain of 188 dB/cm and bandwidth of 40.5 THz for a ~4-pJ, 100-fs pump pulse using the techniques described in [21].

Experimental Scheme
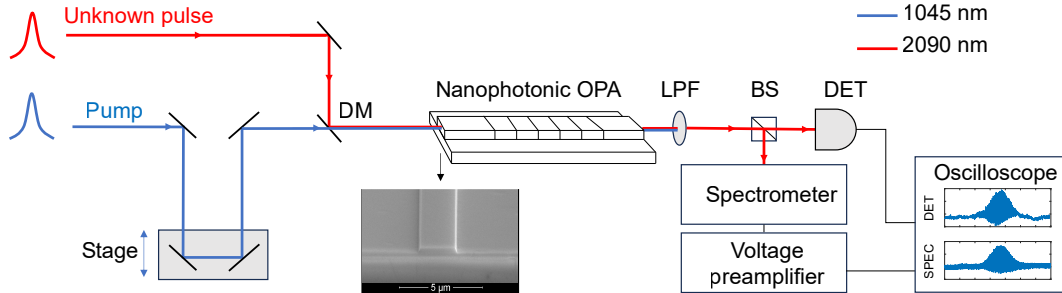
Figure 6.2: **Experimental setup.** DM, Dichroic Mirror; OPA, Optical Parametric Amplifier; LPF, Low Pass Filter; BS, Beam Splitter; DE, Detector. Inset: Scanning electron microscope image of chip facet

Figure 6.2 shows the experimental setup used for DOPA-XFROG. A 100-fs mode-locked fiber laser centered at 1045 nm pumps a home-built optical parametric oscillator (OPO) and the DOPA-XFROG. The output of the OPO is at 2090 nm which is used as the "unknown pulse" to be characterized. Both the pump and OPO

output are characterized with a traditional table-top XFROG to create the reference pulses seen in Fig. 6.4 (right). The unknown pulse is gated by the pump in the nanophotonic OPA for different delays controlled by a linearized motor stage. The resulting signal from the OPA is low-pass filtered and collected in a spectrometer and slow detector. The stage is set to scan continuously and the spectrometer measures the spectrum as a function of delay one wavelength component at a time from 1790 nm to 2390 nm with a 2 nm resolution. The analog output of the spectrometer is amplified using a voltage preamplifier and sent to an oscilloscope. The signal collected by the slow detector used for calibration during postprocessing is also sent to the same oscilloscope. The oscilloscope is set to trigger data collection when the slow detector signal passes a threshold voltage level indicating temporal overlap of the two pulses for each scan of the delay stage. The spectrometer updates the collected wavelength center between subsequent scans by increments of 2 nm. The detector and spectrometer traces are saved on the oscilloscope for each stage scan to create the calibration matrix and raw spectrogram.
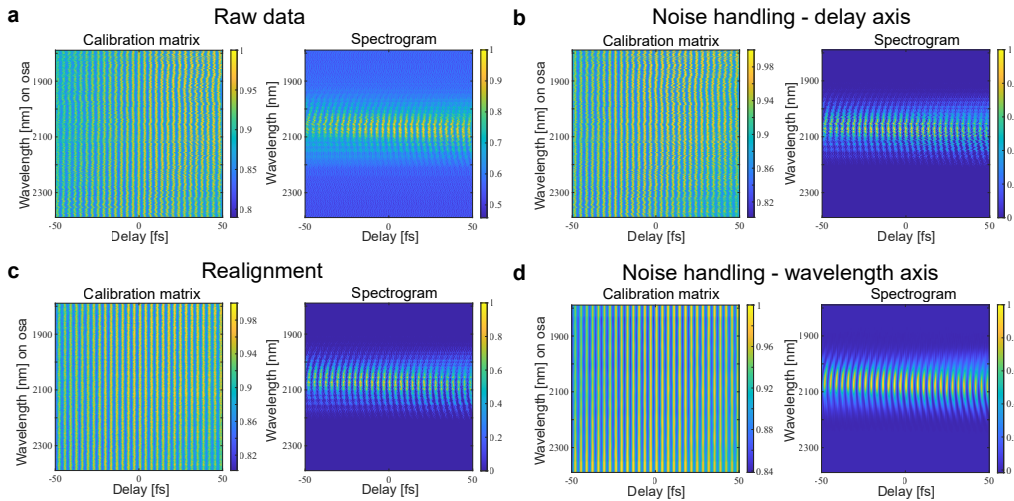
Figure 6.3: **Postprocessing.** Each sub-panel displays the calibration matrix created from the detector signal and the spectrogram created from the spectrometer signal at each step of the postprocessing. **a**, Raw data collected from the experimental measurement. **b**, Matrices after lowpass filtering along the delay axes for both the matrices and thresholding the spectrogram. **c**, Result of realignment and linearization. **d**, Result of lowpass filtering the wavelength axis and renormalization.

Figure 6.3 illustrates the postprocessing algorithm used for calibrating the spectrogram. The calibration process includes noise handling and realignment. The noise handling accounts for electronic noise and optical power fluctuations and is achieved

through low-pass filtering, thresholding, and renormalization. The realignment procedure accounts for optical phase variations caused by timing jitter between pulses, stage non-repeatability/nonlinearity, etc. Additional details about the postprocessing can be found in Section 6.5. The calibrated spectrogram (Fig. 6.3d, right) can now be used with the DOPA-XFROG recovery algorithm to recover the intensity and phase of the unknown pulse.

6.3   Results
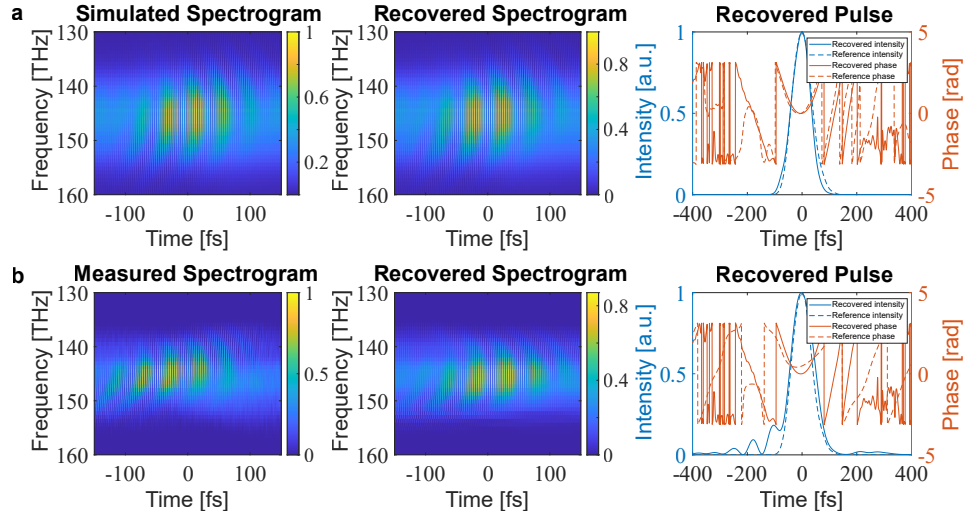
Figure 6.4: **DCOPA-XFROG results. a**, Simulation results. (Left) Simulated spectrogram for a reference pulse. (Center) Recovered spectrogram using DOPA-XFROG algorithm. (Right) Comparison of recovered pulse profile with reference pulse. **b**, Experimental results. (Left) Experimentally measured spectrogram. (Center) Recovered spectrogram using DOPA-XFROG algorithm. (Right) Comparison of recovered pulse profile with expected profile (measured with a tabletop FROG).

The custom algorithm was tested by simulating the DOPA-XFROG. Figure 6.4a (left) shows a spectrogram simulated using the experimental pulse profiles (measured using a standard tabletop XFROG) and the nonlinear equation defined by Eq. 6.1. This spectrogram was passed through the custom recovery algorithm which converged to the recovered spectrogram in Fig. 6.4a (center) with an RMS error of 0.00048 after 250 iterations. The intensity and phase of the recovered field along with the expected profile for comparison are displayed in Fig. 6.4a (right). The phase-sensitive nature of the process can be seen in the intensity spectrogram in the form of periodic fringes. The frequency dependence of the fringe locations marked by the curvature along the frequency axes in the intensity spectrogram is a sign of using chirped pulses.

Figure 6.4b (left) shows the experimentally measured spectrogram after postprocessing using a ~ 1-fJ pulse at 2090 nm gated with ~ 60-fJ pulse at 1045 nm. The pulse energies were estimated on-chip using the previously demonstrated input coupling characterization technique [21]. The spectrogram was passed to the DOPA-XFROG algorithm which recovered the spectrogram displayed in Fig. 6.4b (center) after 500 iterations with an error of 0.003. Figure 6.4b (right) shows a comparison of the recovered pulse intensity and phase with the expected pulse profile. Figure 6.4 demonstrates that the DOPA-XFROG can successfully characterize ultrashort pulses. The performance of DOPA-XFROG — retrieval accuracy, measurement time, postprocessing complexity, and energy efficiency — could be improved by eliminating the calibration process by using a fast spectrometer and improving fabrication capabilities to achieve higher nonlinear conversion efficiencies.

6.4 Discussion

We developed a novel pulse characterization technique, named DOPA-XFROG, and demonstrated how it can be used for ultrafast pulse measurements in a nanophotonic lithium niobate chip. The spatio-temporal confinement of dispersion-engineered nanophotonics enables leveraging the high gain-bandwidth OPAs for energy-efficient pulse characterization using weak gate pulses. Measurements of fJ pulses in bulk OPA-XFROG setups typically required tens of μJ of gate pulse energies [15, 20]. In comparison, we demonstrate pulse characterization of ~ 1-fJ pulses using gate pulses with energy as low as ~ 60-fJ.

Attempts at experimentally measuring weaker pulses are currently limited by parasitic nonlinear effects resulting from pump depletion. Measurement of weaker pulses requires a stronger unsaturated gain to measure an intensity spectrogram with a similar signal-to-noise ratio as the one obtained for the ~ 1 fJ pulse measurement demonstrated here. However, pumping with stronger optical pulses in our nanophotonic waveguides results in optical pump depletion resulting in a deviation from the mathematical model defined in Eq. 1. Since the nonlinear constraint is no longer valid in the algorithm, the recovery algorithm can-not be used for this case. Using shorter OPAs with larger pump pulse energies may enable the measurement of sub-atto-Joule pulses on-chip. This technique could be especially useful for system integration where a small amount of pulse energy could be tapped from a highly integrated photonic circuit for further on-chip pulse characterization.

6.5 Supporting Information

Detailed Workflow

Figure 6.5 describes the workflow for the DOPA-XFROG experiment. Figure 6.5a displays the experimental setup described in Section 6.2. Traditionally, FROGs generate the spectrogram by sequentially measuring the entire spectrum for different gate delays. However, the phase-sensitive nature of the amplification process necessitates a modified spectrogram measurement technique. The modified measurement technique requires iteratively recording single frequency components as a function of the gate delay instead of the typical measurement of the entire spectrum for single gate delay values. This technique requires an additional calibration signal collected using a slow detector that is used to stitch the distinct frequency components together to create a spectrogram. The detector and spectrometer traces are saved on the oscilloscope for each stage scan to create the calibration matrix and raw spectrogram in Fig. 6.5b (left). The calibration matrix and raw spectrogram are then passed through the postprocessing algorithm described in Section 6.5 which produces a calibrated spectrogram (Fig. 6.5b, right). The calibrated spectrogram can now be used with the DOPA-XFROG recovery algorithm to recover the intensity and phase of the unknown pulse (See Fig. 6.5c).

Postprocessing

The degenerate parametric amplification process is sensitive to the phase difference between the carrier frequencies of the unknown signal and the known gate pulse. This results in the nonlinear process being extremely sensitive to experimental variations such as timing jitter between pulses, path length differences caused by thermal fluctuations, alignment variations, stage non-repeatability/non-linearity, etc. This phase sensitivity makes it challenging to record a reliable spectrogram using the standard FROG technique due to the slow nature of the measurement.

To account for these experimental variations, we use a variation of the traditional FROG measurement technique that allows us to generate a calibration signal. In a standard FROG, the intensity spectrogram is generated by recording all frequency components simultaneously for each distinct delay value in an iterative manner. This would be equivalent to iteratively filling each column in the spectrogram. Here, we record all the delay values for each distinct frequency component in an iterative manner (in other words, iteratively filling each row in the spectrogram). This is done experimentally by scanning the stage and recording the output signal one frequency component at a time. Experimentally this was done by sequentially
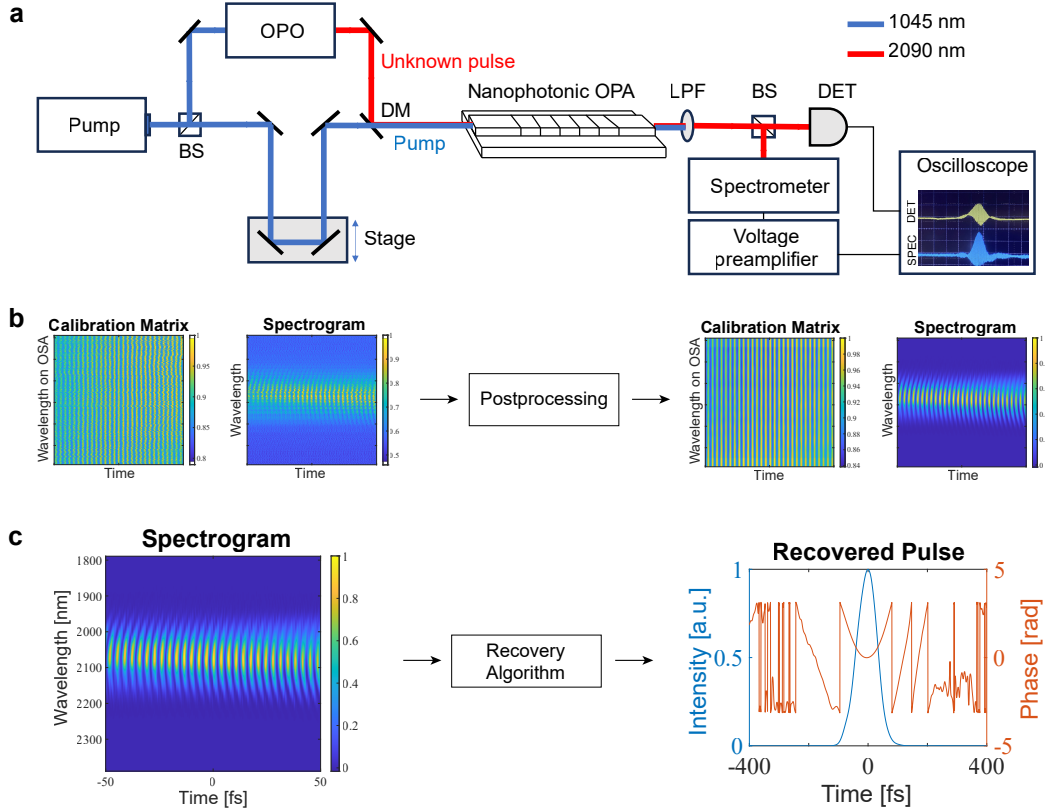
Figure 6.5: **Detailed workflow. a**, Detailed experimental setup. BS, Beam Splitter; OPO, Optical Parametric Oscillator; DM, Dichroic Mirror; OPA, Optical Parametric Amplifier; LPF, Low Pass Filter; DET, Detector. **b**, The calibration matrix, consisting of the measured detector signal, calibrates the spectrogram in postprocessing. **c**, The processed spectrogram is passed through the recovery algorithm for pulse retrieval.

measuring contributions to wavelengths from 1890 nm to 2390 nm with a bandwidth of 2 nm. This allows us to use an additional slow detector that can be used as a calibration tool.

In an ideal case, the slow detector would be expected to record the same signal from one iteration to the next. Any variations in the recorded signal can hence be attributed to experimental fluctuations that can now be calibrated for. The calibration process includes noise handling and realignment. The noise handling accounts for electronic noise, optical power fluctuations, and is achieved through low-pass filtering, thresholding, and renormalization. The realignment procedure accounts for optical phase variations that can be caused due to timing jitter between pulses, stage nonrepeatability/nonlinearity, etc. The phase variations appear as

nonrepeating rows in the calibration matrix. These variations are calibrated for by compensating for them from one iteration to the next in the calibration matrix and applying the identical changes to the corresponding spectrogram. This is done in two steps - we first realign the carrier and the envelope of each row of the calibration matrix to the first row. We then linearize the calibration matrix by interpolating the peaks and troughs of each row to be the expected distance of $\pi/2$ apart (where 2π corresponds to one optical cycle at the signal wavelength). This $\pi/2$ difference is analytically true only for transformed limited pulses. However, for dispersed pulses, the distance between an adjacent peak and trough was heuristically found to be close to $\pi/2$ through simulations. Additionally, the overdetermined [14] nature of the FROG retrieval algorithm, enables the successful retrieval of chirped pulses even with this transformation. Figure 6.1 describes the postprocessing workflow. Each panel contains the calibration matrix (detector signal) and the corresponding spectrogram. Fig. 6.1a shows a zoomed-in version of the raw data that is collected from the measurement. Notice the variations between the different rows of the calibration matrix. Fig. 6.1b shows the calibration matrix and spectrogram after low pass filtering the delay axis of both matrices and thresholding the spectrogram. The threshold for the spectrogram was set to the maximum value at 1800 nm (which determines the spectrometer noise level since no signal is expected). The calibration matrix and corresponding spectrogram values are then realigned and linearized and are displayed in Fig. 6.1c. Finally, the matrices are passed through a low pass filter along the frequency axis resulting in Fig. 6.1d.

6.6 Gradient Descent

As mentioned in Section 6.2, the OPA process can be mathematically modeled as follows

$$
E^{DOPA}(t, \tau) = E(t) \cosh(\kappa |G(t - \tau)|)
$$
$$
+ iE^*(t) \sinh(\kappa |G(t - \tau)|) \exp(i\angle G(t - \tau)) \quad (6.2)
$$

where $E^{DOPA}(t, \tau)$ is the pulse emerging from the degenerate amplification process, $E(t)$ is the unknown signal pulse to be measured, $G(t)$ is the gate pulse that pumps the OPA, and τ is the time delay between the signal and the pump. $\kappa = \frac{2zd_{eff}\omega^2}{kc^2}$ is the gain parameter for the OPA where d_{eff} is the nonlinear coefficient, z is the length of the OPA, and ω, k are the angular frequency and wavenumber of the signal, respectively.

The recovery algorithm follows the standard generalized projects algorithm [14] with a modified loss function to account for the new nonlinearity constraint. The loss function, Z, can be written as

$$Z_{DOPA} = \sum_{i,j=1}^{N} |E_{DOPA}^{(k)}(t_i, \tau_j) - E_{DOPA}^{(k+1)}(t_i, \tau_j)|^2 \tag{6.3}$$

where $E_{DOPA}^{(k)}(t_i, \tau_j)$ is the complex interferogram from the kth iteration. The goal is to find the electric field $E^{(k+1)}(t)$ that satisfies the nonlinearity condition defined in Eq. 6.2 and minimizes the functional distance Z_{DOPA}.

The minimization is performed through gradient descent for which the gradient $-\partial Z/\partial E^{(k+1)}(t_i)$ were calculated analytically for the real and imaginary parts to be

$$\frac{\partial Z_{DOPA}}{\partial Re\{E(t_l^{(k+1)})\}} = \sum_{j=1}^{N} (-E_{DOPA}^{*(k)}(t_l, \tau_j) f(t_l - \tau_j) - E_{DOPA}^{*(k)}(t_l, \tau_j) g(t_l - \tau_j))$$
$$+ E^{*(k+1)}(t_l)|f(t_l - \tau_j)|^2 + E^{*(k+1)}(t_l) f^*(t_l - \tau_j) g(t_l - \tau_j)$$
$$+ E^{(k+1)}(t_l) g^*(t_l - \tau_j) f(t_l - \tau_j) + E^{(k+1)}(t_l)|g(t_l - \tau_j)|^2)$$
$$+ c.c.,$$

$$\frac{\partial Z_{DOPA}}{\partial Im\{E(t_l^{(k+1)})\}} = \sum_{j=1}^{N} (-iE_{DOPA}^{*(k)}(t_l, \tau_j) f(t_l - \tau_j) + iE_{DOPA}^{*(k)}(t_l, \tau_j) g(t_l - \tau_j))$$
$$+ iE^{*(k+1)}(t_l)|f(t_l - \tau_j)|^2 - iE^{*(k+1)}(t_l) f^*(t_l - \tau_j) g(t_l - \tau_j)$$
$$+ iE^{(k+1)}(t_l) g^*(t_l - \tau_j) f(t_l - \tau_j) - iE^{(k+1)}(t_l)|g(t_l - \tau_j)|^2)$$
$$+ c.c.,$$

$$\tag{6.4}$$

respectively, where $f(t) = \cosh(\kappa|G(t)|)$ and $g(t) = i \sinh(\kappa|G(t)|) \exp(i\angle G(t))$ have been used as variables for simplification.

BIBLIOGRAPHY

[1] Lin Chang, Songtao Liu, and John E. Bowers. "Integrated optical frequency comb technologies." In: *Nature Photonics* 16.2 (2022), pp. 95–108.

[2] Qiushi Guo, Benjamin K. Gutierrez, Ryoto Sekine, Robert M. Gray, James A. Williams, Luis Ledezma, Luis Costa, Arkadev Roy, Selina Zhou, Mingchen Liu, et al. "Ultrafast mode-locked laser in nanophotonic lithium niobate." In: *Science* 382.6671 (2023), pp. 708–713. DOI: 10.1126/science.adj5438.

[3] Mengjie Yu, David Barton III, Rebecca Cheng, Christian Reimer, Prashanta Kharel, Lingyan He, Linbo Shao, Di Zhu, Yaowen Hu, Hannah R Grant, et al. "Integrated femtosecond pulse generator on thin-film lithium niobate." In: *Nature* 612.7939 (2022), pp. 252–258.

[4] Michael L. Davenport, Songtao Liu, and John E. Bowers. "Integrated heterogeneous silicon/III–V mode-locked lasers." In: *Photonics Research* 6.5 (2018), pp. 468–478.

[5] Zhiquan Yuan, Maodong Gao, Yan Yu, Heming Wang, Warren Jin, Qing-Xin Ji, Avi Feshali, Mario Paniccia, John Bowers, and Kerry Vahala. "Soliton pulse pairs at multiple colours in normal dispersion microresonators." In: *Nature Photonics* 17.11 (2023), pp. 977–983.

[6] Zachary L. Newman, Vincent Maurice, Tara Drake, Jordan R. Stone, Travis C Briles, Daryl T. Spencer, Connor Fredrick, Qing Li, Daron Westly, Bojan R. Ilic, et al. "Architecture for the photonic integration of an optical atomic clock." In: *Optica* 6.5 (2019), pp. 680–685.

[7] Rajveer Nehra, Ryoto Sekine, Luis Ledezma, Qiushi Guo, Robert M. Gray, Arkadev Roy, and Alireza Marandi. "Few-cycle vacuum squeezing in nanophotonics." In: *Science* 377.6612 (2022), pp. 1333–1337. DOI: 10.1126/science.abo6213.

[8] Qiushi Guo, Ryoto Sekine, Luis Ledezma, Rajveer Nehra, Devin J. Dean, Arkadev Roy, Robert M. Gray, Saman Jahani, and Alireza Marandi. "Femtojoule femtosecond all-optical switching in lithium niobate nanophotonics." In: *Nature Photonics* 16.9 (2022), pp. 625–631. DOI: 10.1038/s41566-022-01071-2.

[9] Huakang Yu, Yipeng Lun, Jintian Lin, Yantong Li, Xingzhao Huang, Bodong Liu, Wanling Wu, Chunhua Wang, Ya Cheng, Zhi-yuan Li, et al. "Frequency-resolved optical gating in transverse geometry for on-chip optical pulse diagnostics." In: *Laser & Photonics Reviews* 17.12 (2023), p. 2201017.

[10] Alessia Pasquazi, Marco Peccianti, Yongwoo Park, Brent E. Little, Sai T. Chu, Roberto Morandotti, José Azaña, and David J. Moss. "Sub-picosecond phase-sensitive optical pulse characterization on a chip." In: *Nature Photonics* 5.10 (2011), pp. 618–623.

[11] Claudius Riek, Philipp Sulzer, Maximilian Seeger, Andrey S. Moskalenko, Guido Burkard, Denis V. Seletskiy, and Alfred Leitenstorfer. "Subcycle quantum electrodynamics." In: *Nature* 541.7637 (2017), pp. 376–379.

[12] Martin Wegener. *Extreme nonlinear optics: An introduction.* Advanced Texts in Physics. Springer Berlin Heidelberg, 2006. ISBN: 9783540266884. URL: `https://books.google.com/books?id=pZI0erZXgdcC`.

[13] Gordon H. Y. Li, Christian R Leefmans, James Williams, Robert M. Gray, Midya Parto, and Alireza Marandi. "Deep learning with photonic neural cellular automata." In: *Light: Science & Applications* 13.1 (2024), p. 283. DOI: `10.1038/s41377-024-01651-7`.

[14] Rick Trebino. *Frequency-resolved optical gating: The measurement of ultrashort laser pulses.* Springer Science & Business Media, 2012.

[15] Jing-yuan Zhang, Aparna Prasad Shreenath, Mark Kimmel, Erik Zeek, Rick Trebino, and Stephan Link. "Measurement of the intensity and phase of attojoule femtosecond light pulses using optical-parametric-amplification cross-correlation frequency-resolved optical gating." In: *Optics Express* 11.6 (2003), pp. 601–609.

[16] Gero Stibenz and Günter Steinmeyer. "Interferometric frequency-resolved optical gating." In: *Optics Express* 13.7 (2005), pp. 2617–2626.

[17] Houxun Miao, Shang-Da Yang, Carsten Langrock, Rostislav V. Roussev, Martin M. Fejer, and Andrew M. Weiner. "Ultralow-power second-harmonic generation frequency-resolved optical gating using aperiodically poled lithium niobate waveguides." In: *Journal of the Optical Society of America B* 25.6 (2008), A41–A53.

[18] Houxun Miao, Andrew M. Weiner, Carsten Langrock, Rostislav V. Roussev, and Martin M. Fejer. "Polarization-insensitive ultralow-power second-harmonic generation frequency-resolved optical gating." In: *Optics Letters* 32.7 (2007), pp. 874–876.

[19] Shang-Da Yang, Andrew M. Weiner, Krishnan R. Parameswaran, and Martin M. Fejer. "Ultrasensitive second-harmonic generation frequency-resolved optical gating by aperiodically poled LiNbO 3 waveguides at 1.5 μm." In: *Optics Letters* 30.16 (2005), pp. 2164–2166.

[20] Jing-Yuan Zhang, Chao-Kuei Lee, Jung Y Huang, and Ci-Ling Pan. "Sub femto-joule sensitive single-shot OPA-XFROG and its application in study of white-light supercontinuum generation." In: *Optics Express* 12.4 (2004), pp. 574–581.

[21]   Luis Ledezma, Ryoto Sekine, Qiushi Guo, Rajveer Nehra, Saman Jahani, and Alireza Marandi. "Intense optical parametric amplification in dispersion-engineered nanophotonic lithium niobate waveguides." In: *Optica* 9.3 (2022), pp. 303–308. DOI: 10.1364/OPTICA.442332.

[22]   Marc Jankowski, Nayara Jornod, Carsten Langrock, Boris Desiatov, Alireza Marandi, Marko Lončar, and Martin M. Fejer. "Quasi-static optical parametric amplification." In: *Optica* 9.3 (2022), pp. 273–279.

Chapter 7

MULTI-OCTAVE FREQUENCY COMB FROM AN ULTRA-LOW-THRESHOLD NANOPHOTONIC PARAMETRIC OSCILLATOR

Ryoto Sekine[*], **Robert M. Gray**[*], Luis Ledezma, Selina Zhou, Qiushi Guo, and Alireza Marandi. "Multi-octave frequency comb from an ultra-low-threshold nanophotonic parametric oscillator." In: *arXiv preprint arXiv:2309.04545* (2023). DOI: 10.48550/arXiv.2309.04545.

7.1   Introduction

Broadband optical frequency combs are among the great achievements of modern optics [1, 2]. Recently, increasing efforts are focused on the realization of broadband frequency combs in nanophotonic platforms [3–5] with applications including dual-comb spectroscopy [6], optical communications [7], optical frequency synthesis [8, 9], and laser ranging [10]. However, the spectral coverage of integrated frequency comb sources remains far behind their table-top counterparts using high-pulse-energy lasers and discrete components, which have recently surpassed six-octave spectra [11, 12]. Such multi-octave frequency combs are valuable for applications such as ultrashort pulse synthesis [13], attosecond science [14], and bio-chemical sensing and imaging [15–17].

Integrated sources of short-pulse frequency combs typically generate picojoules or femtojoules of pulse energies [2, 4, 18–20] and their spectral coverage barely reaches an octave [21, 22]. This has necessitated further spectral broadening stages for many applications, which so far have been realized strictly using table-top systems with discrete amplifiers and components [1, 8, 23]. A femtojoule-level multi-octave coherent spectral broadening mechanism has so far been beyond the reach of current photonic technologies, and hence, a path towards a fully integrated multi-octave frequency comb has remained elusive.

Substantial spectral broadening is typically achieved by passing femtosecond or picosecond pulses with 0.1-10 nJ of energy through waveguides, crystals or fibers with quadratic ($\chi^{(2)}$) or Kerr ($\chi^{(3)}$) nonlinearity with various designs [1, 24–28]. Among these schemes, waveguides with quadratic nonlinearity are becoming increasingly

more efficient, especially because of the recent progress on quasi-phase matching and dispersion engineering [24, 26, 29] and show superior performances over their cubic counterparts. However, to reach an octave of coherent spectrum and beyond they still need 10's of picojoules of energy [29], which is far beyond the current capability of integrated frequency comb sources.

Resonant enhancement of spectral broadening is expected to improve the energy requirements. However, such experiments have so far remained below an octave [23, 30, 31]. This is mainly because of the overly constrained dispersion requirements of cubic coherent spectral broadening schemes especially when combined with high-Q requirements. In fact, even linear components in nanophotonics with multi-octave spectral response are still challenging to design and realize [32]. In contrast, quadratic nonlinearity not only leads to lower energy requirements in single-pass configurations, but it also offers a wider range of nonlinear processes for ultrawide coherent spectral broadening resulting from nonlinear interactions of distant portions of the spectrum [11, 12]. However, a proper resonator design is necessary to enable an operation regime where a sequence of quadratic nonlinear processes can yield coherent spectral broadening towards multi-octave operation.

A promising path towards such a multi-octave nonlinear resonator is based on synchronously (sync-) pumped degenerate OPOs, which so far have been successfully used in bulk optics for efficient phase-locked down-conversion via half-harmonic generation of broadband frequency combs [15, 33–36]. Recent studies indicate the potential of sync-pumped OPOs for extreme pulse shortening and spectral broadening while preserving the coherence properties of the pump [37]. However, lack of dispersion engineering in bulk nonlinear crystals, low parametric gain bandwidths, and multi-picojoule thresholds have put limitations on their applicability for compact and ultrabroadband frequency comb applications. Recent developments of dispersion-engineered OPAs [38] and narrowband sync-pumped OPOs [39] in lithium niobate nanophotonics promise a path towards overcoming these limitations and accessing a new regime of ultrabroadband ultra-low-energy nonlinear optics that has not been accessible before.

In this work, in sharp contrast to previous realizations of nonlinear photonic resonators, we judiciously design and realize an on-chip sync-pumped OPO featuring a low-finesse resonator which couples only frequencies near the half-harmonic of the pump while leaving the pump and its high-harmonics non-resonant. It is near-zero dispersion engineered for the pump and its half-harmonic. The nanophotonic sync-

pumped OPO operates with a record-low threshold of ~18 fJ. Due to its low-energy, intense, phase-sensitive amplification, we discovered an operation regime of the OPO where the nonlinear phase compensates the cavity detuning, yielding a multi-octave coherent spectrum. We measured a 2.6 octave frequency comb at ~121 fJ of pump energy and experimentally confirmed its coherence. We numerically replicate the broadband nonlinear dynamics associated with such a multi-octave broadening and provide design guidelines for even broader outputs.

7.2 Results

Operating Principle and Design
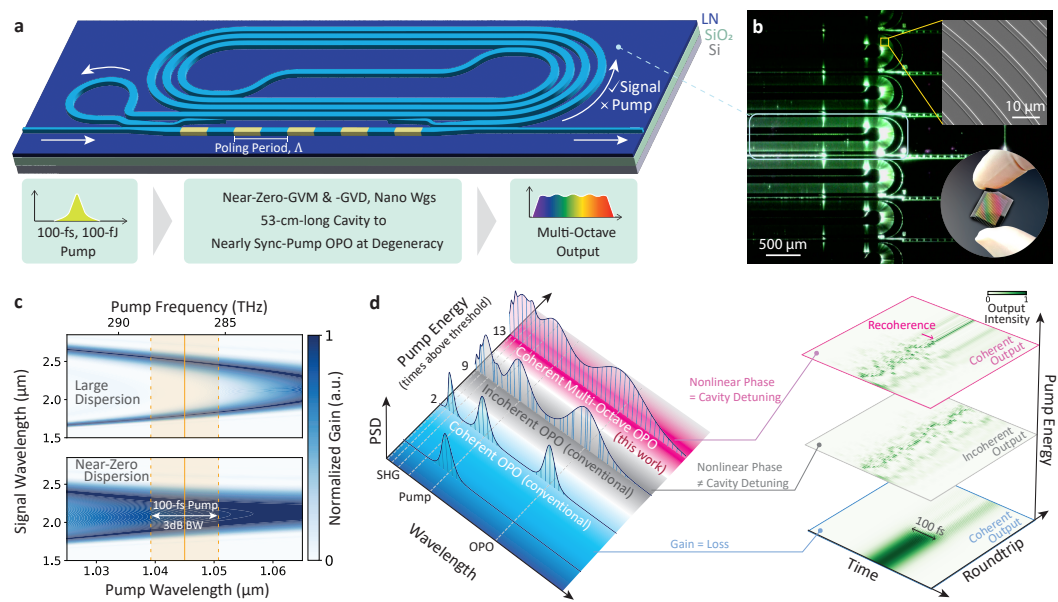
Figure 7.1: **Principle and design of the multi-octave nanophotonic OPO**. **a,** Illustration of the sync-pumped OPO on thin-film lithium niobate with key features highlighted. **b,** Microscope image of several devices when the one in the center is pumped at 1 μm. The chip glows green due to second harmonic generation (SHG). The top inset is a scanning electron microscope image of the spiral region and the bottom is a picture of the entire chip containing 16 OPOs. **c,** Illustration showcasing how short pump pulses can take advantage of near-zero-dispersion-engineered OPAs. The simulated gain profiles are shown in the top for a waveguide with 60 fs^2/mm half-harmonic GVD and 26 fs/mm GVM and in the bottom for the fabricated near-zero-dispersion waveguide. The solid orange line marks the center wavelength of the pump and the orange shaded regions mark the 3-dB bandwidth (BW) of the 100-fs source. **d,** Depiction of the different regimes of operation of the OPO as a function of pump pulse energy, along with the roundtrip-to-roundtrip temporal output of the OPO in each regime.

Figure 7.1a illustrates the design of the on-chip sync-pumped OPO, with the fabricated device shown in Fig. 7.1b. The input/output couplers are designed to allow resonance only around the half-harmonic of the pump (see Section 7.4), and the cavity is designed to be minimally dispersive for these wavelengths. To phase and frequency lock the OPO, the OPO is nearly sync-pumped at degeneracy, requiring a cavity round-trip time of 4 ns for a pump comb with a 250 MHz repetition rate. With the effective index of our nanophotonic lithium niobate waveguides (wgs), this amounts to a 53-cm-long-cavity.

To achieve the ultra-high, ultra-broad, phase-sensitive gain at fJ pump pulse energies that enables coherent broadband comb generation, the OPO includes a 10.8 mm OPA with proper dispersion engineering and QPM. Specifically, we target minimizing the GVD of the pump and signal, as well as the GVM between the pump and signal [38]. Figure 7.1d illustrates the large gain bandwidth that can be accessed when coupling a 100-fs pump to a near-zero dispersion engineered waveguide, as opposed to one with large dispersion that is favored for broadly tunable OPOs [39, 40]. The designs for the poling period, cavity length, and couplers for sync-pumped operation can be found in the Section 7.4.

Figure 7.1d illustrates the different regimes of operation of this nanophotonic OPO. At low pump pulse energies, the OPO goes above threshold when the gain overcomes the loss inside the cavity. This is conventionally the regime where OPOs are operated to yield coherent outputs phase-locked to the pump [34]. At higher pump pulse energies a degenerate OPO is known to transition to an unstable operation regime where the phase-locked operation diminishes [41–43]. Here however, we find that far above threshold, the OPO can undergo a transition to the phase-locked regime as a result of the nonlinear phase being compensated by the cavity. This recoherence is emphasized in the accompanying time domain plots, where after a finite number of roundtrips the output pulse intensity is seen to stabilize with ultrashort features in the multi-octave case. It is worth noting that the dynamics of such far-above-threshold OPOs, including this reemergence of coherence, are not well described by existing reduced models [41].

Measurement of Multi-Octave Frequency Comb

In Fig. 7.2a-c, we show the near-threshold performance of the nanophotonic OPO. Scanning the repetition rate of the pump by 600 Hz, we observe the oscillation peaks of the OPO as depicted in Fig. 7.2a. These peaks are characteristic of doubly-

resonant operation [34]. We can actively lock the pump repetition rate to the center of each of these peaks, and the near-threshold signal spectra of three such peaks at distinct detunings between the pump repetition period and cavity round-trip time, ΔT_{RT}, are shown in Fig. 7.2b. In Fig. 7.2c we show the measured input-output pulse energy growth of these same peaks. We can extrapolate the threshold and slope efficiencies, η_{SL}, and define the peak with the lowest threshold as the zero cavity detuned state. For this peak we estimate an OPO threshold of ~18 fJ.
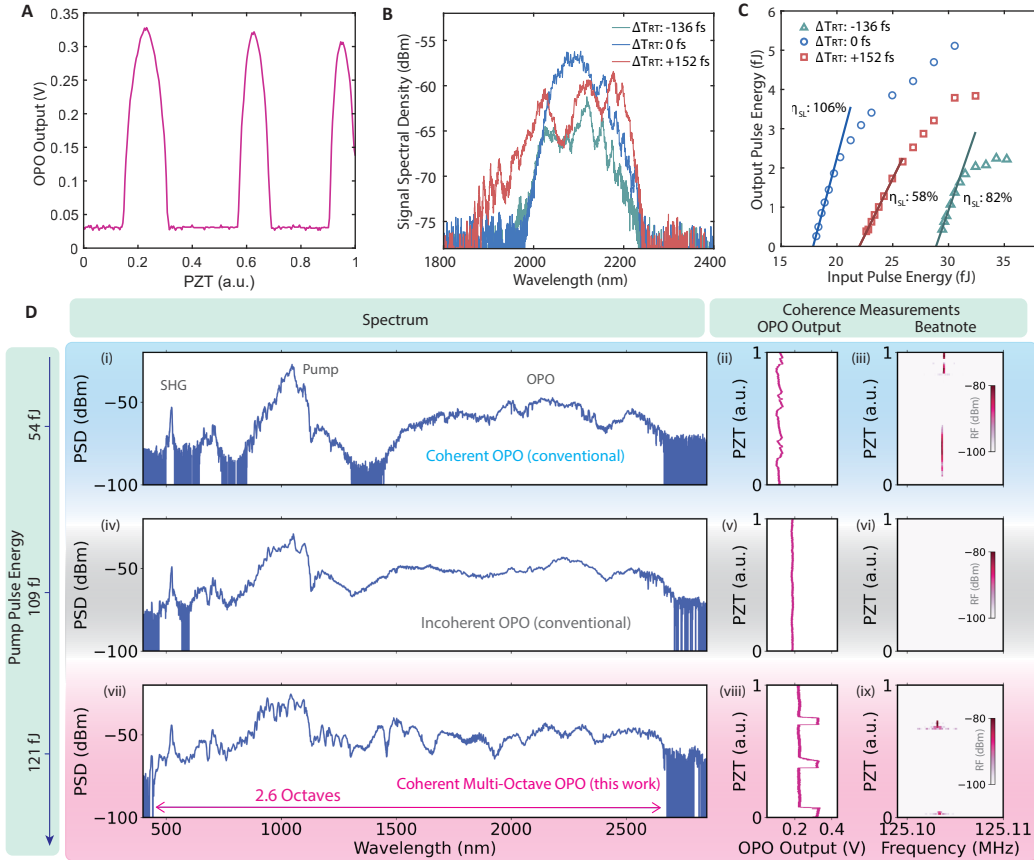
Figure 7.2: **OPO characterization. a,** Oscillation peaks of the OPO near-threshold as the pump repetition rate is modulated by a piezoelectric transducer (PZT) in the pump laser cavity at 600 Hz. **b,** Signal spectrum at 35 fJ of pump energy for three different roundtrip detunings and **c,** the corresponding OPO signal growth as a function of pump energy for different oscillation peaks and their slope efficiencies, η_{SL}. **d**, Output spectra, OPO oscillation peaks, and beatnote measurements from the OPO cavity at 54 fJ, 109 fJ, and 121 fJ of pump. The OPO oscillation peaks (ii), (v), (viii) were taken under the same detector amplification settings. The RF beatnotes (iii), (vi), (ix) were taken between a free space and on-chip OPO that share the same pump, the rep rate of which is tuned over time.

In Fig. 7.2d, we show three characteristic output spectra of the OPO. At 54 fJ of pump we observe conventional OPO behavior. The pump, half-harmonic and second-harmonic are all spectrally broadened, and there is noticeable SFG between the pump and half harmonic. At 109 fJ of pump, we observe continuous spectra from 600 nm to 2710 nm, and at 121 fJ we observe continuous spectra from 443 nm to 2676 nm. The dip at 2.8 µm is associated with the OH absorption peak in the LN and/or the buffer layer [40, 44], and kinks near 680 nm and 1135 nm are due to mode crossings (see Section 7.4). It is also worth noting that the spectra at 121 fJ has some distinctive signatures on the long wavelength side of the spectrum that are absent in the 109 fJ pumped cases.

To characterize the coherence of the OPO at these pump pulse energies, we interfere the chip output with that of a free-space OPO pumped by the same laser using a filter centered around 2.1 µm. When operated in a coherent regime, the half-harmonic output comb from a degenerate OPO above threshold can have two possible CEO frequencies which differ by half of the pump repetition rate, $f_{rep}/2$, depending on the oscillation peak [34]. When the on-chip OPO output comb has a different CEO frequency from the free-space OPO output comb, upon spatially and temporally overlapping their outputs, beatnotes at $f_{rep}/2$ should be observed. For the coherence measurements in Fig. 7.2d, we scan the pump-cavity detuning over time via a piezoelectric (PZT) actuator which controls the pump repetition rate. At 54 fJ of pump, Fig. 7.2d(ii) shows that the on-chip OPO exhibits features at certain detunings, the coherence of which are reflected by the $f_{rep}/2$ beatnotes between the OPOs in Fig. 7.2d(iii). The lack of these signatures both in the OPO power and beatnotes at 109 fJ of pump, indicate that the on-chip OPO has transitioned from a coherent to incoherent regime. At 121 fJ however, the OPO peak structures and RF beatnote reappear, signifying the reemergence of a coherent operating regime.

The coherence of the second-harmonic portions of these spectra were confirmed using a spectrally broadened output of the pump by a photonic crystal fiber. We interfere this broadened pump with the second-harmonic portion of the on-chip OPO and observe beatnotes of the resultant carrier-envelope offset frequency, f_{CEO}, along with the pump repetition rate at 250 MHz for all of the pump pulse energies in Fig. 7.2d, irrespective of the detuning (see Section 7.4). In particular, at 121 fJ of pump, because both the half-harmonic and second harmonic combs are coherent with respect to the pump and all frequency portions of our spectrum are generated through parametric processes of these three combs [29], we conclude that

the continuous 2.6 octave spectrum in Fig. 7.2d is coherent. We have experimentally observed that the regime exists stably within a few percent change of the input power, which is consistent with our numerical simulations. As such, we could even lock the rep rate of the pump to keep the OPO oscillating in this state, and in Section 7.4 we show the beatnote signal being maintained over several minutes.
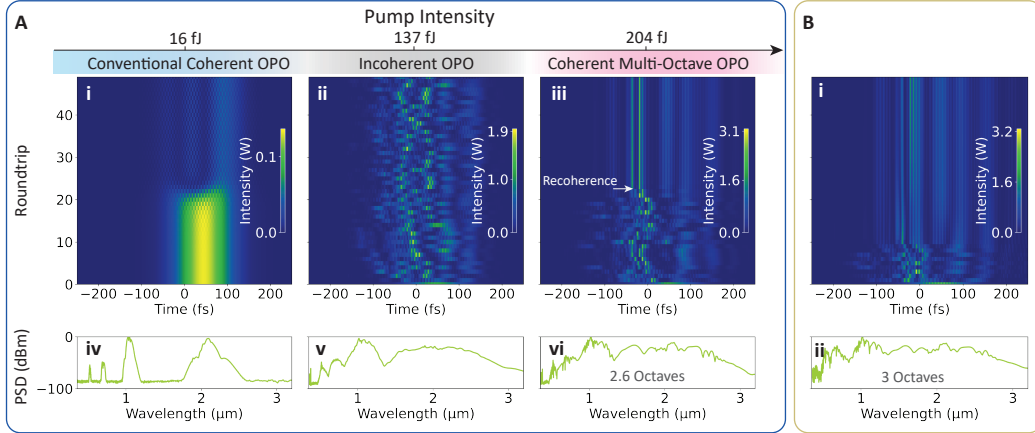
Figure 7.3: **Simulation results showing different operation regimes of the nanophotonic OPO**. **a**, Transition from (i) near-threshold coherent operation to (ii) incoherent operation and (iii) back to coherent operation when the pump energy is increased. The roundtrip temporal evolution (i-iii) and output spectra (iv-vi) are shown for three different pump intensities using experimental parameters and at a cavity detuning of -10.5 fs. **b**, A three-octave coherent OPO. The same experimental parameters are used except that the last one mm of the PPLN was replaced with a chirped poling period. The pump pulse energy was at 250 fJ.

To explain the dynamics of this OPO far above threshold and how coherence can be established over such a broad spectrum, we turn to numerical simulations. To capture the multi-octave nonlinear interactions occurring in the OPO, we modeled the electric field in the nanophotonic cavity as a single envelope in frequency domain which is evolved using the split-step Fourier method for propagation in the PPLN region and a linear filter for the cavity feedback (see Section 7.4). In Fig. 7.3a, we show how this captures distinct regimes of operation when using parameters matching that of the experiment. At 16 fJ (i), the OPO goes above threshold and stabilizes after ~20 roundtrips. As the pump pulse energy is increased, fewer roundtrips are required for the OPO to form, and at 137 fJ (ii) of pump (~9× above threshold), we see that the OPO output is incoherent. Finally, at roughly 204 fJ (iii) of pump (~13× above threshold), the half-harmonic is seen to regain coherence, establishing a two-octave continuous comb with temporal features as short as 4 fs.

In our simulations, this recoherence is observed to occur in a regime where a nonlinear phase of π is accumulated during by the half-harmonic due to its interaction with the pump in the single-pass, which can be balanced by the cavity detuning. This is the case in the presented simulations, performed for a detuning of -10.5 fs, where the resonant half-harmonic signal accumulates a linear phase of π over the roundtrip propagation. The π phase shift may be observed as a 2-roundtrip periodic temporal shift in the fringes caused by the pump-signal interference in the 16-fJ temporal evolution plot of Fig. 7.3a(i). In the recoherent regime of Fig. 7.3a(ii), however, no such fluctuation in the fringes are observed as this π roundtrip phase exactly compensates the accumulated nonlinear phase.

In the multi-octave coherent regime, we further observe that the average output spectrum (Fig. 7.3a(vi)) displays distinct spectral fringes absent in the incoherent regime (Fig. 7.3a(v)). This is because the averaging washes out the features in the incoherent regime which fluctuates from roundtrip to roundtrip. This contrast is also evident in the measured spectra of Fig. 7.2d(iv) and (vii), corresponding to the incoherent and multi-octave coherent regimes, respectively.

In simulation, we further investigate how to extend the coherent operation of the OPO to even broader spectra. By replacing the last one mm of the PPLN region with a chirped poling period for efficient second harmonic and sum-frequency generation, we achieve a coherent three-octave continuous frequency comb with ~250 fJ of pump energy as shown in Fig. 7.3b.

7.3 Discussion

In Fig. 7.4 we compare our results with other integrated spectral broadening schemes and sync-pumped OPOs. The figure highlights how our nanophotonic OPO design and its operation regime enable orders-of-magnitude improvement in the energy efficiency of coherent spectral broadening. Our work represents the lowest threshold sync-pumped OPO which is enabled by its near-zero-dispersion design. This ultralow-threshold operation enabled accessing a previously unexplored operation regime of the OPO far above threshold, where ultrabroad coherent spectral broadening is established as a consequence of the balance between cavity detuning and nonlinear phase shift.

In summary, we have experimentally demonstrated a nearly sync-pumped nanophotonic OPO operating in the near zero-GVM, zero-GVD, fs-pumped, high-gain low-finesse regime resulting in an ultra-broadband coherent output with only ~121
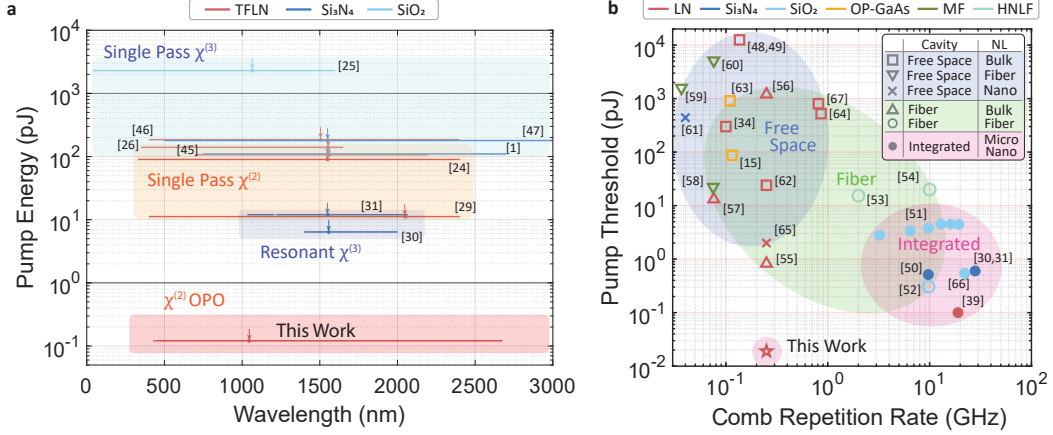
Figure 7.4: **Performance comparison of integrated spectral broadening and frequency comb sync-pumped OPOs**. **a**, Wavelength coverage and pump pulse energies of integrated frequency comb spectral broadening schemes. The arrows indicate the pump wavelength. **b**, Comb repetition rates and pump threshold energies of sync-pumped OPOs. The marker shapes denote the different cavity and nonlinear (NL) element compositions for each OPO, the categories being free space, fiber, integrated and bulk, fiber, nanophotonic, respectively. In both figures, the top legend denotes the material of the nonlinear element. Abbreviations, TFLN: thin-film lithium niobate, OP: orientation patterned, MF: microstructured fiber, HNLF: highly nonlinear fiber.

fJ of energy. The 2.6 octave frequency comb enables unprecedented opportunities for on-chip applications including wavelength division multiplexing [7], dual-comb spectroscopy [16], and frequency synthesis [5]. We show the OPO transitions from an incoherent to coherent operation regime and demonstrate a path towards much broader frequency comb sources in the femtojoule regime.

7.4 Supporting Information
Chip Design
OPO Design

The spatiotemporal profile of pulses propagating through our nanophotonic waveguides can be sculpted by a few key fabrication parameters. Labeled in Fig. 7.5a, these are the LN thickness, etch depth, top width, and sidewall angle. All of these parameters directly affect the effective index of the waveguide which, in turn, determines the near-zero dispersion geometry, quasi-phase-matching poling period, and required cavity length for synchronous pumping of our OPO, as shown in Figs. 7.5b-d. We fabricated our device with a constant poling period of 5.075 µm and a
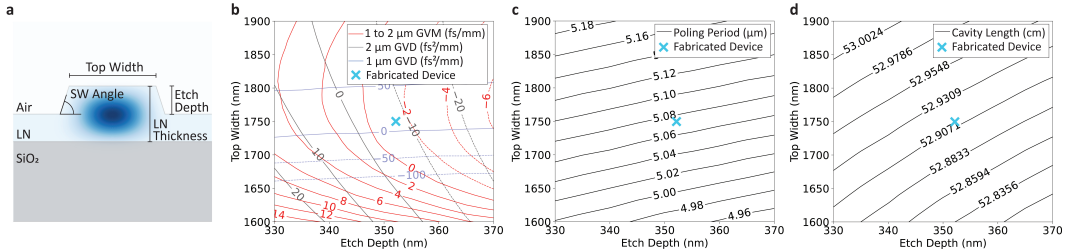
Figure 7.5: **Key OPO design parameters as a function of waveguide geometry. a,** Parameters for tuning spatiotemporal confinement of pulses propagating through our nanophotonic waveguides. An example fundamental TE mode at 1 µm is shown in the core of the waveguide. **b,** Dispersion profile **c,** Phase-matched poling period, and **d,** Optimal sync-pumping cavity length as a function of waveguide top width and etch depth variations. The actual measured dimensions of our fabricated device are indicated by the cross.

cavity length of 52.92 cm, and we measured a waveguide etch depth and top width of 352 nm and 1753 nm, respectively. These dimensions are marked by crosses in Fig. 7.5b-d and show that we successfully engineered our device to be close to optimal parameters for phase-matched operation with near-zero GVM and GVD. The resulting simulated effective index, n_{eff}, and fabricated poling period are shown in Fig. 7.6, along with the simulated bending loss as a function of bend radius and wavelength. The dotted blue line in Fig. 7.6c at 77 µm indicates the minimum bend radius used in fabricating the spiral, showing small bending loss for wavelengths shorter than 3.3 µm at all points in the spiral.
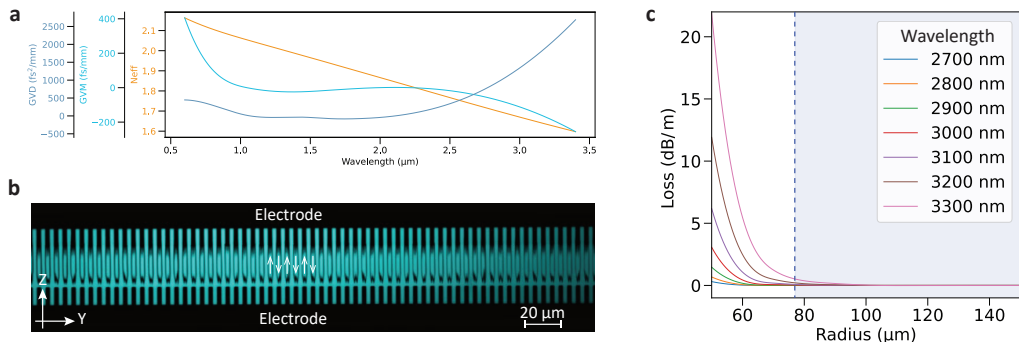
Figure 7.6: **Additional OPO parameters given the waveguide geometry shown in Fig. 7.5. a,** Effective index, GVD, and GVM with respect to the pump for the fundamental TE mode of the waveguide **b,** Second harmonic microscope image of the periodic poling pre-waveguide patterning, and **c,** Simulated propagation loss as a function of bend radius for different signal wavelengths. The dotted blue line is at 77 µm, the minimum bend radius employed when designing the OPO cavity.

Input/Output Coupler Design

The input and output couplers of the OPO, as defined in Fig. 7.7a, are symmetrically identical and take the adiabatic shape depicted in Fig. 7.7b, where the parameters for w_1, w_2, gap, and L are 1753 nm, 1900 nm, 980 nm, and 750 µm, respectively. Adiabatic couplers were chosen for their broadband response and comparative fabrication insensitivity compared to other coupler geometries. The fundamental TE mode profiles at 1 µm and 2 µm for the waveguide design with top width w_2 are shown in Fig. 7.7c. Pulses propagating through this adiabatic coupler follow the coupled mode equations,

$$\begin{cases} \dfrac{da_1}{dz} = -j\kappa e^{j\Delta\beta z} a_2(z) \\ \dfrac{da_2}{dz} = -j\kappa e^{-j\Delta\beta z} a_1(z) \end{cases} \tag{7.1}$$

where a_1 and a_2 are the amplitudes of the modes in each waveguide, κ is the coupling coefficient between the waveguides, and $\Delta\beta = |\beta_1 - \beta_2|$ is the phase mismatch between the two waveguides. Solving eq. (7.1) for our geometry, we obtain the power coupling curve in Fig. 7.7d. We see that only signal wavelengths above 2 µm experience significant coupling. In Fig. 7.7e we compare the spectral output of our OPO (device with coupler and cavity) against that from an adjacent straight waveguide without any couplers but sharing the same poling and waveguide parameters. We find that the simulated dips and peaks in the adiabatic coupler are reflected in the measured spectra from the nanophotonic OPO but are absent from the periodically poled straight waveguide, matching our theoretically predicted coupler response.

Chip Characterization
Experimental Setup

Our experimental setup is shown in Fig. 7.8. The detector in the PID loop allows the repetition rate of the pump comb to be locked to disparate oscillation peaks of the OPO while the spectra is being collected on an OSA. The synergistic features of the pump and OPO that enable multi-octave frequency comb generation are emphasized in the figure.
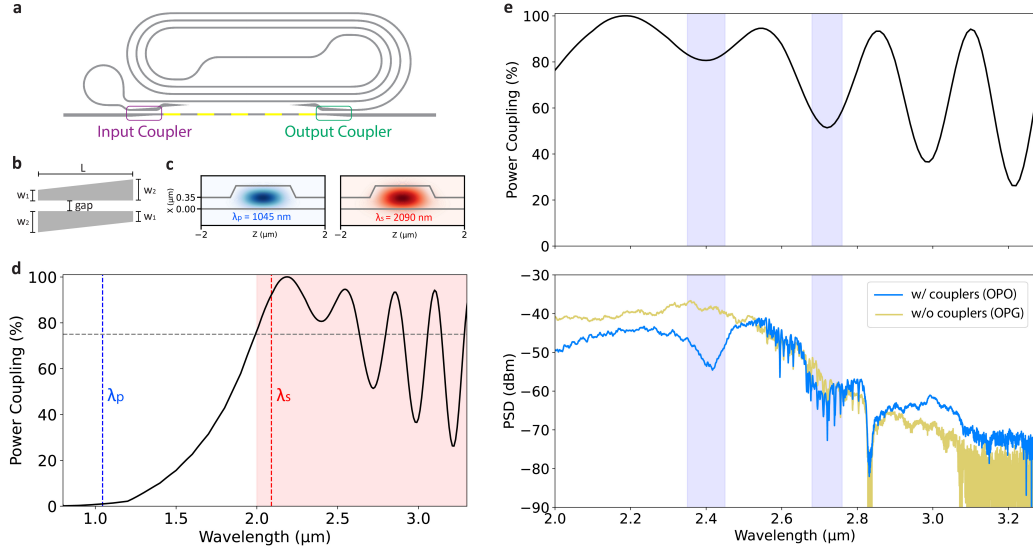
Figure 7.7: **OPO coupler design. a,** Definition of the input/output coupler and **b,** an illustration of the output coupler adiabatic design. Here, the widths and gaps refer to those at the top of the waveguide. **c,** The waveguide fundamental TE modes at 1 µm and 2 µm. **d,** The simulated coupler response using the fabricated waveguide geometry. **e,** Comparing the theoretical coupler behavior to measured spectra at 380 fJ of pump for otherwise identical devices with and without couplers.

Extended Experimental Data to Three Octave Spectra

Using the experimental setup shown in Fig. 7.8, we investigated the output spectra of the OPO at different pump pulse energies, a subset of which was shown in Fig. 7.2d. In Fig. 7.9a, we show the extension to even higher pump pulse energies. At 380 fJ of pump, we observe three-octave-spanning spectra from 362 nm to 3261 nm. The beatnote analysis with a free space OPO shown in Fig. 7.9b however, following the procedure in Fig. 7.12, indicates that the OPO here is incoherent.

Molecular Absorption Features

For the measured spectra above 2.5 µm in Fig. 7.9a, we observe features that appear to be from spectral absorption lines coming from ambient molecules. In Fig. 7.10, we compare the experimental OPO spectra to the spectral lines of H_2O, CO_2, and CH_4. The overlap between water and the OPO's spectral features is especially close, likely because H_2O is the strongest absorber in this spectral region at atmospheric concentrations. We calculate that 9 % of the 3 µm mode inside the spiral region is evanescent, suggesting that with the 53 cm spiral, on-chip sensing may be possible. Here, however, we expect that the absorption primarily occurs between the output
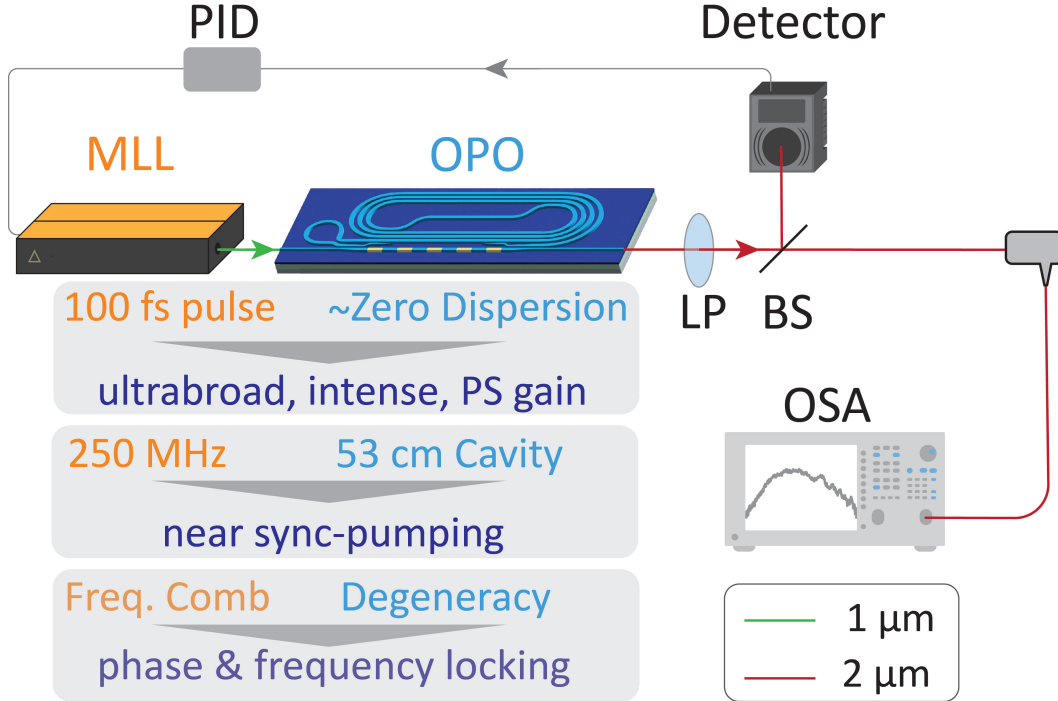
Figure 7.8: **Experimental setup**. Abbreviations, PS: phase sensitive, MLL: mode locked laser, LP: long pass, BS: beam splitter.

of the chip and the detector as none of the systems in this experiment were purged. Furthermore, these absorption features result from ambient molecules existing in the lab as no gas cells were prepared.

The notch at 2.83 µm is due to an OH absorption peak in the LN and/or SiO_2 substrate buffer layer. Studies of the absorption of SiO_2 employed as a buffer layer for Si waveguides [69–71] indicate that the SiO_2 bottom-cladding will become prohibitively narrow around 2.8 µm and above 3.5 µm. For current thin-film lithium (TFLN) niobate devices with a SiO_2 buffer and Si substrate, the upper absorption appears to set in around 3.25 µm [39]. Wavelengths between, 2.8-3.8 µm, however have been measured on TFLN waveguides on a sapphire substrate [72], suggesting a path towards making a multi-octave frequency comb with even longer wavelength components.

Mode Crossings

In Fig. 7.9, there are spectral kinks at 680 nm and 1135 nm evident over all pump pulse energies. These correspond to the two mode crossings shown in Fig. 7.11a. M1 is the mode crossing between the fundamental TE mode and second order TM
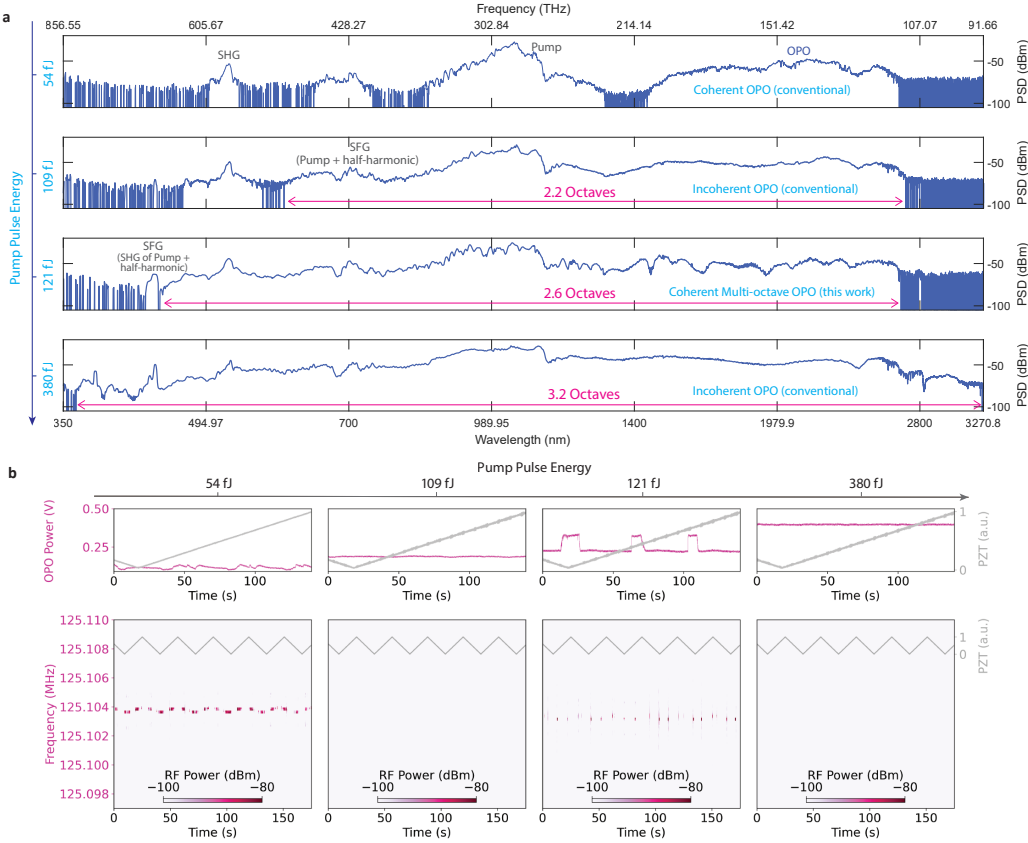
Figure 7.9: **Extended measurements to ∼ 20× above threshold**. **a** Output spectra from the OPO cavity up to 380 fJ of pump pulse energy. **b** For the same energies, the top panels show the OPO oscillation peaks as the pump rep rate is scanned by a PZT. The bottom panels show the RF beatnote between a free space and on-chip OPO that share the same pump, the rep rate of which is tuned over time at 63.58 mHz.
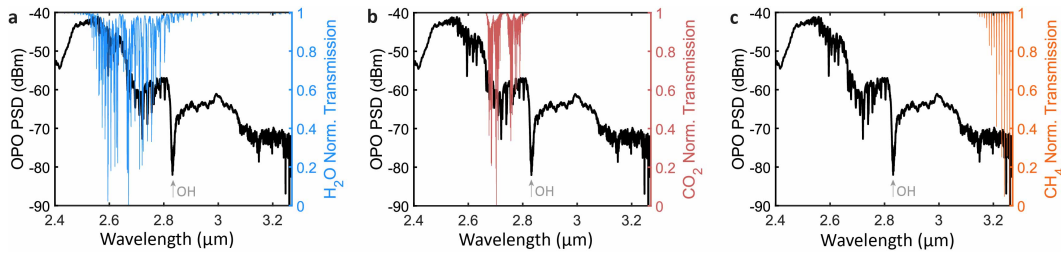
Figure 7.10: **Absorption features of atmospheric molecules compared to the OPO spectra measured at 380 fJ of pump**. The spectral lines were taken from the HITRAN database[68].

mode (Fig. 7.11b) whereas M2 is the mode crossing between the fundamental TE and TM modes (Fig. 7.11c). Indeed, these mode crossings, as well as the OH
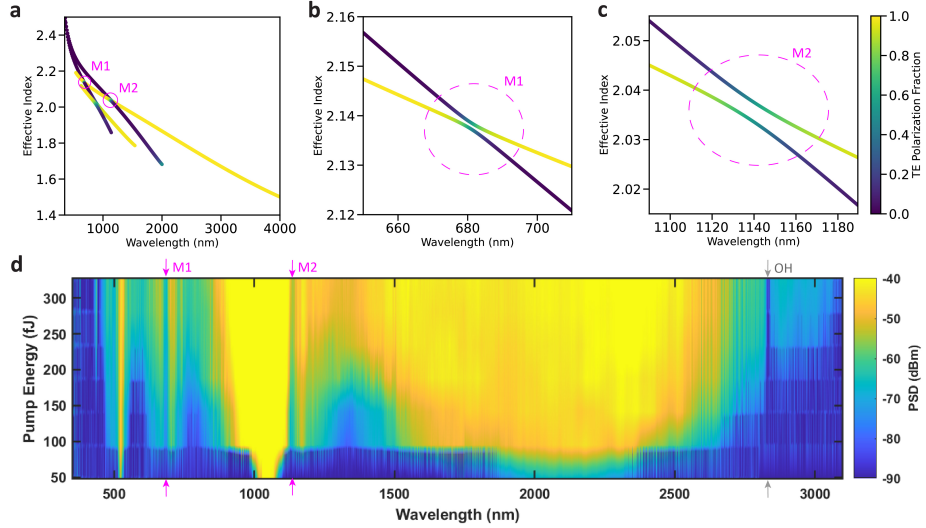
Figure 7.11: **Simulated mode crossings compared to measured straight wave-guide spectra**. **a**, Simulated modes at the periodically poled region of the chip. The mode crossings experienced by the fundamental TE mode are marked as M1 and M2. Close-ups of these are shown in **b** and **c**, respectively. **d**, The measured power spectral density of a periodically poled nanophotonic waveguide with no OPO cavity as a function of pump pulse energy. The locations of M1 (680 nm) and M2 (1135 nm) are indicated by arrows.

absorption discussed in Section IIB, are even evident in the spectra measured from a straight waveguide with the same waveguide geometry and poling period as the OPO and plotted in Fig. 7.11d. As this straight waveguide does not have a cavity, its half-harmonic spectra is due to OPG.

Beatnote Measurement

Down-Conversion Beatnote

The coherence of the down-converted portion of the comb around the half-harmonic was investigated using the experimental setup in Fig. 7.12a. The output of an on-chip and free space OPO pumped by the same laser were interfered. Depending on the detuning peak l of each OPO, we expect to see different signatures in their radio frequency (RF) spectrum and interference patterns. Here, we use the dimensionless detuning parameter $l = 2f_s\Delta T_{RT}$, where ΔT_{RT} is the mismatch between the cavity roundtrip time and pump repetition period and f_s is the signal frequency. While OPOs with even l have output comb lines aligned with that of the pump, near-threshold OPOs with odd l have output comb lines shifted by $f_{rep}/2$ [34, 73]. This is illustrated in Fig. 7.12b.
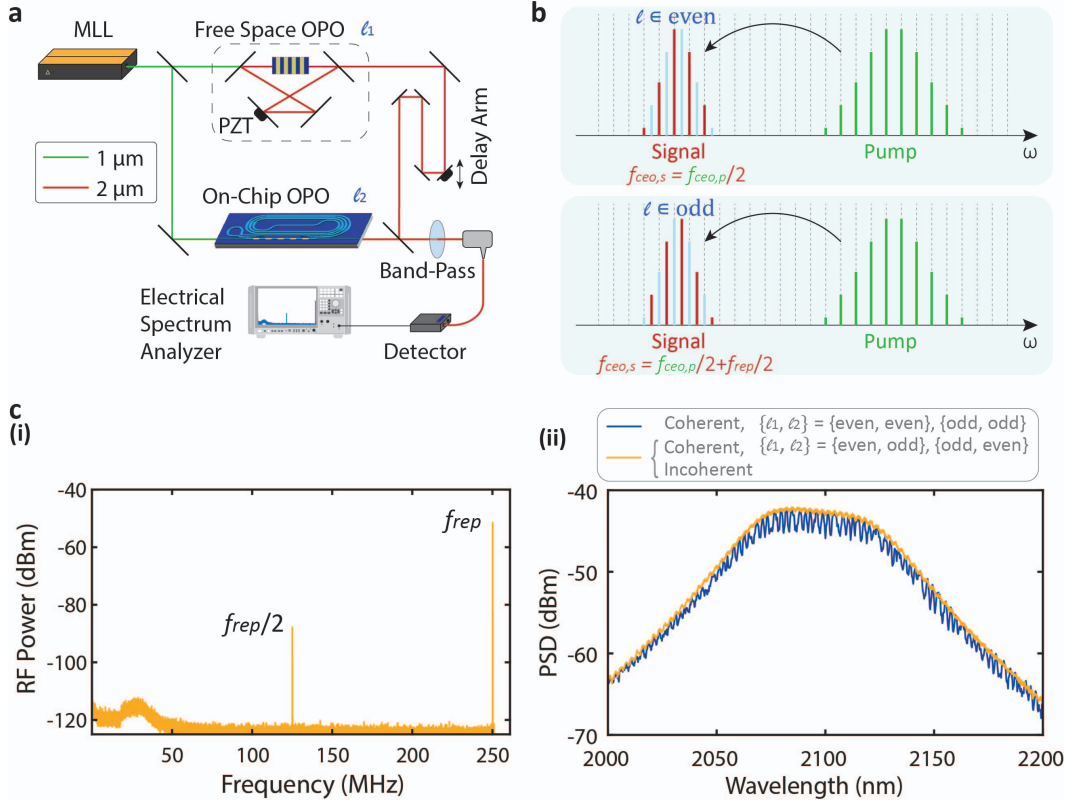
Figure 7.12: **OPO beatnote measurement. a,** Experimental setup. **b,** Illustration of the two near-threshold f_{CEO} states possible for the OPO comb depending on the detuning peak, l, being even or odd. **c,** (i) RF beatnote and (ii) spectral overlap, showing interference fringes (blue) as the relative output delay between the OPOs is scanned in the case where they share an f_{CEO} in the recoherent regime.

As discussed above, a key feature of the recoherent regime is the presence of a strong nonlinear phase accumulation. In this scenario, the a shared f_{CEO} between pump and signal may occur for different values of l compared to the near-threshold case. However, as we show, both scenarios of the signal comb either sharing an f_{CEO} with the pump comb or being shifted by $f_{\mathrm{rep}}/2$ may still occur.

When the on-chip and free-space OPO output combs have f_{CEO}'s which are shifted by $f_{\mathrm{rep}}/2$, the temporally and spatially overlapped OPO outputs show a beatnote at $f_{\mathrm{rep}}/2$, as shown in the RF spectrum measurement in Fig. 7.12c(i). Furthermore, in this case where the two combs have different f_{CEO} frequencies, we do not expect to see interference fringes as the delay between the two coherent OPO outputs is scanned. As shown by the orange trace in Fig. 7.12c(ii), no fringe is observed.

In the case that the OPOs are coherent and share the same f_{CEO}, however, we do

not expect and did not observe a beatnote at $f_{\text{rep}}/2$. Furthermore, since the combs share an f_{CEO}, we expect to see an interference fringe as their relative delay is scanned. This is indeed what we measured, as shown by the blue curve in Fig. 7.12c(ii). At 109 fJ and 380 fJ of pump, where the down-converted portion of the nanophotonic OPO output is incoherent, we observed neither a $f_{\text{rep}}/2$ beatnote nor the blue interference fringe of Fig. 7.12c(ii).

Finally, the pump rep rate can be locked to features in the OPO output signal. In Fig. 7.13, we show that we can indeed lock to and stabilize the on-chip OPO output to the 2.6 octave comb state in the recoherent regime.

Up-Conversion Beatnote

The coherence of the up-converted portion of the pump was investigated using similar methodologies to [29, 35]. Specifically, a spectrally broadened portion of the pump was interfered with the second harmonic portion of the on-chip OPO, as illustrated in Fig. 7.14a. The spectral overlap for three of the pump pulse energies mentioned in Fig. 7.2d are shown in Fig. 7.14b, with the corresponding beatnotes presented in Figs. 7.14c-e. In each case we confirmed the beatnotes correspond to the f_{CEO} by recording its shift as the pump f_{CEO} is tuned. We conclude that the up-converted porion of the pump reamins coherent irrespective of the pump pulse energy or cavity detuning, which is as expected [29, 35].

OPO Simulations
Method

We model the ultrabroad spectral dynamics of the nanophotonic OPO by representing the total electric field in the nanophotonic waveguide using a single envelope in the frequency domain [38, 74–77],

$$\mathbf{E}(x, y, \omega) = A(z, \Omega)\mathbf{e}(x, y, \omega)e^{-i(\beta_0 - \omega_0/v_{\text{ref}})z}, \tag{7.2}$$

where ω and $\Omega = \omega - \omega_0$ are the optical and envelope angular frequencies, ω_0 is the simulation center frequency, β_0 is the waveguide propagation constant at ω_0, v_{ref} is the simulation reference frame velocity, x and y are the transversal waveguide coordinates, $\mathbf{e}(x, y, \omega)$ is the mode transversal field distribution, and $A(z, \omega)$ is the complex amplitude of the field that evolves during propagation. In our OPO simulation, ω_0 is chosen to be the center of the half-harmonic signal at 2090 nm, and v_{ref} is the group velocity of the half-harmonic. $A(z, \omega) = A(z, \Omega)e^{-i\omega_0 t}$ is a rapidly-varying envelope which contains the phase factor $e^{-i\beta(\omega)z}$ acquired during
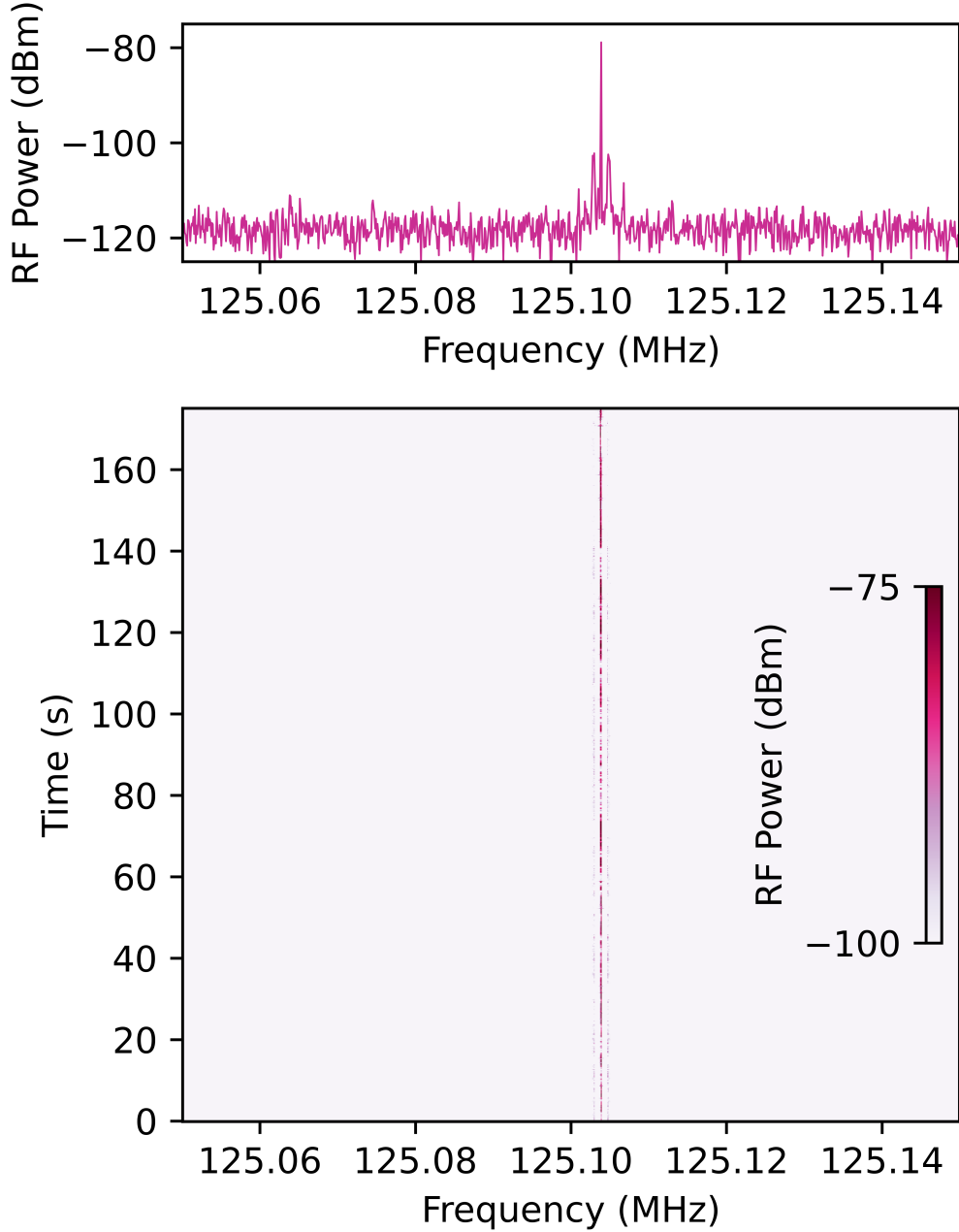
Figure 7.13: **OPO beatnote locked in the recoherent regime.** The pump here is at 121 fJ, and the pump rep rate is locked to the OPO peak structures seen in the OPO oscillation peaks in Fig. 7.2d(viii). The top panel shows the $f_{\mathrm{rep}}/2$ beatnote at a representative time, and the bottom panel shows the beatnote persist over time. The dither signals of the free-space and on-chip OPO cavity locks cause the two sets of side fringes to the main $f_{\mathrm{rep}}/2$ beatnote.
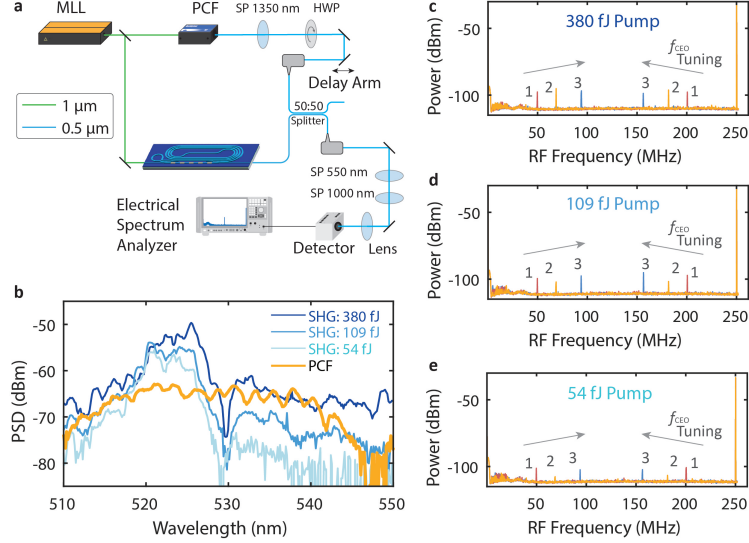
Figure 7.14: **SHG beatnote measurement. a,** Experimental setup. **b,** Spectral overlap between the chip SHG outputs and the PCF. Sample beatnotes measured at **c,** 380 fJ, **d,** 109 fJ, and **e,** 54 fJ with the different colors corresponding to different pump f_{CEO}'s. Abbreviations, SP: short pass, PCF: photonic crystal fiber (Menlo Systems), HWP: half wave plate.

linear propagation. Additionally, $A(z, \omega)$ is an analytic signal, meaning it only contains positive frequencies ($A(z, \omega < 0) = 0$). The code used for finding both the effective index and solving the nonlinear propagation is based on the SNOW library[78].

Our simulation models each round-trip in the OPO in two parts. The first accounts for the nonlinear propagation in the poled region of the waveguide, while the second consists of a linear filter which models the round-trip evolution in the spiral resonator [79]. The output of this round-trip evolution is fed back as a seed for the subsequent nonlinear propagation. The first round-trip is seeded by white noise for all frequencies besides the pump, which is taken to be an 80-fs pulse with a sech pulse profile, centered at 1045 nm.

We find a uni-directional equation of motion describing the nonlinear propagation of $A(z, \Omega)$ by ignoring counter-propagating terms (which are usually phase mismatched) and assuming a constant nonlinear coefficient and mode overlap integral, both of which are weak functions of frequency away from any material resonances. No limitations are placed upon the maximum spectral bandwidth of the simulation.

The resulting propagation equation is,

$$\frac{\partial A}{\partial z} = -i\left[\beta(\omega) - \beta_0 - \frac{\Omega}{v_{\text{ref}}} - i\frac{\alpha}{2}\right]A$$
$$- \frac{i\omega\epsilon_0 X_0}{8}d(z)\mathcal{F}_\Omega\left\{a^2(z,t)e^{j\phi(z,t)} + 2a(z,t)a^*(z,t)e^{-j\phi(z,t)}\right\}, \quad (7.3)$$

where $d(z) = \pm 1$ is the sign of the quadratic nonlinear coefficient that is modulated in quasi-phase matching, α is the propagation loss coefficient, $a(z,t)$ is the time domain representation of $A(z,\Omega)$, $\phi(z,t) = \omega_0 t - (\beta_0 - \omega_0/v_{\text{ref}})z$, $\mathcal{F}_\Omega$ is the Fourier transform in the Ω variable. The effective nonlinear coefficient X_0 is defined as:

$$X_0 = \sum_{ijk} \chi_{ijk}^{(2)} \int e_i^*(\omega_1) e_j(\omega_2) e_k(\omega_1 - \omega_2) \, dS, \quad (7.4)$$

where $\chi_{ijk}^{(2)}$ is the quadratic nonlinear susceptibility tensor, and j, k, l denote Cartesian components.

The nonlinear propagation in each round-trip involves solving the evolution equation (7.3) using the split-step Fourier technique over the length of the poled waveguide, L = 10.8 mm. The nonlinear step employs the fourth-order Runge-Kutta method in the interaction picture (RK4IP) [80].

Propagation in the spiral resonator is modeled through application of a linear feedback function to the output of the poled region. In particular, the signal fed back to the input of the poled region for the $(n+1)^{th}$ round-trip, $A_{in}^{n+1}(0, \omega)$, is related to the field out of the poled region on the nth round-trip, $A_{out}^n(L, \omega)$, by the expression:

$$A_{in}^{n+1}(0, \omega) = A_{out}^n(L, \omega) R(\omega) e^{-j(D_{\text{RT}}(\omega)L_{\text{RT}} + \Delta T_{\text{RT}}\omega + \phi_0)}. \quad (7.5)$$

Here, $R(\omega)$ is the frequency-dependent coupling factor of the designed adiabatic couplers, $D_{\text{RT}} = \beta(\omega) - \beta_0 - \frac{\Omega}{v_{\text{ref}}} - i\frac{\alpha_{\text{RT}}}{2}$ is the complex dispersion operator describing propagation in the round-trip waveguide with parameters defined as above for the poled waveguide, $L_{\text{RT}} = 518.4$ mm is the length of the round-trip cavity, ΔT_{RT} is the cavity detuning parameter which accounts for any timing mismatch between the pump repetition period and cavity roundtrip time, and ϕ_0 is a constant phase offset. We further note that the quantity $\Delta T_{\text{RT}}\omega = \Delta T_{\text{RT}}(\Omega + \omega_0)$ in terms of the envelope angular frequency, Ω, and therefore consists of two terms, a linear phase accumulation (corresponding to a temporal shift) and an absolute phase

accumulation, $\phi_{\mathrm{RT}} = \Delta T_{\mathrm{RT}}\omega_0$. We also frequently utilize the normalized detuning parameter, l, defined as $l = \frac{\Delta T_{\mathrm{RT}}\omega_0}{\pi}$. In addition to this fed back signal, a new pump pulse is also injected, centered at t = 0 on the fast time axis.

Simulations are conducted on a Fourier grid of size 4096 with a bandwidth of 2.4 PHz. The corresponding time window is 1.7 ps. To avoid wrapping in the time window during the nonlinear propagation, a Tukey filter padded with zeros on the edges is applied in the time domain after each nonlinear step. Additionally, before application of the linear filter, all frequency components which will walk out of the time window over the course of the 518-mm propagation in the spiral resonator are filtered out. This has the undesirable effect of effectively reducing the simulated power in frequency modes which are far from the reference frequency (and thus experience significant walk-off with respect to the reference velocity of the simulation), but it ensures the validity of the simulated nonlinear interaction.

In this context we consider nonlinear phase to be the phase accumulated in the PPLN section of the resonator due to the nonlinear process (excluding the linear phase accumulation). We explicitly focus on a narrow spectral range around the pump and its half-harmonic for the spectral analysis and around the peak intensities for the pump and half-harmonic in the temporal analysis.

OPO Dynamics under Different Conditions

As discussed in Section 7.2, the ultrabroadband OPO enters different regimes of operation high above threshold. An extended version of the regimes shown in Fig. 7.1 is shown in Fig. 7.15a. Whether our near-zero dispersion OPO can reach the coherent multi-octave state denoted as (iii) in the figure, largely depends on the pump energy and cavity phase, adjusted either through the detuning (shown in Fig. 7.15b) or absolute phase parameter, ϕ_0. We find that the dynamics of our OPO largely depend on whether it has an even or odd detuning peak, l, and whether ϕ_0 is 0 or π. We will dive into each of these cases in more depth below.

$l \in$ even, $\phi_0 = 0$

When $l \in$ even and $\phi_0 = 0$, we find that while the OPO nearly reaches a coherent, multi-octave comb, it never quite manages to. As an example, we show the case of of $l = -2$ in Fig. 7.16, where this approximate coherence is emphasized by the label (Nearly iii). In this case, we see that in regime (i), near threshold, the roundtrip-to-roundtrip phase of the coherent OPO remains fixed once the OPO goes
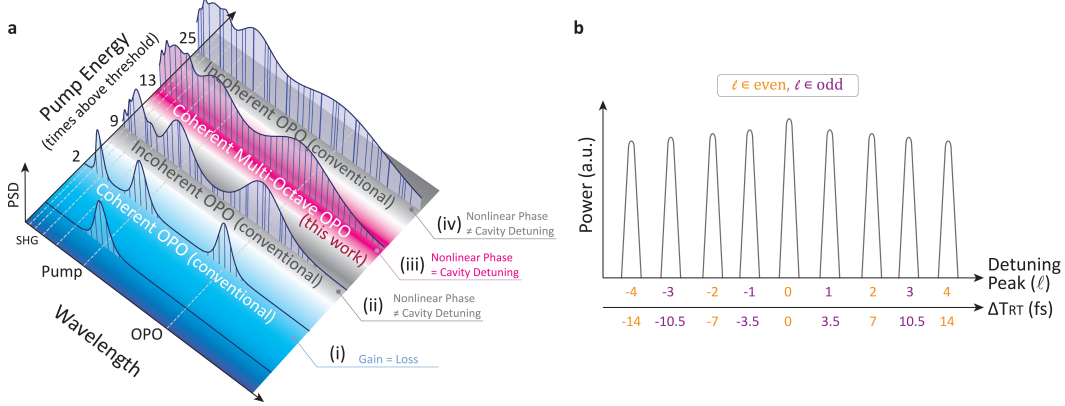
Figure 7.15: **Simulated OPO regimes**.**a**, Extended illustration of the operating regimes of the nanophotonic OPO. In the simulations presented below, regimes (i)–(v) correspond to typical pump pulse energies of 16, 127, 205, and 400 femto-joules, respectively. **b**, OPO resonances labeled in terms of detuning peak (l), and cavity roundtrip detuning (ΔT_{RT}).

above threshold. After transitioning though an incoherent state in regime (ii), the OPO phase is seen to flip roundtrip-to-roundtrip by π in pump regime (iii). This roundtrip signal phase accumulation relative to the pump manifests as a periodic beating between the pump and half-harmonic components, as well as upconverted components resulting from their interaction, which may be observed in the time and frequency evolution plots. At even higher pump energies, the OPO enters the completely saturated, incoherent regime of (iv).

$l \in odd,\ \phi_0 = 0$

The roundtrip-to-roundtrip π phase flips in the $\sim$200 fJ-pumped cases when $l \in$ even and $\phi_0 = 0$ suggest that if the cavity phase can be detuned by π, a multi-octave coherent comb can be sustained. One way of obtaining such a detuning is to select OPO peaks where $l \in$ odd while maintaining $\phi_0 = 0$, and in Fig. 7.17, we show the dynamics of the case where $l = -3$. As expected, near threshold, i.e, in regime (i), the OPO shows roundtrip-to-roundtrip π phase flips. In regime (iii), however, we find that the OPO recoheres and is able to stabilize, showing a fixed roundtrip-to-roundtrip phase.

The coherence of the two octave spectra in regime (iii) can be further verified by means of calculating the $g^{(1)}$ coherence over pairs of output pulses as well as by directly inspecting the overlap of the half-harmonic, pump, second harmonic, and sum-frequency generated combs. As can be seen in the top panel of Fig. 7.18a,
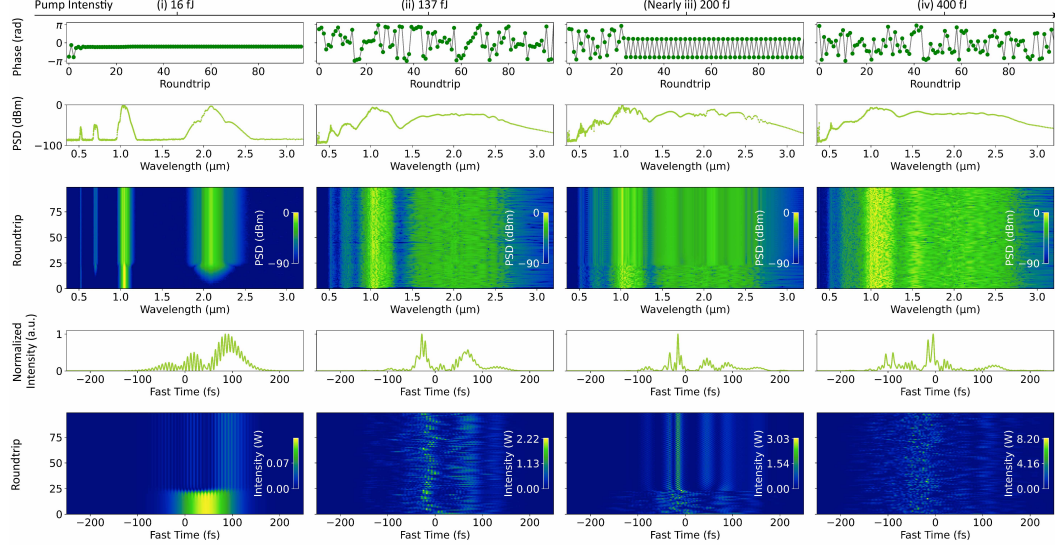
Figure 7.16: **OPO characterization:** $l = -2$, $\phi_0 = 0$. The top row shows the phase of the OPO output as a function of round trip for each operating regime indicated in Fig. 7.15. The second and third rows present the spectral intensity: the third row from the bottom shows the spectral buildup over round trips, while the second row from the bottom shows the spectral intensity after 100 round trips. Similarly, the bottom row illustrates the evolution of the temporal intensity over round trips, and the row above it shows the final temporal intensity after 100 round trips.

we see through measurement of the $g^{(1)}$ coherence between pairs of pulses taken from the last 15 roundtrips of our simulation, the device displays over two octaves of coherent spectra. This can be further verified by looking at the the actual comb lines of the two-octave comb. The full comb spectrum, as well as a close-up of the comb lines corresponding to different harmonic combs, shifted by the nearest multiple of f_{rep} which centers them at zero, are shown in Fig. 7.18b. The good overlap between the comb lines is a further indication that the combs share an f_{CEO} and are thus coherent. Note that the second harmonic comb at 500 nm is not expected to share an f_{CEO} with the other harmonics except in the case where the pump comb at 1 µm has an f_{CEO} of 0, which is generally assumed in our simulation.

$l \in$ even, $\phi_0 = \pi$

Along with picking an odd detuning peak, a roundtrip phase of π can be directly added in the case where $l \in$ even, corresponding to $\phi_0 = \pi$. This helps to decouple the effects from any additional temporal dynamics which can occur due to the detuning parameter, ΔT_{RT}. An example of this is shown in Fig. 7.19 for $l = -2$. Similar to the case of $l \in$ odd with $\phi_0 = 0$, the OPO shows roundtrip-to-roundtrip
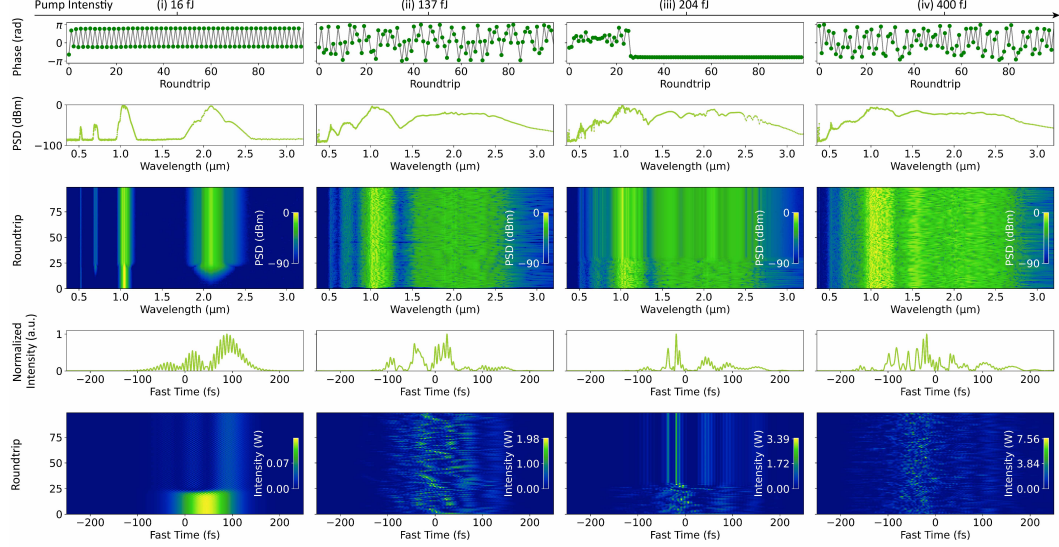
Figure 7.17: **OPO characterization:** $l = -3$, $\phi_0 = 0$. The top row shows the OPO output phase as a function of round trip for each regime in Fig. 7.15. The second and third rows display the spectral intensity: the third row shows spectral buildup with round trips, and the second row shows the intensity after 100 round trips. The bottom row depicts the temporal intensity evolution, with the row above it showing the final temporal intensity after 100 round trips.
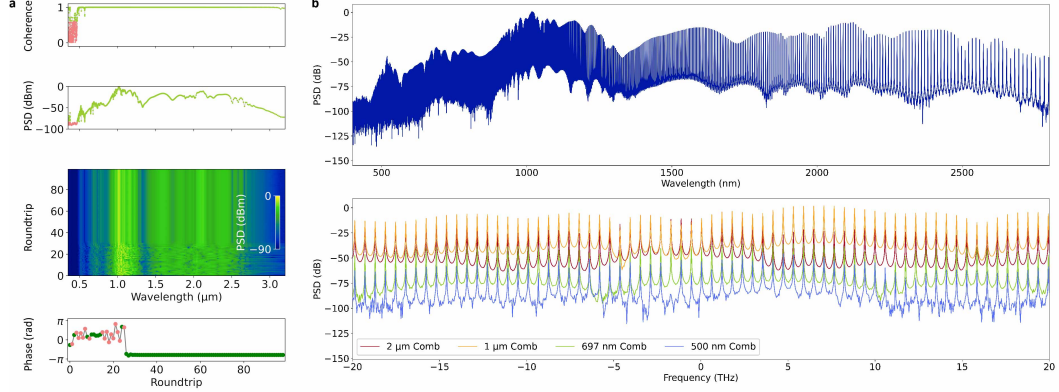
Figure 7.18: **Further characterization of the coherence of regime (iii) for $l = -3$, $\phi_0 = 0$. a**, $g^{(1)}$ coherence as a function of wavelength, PSD, and roundtrip spectra, where points with simulated coherence greater than 0.6 are denoted by a light green dot, with the rest colored in pink. For the roundtrip phase plot, points where the difference in phase compared to the prior roundtrip is smaller than $\pi/6$ are plotted in green with the other points marked in pink. **b**, Simulated comb lines at the output. The 2-μm, 1-μm, 69-nm, and 500-nm combs correspond to the half-harmonic, pump, sum-frequency generation of the pump and half-harmonic, and second harmonic of the pump, respectively.

phase flips at low powers of regime (i) and enters the oscillatory state of regime (ii) until ultimately landing in a steady-state at 200 fJ of pump.
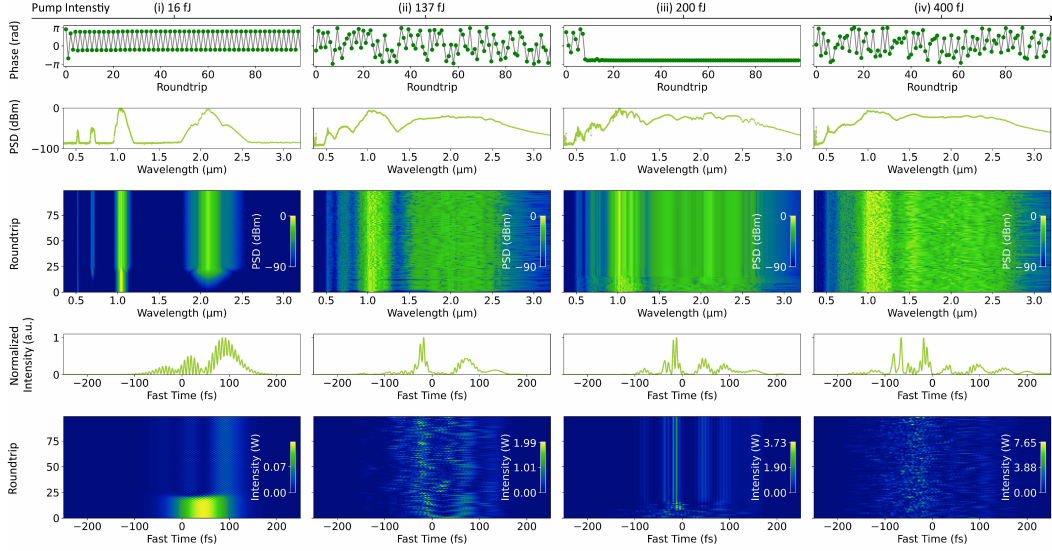

Figure 7.19: **OPO characterization: Peak -2,** $\phi_0 = \pi$. The top row shows the OPO output phase as a function of round trip for each regime in Fig. 7.15. The second and third rows display the spectral intensity: the third row shows spectral buildup with round trips, and the second row shows the intensity after 100 round trips. The bottom row depicts the temporal intensity evolution, with the row above it showing the final temporal intensity after 100 round trips.

Recoherent Regime

Mechanism

In Fig. 7.2d, we experimentally demonstrated that as the input pump pulse energy is increased, our OPO transitions from a conventional operational regime, where it is coherent, to an incoherent one, but then it recovers its coherence at higher pump pulse energies with an appropriate cavity detuning. In Fig. 7.21, we show the intensity and phase propagation of the pump and half-harmonic in the periodically poled region of the cavity at ~200 fJ of pump (i.e., in the recoherent regime). The evolution of the half-harmonic phase in a(ii) clearly shows a phase flip from $-\pi \rightarrow 0$ in locations where the half-harmonic has substantial intensity.

Above, we showed that this π phase flip in the half-harmonic in each single-pass through the PPLN can be compensated by detuning the cavity by an odd number of OPO peaks, or by adding a constant cavity phase of π, ϕ_0. Fig. 7.17 is an example of the former. Near threshold (16 fJ), the OPO output experiences a π phase flip in

every roundtrip, but it is able to stabilize to a constant phase output in the case of 204 fJ of pump. An example of the latter approach of choosing an even detuning peak but ϕ_0 of π, is Fig. 7.19. Again, we observe that in the recoherent regime of 200 fJ of pump, the output phase can stabilize after ~40 cavity roundtrips. These examples show that compensating the single pass phase accumulation in the PPLN by appropriately detuning the cavity, or ϕ_0, is the key to operating in the recoherent regime. Thus, the pump pulse energy of where recoherence occurs is dependent on the OPO dispersion and nonlinear gain that induces π phase flips between the half-harmonic and the pump.
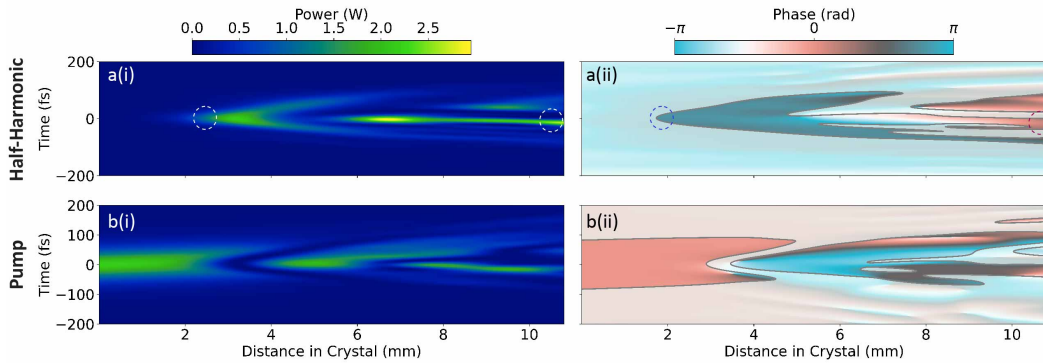
Figure 7.20: **Intensity and phase evolution inside the crystal for the half-harmonic (top) and pump (bottom) of regime (iii) for $l = -3$, $\phi_0 = 0$.** For a(ii) and b(ii), the phase of regions with intensity greater than ~ 0.2 W are encircled, and phases of locations with lower intensities are made more transparent.

Short Pulse Formation As mentioned in Section 7.2, the coherent multi-octave OPO can support ultrafast features at the output of the OPO. In Fig. 7.21, we explicitly show the simulated temporal output of this regime for the cases of $l = \{-3, -1, 1, 3\}$ with $\phi_0 = 0$. Features as narrow as 4.2 fs can be observed, suggesting that the coherent multi-octave comb regime can in the future be leveraged for extreme pulse compression and single/few-cycle pulse synthesis.

Extension to a Three Octave Comb

By employing a chirped poling period targeting energy transfer to the second harmonic and sum frequency generation terms, we can even induce three octaves of coherent spectra. In particular, the poling period in the last 1 mm of the 10.8-mm poled region is assumed to vary smoothly between the period required for quasi-phase-matched OPA between the pump at 1 µm and signal at 2 µm to phase
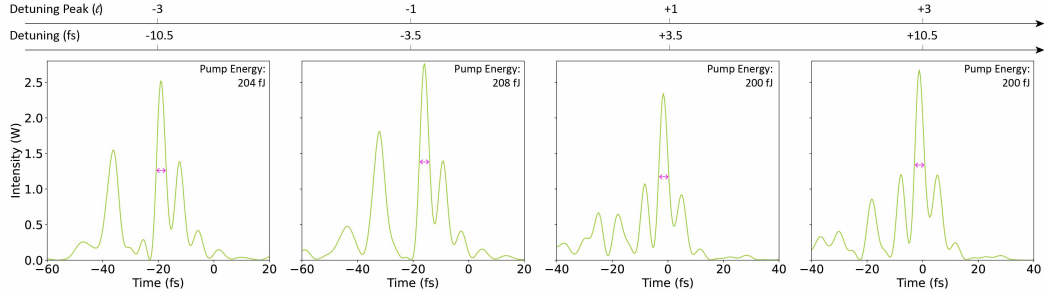
Figure 7.21: **Temporal output of the two-octave combs at different detunings**. In each case, the pink line showing the 3 dB bandwidth of the central feature is ∼ 4.2 fs. Here, $\phi_0 = 0$.

matching the interaction between the pump at 1 µm and its second harmonic at 500 nm. Extended characterization of the results, discussed in Fig. 7.3b, are shown in Fig. 7.22. Of note is that this high-harmonic generation process acts as an effective loss for the 2 µm signal, resulting in a slightly higher threshold for the OPO and larger pump power requirement to reach the recoherent regime. At 248 fJ of pump, however, a multi-octave comb is observed, with the additional high-harmonic processes enabling formation of a coherent three-octave spectrum (Fig. 7.22a-b) by filling the spectral gap between the second harmonic at 500 nm and sum-frequency component at 697 nm (d).
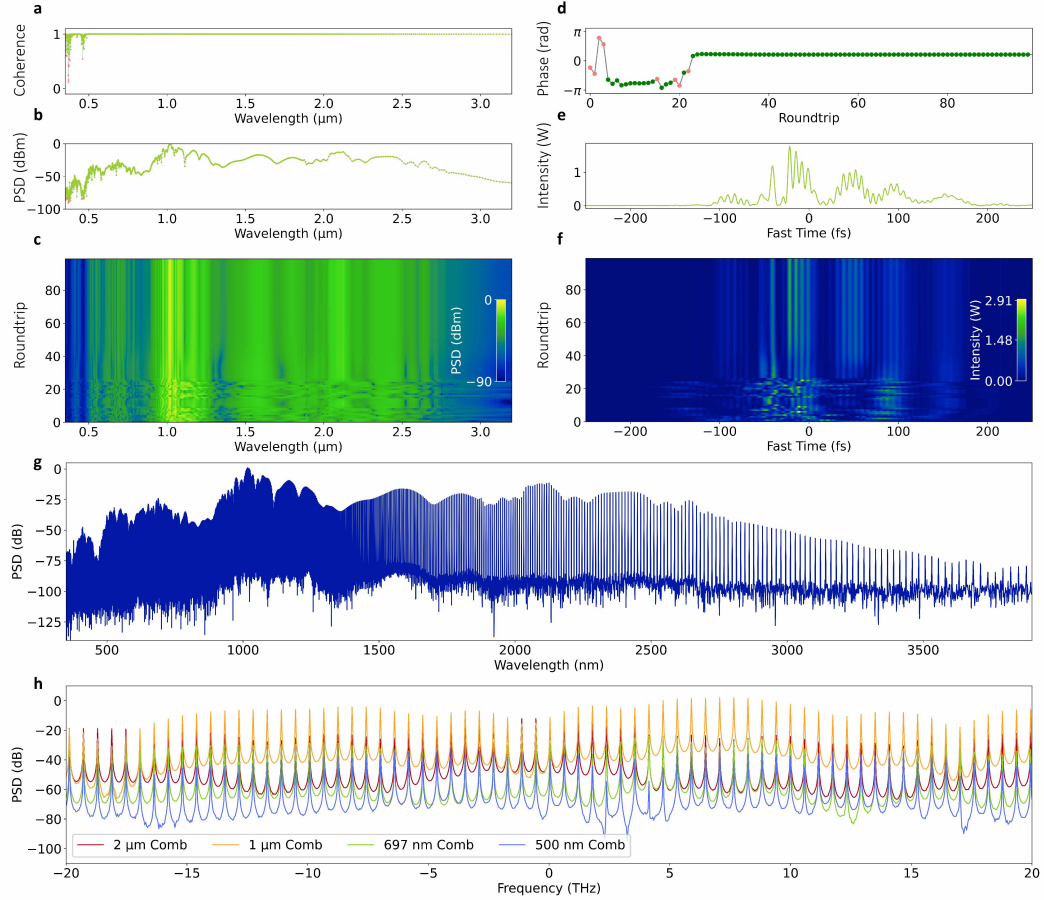
Figure 7.22: **Three octave comb characterization at** $l = 3$, $\phi_0 = 0$. The OPO was simulated with additional duty cycle variations in the poling period, producing a three-octave coherent frequency comb using 248 fJ of pump pulse energy. Panels **a** and **b** show the first-order coherence $g^{(1)}$ and the power spectral density (PSD) after 100 round trips, respectively. Panel **c** illustrates the spectral evolution as a function of round trip, while **d** shows the phase evolution of the OPO output. Panels **e** and **f** present the temporal intensity, with **e** showing the final output after 100 round trips and **f** showing the evolution over all round trips. Panel **g** displays the simulated comb lines spanning the full output spectrum. In panel **h**, comb lines corresponding to different harmonics are shifted by the nearest multiple of f_{rep} to center them at zero. The 2-μm, 1-μm, 69-nm, and 500-nm combs correspond to the half-harmonic, pump, sum-frequency generation of the pump and half-harmonic, and second harmonic of the pump, respectively.

BIBLIOGRAPHY

[1] David R. Carlson, Daniel D. Hickstein, Wei Zhang, Andrew J. Metcalf, Franklyn Quinlan, Scott A. Diddams, and Scott B. Papp. "Ultrafast electro-optic light with subcycle control." In: *Science* 361.6409 (2018), pp. 1358–1363. DOI: 10.1126/science.aat6451. URL: https://www.science.org/doi/abs/10.1126/science.aat6451.

[2] Scott A. Diddams, Kerry Vahala, and Thomas Udem. "Optical frequency combs: Coherently uniting the electromagnetic spectrum." In: *Science* 369.6501 (2020), eaay3676.

[3] Tobias J. Kippenberg, Alexander L. Gaeta, Michal Lipson, and Michael L. Gorodetsky. "Dissipative Kerr solitons in optical microresonators." In: *Science* 361.6402 (2018), eaan8083. DOI: 10.1126/science.aan8083. URL: https://www.science.org/doi/abs/10.1126/science.aan8083.

[4] Lin Chang, Songtao Liu, and John E. Bowers. "Integrated optical frequency comb technologies." In: *Nature Photonics* 16.2 (2022), pp. 95–108.

[5] Alexander L. Gaeta, Michal Lipson, and Tobias J. Kippenberg. "Photonic-chip-based frequency combs." In: *Nature Photonics* 13.3 (Mar. 2019), pp. 158–169. ISSN: 1749-4893. DOI: 10.1038/s41566-019-0358-x. URL: https://doi.org/10.1038/s41566-019-0358-x.

[6] Myoung-Gyun Suh, Qi-Fan Yang, Kiyoul Yang, Xu Yi, and Kerry J. Vahala. "Microresonator soliton dual-comb spectroscopy." In: *Science* 354.6312 (2016), pp. 600–603.

[7] Pablo Marin-Palomo, Juned N. Kemal, Maxim Karpov, Arne Kordts, Joerg Pfeifle, Martin H. P. Pfeiffer, Philipp Trocha, Stefan Wolf, Victor Brasch, Miles H. Anderson, Ralf Rosenberger, Kovendhan Vijayan, Wolfgang Freude, Tobias J. Kippenberg, and Christian Koos. "Microresonator-based solitons for massively parallel coherent optical communications." In: *Nature* 546.7657 (June 2017), pp. 274–279. ISSN: 1476-4687. DOI: 10.1038/nature22387. URL: https://doi.org/10.1038/nature22387.

[8] Daryl T. Spencer, Tara Drake, Travis C. Briles, Jordan Stone, Laura C. Sinclair, Connor Fredrick, Qing Li, Daron Westly, B. Robert Ilic, Aaron Bluestone, et al. "An optical-frequency synthesizer using integrated photonics." In: *Nature* 557.7703 (2018), pp. 81–85. DOI: 10.1038/s41586-018-0065-7.

[9] Minh A. Tran, Chong Zhang, Theodore J. Morin, Lin Chang, Sabyasachi Barik, Zhiquan Yuan, Woonghee Lee, Glenn Kim, Aditya Malik, Zeyu Zhang, Joel Guo, Heming Wang, Boqiang Shen, Lue Wu, Kerry Vahala,

John E. Bowers, Hyundai Park, and Tin Komljenovic. "Extending the spectrum of fully integrated photonics to submicrometre wavelengths." In: *Nature* 610.7930 (Oct. 2022), pp. 54–60. ISSN: 1476-4687. DOI: `10.1038/s41586-022-05119-9`. URL: `https://doi.org/10.1038/s41586-022-05119-9`.

[10]   Johann Riemensberger, Anton Lukashchuk, Maxim Karpov, Wenle Weng, Erwan Lucas, Junqiu Liu, and Tobias J. Kippenberg. "Massively parallel coherent laser ranging using a soliton microcomb." In: *Nature* 581.7807 (May 2020), pp. 164–170. ISSN: 1476-4687. DOI: `10.1038/s41586-020-2239-3`. URL: `https://doi.org/10.1038/s41586-020-2239-3`.

[11]   Daniel M. B. Lesko, Henry Timmers, Sida Xing, Abijith Kowligy, Alexander J. Lind, and Scott A. Diddams. "A six-octave optical frequency comb from a scalable few-cycle erbium fibre laser." In: *Nature Photonics* 15.4 (Apr. 2021), pp. 281–286. ISSN: 1749-4893. DOI: `10.1038/s41566-021-00778-y`. URL: `https://doi.org/10.1038/s41566-021-00778-y`.

[12]   Ugaitz Elu, Luke Maidment, Lenard Vamos, Francesco Tani, David Novoa, Michael H. Frosz, Valeriy Badikov, Dmitrii Badikov, Valentin Petrov, Philip St. J. Russell, and Jens Biegert. "Seven-octave high-brightness and carrier-envelope-phase-stable light source." In: *Nature Photonics* 15.4 (Apr. 2021), pp. 277–280. ISSN: 1749-4893. DOI: `10.1038/s41566-020-00735-1`. URL: `https://doi.org/10.1038/s41566-020-00735-1`.

[13]   Adrian Wirth, Mohammed Th. Hassan, Ivanka Grguraš, Justin Gagnon, Antoine Moulet, Tran Trung Luu, Stefan Pabst, Robin Santra, Zeyad A. Alahmed, Abdallah M. Azzeer, et al. "Synthesized light transients." In: *Science* 334.6053 (2011), pp. 195–200.

[14]   Paul B. Corkum and Ferenc Krausz. "Attosecond science." In: *Nature Physics* 3.6 (June 2007), pp. 381–387. ISSN: 1745-2481. DOI: `10.1038/nphys620`. URL: `https://doi.org/10.1038/nphys620`.

[15]   Andrey V. Muraviev, Viktor O. Smolski, Zachary E. Loparo, and Konstantin L. Vodopyanov. "Massively parallel sensing of trace molecules and their isotopologues with broadband subharmonic mid-infrared frequency combs." In: *Nature Photonics* 12.4 (2018), pp. 209–214. DOI: `10.1038/s41566-018-0135-2`.

[16]   Nathalie Picqué and Theodor W. Hänsch. "Frequency comb spectroscopy." In: *Nature Photonics* 13.3 (2019), pp. 146–157.

[17]   Chein-I Chang. *Hyperspectral imaging*. Springer US, 2003. DOI: `10.1007/978-1-4419-9170-6`. URL: `https://doi.org/10.1007/978-1-4419-9170-6`.

[18] Mengjie Yu, David Barton III, Rebecca Cheng, Christian Reimer, Prashanta Kharel, Lingyan He, Linbo Shao, Di Zhu, Yaowen Hu, Hannah R Grant, et al. "Integrated femtosecond pulse generator on thin-film lithium niobate." In: *Nature* 612.7939 (2022), pp. 252–258.

[19] Qiushi Guo, Benjamin K. Gutierrez, Ryoto Sekine, Robert M. Gray, James A. Williams, Luis Ledezma, Luis Costa, Arkadev Roy, Selina Zhou, Mingchen Liu, et al. "Ultrafast mode-locked laser in nanophotonic lithium niobate." In: *Science* 382.6671 (2023), pp. 708–713. DOI: 10.1126/science.adj5438.

[20] Brian Stern, Xingchen Ji, Yoshitomo Okawachi, Alexander L. Gaeta, and Michal Lipson. "Battery-operated integrated frequency comb generator." In: *Nature* 562.7727 (Oct. 2018), pp. 401–405. ISSN: 1476-4687. DOI: 10.1038/s41586-018-0598-9. URL: https://doi.org/10.1038/s41586-018-0598-9.

[21] Martin H. P. Pfeiffer, Clemens Herkommer, Junqiu Liu, Hairun Guo, Maxim Karpov, Erwan Lucas, Michael Zervas, and Tobias J. Kippenberg. "Octave-spanning dissipative Kerr soliton frequency combs in Si_3N_4 microresonators." In: *Optica* 4.7 (July 2017), pp. 684–691. DOI: 10.1364/OPTICA.4.000684. URL: https://opg.optica.org/optica/abstract.cfm?URI=optica-4-7-684.

[22] Qing Li, Travis C. Briles, Daron A. Westly, Tara E. Drake, Jordan R. Stone, B. Robert Ilic, Scott A. Diddams, Scott B. Papp, and Kartik Srinivasan. "Stably accessing octave-spanning microresonator frequency combs in the soliton regime." In: *Optica* 4.2 (Feb. 2017), pp. 193–203. DOI: 10.1364/OPTICA.4.000193. URL: https://opg.optica.org/optica/abstract.cfm?URI=optica-4-2-193.

[23] Ewelina Obrzud, Monica Rainer, Avet Harutyunyan, Miles H. Anderson, Junqiu Liu, Michael Geiselmann, Bruno Chazelas, Stefan Kundermann, Steve Lecomte, Massimo Cecconi, et al. "A microphotonic astrocomb." In: *Nature Photonics* 13.1 (2019), pp. 31–35. DOI: doi.org/10.1038/s41566-018-0309-y.

[24] Tsung-Han Wu, Luis Ledezma, Connor Fredrick, Pooja Sekhar, Ryoto Sekine, Qiushi Guo, Ryan M. Briggs, Alireza Marandi, and Scott A. Diddams. "Visible-to-ultraviolet frequency comb generation in lithium niobate nanophotonic waveguides." In: *Nature Photonics* 18.3 (Mar. 2024), pp. 218–223. ISSN: 1749-4893. DOI: 10.1038/s41566-023-01364-0. URL: https://doi.org/10.1038/s41566-023-01364-0.

[25] Dong Yoon Oh, Ki Youl Yang, Connor Fredrick, Gabriel Ycas, Scott A. Diddams, and Kerry J. Vahala. "Coherent ultra-violet to near-infrared generation in silica ridge waveguides." In: *Nature Communications* 8.1 (Jan.

2017), p. 13922. ISSN: 2041-1723. DOI: `10.1038/ncomms13922`. URL: `https://doi.org/10.1038/ncomms13922`.

[26] Markus Ludwig, Furkan Ayhan, Tobias M. Schmidt, Thibault Wildi, Thibault Voumard, Roman Blum, Zhichao Ye, Fuchuan Lei, François Wildi, Francesco Pepe, et al. "Ultraviolet astronomical spectrograph calibration with laser frequency combs from nanophotonic lithium niobate waveguides." In: *Nature communications* 15.1 (2024), p. 7614.

[27] John M. Dudley, Goëry Genty, and Stéphane Coen. "Supercontinuum generation in photonic crystal fiber." In: *Reviews of Modern Physics* 78.4 (2006), pp. 1135–1184.

[28] Sergey Vasilyev, Viktor Smolski, Jeremy Peppers, Igor Moskalev, Mike Mirov, Yury Barnakov, Sergey Mirov, and Valentin Gapontsev. "Middle-IR frequency comb based on Cr: ZnS laser." In: *Optics Express* 27.24 (2019), pp. 35079–35087.

[29] Marc Jankowski, Carsten Langrock, Boris Desiatov, Alireza Marandi, Cheng Wang, Mian Zhang, Christopher R. Phillips, Marko Lončar, and Martin M. Fejer. "Ultrabroadband nonlinear optics in nanophotonic periodically poled lithium niobate waveguides." In: *Optica* 7.1 (2020), pp. 40–46.

[30] Miles H. Anderson, Romain Bouchand, Junqiu Liu, Wenle Weng, Ewelina Obrzud, Tobias Herr, and Tobias J. Kippenberg. "Photonic chip-based resonant supercontinuum via pulse-driven Kerr microresonator solitons." In: *Optica* 8.6 (June 2021), pp. 771–779. DOI: `10.1364/OPTICA.403302`. URL: `https://opg.optica.org/optica/abstract.cfm?URI=optica-8-6-771`.

[31] Miles H. Anderson, Wenle Weng, Grigory Lihachev, Alexey Tikan, Junqiu Liu, and Tobias J. Kippenberg. "Zero dispersion Kerr solitons in optical ." In: *Nature Communications* 13.1 (Aug. 2022), p. 4764. DOI: `10.1038/s41467-022-31916-x`. URL: `https://doi.org/10.1038/s41467-022-31916-x`.

[32] Sean Molesky, Zin Lin, Alexander Y. Piggott, Weiliang Jin, Jelena Vucković, and Alejandro W. Rodriguez. "Inverse design in nanophotonics." In: *Nature Photonics* 12.11 (Nov. 2018), pp. 659–670. ISSN: 1749-4893. DOI: `10.1038/s41566-018-0246-9`. URL: `https://doi.org/10.1038/s41566-018-0246-9`.

[33] Peter L. McMahon, Alireza Marandi, Yoshitaka Haribara, Ryan Hamerly, Carsten Langrock, Shuhei Tamate, Takahiro Inagaki, Hiroki Takesue, Shoko Utsunomiya, Kazuyuki Aihara, et al. "A fully programmable 100-spin coherent Ising machine with all-to-all connections." In: *Science* 354.6312 (2016), pp. 614–617. DOI: `10.1126/science.aah5178`.

[34] Alireza Marandi, Nick C. Leindecker, Vladimir Pervak, Robert L. Byer, and Konstantin L. Vodopyanov. "Coherence properties of a broadband femtosecond mid-IR optical parametric oscillator operating at degeneracy." en. In: *Optics Express* 20.7 (Mar. 2012), p. 7255. ISSN: 1094-4087. DOI: 10.1364/OE.20.007255. URL: https://opg.optica.org/oe/abstract.cfm?uri=oe-20-7-7255 (visited on 03/17/2025).

[35] Alireza Marandi, Kirk A. Ingold, Marc Jankowski, and Robert L. Byer. "Cascaded half-harmonic generation of femtosecond frequency combs in the mid-infrared." In: *Optica* 3.3 (2016), pp. 324–327.

[36] Jinghua Sun, Barry J. S. Gale, and Derryck T. Reid. "Composite frequency comb spanning 0.4-2.4µm from a phase-controlled femtosecond Ti:sapphire laser and synchronously pumped optical parametric oscillator." In: *Optics Letters* 32.11 (June 2007), pp. 1414–1416. URL: https://opg.optica.org/ol/fulltext.cfm?uri=ol-32-11-1414&id=133455.

[37] Arkadev Roy, Rajveer Nehra, Saman Jahani, Luis Ledezma, Carsten Langrock, Martin Fejer, and Alireza Marandi. "Temporal walk-off induced dissipative quadratic solitons." In: *Nature Photonics* 16.2 (2022), pp. 162–168. DOI: 10.1038/s41566-021-00942-4.

[38] Luis Ledezma, Ryoto Sekine, Qiushi Guo, Rajveer Nehra, Saman Jahani, and Alireza Marandi. "Intense optical parametric amplification in dispersion-engineered nanophotonic lithium niobate waveguides." In: *Optica* 9.3 (2022), pp. 303–308. DOI: 10.1364/OPTICA.442332.

[39] Arkadev Roy, Luis Ledezma, Luis Costa, Robert Gray, Ryoto Sekine, Qiushi Guo, Mingchen Liu, Ryan M. Briggs, and Alireza Marandi. "Visible-to-mid-IR tunable frequency comb in nanophotonics." In: *Nature Communications* 14.1 (2023), p. 6549. DOI: 10.1038/s41467-023-42289-0.

[40] Luis Ledezma, Arkadev Roy, Luis Costa, Ryoto Sekine, Robert Gray, Qiushi Guo, Rajveer Nehra, Ryan M. Briggs, and Alireza Marandi. "Octave-spanning tunable infrared parametric oscillators in nanophotonics." In: *Science Advances* 9.30 (2023), eadf9711. DOI: 10.1126/sciadv.adf9711.

[41] Ryan Hamerly, Alireza Marandi, Marc Jankowski, Martin M. Fejer, Yoshihisa Yamamoto, and Hideo Mabuchi. "Reduced models and design principles for half-harmonic generation in synchronously pumped optical parametric oscillators." In: *Physical Review A* 94.6 (2016), p. 063809.

[42] Chengxiao Ning, Xi Feng, Jiaxing Heng, and Zhaowei Zhang. "Supercontinuum generation from a quasi-stationary doubly resonant optical parametric oscillator." In: *Optics Letters* 46.17 (2021), pp. 4280–4283.

[43] Pierre Suret, Marc Lefranc, Dominique Derozier, Jaouad Zemmouri, and Serge Bielawski. "Fast oscillations in an optical parametric oscillator." In: *Optics Communications* 200.1-6 (2001), pp. 369–379.

[44] Markus Leidinger, Stephan Fieberg, Niklas Waasem, Frank Kühnemann, Karsten Buse, and Ingo Breunig. "Comparative study on three highly sensitive absorption measurement techniques characterizing lithium niobate over its entire transparent spectral range." In: *Optics Express* 23.17 (Aug. 2015), pp. 21690–21705. DOI: 10.1364/OE.23.021690. URL: https://opg.optica.org/oe/abstract.cfm?URI=oe-23-17-21690.

[45] Yoshitomo Okawachi, Mengjie Yu, Boris Desiatov, Bok Young Kim, Tobias Hansson, Marko Lončar, and Alexander L. Gaeta. "Chip-based self-referencing using integrated lithium niobate waveguides." In: *Optica* 7.6 (June 2020), pp. 702–707. DOI: 10.1364/OPTICA.392363. URL: https://opg.optica.org/optica/abstract.cfm?URI=optica-7-6-702.

[46] Mengjie Yu, Boris Desiatov, Yoshitomo Okawachi, Alexander L. Gaeta, and Marko Lončar. "Coherent two-octave-spanning supercontinuum generation in lithium-niobate waveguides." In: *Optics Letters* 44.5 (Mar. 2019), pp. 1222–1225. DOI: 10.1364/OL.44.001222. URL: https://opg.optica.org/ol/abstract.cfm?URI=ol-44-5-1222.

[47] David R. Carlson, Daniel D. Hickstein, Alex Lind, Judith B. Olson, Richard W. Fox, Roger C. Brown, Andrew D. Ludlow, Qing Li, Daron Westly, Holly Leopardi, Tara M. Fortier, Kartik Srinivasan, Scott A. Diddams, and Scott B. Papp. "Photonic-chip supercontinuum with tailored spectra for counting optical frequencies." In: *Physical Review Applied* 8 (1 July 2017), p. 014027. DOI: 10.1103/PhysRevApplied.8.014027. URL: https://link.aps.org/doi/10.1103/PhysRevApplied.8.014027.

[48] Ben Spaun, P. Bryan Changala, David Patterson, Bryce J. Bjork, Oliver H. Heckl, John M. Doyle, and Jun Ye. "Continuous probing of cold complex molecules with infrared frequency comb spectroscopy." In: *Nature* 533.7604 (May 2016), pp. 517–520. ISSN: 1476-4687. DOI: 10.1038/nature17440. URL: https://doi.org/10.1038/nature17440.

[49] Bryce J. Bjork, Thinh Q. Bui, Oliver Hubert Heckl, P. Bryan Changala, Ben Spaun, Paula Heu, David Follman, Christoph Deutsch, Garrett D. Cole, Markus Aspelmeyer, et al. "Direct frequency comb measurement of OD + CO → DOCO kinetics." In: *Science* 354.6311 (2016), pp. 444–448. DOI: 10.1126/science.aag1862. URL: https://www.science.org/doi/abs/10.1126/science.aag1862.

[50] Wenle Weng, Aleksandra Kaszubowska-Anandarajah, Jijun He, Prajwal D. Lakshmijayasimha, Erwan Lucas, Junqiu Liu, Prince M. Anandarajah, and Tobias J. Kippenberg. "Gain-switched semiconductor laser driven soliton microcombs." In: *Nature Communications* 12.1 (Mar. 2021), p. 1425. ISSN: 2041-1723. DOI: `10.1038/s41467-021-21569-7`. URL: `https://doi.org/10.1038/s41467-021-21569-7`.

[51] Yiqing Xu, Yi Lin, Alexander Nielsen, Ian Hendry, Stéphane Coen, Miro Erkintalo, Huilian Ma, and Stuart G. Murdoch. "Harmonic and rational harmonic driving of microresonator soliton frequency combs." In: *Optica* 7.8 (Aug. 2020), pp. 940–946. DOI: `10.1364/OPTICA.392571`. URL: `https://opg.optica.org/optica/abstract.cfm?URI=optica-7-8-940`.

[52] Ewelina Obrzud, Steve Lecomte, and Tobias Herr. "Temporal solitons in microresonators driven by optical pulses." In: *Nature Photonics* 11.9 (Sept. 2017), pp. 600–607. ISSN: 1749-4893. DOI: `10.1038/nphoton.2017.140`. URL: `https://doi.org/10.1038/nphoton.2017.140`.

[53] Takahiro Inagaki, Kensuke Inaba, Ryan Hamerly, Kyo Inoue, Yoshihisa Yamamoto, and Hiroki Takesue. "Large-scale Ising spin network based on degenerate optical parametric oscillators." In: *Nature Photonics* 10.6 (June 2016), pp. 415–419. ISSN: 1749-4893. DOI: `10.1038/nphoton.2016.68`. URL: `https://doi.org/10.1038/nphoton.2016.68`.

[54] Preetpaul S. Devgan, Jacob Lasri, Renyong Tang, Vladimir S. Grigoryan, William L. Kath, and Prem Kumar. "10-GHz dispersion-managed soliton fiber-optical parametric oscillator using regenerative mode locking." In: *Optics Letters* 30.5 (2005), pp. 528–530.

[55] Arkadev Roy, Rajveer Nehra, Carsten Langrock, Martin Fejer, and Alireza Marandi. "Non-equilibrium spectral phase transitions in coupled nonlinear optical resonators." In: *Nature Physics* 19.3 (2023), pp. 427–434. DOI: `10.6084/m9.figshare.21252147`.

[56] Kirk A. Ingold, Alireza Marandi, Michel J. F. Digonnet, and Robert L. Byer. "Fiber-feedback optical parametric oscillator for half-harmonic generation of sub-100-fs frequency combs around 2 μm." In: *Optics Letters* 40.18 (2015), pp. 4368–4371.

[57] Carsten Langrock and Martin M. Fejer. "Fiber-feedback continuous-wave and synchronously-pumped singly-resonant ring optical parametric oscillators using reverse-proton-exchanged periodically-poled lithium niobate waveguides." In: *Optics Letters* 32.15 (Aug. 2007), pp. 2263–2265. DOI: `10.1364/OL.32.002263`. URL: `https://opg.optica.org/ol/abstract.cfm?URI=ol-32-15-2263`.

[58] Jay E. Sharping, Marco Fiorentino, Prem Kumar, and Robert S. Windeler. "Optical parametric oscillator based on four-wave mixing in microstructure fiber." In: *Optics Letters* 27.19 (Oct. 2002), pp. 1675–1677. DOI: 10.1364/OL.27.001675. URL: https://opg.optica.org/ol/abstract.cfm?URI=ol-27-19-1675.

[59] Yujun Deng, Qiang Lin, Fei Lu, Govind P. Agrawal, and Wayne H. Knox. "Broadly tunable femtosecond parametric oscillator using a photonic crystal fiber." In: *Optics Letters* 30.10 (May 2005), pp. 1234–1236. DOI: 10.1364/OL.30.001234. URL: https://opg.optica.org/ol/abstract.cfm?URI=ol-30-10-1234.

[60] Jay E. Sharping, Mark A. Foster, Alexander L. Gaeta, Jacob Lasri, Ove Lyngnes, and Kurt Vogel. "Octave-spanning, high-power microstructure-fiber-based optical parametric oscillators." In: *Optics Express* 15.4 (Feb. 2007), pp. 1474–1479. DOI: 10.1364/OE.15.001474. URL: https://opg.optica.org/oe/abstract.cfm?URI=oe-15-4-1474.

[61] Ming Gao, Niklas M. Lüpken, Klaus-J. Boller, and Carsten Fallnich. "Optical parametric oscillator based on silicon nitride waveguides." In: *Optica Advanced Photonics Congress 2022*. Optica Publishing Group, 2022, JTh4A.3. DOI: 10.1364/BGPPM.2022.JTh4A.3. URL: https://opg.optica.org/abstract.cfm?URI=BGPPM-2022-JTh4A.3.

[62] Alireza Marandi, Zhe Wang, Kenta Takata, Robert L. Byer, and Yoshihisa Yamamoto. "Network of time-multiplexed optical parametric oscillators as a coherent Ising machine." In: *Nature Photonics* 8.12 (2014), pp. 937–942. DOI: 10.1038/nphoton.2014.249.

[63] Oliver H. Heckl, Bryce J. Bjork, Georg Winkler, P. Bryan Changala, Ben Spaun, Gil Porat, Thinh Q. Bui, Kevin F. Lee, Jie Jiang, Martin E. Fermann, et al. "Three-photon absorption in optical parametric oscillators based on OP-GaAs." In: *Optics Letters* 41.22 (Nov. 2016), pp. 5405–5408. DOI: 10.1364/OL.41.005405. URL: https://opg.optica.org/ol/abstract.cfm?URI=ol-41-22-5405.

[64] Derryck T. Reid, Gordon T. Kennedy, Alan Miller, Wilson Sibbett, and Majid Ebrahim-Zadeh. "Widely tunable, near- to mid-infrared femtosecond and picosecond optical parametric oscillators using periodically poled LiNbO/sub 3/ and RbTiOAsO/sub 4/." In: *IEEE Journal of Selected Topics in Quantum Electronics* 4.2 (1998), pp. 238–248. DOI: 10.1109/2944.686729.

[65] Ryoto Sekine, Robert Gray, Luis Ledezma, Qiushi Guo, and Alireza Marandi. "Sync-pumped femtosecond OPO based on dispersion-engineered nanophotonic PPLN with 3-octave spectrum." In: *Conference on Lasers and Electro-Optics*. Optica Publishing Group, 2022, SM5K.2. DOI: 10.1364/CLEO_SI.2022.SM5K.2. URL:

```
https://opg.optica.org/abstract.cfm?URI=CLEO_SI-
2022-SM5K.2.
```

[66]   Jiang Li, Chengying Bao, Qing-Xin Ji, Heming Wang, Lue Wu, Stephanie Leifer, Charles Beichman, and Kerry Vahala. "Efficiency of pulse pumped soliton microcombs." In: *Optica* 9.2 (Feb. 2022), pp. 231–239. DOI: `10.1364/OPTICA.443060`. URL: `https://opg.optica.org/optica/abstract.cfm?URI=optica-9-2-231`.

[67]   Kent C. Burr, Chung L. Tang, Mark A. Arbore, and Martin M. Fejer. "Broadly tunable mid-infrared femtosecond optical parametric oscillator using all-solid-state-pumped periodically poled lithium niobate." In: *Optics Letters* 22.19 (Oct. 1997), pp. 1458–1460. DOI: `10.1364/OL.22.001458`. URL: `https://opg.optica.org/ol/abstract.cfm?URI=ol-22-19-1458`.

[68]   Iouli E. Gordon, Laurence S. Rothman, Robert J. Hargreaves, R. Hashemi, Ekaterina V. Karlovets, Frances M. Skinner, Eamon K. Conway, Christian Hill, Roman V. Kochanov, Yan Tan, et al. "The HITRAN2020 molecular spectroscopic database." In: *Journal of Quantitative Spectroscopy and Radiative Transfer* 277 (2022), p. 107949.

[69]   Richard A. Soref, Stephen J. Emelett, and Walter R. Buchwald. "Silicon waveguided components for the long-wave infrared region." In: *Journal of Optics A: Pure and Applied Optics* 8.10 (Aug. 2006), p. 840. DOI: `10.1088/1464-4258/8/10/004`. URL: `https://dx.doi.org/10.1088/1464-4258/8/10/004`.

[70]   Steven A. Miller, Mengjie Yu, Xingchen Ji, Austin G. Griffith, Jaime Cardenas, Alexander L. Gaeta, and Michal Lipson. "Low-loss silicon platform for broadband mid-infrared photonics." In: *Optica* 4.7 (July 2017), pp. 707–712. DOI: `10.1364/OPTICA.4.000707`. URL: `https://opg.optica.org/optica/abstract.cfm?URI=optica-4-7-707`.

[71]   Hongtao Lin, Zhengqian Luo, Tian Gu, Lionel C. Kimerling, Kazumi Wada, Anu Agarwal, and Juejun Hu. "Mid-infrared integrated photonics on silicon: A perspective." In: *Nanophotonics* 7.2 (2018), pp. 393–420. DOI: `doi:10.1515/nanoph-2017-0085`. URL: `https://doi.org/10.1515/nanoph-2017-0085`.

[72]   Jatadhari Mishra, Marc Jankowski, Alexander Y. Hwang, Hubert S. Stokowski, Timothy P. McKenna, Carsten Langrock, Edwin Ng, David Heydari, Hideo Mabuchi, Amir H. Safavi-Naeini, et al. "Ultra-broadband mid-infrared generation in dispersion-engineered thin-film lithium niobate." In: *Optics Express* 30.18 (Aug. 2022), pp. 32752–32760. DOI: `10.1364/OE.467580`. URL: `https://opg.optica.org/oe/abstract.cfm?URI=oe-30-18-32752`.

[73]   Marc Jankowski. *Pulse formation and frequency conversion in dispersion-engineered nonlinear waveguides and resonators.* Stanford University, 2020.

[74]   Christopher R. Phillips, Carsten Langrock, Jason S. Pelc, Martin M. Fejer, Ingmar Hartl, and Martin E. Fermann. "Supercontinuum generation in quasi-phasematched waveguides." In: *Optics Express* 19.20 (Sept. 2011), pp. 18754–18773. ISSN: 1094-4087. DOI: 10.1364/OE.19.018754. (Visited on 02/18/2019).

[75]   Matteo Conforti, Fabio Baronio, and Costantino De Angelis. "Nonlinear envelope equation for broadband optical pulses in quadratic media." In: *Phys. Rev. A* 81 (5 May 2010), p. 053841. DOI: 10.1103/PhysRevA.81.053841. URL: https://link.aps.org/doi/10.1103/PhysRevA.81.053841.

[76]   Miroslav Kolesik, Jerome V. Moloney, and Michal Mlejnek. "Unidirectional optical pulse propagation equation." In: *Physical Review Letters* 89 (28 Dec. 2002), p. 283902. DOI: 10.1103/PhysRevLett.89.283902. URL: https://link.aps.org/doi/10.1103/PhysRevLett.89.283902.

[77]   Thomas Brabec and Ferenc Krausz. "Nonlinear optical pulse propagation in the single-cycle regime." In: *Physical Review Letters* 78 (17 Apr. 1997), pp. 3282–3285. DOI: 10.1103/PhysRevLett.78.3282. URL: https://link.aps.org/doi/10.1103/PhysRevLett.78.3282.

[78]   Luis Ledezma. *SNOW: Simulator for nonlinear optical waveguides.* https://github.com/ledezmaluism/snow. 2025.

[79]   Marc Jankowski, Alireza Marandi, Christopher R. Phillips, Ryan Hamerly, Kirk A. Ingold, Robert L. Byer, and Martin M. Fejer. "Temporal simultons in optical parametric oscillators." In: *Physical Review Letters* 120.5 (2018), p. 053904.

[80]   Johan Hult. "A fourth-order Runge–Kutta in the interaction picture method for simulating supercontinuum generation in optical fibers." In: *Journal of Lightwave Technology* 25.12 (Dec. 2007), pp. 3770–3775. ISSN: 1558-2213. DOI: 10.1109/JLT.2007.909373.

C h a p t e r   8

MULTI-OCTAVE COMB FORMATION DYNAMICS IN OPTICAL PARAMETRIC OSCILLATORS

8.1 Introduction

As motivated in Chapter 7, broadband optical frequency combs play a prominent role in modern optical technologies [1–3], with wide application in areas including spectroscopy [4–6], metrology and timekeeping [7, 8], communications [9, 10], and information processing [11]. Combs spanning greater than one octave are of particular importance due to their use in single-cycle pulse synthesis [12, 13] and their compatibility with self-referencing schemes used for carrier-envelope phase control and stabilization. Multi-octave frequency combs are typically realized through supercontinuum generation via coherent spectral broadening mechanisms based on $\chi^{(2)}$ or $\chi^{(3)}$ nonlinearities [14, 15]. Such supercontinuum generation has usually relied on driving a nonlinear medium such as an optical fiber or bulk crystal with high-energy (~nJ) pulses from an ultrafast source [16, 17].

Photonic integration has brought many new opportunities for reducing the size and energy requirements for supercontinuum generation [18]. In particular, the strong spatial confinement offers increased nonlinear interaction strength while simultaneously enabling dispersion engineering, both key parameters in the design of supercontinuum generation systems. These properties have been leveraged in $\chi^{(2)}$ waveguides on the TFLN platform to achieve multi-octave supercontinuum generation [19, 20]. However, these demonstrations have required 10s of pJ pump pulse energies to achieve significant coverage beyond an octave, beyond the reach of current integrated laser sources [1, 2, 21–23]. Furthermore, the usual broadening mechanism relies on second-harmonic generation, thus necessitating an infrared pump source to achieve spectral coverage in the long-wavelength spectral region [24].

On the other hand, recent efforts to reduce the complexity of supercontinuum sources have turned to resonant configurations, in which the nonlinear medium responsible for the supercontinuum generation is placed inside an optical resonator or laser cavity [25]. One challenge of this configuration, however, is that the nonlinear phase accumulated during the nonlinear broadening process can destabilize the system, leading to an incoherent output at high pump powers. Recent demonstrations have

leveraged Mamyshev configurations [26–28], or other forms of intracavity filtering [29], and additionally exploited nonlinear attractor dynamics such as similariton formation [30, 31] to extend the coherent regime.

Among nonlinear resonators, OPOs are of particular interest due to their ability to translate pump combs to disparate spectral windows where direct lasing remains challenging [32, 33]. At degeneracy, OPOs further benefit from an intrinsic phase and frequency locking between pump and signal whereby the pump and signal may share the same set of comb lines requiring no additional stabilization [34]. This ability to translate the coherence properties of the pump comb between disparate frequency bands makes OPOs a particularly attractive candidate for the generation of multi-octave frequency combs; however, previous demonstrations of far-above threshold OPOs have typically suffered from similar decoherence mechanisms due to the strong nonlinear phase accumulation [35, 36].

More recently, integrated OPOs have been demonstrated in TFLN, offering both a reduced size and threshold compared to their bulk counterparts [37–40]. In particular, we demonstrated in Chapter 7 multi-octave frequency comb generation from a dispersion-engineered nanophotonic parametric oscillator which was synchronously pumped with 100-fs pulses at 1045 nm [41]. The system was marked by an ultralow threshold energy of $\sim$ 18 fJ as well as a distinct transition as the pump power was increased from coherence to incoherence followed by recoherence at a pump pulse energy of $\sim$ 121 fJ, leading to the observed coherent multi-octave spectrum. In contrast to previous demonstrations of far above threshold OPOs, we observed that the nonlinear phase was again balanced by the cavity detuning in this regime to achieve coherence.

Here, we analyze the dynamics responsible for such coherent multi-octave continuum formation in OPOs. By analyzing the simulated propagation dynamics through the lens of the temporal mode basis of the linearized OPA, we find that the combined effects of the dispersion and nonlinearity result in an effective spectral filtering effect in the cavity roundtrip, leading to the OPA input being dominated by the fundamental temporal mode of the amplifier in cases where coherence is observed. Our numerical results are supported by spectral and temporal characterization of several different regimes of our nanophotonic OPO device. Through our analysis, we draw analogy between our system and previous demonstrations of intracavity supercontinuum generation based on self-similar propagation and intracavity filtering. Our results offer important insight into the design of OPOs capable of supporting

such multi-octave coherent continuum as well as the dynamics of highly nonlinear resonators more broadly.
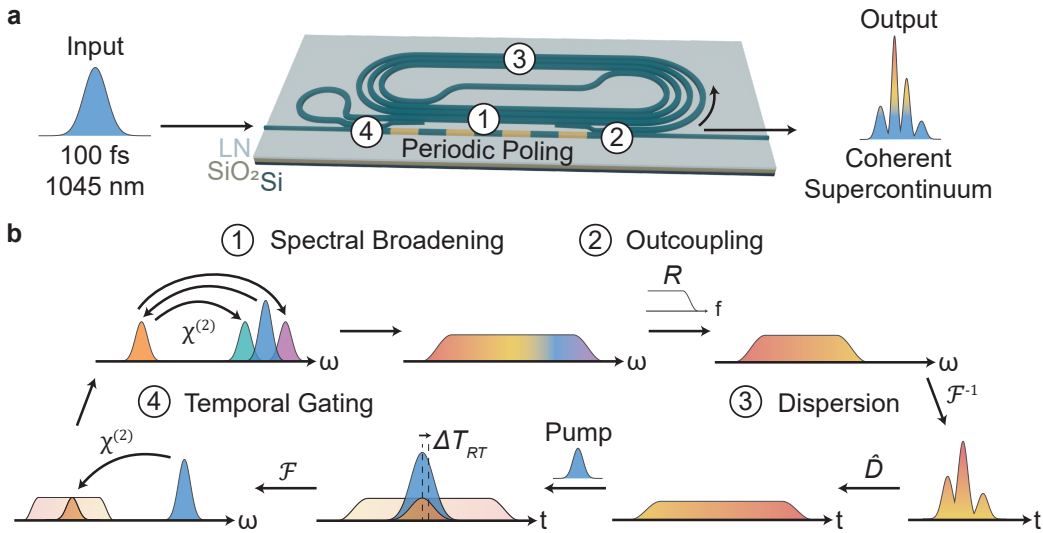
Figure 8.1: **Dynamics of coherent supercontinuum generation**. **a**, Schematic of the OPO device, with labels indicating four key dynamical regions. **b**, Far above threshold, back-and-forth conversion between the pump and half-harmonic signal in the periodic poled region ① leads to spectral broadening. Part of the half-harmonic signal is then filtered out and sent to the spiral resonator at the outcoupler in region ②. In the cavity, region ③, dispersion causes the various frequency components to spread out in time. Finally, at the input coupler, region ④, a new pump pulse is injected which temporally gates a portion of the circulating signal. This corresponds to filtering a limited band of frequencies, depending on the roundtrip group delay, ΔT_{RT}, which seed the subsequent roundtrip. $\chi^{(2)}$, second-order susceptibility; $\mathcal{F}$, Fourier transform; ΔT_{RT}, roundtrip group delay; $\hat{D}$, dispersion operator; R, power coupling.

8.2 Results

The measured OPO device is shown in Fig. 8.1a, as described in Chapter 7 [41]. A 10.8-mm-long periodically poled region ① facilitates phase-matched interaction between the 100-fs pump pulses at 1045 nm and the half-harmonic signal at 2090 nm. Dispersion engineering ensures near-0 GVM and GVD between the pump and half-harmonic, ensuring large and broadband gain for the signal. Adiabatic couplers in regions ② and ④ enable coupling of the half-harmonic while transmitting the pump. The 53-cm spiral cavity, region ③, ensures the pump repetition rate of 250 MHz is matched to the cavity FSR.

Figure 8.1b describes the signal propagation dynamics at different points in the

roundtrip for the coherent supercontinuum generation. In the periodically poled region ①, cascaded $\chi^{(2)}$ processes due to gain saturation and subsequent back-and-forth conversion between the pump and signal result in spectral broadening, forming the multi-octave continuum. Next, the outcoupler in region ② filters out the high-frequency components while feeding back the low-frequency components, though the signal still remains confined in the time domain. However, during the cavity roundtrip, corresponding to region ③, higher-order dispersion results in the pulse becoming spread out in time, with different temporal locations corresponding to distinct frequency components. This dispersed pulse is then recombined with the next injected pump pulse at the input coupler, region ④. Prior to saturation, for a Gaussian input pulse, the amplifier acts most strongly along the fundamental temporal mode of the OPA, which is well-approximated by the fundamental Hermite-Gaussian in both the time and frequency domain, centered around degeneracy [42]. This leads to an effective temporal gating and corresponding frequency filtering effect in the first few millimeters of propagation in the amplifier, which can be optimized by adjusting the roundtrip group delay, ΔT_{RT}, to maximize the contribution from the fundamental mode at the OPA input. This filtering effect helps to ensure the same signal seeds the spectral broadening process in subsequent roundtrips, such that coherence is maintained.

To verify this dynamical behavior, we turn to both numerical simulation and experimental measurements. Our simulation is similar to that described in Section 7.4, but we additionally utilize the refractive index profile calculated using Lumerical to imrpove the accuracy of the simulation. Likewise, our measurement setup is similar to the setup described in Section 7.4, though we additionally utilize the FROG system described in Section 5.7. To begin, we simulate the OPO behavior for pump energy levels between 0 pJ and 0.4 pJ across several values fo ΔT_{RT} and characterize the output in terms of whether it is coherent, incoherent, or periodic, as shown in Figs. 8.2a and 8.2b for $\Delta T_{\mathrm{RT}} \approx 0$ fs and $\Delta T_{\mathrm{RT}} \approx 14$ fs, respectively. Periodic here refers to output state which is seen to repeat over the course of several roundtrips, with some regimes exhibiting periodicity at an exact integer number of roundtrips while others exhibit periodicity over a non-integer multiple of the roundtrip number, as is typical of non-degenerate OPO operation. Further study of these periodic regimes is not the focus of this work, although similar observation of such periodic and limit-cycle behaviors has been reported in studies of other highly nonlinear resonators [35, 43, 44]. In terms of coherent regimes, we observe the disappearance and reemergence of coherence in the $\Delta T_{\mathrm{RT}} \approx 14$ fs case but not in the case where $\Delta T_{\mathrm{RT}} \approx 0$ fs,
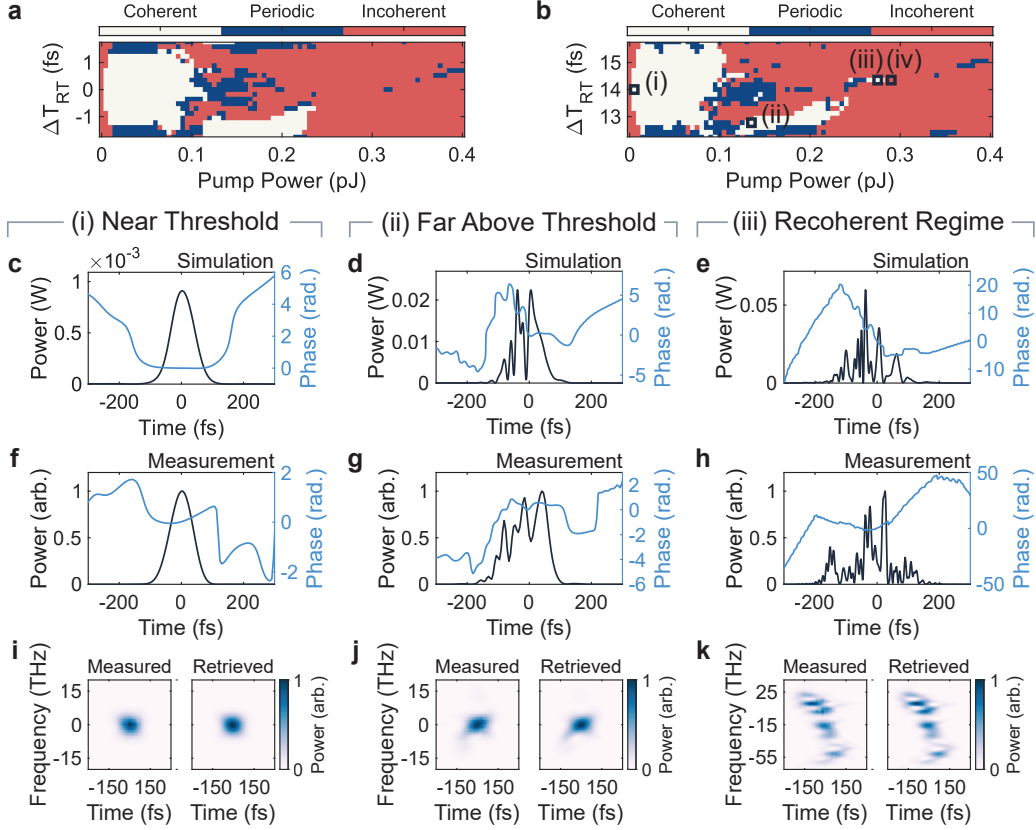
Figure 8.2: **Temporal characterization**. **a**, Map of coherent, incoherent and periodic regimes around $\Delta T_{\mathrm{RT}} = 0$ fs and **b**, $\Delta T_{\mathrm{RT}} = 14$ fs, demonstrating the reliance of the recoherent regime on the detuning, ΔT_{RT}. **c-e**, Simulated temporal profile in the **c**, near threshold, **d**, far above threshold, and **e**, recoherent regimes, labeled (i), (ii), and (iii) in **b**. **f-h**, Corresponding experimentally measured temporal profiles. **i-k**, Associated measured (left) and retrieved (right) FROG traces for the plots of **f-h**. We observe FROG errors of 0.00188, 0.00177, and 0.00481 for the traces of **i**, **j**, and **k**, respectively.

indicating the sensitivity of such the recoherent regime to the detuning parameter.

Four pump energy regimes are indicated on Fig. 8.2b, which will be the primary focus of the remainder of our analysis, the near threshold regime (i), the far above threshold regime (ii), the recoherent regime (iii), and the incoherent regime (iv). The temporal profiles of the simulated and measured half-harmonic outputs in each of these regimes are shown in Figs. 8.2c-e and Figs. 8.2f-h, respectively, with Figs. 8.2i-k presenting the FROG traces corresponding to the measured data. Near threshold, the simulated (Fig. 8.2c) and measured (Fig. 8.2f) pulses are nearly transform-limited with a FWHM duration of ~ 80 fs. As the pump energy is

increased, back-and-forth conversion between the pump and signal leads to the formation of sharp features in the time domain, as observed for the far above threshold regime of Fig. 8.2d and Fig. 8.2g. Furthermore, significant phase variations may be observed across the pulse due to the strong nonlinear phase accumulation. We see even sharper temporal features on the order of $\sim 15 - 20$ fs in the recoherent regime, shown in Figs. 8.2e and 8.2h. Good qualitative agreement is observed between the simulated and measured pulse shapes in all regimes.
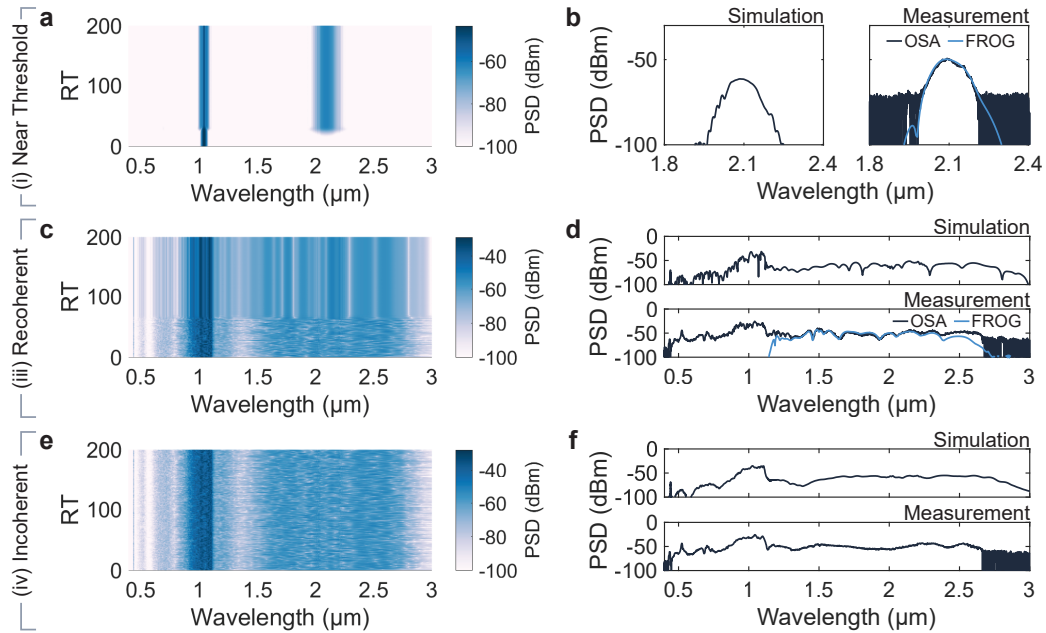
Figure 8.3: **Spectral characterization.** **a**, Simulated roundtrip evolution of the spectrum in the near threshold regime (i). **b**, Simulated (left) and measured (right) average PSD in the near threshold regime; the retrieved FROG spectrum is overlaid on the experimental plot for comparison. **c**, Spectral evolution in the recoherent regime (iii). **d**, Simulated (top) and measured (bottom) average PSD in the recoherent regime, exhibiting good agreement. Again, the measured FROG spectrum is overlaid for comparison. **e**, Simulated roundtrip evolution in the incoherent regime, labeled (iv) in Fig. 8.2b, showing that the system fails to reach steady-state. **f**, Simulated (top) and measured (bottom) average PSDs again exhibit good agreement.

Figure 8.3 shows our corresponding spectral characterization of the OPO, focusing on the near threshold, recoherent, and incoherent regimes. Figures 8.3a, 8.3c, and 8.3e show the roundtrip evolution for the three different regimes, whereas Figs. 8.3b, 8.3d, and 8.3f show the average simulated and measured power spectral density at the output. Near threshold, the signal smoothly builds up until reaching steady-state after around 20 roundtrips (Fig. 8.3a), leading to well-separated pump and

signal bands. The signal output (Fig. 8.3b) consists of only a single spectral lobe around the degenerate half-harmonic wavelength, 2090 nm, with good agreement between the simulation and measurement as well as the measured trace on the OSA and retrieved FROG spectrum. The recoherent regime exhibits different build-up dynamics (Fig. 8.3c) as the pump power is sufficient for the signal to nearly saturate the gain in just a single pass. The high-power signal is then seen to oscillate for around 60 roundtrips before finally reaching the coherent steady-state solution. In the average output PSD (Fig. 8.3d), we observe multi-octave supercontinuum. For the bandwidth of the FROG measurement, good agreement is again also observed between the reconstructed FROG spectrum and the measurement. Finally, we analyze the incoherent regime. As shown in Fig. 8.3e, the system never reaches a steady-state in this regime. Likewise, for the average spectra of Fig. 8.3f, despite being multi-octave, the structure observed in the recoherent regime is washed out due to the roundtrip-to-roundtrip fluctuations.
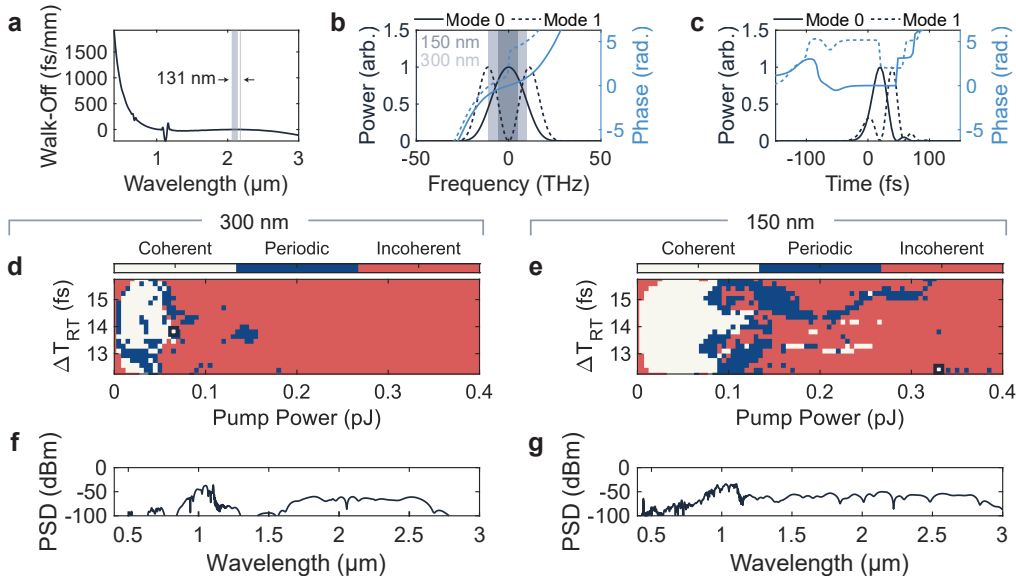
Figure 8.4: **Modal filtering. a**, Walk-off relative to 2090 nm of different spectral components. The highlighted region with a bandwidth of 131 nm shows the spectral content which walks less than 100 fs in the roundtrip. **b**, Spectral profile of modes 0 and 1 of the optical parametric amplifier. The highlighted regions show the filtered content corresponding to a pass band of 150 nm (dark gray) and 300 nm (light gray). **c**, Corresponding temporal mode shapes. **d-e**, Coherence maps corresponding to a dispersion-free cavity with an intracavity filter bandwidth of **d**, 300 nm, and **e**, 150 nm. **f-g**, Spectra corresponding to the points indicated by black squares in **d** (for **f**) and **e** (for **g**).

Having verified the ability of our numerical simulation to qualitatively capture the

different dynamical regimes of our experimentally measured OPO device, we next seek to understand the key features responsible for the recoherence. As shown pictorially in Fig. 8.1, we are especially interested in the interplay between the roundtrip dispersion and temporal gating through the nonlinearity, which has a filtering effect on the signal. This behavior is explored through our results presented in Fig. 8.4. Figure 8.4a presents the walk-off relative to the half-harmonic wavelength (2090 nm) in fs/mm based on the calculated effective index of our designed device. The highlighted region shows the spectral components which walk off less than 100 fs in the course of the roundtrip propagation, the total bandwidth of which is approximately 130 nm. For comparison, we plot the spectral (Fig. 8.4b) and temporal (Fig. 8.4c) profiles of the first two temporal modes of the linearized OPA [42]. We further consider two filter bandwidths, 150 nm and 300 nm, shown by the dark and light gray highlighted regions of Fig. 8.4b, respectively. From this, we see that the 150 nm filter (similar to the effective filtering provided by the combined dispersion and nonlinearity) preserves much of mode 0 while filtering out most of mode 1, whereas the 300 nm filter contains a significant portion of mode 1 in addition to mode 0.

In Figs. 8.4d and 8.4e, we plot the simulated coherence map for a modified version of our cavity, where the roundtrip dispersion has been set to 0 and instead replaced by an intracavity filter with a bandwidth of 300 nm (Fig. 8.4d) and 150 nm (Fig 8.4e). With the 300 nm filter, once the coherence breaks, for increasing pump energies, no recoherent regime is attained. However, with the 150 nm filter, we observe dynamics more similar to those of our experimental system, where recoherence is achieved at higher pump powers. We furthermore plot the spectra corresponding to the highest power coherent regime for both filter bandwidths in the plots of Figs. 8.4f and 8.4g. Here, we see that the 300 nm filter does not permit the formation of coherent multi-octave supercontinuum, as the pump and half-harmonic bands remain disconnected (Fig. 8.4f), whereas the 150 nm filter is able to support such coherent supercontinuum generation.

To further explore this effective mode filtering behavior, we turn in Fig. 8.5 to the simulated propagation dynamics of the OPA. We again consider the near threshold, recoherent, and incoherent regimes of Fig. 8.2. The near threshold regime is depicted in Figs. 8.5a-c. Figure 8.5a presents the simulated temporal profile (bottom) of the half-harmonic at the input to the OPA as well as its decomposition onto the first 50 input modes of the linearized OPA (dashed, red line), along with the corresponding modal distribution (top). In this regime, the fundamental mode is
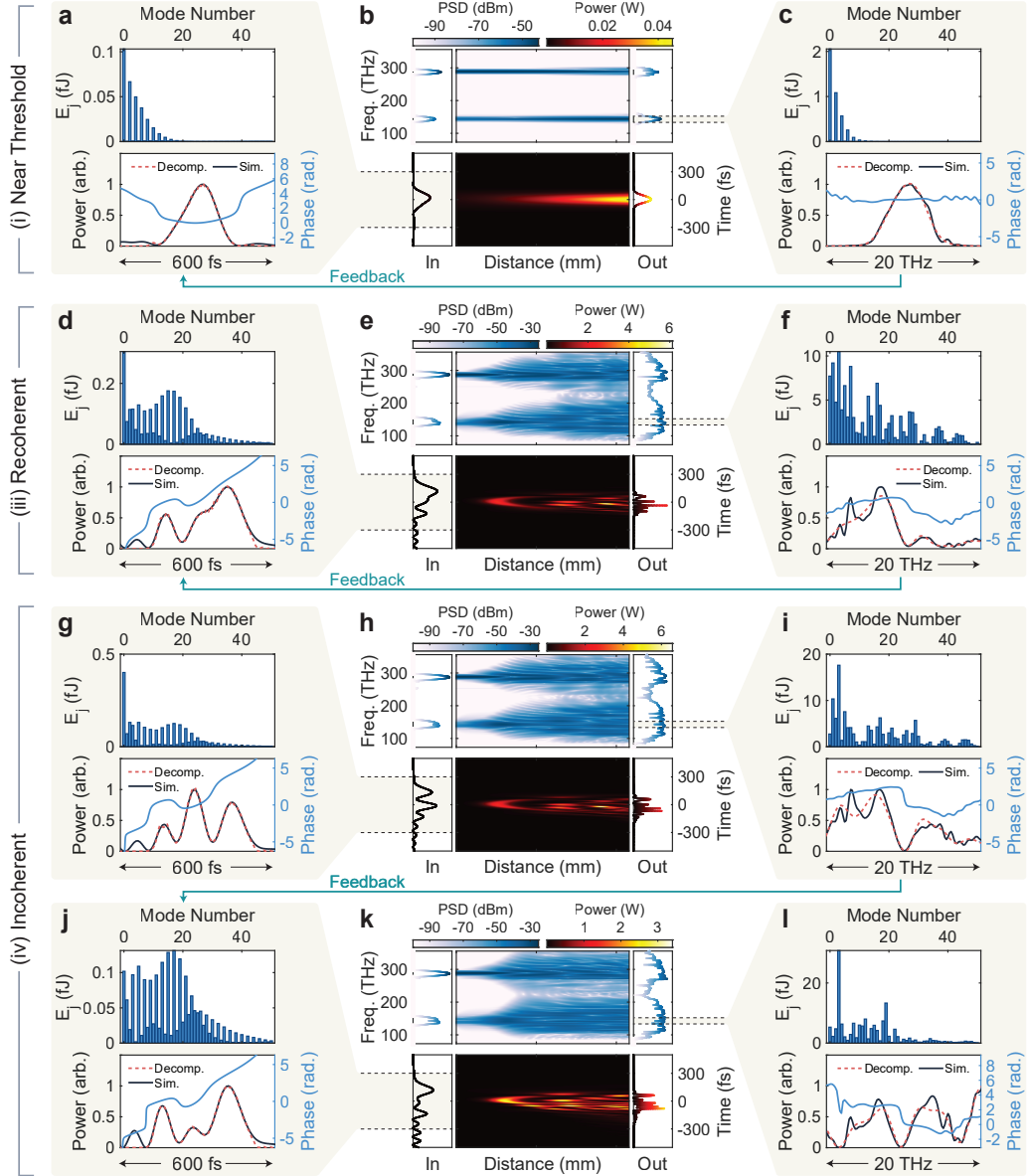
Figure 8.5: **Propagation dynamics. a**, Mode distribution (top) and temporal profile (bottom) of the half-harmonic OPA input for the steady-state near threshold OPO. The mode decomposition fit is shown with a dashed, red line. **b**, Spectral (top) and half-harmonic temporal (bottom) evolution in the OPA. Input (output) profiles are shown in the left (right) insets. **c**, Mode distribution (top) and spectral profile (bottom) of the half-harmonic OPA output. Equivalent plots are shown for **d-f**, the recoherent regime at steady-state as well as **g-i** and **j-l**, subsequent roundtrips in the incoherent regime.

seen to dominate, and the symmetry of the pulse correspondingly presents as even modes exhibiting the highest modal amplitudes. Figure 8.5b shows the spectral (top) and half-harmonic temporal (bottom) evolution through the crystal. Left

(right) insets show the input (output) spectrum and temporal profiles. Here, we observe the monotonic transfer of power from the pump to the signal, with limited back-conversion to the pump. This results in limited spectral broadening. Figure 8.5c depicts the simulated output half-harmonic spectral profile (bottom) and its corresponding mode decomposition (dashed, red line) as well as the corresponding distribution in mode number (top). In this regime, since the lower mode numbers exhibit the highest gain, the distribution is further weighted towards the fundamental mode. The modal distribution is again dominated by the even modes.

Figures 8.5d-f present the equivalent plots for the recoherent regime. Here, we again see that the OPA input (Fig. 8.5d) is dominated by the fundamental mode, although the mode decomposition does not exhibit the same monotonic drop-off as was observed in the near threshold regime. Due to this strong presence of the fundamental mode, we observe that the amplifier initially acts monotonically in the first few millimeters of propagation (Fig. 8.5e, as in the case of the near threshold regime. Subsequent back-and-forth conversion, however, lead to supercontinuum generation accompanied by significant distortion in the temporal and spectral profiles. In terms of the modal decomposition (Fig. 8.5f), the output is extremely messy and contains strong contributions from many of the higher-order modes. However, the fundamental mode remains strong enough that, following the cavity feedback, it is able to return to the input state of Fig. 8.5d containing a dominant contribution from the fundamental mode.

Finally, Figs. 8.5g-i and 8.5j-l contain equivalent plots for subsequent roundtrips in the incoherent regime. We select in Figs. 8.5g-i a roundtrip which exhibits a qualitatively similar input to that of the recoherent regime. As can be seen in Fig. 8.5g, the input contains a dominant contribution from the fundamental mode. However, the stronger pump in this regime leads to a slightly faster back-and-forth conversion (Fig. 8.5h) compared to the recoherent regime. The result is that the output contains very little contribution from the fundamental mode (Fig. 8.5i) such that the cavity feedback is insufficient to seed the same state in the amplifier as the preceding roundtrip. The resulting temporal profile and mode decomposition following the feedback is shown in Fig. 8.5j. The presence of many higher-order modes at the amplifier input leads to a faster breakup of the pulse during propagation (Fig. 8.5k) and an output which is again dominated by the presence of higher-order modes (Fig. 8.5l).

8.3 Discussion

From our results, we see that the generated coherent supercontinuum relies on two dominant effects: spectral broadening due to gain saturation and subsequent back-and-forth conversion in the parametric amplifier along with an effective filtering effect due to the interplay between dispersion and temporal gating due to action of the pump on the signal in the parametric amplifier. These dynamics bear strong resemblance to those observed in oscillators based on self-similar pulse propagation as well as the Mamyshev principle. In our system, the fundamental OPA mode can be viewed analogously to the self-similar solution of a laser amplifier [30], in that it represents a pulse of a given phase and amplitude profile which experiences gain but otherwise remains undistorted in the unsaturated amplifier. Furthermore, it is an approximate attractor of the nonlinear element, since the fundamental mode exhibits the highest gain; hence, the relative contribution from higher-order modes is reduced during propagation in the unsaturated OPA, as observed in the near threshold case of Fig. 8.5a-c. In the recoherent regime, this attractive behavior occurs only prior to saturation, in the first few millimeters of propagation (Fig. 8.5e). After this, as discussed in the above, gain saturation and subsequent back-and-forth conversion result in a significantly distorted pulse profile at the output of the nonlinear region. Robustness against the accumulated nonlinear phase due to these distortions is achieved in our system due to the effective filtering effect created by the interplay of the roundtrip dispersion paired with temporal gating in the nonlinearity through the finite duration of our pump pulse. This is similar to the robustness observed in oscillators based on the Mamyshev principle to nonlinear phase accumulation [26], due to the pulse shaping achieved via spectral filtering in each of the Mamyshev regenerator elements.

In conclusion, we have studied the formation of multi-octave supercontinuum in OPOs driven far above threshold. Through a mixture of experimental results and numerical simulations, we have found the key ingredients responsible for the multi-octave coherent supercontinuum formation, with the dominant contribution coming from an effective filtering effect arising due to the interplay of dispersion and non-linearity in our system. This allows the spectral broadening process in the saturated OPA to be dominantly seeded by the fundamental mode of the unsaturated OPA in each roundtrip for the regimes in which coherence is achieved. Our results can inform the design of future supercontinuum generation based on OPOs, which can benefit from several design modifications compared to our current device. Primarily, in our current device, we have utilized a broadband coupler with approximately 98%

coupling at the half-harmonic wavelength of 2090 nm; however, as illustrated by our theoretical analysis, only a small portion of the recirculating spectrum contributes to the supercontinuum generation in the subsequent roundtrip. Furthermore, much of the recirculating signal is lost due to the large propagation losses in the roundtrip. Thus, a system with reduced roundtrip losses as well as a more narrow-band coupler and larger output coupling across the signal band can offer improved extraction efficiencies for the generated continuum, without significantly altering the threshold. Furthermore, the system could benefit from operation in the vicinity of an alternate attractor of the single pass propagation, or from the incorporation of a more single-mode parametric amplifier.

BIBLIOGRAPHY

[1] Lin Chang, Songtao Liu, and John E. Bowers. "Integrated optical frequency comb technologies." In: *Nature Photonics* 16.2 (2022), pp. 95–108.

[2] Scott A. Diddams, Kerry Vahala, and Thomas Udem. "Optical frequency combs: Coherently uniting the electromagnetic spectrum." In: *Science* 369.6501 (2020), eaay3676.

[3] Alexander L. Gaeta, Michal Lipson, and Tobias J. Kippenberg. "Photonic-chip-based frequency combs." In: *Nature Photonics* 13.3 (Mar. 2019), pp. 158–169. ISSN: 1749-4893. DOI: 10.1038/s41566-019-0358-x. URL: https://doi.org/10.1038/s41566-019-0358-x.

[4] Nathalie Picqué and Theodor W. Hänsch. "Frequency comb spectroscopy." In: *Nature Photonics* 13.3 (2019), pp. 146–157.

[5] Mengjie Yu, Yoshitomo Okawachi, Austin G. Griffith, Nathalie Picqué, Michal Lipson, and Alexander L. Gaeta. "Silicon-chip-based mid-infrared dual-comb spectroscopy." In: *Nature Communications* 9.1 (2018), p. 1869.

[6] Myoung-Gyun Suh, Qi-Fan Yang, Kiyoul Yang, Xu Yi, and Kerry J. Vahala. "Microresonator soliton dual-comb spectroscopy." In: *Science* 354.6312 (2016), pp. 600–603.

[7] Thomas Udem, Ronald Holzwarth, and Theodor W Hänsch. "Optical frequency metrology". In: *Nature* 416.6877 (2002), pp. 233–237.

[8] Travis L. Nicholson, Sara L. Campbell, Ross B. Hutson, G. Edward Marti, Benjamin J. Bloom, Rees L. McNally, Wei Zhang, Murray D. Barrett, Marianna S Safronova, Gregory F. Strouse, et al. "Systematic evaluation of an atomic clock at 2× 10- 18 total uncertainty". In: *Nature Communications* 6.1 (2015), p. 6896.

[9] Pablo Marin-Palomo, Juned N. Kemal, Maxim Karpov, Arne Kordts, Joerg Pfeifle, Martin H. P. Pfeiffer, Philipp Trocha, Stefan Wolf, Victor Brasch, Miles H. Anderson, Ralf Rosenberger, Kovendhan Vijayan, Wolfgang Freude, Tobias J. Kippenberg, and Christian Koos. "Microresonator-based solitons for massively parallel coherent optical communications." In: *Nature* 546.7657 (June 2017), pp. 274–279. ISSN: 1476-4687. DOI: 10.1038/nature22387. URL: https://doi.org/10.1038/nature22387.

[10] Lars Lundberg, Mikael Mazur, Ali Mirani, Benjamin Foo, Jochen Schröder, Victor Torres-Company, Magnus Karlsson, and Peter A. Andrekson. "Phase-coherent lightwave communications with frequency combs". In: *Nature Communications* 11.1 (2020), p. 201.

[11] Peter L. McMahon. "The physics of optical computing." In: *Nature Reviews Physics* 5.12 (2023), pp. 717–734.

[12] Cristian Manzoni, Oliver D. Mücke, Giovanni Cirmi, Shaobo Fang, Jeffrey Moses, Shu-Wei Huang, Kyung-Han Hong, Giulio Cerullo, and Franz X. Kärtner. "Coherent pulse synthesis: Towards sub-cycle optical waveforms." In: *Laser & Photonics Reviews* 9.2 (2015), pp. 129–171. DOI: https://doi.org/10.1002/lpor.201400181. eprint: https://onlinelibrary.wiley.com/doi/pdf/10.1002/lpor.201400181. URL: https://onlinelibrary.wiley.com/doi/abs/10.1002/lpor.201400181.

[13] Adrian Wirth, Mohammed Th. Hassan, Ivanka Grguraš, Justin Gagnon, Antoine Moulet, Tran Trung Luu, Stefan Pabst, Robin Santra, Zeyad A. Alahmed, Abdallah M. Azzeer, et al. "Synthesized light transients." In: *Science* 334.6053 (2011), pp. 195–200.

[14] John M. Dudley, Goëry Genty, and Stéphane Coen. "Supercontinuum generation in photonic crystal fiber." In: *Reviews of Modern Physics* 78.4 (2006), pp. 1135–1184.

[15] Yang Yue, Yuxi Fang, Wenpu Geng, and Changjing Bao. "SCG involving second-order nonlinearity." In: *Integrated Optical Supercontinuum Generation: Physics, Advances, and Applications*. Springer, 2024, pp. 141–160.

[16] Thibaut Sylvestre, Etienne Genier, Amar Nath Ghosh, Patrick Bowen, Goëry Genty, Johann Troles, Arnaud Mussot, Anna C. Peacock, Mariusz Klimczak, Alexander M. Heidt, et al. "Recent advances in supercontinuum generation in specialty optical fibers". In: *Journal of the Optical Society of America B* 38.12 (2021), F90–F103.

[17] Christopher R. Phillips, Carsten Langrock, Jason S. Pelc, Martin M. Fejer, Ingmar Hartl, and Martin E. Fermann. "Supercontinuum generation in quasi-phasematched waveguides." In: *Optics Express* 19.20 (Sept. 2011), pp. 18754–18773. ISSN: 1094-4087. DOI: 10.1364/OE.19.018754. (Visited on 02/18/2019).

[18] Camille-Sophie Brès, Alberto Della Torre, Davide Grassani, Victor Brasch, Christian Grillet, and Christelle Monat. "Supercontinuum in integrated photonics: generation, applications, challenges, and perspectives". In: *Nanophotonics* 12.7 (2023), pp. 1199–1244.

[19] Marc Jankowski, Carsten Langrock, Boris Desiatov, Alireza Marandi, Cheng Wang, Mian Zhang, Christopher R. Phillips, Marko Lončar, and Martin M. Fejer. "Ultrabroadband nonlinear optics in nanophotonic periodically poled lithium niobate waveguides." In: *Optica* 7.1 (2020), pp. 40–46.

[20] Marin Hamrouni, Marc Jankowski, Alexander Y. Hwang, Noah Flemens, Jatadhari Mishra, Carsten Langrock, Amir H. Safavi-Naeini, Martin M. Fejer, and Thomas Südmeyer. "Picojoule-level supercontinuum generation

in thin-film lithium niobate on sapphire". In: *Optics Express* 32.7 (2024), pp. 12004–12011.

[21] Mengjie Yu, David Barton III, Rebecca Cheng, Christian Reimer, Prashanta Kharel, Lingyan He, Linbo Shao, Di Zhu, Yaowen Hu, Hannah R Grant, et al. "Integrated femtosecond pulse generator on thin-film lithium niobate." In: *Nature* 612.7939 (2022), pp. 252–258.

[22] Qiushi Guo, Benjamin K. Gutierrez, Ryoto Sekine, Robert M. Gray, James A. Williams, Luis Ledezma, Luis Costa, Arkadev Roy, Selina Zhou, Mingchen Liu, et al. "Ultrafast mode-locked laser in nanophotonic lithium niobate." In: *Science* 382.6671 (2023), pp. 708–713. DOI: 10.1126/science.adj5438.

[23] Brian Stern, Xingchen Ji, Yoshitomo Okawachi, Alexander L. Gaeta, and Michal Lipson. "Battery-operated integrated frequency comb generator." In: *Nature* 562.7727 (Oct. 2018), pp. 401–405. ISSN: 1476-4687. DOI: 10.1038/s41586-018-0598-9. URL: https://doi.org/10.1038/s41586-018-0598-9.

[24] Marc Jankowski, Carsten Langrock, Boris Desiatov, Marko Lončar, and Martin M. Fejer. "Supercontinuum generation by saturated second-order nonlinear interactions." In: *APL Photonics* 8.11 (2023).

[25] Miles H. Anderson, Romain Bouchand, Junqiu Liu, Wenle Weng, Ewelina Obrzud, Tobias Herr, and Tobias J. Kippenberg. "Photonic chip-based resonant supercontinuum via pulse-driven Kerr microresonator solitons." In: *Optica* 8.6 (June 2021), pp. 771–779. DOI: 10.1364/OPTICA.403302. URL: https://opg.optica.org/optica/abstract.cfm?URI=optica-8-6-771.

[26] Ying-Ying Li, Bo Gao, Chun-Yang Ma, Ge Wu, Jia-Yu Huo, Ying Han, Swelm Wageh, Omar A. Al-Hartomy, Abdullah G. Al-Sehemi, Lie Liu, et al. "Generation of high-peak-power femtosecond pulses in Mamyshev oscillators: Recent advances and future challenges." In: *Laser & Photonics Reviews* 17.4 (2023), p. 2200596.

[27] Chunyang Ma, Ankita Khanolkar, Yimin Zang, and Andy Chong. "Ultra-broadband, few-cycle pulses directly from a Mamyshev fiber oscillator". In: *Photonics Research* 8.1 (2019), pp. 65–69.

[28] Zhanwei Liu, Zachary M. Ziegler, Logan G. Wright, and Frank W. Wise. "Megawatt peak power from a Mamyshev oscillator". In: *Optica* 4.6 (2017), pp. 649–654.

[29] Yiwei Tian, Fanchao Meng, Qi Yan, Changjian Lv, Zhixu Jia, Weiping Qin, Guanshi Qin, and John M Dudley. "Intracavity coherent supercontinuum generation via high-order soliton dynamics in a dissipative soliton fiber laser." In: *Optics Express* 32.27 (2024), pp. 47970–47981.

[30] John M. Dudley, Christophe Finot, David J. Richardson, and Guy Millot. "Self-similarity in ultrafast nonlinear optics". In: *Nature Physics* 3.9 (2007), pp. 597–603.

[31] Norihiko Nishizawa, Toshiki Niinomi, Yoshitaka Nomura, Lei Jin, and Yasuyuki Ozeki. "Octave spanning coherent supercontinuum comb generation based on Er-doped fiber lasers and their characterization". In: *IEEE Journal of Selected Topics in Quantum Electronics* 24.3 (2017), pp. 1–9.

[32] Mingchen Liu, Robert M. Gray, Arkadev Roy, Kirk A. Ingold, Evgeni Sorokin, Irina Sorokina, Peter G. Schunemann, and Alireza Marandi. "High-power mid-IR few-cycle frequency comb from quadratic solitons in an optical parametric oscillator." In: *Laser & Photonics Reviews* 16.11 (2022), p. 2200453. DOI: 10.1002/lpor.202200453.

[33] Andrey V. Muraviev, Viktor O. Smolski, Zachary E. Loparo, and Konstantin L. Vodopyanov. "Massively parallel sensing of trace molecules and their isotopologues with broadband subharmonic mid-infrared frequency combs." In: *Nature Photonics* 12.4 (2018), pp. 209–214. DOI: 10.1038/s41566-018-0135-2.

[34] Alireza Marandi, Nick C. Leindecker, Vladimir Pervak, Robert L. Byer, and Konstantin L. Vodopyanov. "Coherence properties of a broadband femtosecond mid-IR optical parametric oscillator operating at degeneracy." en. In: *Optics Express* 20.7 (Mar. 2012), p. 7255. ISSN: 1094-4087. DOI: 10.1364/OE.20.007255. URL: https://opg.optica.org/oe/abstract.cfm?uri=oe-20-7-7255 (visited on 03/17/2025).

[35] Ryan Hamerly, Alireza Marandi, Marc Jankowski, Martin M. Fejer, Yoshihisa Yamamoto, and Hideo Mabuchi. "Reduced models and design principles for half-harmonic generation in synchronously pumped optical parametric oscillators." In: *Physical Review A* 94.6 (2016), p. 063809.

[36] Chengxiao Ning, Xi Feng, Jiaxing Heng, and Zhaowei Zhang. "Supercontinuum generation from a quasi-stationary doubly resonant optical parametric oscillator." In: *Optics Letters* 46.17 (2021), pp. 4280–4283.

[37] Luis Ledezma, Arkadev Roy, Luis Costa, Ryoto Sekine, Robert Gray, Qiushi Guo, Rajveer Nehra, Ryan M. Briggs, and Alireza Marandi. "Octave-spanning tunable infrared parametric oscillators in nanophotonics." In: *Science Advances* 9.30 (2023), eadf9711. DOI: 10.1126/sciadv.adf9711.

[38] Timothy P. McKenna, Hubert S. Stokowski, Vahid Ansari, Jatadhari Mishra, Marc Jankowski, Christopher J. Sarabalis, Jason F. Herrmann, Carsten Langrock, Martin M. Fejer, and Amir H. Safavi-Naeini. "Ultra-low-power second-order nonlinear optics on a chip." In: *Nature Communications* 13.1 (2022), p. 4532. DOI: 10.1038/s41467-022-31134-5.

[39] Juanjuan Lu, Ayed Al Sayem, Zheng Gong, Joshua B. Surya, Chang-Ling Zou, and Hong X. Tang. "Ultralow-threshold thin-film lithium niobate optical parametric oscillator." In: *Optica* 8.4 (2021), pp. 539–544. DOI: 10.1364/OPTICA.418984.

[40] Jost Kellner, Alessandra Sabatti, Andreas Maeder, and Rachel Grange. "Low threshold integrated optical parametric oscillator with a compact Bragg resonator". In: *Optica* 12.5 (2025), pp. 702–707.

[41] Ryoto Sekine, Robert M. Gray, Luis Ledezma, Selina Zhou, Qiushi Guo, and Alireza Marandi. "Multi-octave frequency comb from an ultra-low-threshold nanophotonic parametric oscillator." In: *arXiv preprint arXiv:2309.04545* (2023). DOI: 10.48550/arXiv.2309.04545.

[42] Wojciech Wasilewski, Alexander I. Lvovsky, Konrad Banaszek, and Czesław Radzewicz. "Pulsed squeezed light: Simultaneous squeezing of multiple modes". In: *Physical Review A—Atomic, Molecular, and Optical Physics* 73.6 (2006), p. 063819.

[43] Petra Groß, Nicoletta Haarlammert, Michael Kues, Till Walbaum, and Carsten Fallnich. "Effects of optical feedback on femtosecond supercontinuum generation". In: *Optical Fiber Technology* 18.5 (2012), pp. 290–303.

[44] Michael Kues, Nicoletta Brauckmann, Till Walbaum, Petra Groß, and Carsten Fallnich. "Nonlinear dynamics of femtosecond supercontinuum generation with feedback". In: *Optics Express* 17.18 (2009), pp. 15827–15841.

Chapter 9

LARGE-SCALE TIME-MULTIPLEXED NANOPHOTONIC PARAMETRIC OSCILLATORS

Robert M. Gray[*], Ryoto Sekine[*], Luis Ledezma, Gordon H. Y. Li, Selina Zhou, Arkadev Roy, Midya Parto, and Alireza Marandi. "Large-scale time-multiplexed nanophotonic parametric oscillators." In: *Newton* (2025). DOI: 10.1016/j.newton.2025.100108.

9.1 Introduction

Nonlinear resonators are emerging as one of the most versatile building blocks for a wide range of photonic systems benefiting applications in quantum information processing [1, 2], stochastic computing [3, 4], metrology [5, 6], and spectroscopy and sensing [7, 8], among others. Coupled nonlinear resonators further promise broad potentials, which have been showcased through a variety of table-top experiments, for instance using OPOs [9–12] and lasers [13, 14]. However, in nanophotonics, demonstrations of coupled nonlinear resonators remain in the small-scale regime [15–18] or suffer from limited programmability [19, 20].

OPOs using quadratic nonlinearity are one of the most promising nonlinear photonic resonators, with a long history as table-top tunable sources in hard-to-access wavelength ranges [21]. More recently, OPOs have been used for a wide range of applications spanning from frequency comb spectroscopy [22] to sensing [23], quantum information processing [24], and computing [25–27]. Advances in thin-film lithium niobate have enabled realization of nanophotonic OPOs [28–30] with substantial miniaturization and threshold enhancement due to the sub-micron modal confinement. Synchronous pumping of dispersion-engineered nanophotonic OPOs with ultrashort pulses is particularly important because it leads to ultralow-threshold operation [31] enabling opportunities for energy-efficient ultrabroad comb sources [32] and quantum information processing [33].

Ultrafast nanophotonic OPOs not only benefit from ultra-low-energy operation, they also enable large-scale time-domain multiplexing (TDM) for realization of programmable OPO networks. Time-multiplexed resonator networks have been demonstrated on table-top experiments for a wide range of studies in optical com-

puting [11, 26, 34], topological photonics [35, 36], and non-equilibrium phase transitions [12], among others. Compared with other multiplexing schemes for realizing nonlinear resonators, such as spatial and spectral multiplexing [37], TDM benefits from scalability, and the strength of nonlinearity [14].

Here, we demonstrate the first nanophotonic realization of large-scale time-multiplexed OPOs in LN. By leveraging a large parametric gain and dispersion engineering, we achieve simultaneous oscillation of as many as 70 independent time-multiplexed OPOs at a 17.5 GHz repetition rate, limited primarily by the speeds of our pump repetition rate and detection electronics. We verify the independence of the oscillators through an interferometric measurement at the output of the chip which confirms the vacuum-seeded randomness of each oscillator.
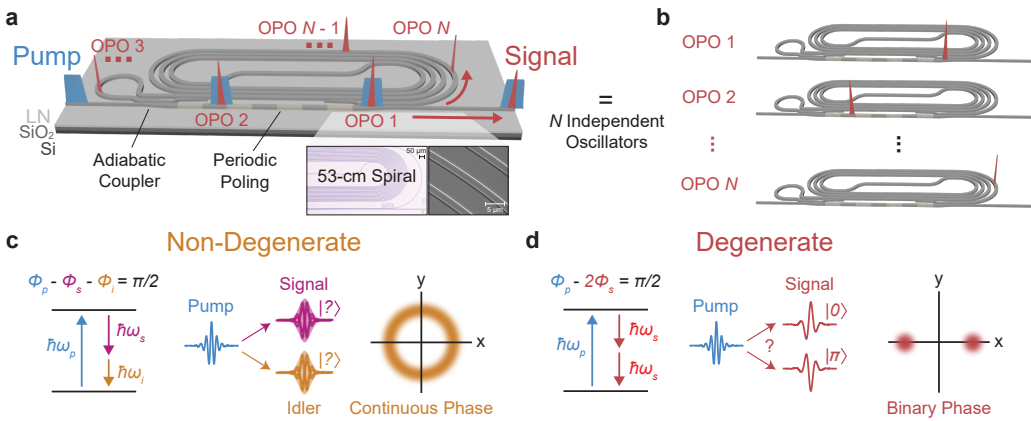
Figure 9.1: **Time-multiplexed nanophotonic OPOs. a**, Schematic of the device based on thin-film lithium niobate. Microscope images of the 53-cm-long spiral resonator are shown in the inset. N pulses in the long cavity are equivalent to **b**, N independent time-multiplexed oscillators. **c**, In the non-degenerate regime, the pump photons split into signal and idler photons at different frequencies. In this case, the phase of each is unconstrained, as shown in the signal phase space diagram. **d**, In the degenerate regime, the pump photons split into indistinguishable signal photons at the half-harmonic of the pump, resulting in a binary phase for the signal.

9.2   Results

Interferometric Measurement Principle

The on-chip time-multiplexed OPO system is schematically depicted in Fig. 9.1a. The inset shows a recolored optical microscope image (left) and scanning electron microscope image (right) of a portion of the 53-cm-long spiral resonator. The temporally separated oscillators, equivalent to the N independent oscillators shown in Fig. 9.1b, share the same optical path length and long periodically poled section.

High gain provided by the periodically poled region ensures a low on-chip threshold pulse energy of a few pJ for the ps pulses used in the experiment. Adiabatic tapers couple more than 96% of the signal light into the resonator while ensuring very little coupling ($\leq 2\%$) for the pump. Finally, dispersion engineering of the waveguide geometry ensures near-zero group velocity mismatch between the pump and signal during the nonlinear interaction to achieve a high gain and gain bandwidth as well as near-zero group velocity dispersion for the signal in the roundtrip, which preserves the short-pulse operation necessary for maintaining the independence of the oscillators.

We operate in both the non-degenerate (Fig. 9.1c) and degenerate (Fig. 9.1d) regimes by adjusting the pump frequency detuning with respect to the cavity. In the non-degenerate regime, pump photons are split into signal and idler photons at different frequencies, and their phase relationship is given by

$$\phi_p - \phi_s - \phi_i = \frac{\pi}{2}, \tag{9.1}$$

where ϕ_p, ϕ_s, and ϕ_i are the pump, signal, and idler phase, respectively. Taking the pump phase as determined, this relationship leaves the signal and idler phases free, constraining only their sum. Thus, as illustrated in the phase space diagram of Fig. 9.1c, wherein the radial coordinate represents the pulse amplitude and the angle represents the phase, the phases are random and may take on any value[10].

By contrast, in the degenerate regime, the signal and idler both resonate at the half-harmonic of the pump and thus are indistinguishable from one another. In this case, equation 9.1 consolidates to

$$\phi_p - 2\phi_s = \frac{\pi}{2}, \tag{9.2}$$

such that signal phase is restricted to one of two phase states (Fig. 9.1d), which we refer to as $|0\rangle$ and $|\pi\rangle$ [26].

Figure 9.2 shows the measurement protocol for ensuring independence of the N oscillators in the time-multiplexed OPO cavity. The measurement setup is shown in Fig. 9.2a and is described in further detail in Section 9.4. The cavity is pumped by ps pulses at 1045 nm generated by an electro-optic (EO) comb with a variable repetition rate. TDM is achieved through selecting a pump repetition period, T_{rep}, that is a harmonic of the cavity roundtrip time, T_{RT}, meaning $T_{\text{rep}} = T_{\text{RT}}/N$, such
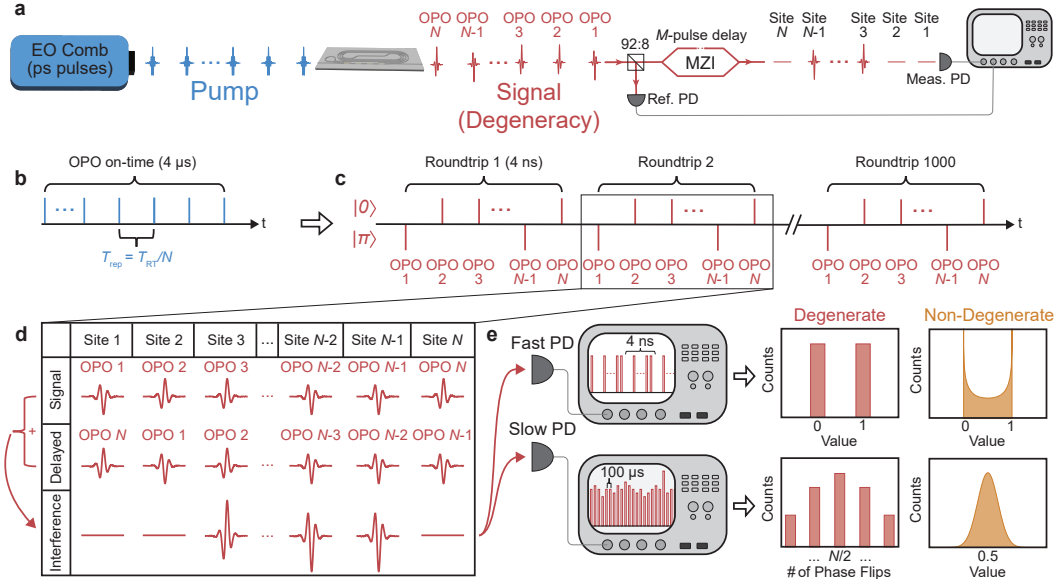
Figure 9.2: **Measurement of independent oscillators. a,** Schematic of the measurement setup. The nanophotonic chip is pumped by the output of an EO comb which provides ps pulses at GHz repetition rates. The output is passed through a fiber interferometer with an M-pulse delay for characterizing the relative phases of the output pulses. **b,** Illustration of the pump pulse train, with 4-µs on-time. **c,** Example signal pulse train at degeneracy, showing the binary phase of the output. Each OPO iteration contains a repeating 4-ns random pattern of $|0\rangle$ and $|\pi\rangle$. **d,** Principle of the interferometric measurement of the signal, illustrated with a 1-pulse delay. **e,** Theoretically expected outputs for pulse-to-pulse (fast) and average (slow) measurements. EO, electro-optic; PD, photodetector; T_{rep}, repetition period; T_{RT}, roundtrip time.

that N OPOs are made to oscillate simultaneously in the long spiral cavity. In our system, the 53-cm spiral results in a roundtrip time of 4 ns and corresponding 250-MHz FSR.

The signal is coupled into an unbalanced Mach-Zehnder interferometer (MZI), here meaning the two interferometer arms have different path lengths, the output of which is collected on a photodetector. This allows for measurement of the relative phases of the output pulse train. A 92:8 splitter placed before the MZI additionally sends a fraction of the signal to a reference photodetector for normalizing the measurement.

Figures 9.2b and 9.2c illustrate an example of the pump and signal pulse trains, respectively. The pump (Fig. 9.1b) consists of a train of ps pulses to pump N time-multiplexed OPOs which are kept on for 1000 roundtrips (4 µs). The resulting signal (Fig. 9.2c) is composed of a train of N pulses with phases sampled randomly

from the allowed phase states of the system. In the depicted case of degeneracy, they are sampled from the binary states $|0\rangle$ and $|\pi\rangle$.

Figure 9.2d depicts the passage of the signal through the MZI for each measurement. Here, a 1-pulse delay is assumed for simplicity. The top row shows the signal arm while the middle row shows the delayed arm. Their recombination results in the interference signal shown in the bottom row, which is finally sent to the measurement detector. In our experiment, this measurement is repeated every 100 µs by turning the system off and sending another 4-µs set of pump pulses for collecting statistics. As shown in Fig. 9.2e, we have employed both a fast detector for shot-to-shot measurement of the resulting intensity in each pulse site and a slow detector for averaging over the MZI output for each 4-µs set of pump pulses.

Each time the time-multiplexed OPOs are turned on, referred to in the following as an OPO iteration, each independent OPO signal takes a random phase. We test for the independence by comparing the output statistics of our measurements to the theoretically expected distributions, derived in Section 9.4 and repeated below. In the case of fast detector measurements (Fig. 9.2e, top) and degenerate operation, the normalized pulse peak intensity distribution taken across many OPO iterations should resemble a Bernoulli distribution with a 50% probability for obtaining either 0 or 1, such that the probability mass function (PMF) is given by

$$
f(x) = \begin{cases} 0.5 & x = 0, \\ 0.5 & x = 1, \\ 0 & \text{otherwise.} \end{cases}
\tag{9.3}
$$

By contrast, in the non-degenerate case, the expected theoretical distribution may be derived by considering the result of the interference between pulses with a uniformly distributed random phase. It is given by the probability density function (PDF)

$$
f(x) = \begin{cases} \dfrac{1}{\pi\sqrt{x(1-x)}} & 0 \leq x < 1, \\ 0 & \text{otherwise.} \end{cases}
\tag{9.4}
$$

In the case of slow detector measurements (Fig. 9.2e, bottom), the average value of the MZI signal over the 4-ns pulse train should be considered. Such a measurement is helpful for obtaining statistics over a larger number of OPO iterations as well as for improving measurement SNR in the case where the pump repetition rate approaches

the detection bandwidth of the fast measurement system. In the degenerate case, the measured value is dependent on how many phase flips occur between neighboring pulses over the 4-ns pulse train. Assuming 0 roundtrip phase in the OPO such that phase flips always occur in pairs, the resulting PMF is found to be

$$f(x) = \begin{cases} \frac{1}{2^{N-1}}\binom{N}{x} & x \text{ even,} \\ 0 & \text{otherwise,} \end{cases} \tag{9.5}$$

where $x \in 0, 1, ..., N$ is the number of phase flips between consecutive pulses in the train of N pulses. Meanwhile, for large N, the central limit theorem suggests the non-degenerate system should tend towards a normal distribution,

$$f(x) = \frac{1}{\sqrt{0.25\pi}} e^{-\frac{(x-0.5)^2}{0.25}}. \tag{9.6}$$

Operation with $N = 40$

We first measure the case where $N = 40$, meaning the repetition rate of the pump is set to be 10 GHz, the results of which are presented in Fig. 9.3. Figures 9.3a-d contain the results of the interferometric measurement on an 18-GHz fast detector, with Figs. 9.3a-b showing the output when the laser is detuned to degeneracy while Figs. 9.3c-d show the output in the non-degenerate case. For ease of comparison between the experiment and theory, the measured detector voltages have been shifted and scaled such that the mean and variance of the resulting distributions match those of the theoretically predicted distributions from equations 9.3 and 9.4, where 1 corresponds to constructive interference and 0 corresponds to destructive interference. Figures 9.3a and 9.3c show examples of the directly measured interference pulse trains. As expected theoretically, the MZI output is binary in the case of degeneracy (Fig. 9.3a). This is further confirmed by the histogram of the peak pulse intensities over 30 OPO iterations shown in Fig. 9.3b, where we observe two well-separated lobes around 1 and 0 with nearly equal probability. As discussed in Section 9.4, one key difference between our measurement and theory is the addition of detector noise which results in the measured distribution looking like the convolution of the expected theoretical distribution with a Gaussian. Meanwhile, the MZI output in the non-degenerate regime can take on any value between 0 and 1 (Fig. 9.3c). By taking the histogram of the pulse peaks over 25 OPO iterations, we obtain the distribution shown in Fig. 9.3d. As expected, the measured distribution is bimodal, and it agrees well with the theoretical fit.
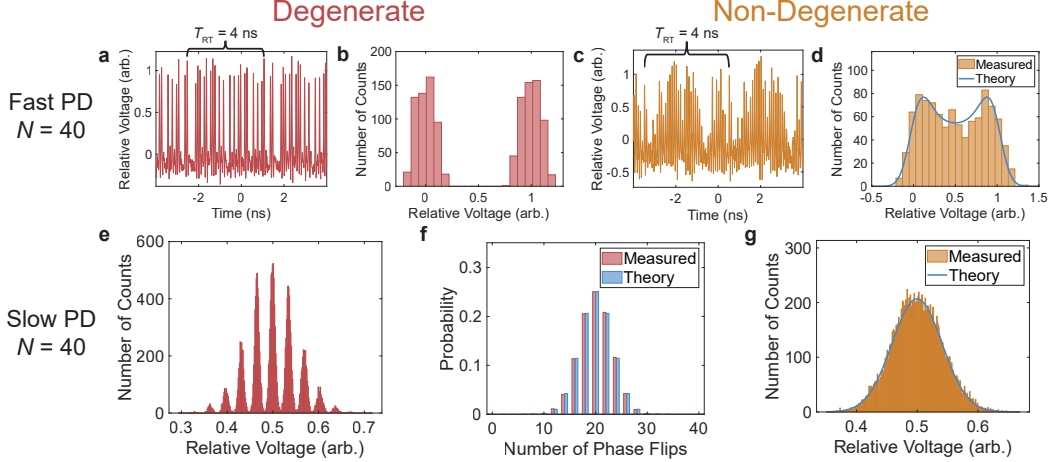
Figure 9.3: **Interference measurements for N = 40. a-d**, Fast detector measurements in the degenerate (**a** and **b**) and non-degenerate (**c** and **d**) regimes. Examples of the measured interference pulse trains are shown in **a** and **c**. Histograms of the measured peak pulse intensities over 30 degenerate (**b**) and 25 non-degenerate (**d**) interference measurements show good agreement with theoretical expectations. **e-g**, Slow detector measurements in the degenerate (**e** and **f**) and non-degenerate (**g**) regimes. Histograms of the measured value over 19,999 OPO iterations are shown in (**e**) and (**g**). As expected theoretically, discrete peaks are observed in the degenerate case (**e**), whereas a continuous distribution is seen in the the non-degenerate case (**g**). The discrete peaks in the degenerate case are binned for comparison with theory (**f**), showing good agreement.

The independence of the pulses is further confirmed through the slow detector measurements shown in Fig. 9.3e-g. The histogram of Fig. 9.3e contains the peak values from 2 s of slow detector data, corresponding to 19,999 OPO iterations. Here, the observance of a discretization in the measured values confirms operation in the degenerate regime. Further comparison between the measurement and the expected theoretical distribution in Fig. 9.3f shows strikingly good agreement, verifying the independence of the OPOs in the time-multiplexed system. The corresponding histogram for the non-degenerate measurement is shown in Figs. 9.3g, again corresponding to 2 s of data. In contrast to the degenerate case, the measurement is not discretized. A Gaussian fit over the histogram shows good agreement between the measured data and the theoretically expected distribution.

Operation with N = 70

One advantage of the TDM scheme is the ability to change the number of sites without significant additional overhead, making computation of problems of different sizes readily achievable. We demonstrate this by pushing our system to N

= 70 at a pump repetition rate of 17.5 GHz. Our current measurement is limited by the modulators used in the EO comb and bandwidth of our fast photodetector. However, as faster nanophotonic pump sources become available, we believe the current time-multiplexed system will be capable of supporting much larger Ns and over an order of magnitude faster pump repetition rates, benefiting from the large and broadband gain paired with low dispersion in the roundtrip (see Section 9.4).
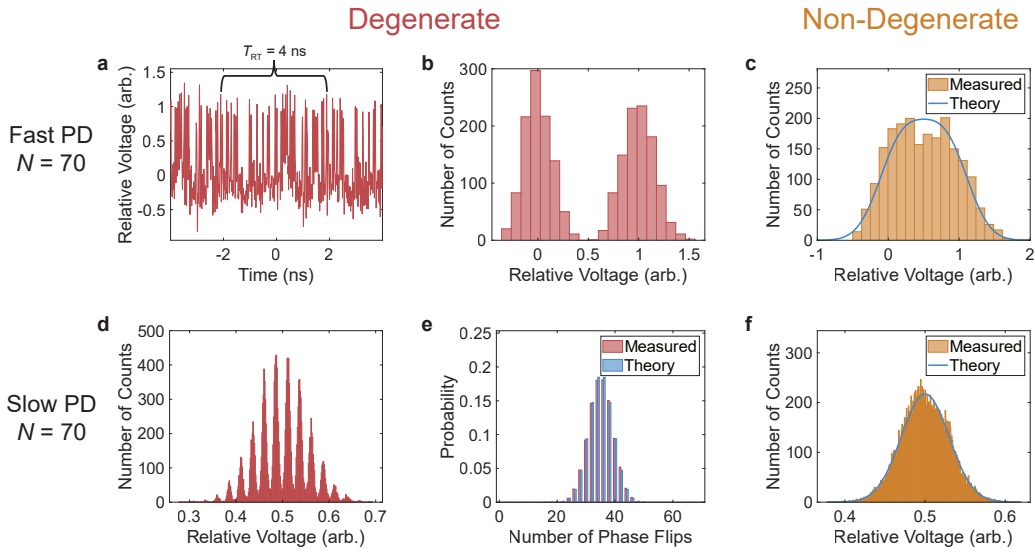
Figure 9.4: **Extension to $N = 70$. a**, Example interference pulse train on the fast detector in the degenerate case. **b**, Histogram of peak pulse intensities over 30 degenerate OPO iterations, exhibiting the expected Bernoulli distribution. **c**, Corresponding histogram of fast detector measurements in the non-degenerate regime and theoretical fit. **f**, Histogram of slow detector measurements in the degenerate regime. **e**, Theoretical comparison after binning the distribution from (**d**) showing close agreement. **f**, Histogram of non-degenerate interference data and corresponding Gaussian fit.

Figure 9.4 presents the results for pumping with $N = 70$. As can be seen in the raw data of Fig. 9.4a measured with the fast detector, pumping near the limits of our electronics results in a reduced signal-to-noise compared to the case of $N = 40$. However, the histogram of fast detector measurements at degeneracy over 30 OPO iterations depicted in Fig. 9.4b again shows a clear Bernoulli distribution, in accordance with the theory. This stands in contrast with the non-degenerate case of Fig. 9.4c, which also agrees well with the theoretical fit. Here, the bimodality is less prevalent because of the relatively larger detector noise. The slow detector measurements in Figs. 9.4d-f further confirm that independence is maintained. At degeneracy, discrete values are again observed in the histogram (Fig. 9.4d), and the

distribution is shown in Fig. 9.4e to match the theoretically expected distribution. Likewise, the non-degenerate measurement shown in Fig. 9.4f agrees well with the Gaussian fit.

9.3 Discussion

In this work, we have demonstrated a large-scale system of time-multiplexed OPOs in lithium niobate nanophotonics and shown the independence of the oscillators in both the degenerate and non-degenerate regimes through interferometric measurements of the device output. Already the device can find application in random number generation [3, 38, 39], benefiting areas such as cryptography and stochastic simulation [40]. Below threshold, it may serve as a source of N independent identical squeezers for creating high-dimensional entangled states [1, 2, 41–43].
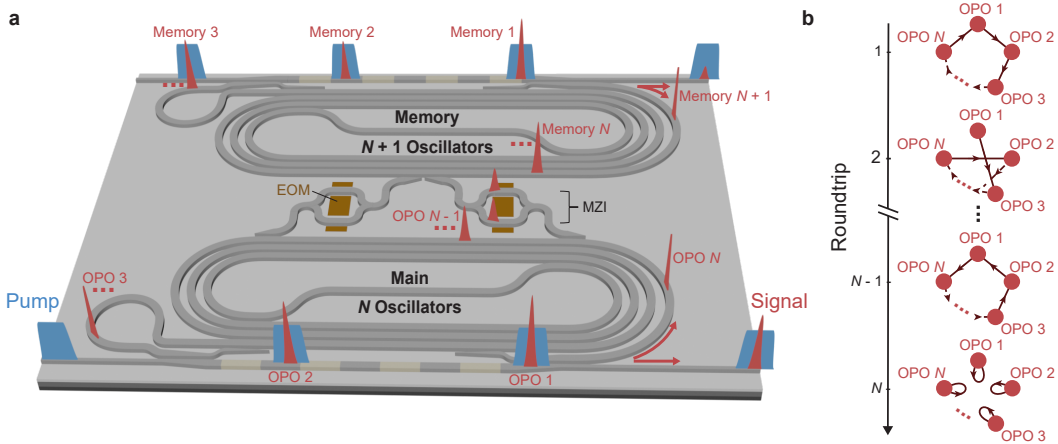
Figure 9.5: **Time-multiplexed architecture for programmable all-to-all coupled nonlinear resonators. a**, The main resonator (bottom) with N time-multiplexed OPOs is coupled to a secondary memory cavity (top), designed to have $N + 1$ sites. Losses in the memory cavity are compensated by a secondary pump and poled region. EOMs in the coupling regions are used to program an MZI-based intensity modulator, which can be used to tune the strength of the coupled pulse. **b**, Connectivity diagrams showing how arbitrary couplings are achieved over N roundtrips. EOM, electro-optic modulator; MZI, Mach-Zehnder interferometer.

The addition of programmable couplings between the oscillators will further allow for exploration of a multitude of fundamental phenomena and enable large-scale, all-optical information processing. Towards this end, we propose the architecture illustrated in Fig. 9.5a, which we call the all-time-multiplexed architecture. Here, the main cavity consisting of N time-multiplexed OPOs is accompanied by a secondary memory cavity with $N + 1$ sites. The cavities are coupled such that pulses in the main

and memory cavities can interact, and the strength of the coupling is set through MZI-based intensity modulators using fast electro-optic modulators (EOMs) [44]. A second pump and periodically poled region in the memory cavity is used to compensate the roundtrip loss.

In general, information processing requires a mixture of both linear and nonlinear operations. In this architecture, linear operations, such as multiply-accumulate operations or dot products, are achieved through arbitrary all-to-all couplings which may be implemented over $N + 1$ roundtrips of the memory cavity. In the first roundtrip, pulses from the main cavity are coupled to the memory cavity through the right MZI channel. In the subsequent N roundtrips, couplings occur as illustrated in the connectivity diagrams of Fig. 9.5b from the memory cavity back to the main cavity through the left MZI channel. The memory cavity may then be emptied of pulses to allow the next coupling cycle to begin. Meanwhile, all-optical nonlinear functions [45] may be applied by modulating the pump in the main cavity.

Compared to previous time-multiplexed computing architectures based on physical delay lines [26], the all-time-multiplexed architecture offers a significantly more compact footprint for facilitating all-to-all connections. Meanwhile, when compared with the measurement-feedback approach [9], the scheme reduces the system reliance on electronic feedback which limits the system clock rate and adds an undesirable digital element to the otherwise analog optical computing scheme. However, the all-time-multiplexed architecture incurs an additional factor of N overhead in the computation time due to the couplings requiring N roundtrips to be implemented. Further comparison with other TDM architectures may be found in Section 9.4.

As motivated in the introduction, the all-time-multiplexed approach also offers a more compact footprint and promises improved scalability and programmability over other integrated approaches based on spatial multiplexing, which require, for example, large interferometer meshes to achieve all-to-all couplings [18, 43]. In total, the all-time-multiplexed architecture offers a flexible platform for studying systems of coupled nonlinear resonators and will therefore be the subject of future studies in integrated time-multiplexed systems. Beyond serving as an Ising [27] and XY solver [10], one can envisage uses for the all-time-multiplexed system in general-purpose computing [46], machine learning [47], topological photonics [35], and quantum computing [48, 49]. For many such applications, the demonstrated system size of $N = 70$ is already sufficiently large for tackling problems of interest [42, 50]. This versatility of application highlights the importance of our demonstrated

time-multiplexed OPOs as a first step towards achieving integrated ultrafast, energy-efficient, and scalable all-optical information processing systems.

9.4   Supporting Information

Setup and Measurement Principle

The full experimental setup is shown in Fig. 9.6a. As mentioned in the Section 9.2, our pump source is an EO comb consisting of an intensity modulator (IM) followed by three phase modulators (PM) applied to the output of a tunable CW laser, similar to that used in ref. [31]. The comb repetition rate is variable through tuning of the radio frequency (RF) signal generator which drives the modulators. Subsequent booster optical amplifier (BOA), waveshaper, and ytterbium-doped fiber amplifiers (YDFA) are used for amplification and pulse compression. Typical spectra of the direct EO comb output in both the 40- and 70-pulse cases can be observed in Figs. 9.6b and 9.6e, respectively. The repetition rates in the two cases are 10.0 GHz (40-pulse) and 17.5 GHz (70-pulse). 17.5 GHz is just fast enough to where the optical spectrum analyzer can begin to resolve the comb lines, which can be observed in Fig. 9.6e. The corresponding spectra after amplification and spectral shaping may be observed in Figs. 9.6c and 9.6f. Amplified spontaneous emission (ASE) from the amplifiers can be observed on the wings of the spectrum.

In addition to using it for amplification, we may modulate the gain of the BOA to switch between a continuous pulsed drive of the system and a periodic pulse driving. With continuous driving, we use an autocorrelator to characterize the pulses following the dispersion compensation in the waveshaper. The resulting autocorrelation traces in the case of $N = 40$ and $N = 70$ are shown in Figs. 9.6d and 9.6g, respectively. The measured autocorrelation widths are 1.6 ps and 1.05 ps, corresponding to pulse widths of 1.13 ps and 735 fs assuming a Gaussian pulse shape. As expected, we see an inverse scaling with the change in comb repetition rate.

Meanwhile, our experiments are primarily conducted with periodic on-off modulation of the BOA to automatically iterate through many OPO instances. For this, we use a 10 kHz modulation with a duty cycle of 4%, corresponding to an on-time of 4 µs and a period of 100 µs between subsequent OPO iterations. The on-time is selected to give sufficiently many roundtrips (1000) to ensure steady-state is reached, while the low duty cycle is helpful in reducing the risk of thermal damage to the facet. Based on an estimated propagation loss of 0.2 dB/cm, the total loss in the
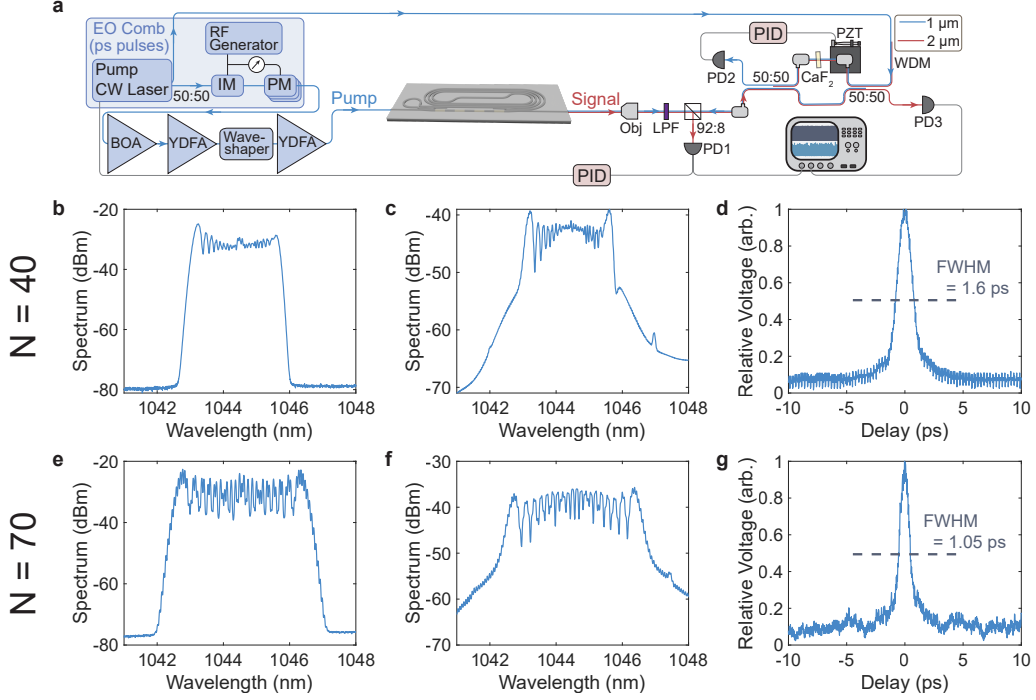
Figure 9.6: **Experimental setup and pump characterization. a**, Schematic of the experimental setup. **b**, Direct measurement of the spectrum out of the EO comb with $N = 40$. **c**, Corresponding spectrum after amplification and pulse shaping. **d**, Autocorrelation of output pulses with $N = 40$, showing an autocorrelation width of 1.6 ps. **e**-**g**, Equivalent plots for $N = 70$. Here, the comb structure is just barely resolved by the spectrum analyzer. A shorter autocorrelation width of 1.05 ps is observed. EO, electro-optic; RF, radio frequency; CW, continuous-wave; IM, intensity modulator; PM, phase modulator; BOA, booster optical amplifier; YDFA, ytterbium-doped fiber amplifier; PD, photodetector; Obj, objective; LPF, long-pass filter; PZT, piezoelectric stack; PID; proportional-integral-derivative control; WDM, wavelength-division multiplexing fiber.

roundtrip is around 10 dB. Therefore, faster iterating through OPO instances with a dead time on the order of 10 roundtrips is theoretically possible without risk of biasing new instances.

The pump is coupled into the nanophotonic chip using a lensed, tapered fiber. The resulting signal is outcoupled from the waveguide using a reflective objective, passed through a LPF to eliminate any residual pump light, and sent to the measurement setup. A 92:8 pellicle beamsplitter is used to siphon off a small portion of the output signal for measurement on a slow (1 MHz) photodetector (PD1, Ref. PD in Fig. 9.2). This output is used to perform side-of-fringe locking of the pump center frequency to an OPO resonance. This signal is additionally measured directly to be

used as a reference for any intensity noise fluctuations which occur over the course of the measurement.

The remainder of the signal is sent to a fiber collimator. The output fiber is first sent to an optical spectrum analyzer to confirm degenerate or non-degenerate operation. Example spectra in both regimes for both the $N = 40$ and $N = 70$ cases are shown in Fig. 9.7. After the system is locked in the desired state, the fiber is routed to an unbalanced MZI. the unbalanced MZI has an approximately 500-ps delay between the two interferometer arms, resulting in 5-pulse and 9-pulse delays for the cases of $N = 40$ and $N = 70$, respectively, which allows for measurement of the relative phases of the output pulse train. The interferometer is locked using back-propagating light at 1 µm, taken from the original pump source, which is measured on a second detector (PD2). A dither-and-lock scheme is employed for top-of-fringe locking using piezoelectric actuators placed on the fiber-free space delay line. A CaF_2 window placed on a rotating stage in the free-space arm of the interferometer allows for tuning of the relative delays of the back-propagating 1-µm light and forward-propagating signal at 2 µm to ensure that the lock point (corresponding to the maximum of the 1 µm interference) also corresponds to the maximum contrast for the 2 µm interference. The interferometer output is finally sent to photodetector PD3 (Meas. PD in Fig. 9.2), which may be swapped between a fast 18-GHz 2 µm detector and a slow 1-MHz detector. This signal is measured simultaneously with the output of PD1 on an oscilloscope, which has a maximum sampling rate of 80 Gs/s. The oscilloscope shares a 10-MHz reference with the signal generator used to drive the EO comb.

Data Processing

Following pump preparation, system stabilization, and measurement, some post-processing is applied to extract the signal of interest. The post-processing for the slow detector measurement is as follows. First, a moving average filter (MATLAB smooth) is applied to the output signal collected after the MZI on PD3 and the reference measured directly out of the OPO on PD1 and the minimum value of each measurement is subtracted. Then, the peak values of each OPO iteration are detected for both the signal and reference. Next, these detected peak values are independently normalized to have a mean of 0.5. The normalized measured signals corresponding to the non-degenerate and degenerate histograms of Fig. 9.3e-g are shown in Figs. 9.8a and 9.8b, respectively. Finally, the signal peaks are divided by their corresponding reference peaks; by normalizing our measured signal to this
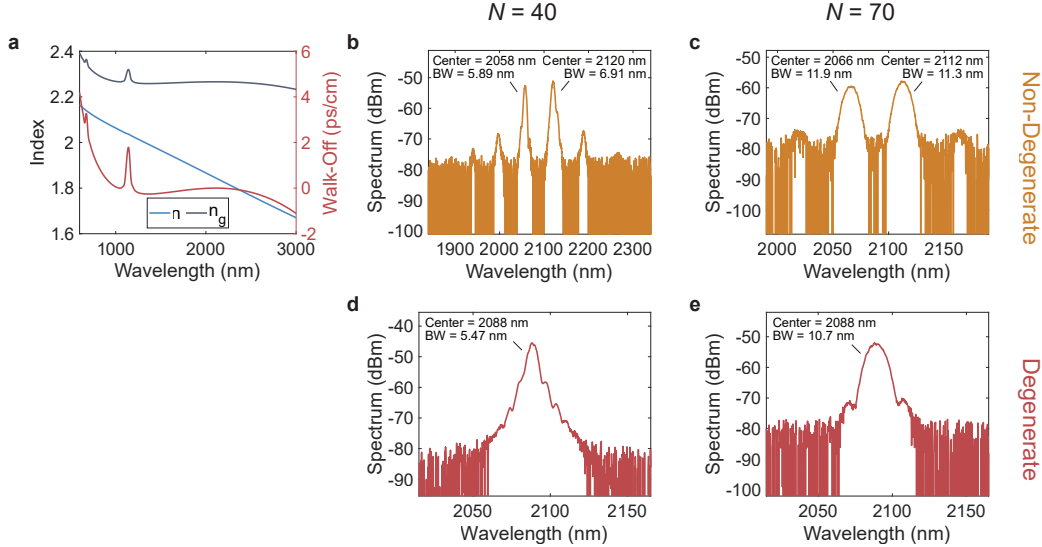
Figure 9.7: **Dispersion and output spectra. a**, Effective index and group index curves as well as walk-off relative to the degenerate frequency of 2090 nm for the measured device. **b-e**, Spectra, taken in the non-degenerate (**b** and **c**) and degenerate (**d** and **e**) regimes for $N = 40$ (**b** and **d**) and $N = 70$ (**c** and **e**).

reference, we reduce the impact of intensity noise fluctuations on the measurement. The resulting normalized peak values are used to generate the histograms of Fig. 9.3. By comparison, we replicate the plots of Figs. 9.8b and 9.3e-f with no post-processing in Fig. 9.8c-e. Figure 9.8c shows snippets of the raw data measured by the slow detectors, both signal and reference. A corresponding histogram of the raw data is shown in Fig. 9.8d. While the expected discretization is still evident, the bins are clearly less well-defined than those of Fig. 9.3e. Similarly, comparison with theory, as in Fig. 9.8e, shows worse agreement compared to the plot of Fig. 9.3f, though the discrepancies are still more than tolerable.

Similarly, some post-processing is applied for the fast detector measurement. An example of a raw non-degenerate trace measured by the fast detector is shown in Fig. 9.8f. To improve the signal-to-noise ratio (SNR), the output pulse train is first averaged over 150 roundtrips; in particular, as we expect the output signal to repeat with a period given by the roundtrip time of the resonator, points with a spacing of NT_{rep}, where T_{rep} is the repetition period of the pump, are averaged together. The resulting trace after this averaging is shown in Fig. 9.8g. A zoomed-in version of the indicated region of Fig. 9.8g, showing the pulses of this averaged data with no additional processing, is presented in Fig. 9.8h. This pulse train corresponds to the post-processed pulse train of Fig. 9.3c, with a small time shift.
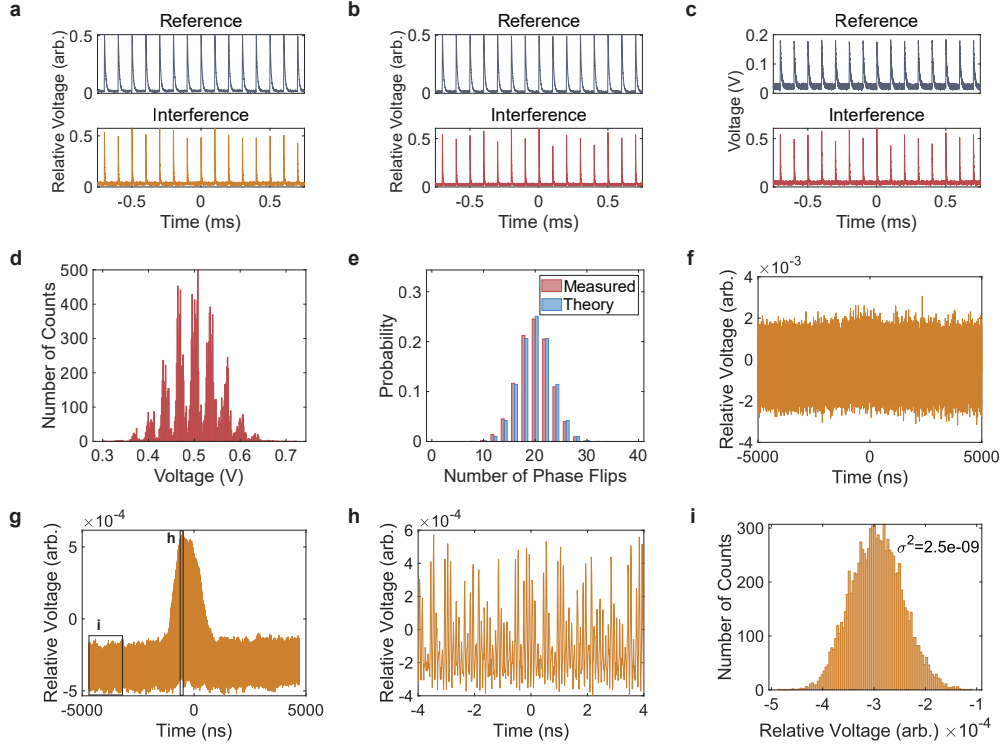
Figure 9.8: **Data processing of slow and fast detector measurements.** **a-b**, Processed data from the slow detector in the non-degenerate (**a**) and degenerate (**b**) regimes corresponding to the histograms of Fig. 9.3 ($N = 40$). **c**, Snippet of raw data corresponding to **b**. **d**, Histogram of measured peaks with no post-processing. **e**, Theoretical comparison with measured distribution of **d**. **f**, Raw trace measured on the fast detector in the non-degenerate case with $N = 40$. **g**, Trace of **f** after 150x averaging, showing significant signal-to-noise improvement. **h**, Zoom-in of indicated region of **g** showing the fast pulse train. **i** Histogram of the noise after averaging, taken from the indicated region of **g**.

The next step of our processing involves application of a high-pass filter to remove any DC offset and low-frequency noise. After this, a 1-D Fast Fourier Transform interpolation (MATLAB interpft) is used to help smooth the output, given the limited number of samples per pulse in our measurement. Statistics are generated by taking the maximum value in each time bin, as specified by the repetition period of the pump. As shown in the following subsections, N - 1 time bins are independent while the full set of N are not, so only N - 1 time bins are sampled for a given measurement. The resulting distribution is scaled according to the theoretically expected mean and variance for a normalized measurement, in accordance with the theory in the following subsections. In the case of non-degeneracy, in particular, this requires using the distribution of the noise, shown in Fig. 9.8i, to help calculate the expected

variance. After the distribution has been scaled, it is then fit with the theoretical distribution using the MATLAB fit function, seeded by the theoretical mean and variance. These same scaling factors are applied to the signal for generating the representative pulse trains shown in, for example, Fig. 9.3.

Device Fabrication and Characterization

The design of the measured device is described fully in ref. [32] and follows the fabrication procedure described in ref. [30]. The device is fabricated on 700-nm-thick X-cut MgO-doped thin-film lithium niobate on a SiO_2/Si substrate (NANOLN). The chip contains 16 devices with fixed poling periods ranging from 4.955-5.18 µm. To achieve the periodic poling, we pattern Cr/Au poling electrodes using lift-off and subsequently apply a voltage to periodically flip the ferroelectric domains. Following poling, we remove the electrodes and etch the waveguides using Ar-milling with HSQ as the etch mask. Finally, mechanical polishing of the waveguide facets is performed to enable end-fire coupling into the devices. The total OPO device footprint is 0.5 mm × 13 mm.

The measured OPO device has a constant poling period of 5.075 µm over the 10.8-mm-long poled region for phase-matched interaction between the pump at 1045 nm and signal at 2090 nm. The spiral cavity has a length of 52.92 cm, resulting in a roundtrip time of 4 ns. We measure the fabricated waveguides to have an etch depth of 352 nm and top width of 1753 nm. The resulting effective index, n (blue), group index, n_g (gray), and walk-off (red) relative to the degenerate wavelength of 2090 nm are shown in Fig. 9.7a. Specifically, we find a GVM of approximately 1 fs/mm and a GVD of -7 fs^2/mm for the signal and 11 fs^2/mm for the pump. Such near-zero GVM/GVD enables the high gain responsible for the low-threshold operation and is critical for maintaining the independence of the oscillators during roundtrip propagation.

In particular, by comparing the calculated walk-off to the measured spectra, we see that within the wavelength region between 1900 nm and 2300 nm, where all of the measured spectral content is observed in both the degenerate and non-degenerate regimes, the largest value of the walk-off compared to the center wavelength of 2090 nm is less than 0.05 ps/cm. This suggests that the spectral components within the pulse walk off by at most 2.6 ps in a single roundtrip, far less than the 57-ps pulse separation in the 70-pulse case. Considering the high roundtrip loss in the cavity (approximately 10 dB given 0.2 dB/cm propagation loss), this

signifies that even the most non-degenerate components will be attenuated by a factor of >200 dB before overlapping with a neighboring pulse. Given a total pulse energy on the order of pJs for the pulses used in the experiment, these far spectral components contain at most fJs of energy after amplification. They should, therefore, be attenuated to approximately 10^{-35} J before interacting with a neighboring pulse, about 16 orders of magnitude below single-photon energy levels. This shows how the dispersion engineering of the device can enable the independent operation of the time-multiplexed OPOs.

If we focus on the degenerate case and consider a bandwidth of 100 nm about the center frequency, we observe that the maximum walk-off of any two spectral components is 0.004 ps/cm, resulting in a walk-off per roundtrip of 212 fs. From the previous argument, we can see that the widest spectral components which walk the farthest should be well-attenuated below single-photon energy levels within approximately 5 roundtrips. Thus, a pulse separation of 2 ps should be more than sufficient to avoid cross-talk in the present system. This suggests that, barring limitations imposed by electronic components, computational clock rates exceeding 500 GHz may be realized in our system.

Threshold Estimate

The OPO threshold may be calculated through measurement of the off-chip pump power at the lowest point for which the OPO is observed to oscillate, which we measure to be 8 mW in the 40-pulse case. By accounting for the 4% duty cycle of the BOA, the pulse repetition rate of 10 GHz, and our estimated fiber-to-chip coupling loss of 10 dB, we calculate an on-chip threshold pulse energy of about 2 pJ.

Probability Theory

In this section, we derive the theoretical probability distributions presented in Section 9.2. Additionally, the theory given in Section 9.2 all assumes that the OPO signal acquires no phase in the roundtrip propagation; in this case, a given pulse maintains the same phase state across consecutive roundtrips at steady state. However, the OPO may also stably oscillate in a resonance where pulses acquire a roundtrip phase of π. The theoretical distributions and experimental results for such a condition are also presented. The results of this section may be derived using the contents of most introductory probability theory texts as a guide; here, we have been guided by [51].

Degeneracy

Probability Mass Function (Fast Detector)

Let us begin by first considering the degenerate case. Here, our OPO output consists of N pulses. Let us denote the phase of pulse i as ϕ_i, where $i \in \{1, 2, ..., N\}$. In the case of degeneracy, ϕ_i is a Bernoulli random variable, taking on one of the two phase states $|0\rangle$ or $|\pi\rangle$ with equal probability of 1/2. We will interchangeably refer to $|0\rangle$ or $|\pi\rangle$ as 0 and 1, respectively, for the sake of the following discussion. Let us now define a new random variable, I_i, which represents the detected output on the fast detector of the interference measurement performed on neighboring pulses. This was depicted in Fig. 9.2 for the case of a 1-bit delay; here, we may assume the same without loss of generality.

To understand the relationship between I_i and ϕ_i, we first consider the case where the delay line is locked such that pulses in the same phase state will constructively interfere. In this case, given the above definitions, $I_i = \phi_i \odot \phi_{i+1}$ for $i \in \{1, 2, ..., N-1\}$, where $\odot$ is the XNOR operator. I_N must be separately defined as $I_N = \phi_N \odot \phi_1$, as our OPO output repeats every N pulses. We begin by considering the probabilities of I_i taking on a value of 0 and 1

$$P(I_i = 1) = P(\phi_i \odot \phi_{i+1} = 1) = P((\phi_i = 0) \wedge (\phi_{i+1} = 0))$$
$$+ P((\phi_i = 1) \wedge (\phi_{i+1} = 1)) = 0.5, \quad (9.7a)$$

$$P(I_i = 0) = P(\phi_i \odot \phi_{i+1} = 1) = P((\phi_i = 0) \wedge (\phi_{i+1} = 1))$$
$$+ P((\phi_i = 1) \wedge (\phi_{i+1} = 0)) = 0.5, \quad (9.7b)$$

where $\wedge$ represents logical AND. From this, it is clear that I_i is also a Bernoulli random variable with probability 1/2 of taking a value of either 1 or 0, corresponding to constructive and destructive interference between the two interferometer arms. Thus, the PMF of I_i, as described in equation 9.3, is given by

$$f(x) = \begin{cases} 0.5 & x = 0, \\ 0.5 & x = 1, \\ 0 & \text{otherwise.} \end{cases} \quad (9.8)$$

One may note that the delay line could also be locked such that pulses with the opposite phase state will constructively interfere. In this case, we must replace the XNOR operator, $\odot$, with the XOR operator, $\oplus$, in the above discussion, but the general conclusion remains the same.

Independence

Let us now turn to the question of independence of the defined random variables I_i. Here, we assume that the ϕ_i's are independent, as expected in our experiment. For this, we first turn to the simplest case of $N = 2$ and then look at larger system sizes. For $N = 2$, independence would suggest

$$P((I_1 = x_1) \wedge (I_2 = x_2)) = P(I_1 = x_1)P(I_2 = x_2). \tag{9.9}$$

It can be clearly shown through a counterexample, however, that this is not the case. Let's consider the probability $P((I_1 = 1) \wedge (I_2 = 0))$. From our previous definition of I_i, we see that $I_1 = 1 \equiv \phi_1 \odot \phi_2 = 1$. However, based on the definition of I_2 when $N = 2$, we have that $(I_2 = 0) \equiv (\phi_2 \odot \phi_1 = 0)$. From the commutativity of the XOR operator, we see that the statements $\phi_2 \odot \phi_1 = 0$ and $\phi_1 \odot \phi_2 = 1$ are contradictions, so the probability of their joint occurrence must be 0. Finally, we conclude that $P((I_1 = 1) \wedge (I_2 = 0)) = 0$, which is not equal to $P(I_1 = 1)P(I_2 = 0) = 0.25$, suggesting that I_1 and I_2 are not independent, as the definition of equation 9.9 is not satisfied.

Let us now look to the case of $N = 3$. Here, mutual independence implies

$$P((I_1 = x_1) \wedge (I_2 = x_2) \wedge (I_3 = x_3)) = P(I_1 = x_1)P(I_2 = x_2)P(I_3 = x_3). \tag{9.10}$$

Again, we may use a counterexample to show that mutual independence is not maintained. Consider the probability $P((I_1 = 1) \wedge (I_2 = 1) \wedge (I_3 = 0))$. For the given statement to occur, we must have that $\phi_1 \odot \phi_2 = 1$, $\phi_2 \odot \phi_3 = 1$, and $\phi_3 \odot \phi_1 = 0$. Noting that $(\phi_2 \odot \phi_3 = 1) \equiv (\phi_2 = \phi_3)$, we see again that we reach a contradiction as we require $\phi_2 \odot \phi_1 = 0$ and $\phi_1 \odot \phi_2 = 1$. Finally, we conclude that $P((I_1 = 1) \wedge (I_2 = 1) \wedge (I_3 = 0)) = 0$, which is not equal to $P(I_1 = 1)P(I_2 = 1)P(I_3 = 0) = 0.125$, suggesting that the I_i's are not mutually independent as the definition given in equation 9.10 is not satisfied.

Now, we turn to the pairwise independence of the I_i's in the case of $N = 3$. Let us consider specifically the pair I_1 and I_2, where their pairwise independence would require satisfying the equation 9.9. From the definition of the I_i's, we know $P((I_1 = x_1) \wedge (I_2 = x_2)) = P((\phi_1 \odot \phi_2 = x_1) \wedge (\phi_2 \odot \phi_3 = x_2))$. Let us first assume that $\phi_2 = 1$. In this case, we have $P((\phi_1 \odot 1 = x_1) \wedge (1 \odot \phi_3 = x_2)) = P((\phi_1 = x_1) \wedge (\phi_3 = x_2)) = P(\phi_1 = x_1)P(\phi_2 = x_2)$ since the ϕ_i's are independent. As both the ϕ_i's and I_i's are Bernoulli random variables with a probability, p, of 1/2 of taking the value 1 or 0, $P(\phi_1 = x_1)P(\phi_2 = x_2) = P(I_1 = x_1)P(I_2 = x_2)$. Thus, we have shown that for $\phi_2 = 1$, $P((I_1 = x_1) \wedge (I_2 = x_2)) = P(I_1 = x_1)P(I_2 = x_2)$.

We next consider the case where $\phi_2 = 0$. Similar to that of $\phi_2 = 1$, this implies $P((\phi_1 \odot 0 = x_1) \wedge (0 \odot \phi_3 = x_2))$ or, equivalently, $P((\neg\phi_1 = x_1) \wedge (\neg\phi_3 = x_2))$, where $\neg$ symbolizes negation. From the independence of the ϕ_i's, this is equal to $P(\neg\phi_1 = x_1)P(\neg\phi_2 = x_2)$. Since the ϕ_i's are Bernoulli random variables with $p = 1/2$, $\neg\phi_i$ is also a Bernoulli random variable with $p = 1/2$. Finally, we find that for $\phi_2 = 0$, $P((I_1 = x_1) \wedge (I_2 = x_2)) = P(\neg\phi_1 = x_1)P(\neg\phi_2 = x_2) = P(I_1 = x_1)P(I_2 = x_2)$. As $(P(I_1 = x_1) \wedge (I_2 = x_2)) = P(I_1 = x_1)P(I_2 = x_2)$ for both $\phi_2 = 1$ and $\phi_2 = 0$, exhausting all possible cases for the value of ϕ_2, we conclude that I_1 and I_2 are pairwise independent in the case where $N = 3$. A similar exercise may be conducted to show the pairwise independence of all combinations of I_i's in this case.

We now scale these arguments to the case of arbitrary N. Here, mutual independence requires that

$$P((I_1 = x_1) \wedge (I_2 = x_2) \wedge ... \wedge (I_N = x_N)) = P(I_1 = x_1)P(I_2 = x_2)...P(I_N = x_N).$$
(9.11)

That the I_i's are not mutually independent is easily seen by considering an extension of the previous counterexample. Here, we look at the probability $P((I_1 = 1) \wedge (I_2 = 1) \wedge ... \wedge (I_{N-1} = 1) \wedge (I_N = 0))$. Through cascading the argument that $(\phi_i \odot \phi_j = 1) \equiv (\phi_i = \phi_j)$, we again arrive at a contradiction as the considered statement would imply that $\phi_1 \odot \phi_N = 1$ and $\phi_N \odot \phi_1 = 0$. This suggests that $P((I_1 = 1) \wedge (I_2 = 1) \wedge ... \wedge (I_{N-1} = 1) \wedge (I_N = 0)) = 0$, which is not equal to $P(I_1 = 1)P(I_2 = 1)...P(I_{N-1} = 1)P(I_N = 0) = \frac{1}{2^N}$, verifying the lack of mutual independence between I_i's.

Let us finally consider the mutual independence of a subset of the I_i's of size j,

where $j < N$. For $j = 2$, there are two cases that must be considered: the case when the I_i's are sequential and the case when they are separate. The sequential case follows immediately from the argument made above for pairwise independence when $N = 3$. Thus, we must only consider the non-sequential case, which demands the pairwise independence of I_i and I_k, where $|k - i| > 1$, requiring $P((I_i = x) \wedge (I_k = y)) = P(I_i = x)P(I_k = y)$. Rewriting the left-hand side, we have $P((\phi_i \odot \phi_{i+1} = x) \wedge (\phi_k \odot \phi_{k+1} = y))$. Due to the independence of ϕ_i, ϕ_{i+1}, ϕ_k, and ϕ_{k+1}, it follows that $f(\phi_i, \phi_{i+1})$ and $g(\phi_k, \phi_{k+1})$ are independent. We may then directly write that $P((I_i = x) \wedge (I_k = y)) = P((\phi_i \odot \phi_{i+1} = x) \wedge (\phi_k \odot \phi_{k+1} = y)) = P(\phi_i \odot \phi_{i+1} = x)P(\phi_k \odot \phi_{k+1} = y) = P(I_i = x)P(I_k = y)$, proving the pairwise independence of non-sequential I_i's.

We now move on to the case of arbitrary j. For non-sequential I_i's, the extension of the previous argument is obvious. Since I_i is a function of the ϕ_i's, which are independent, non-sequential I_i's are clearly independent as they share no ϕ_i's and are thus functions of independent variables. This same logic will additionally apply to clusters of separated sequential I_i's, given the clusters themselves are mutually independent. As such, we turn our focus to proving the independence of sequential I_i's for arbitrary j. In this case, we require that $P((I_1 = x_1) \wedge (I_2 = x_2) \wedge ... \wedge (I_j = x_j)) = P(I_1 = x_1)P(I_2 = x_2) ... P(I_j = x_j)$. As before, we re-write $P((I_1 = x_1) \wedge (I_2 = x_2) \wedge ... \wedge (I_j = x_j))$ as $P((\phi_1 \odot \phi_2 = x_1) \wedge (\phi_2 \odot \phi_3 = x_2) \wedge ... \wedge (\phi_j \odot \phi_{j+1} = x_j))$. Let's begin by assuming ϕ_1 is known. Then, to satisfy the first equation, $\phi_1 \odot \phi_2 = x_1$, we observe that ϕ_2 must be given by $\phi_2 = \phi_1 \odot x_1$. That this is correct is easily verified by plugging this expression for ϕ_2 into the first equation, yielding $\phi_1 \odot \phi_1 \odot x_1 = 1 \odot x_1 = x_1$.

Turning now to the second equation, $\phi_2 \odot \phi_3 = x_2$, we find a similar expression for ϕ_3, $\phi_3 = \phi_2 \odot x_2$. We may now plug our first expression for ϕ_2 in to find that $\phi_3 = \phi_1 \odot x_1 \odot x_2$. Following this pattern, for the jth equation, we find the relationship

$$\phi_{j+1} = \phi_1 \odot x_1 \odot x_2 \odot ... \odot x_j. \tag{9.12}$$

Finally, we may equivalently re-express the original joint probability as $P((\phi_2 = \phi_1 \odot x_1) \wedge ... \wedge (\phi_{j+1} = \phi_1 \odot x_1 \odot x_2 \odot ... \odot x_j))$. Given the independence of the ϕ_i's, $P((\phi_2 = \phi_1 \odot x_1) \wedge ... \wedge (\phi_{j+1} = \phi_1 \odot x_1 \odot x_2 \odot ... \odot x_j)) = P(\phi_2 = \phi_1 \odot x_1)P(\phi_3 = \phi_1 \odot x_1 \odot x_2) ... P(\phi_{j+1} = \phi_1 \odot x_1 \odot x_2 \odot ... \odot x_j)$. As before, since the ϕ_i's and I_i's

are both Bernoulli random variables with p = 1/2, the expression on the right-hand side is equivalent to $P(I_1 = x_1)P(I_2 = x_2) \dots P(I_j = x_j)$, proving the independence of the set of j sequential I_i's, where $j < N$. The lack of independence in the case of $j = N$ also is clear from the above logic, as the relationship given by equation 9.12 for the I_N term would've been $\phi_1 = \phi_1 \odot x_1 \odot x_2 \odot \dots \odot x_N$, which presents a contradiction for many values of x_i, as was the case in the counterexample above.

Summary

To summarize our above findings, we see that for a given system of N degenerate OPOs, the binary random phases of the output may be described by the a set of independent Bernoulli random variables with $p = 1/2$, ϕ_i, where $i \in \{1, 2, \dots, N\}$. Then, the resultant output amplitudes from the interference of consecutive pulses may be described by a set of Bernoulli random variables with $p = 1/2$, I_i, where $I_i = \phi_i \odot \phi_{i+1}$ for $i \in \{1, 2, \dots, N\}$ and $I_N = \phi_N \odot \phi_1$. Through investigating the independence of the I_i's, we find that any subset of $N - 1$ or fewer I_i's is independent, but the full set of N I_i's is not independent. Another way to see this is by noting that the values of the I_i's remain the same under negation of all of the ϕ_i's. This equates to there being exactly two sets of ϕ_i's which result in any given set of I_i's. As the ϕ_i's are binary variables, this suggests the dimension of the set of I_i's should be one less than the dimension, N, of the set of ϕ_i's, meaning the dimension of the set of I_i's should be $N - 1$.

Probability Mass Function (Slow Detector)

Let us now look at the expected output on the slow detector. Here, the slow detector measures the average value of the N interfered pulses, essentially asking the question of how many of the I_i's are equal to 1 (or, conversely, how many of the I_i's are equal to 0). We denote this with the random variable X. Were the I_i's independent, we'd expect X to follow the binomial distribution $\frac{1}{2^N}\binom{N}{x}$, where $x \in 0, 1, \dots, N$, but we know from the above that this is not the case. We may then observe that, in accordance with their lack of independence, the construction of the I_i's requires 0s to appear in pairs. This condition can be found by again considering the expression $\phi_1 = \phi_1 \odot x_1 \odot x_2 \odot \dots \odot x_N$ given by equation 9.12 in the case where $j = N$. To satisfy this expression, there must be an even number of x_i's which are equal to 0 such that $x_1 \odot x_2 \dots \odot x_N = 1$. Another way of stating this is that phase flips between consecutive pulses must come in pairs. Thus, if x is the number of phase flips, we
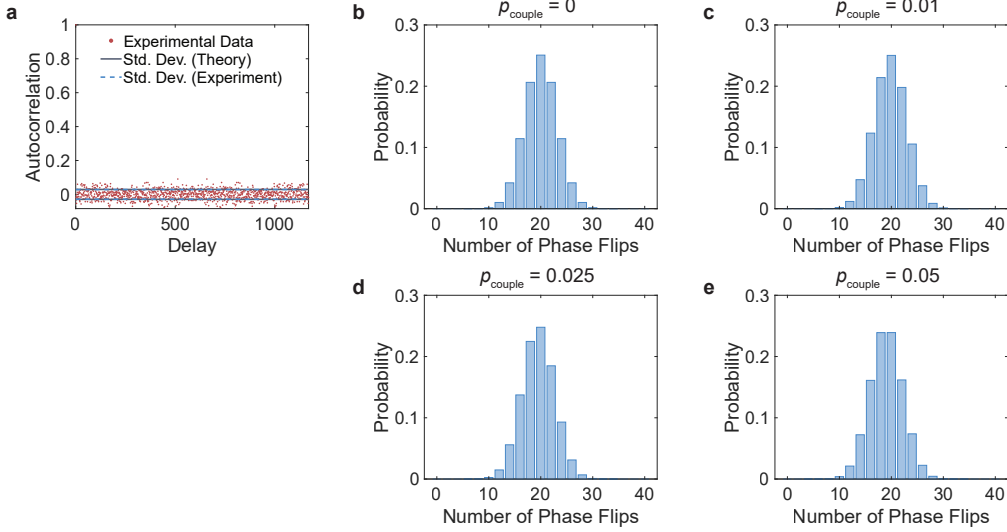
Figure 9.9: **Impact of crosstalk.** **a**, Autocorrelation of thresholded fast detector measurements. **b-e**, Expected distributions in the presence of coupling between neighboring pulses, with coupling probability p_{couple}.

expect $P(X = x) = 0$ for x odd. Finally, we seek the expression for $P(X = x)$ with x even. Because the ϕ_i's are Bernoulli random variables with $\text{p} = 1/2$, we start with the total number of combinations, 2^N, which will form the denominator of the desired expression. Next, we observe that there are $\binom{N}{x}$ combinations of I_i's which correspond to there being x total phase flips (or, equivalently, k 0s amongst the I_i's). However, because there are two sets of ϕ_i's which result in a given set of I_i's (due to the symmetry of the I_i's with respect to negation of all ϕ_i's discussed above), the number of combinations of ϕ_i's is $2\binom{N}{x}$. Finally, then, we find that $P(X = x) = \frac{1}{2^{N-1}}\binom{N}{x}$ for x even. This results in the full PMF, $f_{I_i}(x)$ for I_i, as given in equation 9.5,

$$f_{I_i}(x) = \begin{cases} \frac{1}{2^{N-1}}\binom{N}{x} & x \text{ even,} \\ 0 & \text{otherwise.} \end{cases} \tag{9.13}$$

Impact of Crosstalk

Having derived the expressions considered in Section 9.2 for the probabilities in a conventional degenerate time-multiplexed OPO with a roundtrip phase of 0, we now turn to the question of how crosstalk between the OPOs would impact our measurements. To begin, we consider an autocorrelation of our measured data from

the fast detector, as demonstrated in ref. [39]. Here, we take our fast detector data from the 40-pulse case over 30 OPO instances, as shown in Fig. 9.3b, and apply a threshold such that each interference measurement is encoded as $s_n \in \{+1, -1\}$ corresponding to constructive or destructive interference as measured on the fast detector. With this output encoding, we compute the autocorrelation function

$$K(n) = \frac{1}{N} \sum_{m=0}^{N} s_m \cdot s_{m+n}. \tag{9.14}$$

The result is shown in Fig. 9.9a. As expected, the autocorrelation for a delay of $n = 0$ is 1. The standard deviations of the experimentally measured data and ideal Bernoulli distributions are also plotted, with near-perfect agreement. In the presence of significant crosstalk, it is expected that the experimental data would exhibit strong correlations for some $n \neq 0$, which is not observed. This test further verifies the independence of the pulses.

Next, we analyze the impact of crosstalk on the slow detector distribution. To do so, we consider the case where neighboring pulses become coupled with a probability given by p_{couple}. If we consider the initial system size to be N, the impact of k coupling events is to reduce the effective system size to $M = N - k$. Assuming that a coupling event is binary (either the pulses couple or do not couple), they may be modeled by a Bernoulli distribution with $p = p_{\text{couple}}$. Thus, the probability that k pulses couple is given by a Binomial distribution such that $P(k) = \binom{N}{k} p_{\text{couple}}^k (1 - p_{\text{couple}})^{N-k}$. The probability of there being x phase flips, assuming that k pulses have coupled, is then given by equation 9.5 with N replaced by $N = N - k$. The total PMF for this case may therefore be written as the following modified version of equation 9.5,

$$f_{I_i}(x) = \begin{cases} \sum_{k=0}^{N} \binom{N}{k} p_{\text{couple}}^k (1 - p_{\text{couple}})^{N-k} \frac{1}{2^{(N-k)-1}} \binom{(N-k)}{x} & x \text{ even,} \\ 0 & \text{otherwise.} \end{cases} \tag{9.15}$$

Several example distributions for different values of p_{couple} are given in Figs. 9.9b-e. As can be observed, even for small coupling probabilities, the impact of the coupling is to shift the total number of phase flips towards smaller values, creating an asymmetric skew in the probability distribution. Such a bias was not observed in our measurement.
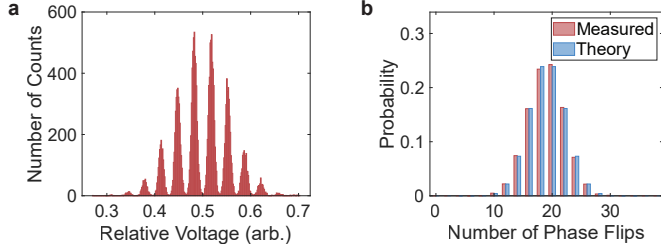
Figure 9.10: **Slow detector distribution at degeneracy for π roundtrip phase and $N = 40$. a,** Histogram of peak values measured from slow detector output. **b,** Comparison with theoretical distribution corresponding to the measurement in **a**.

Probability Mass Function (Slow Detector, π Roundtrip Phase)

As a final consideration, we analyze the case where the OPO is detuned to have a roundtrip phase of π. In this case, the train degenerate pulses will switch phase states each roundtrip. As such, the output pulse train has phase states given by

$$\phi_1, \phi_2, ...\phi_N, \neg\phi_1, \neg\phi_2, ...\neg\phi_N, \phi_1, ...\phi_N, \neg\phi_1, ...\neg\phi_N, ... \qquad (9.16)$$

Since $(\phi_i \odot \phi_j) = (\neg\phi_i \odot \neg\phi_j)$, the impact of this on the I_i's for $i < N$ is minimal. However, it does change the value of I_N which is now given by $I_N = \phi_N \odot \neg\phi_1$. As such, equation 9.12 with $j = N$ becomes $\neg\phi_1 = \phi_1 \odot x_1 \odot x_2 \odot ... \odot x_N$, requiring that $x_1 \odot x_2 \odot ... \odot x_N = 0$. In other words, compared to the previous case with no roundtrip phase, this additional negation requires that there be an odd number of 0s rather than an even number of 0s amongst the I_i's. Without repeating the entire analysis from before, the consequence of this is that the distribution for the random variable X describing the total number of 0s which occur amongst the I_i's becomes $P(X = x) = \frac{1}{2^{N-1}} \binom{N}{x}$ for x odd and $P(X = x) = 0$ for x even, where k is the number of phase flips between consecutive pulses. An example of the measured output in such an OPO configuration is shown in Fig. 9.10.

Non-Degeneracy

Probability Density Function (Fast Detector)

Having found the expected output distributions in the case of degeneracy, we now turn to the case of non-degeneracy. In the non-degenerate case, the signal phase of the ith pulse may take on any value and thus can be represented as a uniform random

variable, ϕ_i, with a value between 0 and 2π. Specifically, the probability density function (PDF) of ϕ_i is given by

$$f_{\Phi_i}(\phi) = \frac{1}{2\pi}\text{rect}(\frac{\phi - \pi}{2\pi}), \tag{9.17}$$

meaning that ϕ takes on the value $\frac{1}{2\pi}$ for ϕ in $[0, 2\pi)$ and 0 elsewhere. As before, $i \in \{1, 2, ..., N\}$ where N is the number of pulses in the time-multiplexed OPO.

Next, as we did in the case of degeneracy, we turn the the detected signal at the output of the interferometer, beginning with the signal on the fast detector. The case of non-degeneracy requires slightly more care, however, as the full interference function must be taken into consideration, whereas we could simply treat the output as a binary in the case of degeneracy. Let us assume that electric field of the ith output pulse takes the form

$$E_i(t) = \mathcal{E}(t)e^{i(\omega t + \phi_i)} \tag{9.18}$$

Here, $\mathcal{E}(t)$ is the slowly-varying field envelope function, ω is the carrier frequency, and ϕ_i is the phase as defined above. The output of the interference signal measured on the detector is then defined to be

$$I_i(t) = \left|\frac{E_i(t) + E_{i+1}(t)}{2}\right|^2 = |\mathcal{E}(t)|^2[1 + \cos{(\phi_i - \phi_{i+1})}]. \tag{9.19}$$

By ignoring the slowly-varying envelope, which we assume to be the same across all output pulses, and re-scaling by a factor of 2 to keep the output values between 0 and 1, we obtain an expression for the random variable describing the normalized detector signal, which we call

$$I_i = \frac{1}{2}(1 + \cos{(\phi_i - \phi_{i+1})}) \tag{9.20}$$

for $i \in \{1, 2, ..., N - 1\}$. For the final pulse, we have $I_N = \frac{1}{2}(1 + cos(\phi_N - \phi_1))$. We wish to ultimately find the PDF for this output pulse, but let us first consider the argument of the cosine, which we will call $\zeta_i = \phi_i - \phi_{i+1}$. Since ϕ_{i+1} is uniform between 0 and 2π, $-\phi_{i+1}$ is uniform between -2π and 0. Additionally, noting that ϕ_i and $-\phi_{i+1}$ are independent random variables, we know that the PDF of ζ_i is given by the convolution of their PDFs, yielding

$$f_{Z_i}(\zeta) = \frac{1}{2\pi}\text{tri}(\frac{\zeta}{2\pi}) \tag{9.21}$$

where $\text{tri}(x)$ is given by $1 - |x|$ for $|x| < 1$ and 0 otherwise.

Now, we turn to finding the PDF of I_i. To do so, we first seek the cumulative distribution function (CDF), which is given by $P(I_i \leq x) = P(\frac{1}{2}(1+\cos(\zeta_i)) \leq x)$. The next step is to invert the function on the left; however, care is required as cosine is not a monotonic function, such that its inverse, $\arccos(x)$, only outputs values in $[0, \pi)$ for x in $[-1, 1]$, whereas ζ_i as defined contains values from $(-2\pi, 2\pi)$. To begin, due to the cosine function being 2π-periodic, we may replace ζ_i with a different random variable, $\tilde{\zeta}_i$, which is given by $\tilde{\zeta}_i = \text{mod}(\zeta_i, 2\pi)$. In this expression, $\text{mod}(a, b)$ gives the output of a modulo b, or the remainder after division of a by b. We can see from the symmetry of the PDF of ζ_i with respect to the y-axis that the new variable $\tilde{\zeta}_i$ is uniform on $[0, 2\pi)$. Making that substitution, let us consider $P(\frac{1}{2}(1+\cos(\tilde{\zeta}_i)) \leq x)$. For a given value of x in $[0, 1]$, we note that this is equivalent to $P(\tilde{\zeta}_i \leq \pi - \arccos(2x - 1)) + P(\pi < \tilde{\zeta}_i \leq \arccos(-2x + 1) + \pi)$. In this step, we have essentially inverted the function on the left-hand side while applying the proper manipulations to both account for the mentioned π ambiguity in the arccos function and ensure the resulting function is monotonically increasing with x. By recognizing that $\pi - \arccos(2x - 1) = \arccos(-2x + 1)$ and that $P(\tilde{\zeta}_i \leq \arccos(-2x + 1)) = P(\pi < \tilde{\zeta}_i \leq \arccos(-2x + 1) + \pi)$, we finally obtain an expression for the CDF, $F_{I_i}(x)$,

$$F_{I_i}(x) = 2P(\tilde{\zeta}_i \leq \arccos(-2x + 1)) = 2F_{\tilde{Z}_i}(\arccos(-2x + 1)) = \frac{1}{\pi}\arccos(-2x + 1). \tag{9.22}$$

In this expression, we have used that the CDF of $\tilde{\zeta}_i$ is given by $F_{\tilde{Z}_i}(\zeta) = \frac{\zeta}{2\pi}$ for ζ in $[0, 2\pi)$ and 0 elsewhere. Having now obtained the CDF of I_i, we can easily find the PDF, $f_{I_i}(x)$, by taking its derivative

$$f_{I_i}(x) = \frac{d}{dx}F_{I_i}(x) = \frac{1}{\pi}\frac{1}{\sqrt{x(1 - x)}}. \tag{9.23}$$

This PDF is also given in equation 9.4.

Independence

To conclude the discussion around the fast detector measurement, as we did for the case of degeneracy, we consider the independence of the I_i's. For simplicity, however, we will use the $\tilde{\zeta}_i$'s as a proxy for the I_i's, as the I_i's are merely a function of the $\tilde{\zeta}_i$'s. As in the degenerate case, the independence of non-consecutive $\tilde{\zeta}_i$'s is easily shown. Towards this end, we consider $\tilde{\zeta}_i = \mod(\phi_i - \phi_{i+1}, 2\pi)$ and $\tilde{\zeta}_j = \mod(\phi_j - \phi_{j+1}, 2\pi)$, where $i, j \in \{1, 2, ...N\}$ and $|i - j| > 1$. To show their independence, we consider the probability $P((\tilde{\zeta}_i \in A_i) \wedge (\tilde{\zeta}_j \in A_j))$. Using the definition of the $\tilde{\zeta}_i$'s, we find that this is equivalent to $P((\mod(\phi_i - \phi_{i+1}, 2\pi) \in A_i) \wedge (\mod(\phi_j - \phi_{j+1}, 2\pi) \in A_j))$. By the independence of the ϕ_i's, and by noting that no ϕ_i's are shared amongst the two expressions since we specified that ζ_i and ζ_j are non-consecutive, we have that $P((\mod(\phi_i - \phi_{i+1}, 2\pi) \in A_i) \wedge (\mod(\phi_j - \phi_{j+1}) \in A_j)) = P(\mod(\phi_i - \phi_{i+1}, 2\pi) \in A_i)P(\mod(\phi_j - \phi_{j+1}, 2\pi) \in A_j) = (\tilde{\zeta}_i \in A_i)P(\tilde{\zeta}_j \in A_j)$, demonstrating the independence of two non-overlapping $\tilde{\zeta}_i$'s. Like the degenerate case, this argument may easily be scaled to larger numbers of non-consecutive $\tilde{\zeta}_i$'s, as well as to distinct clusters of sequential $\tilde{\zeta}_i$'s, as long as the clusters themselves are shown to be independent.

What remains, then, is to evaluate the independence of j consecutive $\tilde{\zeta}_i$'s. For this, we consider the expression $P((\tilde{\zeta}_1 \in A_1) \wedge (\tilde{\zeta}_2 \in A_2) \wedge ... \wedge (\tilde{\zeta}_j \in A_j))$. Let us begin by considering $j = 2$ and $N = 2$. In this case, we consider the joint probability $P((\tilde{\zeta}_1 \in A_1) \wedge (\tilde{\zeta}_2 \in A_2)) = P((\mod(\phi_1 - \phi_2, 2\pi) \in A_1) \wedge (\mod(\phi_2 - \phi_1, 2\pi) \in A_2))$. Noting that $\mod(\phi_2 - \phi_1, 2\pi) = 2\pi - \mod(\phi_1 - \phi_2, 2\pi)$, we see that this is equivalent to $P((\mod(\phi_1 - \phi_2, 2\pi) \in A_1) \wedge (\mod(\phi_1 - \phi_2, 2\pi) \in 2\pi - A_2))$. Clearly, then, $\tilde{\zeta}_1$ and $\tilde{\zeta}_2$ are not independent in this case, as this probability must be 0 if A_1 and $2\pi - A_2$ are non-overlapping intervals, whereas independence would require this probability to be equal to $P(\tilde{\zeta}_1 \in A_1)P(\tilde{\zeta}_2 \in A_2) \neq 0$.

Next, we turn to the case where $j = 2$ and $N = 3$ and again consider the joint probability $P((\tilde{\zeta}_1 \in A_1) \wedge (\tilde{\zeta}_2 \in A_2))$, which under these conditions is equal to $P((\mod(\phi_1 - \phi_2, 2\pi) \in A_1) \wedge (\mod(\phi_2 - \phi_3, 2\pi) \in A_2))$. By inverting the functions on the left-hand side to bring ϕ_2 to the right-hand side in each expression, we see that this is equal to $P((\phi_1 \in \mod(A_1 + \phi_2, 2\pi)) \wedge (\phi_3 \in \mod(\phi_2 - A_2, 2\pi)))$. Here, we make two important observations. The first is that, as the ϕ_i's are uniform random variables, $P(\phi_i \in A) = P(\phi_i \in B)$ where A is the interval $[a_1, a_2)$ and B is the interval $[b_1, b_2)$ as long as $b_2 - b_1 = a_2 - a_1$. Secondly, we note that ϕ_2 is a free variable and essentially represents a static offset to A_1 and A_2. From these

observations, we may conclude that $P((\phi_1 \in \mathrm{mod}(A_1 + \phi_2, 2\pi)) \wedge (\phi_3 \in \mathrm{mod}(\phi_2 - A_2, 2\pi))) = P((\phi_1 \in A_1) \wedge (\phi_3 \in A_2))$. Due to the independence of the ϕ_i's and the fact that they share the same distribution as the $\tilde{\zeta}_i$'s, we may directly rewrite this as $P(\phi_1 \in A_1)P(\phi_3 \in A_2) = P(\tilde{\zeta}_1 \in A_1)P(\tilde{\zeta}_2 \in A_2)$, demonstrating the pairwise independence of $\tilde{\zeta}_1$ and $\tilde{\zeta}_2$ in the case of $j = 2$ and $N = 3$. A similar argument may be constructed to demonstrate the pairwise independence of all $\tilde{\zeta}_i$'s in this case.

Next, we consider the case of $j = 3$ with $N = 3$, which would signify the mutual independence of the $\tilde{\zeta}_i$'s with $N = 3$. Here, the quantity of interest is $P((\tilde{\zeta}_1 \in A_1) \wedge (\tilde{\zeta}_2 \in A_2) \wedge (\tilde{\zeta}_3 \in A_3))$. Re-writing this in terms of the ϕ_i's gives $P((\mathrm{mod}(\phi_1 - \phi_2, 2\pi) \in A_1) \wedge (\mathrm{mod}(\phi_2 - \phi_3, 2\pi) \in A_2) \wedge (\mathrm{mod}(\phi_3 - \phi_1, 2\pi) \in A_3))$. Rearranging the second expression, we find the condition $\phi_2 \in \mathrm{mod}(A_2 + \phi_3, 2\pi)$. From the first expression, we similarly have that $\phi_1 \in \mathrm{mod}(A_1 + \phi_2, 2\pi)$. Combining these two, we see that we must have $\phi_1 \in \mathrm{mod}(A_1 + A_2 + \phi_3, 2\pi)$, where for $A_1 = [x_1, x_2)$ and $A_2 = [y_1, y_2)$, $A_1 + A_2 = [x_1 + y_1, x_2 + y_2)$. As this is a more relaxed constraint on ϕ_1, since it serves to expand the considered interval for ϕ_1, we have that $P((\mathrm{mod}(\phi_1 - \phi_2, 2\pi) \in A_1) \wedge (\mathrm{mod}(\phi_2 - \phi_3, 2\pi) \in A_2) \wedge (\mathrm{mod}(\phi_3 - \phi_1, 2\pi) \in A_3)) \leq P((\phi_1 \in \mathrm{mod}(A_1 + A_2 + \phi_3, 2\pi)) \wedge (\phi_2 \in \mathrm{mod}(A_2 + \phi_3, 2\pi)) \wedge (\mathrm{mod}(\phi_3 - \phi_1, 2\pi) \in A_3))$. Finally, we re-write the rightmost term as $\phi_1 \in \mathrm{mod}(\phi_3 - A_3, 2\pi)$, giving $P((\phi_1 \in \mathrm{mod}(A_1 + A_2 + \phi_3, 2\pi)) \wedge (\phi_2 \in \mathrm{mod}(A_2 + \phi_3, 2\pi)) \wedge \phi_1 \in \mathrm{mod}(\phi_3 - A_3, 2\pi))$. After re-expressing the probability in this way, we see that if $\mathrm{mod}(\phi_3 - A_3, 2\pi)$ and $\mathrm{mod}(A_1 + A_2 + \phi_3, 2\pi)$ are non-overlapping intervals, the probability is equal to 0. In such a case, we would therefore have that $P((\tilde{\zeta}_1 \in A_1) \wedge (\tilde{\zeta}_2 \in A_2) \wedge (\tilde{\zeta}_3 \in A_3)) = 0 \neq P(\tilde{\zeta}_1 \in A_1)P(\tilde{\zeta}_2 \in A_2)P(\tilde{\zeta}_3 \in A_3)$, demonstrating that the $\tilde{\zeta}_i$'s are not independent.

Finally, we turn to the case of arbitrary N. For $j = N$, the arguments made in the case of $N = 3$ can be readily scaled to show the lack of mutual independence amongst the $\tilde{\zeta}_i$'s. In particular, we begin with the expression $P((\tilde{\zeta}_1 \in A_1) \wedge (\tilde{\zeta}_2 \in A_2) \wedge \dots \wedge (\tilde{\zeta}_N \in A_N)) = P((\mathrm{mod}(\phi_1 - \phi_2, 2\pi) \in A_1) \wedge (\mathrm{mod}(\phi_2 - \phi_3, 2\pi) \in A_2) \wedge \dots \wedge (\mathrm{mod}(\phi_N - \phi_1, 2\pi) \in A_N))$. By cascading the argument made before, we may show that $P((\mathrm{mod}(\phi_1 - \phi_2, 2\pi) \in A_1) \wedge (\mathrm{mod}(\phi_2 - \phi_3, 2\pi) \in A_2) \wedge \dots \wedge (\mathrm{mod}(\phi_N - \phi_1, 2\pi) \in A_N)) \leq P((\phi_1 \in \mathrm{mod}(A_1 + A_2 + \dots + A_{N-1} + \phi_N, 2\pi)) \wedge \dots \wedge (\phi_1 \in \mathrm{mod}(\phi_N - A_N, 2\pi)))$. From this, we see that if $\mathrm{mod}(A_1 + A_2 + \dots + A_{N-1} + \phi_N, 2\pi)$ and $\mathrm{mod}(\phi_N - A_N, 2\pi)$ are non-overlapping, the probability must be $0 \neq P(\tilde{\zeta}_1 \in A_1)P(\tilde{\zeta}_2 \in A_2) \dots P(\tilde{\zeta}_N \in A_N)$, indicating that the $\tilde{\zeta}_i$'s are not independent.

Similarly, the arguments made for the case where $j = 2$ and $N = 3$ can be help-

ful in evaluating the independence for arbitrary N with $j < N$. However, while we have been considering the joint probability in constructing our previous arguments, here we consider the conditional probability $P(\tilde{\zeta}_1 \in A_1 | (\tilde{\zeta}_2 = x_1) \wedge (\tilde{\zeta}_3 = x_2) \wedge ... \wedge (\tilde{\zeta}_j = x_j))$. As before, we now re-write this expression in terms of the ϕ_i's as $P(\text{mod}(\phi_1 - \phi_2, 2\pi) \in A_1 | (\text{mod}(\phi_2 - \phi_3, 2\pi) = x_1) \wedge (\text{mod}(\phi_3 - \phi_4, 2\pi) = x_2) \wedge ... \wedge (\text{mod}(\phi_j - \phi_{j+1}, 2\pi) = x_j))$. The rightmost term may be re-written as $\phi_j = \text{mod}(x_j + \phi_{j+1}, 2\pi)$. Plugging this into the corresponding expression for $j - 1$ yields that $\phi_{j-1} = \text{mod}(x_{j-1} + x_j + \phi_{j+1}, 2\pi)$. By cascading this argument, we arrive at an expression for ϕ_2, giving $\phi_2 = \text{mod}(x_2 + x_3 + ... + x_j + \phi_{j+1}, 2\pi)$. Finally, the conditional probability may be re-expressed as $P(\phi_1 \in \text{mod}(A_1 + x_2 + x_3 + ... + x_j + \phi_{j+1}, 2\pi) | (\phi_2 = \text{mod}(x_2 + x_3 + ... + x_j + \phi_{j+1}, 2\pi)) \wedge (\phi_3 = \text{mod}(x_3 + ... + x_j + \phi_{j+1}, 2\pi)) \wedge ... \wedge (\phi_j = \text{mod}(x_j + \phi_{j+1}, 2\pi))$. By noting that the shared ϕ_{j+1} term is unconstrained and thus may take on any value and recalling that $P(\phi_i \in A) = P(\phi_i \in B)$ if A and B represent intervals of the same width since ϕ_i is uniformly distributed, we have through the independence of the ϕ_i's that $P(\phi_1 \in \text{mod}(A_1 + x_2 + x_3 + ... + x_j + \phi_{j+1}, 2\pi) | (\phi_2 = \text{mod}(x_2 + x_3 + ... + x_j + \phi_{j+1}, 2\pi)) \wedge (\phi_3 = \text{mod}(x_3 + ... + x_j + \phi_{j+1}, 2\pi)) \wedge ... \wedge (\phi_j = \text{mod}(x_j + \phi_{j+1}, 2\pi)) = P(\phi_1 \in \text{mod}(A_1 + x_2 + x_3 + ... + x_j + \phi_{j+1}, 2\pi)) = P(\phi_1 \in A_1)$. Finally, since ϕ_1 and $\tilde{\zeta}_1$ are both uniform on $[0, 2\pi)$, $P(\phi_1 \in A_1) = P(\tilde{\zeta}_1 \in A_1)$, proving the independence of this subset of $\tilde{\zeta}_i$'s. Such an argument can be extended to show the independence of arbitrary subsets of $\tilde{\zeta}_i$'s of size j, with $j < N$.

Probability Density Function (Slow Detector)

Having derived the expected distribution for the I_i's on the fast detector and considered the independence of the I_i's using the $\tilde{\zeta}_i$'s as a proxy, we now turn to the response on the slow detector. Here, similar to the degenerate case, the slow detector response is given by the sum over the I_i's. To this end, we consider the random variable X, defined as

$$X = \frac{1}{\sqrt{N}} \sum_{i=1}^{N} I_i, \tag{9.24}$$

which we may use to represent the slow detector response, as multiplication with $\frac{1}{\sqrt{N}}$ just has the impact of scaling the mean and variance. We wish to find the PDF of X. To do so, we first consider the mean, μ, and variance, σ^2, of I_i. The mean is given by

$$\mu = \int_{-\infty}^{\infty} x f_{I_i}(x) dx = \int_0^1 \frac{x}{\pi\sqrt{x(1-x)}} dx = 0.5. \tag{9.25}$$

Similarly, the variance is given as

$$\sigma^2 = \int_{-\infty}^{\infty} (x - \mu)^2 f_{I_i}(x) dx = \int_0^1 \frac{(x-\mu)^2}{\pi\sqrt{x(1-x)}} dx = 0.125 \tag{9.26}$$

Now, we break the definition of X from equation 9.24 into 2 components

$$X = \frac{1}{\sqrt{N}} \sum_{i=1}^{N-1} I_i + \frac{1}{\sqrt{N}} I_N = \tilde{X} + \frac{1}{\sqrt{N}} I_N. \tag{9.27}$$
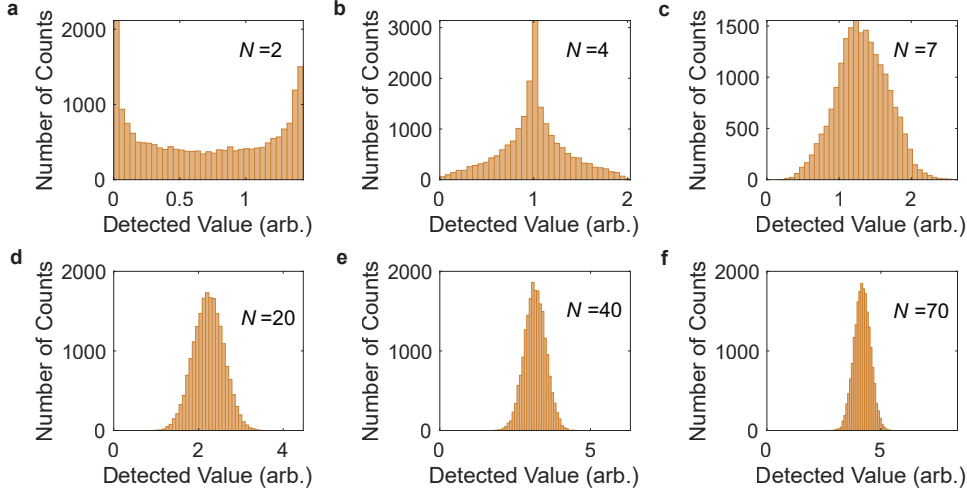
Figure 9.11: **Simulated slow detector distribution in the non-degenerate regime.**
Several values of N are considered including **a**, $N = 2$, **b**, $N = 4$, **c**, $N = 7$, **d**, $N = 20$,
e, $N = 40$, and **f**, $N = 70$.

As shown above, a number $j < N$ of I_i's are independent and identically distributed,
so we may apply the Central Limit Theorem to find that $\tilde{X}$ approaches a normal
distribution with a mean of $\mu = 0.5$ and variance of $\sigma^2 = 0.125$ as $N \to \infty$.
Meanwhile, $\frac{1}{\sqrt{N}} I_N$ tends towards having a mean and variance of 0 as $N \to \infty$. In
other words, as $N \to \infty$, $X \to \tilde{X}$ such that we expect the measured distribution
on the slow detector to be approximately Gaussian. This convergence to a normal
distribution for large N is shown in Fig. 9.11. Here, the theoretical distribution
for X, as defined in equation 9.24, is simulated using pseudorandom numbers in
MATLAB. In each case, we model the output of 20,000 OPO iterations measured

on the slow detector. One may observe reasonably good convergence to a Gaussian by $N = 20$.

Probability Density Function (Slow Detector, π Roundtrip Phase)

As a final note, we briefly consider the case where the OPO has a roundtrip phase of π. Like the degenerate case, we note that the output pulse train has phases given by

$$\phi_1, \phi_2, ...\phi_N, (\phi_1+\pi), (\phi_2+\pi), ...(\phi_N+\pi), \phi_1, ...\phi_N, (\phi_1+\pi), ...(\phi_N+\pi), ... \quad (9.28)$$

Like the degenerate case, this is largely without consequence for I_i's, since $\mathrm{mod}(((\phi_i + \pi) - (\phi_{i+1} + \pi), 2\pi) = \mathrm{mod}(\phi_i - \phi_{i+1}, 2\pi)$. The exception, as before, is I_N since $\tilde{\zeta}_N = \mathrm{mod}(\phi_N - (\phi_1 + \pi), 2\pi)$ now has a phase shift of π. The impact on X is minimal, however, as it will still tend towards a Gaussian for large N.

Addition of Detector Noise

Having derived the theoretical distributions expected from an ideal, we now consider briefly the impact of noise in our detection. As our signal is relatively weak, we expect the measurement to be detector noise limited. In such a case, we may assume the noise is independent of our signal. We may also, to good approximation, assume our detector noise to be normally distributed. Under these considerations, we expect that our measured distributions will look like the convolution of the theoretically calculated PMF/PDF with a Gaussian. For the case of degeneracy, where the expected PMF is discrete, we may still bin the output for comparison with the theory as long as the SNR is sufficient. This is how the theoretical comparisons of Figs. 9.3f and 9.4e are produced. In the non-degenerate case, since the expected distribution from the slow detector is Gaussian, the addition of Gaussian detector noise does not alter its shape (though it may serve to scale the variance). In fitting the distribution from the fast detector, however, we must convolve the predicted distribution of equation 9.4 with a Gaussian to produce an accurate result. This is what accounts for the bimodal distributions of Figs. 9.3d and 9.4c.

Comparison of Time-Multiplexed OPO Architectures

In this section, we discuss in more detail the primary architectures that exist for information processing using time-multiplexed OPOs. We use this to further motivate

the proposed all-time multiplexed architecture. The three main architectures are schematically depicted in Fig. 9.12 and consist of using physical delay lines (Fig. 9.12a), measurement-feedback (Fig. 9.12b), and all-time-multiplexing (Fig. 9.12c).
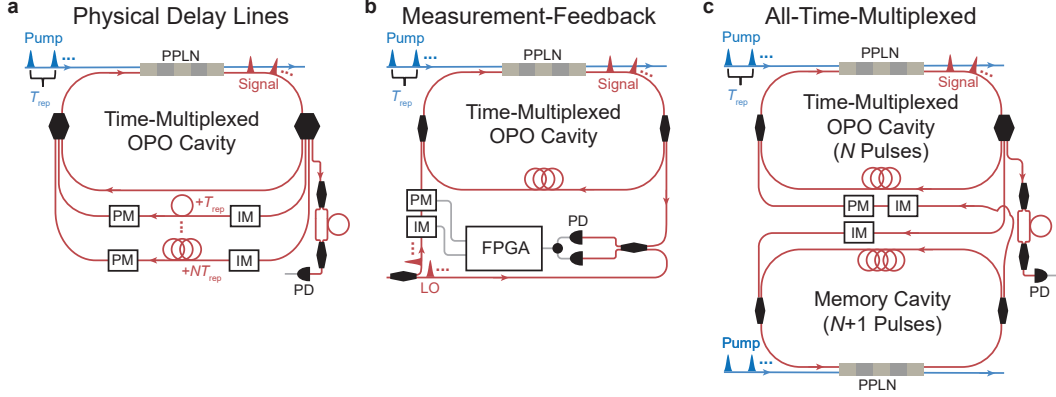

Figure 9.12: **Architectures for time-multiplexed information processing using OPOs. a**, Physical delay line approach, where N delay lines couple the N time-multiplexed OPOs. **b**, Measurement-feedback approach, where pulse amplitudes and phases are read out by an FPGA each roundtrip and used to implement couplings via an injected local oscillator. **c**, All-time architecture, where a secondary memory cavity with $N + 1$ sites is used to store and reinject pulses into the time-multiplexed OPO, implementing all-to-all couplings over the course of N roundtrips. T_{rep}, repetition period; PPLN, periodically poled lithium niobate; PM, phase modulator; IM, intensity modulator; PD, photodetector; FPGA, field-programmable gate array

Many of the first computing demonstrations using OPOs were done using physical delay lines (Fig. 9.12a) [26]. In this approach, all-to-all coupling between the N pulses in the time-multiplexed OPO cavity may be achieved with $N - 1$ delay lines. Inclusion of an Nth delay line allows for a self-interaction term. Arbitrary coupling phase and coupling strength may be achieved by including phase and amplitude modulators along each delay line. The output of the computation can be read out via a phase-sensitive measurement. Here, we depict an unbalanced interferometry setup with a 1-bit delay, similar to that used in our experiment.

This approach is theoretically quite powerful, as couplings are implemented simultaneously through the spatially separated delay lines, enabling operations to be done in parallel. Furthermore, information is stored and processed all-optically, requiring opto-electronic conversion only for read-out following the computation. However, it suffers from the drawback of being extremely challenging to scale due to the required number of delay lines scaling with the system size.

The measurement-feedback approach (Fig. 9.12b) has provided an alternative to using physical delay lines, which has largely solved the scaling issue [9]. In this approach, only one time-multiplexed OPO cavity is required. To provide couplings, signal pulse amplitudes and phases are measured each roundtrip via a homodyne measurement with a local oscillator (LO) and fed into a field-programmable gate array (FPGA). The FPGA then uses the measurement to drive a phase and intensity modulator which shape a newly injected LO pulse to implement the correct coupling amplitude and phase.

This approach has become ubiquitous for performing computations using time-multiplexed OPO systems and has enabled system sizes of $N = 100,000$, as in ref. [11]. However, the approach is ultimately bottle-necked by its requiring opto-electronic and electro-optic conversions in every roundtrip to implement the couplings. Such conversions fundamentally limit the achievable computation speeds to those of the electronic hardware used in the feedback. Additionally, the digitization and subsequent pulse injection can limit the scope of application of this method, for example when the OPO is used in the non-degenerate regime which can take on an arbitrary phase or in the context of quantum information processing where the state is non-classical.

In this work, we propose an all-time-multiplexed (Fig. 9.12c) architecture which seeks to address the primary challenges of both the physical delay line architecture and the measurement-feedback approach. As described in Section 9.3, the approach consists of utilizing two coupled cavities, the main cavity which supports N time-multiplexed OPOs and the memory cavity which supports $N+1$. Here, the N physical delay lines of Fig. 9.12a are instead implemented in a time-multiplexed way. This is done by storing the states of the N pulses from the main cavity in the memory cavity and implementing all-to-all couplings over the course of N roundtrips by re-injecting the stored pulses with the correct coupling amplitude and phase into the main cavity (Fig. 9.5).

As with the physical delay line approach, the all-time-multiplexed approach requires opto-electronic conversion only at the end of the computation and thus can take full advantage of the speed of optics for performing the computation. However, the architecture requires only the addition of the second (memory) cavity, which allows it to be scaled to large system sizes, similar to the measurement-feedback approach. The cost, however, is an additional factor of N overhead in the computation time due to the approach requiring N roundtrips for all-to-all couplings to be achieved. By

combining these two advantages of the different platforms, the all-time-multiplexed approach offers a flexible system for tackling a variety of computing tasks.

BIBLIOGRAPHY

[1] Warit Asavanant, Yu Shiozawa, Shota Yokoyama, Baramee Charoensombutamon, Hiroki Emura, Rafael N. Alexander, Shuntaro Takeda, Jun-ichi Yoshikawa, Nicolas C. Menicucci, Hidehiro Yonezawa, et al. "Generation of time-domain-multiplexed two-dimensional cluster state." In: *Science* 366.6463 (2019), pp. 373–376. DOI: 10.1126/science.aay2645.

[2] Mikkel V. Larsen, Xueshi Guo, Casper R. Breum, Jonas S. Neergaard-Nielsen, and Ulrik L. Andersen. "Deterministic generation of a two-dimensional cluster state." In: *Science* 366.6463 (2019), pp. 369–372. DOI: 10.1126/science.aay4354.

[3] Alireza Marandi, Nick C. Leindecker, Konstantin L. Vodopyanov, and Robert L. Byer. "All-optical quantum random bit generation from intrinsically binary phase of parametric oscillators." In: *Optics Express* 20.17 (2012), pp. 19322–19330. DOI: 10.1364/OE.20.019322.

[4] Charles Roques-Carmes, Yannick Salamin, Jamison Sloan, Seou Choi, Gustavo Velez, Ethan Koskas, Nicholas Rivera, Steven E. Kooi, John D. Joannopoulos, and Marin Soljačić. "Biasing the quantum vacuum to control macroscopic probability distributions." In: *Science* 381.6654 (2023), pp. 205–209. DOI: 10.1126/science.adh4920.

[5] Ewelina Obrzud, Monica Rainer, Avet Harutyunyan, Miles H. Anderson, Junqiu Liu, Michael Geiselmann, Bruno Chazelas, Stefan Kundermann, Steve Lecomte, Massimo Cecconi, et al. "A microphotonic astrocomb." In: *Nature Photonics* 13.1 (2019), pp. 31–35. DOI: doi.org/10.1038/s41566-018-0309-y.

[6] Daryl T. Spencer, Tara Drake, Travis C. Briles, Jordan Stone, Laura C. Sinclair, Connor Fredrick, Qing Li, Daron Westly, B. Robert Ilic, Aaron Bluestone, et al. "An optical-frequency synthesizer using integrated photonics." In: *Nature* 557.7703 (2018), pp. 81–85. DOI: 10.1038/s41586-018-0065-7.

[7] Zhaowei Zhang, Tom Gardiner, and Derryck T. Reid. "Mid-infrared dual-comb spectroscopy with an optical parametric oscillator." In: *Optics Letters* 38.16 (2013), pp. 3148–3150. DOI: 10.1364/OL.38.003148.

[8] Liron Stern, Jordan R. Stone, Songbai Kang, Daniel C. Cole, Myoung-Gyun Suh, Connor Fredrick, Zachary Newman, Kerry Vahala, John Kitching, Scott A. Diddams, et al. "Direct Kerr frequency comb atomic spectroscopy and stabilization." In: *Science Advances* 6.9 (2020), eaax6230. DOI: 10.1126/sciadv.aax6230.

[9] Peter L. McMahon, Alireza Marandi, Yoshitaka Haribara, Ryan Hamerly, Carsten Langrock, Shuhei Tamate, Takahiro Inagaki, Hiroki Takesue, Shoko Utsunomiya, Kazuyuki Aihara, et al. "A fully programmable 100-spin coherent Ising machine with all-to-all connections." In: *Science* 354.6312 (2016), pp. 614–617. DOI: `10.1126/science.aah5178`.

[10] Yutaka Takeda, Shuhei Tamate, Yoshihisa Yamamoto, Hiroki Takesue, Takahiro Inagaki, and Shoko Utsunomiya. "Boltzmann sampling for an XY model using a non-degenerate optical parametric oscillator network." In: *Quantum Science and Technology* 3.1 (2017), p. 014004. DOI: `10.1088/2058-9565/aa923b`.

[11] Toshimori Honjo, Tomohiro Sonobe, Kensuke Inaba, Takahiro Inagaki, Takuya Ikuta, Yasuhiro Yamada, Takushi Kazama, Koji Enbutsu, Takeshi Umeki, Ryoichi Kasahara, et al. "100,000-spin coherent Ising machine." In: *Science Advances* 7.40 (2021), eabh0952. DOI: `10.1126/sciadv.abh0952`.

[12] Arkadev Roy, Rajveer Nehra, Carsten Langrock, Martin Fejer, and Alireza Marandi. "Non-equilibrium spectral phase transitions in coupled nonlinear optical resonators." In: *Nature Physics* 19.3 (2023), pp. 427–434. DOI: `10.6084/m9.figshare.21252147`.

[13] Geva Arwas, Sagie Gadasi, Igor Gershenzon, Asher Friesem, Nir Davidson, and Oren Raz. "Anyonic-parity-time symmetry in complex-coupled lasers." In: *Science Advances* 8.22 (2022), eabm7454. DOI: `10.1126/sciadv.abm745`.

[14] Christian R. Leefmans, Midya Parto, James Williams, Gordon HY Li, Avik Dutt, Franco Nori, and Alireza Marandi. "Topological temporally mode-locked laser." In: *Nature Physics* (2024), pp. 1–7. DOI: `10.1038/s41567-024-02420-4`.

[15] Arghadeep Pal, Alekhya Ghosh, Shuangyou Zhang, Lewis Hill, Haochen Yan, Hao Zhang, Toby Bi, Abdullah Alabbadi, and Pascal Del'Haye. "Linear and nonlinear coupling of light in twin-resonators with Kerr nonlinearity." In: *Photonics Research* 12.11 (2024), pp. 2733–2740. DOI: `10.1364/PRJ.535301`.

[16] Mian Zhang, Cheng Wang, Yaowen Hu, Amirhassan Shams-Ansari, Tianhao Ren, Shanhui Fan, and Marko Lončar. "Electronically programmable photonic molecule." In: *Nature Photonics* 13.1 (2019), pp. 36–40. DOI: `10.1038/s41566-018-0317-y`.

[17] Jae K. Jang, Alexander Klenner, Xingchen Ji, Yoshitomo Okawachi, Michal Lipson, and Alexander L. Gaeta. "Synchronization of coupled optical microresonators." In: *Nature Photonics* 12.11 (2018), pp. 688–693. DOI: `10.1038/s41566-018-0261-x`.

[18]   Yoshitomo Okawachi, Mengjie Yu, Jae K. Jang, Xingchen Ji, Yun Zhao, Bok Young Kim, Michal Lipson, and Alexander L. Gaeta. "Demonstration of chip-based coupled degenerate optical parametric oscillators for realizing a nanophotonic spin-glass." In: *Nature Communications* 11.1 (2020), p. 4119. DOI: `10.1038/s41467-020-17919-6`.

[19]   Miguel A. Bandres, Steffen Wittek, Gal Harari, Midya Parto, Jinhan Ren, Mordechai Segev, Demetrios N. Christodoulides, and Mercedeh Khajavikhan. "Topological insulator laser: Experiments." In: *Science* 359.6381 (2018), eaar4005. DOI: `10.1126/science.aar4005`.

[20]   Sunil Mittal, Gregory Moille, Kartik Srinivasan, Yanne K. Chembo, and Mohammad Hafezi. "Topological frequency combs and nested temporal solitons." In: *Nature Physics* 17.10 (2021), pp. 1169–1176. DOI: `10.1038/s41567-021-01302-3`.

[21]   Malcolm H. Dunn and Majid Ebrahim-Zadeh. "Parametric generation of tunable light from continuous-wave to femtosecond pulses." In: *Science* 286.5444 (1999), pp. 1513–1517. DOI: `10.1126/science.286.5444.1513`.

[22]   Andrey V. Muraviev, Viktor O. Smolski, Zachary E. Loparo, and Konstantin L. Vodopyanov. "Massively parallel sensing of trace molecules and their iso-topologues with broadband subharmonic mid-infrared frequency combs." In: *Nature Photonics* 12.4 (2018), pp. 209–214. DOI: `10.1038/s41566-018-0135-2`.

[23]   Robert M. Gray, Mingchen Liu, Selina Zhou, Arkadev Roy, Luis Ledezma, and Alireza Marandi. "Quadratic-soliton-enhanced mid-IR molecular sensing." In: *Nature Communications* 15.1 (2024), p. 9086. DOI: `10.1038/s41467-024-53447-3`.

[24]   Shunya Konno, Warit Asavanant, Fumiya Hanamura, Hironari Nagayoshi, Kosuke Fukui, Atsushi Sakaguchi, Ryuhoh Ide, Fumihiro China, Masahiro Yabuno, Shigehito Miki, et al. "Logical states for fault-tolerant quantum computation with propagating light." In: *Science* 383.6680 (2024), pp. 289–293. DOI: `10.1126/science.adk7560`.

[25]   Zhe Wang, Alireza Marandi, Kai Wen, Robert L. Byer, and Yoshihisa Yamamoto. "Coherent Ising machine based on degenerate optical parametric oscillators." In: *Physical Review A* 88.6 (2013), p. 063853. DOI: `10.1103/PhysRevA.88.063853`.

[26]   Alireza Marandi, Zhe Wang, Kenta Takata, Robert L. Byer, and Yoshihisa Yamamoto. "Network of time-multiplexed optical parametric oscillators as a coherent Ising machine." In: *Nature Photonics* 8.12 (2014), pp. 937–942. DOI: `10.1038/nphoton.2014.249`.

[27] Yoshihisa Yamamoto, Kazuyuki Aihara, Timothee Leleu, Ken-ichi Kawarabayashi, Satoshi Kako, Martin Fejer, Kyo Inoue, and Hiroki Takesue. "Coherent Ising machines—optical neural networks operating at the quantum limit." In: *npj Quantum Information* 3.1 (2017), p. 49. DOI: `10.1038/s41534-017-0048-9`.

[28] Timothy P. McKenna, Hubert S. Stokowski, Vahid Ansari, Jatadhari Mishra, Marc Jankowski, Christopher J. Sarabalis, Jason F. Herrmann, Carsten Langrock, Martin M. Fejer, and Amir H. Safavi-Naeini. "Ultra-low-power second-order nonlinear optics on a chip." In: *Nature Communications* 13.1 (2022), p. 4532. DOI: `10.1038/s41467-022-31134-5`.

[29] Juanjuan Lu, Ayed Al Sayem, Zheng Gong, Joshua B. Surya, Chang-Ling Zou, and Hong X. Tang. "Ultralow-threshold thin-film lithium niobate optical parametric oscillator." In: *Optica* 8.4 (2021), pp. 539–544. DOI: `10.1364/OPTICA.418984`.

[30] Luis Ledezma, Ryoto Sekine, Qiushi Guo, Rajveer Nehra, Saman Jahani, and Alireza Marandi. "Intense optical parametric amplification in dispersion-engineered nanophotonic lithium niobate waveguides." In: *Optica* 9.3 (2022), pp. 303–308. DOI: `10.1364/OPTICA.442332`.

[31] Arkadev Roy, Luis Ledezma, Luis Costa, Robert Gray, Ryoto Sekine, Qiushi Guo, Mingchen Liu, Ryan M. Briggs, and Alireza Marandi. "Visible-to-mid-IR tunable frequency comb in nanophotonics." In: *Nature Communications* 14.1 (2023), p. 6549. DOI: `10.1038/s41467-023-42289-0`.

[32] Ryoto Sekine, Robert M. Gray, Luis Ledezma, Selina Zhou, Qiushi Guo, and Alireza Marandi. "Multi-octave frequency comb from an ultra-low-threshold nanophotonic parametric oscillator." In: *arXiv preprint arXiv:2309.04545* (2023). DOI: `10.48550/arXiv.2309.04545`.

[33] Ryotatsu Yanagimoto, Edwin Ng, Marc Jankowski, Rajveer Nehra, Timothy P. McKenna, Tatsuhiro Onodera, Logan G. Wright, Ryan Hamerly, Alireza Marandi, Martin M. Fejer, et al. "Mesoscopic ultrafast nonlinear optics—the emergence of multimode quantum non-Gaussian physics." In: *Optica* 11.7 (2024), pp. 896–918. DOI: `10.1364/OPTICA.514075`.

[34] Gordon H. Y. Li, Christian R. Leefmans, James Williams, and Alireza Marandi. "Photonic elementary cellular automata for simulation of complex phenomena." In: *Light: Science & Applications* 12.1 (2023), p. 132. DOI: `10.1038/s41377-023-01180-9`.

[35] Christian Leefmans, Avik Dutt, James Williams, Luqi Yuan, Midya Parto, Franco Nori, Shanhui Fan, and Alireza Marandi. "Topological dissipation in a time-multiplexed photonic resonator network." In: *Nature Physics* 18.4 (2022), pp. 442–449. DOI: `10.1038/s41567-021-01492-w`.

[36] Midya Parto, Christian Leefmans, James Williams, Franco Nori, and Alireza Marandi. "Non-Abelian effects in dissipative photonic topological lattices." In: *Nature Communications* 14.1 (2023), p. 1440. DOI: 10.1038/s41467-023-37065-z.

[37] Tomoki Ozawa and Hannah M. Price. "Topological quantum matter in synthetic dimensions." In: *Nature Reviews Physics* 1.5 (2019), pp. 349–357. DOI: 10.1038/s42254-019-0045-3.

[38] Liam Quinn, Gang Xu, Yiqing Xu, Zongda Li, Julien Fatome, Stuart G. Murdoch, Stéphane Coen, and Miro Erkintalo. "Random number generation using spontaneous symmetry breaking in a Kerr resonator." In: *Optics Letters* 48.14 (2023), pp. 3741–3744. DOI: 10.1364/OL.493731.

[39] Konstantin S. Manannikov, Ekaterina I. Mironova, Andrei S. Poliakov, Alexander Mikhaylov, Alexander E. Ulanov, and Alexander I. Lvovsky. "Spontaneous symmetry breaking of an optical polarization state in a polarization-selective nonlinear resonator." In: *Optics Letters* 50.3 (2025), pp. 792–795. DOI: 10.1364/OL.543643.

[40] Miguel Herrero-Collantes and Juan Carlos Garcia-Escartin. "Quantum random number generators." In: *Reviews of Modern Physics* 89.1 (2017), p. 015004. DOI: 10.1103/RevModPhys.89.015004.

[41] Lars S. Madsen, Fabian Laudenbach, Mohsen Falamarzi Askarani, Fabien Rortais, Trevor Vincent, Jacob F. F. Bulmer, Filippo M. Miatto, Leonhard Neuhaus, Lukas G. Helt, Matthew J. Collins, et al. "Quantum computational advantage with a programmable photonic processor." In: *Nature* 606.7912 (2022), pp. 75–81. DOI: 10.1038/s41586-022-04725-x.

[42] Manuel Erhard, Mario Krenn, and Anton Zeilinger. "Advances in high-dimensional quantum entanglement." In: *Nature Reviews Physics* 2.7 (2020), pp. 365–381. DOI: 10.1038/s42254-020-0193-5.

[43] Juan M. Arrazola, Ville Bergholm, Kamil Brádler, Thomas R. Bromley, Matt J. Collins, Ish Dhand, Alberto Fumagalli, Thomas Gerrits, Andrey Goussev, Lukas G. Helt, et al. "Quantum circuits with many photons on a programmable nanophotonic chip." In: *Nature* 591.7848 (2021), pp. 54–60. DOI: 10.1038/s41586-021-03202-1.

[44] Mian Zhang, Cheng Wang, Prashanta Kharel, Di Zhu, and Marko Lončar. "Integrated lithium niobate electro-optic modulators: When performance meets scalability." In: *Optica* 8.5 (2021), pp. 652–667. DOI: 10.1038/s41586-018-0551-y.

[45] Gordon H. Y. Li, Ryoto Sekine, Rajveer Nehra, Robert M. Gray, Luis Ledezma, Qiushi Guo, and Alireza Marandi. "All-optical ultrafast ReLU function for energy-efficient nanophotonic deep learning." In: *Nanophotonics* 12.5 (2023), pp. 847–855. DOI: 10.1515/nanoph-2022-0137.

[46] Gordon Li and Alireza Marandi. "Turing-completeness and undecidability in coupled nonlinear optical resonators." In: *arXiv preprint arXiv:2501.06966* (2025).

[47] Tingzhao Fu, Jianfa Zhang, Run Sun, Yuyao Huang, Wei Xu, Sigang Yang, Zhihong Zhu, and Hongwei Chen. "Optical neural networks: Progress and challenges." In: *Light: Science & Applications* 13.1 (2024), p. 263. DOI: `10.1038/s41377-024-01590-3`.

[48] Seth Lloyd and Samuel L. Braunstein. "Quantum computation over continuous variables." In: *Physical Review Letters* 82.8 (1999), p. 1784. DOI: `10.1103/PhysRevLett.82.1784`.

[49] Nicolas C. Menicucci, Peter Van Loock, Mile Gu, Christian Weedbrook, Timothy C. Ralph, and Michael A. Nielsen. "Universal quantum computation with continuous-variable cluster states." In: *Physical review letters* 97.11 (2006), p. 110501. DOI: `10.1103/PhysRevLett.97.110501`.

[50] Naeimeh Mohseni, Peter L. McMahon, and Tim Byrnes. "Ising machines as hardware solvers of combinatorial optimization problems." In: *Nature Reviews Physics* 4.6 (2022), pp. 363–379. DOI: `10.1038/s42254-022-00440-8`.

[51] Sheldon M. Ross. *A First Course in Probability.* Vol. 2. Macmillan New York, 1976.

Chapter 10

OUTLOOK

Through our presented work, we have demonstrated several areas in which quadratic nonlinear phenomena can be leveraged for application in ultrafast source development and application. Here, we briefly comment on some additional research areas which will benefit from further study in the near future.

10.1 Quadratic Solitons

In this thesis, we have explored several quadratic solitons, including temporal simultons and two-color bright solitons. However, many other soliton solutions are predicted in both quadratic waveguides and resonators, including two-color bright-bright solitons, dark-dark solitons, and bright-dark solitons, single-color bright solitons and dark solitons, and topological solitons, among others [1–7]. With a significant body of theoretical literature on existence regimes for quadratic soliton solutions to draw from, the novel opportunities for engineering the dispersion and phase mismatch afforded by nanophotonics provide ideal conditions for the realization of various solitonic states. Already, we have observed early signatures of domain wall formation and bright soliton generation in a degenerate optical parametric oscillator [8, 9]. We believe the variety of soliton solutions native to quadratic nonlinear systems can serve as versatile generators as ultrashort pulses and frequency combs with wide application.

10.2 Highly Nonlinear Resonators

Our demonstration of multi-octave frequency comb formation in a far-above threshold nanophotonic optical parametric oscillator represents a first demonstration of what may be achieved by exploiting the strong quadratic nonlinearity afforded by nanophotonics in a resonant configuration. Theoretical investigation into this phenomenon suggests that significant intracavity manipulation of the signal pulse is viable, as long as the pulse phase within the gain bandwidth set by the pump pulse length is sufficiently clean prior to their interaction in the nonlinear crystal in each roundtrip. This process bears similarity to other recent demonstrations of intracavity supercontinuum generation [10] and Mamyshev oscillation [11, 12].

In the present system, however, much of the power is being lost due to the broad bandwidth of the coupler response and subsequent high loss in the roundtrip propagation. Thus, we envisage significant improvement to the spectral flatness of the generated supercontinuum may be made by utilizing a more narrow-band coupler with higher outcoupling.

Additionally, we believe that improved coherence and stability properties may be realized through operation of the system near a dynamical attractor of the nonlinear waveguide. This may be readily achieved by engineering the feedback to shape the recirculating pulse towards such a solution.

Further characterization of the different regimes of operation in such highly nonlinear cavities is also of interest, and would benefit from improved theoretical models. One particularly interesting state which has been observed both in simulation and experiment, but not well understood, involves the generation of periodic states, for which the output oscillates at exact integer sub-harmonics of the cavity repetition rate.

10.3 Integrated Extreme Nonlinear Optics

As motivated in our discussion of demonstrated two-color soliton pulse compression, extension of this work to integrated single-cycle pulse synthesis is readily achievable through CEP stabilization of the pump laser, and addition of an electro-optic modulator. Additionally, the tight mode confinement afforded by the nanophotonic platform reduces the pulse energies required to attain sufficiently large peak powers for entry into the extreme nonlinear optics regime [13]. As such, development of integrated extreme nonlinear optical systems should be achievable in the relatively near future. Several components may be developed in this direction.

The first is the development of CEP-stabilized integrated sources. Such a source will require either the pairing of integrated MLLs [14, 15] or other integrated pulse generators [16] with integrated supercontinuum generation [17–19] for self-referencing and stabilization of the CEP phase, or the use of intrapulse DFG [20, 21] to directly obtain CEP stabilized pulses. Both techniques are readily amenable to the quadratic nonlinearity.

A second key development in this direction would be the integration of OPCPA systems [22–24]. OPCPA may also be directly implemented in the quadratic nonlinear waveguide, and will greatly help to increase the pulse energies to the levels required for driving extreme nonlinear optical phenomena.

10.4 Detector-Free Intractivity Sensing and Spectroscopy

As was motivated in the simulton sensing work, both CW theory and soliton theory suggest that OPOs exhibit preferable scaling behaviors for intracavity sensing and spectroscopy based on threshold sensing when compared to laser systems [25]. However, exploration in this direction has been limited [26, 27].

One proposed approach which we have begun to explore in this thesis is towards detector-free intracavity sensing and spectroscopy [28]. In this scheme, the analyte is placed inside the OPO, and the pump-cavity detuning is scanned, either through an intracavity modulator or through direct tuning of the pump frequency. As each of the output oscillation peaks contains different frequency content, the molecular signature is uniquely imprinted into the resulting relative change in power of the oscillation peaks. Through performing the correct inverse transformation, the analyte concentration may be identified without requiring a spectrally-resolved measurement [29].

10.5 Extension of FROG to Quantum State Tomography

Pulsed systems hold significant promise for high-speed quantum optical information processing. However, a significant challenge in pulsed quantum optics is the multi-mode nature of typically generated pulsed quantum states. As such, working with pulsed quantum optical systems demands new tools capable of temporally characterizing quantum pulses [30–33].

Our demonstration of FROG in a nanophotonic, high-gain OPA suggests that the technique should be compatible with ultra-weak quantum pulses. Furthermore, we have recently demonstrated use of the phase sensitivity of the OPA process for state tomography [34, 35]. Following these developments, we have begun exploring the potentials of using FROG to fully characterize quantum states of interest, and early indications show significant promise for this direction.

BIBLIOGRAPHY

[1] Carlos Mas Arabi, Pedro Parra-Rivas, Tobias Hansson, Lendert Gelens, Stefan Wabnitz, and François Leo. "Localized structures formed through domain wall locking in cavity-enhanced second-harmonic generation." In: *Optics Letters* 45.20 (2020), pp. 5856–5859.

[2] Dmitry V Skryabin. "Sech-squared Pockels solitons in the microresonator parametric down-conversion." In: *Optics Express* 29.18 (2021), pp. 28521–28529.

[3] Pedro Parra-Rivas, Lendert Gelens, Tobias Hansson, Stefan Wabnitz, and François Leo. "Frequency comb generation through the locking of domain walls in doubly resonant dispersive optical parametric oscillators." In: *Optics Letters* 44.8 (2019), pp. 2004–2007.

[4] Gian-Luca Oppo, Alison M. Yao, and Domenico Cuozzo. "Self-organization, pattern formation, cavity solitons, and rogue waves in singly resonant optical parametric oscillators." In: *Physical Review A* 88.4 (2013), p. 043813. DOI: 10.1103/PhysRevA.88.043813.

[5] Alexander V. Buryak, Paolo Di Trapani, Dmitry V. Skryabin, and Stefano Trillo. "Optical solitons due to quadratic nonlinearities: From basic physics to futuristic applications." In: *Physics Reports* 370.2 (2002), pp. 63–235.

[6] Hao He, Michael J. Werner, and Peter D. Drummond. "Simultaneous solitary-wave solutions in a nonlinear parametric waveguide." In: *Physical Review E* 54.1 (1996), p. 896.

[7] Stefano Trillo, Marc Haelterman, and Adrian Sheppard. "Stable topological spatial solitons in optical parametric oscillators." In: *Optics Letters* 22.13 (1997), pp. 970–972.

[8] Nicolas Englebert, Robert M. Gray, Ryoto Sekine, Thomas Zacharias, Luis Ledezma, Selina Zhou, Carlos Mas Arabi, Simon-Pierre Gorza, François Leo, and Alireza Marandi. "Purely quadratic cavity solitons in a nano-photonic parametric oscillator." In: *2024 Conference on Lasers and Electro-Optics (CLEO)*. IEEE. 2024, pp. 1–2.

[9] Nicolas Englebert, Robert M. Gray, Luis Ledezma, and Alireza Marandi. "Topological soliton formation in a nanophotonic optical parametric oscillator." In: *2024 Conference on Lasers and Electro-Optics (CLEO)*. IEEE. 2024, pp. 1–2.

[10] Yiwei Tian, Fanchao Meng, Qi Yan, Changjian Lv, Zhixu Jia, Weiping Qin, Guanshi Qin, and John M Dudley. "Intracavity coherent supercontinuum generation via high-order soliton dynamics in a dissipative soliton fiber laser." In: *Optics Express* 32.27 (2024), pp. 47970–47981.

[11] Xing Luo, Tong Hoang Tuan, Takenobu Suzuki, and Yasutake Ohishi. "Intracavity supercontinuum generation in a mode-locked erbium-doped fiber laser based on the Mamyshev mechanism with highly nonlinear fiber." In: *Optics Letters* 45.9 (2020), pp. 2530–2533.

[12] Ying-Ying Li, Bo Gao, Chun-Yang Ma, Ge Wu, Jia-Yu Huo, Ying Han, Swelm Wageh, Omar A. Al-Hartomy, Abdullah G. Al-Sehemi, Lie Liu, et al. "Generation of high-peak-power femtosecond pulses in Mamyshev oscillators: Recent advances and future challenges." In: *Laser & Photonics Reviews* 17.4 (2023), p. 2200596.

[13] Martin Wegener. *Extreme nonlinear optics: An introduction.* Advanced Texts in Physics. Springer Berlin Heidelberg, 2006. ISBN: 9783540266884. URL: https://books.google.com/books?id=pZI0erZXgdcC.

[14] Michael L. Davenport, Songtao Liu, and John E. Bowers. "Integrated heterogeneous silicon/III–V mode-locked lasers." In: *Photonics Research* 6.5 (2018), pp. 468–478.

[15] Qiushi Guo, Benjamin K. Gutierrez, Ryoto Sekine, Robert M. Gray, James A. Williams, Luis Ledezma, Luis Costa, Arkadev Roy, Selina Zhou, Mingchen Liu, et al. "Ultrafast mode-locked laser in nanophotonic lithium niobate." In: *Science* 382.6671 (2023), pp. 708–713. DOI: 10.1126/science.adj5438.

[16] Mengjie Yu, David Barton III, Rebecca Cheng, Christian Reimer, Prashanta Kharel, Lingyan He, Linbo Shao, Di Zhu, Yaowen Hu, Hannah R Grant, et al. "Integrated femtosecond pulse generator on thin-film lithium niobate." In: *Nature* 612.7939 (2022), pp. 252–258.

[17] Marc Jankowski, Carsten Langrock, Boris Desiatov, Alireza Marandi, Cheng Wang, Mian Zhang, Christopher R. Phillips, Marko Lončar, and Martin M. Fejer. "Ultrabroadband nonlinear optics in nanophotonic periodically poled lithium niobate waveguides." In: *Optica* 7.1 (2020), pp. 40–46.

[18] Marc Jankowski, Carsten Langrock, Boris Desiatov, Marko Lončar, and Martin M. Fejer. "Supercontinuum generation by saturated second-order nonlinear interactions." In: *APL Photonics* 8.11 (2023).

[19] Ryoto Sekine, Robert M. Gray, Luis Ledezma, Selina Zhou, Qiushi Guo, and Alireza Marandi. "Multi-octave frequency comb from an ultra-low-threshold nanophotonic parametric oscillator." In: *arXiv preprint arXiv:2309.04545* (2023). DOI: 10.48550/arXiv.2309.04545.

[20] Ioachim Pupeza, Daniel Sánchez, Jinwei Zhang, Nicolai Lilienfein, Marcus Seidel, Nicholas Karpowicz, Tim Paasch-Colberg, Irina Znakovskaya, M. Pescher, Wolfgang Schweinberger, et al. "High-power sub-two-cycle mid-infrared pulses at 100 MHz repetition rate." In: *Nature Photonics* 9.11 (2015), pp. 721–724.

[21] Christian Gaida, Martin Gebhardt, Tobias Heuermann, Fabian Stutzki, Cesar Jauregui, Jose Antonio-Lopez, Axel Schülzgen, Rodrigo Amezcua-Correa, Andreas Tünnermann, Ioachim Pupeza, et al. "Watt-scale super-octave mid-infrared intrapulse difference frequency generation." In: *Light: Science & Applications* 7.1 (2018), p. 94.

[22] Jan Rothhardt, Stefan Demmler, Steffen Hädrich, Jens Limpert, and Andreas Tünnermann. "Octave-spanning OPCPA system delivering CEP-stable few-cycle pulses and 22 W of average power at 1 MHz repetition rate." In: *Optics Express* 20.10 (2012), pp. 10870–10878.

[23] Benedikt W. Mayer, Christopher R. Phillips, Lukas Gallmann, and Ursula Keller. "Mid-infrared pulse generation via achromatic quasi-phase-matched OPCPA." In: *Optics Express* 22.17 (2014), pp. 20798–20808.

[24] Jeffrey Moses, Cristian Manzoni, Shu-Wei Huang, Giulio Cerullo, and Franz X. Kaertner. "Temporal optimization of ultrabroadband high-energy OPCPA." In: *Optics Express* 17.7 (2009), pp. 5540–5555.

[25] Valery M. Baev, Torsten Latz, and Peter E. Toschek. "Laser intracavity absorption spectroscopy." In: *Applied Physics B* 69.3 (1999), pp. 171–202.

[26] Witlof Brunner and Harry Paul. "The optical parametric oscillator as a means for intracavity absorption spectroscopy." In: *Optics Communications* 19.2 (1976), pp. 253–256.

[27] Magnus W. Haakestad, Tobias P. Lamour, Nick Leindecker, Alireza Marandi, and Konstantin L. Vodopyanov. "Intracavity trace molecular detection with a broadband mid-IR frequency comb source." In: *Journal of the Optical Society of America B* 30.3 (2013), pp. 631–640.

[28] Selina Zhou, Robert Gray, Mingchen Liu, Arkadev Roy, and Alireza Marandi. "Towards gas sensing without spectroscopy using mid-infrared optical parametric oscillators." In: *Optical Sensors*. Optica Publishing Group. 2022, SM1E–1.

[29] Zongyin Yang, Tom Albrow-Owen, Weiwei Cai, and Tawfique Hasan. "Miniaturization of optical spectrometers." In: *Science* 371.6528 (2021), eabe0722.

[30] Claudius Riek, Philipp Sulzer, Maximilian Seeger, Andrey S. Moskalenko, Guido Burkard, Denis V. Seletskiy, and Alfred Leitenstorfer. "Subcycle quantum electrodynamics." In: *Nature* 541.7637 (2017), pp. 376–379.

[31] Andreas Eckstein, Benjamin Brecht, and Christine Silberhorn. "A quantum pulse gate based on spectrally engineered sum frequency generation." In: *Optics Express* 19.15 (2011), pp. 13770–13778.

[32] Vahid Ansari, Georg Harder, Markus Allgaier, Benjamin Brecht, and Christine Silberhorn. "Temporal-mode measurement tomography of a quantum pulse gate." In: *Physical Review A* 96.6 (2017), p. 063817.

[33]   Nan Huo, Yuhong Liu, Jiamin Li, Liang Cui, Xin Chen, Rithwik Palivela, Tianqi Xie, Xiaoying Li, and ZheYu Ou. "Direct temporal mode measurement for the characterization of temporally multiplexed high dimensional quantum entanglement in continuous variables." In: *Physical Review Letters* 124.21 (2020), p. 213603.

[34]   James Williams, Elina Sendonaris, Rajveer Nehra, Robert M. Gray, Ryoto Sekine, Luis Ledezma, and Alireza Marandi. "Ultrafast all-optical measurement of squeezed vacuum in a lithium niobate nanophotonic circuit." In: *arXiv preprint arXiv:2502.00518* (2025). DOI: 10.48550/arXiv.2502.00518.

[35]   Rajveer Nehra, Ryoto Sekine, Luis Ledezma, Qiushi Guo, Robert M. Gray, Arkadev Roy, and Alireza Marandi. "Few-cycle vacuum squeezing in nanophotonics." In: *Science* 377.6612 (2022), pp. 1333–1337. DOI: 10.1126/science.abo6213.